JACS
JOURNAL OF THE AMERICAN CHEMICAL SOCIETY

Article

pubs.acs.org/JACS

Water Oxidation Catalysis by Co(II) Impurities in Co(III)$_4$O$_4$ Cubanes

Andrew M. Ullman,[†] Yi Liu,[†] Michael Huynh,[†] D. Kwabena Bediako,[†] Hongsen Wang,[‡] Bryce L. Anderson,[†] David C. Powers,[†] John J. Breen,[§] Héctor D. Abruña,[‡] and Daniel G. Nocera*,[†]

[†]Department of Chemistry and Chemical Biology, Harvard University, 12 Oxford Street, Cambridge, Massachusetts 02138, United States

[‡]Baker Laboratory, Department of Chemistry and Chemical Biology, Cornell University, Ithaca, New York 14853, United States

[§]Department of Chemistry and Biochemistry, Providence College, 1 Cunningham Square, Providence, Rhode Island 02918, United States

Ⓢ *Supporting Information*

ABSTRACT: The observed water oxidation activity of the compound class $Co_4O_4(OAc)_4(Py{-}X)_4$ emanates from a Co(II) impurity. This impurity is oxidized to produce the well-known Co-OEC heterogeneous cobaltate catalyst, which is an active water oxidation catalyst. We present results from electron paramagnetic resonance spectroscopy, nuclear magnetic resonance line broadening analysis, and electrochemical titrations to establish the existence of the Co(II) impurity as the major source of water oxidation activity that has been reported for Co_4O_4 molecular cubanes. Differential electrochemical mass spectrometry is used to characterize the fate of glassy carbon at water oxidizing potentials and demonstrate that such electrode materials should be used with caution for the study of water oxidation catalysis.

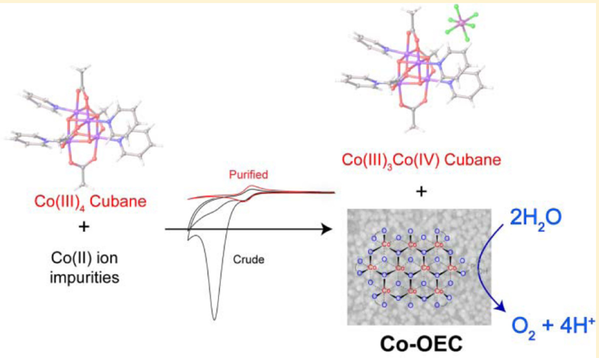

■ INTRODUCTION

The design of efficient water oxidation catalysts (WOCs) based on nonprecious materials remains an important challenge for achieving a clean and sustainable solar fuels-based energy economy.[1−3] We have previously shown that active WOCs can be formed by anodic electrodeposition of metal-oxides from neutral and near-neutral buffered aqueous solutions of cobalt,[4,5] nickel,[6,7] and recently, manganese.[8,9] In particular, the cobalt oxygen-evolving catalyst (Co-OEC) has been studied in detail, resulting in an understanding of the electrochemical kinetic mechanisms of its formation,[10] catalysis,[11] and charge transport.[12] The structural and electronic properties of Co-OEC have been clarified using XAS,[13] X-ray PDF,[14,15] EPR,[16] and X-ray GID.[17] These studies have revealed that the electrodeposited catalyst films comprise molecular to nanoscale-sized metalate clusters composed of edge-sharing CoO_6 octahedra with a mixed valence Co(III/IV) resting state.

The development of soluble molecular WOCs based on Co[18−21] as well as other transition metals, such as Ir,[22] Ru,[23] Cu,[24] and Fe[25] have also been a subject of intense focus. Molecular WOCs are attractive research targets because they provide a tractable means to characterize catalytic mechanisms and to identify reactive intermediates, thus forming the basis for the continued development of new WOCs. However, the true identity of the active catalyst must be clarified prior to a detailed interrogation of the WOC mechanism. Indeed, some molecules that were thought to be WOCs have subsequently been shown to be precursors of heterogeneous or colloidal materials, which are the active catalysts.[26−29] Proper catalyst identification is especially challenging for the study of molecular cobalt WOCs because extremely small amounts of Co-OEC may be produced from the decomposition of the molecular catalyst.[30,31] An exemplar of this challenge is the all-inorganic cobalt polyoxometalate $[Co_4(H_2O)_2(PW_9O_{34})_2]^{10-}$ (Co_4POM), which was suggested as a WOC.[32] Re-examination of the molecule showed that electrochemically driven oxygen evolution arose from the formation of Co-OEC on glassy carbon (GC) electrodes at 1.1 V vs Ag/AgCl.[30] Because the Co_4POM was unstable at higher potentials, water oxidation activity could not be conclusively attributed to the Co_4POM, as opposed to its role as a molecular precursor to Co-OEC.[33] The Co_4POM has now been suggested to exhibit water oxidation activity but under specific photochemical conditions where $Ru(bpy)_3^{3+}$ is the oxidant.[34,35]

Against this backdrop, cubane Co_4O_4 clusters, such as $Co_4O_4(OAc)_4(Py)_4$, (**1**, Figure 1), have come under investigation as a class of molecular cobalt complexes that are potential WOCs.[36−40] We had previously investigated **1**, first synthesized by Das and co-workers,[41] and a related Co_4O_4 cubane of Christou,[42] in order to gain valuable insights into the electronic characteristics and proton-coupled electron transfer (PCET) behavior of Co(III/IV) in a Co-OEC environment.[43,44] The structure of **1** has been previously reported

Received: October 27, 2014
Published: November 18, 2014

dx.doi.org/10.1021/ja5110393 | *J. Am. Chem. Soc.* 2014, 136, 17681−17688

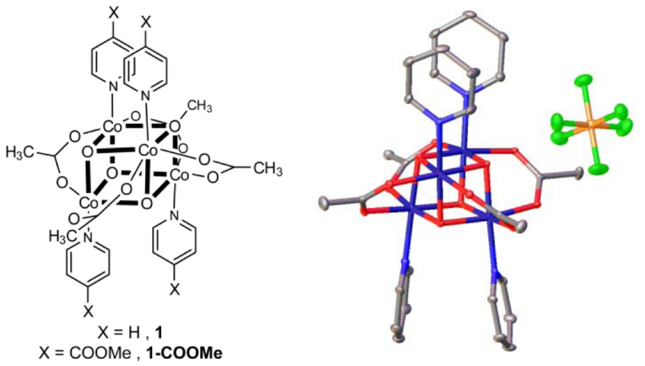

Figure 1. (left) Molecular structure of Co_4O_4 cubane structure **1** and (right) thermal ellipsoid representation at the 50% probability level of the one-electron oxidized cubane, **1**[**PF**$_6$]. Hydrogen atoms and an acetonitrile molecule have been omitted for clarity. Atoms are color-coded: gray (carbon), blue (nitrogen), red (oxygen), dark blue (cobalt), green (fluorine), and yellow (phosphorus).

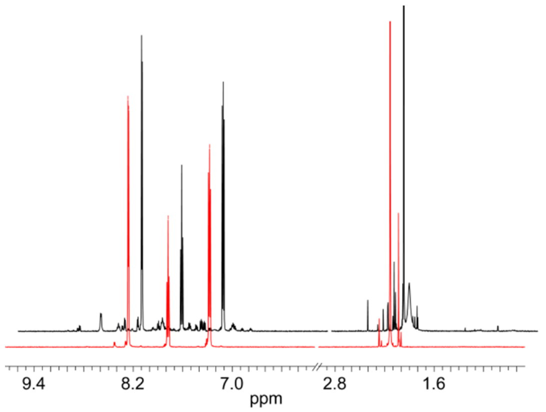

Figure 2. A comparison of the ^{1}H NMR spectra of (black line) 10 mM crude **1** and (red line) 10 mM pure **1** in D_2O.

(Figure S1, Supporting Information);[41] the crystal structure of the oxidized cubane 1^+ was known as a perchlorate salt[45] and is now obtained as a PF_6^- salt, as shown in Figure 1. In our studies, we did not find any evidence that these cubanes were active WOCs. Motivated by the recent reports to the contrary[36−39] and subsequent computational work outlining a detailed mechanistic pathway for **1** as a WOC,[46] we renewed our investigation of these molecules.

Herein, we report that a Co(II) impurity in as-synthesized cubane **1** is primarily responsible for the reported catalytic water oxidation activity. We present a series of experiments that are useful for determining whether a small amount of a Co(II) impurity may lead to formation of a heterogeneous WOC. We further emphasize the utility of differential electrochemical mass spectrometry (DEMS) for clarifying how anodic potentials affect the decomposition of glassy carbon electrodes, which are commonly used in the study of WOCs. The reported experiments are aimed at establishing a standardized approach to evaluate the presence of Co(II) impurities in molecular complexes under investigation as water oxidation catalysts.

■ RESULTS

Synthesis. We synthesized and isolated **1** by precisely following the one-pot procedure developed by others.[36,39] Despite satisfactory elemental analyses for **1** (Table S1), we determined that this as-synthesized material, which was isolated by concentrating a dichloromethane (DCM) extraction, was not pure. The presence of impurities was indicated by the observation of many small peaks in the ^{1}H NMR spectrum (Figures 2 and S2−S4) and by the presence of slowly moving bands that eluted behind the product band on a silica thin layer chromatography (TLC) plate (Figure S5). On the basis of the TLC result, purification of the compound was performed by column chromatography on silica, eluting with a gradient of 2−10% MeOH in DCM. Along with the slowly moving green bands, a red coloration was consistently observed at the top of the column. A comparison of ^{1}H NMR spectra for crude (i.e., as-synthesized) and purified **1** is shown in Figure 2. Several peaks that are observed in the aromatic region in the NMR of the crude sample are absent in the NMR of the purified sample. Molecular impurities are also indicated by many peaks in the m/z range of 300−700 in the ESI-MS of crude **1**; these peaks are absent in the purified sample (Figure S6). A structural variant, **1-COOMe**, was also synthesized according to Das' original procedure;[41] the final product was isolated by precipitation and filtration. No diamagnetic impurities were detected in the ^{1}H NMR spectra of the precipitated **1-COOMe**. However, to remove possible paramagnetic impurities, the precipitated **1-COOMe** was subject to further purification by chromatography. Interestingly, the same ^{1}H NMR spectrum was obtained for precipitated and chromatographed **1-COOMe** (Figure S7), though the former was observed to have impurities that were not removed by precipitation.

Electrochemistry. The reported water oxidation activity of **1**[36,39] could not be replicated using purified samples. Figure 3 compares the CVs of crude and purified **1** (0.852 mg/mL, 1 mM assuming 100% purity). The catalytic current, peaking at 1.3 V (all potentials are referenced to Ag/AgCl), in the crude sample is consistent with the WOC activity that has been previously reported of **1** in the presence of proton accepting electrolytes. However, a similar catalytic wave in the purified sample is completely absent; only a reversible $Co(III)_3Co(IV)/Co(III)_4$ couple centered at $E_{1/2}$ = +1.05 V is observed. Interestingly, the catalytic current detected with the crude sample is only prominent in the first scan of the CV. A similar behavior is observed for **1-COOMe** where precipitated samples exhibit a large catalytic current in the CV and chromatographed samples show only the reversible $Co(III)_3Co(IV)/Co(III)_4$ couple, as shown in Figure S8. The $E_{1/2}$ of the reversible couple is at a more positive potential than for **1**, due to the

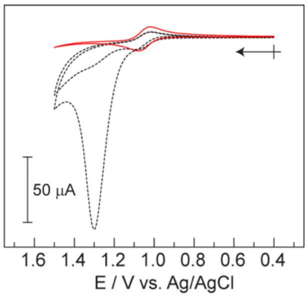

Figure 3. Background corrected CVs of crude (black dotted) and purified (red solid) samples of **1** (0.852 mg/mL) in 0.2 M KP_i buffer, pH = 7. Two scans are presented for the crude sample demonstrating the loss of activity upon the second scan. Crossed arrow indicates initial point and direction of scan.

electron withdrawing nature of the methyl ester substituents on the pyridine ligands.

The electrochemistry of **1** was also investigated in carbonate buffer at pH = 7. The crude sample also showed a catalytic current (E_p = ~1.4 V, Figure S9), which was absent in the purified sample. The only observed difference between the CVs in carbonate and phosphate electrolyte is that the catalytic peak current of the crude sample occurs at a more positive (~80 mV) potential in carbonate electrolyte.

To confirm that the catalytic current in the crude sample was associated with the oxygen evolution reaction, electrochemical oxidation was performed in a DEMS experimental setup, which allows for the immediate and simultaneous detection of all gaseous products formed at the electrode surface.[47] The catalytic current from an unpurified sample shown in the red trace of the top of Figure 4A is accompanied by the production of O_2, as shown in the middle panel of Figure 4A. Purified **1** and **1-COOMe** were also investigated using DEMS under the identical conditions employed for that of the crude sample. As shown in the top panels of Figure 4B,C for purified **1** and **1-COOMe**, respectively, the Faradaic current density decreases by over an order of magnitude from that of the crude sample. The waveform of the CVs in Figure 4 are different than those of CVs taken on stationary GC electrodes (e.g., Figure 3, red trace) owing to the flow conditions of the DEMS experiment; similar waveforms are observed, for instance, at rotating disk electrodes where there is forced solution flow across an electrode surface.[48] The signal from the mass channel of O_2 for the purified samples (middle panels in Figure 4B,C) shows no O_2 production for applied potentials below 1.4 V; at potentials of 1.4 V or greater, an extremely small amount of O_2 is observed (pA intensities as opposed to nA intensities of crude samples). We note that for all three samples, the mass channel of CO_2 exhibits a sizable signal when the electrode potential surpasses ~1.2 V. The high level of evolved CO_2 is observed even in the background scans of blank GC electrodes (black lines in the bottom panels in Figure 4A–C).

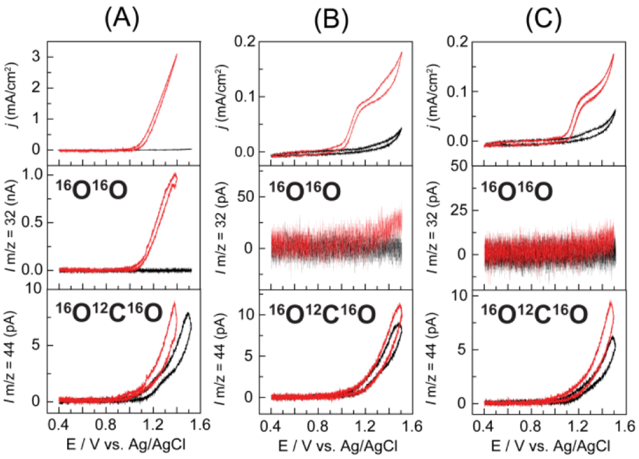

Figure 4. DEMS experimental data for three samples: (A) crude **1-COOMe**, (B) purified **1** and (C) purified **1-COOMe**. Top panels display the Faradaic current density vs potential; middle and bottom panels display the current collected for mass channels 32 (O_2) and 44 (CO_2) *m/z*, respectively. Red lines are representative data from the samples, and black lines are the data from the corresponding blank GC electrodes.

We sought to place a limit on the level of O_2 produced by the cubane cluster within the error of our measurements. The middle panel of Figure 4B indicates that there is a small but non-negligible amount of O_2 produced in purified samples of **1** at applied potentials >1.4 V. We therefore wished to quantify the amount charge passed with the current associated with the slight downturn in the red CV trace at potentials above 1.4 V in Figure 3. Three separate voltammograms (using three independently prepared GC electrodes) were collected with a sample of purified **1** (black traces in Figure S10b–d). A simulated CV (Figure S10a) was subtracted from the background corrected raw data to remove the current that is due to the reversible $Co(III)_3Co(IV)/Co(III)_4$ couple, thus leaving only the current that may be attributed to oxygen evolution (red traces in Figure S10b–d). From these data, the average current density was 0.11 ± 0.04 mA/cm^2 at 1.5 V. Assuming that all of this current leads to the production of O_2, then a TOF of 0.06 mol O_2/mol catalyst is calculated at an overpotential of 0.89 V (see SI for details). This low current density and TOF is consistent with catalysis from ppb concentrations of Co(II) produced from decomposition of the cubane (see Discussion).

To exclude the possibility of chemistry specific to a **1**:GC interaction, Pt, Au, and FTO were also employed as electrode materials. In all three cases, a similar behavior was obtained as for the GC experiments: the CVs of the crude **1** showed significant water oxidation current, which was absent in the CVs of the purified material (Figure S11).

Photochemistry. In addition to electrochemical WOC activity, photochemical water oxidation has been reported for as-synthesized samples of **1** using the $Ru(bpy)_3^{2+}/S_2O_8^{2-}$ sacrificial oxidant system. The photochemical assay was performed in triplicate according to the literature procedure,[36] with the exception that phosphate buffer was used instead of carbonate (see SI for details). The concentration of O_2 was measured for samples of crude **1**, purified **1**, and without added catalyst. A fluorescence-based O_2 sensor was immersed into N_2 purged solutions containing $[Ru(bpy)_3^{2+}]$ = 0.5 mM, $[S_2O_8^{2-}]$ = 35 mM, and [**1**] = 0.33 mM, and the cuvettes were photolyzed with a Hg/Xe arc lamp (λ_{exc} > 400 nm). The yield of O_2 over 400 s of photolysis decreased from 167 ± 15 μM for the crude samples to 31 ± 6 μM for the purified samples (Figure 5).

Identification and Quantification of Impurities. To identify and quantify the impurity found in the crude samples

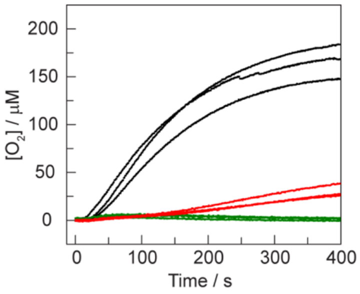

Figure 5. Solution $[O_2]$ measurements during illumination of crude samples of **1** (black), purified **1** (red), and without added **1** (green). Photochemical reactions were performed in the presence of 0.5 mM $Ru(bpy)_3^{2+}$, 35 mM $Na_2S_2O_8$, and 100 mM KPi pH = 7 buffer. The concentration of crude and purified **1** was 0.33 mM, assuming 100% purity for the crude material.

of **1**, a series of spectroscopic and electrochemical experiments were performed. The EPR spectrum of a solid sample of crude **1** reveals a broad paramagnetic signal over the range g = 10 to 2, which is absent in the purified sample (Figure S12). This signal is consistent with a paramagnetic Co(II) species.[16] To confirm the presence of a Co(II) impurity, EDTA was titrated into a CV solution of the crude sample. Figure 6 shows the CVs for the addition of EDTA (0−0.5 mM) into a 2 mM solution (assuming 100% purity) of crude **1** in 0.2 M KP_i pH = 7. Nearly complete suppression of the catalytic current was observed at 0.5 mM EDTA addition. As a control, a 50 μM solution of purified **1** was treated with 10 mM EDTA in 0.2 M KP_i at pH = 7 for 1 h, and no changes in absorbance were observed (Figure S13), confirming that **1** is kinetically stable in the presence of EDTA. The CV wave of the Co(III)/Co(IV) couple of purified **1** with addition of EDTA (Figure S14) is fully reversible, indicating that $\mathbf{1}^+$ is also stable to EDTA on the time scale of the CV experiment.

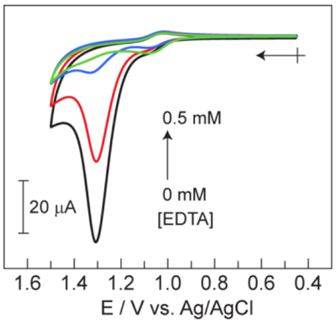

Figure 6. CVs of 2 mM (assuming 100% purity) crude **1** and [EDTA] = 0 (black), 0.10 (red), 0.25 (blue) and 0.50 (green) mM in 0.2 M KPi (pH = 7). Arrow and cross indicates the initial point and direction of scan.

The amount of Co(II) introduced by dissolving the crude preparation of **1** in aqueous media could be quantified by applying ^{31}P NMR line broadening analysis, which we previously employed to quantify the self-healing properties of Co-OEC.[10] A calibration curve was constructed by adding increasing amounts of a 1:1 mixture of $Co(OAc)_2$:pyridine to a 0.5 mM solution (0.426 mg/mL) of purified **1** in 0.2 M KP_i buffer (Figure 7, see SI for experimental details). This calibration curve was used to determine the amount of Co(II) in batches of crude **1**. Although CV experiments were performed with **1** at a concentration of 0.852 mg/mL, at this concentration of crude **1**, the broadening of the phosphate signal is too great to construct a calibration curve over a wide enough range. Thus, we performed ^{31}P NMR line broadening experiments at half the concentration used for CV experiments. Figure 7 shows the ^{31}P NMR signals of phosphate upon dissolving 0.426 mg/mL of crude **1** for three separately prepared batches. Per the calibration curve, we determine that the Co(II) ion concentration in solution is [Co(II)] = 0.086 ± 0.004 mM, 0.091 ± 0.008 mM and 0.065 ± 0.006 mM for samples (c), (d) and (e), respectively ($[\mathrm{Co(II)}]_{\mathrm{avg}}$ = 0.08 ± 0.01 mM). Translating this result to the concentrations used for CV experiments, a sample of 0.852 mg/mL of crude **1** introduces an average concentration of [Co(II)] = 0.16 ± 0.02 mM into solution.

The results of the ^{31}P NMR experiments were confirmed by an electrochemical titration, in which [Co(II)] was correlated with the catalytic current observed by CV (Figure S15). With increasing [Co(II)], the peak current of the catalytic wave at 1.3 V increases linearly. A calibration curve was again constructed and used to assess [Co(II)] in the three batches of crude **1** at the concentration used for CV experiments. The results of this assay shows excellent agreement with the ^{31}P NMR experiment, albeit with larger error bars, giving 0.153 ± 0.019 mM, 0.178 ± 0.020 mM, and 0.120 ± 0.016 mM for the three samples, with a $[\mathrm{Co(II)}]_{\mathrm{avg}}$ = 0.15 ± 0.03 mM.

Because of the insolubility of $Co_3(PO_4)_2$ in aqueous media, the measured Co(II) concentration could be diminished due to loss of cobalt in the form of a $Co_3(PO_4)_2$ precipitate. However,

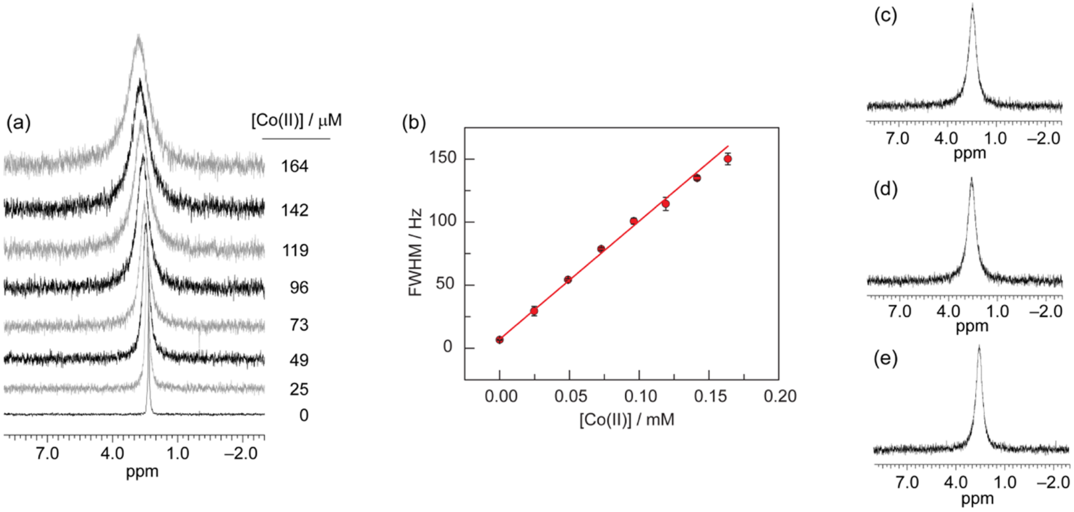

Figure 7. (a) ^{31}P NMR spectra of the phosphate signal of a 0.5 mM solution (0.426 mg/mL) of purified **1** in 0.2 M KPi (pH = 7) with added Co(II) at the indicated concentrations. (b) The measured full-width at half-maximum (fwhm) of the phosphate ^{31}P NMR signal is linearly dependent on the concentration of added Co(II). The equation of the linear calibration curve is fwhm = {(936 ± 8) × [Co(II)]} + (7.2 ± 0.4). (c−e) ^{31}P NMR spectra of the phosphate signal for three separate batches of 0.426 mg/mL of crude **1** in 0.2 M KPi at pH = 7. Using the calibration curve of (b), the amount of line broadening corresponds to a Co(II) concentration of 0.086 ± 0.004 mM, 0.091 ± 0.008 mM, and 0.065 ± 0.006 mM for samples (c), (d) and (e), respectively.

at these low [Co(II)], precipitation of Co(II) by phosphate is negligible due to the slow kinetics of formation of the $Co_3(PO_4)_2$ on the time scale of the electrochemical or photochemical experiments, which take minutes to complete. To experimentally verify that no $Co_3(PO_4)_2$ formed under our experimental conditions, a 0.15 mM solution of a 1:1 mixture of $Co(OAc)_2$:pyridine in the presence of 0.2 M KPi at pH = 7 was monitored by ^{31}P NMR line broadening over a 4 h period (Figure S16). The ^{31}P NMR spectrum establishes that the concentration of Co(II) in solution does not significantly decrease over this time period.

The ^{31}P NMR line broadening experiment is also a sensitive measure of compound stability. Solids of purified **1** can be stored on the benchtop for at least 25 days without decomposition. The ^{31}P NMR line broadening analysis of 0.5 mM **1** in 0.2 M KP_i buffer solution shows that the presence of Co(II) ions after 25 days is negligible (Figure S17). In addition, comparison of the ^1H NMR spectra of **1**, hours after purification and after 25 days are identical (Figure S18).

Characterization of Electrode Surface. Since crude **1** introduces Co(II) into the solution, we would expect that at anodic potentials, Co-OEC will be deposited. Indeed, bulk electrolysis of a 1 mM solution of crude **1** at 1.2 V for 5 min resulted in the deposition of Co-OEC material on the electrode surface, which was readily observed by scanning electron microscopy (SEM) and energy dispersive X-ray spectroscopy (EDS) (Figures S19a and S20a, respectively). Bulk electrolysis of the crude sample at a higher potential of 1.4 V results in significantly less Co-OEC detected on the electrode surface (Figures S19c and S20c), despite more charge being passed (Figure S21). Per the DEMS experiment, current is redirected from water splitting (O_2 production) to degradation of the GC electrode (CO_2 production at higher potential).

Although bulk electrolysis performed over 300 s of a purified sample at 1.2 V resulted in an EDS spectrum that is indistinguishable from that of a blank sample (Figure S20b,d), the SEM images of the pure and blank samples showed a subtle difference. The density of light contrast material was increased in the pure sample as compared to that of the blank sample. We therefore pursued further characterization of the electrode surface by XPS analysis, which is more selective to analysis of surface materials than EDS. A comparison of high-resolution Co 2p XPS spectra of crude, pure, and blank GC electrodes after 300 s of bulk electrolysis at 1.2 V is shown in Figure S22. A trace signal at the Co $2p_{3/2}$ peak of the pure sample is barely distinguishable over background, whereas a large Co $2p_{3/2}$ signal is observed for electrodes removed from bulk-electrolyzed solutions of crude **1**.

■ DISCUSSION

As-synthesized samples of **1** contain significant amounts of impurities in two forms. The many aromatic peaks in the ^1H NMR spectra of crude **1** (Figure 2) and the slowly eluting bands on TLC plates are likely Co(III) clusters of smaller nuclearity, which are known to be stable compounds.[49] Of greater significance, as demonstrated by EPR spectroscopy (Figure S12), electrochemical measurements in the presence of the ion scavenging EDTA (Figure 6) and ^{31}P NMR line broadening analysis (Figure 7), a Co(II) impurity is present in crude samples of **1**. Electrochemical titration experiments and ^{31}P NMR line broadening experiments quantify significant amounts of Co(II) in as-synthesized preparations of **1**. Repeated experiments on different batches of as-synthesized **1** show that the concentration of Co(II) is 16% of the expected concentration of the cubane molecule, **1**. Because the Co(II) impurity is soluble in DCM, the ligation of the Co(II) ion likely involves solubilizing organic groups, such as the acetate or pyridine reactants of **1**, as salts of Co(II) with outer-sphere anions, such as acetate or nitrate, are unlikely to have significant solubility in DCM. Ligation of the solubilizing groups appears to be sufficiently weak that Co-OEC is easily formed (vide infra). As a cautionary note, the absence of line broadening in the ^1H NMR spectra of **1** does not provide sufficient evidence that Co(II) is not present in solution.[36] The lack of significant line broadening in the ^1H NMR spectra upon titrating 1:1 $Co(OAc)_2$:pyridine into a sample of purified **1** (Figure S23) indicates that this is not a sensitive measure of paramagnetic impurities, presumably because **1** (a neutral, weakly basic molecule) does not interact significantly with the Co(II) ion. As Figure 7 demonstrates, the phosphate ^{31}P NMR signal is a much more sensitive measure of the presence of Co(II) impurities. The Co(II) ion impurities do not elute on silica and thus are easily removed from **1**. The same behavior is observed for **1-COOMe**, where silica gel chromatography can be used to remove Co(II) impurities from as-synthesized or precipitated samples.

The Co(II) impurity acts as a source for the formation of the known water oxidation catalyst, Co-OEC. The formation of heterogeneous Co-OEC occurs from solutions of Co(II) with any proton accepting electrolyte, as long as the concentration of the electrolyte is sufficiently high to control pH.[10,17] Moreover, Co-OEC will be formed from Co(II) either electrochemically or (photo)chemically as long as the potential is sufficient to oxidize Co(II) to Co(III) in the presence of electrolytes such as phosphate or carbonate. Consistent with the formation of Co-OEC, the catalytic wave in Figure 3 has the same peak potential and onset current as found for a CV of Co(II) solutions from which Co-OEC electrodeposits (Figure S24). However, unlike a well-behaved catalytic process, as is typical of Co-OEC on FTO, a peak response is observed in the cyclic voltammogram. A peak in the catalytic wave will result from either depletion of substrate or catalyst deactivation.[50] Since the solvent, H_2O, is the substrate, pH is maintained by a high concentration of phosphate, and current densities are low, we can safely rule out substrate depletion as the cause for the peak in Figure 3. However, a peak will result if the catalyst were to be removed from the electrode in a parasitic side reaction, or as in this case, if oxidative degradation of the electrode is significant (vide infra).

Once the impurities are removed by column chromatography, the large catalytic waves in CVs of solutions of unpurified **1** (Figure 3) and **1-COOMe** (Figure S8) disappear completely. This behavior is observed on other electrode materials (Pt, Au, and FTO, Figure S11) as well. Crude **1** shows higher currents at anodic potentials than purified **1**, providing further evidence that an impurity is responsible for the WOC, as opposed to spurious activity arising from a specific deleterious interaction between the cobalt cubane molecule, **1**, and a GC electrode. SEM, EDS, and XPS support the formation of a heterogeneous Co catalyst, which we attribute to Co-OEC, which deposits on electrodes from bulk electrolyzed solutions of crude **1**. Even in purified samples of **1**, XPS indicates that indeed a small amount of cobalt can be detected on the electrode. The production of Co-OEC from purified **1** explains the small amount of O_2 observed in the DEMS experiment (Figure 4B, middle panel) and the minute amount of current beyond background (Figure 3, red trace) at potentials above 1.4 V vs Ag/AgCl. If all the current at 1.5 V goes to the production of O_2, the TOF at this potential would be 0.06 mol O_2/mol of **1**. However, only an extremely small amount of cobalt in the form of Co-OEC is needed to support the current density associated with this TOF. Using the Tafel slope and the known dependence of the exchange current density on the thickness (i.e., Co content) of films of Co-OEC,[12] it was determined that only ~70 ppb of **1**, with its 4 cobalt atoms, would need to decompose to furnish enough cobalt to form Co-OEC and produce this observed current density (see SI for details of the calculation). However, we note that the amount of Co-OEC and O_2 produced is negligible as compared to the Co-OEC formed from as-synthesized samples of **1**.

At potentials above 1.4 V, the DEMS results show that the observed current is predominantly due to the production of CO_2 when a GC electrode is used as the anode. As EDS and XPS results show, the process is so efficient at 1.4 V, that the current is largely redirected from Co-OEC production from the Co(II) impurity to oxidative degradation of the electrode. Importantly, the direct evidence of CO_2 formation (Figure 4A, bottom) under conditions that thermodynamically favor the formation of Co-OEC argues against the possibility that the Co-OEC catalyst is unstable at these high potentials. If the potential is such that the rate of degradation of the GC surface is rapid, as Stracke et al.[33] have noted, one cannot interpret the *absence* of deposited heterogeneous material after electrolysis as evidence of actual molecular catalysis, since surface catalyst will be lost upon degradation of the underlying electrode. Consistent with this argument, SEM and EDS analysis show a decrease of observable Co-OEC on the electrode for bulk electrolysis experiments performed at 1.4 V vs 1.2 V (Figures S19 and S20). Any carbon material (e.g., graphene, carbon nanotubes. etc.) may be compromised due to degradation at high anodic potentials and thus water oxidation experiments performed on carbon-based anodes should be subject to DEMS or other mass spectrometric analysis to ensure that the current is not due to electrode oxidation to CO_2.

As in electrochemical experiments, removing the Co(II) impurity from photochemically driven WOC also leads to a dramatic reduction in the amount of O_2 observed (Figure 5). In the photolysis experiment, persulfate ($S_2O_8^{2-}$) is used as a sacrificial oxidant to form $Ru(bpy)_3^{3+}$ upon irradiation. The reduction potential of $Ru(bpy)_3^{3+}$ is 1.06 V vs Ag/AgCl. At pH = 7, Co-OEC is formed from Co(II) at potentials in the range of 0.75−0.80 V vs Ag/AgCl.[10] Therefore, under the conditions of the photolysis experiment, Co(II) can be oxidized to Co-OEC by $Ru(bpy)_3^{3+}$. Furthermore, the onset of WOC by Co-OEC is 0.90−0.95 V vs Ag/AgCl, and so $Ru(bpy)_3^{3+}$ is thermodynamically capable of driving catalyst turnover. In addition, the quenching reaction of $Ru(bpy)_3^{2+}$ by persulfate to produce $Ru(bpy)_3^{3+}$, also produces $SO_4^{\bullet -}$ as a potential oxidant, which has ample overpotential to drive water oxidation ($E^\circ \sim 2.2$ V vs Ag/AgCl).[51] Thus, the major pathway giving rise to water photooxidation activity with as-synthesized **1** is consistent with the formation of Co-OEC from the in situ oxidation of Co(II) ions.

Although all photochemical studies have used as-synthesized **1**,[36−39] and thus water oxidation may be supported by Co-OEC, the present study shows the photochemical oxidation of purified **1** also results in the production of measurable quantities of O_2 (31 ± 6 μM) over 400 s of photolysis, leading to a TOF = 2.3×10^{-4} s^{-1}. At the potential of $Ru(bpy)_3^{3+}$, which is within the $Co(III)_3Co(IV)/Co(III)_4$ wave (Figure 3), no O_2 is produced as measured by DEMS (Figure 4B). Therefore, $Ru(bpy)_3^{3+}$ is not a potent enough oxidant to turn over **1**;[37] a greater overpotential is required, if **1** is indeed a molecular catalyst under these specific photochemical conditions. As noted above, the protocol of the photochemical experiment produces the strongly oxidizing species $SO_4^{\bullet -}$. This species is free not only to react directly with $Ru(bpy)_3^{2+}$ but also to react with **1** because the concentrations of $[Ru(bpy)_3^{2+}]$ = 0.5 mM and [**1**] = 0.33 mM are similar. Therefore, the observed O_2 emanating from the photolysis conditions used for purified **1** in Figure 5 is likely due to the interaction of **1** with $SO_4^{\bullet -}$, which has a considerably more positive reduction potential than $Ru(bpy)_3^{3+}$.

We envision photochemical WOC activity to be promoted by $SO_4^{\bullet -}$. This species is capable of breaking the O−H bond (BDFE = 123 kcal/mol)[52] of water directly to produce the radical, •OH.[53] We do not expect the C−H bonds of the ligands, and thus the molecule itself, to be thermodynamically stable with respect to hydrogen atom abstraction given the extreme potentials provided by the electron accepting $SO_4^{\bullet -}$ and proton accepting phosphate buffer species. If the cubane were to decompose, Co-OEC is a likely product of the decomposition pathway. Alternatively, computational investigations into the mechanism of WOC by **1** suggest that two oxidations of **1** to the level of $Co(III)_2Co(IV)_2$ and an acetate ligand dissociation were required prior to water attack and subsequent O−O bond formation.[46] We cannot confirm if $SO_4^{\bullet -}$ is capable of oxidizing $\mathbf{1}^+$ because the electrochemical window limits the range of potentials for investigating the behavior of **1** at potentials beyond 1.5 V. If a higher oxidized cubane is capable of water oxidation activity, it occurs at extremely high overpotentials.

■ CONCLUSION

Without purification by silica chromatography, the Co(III) oxo cubanes can be contaminated with Co(II) impurities, which are responsible for the observed water oxidation activity reported for these molecules. We have shown that an EDTA titration can be used to test for the presence of Co(II) and a ^{31}P NMR experiment can be used for the Co(II) quantification; these experiments are more definitive than ^{1}H NMR spectroscopy for identifying paramagnetic Co(II) impurities. Beyond Co(II) as an impurity, the use of any Co(II) complex should be assessed as an authentic WOC versus precursors for heterogeneous catalysts such as Co-OEC owing to the proclivity of Co(II) complexes to undergo rapid ligand substitution.[54,55] We note that water oxidation activity of a catalyst should not depend on whether an anodic potential is supplied electrochemically or (photo)chemically for mechanisms involving outer sphere electron transfers. In instances where homogeneous and heterogeneous O_2 evolution experiments do not concur, it is appropriate to consider whether other species are responsible for catalytic activity. Finally, when inspecting carbon-based electrode surfaces for the deposition of heterogeneous catalysts, care must be exercised in the choice of oxidizing potentials, as extreme values can give rise to spurious current that is associated with CO_2 evolution and electrode degradation as established by DEMS.

■ ASSOCIATED CONTENT

Ⓢ Supporting Information

Experimental methods, calculations, X-ray crystallographic data in CIF format, elemental analyses, ^{1}H NMR spectra, ESI-MS data, EPR spectra, UV−vis absorption spectra, ^{31}P NMR calibration curve data, SEM/EDX images, XPS spectra, and further CV data. This material is available free of charge via the Internet at http://pubs.acs.org.

■ AUTHOR INFORMATION

Corresponding Author

dnocera@fas.harvard.edu

Notes

The authors declare no competing financial interest.

■ ACKNOWLEDGMENTS

This material is based upon work supported by the U.S. Department of Energy Office of Science, Office of Basic Energy Sciences under Award Number DE-SC0009565. EPR spectra were recorded on instruments supported by NIH Award Numbers P41 EB-002804 and EB-002026. SEM and XPS imaging was performed at Harvard University's Center for Nanoscale Systems, a member of the National Nanotechnology Infrastructure Network, which is supported by the NSF under ECS-0335765. The DEMS work at Cornell (HW and HDA) was supported as part of the Energy Materials Center at Cornell, an Energy Frontier Research Center funded by the DOE Office of Basic Energy Sciences under Award Number DE-SC0001086. We acknowledge Dr. Yu-Sheng Chen for assistance with X-ray crystallography at ChemMatCARS, APS. ChemMatCARS Sector 15 is principally supported by NSF/CHE-1346572. Use of APS was supported by the DOE under Contract No. DE-AC02-06CH11357. We thank Dr. Mark Symes for his initial support of this work and for subsequent insightful electronic communications.

■ REFERENCES

(1) Lewis, N. S.; Nocera, D. G. *Proc. Natl. Acad. Sci. U. S. A.* **2006**, *103*, 15729−15735.

(2) Bauer, D.; Diamond, D.; Li, J.; Sandalow, D.; Telleen, P.; Wanner, B. *Critical Materials Strategy*; U.S. Department of Energy: Washington, D.C., 2010.

(3) Cook, T. R.; Dogutan, D. K.; Reece, S. Y.; Surendranath, Y.; Teets, T. S.; Nocera, D. G. *Chem. Rev.* **2010**, *110*, 6474−6502.

(4) Kanan, M. W.; Nocera, D. G. *Science* **2008**, *321*, 1072−1075.

(5) Surendranath, Y.; Dincă, M.; Nocera, D. G. *J. Am. Chem. Soc.* **2009**, *131*, 2615−2620.

(6) Dincă, M.; Surendranath, Y.; Nocera, D. G. *Proc. Natl. Acad. Sci. U. S. A.* **2010**, *107*, 10337−10341.

(7) Bediako, D. K.; Surendranath, Y.; Nocera, D. G. *J. Am. Chem. Soc.* **2013**, *135*, 3662−3674.

(8) Huynh, M.; Bediako, D. K.; Nocera, D. G. *J. Am. Chem. Soc.* **2014**, *136*, 6002−6010.

(9) Huynh, M.; Bediako, D. K.; Liu, Y.; Nocera, D. G. *J. Phys. Chem. C* **2014**, *118*, 17142−17152.

(10) Surendranath, Y.; Lutterman, D. A.; Liu, Y.; Nocera, D. G. *J. Am. Chem. Soc.* **2012**, *134*, 6326−6336.

(11) Surendranath, Y.; Kanan, M. W.; Nocera, D. G. *J. Am. Chem. Soc.* **2010**, *132*, 16501−16509.

(12) Bediako, D. K.; Costentin, C.; Jones, E. C.; Nocera, D. G.; Savéant, J.-M. *J. Am. Chem. Soc.* **2013**, *135*, 10492−10502.

(13) Kanan, M. W.; Yano, J.; Surendranath, Y.; Dincă, M.; Yachandra, V. K.; Nocera, D. G. *J. Am. Chem. Soc.* **2010**, *132*, 13692−13701.

(14) Du, P.; Kokhan, O.; Chapman, K. W.; Chupas, P. J.; Tiede, D. M. *J. Am. Chem. Soc.* **2012**, *134*, 11096−11099.

(15) Farrow, C. L.; Bediako, D. K.; Surendranath, Y.; Nocera, D. G.; Billinge, S. J. L. *J. Am. Chem. Soc.* **2013**, *135*, 6403−6406.

(16) McAlpin, J. G.; Surendranath, Y.; Dincă, M.; Stich, T. A.; Stoian, S. A.; Casey, W. H.; Nocera, D. G.; Britt, R. D. *J. Am. Chem. Soc.* **2010**, *132*, 6882−6883.

(17) Liu, Y.; Nocera, D. G. *J. Phys. Chem. C* **2014**, *118*, 17060−17066.

(18) Dogutan, D. K.; McGuire, R.; Nocera, D. G. *J. Am. Chem. Soc.* **2011**, *133*, 9178−9180.

(19) Wasylenko, D. J.; Ganesamoorthy, C.; Borau-Garcia, J.; Berlinguette, C. P. *Chem. Commun.* **2011**, *47*, 4249−4251.

(20) Rigsby, M. L.; Mandal, S.; Nam, W.; Spencer, L. C.; Llobet, A.; Stahl, S. S. *Chem. Sci.* **2012**, *3*, 3058−3062.

(21) Wang, D.; Groves, J. T. *Proc. Natl. Acad. Sci. U. S. A.* **2013**, *110*, 15579−15584.

(22) Thomsen, J. M.; Sheehan, S. W.; Hashmi, S. M.; Campos, J.; Hintermair, U.; Crabtree, R. H.; Brudvig, G. W. *J. Am. Chem. Soc.* **2014**, *136*, 13826−13834.

(23) Duan, L.; Bozoglian, F.; Mandal, S.; Stewart, B.; Privalov, T.; Llobet, A.; Sun, L. *Nat. Chem.* **2012**, *4*, 418−423.

(24) Barnett, S. M.; Goldberg, K. I.; Mayer, J. M. *Nat. Chem.* **2012**, *4*, 498−502.

(25) Panda, C.; Debgupta, J.; Díaz Díaz, D.; Singh, K. K.; Sen Gupta, S.; Dhar, B. B. *J. Am. Chem. Soc.* **2014**, *136*, 12273−12282.

(26) Grotjahn, D. B.; Brown, D. B.; Martin, J. K.; Marelius, D. C.; Abadjian, M.-C.; Tran, H. N.; Kalyuzhny, G.; Vecchio, K. S.; Specht, Z. G.; Cortes-Llamas, S. A.; Miranda-Soto, V.; van Niekerk, C.; Moore, C. E.; Rheingold, A. L. *J. Am. Chem. Soc.* **2011**, *133*, 19024−19027.

(27) Schley, N. D.; Blakemore, J. D.; Subbaiyan, N. K.; Incarvito, C. D.; D'Souza, F.; Crabtree, R. H.; Brudvig, G. W. *J. Am. Chem. Soc.* **2011**, *133*, 10473−10481.

(28) Hocking, R. K.; Brimblecombe, R.; Chang, L.-Y.; Singh, A.; Cheah, M. H.; Glover, C.; Casey, W. H.; Spiccia, L. *Nat. Chem.* **2011**, *3*, 461−466.

(29) Najafpour, M. M.; Moghaddam, A. N.; Dau, H.; Zaharieva, I. *J. Am. Chem. Soc.* **2014**, *136*, 7245−7248.

(30) Stracke, J. J.; Finke, R. G. *J. Am. Chem. Soc.* **2011**, *133*, 14872−14875.

(31) Artero, V.; Fontecave, M. *Chem. Soc. Rev.* **2013**, *42*, 2338−2356.

(32) Yin, Q.; Tan, J. M.; Besson, C.; Geletii, Y. V.; Musaev, D. G.; Kuznetsov, A. E.; Luo, Z.; Hardcastle, K. I.; Hill, C. L. *Science* **2010**, *328*, 342−345.

(33) Stracke, J. J.; Finke, R. G. *ACS Catal.* **2013**, *3*, 1209−1219.

(34) Vickers, J. W.; Lv, H.; Sumliner, J. M.; Zhu, G.; Luo, Z.; Musaev, D. G.; Geletii, Y. V.; Hill, C. L. *J. Am. Chem. Soc.* **2013**, *135*, 14110−14118.

(35) Stracke, J. J.; Finke, R. G. *ACS Catal.* **2014**, *4*, 79−89.

(36) McCool, N. S.; Robinson, D. M.; Sheats, J. E.; Dismukes, G. C. *J. Am. Chem. Soc.* **2011**, *133*, 11446−11449.

(37) Smith, P. F.; Kaplan, C.; Sheats, J. E.; Robinson, D. M.; McCool, N. S.; Mezle, N.; Dismukes, G. C. *Inorg. Chem.* **2014**, *53*, 2113−2121.

(38) Ganga, G. L.; Puntoriero, F.; Campagna, S.; Bazzan, I.; Berardi, S.; Bonchio, M.; Sartorel, A.; Natali, M.; Scandola, F. *Faraday Discuss.* **2012**, *155*, 177−190.

(39) Berardi, S.; La Ganga, G.; Natali, M.; Bazzan, I.; Puntoriero, F.; Sartorel, A.; Scandola, F.; Campagna, S.; Bonchio, M. *J. Am. Chem. Soc.* **2012**, *134*, 11104−11107.

(40) Zhang, B.; Li, F.; Yu, F.; Wang, X.; Zhou, X.; Li, H.; Jiang, Y.; Sun, L. *ACS Catal.* **2014**, *4*, 804−809.

(41) Chakrabarty, R.; Bora, S. J.; Das, B. K. *Inorg. Chem.* **2007**, *46*, 9450−9462.

(42) Dimitrou, K.; Folting, K.; Streib, W. E.; Christou, G. *J. Am. Chem. Soc.* **1993**, *115*, 6432−6433.

(43) McAlpin, J. G.; Stich, T. A.; Ohlin, C. A.; Surendranath, Y.; Nocera, D. G.; Casey, W. H.; Britt, R. D. *J. Am. Chem. Soc.* **2011**, *133*, 15444−15452.

(44) Symes, M. D.; Surendranath, Y.; Lutterman, D. A.; Nocera, D. G. *J. Am. Chem. Soc.* **2011**, *133*, 5174−5177.

(45) Stich, T. A.; Krzystek, J.; Mercado, B. Q.; McAlpin, J. G.; Ohlin, C. A.; Olmstead, M. M.; Casey, W. H.; David Britt, R. *Polyhedron* **2013**, *64*, 304−307.
(46) Li, X.; Siegbahn, P. E. M. *J. Am. Chem. Soc.* **2013**, *135*, 13804−13813.
(47) Wang, H.; Abruña, H. In *Electrocatalysis of Direct Alcohol Fuel Cells: Quantitative DEMS Studies Fuel Cells and Hydrogen Storage*; Bocarsly, A., Mingos, D. M. P., Eds.; Springer: Berlin, 2011; Vol. *141*, pp 33−83.
(48) Bard, A. J.; Faulkner, L. R. *Electrochemical Methods: Fundamentals and Applications*, 2nd ed.; Wiley: New York, 2001; Chapter 9.
(49) Sumner, C. E. *Inorg. Chem.* **1988**, *27*, 1320−1327.
(50) Costentin, C.; Drouet, S.; Robert, M.; Savéant, J.-M. *J. Am. Chem. Soc.* **2012**, *134*, 11235−11242.
(51) Lewandowska-Andralojc, A.; Polyansky, D. E. *J. Phys. Chem. A* **2013**, *117*, 10311−10319.
(52) Warren, J. J.; Tronic, T. A.; Mayer, J. M. *Chem. Rev.* **2010**, *110*, 6961−7001.
(53) Stanbury, D. M. In *Advances in Inorganic Chemistry*; Sykes, A.G., Ed.; Academic Press: San Diego, 1989; Vol. *33*, pp 69−138.
(54) Basolo, F.; Pearson, R. G. *Mechanisms of Inorganic Reactions: A Study of Metal Complexes in Solution*; J. Wiley: New York, 1967; Chapter 3.
(55) Richens, D. T. *Chem. Rev.* **2005**, *105*, 1961−2002.

JOURNAL OF THE AMERICAN CHEMICAL SOCIETY
Communication
pubs.acs.org/JACS

Intermediate-Range Structure of Self-Assembled Cobalt-Based Oxygen-Evolving Catalyst

Christopher L. Farrow,[†] D. Kwabena Bediako,[‡] Yogesh Surendranath,[‡] Daniel G. Nocera,*[,‡] and Simon J. L. Billinge*[,†,§]

[†] Department of Applied Physics and Applied Mathematics, Columbia University, New York, New York 10027, United States
[‡] Department of Chemistry and Chemical Biology, Harvard University, Cambridge, Massachusetts 02138, United States
[§] Condensed Matter Physics and Materials Science Department, Brookhaven National Laboratory, Upton, New York 11973, United States

Supporting Information

ABSTRACT: Continual improvements in solar-to-fuels catalysis require a genuine understanding of catalyst structure–function relationships, not only with respect to local order, but also intermediate-range structure. We report the X-ray pair distribution function analysis of the nanoscale order of an oxidic cobalt-based water-splitting catalyst and uncover an electrolyte dependence in the intermediate-range structure of catalyst films. Whereas catalyst films formed in borate electrolyte (CoB_i) exhibit coherent domains consisting of 3–4 nm cobaltate clusters with up to three layers, films deposited in phosphate electrolyte (CoP_i) comprise significantly smaller clusters that are not coherently stacked. These structural insights are correlated with marked differences in activity between CoP_i and CoB_i films.

Hydrogen and oxygen generation by solar-driven water splitting provides a means to store sunlight in a renewable manner.[1−3] However, the kinetic complexity of water splitting,[4] particularly for the oxygen evolution reaction (OER), mandates the use of catalysts to store and discharge the redox equivalents productively by performing the $4e^-{-}4H^+$ proton-coupled electron transfer (PCET) of the OER at low overpotential.[5−11] Electrodeposited thin-film OER catalysts, which self-assemble from solutions of $Co^{2+}(aq)$[12−14] and $Ni^{2+}(aq)$[15,16] in the presence of a buffering electrolyte, such as phosphate (P_i), methylphosphonate (MeP_i), or borate (B_i), perform the OER remarkably well.[17] Extended X-ray absorption fine structure (EXAFS) investigations[18−20] of these catalyst films establish that they are composed of edge-sharing MO_6 clusters of molecular dimensions. A recent X-ray scattering and PDF analysis study[21] has extended the initial EXAFS studies and demonstrated that the domains of CoP_i films consisted of clusters comprising on the order of 14 Co ions.

Whereas EXAFS provides key insight into the *local* order in these films, atomic pair distribution function (PDF) has the added benefit that it affords a direct probe that is also sensitive to *intermediate*-range structure on the nanoscale.[22−24] Nanoscale structure is a crucial determinant of the electronic structure of a variety of functional materials. In the case of the self-assembled OER catalysts, intermediate-range order in these porous thin films is also anticipated to be critical to charge/mass transport between active sites and hence overall catalytic activity. Indeed, changes in microstructure of thin films and electronic structure would be expected to impact the activity and performance of any OER anode. The kinetics of CoP_i nucleation and film deposition indicates that the electrolyte plays a pivotal role in modulating catalyst self-assembly.[25] We surmised that the identity of the electrolyte could impact the structure of Co-OEC, and in the future permit the tuning of catalytic activity. To this end, the self-assembled $Co\text{-}P_i/B_i$ films offer a unique platform to explore nanoscale structure–activity relationships of OER catalysts at length scales beyond the molecular dimension. We now show by X-ray PDF analysis of CoP_i and CoB_i films that the B_i templates a unique intermediate layered microstructure, thus establishing the importance of film microstructure in overall catalytic activity.

Catalyst films were electrodeposited onto FTO plates (Hartford Glass) by controlled-potential electrolysis of $Co^{2+}(aq)$ solutions containing P_i or B_i at pH 7.0 or 9.2, respectively. Following electrodeposition, films were rinsed and dried in air, and catalyst material was removed from the substrate surface. Nanoparticulate (50 nm) Co_3O_4 was used as received (Sigma-Aldrich), and CoO(OH) was prepared according to an established procedure.[26] Samples were packed into polyimide capillary tubes for X-ray analysis. X-ray analysis was performed at the X7B beamline at the National Synchrotron Light Source (NSLS) at Brookhaven National Laboratory. Diffraction data were collected using the rapid acquisition pair distribution function (RaPDF) technique,[27] utilizing a 2D X-ray detector. Full experimental details pertaining to sample preparation and X-ray analysis are provided in the Supporting Information (SI).

All raw 2D data images were azimuthally integrated and converted to intensity versus 2θ using the software Fit2D,[28] where 2θ is the angle between the incident and scattered X-rays. The data were corrected using PDFgetX3,[29] a home-written data analysis program, to obtain the total scattering structure function, $S(Q)$, where Q is the magnitude of the scattering vector (as defined in the SI) and the PDF, $G(r)$. Plots of $Q(S(Q) - 1)$ for all samples are shown in Figure 1a, and $G(r)$ plots for CoP_i and CoB_i are shown in Figure 1b. PDFs of all samples are presented in Figure S1. Unlike the crystalline analogues which exhibit sharp

Received: February 4, 2013
Published: April 2, 2013

dx.doi.org/10.1021/ja401276f | *J. Am. Chem. Soc.* 2013, 135, 6403−6406

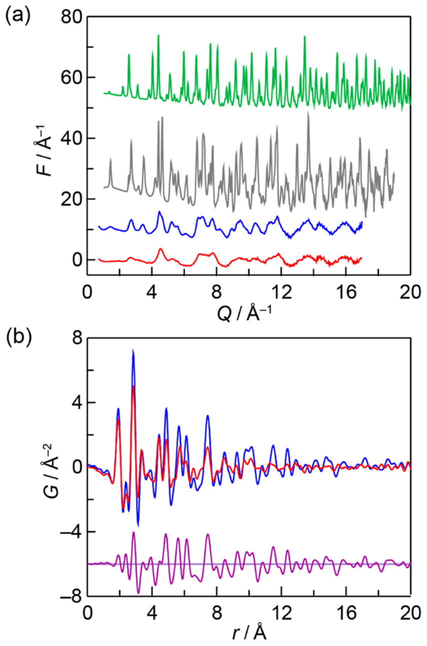

Figure 1. (a) Structure functions for (from top to bottom) crystalline Co_3O_4 (green line), CoO(OH) (grey line), and nanocrystalline samples of CoB_i (blue line) and CoP_i (red line). (b) Comparison of PDFs of CoB_i (blue line) and CoP_i (red line). PDFs have been truncated at $r = 20$ Å to highlight the differences. The difference is shown by the lower trace (purple line), which is offset for clarity.

Bragg peaks in the diffraction pattern (Figure 1a) and possess PDFs that extend to high *r* (Figure S1), the catalyst samples exhibit only diffuse scattering due to finite size effects (Figure 1a). However, PDFs of CoP_i and CoB_i display sharp peaks in real space (Figure 1b), indicating a well-defined local order (i.e., they are not glassy). The peaks diminish with increasing *r*, signifying that the samples are nanocrystalline with domain sizes between 15 and 30 Å. It is also evident from Figure 1b that CoB_i possesses more structural coherence than CoP_i, since there is a wider range of *r* for the former over which structural correlations persist. Whereas Du and co-workers have observed extra features in their PDF data that were attributed to CoO cube defects and distortions to the terminal Co−O positions,[21] we do not observe any evidence for such features. The fact that our samples are catalytically active without the presence of the defect features suggests that they are not essential for the activity, though additional studies are required to resolve this issue.

Two crystalline structural analogues, Co_3O_4 and CoO(OH), were also measured for structural comparison to the CoP_i/B_i samples. Their PDFs were truncated to simulate nanoparticle effects and compared to CoP_i and CoB_i (Figures S2−S5). In general, there is poorer agreement of CoP_i/B_i to Co_3O_4 (Figures S2 and S3) as compared to CoO(OH) (Figures S4 and S5), indicating that the CoP_i/B_i samples are of the cobaltate structure, in agreement with previous EXAFS and PDF structural studies.[18−21] However, there is significantly poorer agreement between CoO(OH) and the CoP_i/B_i at high *r* compared to low *r*, representing some difference in intermediate-range structure. For example, a significant discrepancy in peak position between CoO(OH) and either CoP_i and CoB_i is found in the doublet between 4 and 5 Å. The CoO(OH) structure consists of aligned layers of edge-shared CoO_6 octahedra with hydrogen atoms in the interlayer region.[30] The first peak in the doublet arises from the nearest-neighbor *inter*layer Co−Co distance in the CoO(OH) structure, and the second peak is from the second nearest-neighbor *intra*layer Co−Co distance. Since the largest discrepancy is in the position of the first peak of the doublet, this indicates that CoP_i and CoB_i have the CoO(OH) structure, but with diminished coherence in the stacking direction due to turbostratic disorder between stacked layers, or because the clusters are not coherently stacked at all.

Preliminary modeling was performed using the PDFgui software,[31] with the model PDFs attenuated by the characteristic function for a sphere. Modeling was performed according to standard procedures,[22,32] using the maximum number of parameters allowed by the space groups of the model structures. In agreement with our initial observations, the CoO(OH) model performed better by a considerable margin than Co_3O_4 (Figures S6 and S7), as evidenced by the greatly improved goodness-of-fit parameter, R_w. Both models refined with large cobalt atomic displacement parameters along the *c*-axis of the cell, providing evidence for turbostratic disorder among the stacked layers.[32,33]

More advanced modeling was performed using atomistic nanoparticle models created from the CoO(OH) structure. These models were fit using our recently developed SRREAL and SRFIT programs.[34] Models were created for refinement using a nanoparticle template approach; a geometric shape is used to excise a nanoparticulate model from a crystal structure. This allows us to vary not only the crystal structure, but also the dimensions of the nanoparticle by varying the template. It also allows us to decorate the model with additional scatterers and to distort the model. This was not done here, but will be explored in future modeling efforts. The nanoparticle models for CoB_i and CoP_i were created using a cylindrical template. The template was allowed variable dimensions and location, with the axis of the cylinder aligned with the *c*-axis of the CoO(OH) structure. For simplicity, hydrogen atoms were excluded from the models. Since circular cuts were made in the hexagonal layers, the resulting structures that were used for modeling did not necessarily have fully coordinated Co ions at the perimeter. The resulting finite-sized nanoparticle models are then used to calculate the PDF using the Debye equation. Unlike the PDFgui approach, this method does not use periodic boundary conditions.

The refined PDF fits and models for CoB_i and CoP_i catalysts are shown in Figures 2 and 3, and some structural parameters are tabulated in Table S1. The CoB_i model has three layers on average, and the diameter of the layers is approximately 35 Å. We

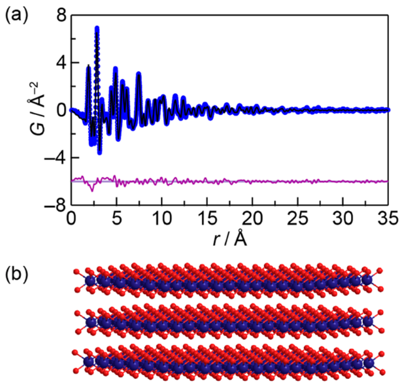

Figure 2. (a) Cylindrical atomistic model fit (black line) to the CoB_i catalyst PDF data (blue circles). The difference curve is shown in purple, and is offset for clarity. (b) View of the refined model for the average coherent domain in CoB_i films.

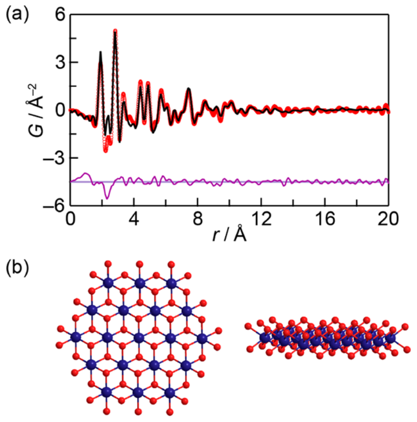

Figure 3. (a) Cylindrical atomistic model fit (black line) to the CoP_i catalyst PDF data (red circles). The difference curve is shown in purple, and is offset for clarity. (b) Two views of the refined model for the average coherent domain in CoP_i films.

attempted to constrain the model to a single layer, but this furnishes a poorer fit (Figure S8), suggesting that the coherent domains of CoB_i do indeed consist of multiple layers of clusters with weak, but significant interlayer correlations. Compared to the crystalline CoO(OH) compound, the *c*-axis is significantly larger (Table S1), which indicates an expansion of the layers, perhaps to accommodate species larger than protons in the interlayer region such as weakly scattering or disordered electrolyte ions, though these were not identified. The refined CoP_i model and fit (Figure 3) indicate that the diameter of the clusters is approximately 14 Å, considerably smaller than those of CoB_i. This model was given the flexibility to form layers, but did not. This suggests that unlike CoB_i, the coherent domains of the catalyst consist of single-layer clusters like those shown in Figure 3b whose arrangements are significantly disordered in the film.

The dependence of structure on deposition potential was evaluated for fixed electrolyte conditions. CoP_i films were deposited at 1.0−1.1 V vs NHE, and CoB_i films were deposited at 0.9−1.0 V vs NHE. No significant differences were observed over this range for films grown in P_i or B_i at varying potentials, indicating that it is the electrolyte, and not the potential, that directs these nanoscale structural changes in catalyst films.

Electrochemical data indicate that the intrinsic activity of CoB_i films is considerably better than that of CoP_i films as film thickness is increased. This is evident in Figure 4, where the geometric current density of the cobalt OER catalysts at a fixed overpotential of 400 mV is shown as a function of film loading. In both cases, the performance of the anode can be improved by depositing thicker films. However, the behavior for CoB_i and CoP_i differs. Whereas the CoB_i films display a monotonic increase in activity with film thickness, the activity of CoP_i attains a limiting activity at catalyst loadings in excess of 1 μmol Co/cm^2. At loadings greater than 0.25 μmol Co/cm^2, CoB_i activity is significantly superior to that of CoP_i. These results suggest that the effective surface area of the CoB_i catalyst increases with increasing film thickness while preserving the intrinsic transport properties within the film. The PDF results now offer a concrete difference in CoP_i and CoB_i, thus allowing the first insight into a tangible structure−function correlation. The mesoscale ordering of the CoB_i film suggests enhanced catalytic activity. Electrochemical and stopped-flow spectroscopic studies using molecular model compounds establish that the mechanism for charge transport in these films is best thought of as involving a series of PCET self-exchange reactions between Co^{III} and Co^{IV} centers of different cluster subunits.[35] Along these lines, the larger domain size of CoB_i relative to CoP_i provides a mechanism to delocalize the mobile holes over a larger region, which can be manifest in more efficient charge transport owing to (1) fewer discrete hole hops needed in a given distance for charge transport among clusters and (2) a reduced reorganizational energy for electron transfer since charge is delocalized over a larger cluster area. Indeed, charge delocalization has been observed to enhance apparent self-exchange rates and attendant hole mobility on polymer[36,37] and nanoparticulate[38] films. In addition, interlayer hopping of holes may be facilitated by less disorder in a film comprising a multilayer CoB_i structure as compared to more disorder in the single-layer structure of CoP_i films. Together, these factors will contribute to an enhanced hole hopping rate, and hence a greater charge transport mobility in CoB_i films, accounting for the ability of these films to sustain higher net activity than CoP_i. In addition, we hypothesize that such nanoscale differences may impact a long-range morphology of these materials, such as their porosity and, by extension, their capacity for *mass* transport. Detailed transport and surface-area measurements will shed more light on these questions.

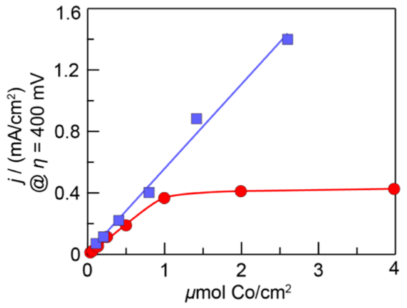

Figure 4. Stead-state current density, *j*, at an overpotential, η, of 400 mV for CoP_i (red circles) and CoB_i (blue squares) films with varying loading operated in KP_i pH 7.0 and KB_i pH 9.2 electrolyte, respectively. Lines are drawn simply as guides to the eye.

The electrolyte in OER self-assembly of Co and Ni/P_i and B_i films has several important roles. First, the anionic electrolyte is a mechanistic element of film nucleation and film growth. Second, the electrolyte is a proton acceptor in the PCET reaction of OER. Third, the electrolyte is the critical determinant of the self-healing nature of these films. The structural insights uncovered here by PDF analysis now indicate yet another important role of the electrolyte as an element that directs the intermediate-range structural order of the oxidic cobalt clusters within the films. Previous kinetic studies have provided a mechanistic framework for understanding the conflicting interactions between the buffering electrolyte as both proton acceptor and adsorbing anion.[25] Whereas the latter role inhibits catalyst assembly, the former serves to assist formation and growth of clusters by facilitating the PCET oxidation of Co^{2+} precursors.[25] Thus, it is reasonable to expect that the size of the domains formed would depend critically on the balance between these factors; a high binding constant between buffering anion and cobalt centers—most likely at the edges of nascent clusters—would favor the formation of new domains versus the growth of existing ones, whereas a weaker adsorption isotherm would promote larger domain sizes. The intercalation of anions between clusters, as observed in solid-state ^{31}P NMR studies of CoP_i,[39] may serve as a mechanism by which the electrolyte defines the degree of coherence in stacking of cobaltate clusters. The fundamental thermodynamic and kinetic parameters that directly regulate catalyst size warrant further investigation, since electrochemical studies show that these nanoscale morphological changes have a marked impact on the activity with film thickness (Figure 4).

The CoP_i/B_i clusters are dimensionally reduced analogues of extended cobalt oxides. These PDF studies now show that this dimensional reduction extends beyond Co oxido cluster subunits, and in CoB_i a mesostructure is realized that captures the nascent layered structure of cobaltates such as $LiCoO_2$. In this regard, CoB_i provides a link between molecular and extended-solid OER catalysts. After nearly a century of research,[40,41] the mechanism of the OER at an atomistic level remains largely unknown for conventional transition metal oxides. Thus the CoB_i OER catalyst offers a molecular-like understanding of the structure−function relationships of OER oxide catalysts. The edges of the clusters are known to be especially important to OER activity in CoP_i and CoB_i films.[42−44] Hence, the results described herein suggest that traditional metal oxides may restructure to give metallate cluster active sites of the type observed in this study. Insights such as these, which provide a bridge between molecular and extended solids, should be useful to accelerating the discovery of both homogeneous and heterogeneous catalysts systems.

■ ASSOCIATED CONTENT

Ⓢ Supporting Information

Full experimental details, additional PDF data, and fitting plots. This material is available free of charge via the Internet at http://pubs.acs.org.

■ AUTHOR INFORMATION

Corresponding Author

dnocera@fas.harvard.edu; sb2896@columbia.edu

Notes

The authors declare no competing financial interest.

■ ACKNOWLEDGMENTS

X-ray experiments were carried out at the National Synchrotron Light Source, Brookhaven National Laboratory, which is supported by the DOE, Division of Materials Sciences and Division of Chemical Sciences, DE-AC02-98CH10886. Work in the Billinge group was supported by the DOE under DE-SC0001085. Work in the Nocera group was supported by Grant DE-SC0009565.

■ REFERENCES

(1) Cook, T. R.; Dogutan, D. K.; Reece, S. Y.; Surendranath, Y.; Teets, T. S.; Nocera, D. G. *Chem. Rev.* **2010**, *110*, 6474.

(2) Barber, J. *Chem. Soc. Rev.* **2009**, *38*, 185.

(3) Lewis, N. S.; Nocera, D. G. *Proc. Natl. Acad. Sci. U.S.A.* **2006**, *103*, 15729.

(4) Surendranath, Y.; Nocera, D. G. *Prog. Inorg. Chem.* **2011**, *57*, 505.

(5) Cukier, R. I.; Nocera, D. G. *Annu. Rev. Phys. Chem.* **1998**, *49*, 337.

(6) Eisenberg, R.; Gray, H. B. *Inorg. Chem.* **2008**, *47*, 1697.

(7) Betley, T. A.; Wu, Q.; Van Voorhis, T.; Nocera, D. G. *Inorg. Chem.* **2008**, *47*, 1849.

(8) Betley, T. A.; Surendranath, Y.; Childress, M. V.; Alliger, G. E.; Fu, R.; Cummins, C. C.; Nocera, D. G. *Philos. Trans. R. Soc. B* **2008**, *363*, 1293.

(9) Hammes-Schiffer, S. *Acc. Chem. Res.* **2009**, *42*, 1881.

(10) Concepcion, J. J.; Jurss, J. W.; Brennaman, M. K.; Hoertz, P. G.; Patrocinio, A. O. T.; Murakami Iha, N. Y.; Templeton, J. L.; Meyer, T. J. *Acc. Chem. Res.* **2009**, *42*, 1954.

(11) Nocera, D. G. *Inorg. Chem.* **2009**, *48*, 10001.

(12) Kanan, M. W.; Nocera, D. G. *Science* **2008**, *321*, 1072.

(13) Surendranath, Y.; Dinca, M.; Nocera, D. G. *J. Am. Chem. Soc.* **2009**, *131*, 2615.

(14) Lutterman, D. A.; Surendranath, Y.; Nocera, D. G. *J. Am. Chem. Soc.* **2009**, *131*, 3838.

(15) Dincă, M.; Surendranath, Y.; Nocera, D. G. *Proc. Natl. Acad. Sci. U.S.A.* **2010**, *107*, 10337.

(16) Bediako, D. K.; Lassalle, B.; Surendranath, Y.; Yano, J.; Yachandra, V. K.; Nocera, D. G. *J. Am. Chem. Soc.* **2012**, *134*, 6801.

(17) Esswein, A. J.; Surendranath, Y.; Reece, S. R.; Nocera, D. G. *Energy Environ. Sci.* **2011**, *4*, 499.

(18) Risch, M.; Khare, V.; Zaharieva; Gerencser, L.; Chernev, P.; Dau, H. *J. Am. Chem. Soc.* **2009**, *131*, 6936.

(19) Kanan, M. W.; Yano, J.; Surendranath, Y.; Dincă, M.; Yachandra, V. K.; Nocera, D. G. *J. Am. Chem. Soc.* **2010**, *132*, 13692.

(20) Risch, M.; Klingan, K.; Ringleb, F.; Chernev, P.; Zaharieva, I.; Fischer, A.; Dau, H. *ChemSusChem* **2012**, *5*, 542.

(21) Du, P.; Kokhan, O.; Chapman, K. W.; Chupas, P. J.; Tiede, D. M. *J. Am. Chem. Soc.* **2012**, *134*, 11096.

(22) Egami, T.; Billinge, S. J. L. *Underneath the Bragg-Peaks: Structural Analysis of Complex Materials*; Plenum: Oxford, 2003.

(23) Billinge, S. J. L.; Kanatzidis, M. G. *Chem. Commun.* **2004**, 749.

(24) Blakemore, J. D.; Mara, M. W.; Kushner-Lenhoff, M. N.; Schley, N. D.; Konezny, S. J.; Rivalta, I.; Negre, C. F. A.; Snoeberger, R. C.; Kokhan, O.; Huang, J.; Stickrath, A.; Tran, L. A.; Parr, M. L.; Chen, L. X.; Tiede, D. M.; Batista, V. S.; Crabtree, R. H.; Brudvig, G. W. *Inorg. Chem.* **2013**, *52*, 1860.

(25) Surendranath, Y.; Lutterman, D. A.; Liu, Y.; Nocera, D. G. *J. Am. Chem. Soc.* **2012**, *134*, 6326.

(26) Amatucci, G. G.; Tarascon, J. M.; Larcher, D.; Klein, L. C. *Solid State Ionics* **1996**, *84*, 169.

(27) Chupas, P. J.; Qiu, X.; Hanson, J. C.; Lee, P. L.; Grey, C. P.; Billinge, S. J. L. *J. Appl. Crystallogr.* **2003**, *36*, 1342.

(28) Hammersley, A. P.; Svenson, S. O.; Hanfland, M.; Hauserman, D. *High Pressure Res.* **1996**, *14*, 235.

(29) Juhas, P.; Davis, T.; Farrow, C. L.; Billinge, S. J. L., arXiv:1211.7126, arXiv.org e-Print archive, 2012; http://arxiv.org/abs/1211.7126 (accessed January 25, 2013).

(30) Delaplane, R. G.; Ibers, J. A.; Ferraro, J. R.; Rush, J. J. *J. Chem. Phys.* **1969**, *50*, 1920.

(31) Farrow, C. L.; Juhás, P.; Liu, J.; Bryndin, D.; Božin, E. S.; Bloch, J.; Proffen, T.; Billinge, S. J. L. *J. Phys: Condens. Mat.* **2007**, *19*, 335219.

(32) Masadeh, A. S.; Božin, E. S.; Farrow, C. L.; Paglia, G.; Juhás, P.; Karkamkar, A.; Kanatzidis, M. G.; Billinge, S. J. L. *Phys. Rev. B* **2007**, *76*, 115413.

(33) Petkov, V.; DiFrancesco, R. G.; Billinge, S. J. L.; Acharya, M.; Foley, H. C. *Philos. Mag. B* **1999**, *79*, 1519.

(34) Farrow, C. L.; Billinge, S. J. L. *Acta Crystallogr. A* **2009**, *65*, 232.

(35) Symes, M. D.; Surendranath, Y.; Lutterman, D. A.; Nocera, D. G. *J. Am. Chem. Soc.* **2011**, *133*, 5174.

(36) Buttry, D. A.; Anson, F. C. *Electroanal. Chem.* **1981**, *130*, 333.

(37) Blaunch, D. N.; Saveant, J. M. *J. Am. Chem. Soc.* **1992**, *114*, 3323.

(38) Hicks, J. F.; Zamborini, F. P.; Osisek, A.; Murray, R. W. *J. Am. Chem. Soc.* **2001**, *123*, 7048.

(39) Harley, S. J.; Mason, H. E.; McAlpin, J. G.; Britt, R. D.; Casey, W. H. *Chem.—Eur. J.* **2012**, *18*, 10476.

(40) Tarasevich, M. R.; Efremov, B. N. In *Electrodes of Conductive Metal Oxides, Part A*; Trasatti, S., Ed.; Elsevier: Amsterdam, 1980; Ch. 5.

(41) Trasatti, S. In *Electrochemistry of Novel Materials*; Lipkowski, J., Ross, P. N., Eds.; VCH: New York, 1994; Ch. 5.

(42) Surendranath, Y.; Kanan, M. W.; Nocera, D. G. *J. Am. Chem. Soc.* **2010**, *132*, 16501.

(43) Gerken, J. B.; McAlpin, J. G.; Chen, J. Y. C.; Rigsby, M. L.; Casey, W. H.; Britt, R. D.; Stahl, S. S. *J. Am. Chem. Soc.* **2011**, *133*, 14431.

(44) Lee, S. W.; Carlton, C.; Risch, M.; Surendranath, Y.; Chen, S.; Furutsuki, S.; Yamada, A.; Nocera, D. G.; Shao-Horn, Y. *J. Am. Chem. Soc.* **2012**, *134*, 16959.

JACS
JOURNAL OF THE AMERICAN CHEMICAL SOCIETY

Proton–Electron Transport and Transfer in Electrocatalytic Films. Application to a Cobalt-Based O_2-Evolution Catalyst

D. Kwabena Bediako,[†] Cyrille Costentin,*[,‡] Evan C. Jones,[†] Daniel G. Nocera,*[,†] and Jean-Michel Savéant*[,‡]

[†]Department of Chemistry and Chemical Biology, 12 Oxford Street, Harvard University, Cambridge, Massachusetts 02138-2902, United States

[‡]Sorbonne Paris Cité, Laboratoire d'Electrochimie Moléculaire, Unité Mixte de Recherche Université - CNRS No 7591, Université Paris Diderot, Bâtiment Lavoisier, 15 rue Jean de Baïf, 75205 Paris Cedex 13, France

S *Supporting Information*

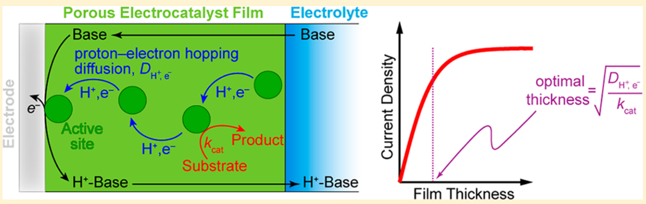

ABSTRACT: Solar-driven electrochemical transformations of small molecules, such as water splitting and CO_2 reduction, pertinent to modern energy challenges, require the assistance of catalysts preferably deposited on conducting or semiconducting surfaces. Understanding mechanisms and identifying the factors that control the functioning of such systems are required for rational catalyst optimization and improved performance. A methodology is proposed, in the framework of rotating disk electrode voltammetry, to analyze the current responses expected in the case of a semigeneral reaction scheme involving a proton-coupled catalytic reaction associated with proton-coupled electron hopping through the film as rate controlling factors in the case where there is no limitation by substrate diffusion. The predictions concern the current density vs overpotential (Tafel) plots and their dependence on buffer concentration (including absence of buffer), film thickness and rotation rate. The Tafel plots may have a variety of slopes (e.g., $F/RT \ln 10$, $F/2RT \ln 10$, 0) that may even coexist within the overpotential range of a single plot. We show that an optimal film thickness exists beyond which the activity of the film plateaus. Application to water oxidation by films of a cobalt-based oxidic catalyst provides a successful test of the applicability of the proposed methodology, which also provides further insight into the mechanism by which these cobalt-based films catalyze the oxidation of water. The exact nature of the kinetic and thermodynamic characteristics that have been derived from the analysis is discussed as well as their use in catalyst benchmarking.

INTRODUCTION

To meet rising global energy demand, inexpensive and carbon-neutral energy sources must be developed to ensure the sustainable development of future generations.[1] Solar-driven electrochemical splitting of water to molecular hydrogen and oxygen,[2] along with the reduction of carbon dioxide[3] are small molecule transformations that hold promise as routes of storing sunlight in energy-dense chemical bonds. Electrochemical recovery of the stored energy would then involve the oxidation of hydrogen or the CO_2-derived fuel in a fuel cell.[4,5]

In most of these cases, high activation penalties require the help of catalysts, usually transition-metal derivatives, which may be operated homogeneously or under the form of a thin film that coats an electrode. The latter arrangement is preferred since it allows compactness and avoids reactant separation problems. Identifying the factors that control the functioning of such devices and understanding their interplay are required for rational catalyst optimization and improved performance. Besides the catalytic reaction itself, two major controlling factors are (i) the transport of electrons from or to the electrode to regenerate the active form of the catalyst and (ii) the transport of the substrate from the bathing solution through the film toward the catalytic centers. In the above-listed reactions and in many others, protons are consumed or produced during catalysis. Proton-coupled electron transfer (PCET) reactions[6] thus play a key role in the catalytic cycle. The transport of protons and/or the acid and basic forms of the buffer often added to the solution may therefore influence the catalytic responses. In such systems, one should consider also that the transport of electrons through the film may be coupled with the transfer of protons. The purpose of the work reported herein was to investigate the interplay of these various, potentially governing factors in the framework of a reasonably general process. A completely general analysis would embark the reader in a taxonomic nightmare with no guarantee of actual generality. In contrast, a reasonably general reaction scheme should retain most of the essential controlling factors, with some simplifying assumptions, allowing a tractable analysis of their interplay. Scheme 1, with some accompanying simplifications and approximations, as detailed in the following study, represents such a reasonably general framework. It is represented for an oxidative process. Transposition to reduction is straightforward. One of the main simplifying assumptions is that the substrate is in large

Received: April 23, 2013
Published: June 12, 2013

dx.doi.org/10.1021/ja403656w | *J. Am. Chem. Soc.* 2013, 135, 10492−10502

Scheme 1. Electrocatalytic Oxidation of the Substrate A into the Products B in the Presence of an Acid−Base Couple (charge not shown) ZH/Z by Means of an Immobilized PH/Q + e$^-$ Catalyst Couple

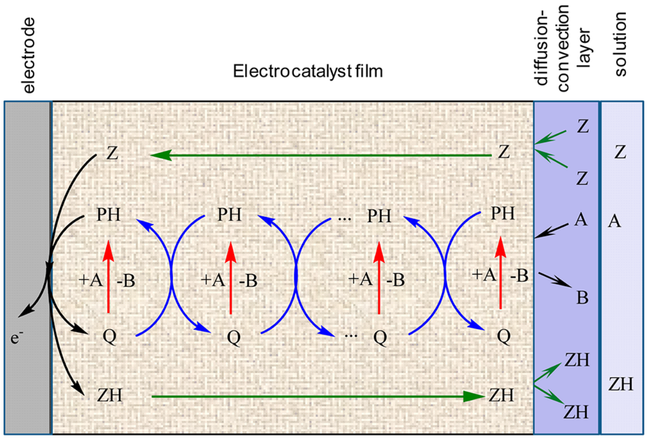

concentration in the solution and in the film, so large that it remains constant as it is the case when the solvent, e.g., water, is the substrate. This simplifying situation is considered in order to focus on the other factors, notably proton transfer and transport. Cases in which penetration and diffusion of the substrate through the film are rate-controlling factors may be treated when necessary by adaptation of the present and previous analyses.[7]

The kinetic responses expected for such processes will be discussed in the first part of this paper, as the result of interplay between the various rate-controlling factors. The second part will be devoted to the application of this methodology to the electrocatalytic oxidation of water by a cobalt oxide film in a family of thin-film oxidic catalysts[8] that have been shown to be promising candidates for direct solar water splitting systems,[9] in large part because of their capacity for self-repair.[10] Self-repair permits their operation under a wide range of pH conditions, including close-to-neutral pHs. Spectroscopic studies[11] of these cobalt-based catalysts (Co−OECs) have established a mixed valence $Co^{III/IV}$ resting state, and mechanistic studies[12] suggest a rapid, one-electron, one-proton equilibrium between $Co^{III}{-}OH$ and $Co^{IV}{-}O$ in which a phosphate species is the proton acceptor, followed by a chemical turnover-limiting process involving oxygen−oxygen bond coupling (Scheme 2). Subsequently, lower valence intermediates are rapidly oxidized to regenerate the resting state species (a net $3e^-$, $3H^+$ process), and thus the kinetics of these steps do not contribute to the overall rate law. As a consequence, the cobalt-based O_2-evolution catalyst may be analyzed according to a simple scheme (Scheme 1) that involves the PH ($Co^{IV}O{-}Co^{III}OH$) and Q ($Co^{IV}O{-}Co^{IV}O$) forms of the catalyst merely considering that $k_{cat} = 4 \times k_C$ in eqs 2 and 3. As porous materials, the accessibility of active sites distributed throughout the film is a key determinant of overall OER activity.[13]

Scheme 2. Electrocatalytic Oxidation of Water into the Products Dioxygen and Protons in the Presence of an Acid−Base Couple (charge not shown) ZH/Z (possibly H_3O^+/H_2O)

$$\begin{array}{lcl}
\text{4 times}\quad Co^{III}OH\text{-}Co^{IV}O + Z & \rightleftharpoons & Co^{IV}O\text{-}Co^{IV}O + ZH + e \\
Co^{IV}O\text{-}Co^{IV}O + 2\,H_2O & \xrightarrow{k_C} & Co^{II}OH_2\text{-}Co^{II}OH_2 + O_2 \\
Co^{IV}O\text{-}Co^{IV}O + Co^{II}OH_2\text{-}Co^{II}OH_2 & \xrightarrow{k > k_C} & Co^{III}OH\text{-}Co^{IV}O + Co^{III}OH\text{-}Co^{II}OH_2 \\
Co^{IV}O\text{-}Co^{IV}O + Co^{III}OH\text{-}Co^{II}OH_2 & \xrightarrow{k' > k_C} & Co^{III}OH\text{-}Co^{IV}O + Co^{III}OH\text{-}Co^{III}OH \\
Co^{IV}O\text{-}Co^{IV}O + Co^{III}OH\text{-}Co^{III}OH & \xrightarrow{k'' > k_C} & 2\,Co^{III}OH\text{-}Co^{IV}O \\
\hline
2\,H_2O + 4\,Z & \longrightarrow & O_2 + 4\,ZH + 4\,e
\end{array}$$

RESULTS AND DISCUSSION

1. Electrocatalytic Oxidation of a Substrate by Means of an Immobilized Proton−Electron Catalyst Couple.

Although any electrochemical nondestructive technique may be used to investigate the kinetic responses of systems like the one shown in Scheme 1, rotating-disk electrode voltammetry (RDEV) is particularly convenient and holds transport characteristics that are similar to those prevailing under preparative-scale conditions. Transport of the reactants in the solution to or from the film/solution may be controlled through the rotating rate, ω, which modulates the size, δ, of the diffusion-convection layer (Scheme 1):

$$\delta(\text{cm}) = 1.61 \times D(\text{cm}^2\text{s}^{-1})^{1/3} \times \nu(\text{cm}^2\text{s}^{-1})^{1/6}\omega(\text{rad s}^{-1})^{-1/2} \tag{1}$$

where D is the diffusion coefficient, ν is the kinematic viscosity, and ω is the rotation rate.

The aim of the analysis is to predict the current/potential curves under the control of the various transport and reactivity factors sketched in Scheme 1. A popular way of representing these relationships is the so-called "Tafel plot" relating the log of the current, or current density, to the electrode potential or to the overpotential (difference between the electrode potential and the equilibrium potential of the reaction being catalyzed).[14] In the following report we will use current densities rather than currents. Historically, the Tafel equation is the irreversible version of the more general Butler−Volmer equation, which describes the relationship between the kinetics of an electrochemical charge-transfer reaction, represented by the log of the current or current density, and its thermodynamics, represented by the overpotential. The ensuing Tafel plots of such reactions are usually linear, in which case they are characterized by their slope and by the value of the exchange current density, i.e., the current density at overpotential zero. The Tafel slope is related to the electrochemical transfer coefficient, α, in this case comprised between 0 and 1. This is often close to 0.5, which corresponds to a $F/2RT \ln 10$ Tafel slope. In fact the "Tafel" slope for electrocatalytic reactions in general, and in particular those depicted in Scheme 1, has no reason to systematically have such a value. The ensuing Tafel plots are not even necessarily linear. Strictly speaking, the current−potential relationships characterizing electrocatalytic systems, such as represented in Scheme 1, are not actual Tafel plots of electrochemical charge-transfer reactions. To conform to usage, we nevertheless retain the appellation Tafel plot in the very broad sense of a log current (or current density) vs overpotential relationship that would result from the interplay of the various rate-controlling factors of an electrocatalytic reaction. A methodology for describing the kinetics as a function of various controlling factors has been developed in the framework of RDEV for electrocatalytic electrode coatings in the 1980s.[7] It must, however, be extended in two directions to meet the requirements of the current study. The earlier approach was essentially focused on the catalytic plateau currents that are encountered with such systems at large overpotentials, whereas the study here is concerned with a description of the foot of the current−potential response, where

Table 1. Characteristic Current Densities[a]

rate-controlling phenomenon	characteristic current density	parameters, remarks
catalytic reaction	$I_k = Fk_{\mathrm{cat}}C_{\mathrm{cat}}d_{\mathrm{f}}$	$k_{\mathrm{cat}} = k_{\mathrm{2nd}}C_{\mathrm{subtr}}$: pseudo first-order rate constant of the catalytic reaction
proton−electron hopping	$I_{\mathrm{H},e} = \frac{FD_{\mathrm{H},e}C_{\mathrm{cat}}}{d_{\mathrm{f}}}$	$D_{\mathrm{H},e}$: proton−electron hopping diffusion coefficient (see text)
proton diffusion in the film	$I_{\mathrm{H,in}} = \frac{FD_{\mathrm{H,in}}C^0_{\mathrm{H}^+}}{d_{\mathrm{f}}}$	$D_{\mathrm{H,in}}$: proton diffusion coefficient in the film
diffusion of the buffer components in the film	$I_{\mathrm{ZH,in}} = \frac{FD_{\mathrm{ZH,in}}C^0_{\mathrm{ZH}}}{d_{\mathrm{f}}}$ $I_{\mathrm{Z,in}} = \frac{FD_{\mathrm{Z,in}}C^0_{\mathrm{Z}}}{d_{\mathrm{f}}}$	$D_{\mathrm{Z,H,in}}$, $D_{\mathrm{Z,in}}$: diffusion coefficients of ZH and Z in the film
proton diffusion in the solution and fast equilibration at the film solution interface	$I_{\mathrm{H,out}} = \frac{FD_{\mathrm{H,out}}C^0_{\mathrm{H}^+}}{\delta}$	$D_{\mathrm{H,out}}$: proton diffusion coefficient in the solution.
diffusion of the buffer components in the solution and fast equilibration at the film solution interface	$I_{\mathrm{ZH,out}} = \frac{FD_{\mathrm{ZH,out}}C^0_{\mathrm{ZH}}}{\delta}$ $I_{\mathrm{Z,out}} = \frac{FD_{\mathrm{Z,out}}C^0_{\mathrm{Z}}}{\delta}$	$D_{\mathrm{ZH,out}}$, $D_{\mathrm{Z,out}}$: diffusion coefficients of ZH and Z in the solution.

[a] d_{f}: film thickness. δ: diffusion layer thickness (eq 1). C_{cat}: total concentration of the catalyst in the film. C_{subtr}: concentration of substrate in the film. C^0_{H},C^0_{ZH},C^0_{Z}: concentrations of H^+, ZH, and Z in the solution, respectively.

the contribution of reactant transport in the solution is expected to be minimal, although not necessarily negligible. The other extension concerns the coupling between electron transfer and proton transfer in electrocatalytic films of the type shown in Scheme 1. PCET reactions have been the object of intense investigation during the past decade with particular emphasis on concerted proton−electron transfers (CPET) in which proton and electron are transferred during a single step.[6,15] In the electrocatalytic films under discussion, coupling between proton and electron transfers comes into play at two levels. One involves the proton−electron hopping through the film, which replaces the single electron hopping of previous studies. The other concerns the production of protons at the electrode from the oxidation of the reduced form of the catalyst (PH yielding Q + H^+) in the presence or absence of a buffer (ZH/Z).

Electrocatalytic films such as those that are object of the present analysis are porous structures where the solvent can penetrate and the substrate, products, solvated protons, and buffer components can diffuse freely in the pores. Proton−electron hopping conduction takes place in the solid sections of the structure where continuity is ensured even at the cost of dynamic percolation.[16] On the whole, the various elements of the structure can be averaged and considered as equivalent to a homogeneously distributed set of catalytic sites between which protons and electrons can hop in a coupled manner and through which substrate, products, solvated protons, and buffer components may diffuse freely through an equivalent isotropic film as sketched in Scheme 1 in a similar manner as already described for polymer electrode coatings.[17]

Additional assumptions, approximations, or restrictions are: (i) The analysis is restricted here to the case where catalysis and proton−electron hopping are performed by the same centers. If necessary, it could be extended to cases where the catalytic and the conduction centers are not the same as previously illustrated with electron-hopping examples. (ii) Proton−electron hopping through the film may follow a concerted pathway (CPET) that goes directly from PH to Q or two stepwise pathways, a PET pathway (proton transfer first, from PH to P, followed by electron transfer between P and Q) or a EPT pathway (electron transfer first, between PH and QH, followed by proton transfer, from QH to Q). We consider the case where the proton transfers involved in the stepwise pathways are fast and unconditionally at equilibrium. It is shown in the Supporting Information (SI) that all three pathways are equivalent. (iii) The electron-transfer reaction at the electrode regenerating Q from the oxidation of PH with production of a proton may likewise follow concerted or stepwise pathways. We consider the cases where the concerted reaction is fast and unconditionally at equilibrium and where the proton- and electron-transfer reactions are all fast and unconditionally at equilibrium in the stepwise pathways. (iv) As mentioned in the Introduction, the substrate, A, is assumed to be in large concentration in the solution and in the film, so large that it remains constant. (v) We further assume that the partition coefficients of H^+, ZH, and Z between the solution in the pores and the solution outside the film are approximately equal to unity.

In the following, each current density is defined as the current intensity divided by the projection of the real surface area on the geometrical electrode surface. It is convenient to represent each of the factors by a characteristic current density as summarized in Table 1. The expressions of these characteristic current densities result from the following analysis.

Proton−electron hopping through the film may be likened to a linear diffusional transport obeying the Fick's diffusional law as shown in the SI (1.1), assuming that there is no electric field effect within the film because the hopping process does not involve net charge transport. Association with the catalytic reaction (Scheme 1) leads to the following steady-state expressions of the Fick's law modified by a kinetic catalytic term.

$$D_{\mathrm{H},e}\frac{d^2C_{\mathrm{PH}}}{dx^2} + k_{\mathrm{cat}}C_{\mathrm{Q}} = 0 \tag{2}$$

$$D_{\mathrm{H},e}\frac{d^2C_\mathrm{Q}}{dx^2} - k_\mathrm{cat}C_\mathrm{Q} = 0 \tag{3}$$

where x is the distance from the electrode and the C is the concentration of the subscript species.

Insofar the proton-transfer steps are at equilibrium (condition ii above) eqs 2 and 3 apply irrespective of the mechanism of proton−electron hopping, albeit $D_{\mathrm{H},e}$ may have different expressions in each case (SI, 1.1).

Condition (iii) above implies that the following equivalent expressions of the Nernst law apply at the electrode surface (x = 0):

$$\frac{(C_\mathrm{Q})_{x=0}\times(C_{\mathrm{H}^+})_{x=0}}{(C_\mathrm{PH})_{x=0}\times C^0} = \exp\left[\frac{F}{RT}\left(E - E^0_{\mathrm{Q+H^+/PH}}\right)\right]$$

$$\frac{(C_\mathrm{Q})_{x=0}\times(C_\mathrm{ZH})_{x=0}}{(C_\mathrm{PH})_{x=0}\times(C_\mathrm{Z})_{x=0}} = \exp\left[\frac{F}{RT}\left(E - E^0_{\mathrm{Q+ZH/PH+Z}}\right)\right]$$

where the two standard potentials characterizing the catalyst PH/Q couple are related by

$$E^0_{\mathrm{Q+ZH/PH+Z}} = E^0_{\mathrm{Q+H^+/PH}} + \frac{RT}{F}\ln\left(\frac{K_\mathrm{a}}{C^0}\right) \tag{4}$$

(K_a is the acidity constant of ZH, C^0 is a normalizing concentration, conveniently taken as equal to 1 M.)

The above Nernst equations may also be expressed as a function of the overpotential $\eta = E - E^\mathrm{eq}_\mathrm{A}$, where E^eq_A is the equilibrium potential of the reaction to be catalyzed. It is not necessarily a standard potential and may contain reactant concentration terms, as e.g., the pH, according to the reaction under consideration and to the most convenient definition the overpotential in each particular case.

Integration of eqs 2 and 3, taking into account the appropriate boundary conditions and noting that we are interested in what happens in the foot of the current responses, leads to (see SI 1.2, Table 1):

$$\frac{(C_\mathrm{Q})_{x=0}}{C_\mathrm{cat}} = \frac{I}{\sqrt{I_k I_{\mathrm{H},e}}\tanh\left(\sqrt{\frac{I_k}{I_{\mathrm{H},e}}}\right)} \tag{5}$$

1.1. High Buffer Concentrations (Insignificant Buffer Consumption Within the Catalyst Film).

Joint control by catalytic reaction and proton−electron hopping is observed when the concentration of buffer is so large that the concentrations of its two components are constant throughout the film. The buffer serves to neutralize the protons generated by the CPET electrode reaction and to convert, at least partially, their diffusion toward the solution into a ZH diffusion toward the solution and a diffusion of Z toward the electrode and, additionally, to participate as reactants to the CPET electrode reaction. Then the Tafel plots are predicted to obey the following equation (see SI 1.2):

$$\log I = \log I_0 + \frac{F}{RT\ln 10}\eta \tag{6}$$

where I_0, the current density at zero overpotential, can be considered as an exchange current density by analogy with electrochemical reaction Tafel plots. It can be expressed as:[18]

$$\begin{aligned}\log I_0 &= \log\left[\frac{C^0}{C^0_{\mathrm{H}^+}}\sqrt{I_k I_{\mathrm{H},e}}\tanh\left(\sqrt{\frac{I_k}{I_{\mathrm{H},e}}}\right)\right] + \frac{F(E^\mathrm{eq}_\mathrm{A} - E^0_{\mathrm{Q+H^+/PH}})}{RT\ln 10}\\ &= \log\left[F\frac{C^0}{C^0_{\mathrm{H}^+}}C_\mathrm{cat}k_\mathrm{cat}d_\mathrm{f}^\mathrm{opt}\tanh\left(\frac{d_\mathrm{f}}{d_\mathrm{f}^\mathrm{opt}}\right)\right] + \frac{F(E^\mathrm{eq}_\mathrm{A} - E^0_{\mathrm{Q+H^+/PH}})}{RT\ln 10}\end{aligned} \tag{7}$$

with

$$d_\mathrm{f}^\mathrm{opt} = \sqrt{\frac{D_{\mathrm{H},e}}{k_\mathrm{cat}}} \tag{8}$$

The Tafel plots are thus predicted to have a $F/RT\ln 10$ slope and to depend on film thickness as pictured in Figure 1a. Below the optimal value, $d_\mathrm{f}^\mathrm{opt}$, the current density response increases in proportion to film thickness, whereas beyond $d_\mathrm{f}^\mathrm{opt}$, the response plateaus off. This is best represented as a variation of the exchange current density with the film thickness as shown in

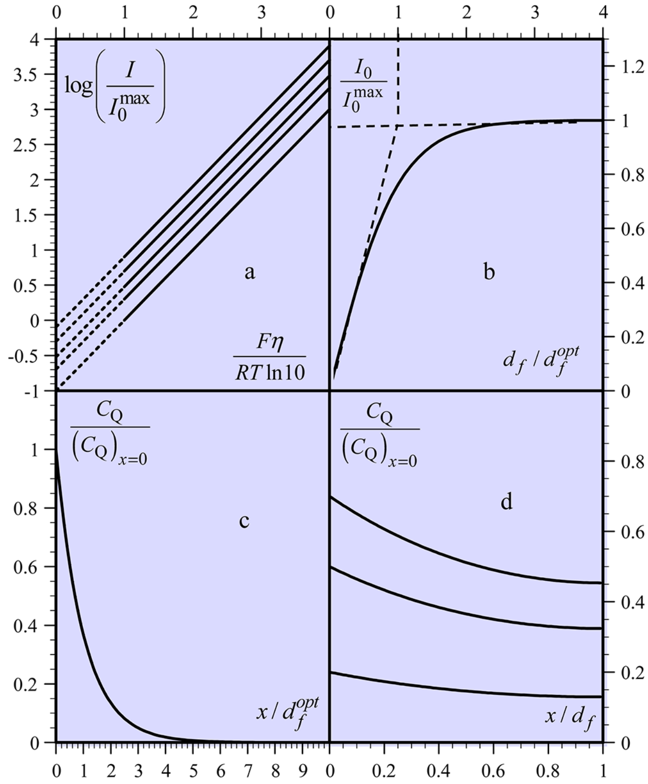

Figure 1. Large buffer concentrations. (a) Tafel plots predicted for a series of increasing thicknesses from bottom to top. (b) Variation of the current density with the film thickness (relative to the optimal film thickness, $d_\mathrm{f}^\mathrm{opt}$) at $\eta = 0$. I_0 and I_0^max are defined in eqs 7, 7′, 9 and 9′, respectively. For d_f see eq 8. (c) Concentration profile of Q (relative to the concentration of Q at the electrode−film interface) for mixed control of the catalytic reaction and the diffusion-like proton−electron hopping under pure kinetic conditions for a film thickness $d_\mathrm{f} = 10\times d_\mathrm{f}^\mathrm{opt}$. (d) Concentration profile of Q (relative to catalyst concentration in the film) as a function of increasing electrode potential (from bottom to top) for a film of thickness equal to $d_\mathrm{f}^\mathrm{opt}$.

Figure 1b where the maximal value reached by I_0, noted $I_0^{\max}$, may be expressed by[19]

$$I_0^{\max} = F\frac{C^0}{C^0_{\mathrm{H}^+}}C_{\mathrm{cat}}\sqrt{k_{\mathrm{cat}}D_{\mathrm{H},e}}\exp\left[\frac{F(E_{\mathrm{A}}^{\mathrm{eq}} - E^0_{\mathrm{Q+H^+/PH}})}{RT}\right]$$
$$= F\frac{C^0}{C^0_{\mathrm{H}^+}}C_{\mathrm{cat}}k_{\mathrm{cat}}d_{\mathrm{f}}^{\mathrm{opt}}\exp\left[\frac{F(E_{\mathrm{A}}^{\mathrm{eq}} - E^0_{\mathrm{Q+H^+/PH}})}{RT}\right] \quad (9)$$

In other words, eq 7 may be recast as

$$I_0 = I_0^{\max}\tanh\left(\frac{d_{\mathrm{f}}}{d_{\mathrm{f}}^{\mathrm{opt}}}\right) \quad (10)$$

More rigorously, the variation of the exchange current density with the film thickness (Figure 1b) shows two limiting behaviors:

$$\text{when } d_{\mathrm{f}}/d_{\mathrm{f}}^{\mathrm{opt}} \to 0\text{: } I_0 \to I_0^{\max}\frac{d_{\mathrm{f}}}{d_{\mathrm{f}}^{\mathrm{opt}}}$$
$$= F\frac{C^0}{C^0_{\mathrm{H}^+}}C_{\mathrm{cat}}k_{\mathrm{cat}}\exp\left[\frac{F(E_{\mathrm{A}}^{\mathrm{eq}} - E^0_{\mathrm{Q+H^+/PH}})}{RT}\right] \times d_{\mathrm{f}}$$

The exchange current density is governed solely by the catalytic reaction, being consequently proportional to film thickness.

When $d_{\mathrm{f}}/d_{\mathrm{f}}^{\mathrm{opt}} \to \infty$, then $I_0 \to I_0^{\max}$

(as given by eq 10).

The exchange current density is then independent of film thickness, being under the mixed control of the catalytic reaction and the diffusion-like proton−electron hopping under "pure kinetic conditions".[20] Under these conditions, the concentration profile of Q (Figure 1c) is independent of the film thickness as a result of mutual compensation of catalytic reaction and diffusion-like proton−electron hopping. It is confined in a reaction-diffusion layer of $(D_{\mathrm{H},e}/k_{\mathrm{cat}})^{1/2}$ thickness.

It follows that there is no advantage to continuing to increase the thickness much beyond $d_{\mathrm{f}}^{\mathrm{opt}}$. It suffices that I_0 reaches a value equal to $I_0^{\max}$ within experimental uncertainty. As shown in Figure 1d, increasing the electrode potential shifts the position of the PH/Q+H$^+$ equilibrium at the electrode−film interface. This consequently leads to greater values of C_{Q} throughout the film and a greater current density (Figure 1a).

We note that the current response is independent of the rotation rate. In other words the "Koutecky−Levich" (KL) plots are horizontal. KL plots in RDEV are plots of the inverse of current density against the inverse of the square root of the rotation rate.[21] In the present discussion they may be taken at any potential along the Tafel plot. When they are linear, the intercept is representative of phenomena occurring in the film, whereas the slope reflects reactant transport in the solution. This approach is actually not general because KL plots are not always linear. Examples of nonlinear KL plots have been given in the analysis of redox polymer film responses.[7] Observing a nonlinear KL plot does not mean that the events taking place in the film are not separable from transport in solution, but that it requires a somewhat less straightforward procedure. Examples will be given in the following analysis.

1.2. Buffer-Free Conditions. Nonlinear KL plots are observed when no buffer has been introduced in the solution, which represents the converse extreme of the case where the whole system was completely buffered as examined earlier. Then (see SI 1.2):

$$\frac{(C_{\mathrm{H}^+})_{x=0}}{C^0_{\mathrm{H}^+}} = I\left(\frac{1}{I_{\mathrm{H,in}}} + \frac{1}{I_{\mathrm{H,out}}}\right) + 1$$

(symbols are defined in Table 1). An extreme of a nonbuffered situation is when the production of protons at the electrode is much larger than the proton concentration in solution, i.e., $(C_{\mathrm{H}^+})_{x=0} \gg C^0_{\mathrm{H}^+}$, leading to

$$\frac{(C_{\mathrm{H}^+})_{x=0}}{C^0_{\mathrm{H}^+}} = I\left(\frac{1}{I_{\mathrm{H,in}}} + \frac{1}{I_{\mathrm{H,out}}}\right)$$

with

$$I_{\mathrm{H,in}} = \frac{FD_{\mathrm{H,in}}C^0_{\mathrm{H}^+}}{d_{\mathrm{f}}}, \qquad I_{\mathrm{H,out}} = \frac{FD_{\mathrm{H,out}}C^0_{\mathrm{H}^+}}{\delta}$$

In most cases the RDEV diffusion-convection layers, δ, are larger than the catalyst film thickness, d_{f} (of the order of 10^{-2}–10^{-3} cm against 10^{-4}–10^{-6} cm, respectively). Since the ratio of the diffusion coefficients is not very different from 1, $I_{\mathrm{H,in}} \gg I_{\mathrm{H,out}}$, and therefore:

$$\frac{(C_{\mathrm{H}^+})_{x=0}}{C^0_{\mathrm{H}^+}} = \frac{I}{I_{\mathrm{H,out}}}$$

In this case, the diffusion of solvated protons out of the film controls the current density jointly with proton−electron hopping. The Tafel plots are then expected to obey eq 11 as represented in Figure 2a (see SI 1.2).

$$\log I = \frac{1}{2}\log(I_0 \times I_{\mathrm{H,out}}) + \frac{F}{2RT\ln 10}\eta \quad (11)$$

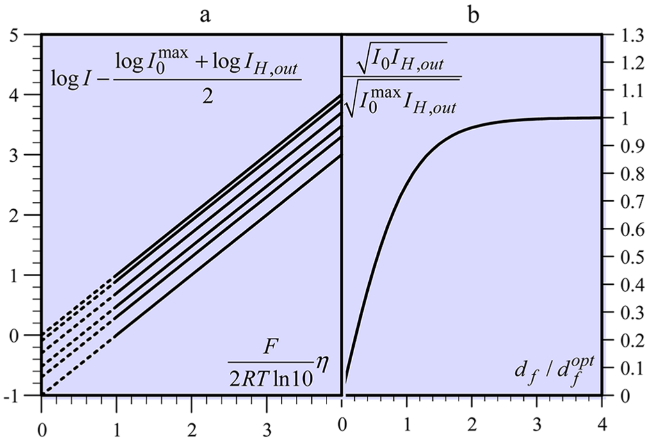

Figure 2. No buffer. (a) Tafel plots predicted for a series of increasing thicknesses from bottom to top. (b) Variation of the current density with the film thickness (relative to the optimal film thickness) at $\eta = 0$. I_0 and $I_0^{\max}$ are defined in eqs 7, 7′, 9 and 9′, respectively. $I_{\mathrm{H,out}}$ is defined in Table 1.

I_0 being given by eqs 7, 7′ or (9, 9′ and 10) and $I_{\mathrm{H,out}}$, which characterizes the proton transport in solution, is defined in Table 1. In the first term of eq 11, I_0 is inversely proportional to $C^0_{\mathrm{H}^+}$ (eq 7′), whereas $I_{\mathrm{H,out}}$ is directly proportional to $C^0_{\mathrm{H}^+}$ (Table 1) making the first term of eq 11 independent of pH. The Tafel plot predicted by eq 11 may, however, be pH dependent if $E_{\mathrm{A}}^{\mathrm{eq}}$, which serves as reference in the definition of the overpotential, depends itself on pH.

The Tafel slope is $F/2RT \ln 10$. KL plots are not linear, even if they may look linear within the necessarily limited range of accessible rotation rates. Figure 3 illustrates this misleading state of affairs. It also shows that, in such a situation, the slope of the apparently linear KL relationship varies with the electrode potential unlike what is expected with truly linear KL relationships.

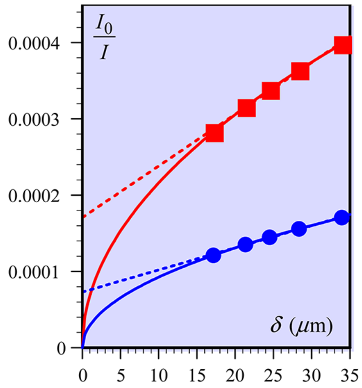

Figure 3. KL plots in absence of buffer: I_0/I as function of diffusion layer thickness δ, for two different values of the overpotential: $\eta = 0.4$ (red squares) and 0.5 (blue dots) with $I_0 = 2 \times 10^{-10}$ A cm^{-2}, $D_{H,out} = 5 \times 10^{-5}$ cm^2 s^{-1}, $C^0_{H^+} = 10^{-6}$ M. Dots correspond to typical rotation rates: 2500, 1600, 1225, 900, and 625 rpm (using eq 1 with $\nu = 10^{-2}$ cm^2/s). Dotted lines correspond to purposely forced linear fitting of the data corresponding to rotation rates between 625 and 2500 rpm.

One could be tempted to define an exchange current density for this case as being the current density at overpotential zero. The "exchange current density" thus obtained, $(I_0 \times I_{H,out})^{1/2}$ is, however, somewhat unusual as compared to conventional electrochemical reactions in the sense that it incorporates the rate of proton transport in the solution and therefore depends on the RDEV rotation rate (through $I_{H,out}$ and eq 1).

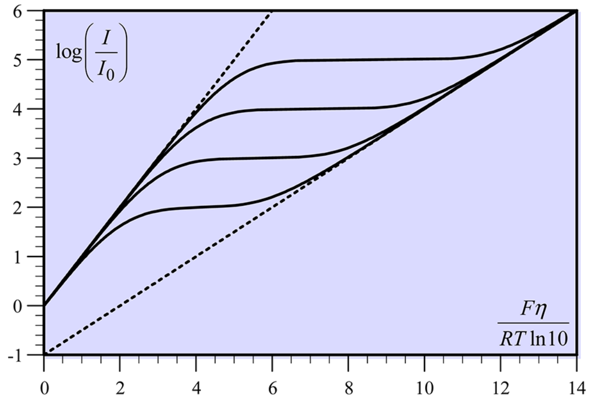

Figure 4. Tafel plots (full lines) predicted for intermediate buffer concentrations, showing the passage from joint control by catalytic reaction and proton−electron hopping (upper dotted line) to joint control by catalytic reaction, proton−electron hopping, and proton diffusion (lower dotted line) for a series of $I_{Z,out}/I_0$ values (10, 100, 1000, 10 000, 100 000 from bottom to top) corresponding to increasing value of buffer concentration ($I_{Z,out} = FD_{Z,out}C^0_Z/\delta$). Figure has been plotted for the following values of the other parameters: $C^0_{ZH}/C^0_Z = 1$ (the pH is equal to the ZH pK_a) and $I_0/I_{H,out} = 100$.

This exchange current density varies with the film thickness as shown in Figure 2b, first proportionally for $d_f \ll d_f^{opt}$ then reaching saturation with a value $(I_0^{max} \times I_{H,out})^{1/2}$ in which the expression of I_0^{max} is the same as in eqs 9 and 9′ introduced previously in the case of perfect buffering.

1.3. Intermediate Buffer Concentrations. For intermediate buffer concentrations, the same assumptions concerning proton transfer and transport lead to a general implicit expression of the Tafel plots given by eq 12 (see SI 1.2):

$$\frac{F}{RT \ln 10}\eta = \log\left(\frac{I}{I_0}\right) + \log\left[\frac{I_{Z,out}}{I_0}\frac{I_0}{I_{H,out}}\frac{\left(\frac{I}{I_0}\frac{I_0}{I_{Z,out}} - 1\right) + \sqrt{\left(\frac{I}{I_0}\frac{I_0}{I_{Z,out}} - 1\right)^2 + 4\left(\frac{I}{I_0}\frac{I_0}{I_{Z,out}} + \frac{C^0_{ZH}}{C^0_Z}\right)\frac{C^0_Z}{C^0_{ZH}}\frac{I_{Z,out}}{I_0}\frac{I_0}{I_{H,out}}}}{2}\right] \tag{12}$$

The exchange current density, I_0, is defined by eqs 7, 7′ or 9, 9′ and 10. The buffer base and proton solution transport characteristic currents, $I_{Z,out}$ and $I_{H,out}$ respectively, are defined in Table 1.

Equation 12 allows the construction of a typical series of such Tafel plots as shown in Figure 4. It is seen that, at a given value of the buffer concentration, the high-buffer behavior tends to be reached at low overpotentials, whereas the no-buffer behavior tends to be reached oppositely at high overpotentials. In between these two limits the Tafel plots plateaus off. The current density is then $I = I_{Z,out}$, obtained when the concentration of the buffer base at the electrode surface comes close to zero as a result of the reaction with the catalytically generated protons. The current response is then solely controlled by the transport of the buffer base from the solution toward the film.

One conclusion of this section is that the combination of the various controlling factors, catalytic reaction, and proton−electron hopping conduction through the film as well as proton transfer and transport may result in quite different Tafel slopes, $F/RT \ln 10$, $F/2RT \ln 10$ or 0. Tafel plots such as those represented in Figure 4 are quite unusual if one refers to conventional electrochemical reactions. Illustrating experimental examples of such behaviors are given in the next section, which is devoted to application of the above analyses and equations to an illustrative experimental example.

2. Application to a Cobalt-Based O_2-Evolution Catalyst.

The cobalt-based O_2-evolution catalyst may be analyzed according to Scheme 1 and the ensuing methodology simply considering that $k_{cat} = 4 \times k_C$ in eqs 2 and 3. In this analysis, the overpotential is defined as

$$\eta = E - E^{eq}_{O_2/H_2O} \text{ with}$$

$$E^{eq}_{O_2/H_2O} = E^0_{O_2/H_2O} - \frac{RT \ln 10}{F}\left(pH - \frac{1}{4}\log\left(\frac{P_{O_2}}{P^0}\right)\right) \tag{13}$$

and $E^0_{O_2/H_2O}$ = 1.23 V vs NHE.[22] A series of RDEV experiments was carried as a function of two main parameters, the concentration of the buffer (including the absence of buffer) and the film thickness. The stationary current density was measured point by point at a series of decreasing electrode potential values and at different rotation rates.

2.1. High Buffer Concentrations (≥100 mM P_i). In presence of a large amount of buffer (0.1 M NaP_i, at pH 7), Tafel plots with a $F/RT \ln 10$ (1/59 mV at 297 K) slope are obtained for a series of film thicknesses (Figure 5a). They were observed to be independent of rotation rates (from 625 to 2500 rpm). The current density increases with film thickness before reaching saturation (Figure 5a). These observations are what is anticipated for joint control by the catalytic reaction and by proton−electron hopping as discussed in the preceding section.

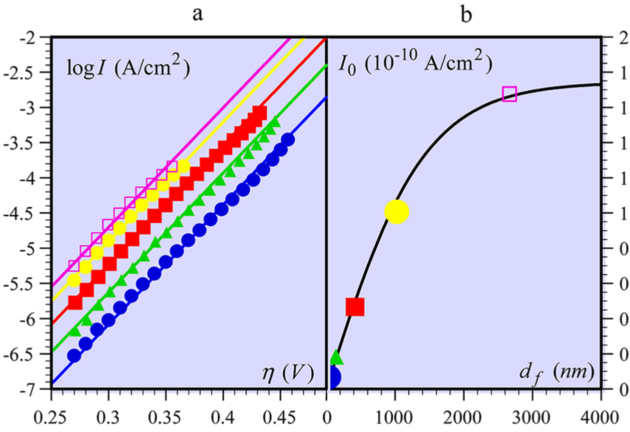

Figure 5. (a) Tafel plots of Co−OEC films operated in 0.1 M KP_i pH 7 electrolyte with increasing film thicknesses: 40 nm (blue dots), 120 nm (green triangles), 400 nm (red squares), 1024 nm (yellow diamonds), 2665 nm (magenta open squares) (for the estimation of the film thickness, see Experimental Section). Rotation rate: 1000 rpm. The slope of the solid lines is $F/RT \ln 10$. (b) Variation of the exchange current density with the film thickness. Solid line: fitting according to $I_0 = I_0^{max}\tanh(d_f/d_f^{opt})$ (eq 10).

The variation of the Tafel intercept at η = 0 (exchange current density) is thus expected to follow the variation shown in Figure 1b and to obey eqs 7, 7′, 8, 9, and 9′. This is what is indeed seen in Figure 5b, while application of these eqs 7−9 leads to

$$d_f^{opt} = \sqrt{\frac{D_{H,e}}{k_{cat}}} = 1440 \text{ nm} \tag{14}$$

and

$$I^{max}_{0,pH=7} = 1.75 \times 10^{-10} \text{A/cm}^2 \tag{15}$$

on the understanding that $E^{eq}_{A,pH=7}$ is then given by eq 13 with P_{O_2}/P^0 = 0.2 and pH = 7, i.e., $E^{eq}_{A,pH=7}$ = 0.807 V vs NHE.

2.2. Buffer-Free Conditions. Tafel plots acquired at pH 6 in absence of buffer display a $F/2RT \ln 10$ slope at various rotation rates for various film thicknesses (Figure 6). In this case the overpotential is defined using a value of $E^{eq}_{O_2/H_2O}$ corresponding to pH 6 by application of eq 13 ($E^{eq}_{A,pH=6}$ = 0.866 V vs NHE). These data are distinct from the background currents associated with the RDE surface alone and are unaltered with changing the ionic strength, supporting electrolyte, or the elimination of CO_2, and therefore carbonate, from the electrolyte. It clearly appears that the response is dependent on film thickness thus ruling out a limitation by the PCET kinetics at the electrode surface. As detailed in the preceding section, the $F/2RT \ln 10$ slopes are coherent with a catalytic PCET process with water as proton acceptor associated with proton−electron hopping and jointly controlled by proton diffusion toward the solution in the absence of buffer. The intercept, logarithm of the current density at zero overpotential, is then $\log((I_{H,out} \times I_0)^{1/2})$. It allows access to the same intrinsic information on the system as in the high buffer concentration situation, yet taking into account the diffusion properties of the proton as required for the estimation of $I_{H,out}$. Because it is partially controlled by proton diffusion toward the solution, the current response is sensitive to the rotation rate of the electrode. This dependence is reported quantitatively in Figure 7a where the variation of $I_{H,out} \times I_0$ with $1/\delta$ is displayed and indeed obeys the simple proportionality predicted from the application of eq 10 and the definition of $I_{H,out}$ in Table 1:

$$I_{H,out} \times I_0 = FD_{H,out}C^0_{H^+}I^{max}_{0,pH=6}\tanh\left(\frac{d_f}{d_f^{opt}}\right) \times \frac{1}{\delta}$$

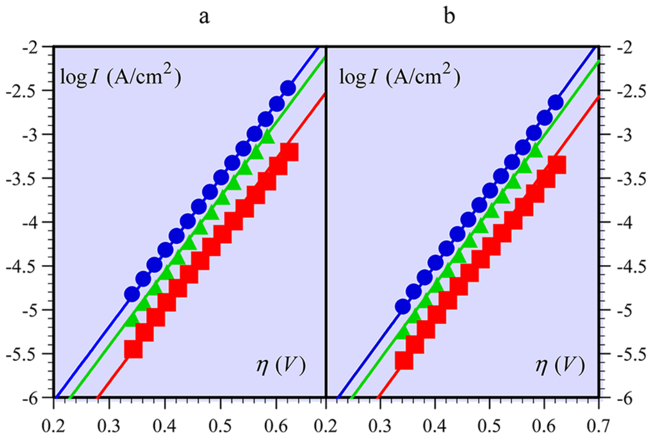

Figure 6. Tafel plots of Co−OEC films operated in 0.1 M $NaClO_4$ pH 6 electrolyte with no buffer present as a function of film thickness (in nm) 48 (red squares), 200 (green triangles), 575 (blue dots) at two rotation rates. (a) 2500 and (b) 625 rpm (data at other rotation rates are given in the SI). The slope of the solid lines is $F/2RT \ln 10$.

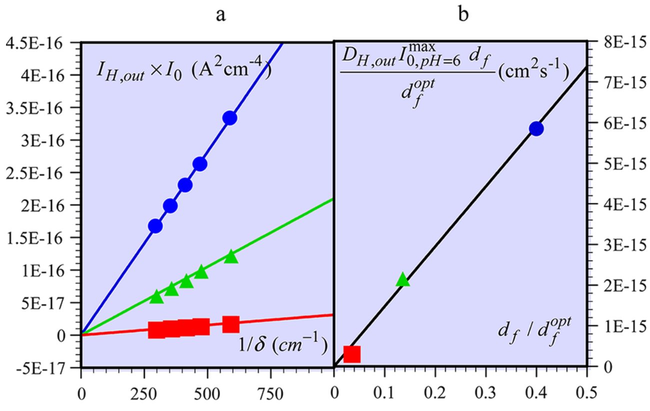

Figure 7. (a) $I_{H,out} \times I_0$ as function of $1/\delta$ (using eq 1 with $D = 5 \times 10^{-5}$ cm^2/s and $\nu = 10^{-2}$ cm^2/s)[21] for films of various thicknesses (in nm) 48 (red square), 200 (green triangles), 575 (blue dots). (b) Slopes of the straight lines in (a).

Since the three films examined in Figure 7 are much thinner than d_f^{opt} (1440 nm), the above equation becomes

$$I_{H,out} \times I_0 = FD_{H,out}C^0_{H^+}I^{max}_{0,pH=6}\frac{d_f}{d_f^{opt}} \times \frac{1}{\delta}$$

A simple proportionality to film thickness is indeed observed as reported in Figure 7b, which plots the slopes of the straight lines in Figure 7a against the film thickness under the form of a $D_{H,out}I^{max}_{0,pH=6}/d_f^{opt}$ vs d_f/d_f^{opt} diagram, the slope of which, $D_{H,out}I^{max}_{0,pH=6}/d_f^{opt}$, may be used to estimate $D_{H,out}$, after $I^{max}_{0,pH=6} = 1.75 \times 10^{-10}$ A/cm², equal to $I^{max}_{0,pH=7}$ (eq 15) by application of eq 9′. The value thus obtained for $D_{H,out}$, 8.5×10^{-5} cm²/s, is in excellent agreement with literature values (9.3×10^{-5} cm²/s),[23] showing the excellent consistency of the data obtained with high buffer concentrations on the one hand and those obtained with no buffer at all on the other.

The effect of varying the pH is displayed in Figure 8.[24] As shown in the first section (eq 11), the variation of the Tafel plots with pH are predicted to follow the variation of $E_A^{eq} = E^{eq}_{O_2/H_2O}$ (eq 13), which served as reference for the definition of the overpotential. The results are therefore best represented by plotting log I vs the electrode potential, E, rather than vs η, leading as expected to a pH-independent plot as indeed seen in Figure 8.

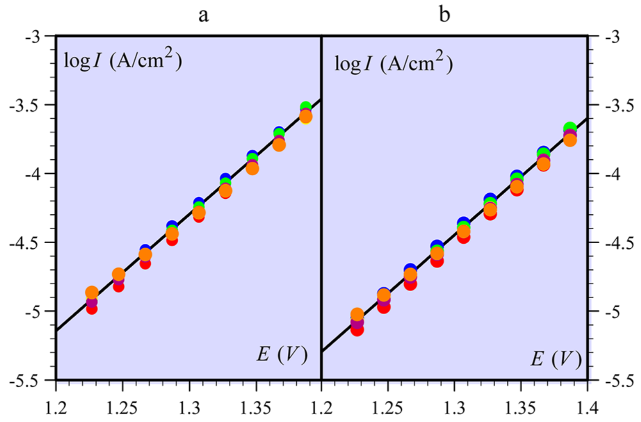

Figure 8. Tafel plots of a 200 nm Co−OEC films operated in operated in 0.1 M NaClO$_4$ with no buffer present, pH: 6.0 (blue), 6.2 (green), 6.4 (red), 6.6 (yellow), 6.8 (magenta), 7.2 (orange), at two rotation rates. (a) 2500 and (b) 625 rpm (data at other rotation rates are given in the SI). The slopes of the straight lines are $F/2RT$ ln 10.

2.3. Weakly Buffered Electrolytes (0.3−10 mM P$_i$).

The mechanism thus established is further confirmed by the results obtained in weakly buffered solutions, which are displayed in Figure 9. The Tafel plots there are strikingly similar to the predictions displayed in Figure 4. Whereas a F/RT ln 10 slope is observed at low overpotential, a $F/2RT$ ln 10 slope is observed at high overpotential with a transition that depends both on buffer concentration and rotation rate. From the intercepts of the F/RT ln 10 slope straight lines we obtain $I_0 = 2.7 \times 10^{-11}$ A/cm² in agreement with the data shown in Figure 5b, and from the intercepts of the $F/2RT$ ln 10 slope straight lines we obtain $I_{H,out} \times I_0$ as a function of $1/\delta$, thus leading to $D_{H,out} = 8 \times 10^{-5}$ cm²/s in full agreement with the previous buffer-free experiments.

The knowing I_0 as well as $I_{H,out}$ at each rotation rate, the whole set of data can be fit at any buffer concentration with a single parameter, $D_{Z,out}$, through $I_{Z,out} = FD_{Z,out}C^0_Z/\delta$ according to eq 12. This is in line with the fact that the transition between both limiting behaviors is controlled by buffer diffusion in solution.[25] Fitting, as shown in Figure 9 leads to $D_{Z,out} = 6 \times 10^{-6}$ cm²/s in agreement with literature values of the diffusion coefficient of PO$_4$H^{2-} (7.6×10^{-6} cm²/s).[26]

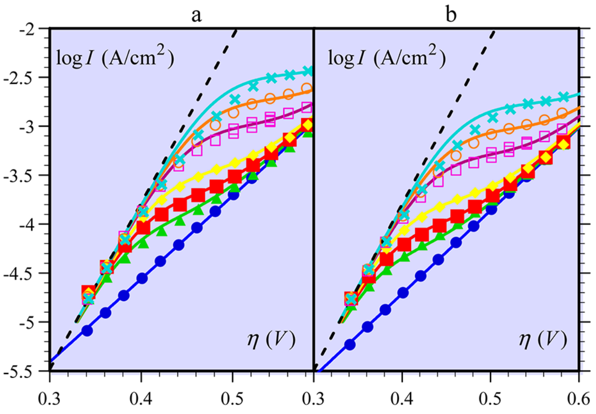

Figure 9. Tafel plots of a 200 nm Co−OEC films operated in 0 (blue dots), 0.3 (green solid triangles), 0.55 (red solid squares), 1 (yellow solid diamonds), 3 (magenta open squares), 5.5 (orange open diamonds), 10 (cyan cross) mM NaP$_i$ pH 6 electrolyte with 0.1 M NaClO$_4$ as supporting electrolyte at various rotation rate. (a) 2500 and (b) 625 rpm data at other rotation rates are given in the SI). The slopes of the straight lines are F/RT ln 10 (dashed black) and $F/2RT$ ln 10 and (solid blue).

The effect of film thickness was systematically investigated at a low P$_i$ concentration (3 mM) at pH 6 at various rotation rates (Figure 10). The data are satisfactorily fitted with eq 12 using the same diffusion parameters as above, i.e. $D_{H,out} = 8 \times 10^{-5}$ cm²/s and $D_{Z,out} = 6 \times 10^{-6}$ cm²/s as well as the same intrinsic parameter $I^{max}_{0,pH=6} = 1.75 \times 10^{-10}$ A/cm². This confirms the full consistency of our proposed mechanism.

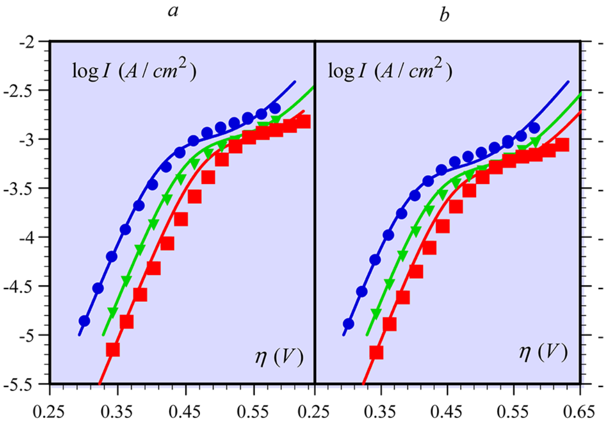

Figure 10. Tafel plots of Co−OEC films operated in 3 mM NaP$_i$ pH 6 electrolyte with 0.1 M NaClO$_4$ as supporting electrolyte with increasing film thicknesses (red squares) 48 (green triangles) 200 (blue dots) 575 nm at various rotation rate. (a) 2500 and (b) 625 rpm (data at other rotation rates are given in the SI). The solid colored lines correspond to fitting of data.

2.4. Kinetic and Thermodynamic Parameters of Co−OEC.

One remarkable aspect of our mechanistic analysis is that the data obtained at high buffer concentrations, with no buffer at all and in weakly buffered solutions, are perfectly consistent being in agreement with the same set of kinetic and thermodynamic characteristics. It is worth having a closer look at what can be precisely derived from the experimental data in terms of kinetic and thermodynamic characteristics. The rate constant of the catalytic reaction, k_{cat}, the equivalent diffusion coefficient of proton−electron hopping, $D_{\text{H},e}$ and the standard potential of the catalyst, $E^0_{\text{Q+ZH/PH+Z}}$ (or $E^0_{\text{Q+H}^+/\text{PH}}$) are three unknowns related by two equations deriving from the experimental determination of $D_{\text{H},e}/k_{\text{cat}}$ from d_f^{opt} (eq 8) and $k_{\text{cat}}C_{\text{cat}}\exp[-(F/RT)(E^0_{\text{Q+ZH/PH+Z}}$ or $E^0_{\text{Q+H}^+/\text{PH}})]$ from $I_0^{\max}$ (eq 9). At the present stage, we do not know these three parameters independently from one another. Progress in this direction will most probably require resorting to faster electrochemical techniques in order to sense the proton−electron hopping rate in conditions where catalysis is made negligible. For the time being, knowing the combined parameter $k_{\text{cat}}C_{\text{cat}}\exp[-(F/RT)(E^0_{\text{Q+ZH/PH+Z}}$ or $E^0_{\text{Q+H}^+/\text{PH}})]$ will nevertheless allow the benchmarking of catalysts for a given reaction similar to the recently advocated comparison between turnover frequencies at zero overpotential.[27] In the present case of a catalytic film whose thickness may be varied, the proton−electron conduction is an additional benchmarking factor: the larger $D_{\text{H},e}/k_{\text{cat}}$, the more globally efficient the catalysis. The optimal thickness, $d_f^{\text{opt}} = (D_{\text{H},e}/k_{\text{cat}})^{1/2}$ being determined experimentally and the actual film thickness being adjusted to this value, the global benchmarking factor may then be derived from $I_0^{\max}$ as

$$F\sqrt{D_{\text{H},e}k_{\text{cat}}}\,C_{\text{cat}}\exp[-(F/RT)(E^0_{\text{Q+ZH/PH+Z}}\text{ or }E^0_{\text{Q+H}^+/\text{PH}})]$$

EXPERIMENTAL SECTION

Materials. $Co(NO_3)_2{\cdot}6H_2O$ 99.999% (Strem) and $NaClO_4$ 99.99% metals basis (Aldrich) were used as received. NaH_2PO_4 99%, KH_2PO_4 99%, NaOH 99%, KOH 88%, and KNO_3 99.0−100.5% were reagent grade and used as received from Macron. All H_2O electrolyte solutions were prepared with type I water (EMD Millipore, 18.2 MΩ cm resistivity).

Electrochemical Methods. All electrochemical experiments were conducted using a CH Instruments 760C or 760D bipotentiostat, a BASi Ag/AgCl reference electrode (soaked in saturated NaCl), and a Pt-mesh counter electrode. Measurements were conducted using a Pine Instruments MSR rotator and a 5 mm diameter Pt-disk rotating electrode (RDE). Electrochemical experiments were performed using a three-electrode electrochemical cell with a porous glass frit separating the working and auxiliary compartments. Experiments were performed at room temperature (24 ± 1 °C) and electrode potentials were converted to the NHE scale using $E(\text{NHE}) = E(\text{Ag/AgCl}) + 0.197$ V.

Film Preparation. Catalyst films were prepared via controlled-potential electrolysis of 0.1 M potassium phosphate (KP_i), pH 7.0 electrolyte solutions containing 0.5 mM Co^{2+}. To minimize precipitation of cobalt(II) phosphate, 25 mL of 0.2 M KP_i was added to 25 mL of 1.0 mM Co^{2+} solution. The solutions thus prepared remained clear over the course of all depositions. Depositions were carried out using a 5 mm diameter Pt disk as the working electrode. Deposition by controlled potential electrolysis was carried out on quiescent solutions at 1.047 V without *i*R compensation. A typical deposition lasted 40 min for a 24 mC/cm^2 film (∼200 nm thick). Following deposition, films were rinsed thoroughly in type I water to remove any adventitious Co^{2+} and P_i. Thinner films were deposited under identical conditions but with passage of the desired amount of charge. Evaluation of film thickness was performed from an estimation of the volume occupied by each Co atom as previously described.[12] The amount of mol Co/cm^2 was determined from ICP analysis of films digested in 2% nitric acid (Fluka TraceSelect). Film thicknesses of 40, 120, 390, 1025, and 2665 nm (as shown in Figure 5) correspond respectively to 5, 15, 30, 150, and 400 mC/cm^2 deposition.

Potentiostatic Tafel Data Collection in Well-Buffered P_i Electrolyte. Current−potential data were obtained by controlled potential electrolysis of 0.1 M KP_i electrolyte pH 7.0 at a variety of applied potentials. Prior to film deposition, the solution resistance of the electrolyte to be used for Tafel data collection was measured using the *i*R test function. The electrolysis solution was exchanged for Co^{2+}-containing KP_i electrolyte, without modifying the relative positions of the working and reference electrodes. The film was prepared by controlled potential electrolysis as described above. Following film preparation, the working electrode was rinsed in water and transferred, without drying, to the same electrolysis bath in which the solution resistance was measured. The electrode was allowed to equilibrate with the electrolysis solution for 5 min while being held at the open circuit potential. The rotation rate was set to 1000 rpm, and steady-state currents were then measured at applied potentials that descended from 1.267 to 1.097 V in 10 mV steps. For current densities greater than 10 μA cm^{-2}, a steady state was reached at a particular potential in <400 s. For current densities lower than 10 μA cm^{-2}, longer electrolysis times (15−20 min) were utilized to ensure that a steady state had been achieved. The solution resistance measured prior to the data collection was used to correct the Tafel plot for ohmic potential losses.

Tafel Data in Low [P_i] Electrolyte, pH 6. A 24 mC/cm^2 catalyst film was prepared onto a Pt RDE as described above. Following Tafel data acquisition in 0.1 M KP_i electrolyte (Section 1.4), the electrode was rinsed thoroughly with type I water, and steady state current densities were acquired in weakly buffered electrolytes (1.0 M $NaClO_4$, pH 6 electrolyte containing [NaP_i] between 30 mM and 0.1 μM) with *i*R compensation (measured prior to film deposition) at rotation rates of 2500, 1600, 1225, 900, and 625 rpm at 20 mV intervals over the desired potential range. When necessary 0.5−5 μL aliquots of 1 M aqueous NaOH were added periodically to ensure minimal drift in bulk pH (±0.01) over the course of the experiment. The experiment was repeated twice more using the same catalyst film. Consecutive runs displayed excellent reproducibility. Following operation in P_i-free electrolyte the electrode was rinsed, and data acquisition was repeated in 0.1 M KP_i electrolyte, as described above.

Background Pt RDE Tafel Data. Tafel data were acquired using a Pt RDE in the absence of a catalyst film. The electrode surface was polished to a mirror finish with 0.05 μm alumina, sonicated for 2 min, rinsed in 1 M H_2SO_4, and rinsed thoroughly in type I water. Those data were compared to data acquired with a 24 mC/cm^2 catalyst film deposited onto a Pt RDE and operated in 1 M $NaClO_4$ pH 7.0 electrolyte. Between 1.39 and 1.2 V the current measured with the catalyst film is 1 order of magnitude higher than the current measured on Pt in the absence of a catalyst film.

Tafel Data in P_i-Free Electrolyte, pH 6. A 24 mC/cm^2 catalyst film was prepared onto a Pt RDE as described above. Following Tafel data acquisition in 0.1 M KP_i electrolyte, the electrode was rinsed thoroughly with type I water, and steady-state current densities were acquired in P_i-free 1 M $NaClO_4$ pH 6.0 electrolyte in a manner identical to that described above. Experiments were repeated for films operated in 0.5 M $NaClO_4$ and 1.0 M KNO_3. Within experimental uncertainty (less than the size of data points), data acquired are identical irrespective of electrolyte concentration or composition. To compare data in an electrolyte, completely lacking dissolved CO_2 and carbonate, O_2 was bubbled through a 1.0 M $NaClO_4$ solution overnight (>12 h), and data were acquired as described previously. Data arising from this measurement were identical to that acquired in 1 M $NaClO_4$ without bubbling O_2, indicating that dissolved carbonate species do not play a role in proton transfers during O_2 evolution in P_i-free media.

CONCLUSION

A methodology has been established to predict the current responses expected in RDEV for the semi-general catalytic reaction scheme depicted in Scheme 1. The predictions concern the Tafel plots and their dependency on buffer concentration (including absence of buffer), film thickness and rotation rate, which are the main operational parameters that can be experimentally varied to uncover the reaction mechanism and determine its kinetic characteristics. To avoid unmanageable complexity, the scheme investigated is not general, but it can be easily implemented for other reactions and controlling factors along the same principles, thanks particularly to the use of characteristic current densities that stand for each particular rate-governing factor involved. One important outcome of the theoretical analysis, whose pertinence is confirmed experimentally, is that the Tafel plots may have a variety of slopes, $F/RT\ln 10$, $F/2RT\ln 10$, 0, that not only may be observed along the whole plot but may also coexist within the overpotential range of a single plot. It is also remarkable that KL plots, relating the inverse of the current density to the inverse of the square root of the rotation rate, are not always linear, making somewhat more cumbersome, albeit still reachable, the separation of the events inside the film from reactant transport in the solution.

Application to water oxidation by films of a cobalt-based oxidic catalyst had a double purpose. One was to provide an experimental example of the viability of the proposed methodology and of its ability to uncover the reaction mechanism and determine its kinetic characteristics. The second was to actually establish kinetic characteristics of this particular catalyst in action, with a new focus on elucidating the reasons for the previously observed behavior in buffer-free electrolytes and the effect of film thickness on OER activity. Moreover, this catalyst seems to be a premiere in the field of catalytic electrode coatings designed for the activation of small molecules required for the resolution of modern energy challenges and this work may therefore serve as a methodological model for future studies.

Some of the features of the cobalt-based oxidic catalyst are remarkable and are worth emphasizing as they could be found with other catalysts of the same reaction or with other OECs or in other catalytic reactions. One of these is that the current response is controlled jointly by the catalytic reaction and proton−electron hopping. This mixed control results in an optimal thickness beyond which any increase is at best useless or may even afford rapidly diminishing returns in net catalytic activity.

Empirically one feels that the best catalysts correspond to a high catalytic rate constant, a high catalyst concentration in the film, a low catalyst standard potential, and also a fast proton−electron hopping conduction in the film. However what counts eventually is the value of the above combination of all these parameters into a global benchmarking index. The exact expression of the benchmarking index depends on the catalytic electron and proton stoichiometries, which are reflected in the Tafel slopes and H^+ reaction order, respectively.[25b] When the stoichiometries are the same a single index can be used. In the other case, the comparison should involve entire Tafel plots with the possibility that the first catalyst is better than the second in a certain range of overpotentials or pH and vice versa. Furthermore, if the catalyst is to be employed in a photoelectrochemical cell, the matching requirements of the targeted semiconductor substrates/assemblies will define the appropriate catalyst to be used.[28]

Deconvolution of the kinetics of the catalytic reaction and of proton−electron hopping conduction is a necessary requirement for a future assessment of the catalytic and conduction mechanisms that may a priori involve stepwise or concerted pathways. Examination of kinetic H/D isotope effects should also be useful in this endeavor.

■ ASSOCIATED CONTENT

Ⓢ Supporting Information

Analysis of the kinetic responses and additional data. This material is available free of charge via the Internet at http://pubs.acs.org.

■ AUTHOR INFORMATION

Corresponding Author

cyrille.costentin@univ-paris-diderot.fr; dnocera@fas.harvard.edu; saveant@univ-paris-diderot.fr

Notes

The authors declare no competing financial interest.

■ ACKNOWLEDGMENTS

Part of this work was supported by a grant from the D.O.E., U.S. D.O.E. Grant DE-SC0009565

■ REFERENCES

(1) (a) Hoffert, M. I.; Caldeira, K.; Jain, A. K.; Haites, E. F.; Harvey, L. D. D.; Potter, S. D.; Schlesinger, M. E.; Schneider, S. H.; Watts, R. G.; Wigley, T. M. L.; Wuebbles, D. J. *Nature* **1998**, *395*, 881. (b) Nocera, D. G. *Inorg. Chem.* **2009**, *48*, 10001. (c) Abbott, D. *Proc. IEEE* **2010**, *98*, 42. (d) Chu, S.; Majumdar, A. *Nature* **2012**, *488*, 294.

(2) (a) Bard, A. J.; Fox, M. A. *Acc. Chem. Res.* **1995**, *28*, 141. (b) Lewis, N. S.; Nocera, D. G. *Proc. Natl. Acad. Sci. U.S.A.* **2006**, *103*, 1529. (c) Liu, F.; Concepcion, J. J.; Jurss, J. W.; Cardolaccia, T.; Templeton, J. L.; Meyer, T. J. *Inorg. Chem.* **2008**, *47*, 1727. (d) Barber, J. *Chem. Soc. Rev.* **2009**, *38*, 185. (e) Cook, T. R.; Dogutan, D. K.; Reece, S. Y.; Surendranath, Y.; Teets, T. S.; Nocera, D. G. *Chem. Rev.* **2010**, *110*, 6474.

(3) (a) Schneider, J.; Jia, H.; Muckerman, J. T.; Fujita, E. *Chem. Soc. Rev.* **2012**, *41*, 2036. (b) Costentin, C.; Robert, M.; Savéant, J.-M. *Chem. Soc. Rev.* **2013**, *42*, 2423. (c) Smieja, J. M.; Sampson, M. D.; Grice, K. A.; Benson, E. E.; Froehlich, J. D.; Kubiak, C. P. *Inorg. Chem.* **2013**, *52*, 2484.

(4) (a) Savéant, J.-M. *Chem. Rev.* **2008**, *108*, 2348. (b) Suntivich, J.; May, K. J.; Gasteiger, H. A.; Goodenough, J. B.; Shao-Horn, Y. *Science* **2011**, *334*, 1383.

(5) Gasteiger, H. A.; Marković, N. M. *Science* **2009**, *324*, 48.

(6) (a) Proton-Coupled Electron Transfer. Thematic Issue. *Chem. Rev.* **2010**, *110*, 6937. (b) Savéant, J.-M. *Energy Environ. Sci.* **2012**, *5*, 7718.

(7) (a) Andrieux, C. P.; Dumas-Bouchiat, J.-M.; Savéant, J.-M. *J. Electroanal. Chem.* **1982**, *131*, 1. (b) Andrieux, C. P.; Savéant, J.-M. *J. Electroanal. Chem.* **1982**, *134*, 163. (c) Andrieux, C. P.; Dumas-Bouchiat, J.-M.; Savéant, J.-M. *J. Electroanal. Chem.* **1984**, *169*, 9. (d) Andrieux, C. P.; Savéant, J.-M. In *Molecular Design of Electrode Surfaces*; Murray, R. W., Ed.; John Wiley and Sons: New York, NY, 1992; Vol. 22, p 207−270. (e) Savéant, J.-M. *Elements of molecular and biomolecular electrochemistry: an electrochemical approach to electron transfer chemistry*; John Wiley & Sons: Hoboken, NJ, 2006.

(8) (a) Kanan, M. W.; Nocera, D. G. *Science* **2008**, *321*, 1072−1075. (b) Kanan, M. W.; Surendranath, Y.; Nocera, D. G. *Chem. Soc. Rev.* **2009**, *38*, 109. (c) Dincă, M.; Surendranath, Y.; Nocera, D. G. *Proc. Natl. Acad. Sci. U.S.A.* **2010**, *107*, 10337. (d) Bediako, D. K.; Lassalle-Kaiser, B.; Surendranath, Y.; Yano, J.; Yachandra, V. K.; Nocera, D. G. *J. Am. Chem. Soc.* **2012**, *134*, 6801.

(9) (a) Steinmiller, E. M. P.; Choi, K.−S. *Proc. Natl. Acad. Sci. U.S.A.* **2009**, *106*, 20633. (b) Zhong, D. K.; Gamelin, D. R. *J. Am. Chem. Soc.* **2010**, *132*, 4202. (c) Pijpers, J. J. H.; Winkler, M. T.; Surendranath, Y.; Buonassisi, T.; Nocera, D. G. *Proc. Natl. Acad. Sci. U.S.A.* **2011**, *108*, 10056−10061. (d) Reece, S. Y.; Hamel, J. A.; Sung, K.; Jarvi, T. D.; Esswein, A. J.; Pijpers, J. J. H.; Nocera, D. G. *Science* **2011**, *334*, 645.

(10) (a) Lutterman, D. A.; Surendranath, Y.; Nocera, D. G. *J. Am. Chem. Soc.* **2009**, *131*, 3838. (b) Surendranath, Y.; Lutterman, D. A.; Liu, Y.; Nocera, D. G. *J. Am. Chem. Soc.* **2012**, *134*, 6326.

(11) (a) McAlpin, J. G.; Surendranath, Y.; Dincă, M.; Stich, T. A.; Stoian, S. A.; Casey, W. H.; Nocera, D. G.; Britt, R. D. *J. Am. Chem. Soc.* **2010**, *132*, 6882. (b) Kanan, M. W.; Yano, J.; Surendranath, Y.; Dincă, M.; Yachandra, V. K.; Nocera, D. G. *J. Am. Chem. Soc.* **2010**, *132*, 13692.

(12) (a) Surendranath, Y.; Kanan, M. W.; Nocera, D. G. *J. Am. Chem. Soc.* **2010**, *132*, 16501−16509. (b) Each Co occupies a cube 5 Å in width; defining a volume of 125 $Å^3$. Each monolayer contains $6.64\ 10^{-10}$ mol of Co/cm^2 (note that there is a mistake in the numerical evaluation

of film thickness in ref 12a in which one monolayer is estimated to correspond to 1.65 10^{-9} mol of Co/cm^2)

(13) (a) Esswein, A. J.; Surendranath, Y.; Reece, S. Y.; Nocera, D. G. *Energy Environ. Sci.* **2011**, *4*, 499. (b) Farrow, C. L.; Bediako, D. K.; Surendranath, Y.; Nocera, D. G.; Billinge, S. J. L. *J. Am. Chem. Soc.* **2013**, *135*, 6403.

(14) (a) Tafel, J.; Hahl, H. 1907, *40*, 3312. (b) Tafel equation is a large overpotential version (where the reaction is irreversible) of the more general Butler−Volmer relationship between current and potential for an electrochemical reaction, which spans the whole range of overpotentials (ref 14c,d). (c) Erdey-Grúz, T.; Volmer, M. *Z. Phys. Chem. (A)* **1930**, *150*, 203. (d) Butler, J. A. V. *Trans. Faraday Society* **1924**, *19*, 729.

(15) Biczok, L.; Linschitz, H. *J. Phys. Chem.* **1995**, *99*, 1843.

(16) Blauch, D. N.; Savéant, J.-M. *J. Am. Chem. Soc.* **1992**, *114*, 3323.

(17) Savéant, J.-M. *J. Electroanal. Chem.* **1991**, *302*, 91.

(18) It may alternatively be expressed in terms of $E^0_{\mathrm{Q+ZH/PH+Z}}$ by application of eq 4:

$$\begin{aligned}\log I_0 &= \log\left[\frac{C^0_{\mathrm{Z}}}{C^0_{\mathrm{ZH}}}\sqrt{I_k I_{\mathrm{H},e}}\tanh\left(\sqrt{\frac{I_k}{I_{\mathrm{H},e}}}\right)\right] \\ &\quad + \frac{F(E^{eq}_{\mathrm{A}} - E^0_{\mathrm{Q+ZH/PH+Z}})}{RT\ln 10} \\ &= \log\left[F\frac{C^0_{\mathrm{Z}}}{C^0_{\mathrm{ZH}}}C_{\mathrm{cat}}k_{\mathrm{cat}}d_{\mathrm{f}}^{\mathrm{opt}}\tanh\left(\frac{d_{\mathrm{f}}}{d_{\mathrm{f}}^{\mathrm{opt}}}\right)\right] \\ &\quad + \frac{F(E^{\mathrm{eq}}_{\mathrm{A}} - E^0_{\mathrm{Q+ZH/PH+Z}})}{RT\ln 10} \qquad (7')\end{aligned}$$

(19) or, alternatively by

$$\begin{aligned}I_0^{\max} &= F\frac{C^0_{\mathrm{Z}}}{C^0_{\mathrm{ZH}}}C_{\mathrm{cat}}\sqrt{k_{\mathrm{cat}}D_{\mathrm{H},e}}\exp\left[\frac{F(E^{\mathrm{eq}}_{\mathrm{A}} - E^0_{\mathrm{Q+ZH/PH+Z}})}{RT}\right] \\ &= F\frac{C^0_{\mathrm{Z}}}{C^0_{\mathrm{ZH}}}C_{\mathrm{cat}}k_{\mathrm{cat}}d_{\mathrm{f}}^{\mathrm{opt}}\exp\left[\frac{F(E^{\mathrm{eq}}_{\mathrm{A}} - E^0_{\mathrm{Q+ZH/PH+Z}})}{RT}\right] \qquad (9')\end{aligned}$$

(20) For the notion of “pure kinetic conditions” see ref 7c, p. 82.

(21) Bard, A. J.; Faulkner, L. R. *Electrochemical Methods: Fundamentals and Applications*, 2nd ed; John Wiley and Sons: New York, 2001; Chapter 9.

(22) *Standard Potentials in Aqueous Solutions*; Bard, A. J., Jordan, J., Parsons, R., Eds.; Marcel Dekker: New York, 1985.

(23) *Handbook of Chemistry and Physics*, 81st ed.; Lide, D. R., Ed.; CRC Press: Boca Raton, FL, 2000−2001; pp 5−95.

(24) Above pH = 7, OH^- start to interfere as an additional CPET proton acceptor. The reactions that have OH^- and other species as proton acceptor are under current investigation.

(25) (a) A similar behavior is observed with Ni−B_i films in unbuffered pH 8.5 electrolyte where the slopes of the KL plots change (see Figure S6 in ref 25b) suggesting that in the later case the limiting factor is diffusion of OH^- which is the acting base in the PCET processes. This ultimately leads to current density that plateaus (see Figure 7 in ref 25b). (b) Bediako, D. K.; Surendranath, Y.; Nocera, D. G. *J. Am. Chem. Soc.* **2013**, *135*, 3662.

(26) *Handbook of Chemistry and Physics*, 81st ed.; Lide, D. R., Ed.; CRC Press: Boca Raton, FL, 2000−2001; pp 5−96.

(27) (a) Costentin, C.; Drouet, S.; Robert, M.; Savéant, J.-M. *J. Am. Chem. Soc.* **2012**, *134*, 11235. (b) Costentin, C.; Drouet, S.; Robert, M.; Savéant, J.-M. *Science* **2012**, *338*, 90. (c) The turnover frequency at zero overpotential introduced in refs 27a,b is in fact the analog of $k_{\mathrm{cat}}\exp[(F/RT)(E^{\mathrm{eq}}_{\mathrm{A}} - E^0_{\mathrm{Q+ZH/PH+Z}}$ or $E^0_{\mathrm{Q+H+/PH}})]$, which implies that C_{cat} in the film could have been estimated.

(28) Surendranath, Y.; Bediako, D. K.; Nocera, D. G. *Proc. Natl. Acad. Sci. U.S.A.* **2012**, *109*, 15617.

JACS JOURNAL OF THE AMERICAN CHEMICAL SOCIETY

Article

pubs.acs.org/JACS

A Functionally Stable Manganese Oxide Oxygen Evolution Catalyst in Acid

Michael Huynh,[†,‡] D. Kwabena Bediako,[†] and Daniel G. Nocera*[,†]

[†]Department of Chemistry and Chemical Biology, Harvard University, Cambridge, Massachusetts 02138, United States

[‡]Department of Chemistry, Massachusetts Institute of Technology, Cambridge, Massachusetts 02139, United States

Supporting Information

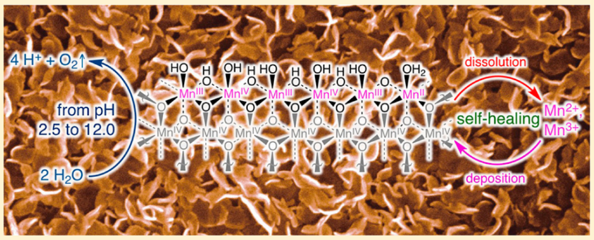

ABSTRACT: First-row metals have been a target for the development of oxygen evolution reaction (OER) catalysts because they comprise noncritical elements. We now report a comprehensive electrochemical characterization of manganese oxide (MnOx) over a wide pH range, and establish MnOx as a functionally stable OER catalyst owing to self-healing, is derived from MnOx redeposition that offsets catalyst dissolution during turnover. To study this process in detail, the oxygen evolution mechanism of MnOx was investigated electrokinetically over a pH range spanning acidic, neutral, and alkaline conditions. In the alkaline pH regime, a ∼60 mV/decade Tafel slope and inverse first-order dependence on proton concentration were observed, whereas the OER acidic pH regime exhibited a quasi-infinite Tafel slope and zeroth-order dependence on proton concentration. The results reflect two competing mechanisms: a one-electron one-proton PCET pathway that is dominant under alkaline conditions and a Mn^{3+} disproportionation process, which predominates under acidic conditions. Reconciling the rate laws of these two OER pathways with that of MnOx electrodeposition elucidates the self-healing characteristics of these catalyst films. The intersection of the kinetic profile of deposition and that of water oxidation as a function of pH defines the region of kinetic stability for MnOx and importantly establishes that a non-noble metal oxide OER catalyst may be operated in acid by exploiting a self-healing process.

1. INTRODUCTION

Solar-driven electrochemical splitting of water to hydrogen and oxygen affords a method to store renewable energy in the form of energy-dense chemical fuels on a scale commensurate with future global energy requirements.[1−6] Of the two half reactions for water splitting, the oxygen evolution reaction (OER) is more kinetically demanding because it requires the coupled transfer of four protons and four electrons from two water molecules[7,8] to release one oxygen molecule.[9,10] The most active OER catalysts comprise "critical" elements that are expensive and lack sufficient abundance to be utilized on a global scale;[5,11] performing OER with commensurate activity by using noncritical elements remains a significant challenge. Discovery paths to noncritical OER catalysts follow two disparate approaches: "top−down" experimental and computational screening for mixed metal oxides[12−15] and a "bottom−up" experimental approach focused on defining the structure and mechanism of unary metal oxides to guide catalyst discovery.[16,17] Adopting the latter methodology with knowledge of the rate laws for catalyst formation (including nucleation and steady-state growth) and turnover, we have shown that conditions may be chosen to achieve promising oxygen evolution activity in neutral and near neutral pH electrolytes by exploiting the self-healing ability of catalysts.[18,19]

Our ability to operate OER catalysts at neutral and near neutral pH electrolytes has enabled our construction of buried junction devices (e.g., the artificial leaf) from noncritical materials.[20,21] To attain appreciable solar-to-fuels efficiencies, the combination of PV, catalyst, and electrolyte requires precise optimization. As described with equivalent circuit analysis,[22] the $j-V$ curves of the PV material and catalyst must be matched for maximizing operating power. Moreover, the stability of different photovoltaic materials vary in different pH regimes and thus provides an imperative to further extend the operation of OER catalysts over wider pH ranges, from basic and neutral to acidic pH regimes. For example, silicon is quickly passivated to silicon dioxide in alkaline media, which necessitates the use of catalysts that are stable in low to moderate pH electrolytes if the catalyst is to be directly integrated with silicon. Late first-row transition metal oxides, such as the Co−OEC,[23,24] Ni−OEC,[25,26] and more conventional "basic" oxides (e.g., from groups I and II elements),[16,17] are not stable in acidic conditions where such catalysts are known to corrode quickly. In contrast, early first-row transition metal oxides are resistant to corrosion in acidic environments and indeed have been used to passivate other more susceptible metal surfaces.[27] Thus, we turned our attention to defining activity profiles of early transition metal oxides and, in particular, to an electrodeposited manganese oxide catalyst (henceforth denoted MnOx). Manganese oxide-based materials have been examined extensively in neutral and basic solutions.[28−40] However, the

Received: January 12, 2014
Published: March 26, 2014

OER activity of manganese oxides has garnered less attention in acidic pH regimes.[41−47] We now extend the understanding of oxidic manganese OER catalysts by elucidating the mechanism of MnOx under a wide pH range with detailed electrokinetics measurements. Tafel and reaction order analysis suggest two distinct OER pathways for MnOx: one prevalent in acidic and the other in alkaline electrolyte conditions. The rate laws of these water oxidation mechanisms are unified with that of catalyst deposition to elucidate the functional stability of MnOx films during OER catalysis, thus enabling us to predict and quantify the self-healing nature of MnOx in acid, a pH regime that hitherto has remained largely undefined for OER catalysts comprising noncritical elements. From this knowledge, we show that a metal oxide OER catalyst may operate with facility in acid, a realm previously dominated by oxides of iridium and ruthenium.

2. EXPERIMENTAL SECTION

2.1. Materials. $MnCl_2 \cdot 4H_2O$ (99.995% trace metals basis, Strem), KOH (88%, Macron), and KNO_3 (99.0−100.5%, Macron) were used as received. Methylphosphonic acid (98%, Aldrich) was recrystallized twice from boiling acetonitrile (HPLC grade, Aldrich). Phosphoric acid (85 wt % in H_2O, 99.99% trace metals basis, Aldrich) was used as received. Type I water (EMD Millipore, 18.2 MΩ cm resistivity) was exclusively used to rinse electrodes and glassware as well as to prepare solutions.

2.2. Solution Preparation. Mn^{2+}-free solutions of phosphate (P_i) were prepared by diluting stock phosphoric acid (85 wt % in H_2O, ∼14.6 M) with reagent water. Additional KNO_3 was added to maintain the ionic strength (μ) of the solution at ∼2 M, which mitigated diffuse double layer effects.[48] Solution pH was adjusted by adding pellets of solid KOH and aliquots of concentrated KOH while monitoring with a pH meter (VWR).

2.3. General Electrochemical Methods. All electrochemical experiments were conducted using a CH Instruments 760D bipotentiostat, a BASi Ag/AgCl reference electrode (filled with saturated KCl), and a Pt-mesh counterelectrode. All measurements were performed using a three-electrode electrochemical cell with a porous glass frit separating the working and auxiliary compartments. Glassware and cells were cleaned by soaking in aqua regia and rinsing with reagent water. All procedures were performed at ambient temperature (23 ± 1 °C), and electrode potentials were converted to the NHE scale using $E(\text{HE}) = E(\text{Ag/AgCl}) + 0.197$ V. All overpotentials for the oxygen evolution reaction (OER) from H_2O were computed using $\eta = E(\text{NHE}) - 0.059 \text{ V} \times \text{pH}$.

Unless otherwise specified, OER studies employed working electrodes of fluorine-doped, tin oxide-coated glass (FTO) with 7 Ω/sq surface resistivity (TEC-7) purchased as precut 1 cm × 2.5 cm pieces from Hartford Glass. FTO slides were sonicated in acetone and rinsed with reagent water prior to use. A 1 cm^2 electrode area was created by using a 0.5 cm wide strip of Scotch tape as a mask. Rotating disk electrode (RDE) experiments employed a Pine Instruments MSR rotator with a 0.196 cm^2 Pt-disk rotating electrode, polished to mirror shine with 0.05 μm alumina (CH Instruments) and cycled ∼50 times at 300 mV/s from −0.2 to 1.5 V in 0.5 M H_2SO_4 (99.999% trace metals basis, Aldrich) before each experiment.

2.4. Film Preparation. MnOx catalyst films were prepared by controlled-potential electrolysis of solutions containing 0.5 mM Mn^{2+} and 50 mM methylphosphonate (MeP_i) at pH 8.0. These solutions remained clear over the course of all depositions. A FTO-coated glass slide was masked to 1 cm^2 and immersed in the quiescent solution. A constant potential of 0.537 V was applied to the electrode with automatic *iR* compensation until the total charge passed reached the desired loading of catalyst. For example, a 6 mC/cm^2 loading required ∼700 s of deposition time. Following deposition, films were immersed in reagent water to remove any trace Mn^{2+} and MeP_i remaining from solution. The films were prevented from drying by quickly transferring them to a Mn^{2+}-free solution for subsequent experiments.

2.5. Determination of Faradaic Efficiency. A fluorescence-based O_2 sensor (Ocean Optics) was employed to determine the Faradaic efficiency of oxygen evolution on MnOx. The total charge passed and the amount of O_2 detected by the sensor over time was recorded and is plotted in Figure S1 in the Supporting Information (SI). The experimental setup employed a custom-built, two-compartment, gastight electrochemical cell with a 14/20 port on each compartment and a Schlenk connection with a Teflon valve on the working compartment. One compartment contained a Pt mesh auxiliary electrode, and the other compartment contained the working and Ag/AgCl reference electrodes. The working electrode consisted of a 10 mC/cm^2 MnOx film electrodeposited on an FTO plate masked with Scotch tape to a 21.5 cm^2 area. The film was operated at 0.3 mA in 0.10 M P_i with 1.75 M KNO_3 electrolyte solution at pH 2.5, 7.0, and 12.0. Prior to measurements, the solution was degassed by bubbling with high purity Ar for 2 h with vigorous stirring. The 14/20 port of the working compartment was fitted with a FOXY OR125-73 mm O_2 sensing probe connected to a multi-frequency phase fluorometer. The phase shift of the O_2 sensor on the FOXY probe was recorded at 2 s intervals and then converted into the partial pressure of O_2 in the headspace using a two-point calibration curve (air, 20.9% O_2; and high purity Ar, 0% O_2). Because the amount of dissolved O_2 was small compared to the amount of generated O_2, no correction of the partial pressures by Henry's law was performed. These pressures were converted using the ideal gas law into O_2 concentration and compared to the theoretical yield of O_2, calculated by dividing the charge passed by 4*F*.

2.6. Electron Microscopy. Field emission scanning electron microscopy (FESEM) was performed on a 100 mC/cm^2 MnOx film electrodeposited on FTO (Figure S4 in the SI). The FESEM instrument (Zeiss Supra55VP) was operated at a beam voltage of 15.0 kV and at a working distance of ∼11 mm with a 30 μm aperture. InLens was used as the detector.

2.7. Tafel Data Collection. The current−voltage (Tafel) properties of the catalyst film in the region of oxygen evolution were measured by controlled potential electrolysis of 6 mC/cm^2 MnOx films in stirred Mn^{2+}-free solutions of 0.10 M P_i buffer in acidic (pH 1.0−3.5, Figure S2a in the SI), neutral (pH 5.5−8.5, Figure S2b in the SI), and alkaline (pH 11.35−13.30, Figure S2c in the SI) regimes. All solutions contained 1.73 M KNO_3 supporting electrolyte to achieve a high μ. The steady-state OER current density (j) was determined as a function of the applied overpotential (η) for freshly prepared 6 mC/cm^2 MnOx (a summary of the plots is shown in Figure 1). The solution was stirred at ∼600 rpm with a Teflon stir bar, and Tafel data were collected by adjusting the electrode potential from high to low values, in fixed mV decrements, across the linear Tafel

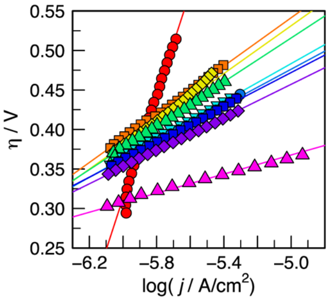

Figure 1. Tafel plots of the OER on 6 mC/cm^2 MnOx operating in 0.10 M P_i and 1.73 M KNO_3 at low pH 2.5 (red, ●); intermediate pH 5.5 (orange, ■), 6.0 (yellow, ◆), 6.5 (green, ▲), 7.0 (light blue, ▼), 7.5 (blue, ●), 8.0 (dark blue, ■), and 8.5 (purple, ◆); and high pH 12.0 (magenta, ▲). The overpotential (η) was used instead of *E* so that plots at different pHs could be displayed on the same scale. Intermediate pH plots have slopes that vary from 153 to 105 mV/decade, centered around 127 mV/decade at pH 7.0. The accessible range of potentials (and current densities) was restricted by corrosion at high potentials in some electrolyte conditions.

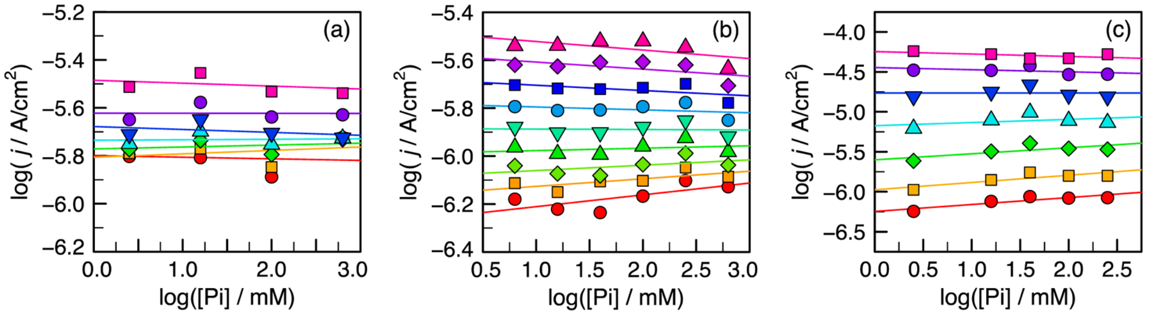

Figure 2. [P_i] dependence for the OER on MnOx (6 mC/cm^2 films) operated over a wide pH range at (a) pH 2.5 for E = 1.467 (red, ●), 1.497 (orange, ■), 1.527 (light green, ◆), 1.557 (light blue ▲), 1.587 (dark blue ▼), 1.617 (purple ●), and 1.647 V (magenta ■); (b) pH 7.0 for E = 0.960 (red ●), 0.970 (orange ■), 0.980 (light green ◆), 0.990 (green ▲), 1.000 (blue green ▼), 1.010 (blue ●), 1.020 (dark blue ■), 1.030 (violet ◆), and 1.040 V (magenta ▲); and (c) pH 12.5 for E = 0.777 (red ●), 0.792 (orange ■), 0.807 (green ◆), 0.822 (light blue ▲), 0.837 (dark blue ▼), 0.852 (purple ●), and 0.867 V (magenta ■) with varying P_i concentrations from 2.5 to 631.0 mM. In all solutions, appropriate amounts of KNO_3 were added to achieve a total ionic strength of 2 M. Data were interpolated at fixed potentials from Tafel plots in Figure S5 in the SI. The average slope in all three plots is zero.

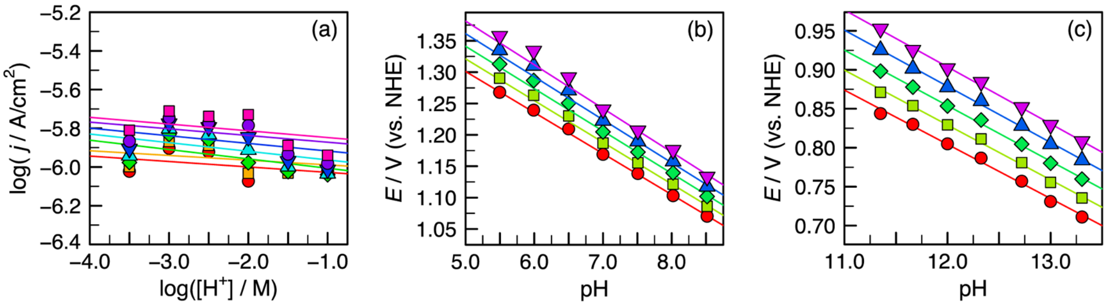

Figure 3. pH dependence for the OER on MnOx (6 mC/cm^2 films) operated in 0.10 M P_i and 1.73 M KNO_3 at (a) acidic pH 1.0 to 3.5, at E = 1.447 (red ●), 1.467 (orange ■), 1.487 (green ◆), 1.507 (light blue ▲), 1.527 (dark blue ▼), 1.547 (purple ●), and 1.567 V (magenta ■); (b) neutral pH 5.5 to 8.5, at log j = −6.10 (red ●), −5.95 (light green ■), −5.80 (green ◆), −5.65 (blue ▲), and −5.50 (magenta ▼); and (c) alkaline pH 11.35 to 13.30, at log j = −6.4 (red ●), −6.0 (light green ■), −5.6 (green ◆), −5.2 (blue ▲), and −4.8 (magenta ▼). Data were interpolated at fixed potentials in (a) and at constant current densities in (b) and (c) from Tafel data in Figure S2 in the SI. The average slope is (a) zero for proton concentration dependence from pH 1.0 to 3.5; (b) −67.5 ± 1.7 mV/pH for E/pH from pH 5.5 to 8.5; and (c) −71.3 ± 1.4 mV/pH for E/pH from pH 11.35 to 13.30.

region. At each potential, data were collected for 60−90 s such that steady-state current density was reached. To minimize any pseudocapacitance, the highest potential (first point in the sweep) was held for 30 min. Solution resistance was measured prior to data collection and automatically compensated. Tafel data collected in succession using the same and different electrodes exhibited good reproducibility and were not dependent on the direction of the potential scan. Performing the same experiments on blank FTO electrodes yielded current densities at least 1 order of magnitude lower than for FTO electrodes coated with a MnOx film, demonstrating low background contribution. Because the concentration of water is ~55 M and well-buffered solutions were used, it was possible to collect activation-controlled current density without the necessity of using a rotating disk electrode (RDE) and attendant Koutecký−Levich (K−L) analysis. Nonetheless, control experiments comparing the Tafel slopes for plots collected on stirred solutions, using a RDE at 2500 rpm, and RDE coupled to K−L analysis established that stirring the solution with a stir bar at ~600 rpm was sufficient to mitigate mass transport effects (Figure S8 in the SI). Film loading studies were performed on MnOx films of varying thicknesses by constant potential deposition on FTO, as described above, with passage of 0.5−500 mC/cm^2 charge and transferred to the Mn^{2+}-free electrolyte without drying (Figure S3 in the SI).

2.8. Phosphate Concentration Dependence. The dependence of P_i concentration on OER activity at pH 2.5, 7.0, and 12.5 was examined by recording Tafel plots on 6 mC/cm^2 MnOx films in stirred solutions at fixed pH of varying [P_i]: 2.5, 15.9, 100.0, and 631.0 mM at pH 2.5; 2.5, 6.3, 15.9, 39.9, 100.0, 251.2, and 631.0 mM at pH 7.0; and 2.5, 15.9, 39.8, 100.0, and 251.2 mM at pH 12.5 (Figure S5 in the SI). All solutions included KNO_3 to maintain a constant μ = 2.0 M so that the pK_a's of phosphoric acid could be accurately established. The data were interpolated at potentials from 1.467 to 1.647 V, incrementing by 30 mV at pH 2.5; 0.960 to 1.040 V, incrementing by 10 mV at pH 7.0; and 0.777 to 0.867 V, incrementing by 15 mV at pH 12.5, by slicing horizontally across the linear Tafel plots, to yield the dependence of activation current density (j_{ac}) on [P_i] (Figure 2).

A fixed ionic strength μ = 2 M was required to reliably prepare solutions of known [P_i]. Equilibrium constants were determined for μ = 2 M with KNO_3 as a supporting electrolyte. The reported pK_a's for phosphoric acid are 2.148, 7.198, and 12.375 at 25 °C.[49−51] An adjusted pK_a for P_i was calculated using specific ion interaction theory (SIT),[52] as implemented in the program *Ionic Strength Corrections using Specific Interaction Theory* (v 2.0);[53] the cation SIT parameter for H^+ (0.07) and the anion SIT parameters for $H_2PO_4^{2-}$ (−0.14), HPO_4^{2-} (−0.10), and PO_4^{3-} (−0.09 with a complex SIT parameter of −0.10) furnished corrected pK_a values of 1.582, 6.251, and 11.185 for electrolytes at μ = 2 M. These pK_a values were then used to calculate the speciation of P_i at various concentrations and to determine the amount of KNO_3 required to achieve the target value of μ = 2 M.

2.9. pH Dependence. The dependence of OER activity on pH was determined by constructing Tafel plots for MnOx films deposited from 6 mC/cm^2 in 0.10 M P_i and 1.73 M KNO_3 solutions at pH values spanning 1.0 to 3.5, incremented by 0.5 in acidic conditions; from pH 5.5 to 8.5, incremented by 0.5 in near-neutral conditions; and from pH 11.35 to 13.30, incremented by about 0.25 in alkaline conditions (Figure S2 in the SI).

The data were interpolated for the acidic cases at fixed potentials of 1.447−1.567 V, in 20 mV increments. The resulting plot presents the dependence of j_{ac} on proton concentration (Figure 3a). The intermediate and alkaline pH cases were interpolated at values of $\log(j_{ac})$: −6.10 to −5.50, in increments of 0.05 at intermediate pH; and −6.4 to −4.8, in 0.4 increments at alkaline pH, to yield the dependence of applied potential on pH (b and c of Figure 3). The slope of E vs. pH plots was multiplied by the negative reciprocal of the Tafel slope to extract the reaction order in pH.

The pH dependence at intermediate pH was also explored by potentiostatic titration of a 6 mC/cm^2 film in 0.10 M P_i and 1.73 M KNO_3 solution. The electrode was operated at a constant potential of 1.30 V, and the steady-state current density (measured after operation for ≥2 min at each pH) was recorded as the pH of the solution (measured *in situ*) was raised in increments of about 0.25 pH units using μL aliquots of 1 M KOH solution from pH 4 to pH 10. The plot of steady-state current density as a function of pH (Figure S6 in the SI) has a slope of 0.44 from pH 6 to 10. Below pH 6, the slope gradually decreases to zero.

2.10. Catalyst Tracking. The kinetic stability of MnOx films was evaluated by ^{31}P NMR where high-spin Mn^{2+} induces paramagnetic line broadening of the ^{31}P NMR signal of phosphate. Chronopotentiometry at 0 (open circuit) and 10 μA/cm^2 was performed on 100 mC/cm^2 MnOx films immersed in rapidly stirred solutions of increasing acidity: 0.10 M P_i with 1.90 M KNO_3 at pH 2.0, 4 M phosphoric acid at pH 0.1, and 4 M HCl with 0.10 M P_i at pH ∼−0.5. Aliquots of the electrolyte solution were sampled every 15 min over the course of 1 h. The Mn^{2+} concentration in each aliquot was quantified by measuring the full-width at half-maximum (fwhm) of the ^{31}P NMR signal for inorganic phosphate in the electrolyte. The magnitude of the broadening is directly proportional to the Mn^{2+} concentration. To produce calibration curves (Figure S7 in the SI), small precalculated microliter amounts of Mn^{2+} were added from a 0.5 mM stock to each electrolyte solution examined, producing solutions of known Mn^{2+} concentrations from 0 to 40 μM, in increments of 10 μM. Since the width of the ^{31}P NMR signal was highly sensitive to instrumental variables, data for the calibration curves were recorded immediately prior to those for the experimental samples in all cases. The measured concentrations were normalized against a fully dissolved 100 mC/cm^2 film ($[Mn^{2+}] = 7.45\ \mu M$) to track the fractional dissolution of the film over time (Figure 4).

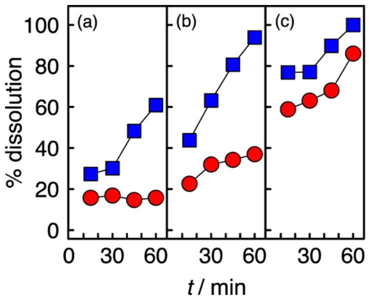

Figure 4. Percent of 100 mC/cm^2 MnOx film dissolved as a function of time (t) for application of 0 (blue, ■) and 10 (red, ●) μA/cm^2 current density in (a) 0.10 M P_i with 1.90 M KNO_3 solution at pH 2.0; (b) 4 M phosphoric acid at pH 0.1; and (c) 4 M HCl with 0.10 M P_i at pH −0.5. Lines are presented as guides.

3. RESULTS

MnOx films were prepared following procedures previously described for MnOx catalyst deposition.[54] FTO-coated glass slides, with 1 cm^2 working area, were polarized at a constant potential of 0.54 V (vs NHE) in quiescent solutions containing 0.5 mM Mn^{2+} and 50 mM MeP_i at pH 8.0. Deposition times varied, depending on the desired amount of catalyst deposited, but default catalyst loadings were 6 mC/cm^2 unless otherwise specified.

Figure S1 in the SI shows the total charge passed and the amount of O_2 detected by a fluorescent-based O_2 sensor. All current passed during the OER can be attributed to O_2 production. No degradation of the catalyst was detected, indicating that the OER Faradaic efficiency of MnOx is unity.

3.1. Tafel Analysis. The Tafel behavior of the OER of MnOx was measured by collecting steady-state current density (j) as a function of the applied overpotential (η) in acidic, neutral, and alkaline regimes of phosphate-buffered electrolyte (Figures 1 and S2 in the SI). Tafel plots in all pH regimes were reproducible under independent runs and were not dependent on the direction of the potential scan, indicating that the films were not altered during data collection. In acidic conditions, the Tafel plots possessed high slopes, over a range of 365−851 mV/decade with an average slope of 653 ± 166 mV/decade (Figure S2a in the SI). Under alkaline pH, the Tafel plots displayed linearity over two decades of current density with an average slope of 60.3 ± 2.9 mV/decade (Figure S2c in the SI). In addition, the Tafel slope remained close to 60 mV/decade over the entire alkaline pH range. At intermediate pHs, Tafel plots had an average slope of 127.4 ± 20.0 mV/decade (Figure S2b in the SI). Closer inspection revealed that the Tafel slopes systematically decreased with increasing pH. For example, Tafel slopes of 152.6, 119.9, and 104.9 mV/decade were observed for pH 5.5, 7.0 and 8.5, respectively.

Thicker MnOx films exhibited greater activities than thinner films, as evidenced by the monotonic shift of the Tafel plots to higher current densities with increased catalyst loadings. These data are shown in Figure S3 in the SI for films deposited with passage of charge from 0.5 to 500 mC/cm^2. Tafel slopes were preserved over a wide range of film thicknesses, indicating that the MnOx films are porous. This contention was supported by SEM images of thick films, which exhibited disc-like features (Figure S4 in the SI). Nonetheless, the activity of films thicker than 32 mC/cm^2 does not scale linearly with increased catalyst loadings. This is consistent with intrinsic limitations associated with proton−electron transport in porous OEC films.[55] In addition, upward bending of the Tafel plot occurred at high catalyst loadings. For these reasons, subsequent studies focus on the behavior of films deposited upon the passage of 6 mC/cm^2 under relatively well-buffered conditions, such that the films behave, in effect, as active sites that are equally accessible by an electric field from the electrode substrate, and may be treated using conventional electrokinetics theory.

3.2. Reaction Order Analysis. The reaction order (ρ) of a species at concentration c_i may be determined from electrokinetic measurements when the concentration of all other species ($c_{k\neq i}$) are held constant, and is given by

$$\rho = \left(\frac{\partial \log \nu}{\partial \log c_i}\right)_{c_{k\neq i}} = \left(\frac{\partial \log j}{\partial \log c_i}\right)_{c_{k\neq i}} \tag{1}$$

where the rate of the reaction, ν, is directly proportional to the current density (j) driving the reaction.[56] Consequently, the reaction order of a species can be determined electrochemically by the slope of a $\log j$ vs $\log [c_i]$ plot at fixed potentials.

Tafel plots were collected at fixed pH while varying the concentration of phosphate, $[P_i]$, to delineate the phosphate dependence of the OER activity of MnOx (Figure S5 in the SI). Horizontal interpolation of the Tafel data at constant potentials resulted in $\log j$ vs $\log [P_i]$ plots where the slope provided a direct measure of P_i reaction order (Figure 2). The observed current densities in Figure 2, in acidic, neutral, and alkaline pH regimes, do not change appreciably over 2.5 magnitudes of $[P_i]$, indicating a zeroth-order dependence on $[P_i]$.

Similarly, the pH dependence of oxygen evolution on MnOx films was investigated by acquiring Tafel data over a pH range at constant $[P_i]$ (Figure S2 in the SI). At acidic pH, the OER activity did not significantly change over four pH units. Indeed, horizontal interpolation of the lower linear region ($E < 1.6$ V) of the Tafel plots at fixed potentials, yielded a zeroth-order dependence on proton concentration (Figure 3a) in acidic conditions.

In the alkaline regime, the Tafel slopes are lower, owing to the greater activity of MnOx in this pH range (Figure S2c in the SI). Consequently, a single "horizontal" slice through all data cannot encompass all Tafel plots. However, vertical interpolation of Tafel plots at fixed current densities yields the pH dependence of the steady-state potential at constant current density $(\partial E/\partial \mathrm{pH})_j$. The reaction order in pH (ρ_{pH}) may then be determined from the following partial derivative:[56]

$$\rho_{\mathrm{pH}} = \left(\frac{\partial \log j}{\partial \mathrm{pH}}\right)_E = -\left(\frac{\partial E}{\partial \mathrm{pH}}\right)_j \Big/ \left(\frac{\partial E}{\partial \log j}\right)_{\mathrm{pH}} \qquad (2)$$

Thus, ρ_{pH} is furnished by dividing the negative of the slope of the potential vs pH plot by the Tafel slope. Applying this procedure to the data of Figure S2c in the SI by vertical interpolation of the Tafel plots at fixed current densities produces a potential vs pH plot with an average slope of −71.3 ± 1.4 mV/pH (Figure 3c). Dividing by the average Tafel slope furnishes a reaction order in pH of 1.2 ± 0.1. Therefore, oxygen evolution by MnOx exhibits an inverse first-order dependence on $[H^+]$ under alkaline conditions.

Applying the same procedure on data collected at intermediate pH (Figure S2b in the SI), vertical interpolation of the Tafel plots at fixed current densities resulted in a potential vs pH plot with an average slope of −67.5 ± 1.7 mV/pH (Figure 3b). Per eq 2, dividing by the negative of the average Tafel slope yielded an apparent reaction order in pH of 0.5 ± 0.2, which implies an inverse half-order in $[H^+]$. This fractional pH dependence at intermediate pH was explored further by potentiometric titration of the films from pH 6 to 10. In the titration, the potential was held constant at 1.3 V while the pH of the solution was slowly adjusted by increments of ~0.05 units, which correspondingly caused an increase in current density. The solution was stirred rapidly, and sufficient time (1−5 min) was permitted for the current density to reach a steady-state value. The resulting log j vs pH plot was linear over four orders of pH; consequently, the slope of this plot directly yields the pH reaction order (Figure S6 in the SI). Consistent with the data of Figure 3b, a pH reaction order of 0.44 is obtained.

3.3. Film Dissolution Analysis. The kinetic stability of MnOx films at low pH was evaluated by measuring the Mn^{2+}-induced paramagnetic line broadening of the ^{31}P NMR peak for inorganic phosphate. MnOx films exhibit high intrinsic stability in intermediate and alkaline pH regimes; however, the degradation rate of MnOx films increases for more acidic solutions. Figure 4 shows the percent dissolution of MnOx films over time in the presence and absence of applied current (at fixed potential) at very acidic pHs (<2). Generally, films held at open circuit were less stable and dissolved more quickly than films operated at 10 μA/cm^2. As Figure 4a demonstrates, catalyst films operated in solutions of pH 2.0 were stable, and negligible dissolution of the films was observed when operated at 10 μA/cm^2. Conversely, removal of applied potential (i.e., no current) led to degradation of the film within an hour. Similarly, electrolysis of MnOx in the pH 0.1 solution exhibited significantly diminished dissolution compared to films held at open circuit (Figure 4b). Only in 4 M HCl (pH approximately −0.5) did the catalyst completely dissolve during operation of the film (Figure 4c).

4. DISCUSSION

The Faradaic efficiency measurements of Figure S1 in the SI establish that the observed current density originates solely from the production of O_2 by OER. To ensure that electrokinetics measurements reliably and reproducibly reflect this OER process, Tafel data must be collected for an activation-controlled reaction at the electrode. A series of experiments was performed to define the experimental conditions that were appropriate for such an activation-controlled OER process.

First, measured current densities must be unencumbered by the mass-transport of reactant to and product from the electrode. Whereas water is readily available as a reactant, even in in quiescent solutions, the production of protons resulting from OER can result in a local pH gradient, which can convolute the collection of Tafel data. To minimize the possibility of mass transport limitations associated with a pH gradient, solutions were stirred during the collection of Tafel data. To confirm that solutions were stirred sufficiently to enable an activation-controlled current to be collected, a series of Tafel plots were constructed for (i) MnOx on a stationary FTO electrode immersed in a stirred (Teflon stir bar at 600 rpm) solution, (ii) MnOx on a Pt RDE rotated at 2500 rpm, and (iii) MnOx on a Pt RDE at "infinite" rotational velocity as ascertained from a Koutecký−Levich (K−L) analysis (Figure S8 in the SI). The Tafel slopes were similar (~120 mV/decade for P_i electrolyte at pH 7.0) and reproducible in all three cases. These results indicate that Tafel data could be collected for stirred solutions in an activation-controlled regime.

Second, capacitive contributions to the observed current density must also be minimal for constructing accurate Tafel plots of the OER process. Upon application of potential, the first few seconds of measured current density that rapidly decays can be ascribed to non-Faradaic current arising from the charging of the double-layer capacitance. Accordingly, current measurements were made in temporal domains beyond this short time scale window. However, additional pesudocapacitive effects over a longer time scale may arise from surface adsorption, intercalation of electrolyte anions, and/or surface structure changes.[56] Therefore, to reach steady-state conditions: (i) freshly deposited MnOx films were preanodized for at least 30 min in the same electrolyte used for subsequent Tafel analysis, and (ii) current density was measured over 30 to 60 s at each potential during Tafel data collection. The combination of both procedures yielded reproducible current densities with minimal capacitance contributions.

In addition, the Tafel behavior of MnOx films of varying thickness was examined. MnOx films were deposited with passage of charge ranging from 0.5 to 500 mC/cm^2 and operated in acidic and neutral P_i solutions (Figure S3 in the SI). As expected, thicker films had greater activities, as evidenced by the shift of the Tafel plot to higher current densities for increased catalyst loadings. Furthermore, Tafel slopes remained

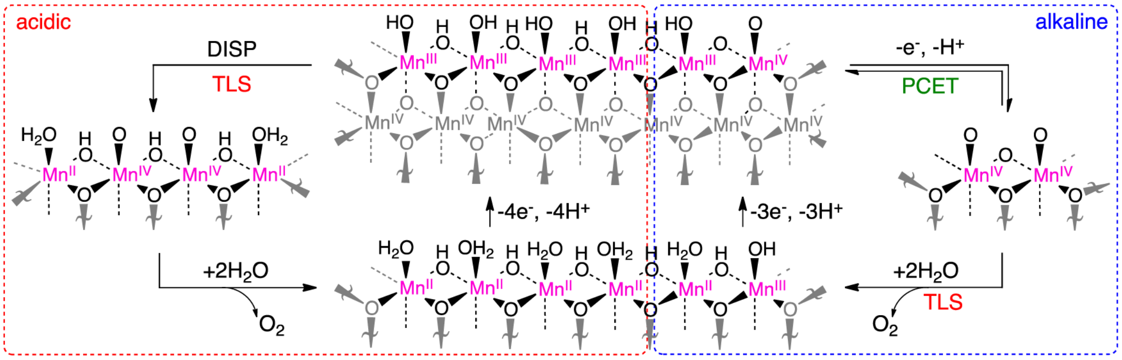

Figure 5. Proposed mechanism for the OER on MnOx in (left) acidic and (right) alkaline pH conditions. In the acidic regime, the resting state composed of Mn^{III} edge sites undergo turnover-limiting cross-site proton-coupled disproportionation to produce adjacent Mn^{IV} sites with terminal oxos. These terminal oxos couple to release O_2. In the alkaline regime, the mixed valent Mn$^{III/IV}$ resting state proceeds through a one-electron, one-proton PCET to generate adjacent Mn^{IV}=O sites. Similarly, these terminal oxos then couple in the turnover-limiting step to produce O_2.

the same over a wide range of film thicknesses (from 0.5 to 250 mC/cm^2) for the same pH. These observations suggest that the electrodeposited MnOx catalyst film is porous, as confirmed by the observation of disc-like structures in the SEM images of a thick film (Figure S4 in the SI). However, the increase in activity did not scale linearly as a function of loading owing to a limit that we have shown is intrinsic to such porous OEC films where proton−electron/hole transport necessarily exists in competition with the consumption of holes in catalytic reactions.[55] In materials such as these, an optimal/critical thickness is reached where electrode activity reaches a plateau. Therefore, thin films deposited with passage of 6 mC/cm^2 were selected for electrochemical measurements since they offered sufficient film thickness while preserving linear Tafel slopes across a wide potential range.

4.1. OER Rate Law in Alkaline Medium. The steady-state water oxidation mechanism of MnOx was initially interrogated using Tafel and reaction order plots at alkaline and acidic pH. In alkaline conditions from pH 11.35 to 13.30, the OER on MnOx exhibits average Tafel slopes of about 60 mV/decade with low deviation, zeroth-order dependence on [P$_i$] (Figures 2c and S5c in the SI) and inverse first-order dependence on [H$^+$] (Figures 3c and S2c in the SI). The electrochemical rate law for alkaline oxygen evolution on MnOx is

$$j_{\mathrm{alkaline}} = j_{0,\mathrm{b}}\exp\left[\frac{F\eta}{RT}\right] = 4Fk_0[\mathrm{H}^+]^{-1}\exp\left[\frac{F\eta}{RT}\right] \qquad (3)$$

where $j_{0,b}$ is the exchange current density, k_0 is the heterogeneous electrochemical rate constant at the reversible potential with units of (mol M)/(s cm^2), and 2.3 × RT/F denotes the 59 mV/decade Tafel slope. A Tafel slope close to 59 mV/decade is consistent with a one-electron pre-equilibrium preceding a turnover-limiting chemical step.[56]

Armed with the electrochemical rate law, a mechanistic model for the OER on MnOx under alkaline pH may be constructed with insights into catalyst resting state. Our work on oxidic metal films indicated that edge sites are particularly important for engendering catalysis.[24,25,57,58] In particular, two critical structural and chemical features of the resting state involve the identity of the oxygen ligands and the oxidation state of manganese at edge sites of MnOx in alkaline conditions.

The nature of the manganese oxidation state is furnished by prior coulometric measurements and XAS studies. Our previous coulometry analysis indicates an average oxidation state of +3.68 for Mn in MnOx;[54] thus, manganese exists in Mn^{III} and Mn^{IV} formal oxidation states. This result is consistent with the stoichiometric composition of $MnO_{1.7-2.0}$ that defines manganese dioxides.[59] Recent *in situ* X-ray absorption (XAS) and UV−vis spectroscopic studies also support the presence of Mn^{III} at the surface of active MnO_2 catalyst films.[37−44] We thus surmise that the resting state of MnOx consists of some Mn^{III}, in addition to Mn^{IV}, at edge sites. *Ex situ* XAS of MnO_2 films electrodeposited under conditions similar to those reported here, at constant potential from aqueous solutions of Mn^{2+} buffered with acetate at pH 6, suggest that these films comprise a pyrolusite material with a short-range structure that exhibits birnessite-like edge-sharing Mn octahedra. The pyrolusite polymorph of MnO_2 has a point of zero charge (PZC) of ~7.[60−62] By definition, at electrolyte pH below the PZC, the surface of the catalyst is positively charged and terminated predominantly by protonated oxygen in the form of bound water molecules and bridging hydroxyl groups. Above the PZC, the surface is negatively charged and is more likely to consist of terminal or bridging di-μ-oxo's. Therefore, in the alkaline regime from pH 11.35 to 13.30, the MnOx surface has partial negative charge, implying a preponderance of terminal hydroxo and oxo groups.

Figure 5 shows a model of MnOx in alkaline solution (blue dashed box) that is consistent with the structural and chemical characteristics of MnOx and the electrokinetics measurements. In the resting state, Mn^{III}−OH is converted to Mn^{IV}=O via a one-electron and one-proton PCET pre-equilibrium. This is followed by the chemical turnover-limiting step (TLS), which is likely O_2 liberation from coupling two adjacent terminal oxygen atoms. Such electrochemical behavior resembles that observed for Co−OEC, which also exhibits a PCET pre-equilibrium from a Co$^{III/IV}$ resting state preceding a chemical TLS step to furnish O_2.

4.2. OER Rate Law in Acidic Medium. In acidic conditions from pH 1.0 to 3.5, the Tafel plots exhibited a high average slope of about 653 mV/decade, zeroth-order dependence on [P$_i$] (Figures 2a and S5a in the SI), and zeroth-order dependence on [H$^+$] (Figures 3a and S2a in the SI). Slopes much greater than 120 mV/decade are classified as quasi-infinite and are consistent with an initial turnover-limiting chemical step.[56] The electrochemical rate law for acidic OER on MnOx is then simply:

$$j_{\mathrm{acidic}} = j_{0,\mathrm{a}} \qquad (4)$$

where $j_{0,a}$ is the potential independent exchange current density.

Possible chemical steps include O−O bond formation, O_2 liberation, deprotonation of surface hydroxyls by water, or disproportionation of surface Mn^{3+}. However, assigning the TLS to O−O bond formation or O_2 liberation is unlikely because both of these steps require that the resting state of the catalyst surface is fully composed of reactive terminal $Mn^{IV}{=}O$, which is inconsistent with the observed average Mn oxidation state, PZC of MnOx, and recent literature, all of which suggest the presence of Mn^{3+} in active manganese oxide water oxidation catalysts. Furthermore, in acidic conditions, bridging di-μ-hydroxyl and terminal hydroxyl groups—not terminal oxos—are favored, and thus OER formation would have to be accompanied by PCET to the electrode, which cannot generally be accommodated by an infinite Tafel slope.

Hence, the remaining possibilities are deprotonation of surface hydroxyls by water and disproportionation of surface-bound Mn^{III}. Considering the former case, there are two possible proton acceptors under acidic conditions: water and adjacent $Mn^{III}{-}OH$ sites. Given that the pK_a of H_3O^+ is −1.7[63] and that of $Mn^{III}{-}OH_2^+$ (from manganite, for comparison) is 5.72,[64] it is significantly more favorable to perform a surface proton transfer to create adjacent $Mn^{III}{-}OH_2^+$ and $Mn^{III}{-}O^-$ groups, which are then poised to disproportionate. Indeed, surface-bound Mn^{3+} oxides have a large equilibrium constant for disproportionation under acidic conditions,[65] as recently observed by Takashima et al.[38] However, on the surface, the disproportionation is likely coupled with a cross-site proton transfer which serves to limit the rate of the process due to the inversion of pK_a required to access $Mn^{III}{-}OH_2^+$ and $Mn^{III}{-}O^-$ intermediates. A similar mechanism is observed in Meyer's surface-bound polypyridyl Ru complexes where two adjacent $Ru^{III}{-}OH$ undergo proton transfer and disproportionation to form $Ru^{II}{-}OH_2$ and $Ru^{IV}{=}O$ species.[66] Thus, assigning the TLS to a cross-site proton-coupled disproportionation is consistent with the observed Tafel and reaction order data in acidic electrolytes. Figure 5 (red dashed box) illustrates this model where four $Mn^{III}{-}OH$ sites disproportionate to two $Mn^{II}{-}OH_2$ and two $Mn^{IV}{=}O$ species. The adjacent $Mn^{IV}{=}O$ sites may then couple terminal oxos and liberate O_2. Four adjacent Mn^{III} sites are needed to generate two neighboring Mn^{IV} sites. The likelihood of sampling a reaction coordinate possessing four contiguous Mn^{III} sites is likely to be small, and thus accounts for the low activity of MnOx in acidic solution.

4.3. OER Rate Law in Intermediate pH Medium.

In neutral conditions at pH 7.0, MnOx displayed an average slope near 120 mV/decade (Figures 1 and S2b in the SI). Although this slope is characteristic of a first-step, turnover-limiting, electron transfer,[56] in this case, the Tafel slope varies systematically over the intermediate pH range from 153 mV/decade (at pH 5.5) to 105 mV/decade (at pH 8.5) and is observed over a narrow range of current density. That is, the 105−150 mV/decade Tafel slopes do not reflect the kinetics of a single mechanism at pH 7 but rather are consistent with a narrow regime displaying mixed-control by two reaction pathways. Thus, Langmuir conditions cannot be assumed.[56] Indeed, the catalyst films exhibit approximately inverse half-order fractional dependence on proton concentration (Figure 3b), which would result from the combination of zeroth-order $[H^+]$ dependence at acidic pH and inverse first-order $[H^+]$ dependence at alkaline pH. These observations suggest that, at intermediate pH, there are two primary competing pathways: (i) in acidic conditions, a disproportionation mechanism with zeroth-order dependence on proton concentration, and (ii) at alkaline pH, a one-electron, one-proton PCET mechanism. In this model, the pH of the electrolyte modulates the contribution of each mechanism. Assuming a surface-bound Mn^{3+} disproportionation reaction described in Figure 5, the propensity for the reaction to occur diminishes exponentially as pH increases. Thus, in alkaline conditions, there is no contribution from the disproportionation mechanism, while in the acidic regime, disproportionation is the dominant pathway. Our results are consistent with a similar conclusion reached by Takashima et al. where Mn^{III} is stabilized in alkaline electrolyte but disproportionate readily in acidic conditions.[41,44] An emerging trend establishes that OER is enhanced in manganese oxides when Mn^{3+} is introduced through voltage cycling protocols[28,31,35,37] or via chemical synthesis.[29,38,39,47] These studies reinforce the important role that Mn^{3+} plays in facilitating OER.

4.4. Stability and Self-Healing.

The stability of MnOx and other metal oxide materials is generally considered within the context of the intrinsic thermodynamic and kinetics properties of the catalyst itself. Generally, the dissolution of metal ions from oxide materials correlates with ligand substitution rates in metal aquo complexes,[67] where the rate is dominated by the electron count of the metal in a given ligand field, most notably octahedral or pseudo-octahedral for metal oxide catalysts. Population of electrons in metal antibonding orbitals, especially in the e_g* set, diminish the metal−ligand bond order and promote substitutional lability.[9,68] Analogously in metal oxides, where both the t_{2g}* and e_g* orbitals of a local metal center are antibonding, increased d-electron counts and high-spin electron configurations weaken the metal−oxygen framework and lead to more facile oxide degradation. Thus, early first-row transition metal oxides, such as MnOx, are more intrinsically stable in contact with acids than are late first-row metal oxides with higher d-electron counts.

Notwithstanding, most metal oxides are also unstable under the conditions of OER. The four-electron chemistry of OER causes metals to cycle through a range of oxidation states. In the mechanism outlined in Figure 5, Mn^{2+} is attendant to O_2 evolution; the high-spin d^5 nature of Mn^{2+} imparts to it exceptional substitutional lability and accelerates the dissolution of the catalyst film. These electronic configurations are augmented by acid−base chemistry. In the case of oxides, acidic pH regimes are especially deleterious to catalyst stability. For these reasons, MnOx naturally leaches into solution in acidic electrolytes and during OER, as established by ^{31}P NMR line broadening experiments.

Though intrinsically unstable, MnOx and more generally, other anodically electrodeposited metal oxide films, may be functionally stable if a self-healing mechanism is introduced as part of the catalytic cycle. As long as MnOx deposition occurs at potentials below those required for OER, the films will remain stable through self-repair owing to the reoxidation of manganese ions in solution. A similar self-healing process has been recently inferred by Casey and Britt[47] during OER for manganese oxide in the presence of a chemical oxidant.

To better visualize the relation between deposition and OER kinetics processes, Tafel plots derived for growth and oxygen evolution on MnOx were combined and reformulated in terms of a single potential (E) vs pH plot (Figure 6). This plot incorporates the inverse first- and zeroth-order dependence on

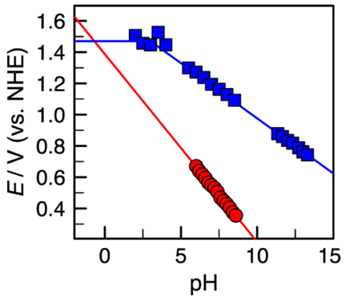

Figure 6. Potential dependence on pH for MnOx deposition (red, ●) and oxygen evolution on MnOx (blue, ■). Data were interpolated at $j = 1.3\ \mu A/cm^2$ from Tafel plots for MnOx deposition (see ref 54) and OER (Figure S2 in the SI). The deposition trace is consistent with an inverse fourth-order dependence on $[H^+]$ in the acidic regime[69] and assumes a Mn^{2+} solution concentration of 50 μM, which is consistent with concentrations for a dissolved 6 mC/cm^2 MnOx film.

$[H^+]$ for the OER in the alkaline and acidic regimes, respectively, and the inverse fourth-order dependence on $[H^+]$ for MnOx deposition near-neutral[54] to acidic[69] pH. The difference in proton order between deposition and oxygen evolution on MnOx results in the deposition potential rising faster than the OER potential as pH is lowered (for the same current density). Eventually, the two traces cross and mark the point where film repair can no longer keep pace with film degradation during the OER process. As indicated in Figure 6, this crossover emerges near pH 0 and provides a prediction of where self-healing ceases and net film dissolution manifests.

To test our prediction and quantify functional stability, film dissolution was examined with Mn^{2+}-induced paramagnetic line broadening of the ^{31}P NMR peak for inorganic phosphate in acidic solutions at pH 2.0, 0.1, and −0.5 (Figure 4). The catalyst displayed characteristics of both intrinsic and functional kinetic stability. The intrinsic stability prevented complete dissolution of the film even at pH 2.0 in the absence of applied current (Figure 4a). Additional stabilization of MnOx was obtained by self-healing the catalyst films and was exemplified by the significantly slower rate of dissolution and diminished overall percent dissolution for the system under operation in 4 M phosphoric acid (pH ≈ 0.1) compared to films held at open circuit (Figure 4b). However, it is only in 4 M HCl with a pH of approximately −0.5 that the operating catalyst films could finally no longer be stabilized and decayed with rate similar to those at open circuit with film dissolution (Figure 4c). These observations concur with the predictions of Figure 6.

5. CONCLUSION

Electrokinetic experiments on electrodeposited MnOx films were performed over a wide pH range (in acidic, neutral, and alkaline P_i electrolytes) and revealed two competing mechanisms. In acidic conditions, a quasi-infinite Tafel slope and lack of proton dependence in the rate law indicated an initial chemical TLS that was assigned to surface Mn^{3+} disproportionation. At alkaline pH, an average Tafel slope of approximately 60 mV/decade contributed to a rate law concordant with a one-electron, one-proton PCET equilibrium preceding a turnover-limiting chemical step. At neutral pH, competition between these two mechanisms resulted in a half-order dependence on proton concentration and Tafel slopes that are intermediate to those observed for the limiting acidic and alkaline regimes.

A key feature that differentiates MnOx from other electrodeposited, late first-row transition metal oxides is its higher intrinsic and functional kinetic stability in acidic electrolytes. Although MnOx is not as catalytically active for OER as late metal oxidic films, such as Co−OEC and Ni−OEC, it is able to perform OER in very acidic environments owing to the increased inertness of MnOx and its ability to maintain self-healing for electrolytes with pH greater than zero. Our results show that self-healing may be predictably quantified by acquiring mechanistic knowledge of the interplay between OER and deposition electrokinetics, and thus self-healing may be incorporated as a general design principle in catalysis development, especially in expanding the operational range of OER catalysts.

■ ASSOCIATED CONTENT

Ⓢ Supporting Information

O_2 sensor measurements, Tafel plots, SEM images, and NMR line broadening calibration curves. This material is available free of charge via the Internet at http://pubs.acs.org.

■ AUTHOR INFORMATION

Corresponding Author

dnocera@fas.harvard.edu

Notes

The authors declare no competing financial interest.

■ ACKNOWLEDGMENTS

This research was supported by DOE DE-SC0009565. SEM imaging was performed at Harvard University's Center for Nanoscale Systems (CNS), a member of the National Nanotechnology Infrastructure Network (NNIN), which is supported by the National Science Foundation under ECS-0335765. We thank Casandra Cox for instruction on O_2 Faradaic efficiency measurement.

■ REFERENCES

(1) Lewis, N. S.; Nocera, D. G. *Proc. Natl. Acad. Sci. U.S.A.* **2006**, *103*, 15729−15735.
(2) Abbott, D. *Proc. IEEE* **2010**, *98*, 42−66.
(3) Hoffert, M. I.; Caldeira, K.; Jain, A. K.; Haites, E. F.; Harvey, L. D. D.; Potter, S. D.; Schlesinger, M. E.; Schneider, S. H.; Watts, R. G.; Wigley, T. M. L.; Wuebbles, D. J. *Nature* **1998**, *395*, 881−884.
(4) Nocera, D. G. *Inorg. Chem.* **2009**, *48*, 10001−10017.
(5) Cook, T. R.; Dogutan, D. K.; Reece, S. Y.; Surendranath, Y.; Teets, T. S.; Nocera, D. G. *Chem. Rev.* **2010**, *110*, 6474−6502.
(6) Barber, J. *Chem. Soc. Rev.* **2009**, *38*, 185−196.
(7) Cukier, R. I.; Nocera, D. G. *Annu. Rev. Phys. Chem.* **1998**, *49*, 337−369.
(8) Huynh, M. H. V.; Meyer, T. J. *Chem. Rev.* **2007**, *107*, 5004−5064.
(9) Betley, T. A.; Wu, Q.; Van Voorhis, T.; Nocera, D. G. *Inorg. Chem.* **2008**, *47*, 1849−1861.
(10) Eisenberg, R.; Gray, H. B. *Inorg. Chem.* **2008**, *47*, 1697−1699.
(11) Hernández-Pagán, E. A.; Vargas-Barbosa, N. M.; Wang, T.; Zhao, Y.; Smotkin, E. S.; Mallouk, T. E. *Energy Environ. Sci.* **2012**, *5*, 7582−7589.
(12) Rossmeisl, J.; Qu, Z.-W.; Zhu, H.; Kroes, G.-J.; Nørskov, J. K. *J. Electroanal. Chem.* **2007**, *607*, 83−89.
(13) Man, I. C.; Su, H.-Y.; Calle−Vallejo, F.; Hansen, H. A.; Martínez, J. I.; Inoglu, N. G.; Kitchin, J.; Jaramillo, T. F.; Nørskov, J. K.; Rossmeisl, J. *ChemCatChem.* **2011**, *3*, 1159−1165.
(14) Woodhouse, M.; Parkinson, B. A. *Chem. Soc. Rev.* **2009**, *38*, 197−210.
(15) Gerken, J. B.; Chen, J. Y. C.; Massé, R. C.; Powell, A. B.; Stahl, S. S. *Angew. Chem., Int. Ed.* **2012**, *51*, 6676−6680.

(16) Trasatti, S. In *The Electrochemistry of Novel Materials*; Lipkowski, J., Ross, P. N., Eds.; VCH: New York, 1994; pp 207−251.
(17) Surendranath, Y.; Nocera, D. G. *Prog. Inorg. Chem.* **2011**, *57*, 505−560.
(18) Lutterman, D. A.; Surendranath, Y.; Nocera, D. G. *J. Am. Chem. Soc.* **2009**, *131*, 3838−3839.
(19) Surendranath, Y.; Lutterman, D. A.; Liu, Y.; Nocera, D. G. *J. Am. Chem. Soc.* **2012**, *134*, 6326−6336.
(20) Nocera, D. G. *Acc. Chem. Res.* **2012**, *45*, 767−776.
(21) Surendranath, Y.; Bediako, D. K.; Nocera, D. G. *Proc. Natl. Acad. Sci. U.S.A.* **2012**, *109*, 15617−15621.
(22) Winkler, M. T.; Cox, C. R.; Nocera, D. G.; Buonassisi, T. *Proc. Natl. Acad. Sci. U.S.A.* **2013**, *110*, E1076−E1082.
(23) Kanan, M. W.; Nocera, D. G. *Science* **2008**, *321*, 1072−1075.
(24) Surendranath, Y.; Kanan, M. W.; Nocera, D. G. *J. Am. Chem. Soc.* **2010**, *132*, 16501−16509.
(25) Bediako, D. K.; Surendranath, Y.; Nocera, D. G. *J. Am. Chem. Soc.* **2013**, *135*, 3662−3674.
(26) Dincă, M.; Surendranath, Y.; Nocera, D. G. *Proc. Natl. Acad. Sci. U.S.A.* **2010**, *107*, 10337−10341.
(27) Revie, R. W., Ed. *Uhlig's Corrosion Handbook*, 3rd ed.; John Wiley: Hoboken, NJ, 2011.
(28) Zaharieva, I.; Chernev, P.; Risch, M.; Klingan, K.; Kohlhoff, M.; Fischer, A.; Dau, H. *Energy Environ. Sci.* **2012**, *5*, 7081−7089.
(29) Robinson, D. M.; Go, Y. B.; Mui, M.; Gardner, G.; Zhang, Z.; Mastrogiovanni, D.; Garfunkel, E.; Li, J.; Greenblatt, M.; Dismukes, G. C. *J. Am. Chem. Soc.* **2013**, *135*, 3494−3501.
(30) Bergmann, A.; Zaharieva, I.; Dau, H.; Strasser, P. *Energy Environ. Sci.* **2013**, *6*, 2745−2755.
(31) Hocking, R. K.; Brimblecombe, R.; Chang, L.-Y.; Singh, A.; Cheah, M. H.; Glover, C.; Casey, W. H.; Spiccia, L. *Nat. Chem.* **2011**, *3*, 461−466.
(32) Zhou, F.; Izgorodin, A.; Hocking, R. K.; Spiccia, L.; MacFarlane, D. R. *Adv. Energy Mater.* **2012**, *2*, 1013−1021.
(33) Fekete, M.; Hocking, R. K.; Chang, S. L. Y.; Italiano, C.; Patti, A. F.; Arena, F.; Spiccia, L. *Energy Environ. Sci.* **2013**, *6*, 2222−2232.
(34) Zhou, F.; Izgorodin, A.; Hocking, R. K.; Armel, V.; Spiccia, L.; Macfarlane, D. R. *ChemSusChem* **2013**, *6*, 643−651.
(35) Gorlin, Y.; Jaramillo, T. F. *J. Am. Chem. Soc.* **2010**, *132*, 13612−13164.
(36) Gorlin, Y.; Jaramillo, T. F. *J. Electrochem. Soc.* **2012**, *159*, H782−H786.
(37) Gorlin, Y.; Lassalle-Kaiser, B.; Benck, J. D.; Gul, S.; Webb, S. M.; Yachandra, V. K.; Yano, J.; Jaramillo, T. F. *J. Am. Chem. Soc.* **2013**, *135*, 8525−8534.
(38) Mette, K.; Bergmann, A.; Tessonnier, J.-P.; Hävecker, M.; Yao, L.; Ressler, T.; Schlögl, R.; Strasser, P.; Behrens, M. *ChemCatChem.* **2012**, *4*, 851−862.
(39) Bergmann, A.; Zaharieva, I.; Dau, H.; Strasser, P. *Energy Environ. Sci.* **2013**, *6*, 2745−2755.
(40) Ramírez, A.; Bogdanoff, P.; Friedrich, D.; Fiechter, S. *Nano Energy* **2012**, *1*, 282−289.
(41) Morita, M.; Iwakura, C.; Tamura, H. *Electrochim. Acta* **1977**, *22*, 325−328.
(42) Morita, M.; Iwakura, C.; Tamura, H. *Electrochim. Acta* **1979**, *24*, 357−362.
(43) Takashima, T.; Hashimoto, K.; Nakamura, R. *J. Am. Chem. Soc.* **2012**, *134*, 1519−1527.
(44) Takashima, T.; Hashimoto, K.; Nakamura, R. *J. Am. Chem. Soc.* **2012**, *134*, 18153−18156.
(45) Najafpour, M. M.; Leonard, K. C.; Fan, F.-R. F.; Tabrizi, M. A.; Bard, A. J.; King'ondu, C. K.; Suib, S. L.; Haghighi, B.; Allakhverdiev, S. I. *Dalton Trans.* **2013**, *42*, 5085−5091.
(46) Najafpour, M. M.; Sedigh, D. J. *Dalton Trans.* **2013**, *42*, 12173−12178.
(47) Najafpour, M. M.; Kompany-Zareh, M.; Zahraei, A.; Jafarian Sedigh, D.; Jaccard, H.; Khoshkam, M.; Britt, R. D.; Casey, W. H. *Dalton Trans.* **2013**, *42*, 14603−14611.
(48) Parsons, R. In *Advances in Electrochemistry and Electrochemical Engineering*; Delahay, P., Ed.; Interscience: New York, 1961; pp 1−64.
(49) Bates, R. G. *J. Res. Natl. Bur. Stand.* **1951**, *47*, 127−134.
(50) Bates, R. G.; Acree, S. F. *J. Res. Natl. Bur. Stand.* **1943**, *30*, 129−155.
(51) Vanderzee, C. E.; Quist, A. S. *J. Phys. Chem.* **1961**, *65*, 118−123.
(52) Grenthe, I.; Plyasunov, A. *Pure Appl. Chem.* **1997**, *69*, 951−958.
(53) Pettit, L. D.; Puigdomenech, I.; Wanner, H.; Sukhno, I.; Buzko, V. *Ionic Strength Corrections using Specific Interaction Theory*; 2008, http://old.iupac.org/projects/2006/2006-010-1-500.html (accessed Jan 12, 2013).
(54) Huynh, M.; Bediako, D. K.; Liu, Y.; Nocera, D. *J. Phys. Chem. C* **2014**, DOI: 10.1021/jp501768n.
(55) Bediako, D. K.; Costentin, C.; Jones, E. C.; Nocera, D. G.; Savéant, J.-M. *J. Am. Chem. Soc.* **2013**, *135*, 10492−10502.
(56) Gileadi, E. *Physical Electrochemistry: Fundamentals, Techniques and Applications*, 1st ed.; Wiley−VCH: Weinheim, 2011.
(57) Wang, L.-P.; Van Voorhis, T. *J. Phys. Chem. Lett.* **2011**, *2*, 2200−2204.
(58) Lee, S. W.; Carlton, C.; Risch, M.; Surendranath, Y.; Chen, S.; Furutsuki, S.; Yamada, A.; Nocera, D. G.; Shao-Horn, Y. *J. Am. Chem. Soc.* **2012**, *134*, 16959−16962.
(59) Pisarczyk, K. *Kirk−Othmer Encyclopedia of Chemical Technology*; John Wiley: New York, 1991; pp 501−532.
(60) Healy, T. W.; Herring, A. P.; Fuerstenau, D. W. *J. Colloid Interface Sci.* **1966**, *21*, 435−444.
(61) Gray, M. J.; Malati, M. A.; Rophael, M. W. *J. Electroanal. Chem. Interfac.* **1978**, *89*, 135−140.
(62) Chabre, Y.; Pannetier. *J. Prog. Sol. State Chem.* **1995**, *23*, 1−130.
(63) Jencks, W. P.; Regenstein, J. In *Handbook of Biochemistry and Molecular Biology*; Lundblad, R. L., MacDonald, F. M., Eds.; CRC Press: Boca Raton, FL, 2010; pp 595−635.
(64) Xyla, A. G.; Sulzberger, B.; Luther, G. W.; Hering, J. G.; Van Cappellen, P.; Stumm, W. *Langmuir* **1992**, *8*, 95−103.
(65) Batchelor-McAuley, C.; Shao, L.; Wildgoose, G. G.; Green, M. L. H.; Compton, R. G. *New J. Chem.* **2008**, *32*, 1195−1203.
(66) Chen, Z.; Vannucci, A. K.; Concepcion, J. J.; Jurss, J. W.; Meyer, T. J. *Proc. Natl. Acad. Sci. U.S.A.* **2011**, *108*, E1461−E1469.
(67) Casey, W. H. *J. Colloid Interface Sci.* **1991**, *146*, 586−589.
(68) Basolo, F.; Pearson, R. G. In *Mechanisms of Inorganic Reactions*; Wiley: New York, 1967.
(69) Fleischmann, M.; Thirsk, H. R.; Tordesillas, I. M. *Trans. Faraday Soc.* **1962**, *58*, 1865−1877.

J|A|C|S
JOURNAL OF THE AMERICAN CHEMICAL SOCIETY

Article

pubs.acs.org/JACS

Mechanistic Studies of the Oxygen Evolution Reaction Mediated by a Nickel–Borate Thin Film Electrocatalyst

D. Kwabena Bediako,[†,‡] Yogesh Surendranath,[†] and Daniel G. Nocera*[,†,‡]

[†]Department of Chemistry, Massachusetts Institute of Technology, 77 Massachusetts Avenue, Cambridge, Massachusetts 02139–4307

[‡]Department of Chemistry and Chemical Biology, Harvard University, 12 Oxford Street, Cambridge, Massachusetts 02138–2902

S Supporting Information

ABSTRACT: A critical determinant of solar-driven water splitting efficiency is the kinetic profile of the O_2 evolving catalyst (OEC). We now report the kinetic profiles of water splitting by a self-assembled nickel–borate (NiB_i) OEC. Mechanistic studies of anodized films of NiB_i exhibit the low Tafel slope of $2.3 \times RT/2F$ (30 mV/decade at 25 °C). This Tafel slope together with an inverse third order rate dependence on H^+ activity establishes NiB_i as an ideal catalyst to be used in the construction of photoelectrochemical devices for water splitting. In contrast, nonanodized NiB_i films display significantly poorer activity relative to their anodized congeners that we attribute to a more sluggish electron transfer from the catalyst resting state. Borate is shown to play two ostensibly antagonistic roles in OEC activity: as a promulgator of catalyst activity by enabling proton-coupled electron transfer (PCET) and as an inhibitor in its role as an adsorbate of active sites. By defining the nature of the PCET pre-equilibrium that occurs during turnover, trends in catalyst activity may be completely reversed at intermediate pH as compared to those at pH extremes. These results highlight the critical role of PCET pre-equilibria in catalyst self-assembly and turnover, and accordingly suggest a reassessment in how OEC activities of different catalysts are compared and rationalized.

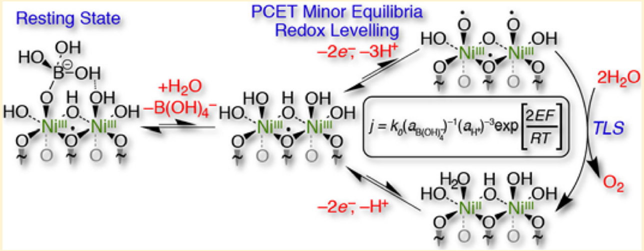

INTRODUCTION

Photodriven water splitting to generate H_2 and O_2 is a promising means of storing solar energy in chemical fuels.[1−5] Viable solar-to-fuels schemes mandate the use of catalysts that can mediate the oxygen evolution reaction (OER) and hydrogen evolution reaction (HER) with minimized overpotentials required to sustain current densities commensurate with the solar flux (ca. 20 mA/cm^2).[4] Of the two half reactions, the OER is more kinetically demanding because it requires a total of four redox equivalents per turnover, and results in the formation of two oxygen−oxygen bonds.[6,7] Accordingly, the majority of the activation overpotential in water splitting usually arises from the OER.[8] Oxygen evolution catalysts (OECs) must therefore be able to accommodate the redox demand of the OER, ideally over a narrow potential range. Such activity profiles (i.e., small current−voltage, Tafel, slopes) are especially important for the integration of catalysts with light harvesting/charge separating materials in a buried-junction configuration.[1,9−12] In a buried-junction semiconductor heterostructure,[11−15] a photovoltage is generated at an internal solid-state junction of a photovoltaic (PV) material that is protected from the electrolyte by an Ohmic coating. Such a configuration is an especially attractive target for direct solar-to-fuels conversion because the catalytic and PV components can be independently optimized, thus permitting the use of a wider variety of semiconductor and catalytic materials.[16] In a buried junction device, the kinetic behavior of the catalysts defines the point of intersection of the electrochemical load of the catalyst with the current density−voltage (j−V) curve of the PV.[14,17] This impedance matching determines the operational current density and voltage, and therefore net solar−to−fuels efficiency (SFE) of the system. The highest SFEs demand that OECs possessing modest exchange current densities and low Tafel slopes be integrated with PVs that have open circuit voltages near the thermodynamic threshold of water splitting.[17] Since the Tafel slope depends on the mechanism of the reaction itself, the development of functionally stable and efficient buried junction systems requires an understanding of the interplay between the kinetics of catalyst formation/decomposition and catalytic turnover.[18] Moreover, catalysts that are stable and operate at intermediate pH regimes are particularly useful because they avoid OER conditions where semiconducting materials are often unstable.

To meet the foregoing requirements, we have elaborated Co−OECs that operate under a range of conditions, including the underexplored intermediate pH regimes.[18−26] The Co−OEC displays a 60 mV/decade Tafel slope and an inverse first order dependence on H^+ activity owing to the presence of a Co^{III}−OH/Co^{IV}−O PCET pre-equilibrium during turnover.[24]

Received: December 27, 2012
Published: January 29, 2013

Although this catalyst has been successfully applied to a myriad of semiconducting materials,[13,27−39] and is the foundation on which the artificial leaf has been built,[9] improvements in SFE may be realized with the development of more active catalysts, particularly those with lower Tafel slopes. To this end, we recently reported a nickel−borate (NiB_i) system that allows for controlled electrodeposition of OEC films that display high activity at intermediate pH.[25] X-ray absorption spectroscopy reveals changes in the nickel oxidation state and local structure that accompany a drastic improvement (ca. 3 orders of magnitude) in activity upon anodization of NiB_i[26] as a result of Tafel slopes of 30 mV/decade (2.3 × RT/2F) in near-neutral pH regimes.[17,26] In line with anodization pretreatment, complementary studies have shown that solution-cast Ni-based and NiFe-based films also furnish low Tafel slopes in alkaline pH regimes.[40] Electrochemical treatment of the crystalline oxide precursors appears to lead to transformation of the films into a nickelate structure[40] that is very similar to that found for NiB_i films in near neutral regimes.[26] Moreover, we have shown that phase changes induced by electrochemical conditioning of conventional crystalline oxides is a crucial factor to consider in OEC development.[41] In light of this emerging trend of increased activity with anodization of Ni−based catalysts, we sought to correlate OEC activity with anodization.

We now report the OER kinetic profile of NiB_i films over a wide pH range (8.5−14) and divulge mechanistic insights into the origin of the considerable activity enhancement that is attendant to anodization. The electrosynthesis of ultrathin OEC films (≤15 monolayers) enables us to avoid internal electronic or ionic transport barriers. Our studies have enabled us to uncover a unique OER mechanism that stands in contrast to frequently invoked OER mechanisms of nickel oxide anodes.[42−50] Furthermore, we find that the apparent specific activity of NiB_i films is significantly greater than that found in CoB_i systems of comparable catalyst loading for pH > 7. However, the same pH-dependent profiles cause CoB_i to supersede NiB_i in activity for pH ≤ 7. By defining the nature of the proton-coupled electron transfer (PCET) pre-equilibrium that occurs during turnover, we find that trends in catalyst activity may be completely reversed at intermediate pH as compared to those at pH extremes. The results presented herein highlight the need for a detailed mechanistic understanding of OER for the construction of direct solar-to-fuels devices that operate at high efficiencies.

■ EXPERIMENTAL SECTION

1. Materials. $Ni(NO_3)_2 \cdot 6H_2O$ 99.9985% was used as received from Strem. KOH 88%, KNO_3 99.0−100.5%, and H_3BO_3 99.9% were reagent grade and used as received from Macron. $NaClO_4$ hydrate (99.99% metals basis) was used as received from Aldrich. All electrolyte solutions were prepared with type I water (EMD Millipore, 18 MΩ cm resistivity). Fluorine−tin−oxide (FTO) coated glass (TEC-7) was purchased as pre-cut 1 cm × 2.5 cm glass pieces from Hartford Glass. Unless stated otherwise, all experiments used FTO with 7 Ω/sq surface resistivity.

2. Electrochemical Methods. Potentiometric and voltammetric measurements were undertaken with a CH Instruments 760C or 760D bipotentiostat, a BASi Ag/AgCl reference electrode (soaked in saturated KCl), and a Pt-mesh counter electrode. Rotating disk electrode (RDE) measurements were conducted using a Pine Instruments MSR rotator and a 5 mm diameter Pt-disk rotating electrode. All electrochemical experiments were performed at 23 ± 1 °C using a three-electrode compartment cell with a porous glass frit separating the working and auxiliary compartments. Electrode potentials were converted to the NHE scale using $E(\text{NHE}) = E(\text{Ag/AgCl}) + 0.197$ V. Overpotentials were computed using $\eta = E(\text{NHE}) - 0.68$ V at pH 9.2. Unless stated otherwise, the electrolyte comprised 0.5 M potassium borate (KB_i), 1.75 M potassium nitrate, pH 9.2 (henceforth referred to as KB_i/KNO_3 electrolyte).

3. Film Preparation. Catalyst films were prepared via controlled-potential electrolysis of 0.1 M KB_i, pH 9.2 electrolyte solutions containing 0.4 mM Ni^{2+}. To minimize precipitation of $Ni(OH)_2$ from these solutions, 25 mL of 0.2 M KB_i was added to 25 mL of 0.8 mM Ni^{2+} solution. The deposition solutions were subsequently filtered through a 0.2 μm syringe filter (Pall) to remove any $Ni(OH)_2$ that formed. The solutions thus prepared remained clear over the course of deposition, which was carried out onto an FTO-coated glass piece. These FTO working electrodes were rinsed with acetone and water prior to use. A ∼0.6 cm wide strip of Scotch tape was applied to the FTO coated side such that a 1 cm^2 area was exposed to solution. Unless stated otherwise, deposition by controlled potential electrolysis was carried out on quiescent solutions at 1.15 V without *iR* compensation and with passage of 1 mC cm^{-2}. A typical deposition lasted 70 s. Following deposition, films were rinsed by dipping briefly in 0.1 M KB_i, pH 9.2 solution to remove any adventitious Ni^{2+}. Anodized films were subsequently electrochemically treated in 1 M KB_i, pH 9.2 electrolyte by passing an anodic current of 3.5 mA cm^{-2} with stirring. A steady potential was obtained after about 30 min of anodization. Unless stated otherwise, films were anodized for 1 h.

4. Potentiostatic Tafel Data Collection. Current−potential data were obtained by conducting controlled potential electrolysis in KB_i/KNO_3 electrolyte pH 9.2 at a variety of applied potentials (E_{appl}). Prior to film deposition and anodization, the solution resistance of the electrolyte to be used for Tafel data collection was measured using the *iR* test function. The electrolysis solution was exchanged for Ni^{2+}-containing KB_i electrolyte, without disturbing the relative positions of the working and reference electrodes and films were deposited. Following film preparation, the working electrode was rinsed in fresh Ni-free KB_i electrolyte and transferred, without drying, to the same electrolysis bath in which the solution resistance was measured. The electrode was allowed to equilibrate with the electrolyte solution for 5 min while being held at the open circuit potential. The solution was stirred, and steady-state currents were then measured at applied potentials that descended from 1.13 to 1.00 V in 7−20 mV steps. For currents greater than 10 μA cm^{-2}, a steady state was reached at a particular potential in less than 400 s. For currents lower than 10 μA cm^{-2}, longer electrolysis times (15−20 min) were utilized to ensure that steady state had been achieved. The solution resistance measured prior to the data collection was used to correct the Tafel plot for Ohmic potential losses. Tafel data collected in succession using the same electrode exhibited good reproducibility, and Tafel slopes were not dependent on the direction of potential change (Figure S2).

5. Cyclic Voltammetry. CVs of anodized catalyst films were recorded in KB_i/KNO_3, pH 9.2 electrolyte. After 2 min at open circuit, catalyst films were held at 1.0 V for 60 s, immediately after which CV scans were initiated from 1.0 V. The potential was decreased at a scan rate of 100 mV s^{-1} with stirring, and with correction for Ohmic potential losses (measured prior to film deposition). At a switching potential of 0.2 V, the direction of scan was reversed, and CVs were terminated at 1.1 V.

6. Dependence of Tafel Data on Film Thickness and Calculation of Lower-Limit TOF. Steady-state polarization data were acquired following anodization of films deposited by passage of 1.0, 0.4, and 0.083 mC cm^{-2}. Deposition durations were about 67, 25, and 11 s, respectively. We note that the charge passed cannot be used as a simple measure of the Ni loading because: (1) non-Faradaic double-layer charging currents for short deposition times (and particularly for the thinnest of these films) accounts for a non-trivial proportion of the total charge passed; and (2) oxygen evolution accompanies deposition, and so a fraction of the charge passed is consumed for OER and not solely for film deposition. Thus, in order to evaluate film loadings, CVs of each film were acquired as described in part 5 of this section, and the charge consumed upon film reduction was determined by integration of the cathodic surface wave. Charges of 0.91, 0.53, and 0.21 mC cm^{-2} were obtained from analysis of the CVs.

We have established that the charge passed upon film oxidation or reduction involves the net transfer of 1.6 electrons per nickel center for films of comparable thickness.[26] Thus, the charges correspond to loadings of about 5.9, 3.4, and 1.4 nmol/cm^2 of Ni centers, corresponding to films of approximate thicknesses of 5, 3, and 1.0 nm.

Knowing the amount of nickel on each electrode, and by interpolating Tafel data for each film at η = 400 mV, respective current densities, *j*, at this overpotential can be converted into turnover frequency per nickel center, given that each turnover requires the removal of four electrons ($j = 4F\nu$, where ν is the turnover velocity of the film per cm^2 and *F* is the Faraday constant). Dividing ν by the catalyst loading returns the TOF per nickel center. Since the number of active sites is expected to be only a fraction of the number of nickel centers, this calculation returns a lower limit for the TOF of each active site. The calculated lower limit on the TOFs at η = 400 mV in 0.5 M KB_i 1.75 M KNO_3, pH 9.2 are 0.92, 0.51, and 0.49 mol O_2 (mol Ni)$^{-1}$ s^{-1} for films deposited by passage of 1.0, 0.4, and 0.08 mC cm^{-2}, respectively. Similarly, in the case of a 1.0 mC cm^{-2} catalyst film operated in 1 M KOH 1 M KNO_3 pH 13.85 electrolyte, we calculate a lower-limit on the TOF of 1.7 mol O_2 (mol Ni)$^{-1}$ s^{-1} at η = 325 mV.

7. Mass Transport Dependence Studies. To verify that Tafel data were not subject to mass transport limitations, a Pt rotating disk electrode (RDE) was used to collect steady state data. The Pt RDE was polished to a mirror finish with 0.05 μm α-alumina (CH Instruments). Prior to film deposition, the Pt disk was electrolyzed at 1.4 V (vs NHE) in 1 M KB_i, pH 9.2 electrolyte for 30 min to anodize the Pt surface exhaustively as to minimize current arising from platinum oxide formation upon application of a potential step. Following this pretreatment, catalyst films were deposited onto the Pt RDE in an otherwise identical manner to that described above. Tafel data were collected in KB_i/KNO_3 electrolyte with E_{appl} stepped from 1.13 to 1.00 V in 7−20 mV increments. At each potential step, steady-state data were collected at rotation rates (ω) of 2000 and 600 rpm; data were also collected in the absence of disk rotation, but in a well-stirred solution. *iR* corrected Tafel data collected under these three conditions are shown in Figure S1. Background currents arising from the OER at the Pt RDE itself are insignificant compared to currents due to the OER mediated by NiB_i. The excellent agreement among Tafel slopes (28 mV/decade) under these disparate conditions reveals that Tafel data are not limited by mass transport over the current/potential range explored. In addition, these experiments demonstrate that the kinetic profile of the catalyst does not depend on the nature of the underlying substrate.

8. Tafel Data in the Absence of Excess Supporting Electrolyte. Tafel data were acquired as in part 2 of this section, with the exception that electrolytes contained only KB_i and no KNO_3. Tafel data were collected in 0.1, 0.2, 0.5, and 1.0 M KB_i, pH 9.2 electrolyte (Figure S3). Apparent Tafel slopes decrease from 40 to 35 mV/decade as the borate concentration (and ionic strength of the electrolyte) increases.

9. Supporting Electrolyte Effect. The surface of a 0.2 cm^2 FTO-coated glass electrode was exposed by application a 1 cm wide piece of scotch tape to isolate a 2.0 mm ×1.0 cm strip. The solution resistances of six electrolytes, each containing 0.1 M KB_i at pH 9.2, with varying concentrations of KNO_3 from 0 to 2 M were measured using the *iR* test function. Without disturbing the relative positions of the working and reference electrodes, a 1.0 mC cm^{-2} catalyst film was deposited and anodized. Following anodization, the catalyst film was operated in each solution at a fixed current density of 0.4 mA cm^{-2}. In this galvanostatic experiment, the potential required to sustain this current density was recorded after at least 300 s had elapsed. Potential values were then corrected for *iR* drop using the measured solution resistances. Prior to operation in each electrolyte, the catalyst film was briefly rinsed in fresh electrolyte of identical composition, to avoid cross-contamination. As shown in Figure S4, KNO_3 concentrations ≥1 M are sufficient to eliminate any diffuse double layer effects and attendant complications arising from elevated local concentrations of borate anions.

10. Open Circuit Decay Transients. NiB_i films were prepared as described in part 3 of this section. Following deposition, the films were immersed in KB_i/KNO_3 pH 9.2 electrolyte and held at 1.1 V (vs NHE) for 10 s, after which E_{appl} was removed. This short duration was sufficient for the current to plateau without the onset of anodization. A second potentiostat, which was connected in parallel, was used to measure the voltage across the working and reference electrodes throughout the potential bias and for 2 min subsequent to the removal of E_{appl} (open circuit). The sampling interval was 5 ms. The open circuit potential (OCP) was plotted as a function of time (see Figure 2). The electrode was then rinsed in water and anodized in 1 M KB_i pH 9.2 electrolyte. Following anodization, films were immersed in KB_i/KNO_3 pH 9.2 electrolyte, and the open circuit decay experiment was repeated, this time with a sampling interval of 2.5 ms. The open circuit potential was plotted as a function of time (see Figure 2). These transients were fit to eq 1 to extract the Tafel slopes for OER for anodized and nonanodized films. The OCP transients were also converted into Tafel plots (Figure 2 inset) using eq 2.

11. Borate Dependence Studies. To determine the reaction order in borate, solutions were prepared with B_i concentrations in the range 0.63−6.3 mM. An appropriate amount of KNO_3 was added to ensure an ionic strength of 2 M. The solution resistance of each electrolyte was recorded without disturbing the relative positions of the working and reference electrodes, and then a 1.0 mC cm^{-2} catalyst film was deposited onto a Pt RDE. Following anodization, the catalyst film was operated at 1.05 V in each solution at ω = 2500, 1600, 900, and 625 rpm. At each rotation rate, the current was allowed to reach its steady-state value before proceeding to the next rate. Prior to operation in each electrolyte, the catalyst was rinsed in fresh electrolyte of identical composition to avoid cross-contamination. The experiment was then repeated at 1.04 and 1.06 V. Ohmic losses due to solution resistance accounted for <1 mV, and they were therefore neglected. Appreciable changes in current values with ω were observed for electrolytes of low buffer strength ($[B_i] < 40$ mM), implying that the reaction was not purely activation controlled. As such, Koutecký−Levich (K−L) plots (i^{-1} as a function of $\omega^{-1/2}$) were constructed to allow for extraction of activation-controlled currents by linear extrapolation to the limit of an infinitely high rotation rate (Figure S5 shows a representative plot). Log *j* was plotted as a function of log $[B_i]$ (see Figure 3) over the $[B_i]$ range 0.63 M−40 mM. In electrolytes of very low buffer strength ($[B_i] < 40$ mM), a slope of ca. zero is observed.

12. pH Dependence Studies in B_i Electrolyte. A 0.2 cm^2 (1 cm × 2 mm) area of an FTO-coated glass electrode was isolated with scotch tape and a 1 mC cm^{-2} catalyst film was deposited. The electrode was operated at a current of 2 μA (equivalent to 10 μA cm^{-2}) in 100 mM KB_i 2 M KNO_3, pH 8.5 electrolyte. The steady state electrode potential (measured after operation for ≥2 min at each pH) was recorded as the pH of the solution was raised up to pH 12.0 in increments of about 0.1 pH units using μL aliquots of 10% KOH solution. Ohmic potential losses amounted to <0.1 mV, and they were ignored. Additionally, at these very low current densities, no local pH gradients arise even when the pH is adjusted outside of the ideal B_i buffering regime. The steady-state electrode potential was plotted as a function of pH (see Figure 4).

A 1.0 mC cm^{-2} catalyst film was prepared onto a Pt RDE. Tafel data were collected in electrolytes with B_i concentrations equal to 0.601, 0.200, 0.110, 0.101, and 0.100 M at pH 8.5, 9.2, 10.2, 11.2, and 12.0, respectively, to ensure that each electrolyte contained ∼0.1 M borate anion, considering the pK_a of 9.2 for B_i buffer. Sufficient KNO_3 was added to each solution to yield a concentration of 0.9 M, and therefore to maintain an ionic strength of 1 M. In each solution, steady state data were collected without *iR* compensation at 2500, 1600, 900, and 625 rpm, and where necessary, K−L analysis was used to extract activation−controlled current values. Although the measured current, and for that matter the *iR* drop, varied with rotation rate, the difference in these Ohmic losses due to solution resistance between different rotation rates at the same applied potential was negligible (<1 mV). The product of the previously measured solution resistance and the average current value over the rotation rate range analyzed was subtracted from the applied potential to yield the *iR*-corrected potential. The upper and lower limits for applied potentials were chosen such that current densities would fall between 3.5 mA cm^{-2} and 10 μA cm^{-2}. Data were recorded at potential intervals of 10 mV to yield Tafel slopes (Figure 5a). Tafel plots were interpolated at 2.5, 0.25, and 0.025 mA cm^{-2} to furnish the potential dependence on pH at constant current density (Figure 5b).

13. pK_a Titrations. A 1.0 mC cm^{-2} catalyst film was prepared onto an FTO-coated glass electrode (0.2 cm^2), and operated at a current of 2 μA (equivalent to 10 μA cm^{-2}) in 100 mM KB$_i$ 2 M KNO$_3$, pH 11.3 electrolyte. The steady-state electrode potential was recorded using a Hg/HgO (1 *m* NaOH) reference electrode as the pH of the solution was raised in increments of 0.2−0.25 pH units up to pH 12, with μL aliquots of 50% KOH solution. The experiment was continued in separate electrolytes of identical composition (100 mM KB$_i$ 2 M KNO$_3$) whose pH had been previously adjusted to pH 12.25, 12.5, 12.8, and 13.15, respectively. Ohmic potential losses amounted to <0.1 mV in each electrolyte and could be safely ignored. The measured potentials (vs Hg/HgO) were converted to the NHE scale using E(NHE) = E(Hg/HgO, 1 *m* NaOH) + 0.108.[51] The corresponding overpotentials were calculated by subtracting the thermodynamic potential for the OER at each pH from the E(NHE) values. The steady state electrode overpotential was plotted as a function of pH at 10 μA cm^{-2} (see Figure 6).

14. Tafel Data in B$_i$-Free Electrolyte, pH 12.9, 13.8. A 1.0 mC cm^{-2} catalyst film was deposited onto a Pt RDE, and Tafel data were acquired in 0.1 M KOH 1.9 M KNO$_3$ and 1.0 M KOH 1.0 M KNO$_3$ solutions (pH 12.9 and 13.8, respectively). For these solutions, no mass transport limitations were encountered over the accessible overpotential range (η = 220−330 mV), and activation-controlled steady state Tafel data were acquired at a single rotation rate of 2000 rpm (Figure 6, inset).

15. Tafel Data in B$_i$-Free Electrolyte, pH 8.5. A 1.0 mC cm^{-2} catalyst film was deposited onto a Pt RDE as described above. The activation-controlled steady state current density was measured with *iR* compensation as a function of applied potential by K−L analysis (see Figure S6 for a representative example) at 20 mV intervals in 1.0 M NaClO$_4$, pH 8.50 electrolyte. There were 1−5 μL aliquots of 1 M NaOH added periodically to ensure minimal drift (±0.01 pH units) in bulk pH over the course of the experiment. Three consecutive runs were acquired, and the Tafel data were averaged (Figure 7). The activities of films in B$_i$ electrolyte (0.5 M KB$_i$ 1.75 M KNO$_3$, pH 9.2 electrolyte) after operation in 1 M NaClO$_4$ pH 8.5 are compared with Tafel data acquired using a fresh catalyst film in Figure S7. Since the activity of a catalyst film after operation in B$_i$-free electrolyte is comparable to that of a fresh film, the possibility of film corrosion causing the Tafel behavior displayed in Figure 7 is excluded.

16. Deposition and Tafel Plots of CoB$_i$ Films. CoB$_i$ catalyst films were prepared via controlled-potential electrolysis of 0.1 M KB$_i$, pH 9.2 electrolyte solutions containing 0.5 mM Co^{2+}. Depositions were carried out using an FTO-coated glass piece as the working electrode. These FTO-coated glass electrodes were rinsed with acetone and water prior to use in all experiments and a ~0.6 cm wide strip of Scotch tape was applied to the FTO coated side such that a 1 cm^2 area was exposed to solution. Deposition by controlled potential electrolysis was carried out on quiescent solutions at 0.9 V (vs NHE) without *iR* compensation and with passage of 0.6 mC cm^{-2} (equivalent to 6 nmol cm^{-2} Co). A typical deposition lasted 12 s.

Current−potential data were obtained for this 0.6 mC cm^{-2} CoB$_i$ film by conducting controlled potential electrolysis in KB$_i$/KNO$_3$ pH 9.2 electrolyte at a variety of applied potentials. Prior to film deposition, the solution resistance of the electrolyte to be used for collection of Tafel data was measured using the *iR* test function. The electrolysis solution was exchanged for Co^{2+}-containing KB$_i$ electrolyte, without disturbing the relative positions of the working and reference electrodes. The film was prepared by controlled-potential electrolysis. Following film preparation, the working electrode was rinsed in fresh Co-free KB$_i$ electrolyte and transferred, without drying, to the same electrolysis bath in which the solution resistance was measured. The electrode was allowed to equilibrate with the electrolysis solution for 5 min while being held at the open circuit potential. The solution was stirred, and steady-state currents were then measured at applied potentials that descended from 1.13 to 1.00 V in 10 mV steps. At each potential, 400 to 600 s were allowed for the film to reach steady state. The solution resistance measured prior to the data collection was used to correct the Tafel plot for Ohmic potential losses (Figure 9a).

■ RESULTS

Catalyst films were prepared by controlled potential electrolysis of 100 mM KB(OH)$_4$/H$_3$BO$_3$ (B$_i$) electrolyte, pH 9.2 containing 0.4 mM Ni^{2+} at an applied potential of 1.15 V (vs NHE) without stirring. Unless otherwise noted, a total charge of 1.0 mC cm^{-2} was passed during deposition over a period of 60−80 s using fluorine−tin−oxide (FTO) coated glass slides as substrate. Following deposition, films were preconditioned with an anodization protocol that involved passage of 3.5 mA cm^{-2} for 1−2 h in stirred solutions of 1.0 M B$_i$ electrolyte, pH 9.2.

1. Tafel Slope Determination. The steady-state current density (j) for oxygen evolution from anodized films was evaluated as a function of the overpotential (η) in stirred Ni-free solutions of 0.5 M B$_i$ pH 9.2 electrolyte (Figure 1). To avoid diffuse double layer effects,[52] a high ionic strength was maintained with 1.75 M KNO$_3$ supporting electrolyte. The applied voltage (E_{appl}) was varied in 7−20 mV increments in the region of water oxidation and maintained until j attained a steady-state value. Compensation of E_{appl} for Ohmic potential losses yielded the corrected potential (E), which was then converted to η by subtraction of the thermodynamic potential for water oxidation ($E°$) under the experimental conditions. Steady-state polarization data were acquired following anodization of films deposited by passage of 1.0, 0.40, and 0.083 mC cm^{-2}.

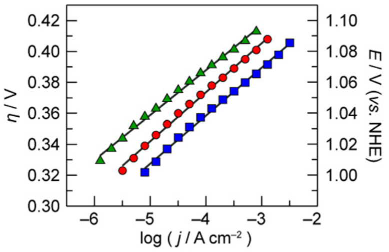

Figure 1. Tafel plots, $E = (E_{\text{appl}} - iR)$, $\eta = (E - E°)$, for anodized catalyst films deposited onto FTO by passage of 1.0 (blue ■), 0.40 (red ●), and 0.083 (green ▲) mC cm^{-2} and operated in 0.5 M KB$_i$ 1.75 M KNO$_3$ pH 9.2 electrolyte. Tafel slopes are 31, 32, and 29 mV/decade, respectively.

The amount of charge passed in oxidation or reduction of NiB$_i$ films involves a net transfer of ca. 1.6 electrons per nickel center.[26] With this knowledge, the charge consumed upon reduction of films by cyclic voltammatery permits a reliable estimation of the number of nickel centers in catalyst films (see subheading 6 of the Experimental Section) and thickness of the films.[26] Film thicknesses of approximately 5, 3, and 1 nm correspond to 15, 9, and 3 monolayers' worth of catalyst, respectively. Although the overall activity of these catalyst films at a specified overpotential increases with thickness, plots of η (or E) as a function of log j (Tafel plots) display similar slopes, b, of 30 mV/decade (2.3 × $RT/2F$), irrespective of loading. These Tafel slopes are indicative of a two-electron transfer in minor equilibrium prior to a chemical turnover-limiting step (TLS), resulting in a transfer coefficient, α ($\alpha = 2.3RT/bF$) of 2.[45,53] Tafel plots of films deposited onto a Pt rotating disk electrode (RDE) are identical irrespective of the rotation rates, ω of 2000 or 600 rpm, or whether stirring is the sole source of convection (Figure S1). These observations confirm that the Tafel slope is representative of activation-controlled OER over the potential range explored. Tafel slopes are also reproducible for sequential runs, and do not depend on the direction of potential change (Figure S2), indicating that the films are not significantly altered over the course of data collection.

Although only a fraction of the nickel centers may be involved in catalysis, a lower-limit value for the oxygen evolution turnover frequency ($\mathrm{TOF_{min}}$) of $\mathrm{NiB_i}$ catalyst films at a specified overpotential can be estimated by determining the rate of turnover per nickel center in the film at that overpotential. At η = 400 mV in 0.5 M $\mathrm{B_i}$ pH 9.2 electrolyte, a $\mathrm{TOF_{min}}$ was determined to be 0.9, 0.5, and 0.5 mol $\mathrm{O_2}$ (mol Ni)$^{-1}$ s^{-1} for films prepared by passage of 1.0, 0.40, and 0.083 mC cm^{-2}, respectively (see subheading 6 of the Experimental Section).

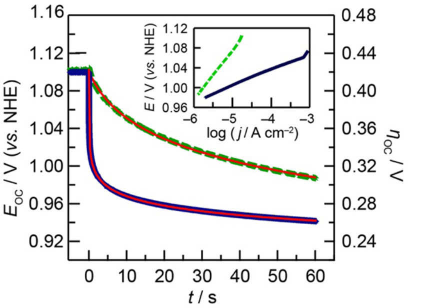

Figure 2. Open circuit potential, E_{OC}, and overpotential, $\eta_{\mathrm{OC}} = (E_{\mathrm{OC}} - E°)$, transients for nonanodized (green ---) and anodized (dark blue —) 1.0 mC cm^{-2} $\mathrm{NiB_i}$ films immediately following a 10 s bias at 1.1 V in 0.5 M $\mathrm{KB_i}$ 1.75 M $\mathrm{KNO_3}$ pH 9.2 electrolyte. The red lines represent fits to eq 1. Tafel slopes are 100 before anodization and 33 mV/decade after anodization. The inset shows the corresponding Tafel plots determined from the E_{OC} transients by calculating log j at each time point using eq 2.

Tafel slopes were also extracted from open circuit potential (E_{OC}) decay transients, following the interruption of a potential pulse. Catalyst films were poised at 1.1 V in 0.5 M $\mathrm{B_i}$ pH 9.2 electrolyte for 5 s. Upon switching to open circuit, the decay in E_{OC} was monitored as a function of time, t (Figure 2). The decrease in E_{OC} arises due to the discharge of the capacitance of the electrode, through the Faradaic resistance, mediated by the catalyst film (i.e., Ni centers in the film are reduced by water via the OER). Thus, the characteristics of the overpotential of the electrode at open circuit ($\eta_{\mathrm{OC}} = E_{\mathrm{OC}} - E°$) versus time depend on the mechanism of $\mathrm{O_2}$ evolution and therefore the Tafel slope, b[43,54,55]

$$\eta_{\mathrm{OC}} = a - b\log(t + \tau) \qquad (1)$$

with $a = b\log(bC/j_0)$ and $\tau = 10^{(-\eta'/b)}bC/j_0$. C is the capacitance of the electrode, j_0 is the exchange current density, and η' is the initial overpotential at t = 0. This open-circuit decay method assumes that any change in C during the experiment is negligible.

E_{OC}−t curves recorded for anodized and non−anodized films are shown in Figure 2.

Owing to their considerably higher catalytic activity, the E_{OC} of anodized films decreases by almost 100 mV within the first 0.1 s after the potential is interrupted. In contrast, over the same duration a minimal decrease (<10 mV) is observed in E_{OC} for nonanodized films. Fitting the decay trace of an anodized film to eq 1 yields a Tafel slope of 33 mV/decade, which is in excellent agreement with the steady-state Tafel plot measurements of Figure 1. In contrast, a much higher Tafel slope of 100 mV/decade is extracted from the open circuit decay trace of nonanodized films. These transients permit the construction of Tafel plots of anodized and nonanodized films by recognizing that the instantaneous OER current density across the catalyst−electrolyte interface (log j_t) can be expressed as a function of the time elapsed during the OCP decay, t[54]

$$\log j_t = \log j_{t=0} - \log(1 + t/\tau) \qquad (2)$$

where log $j_{t=0}$ is the initial current density before open circuit conditions. The resulting Tafel plots (Figure 2 inset) illustrate a significant difference in the activity of anodized versus nonanodized films. We note that the Tafel plot of the anodized film is concordant with that obtained by steady state polarization measurements of Figure 1.

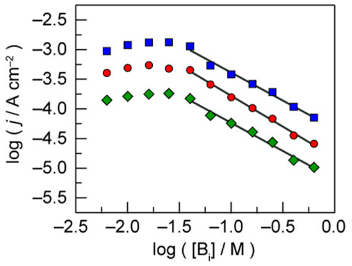

Figure 3. $\mathrm{B_i}$ concentration dependence of steady state catalytic current density at constant potential (E = 1.04 V (green ◆), 1.05 V (red ●), 1.06 V (blue ■)) for an anodized catalyst film deposited onto a Pt RDE by passage of 1.0 mC cm^{-2} and operated in $\mathrm{B_i}$ electrolyte, pH 9.2. Sufficient $\mathrm{KNO_3}$ was added to maintain a constant total ionic strength of 2 M in all electrolytes. Koutecký−Levich analysis was used to extract activation-controlled current densities in weakly buffered electrolyte, where the measured current was dependent on rotation rate. The experimental reaction orders (slopes of the red linear fits) in $\mathrm{B_i}$ are (from top to bottom) −0.95, −1.04, and −0.95.

2. Determination of Reaction Order in $\mathrm{B_i}$. The dependence of reaction rate on buffer strength was interrogated by controlled potential electrolysis of anodized catalyst films at 1.04, 1.05, and 1.06 V in Ni-free electrolyte, pH 9.2 with varying $\mathrm{B_i}$ concentrations [$\mathrm{B_i}$] from 630 to 6.3 mM (Figure 3). Sufficient $\mathrm{KNO_3}$ was added to each solution to preserve a constant high ionic strength of 2 M. Diffuse double layer effects,[52] which lead to spuriously elevated Tafel slopes and distorted reaction orders (Figure S3), can be eliminated by operating at constant ionic strength as well as maintaining a low concentration of buffering species relative to an inert supporting electrolyte (Figure S4).[56] Catalyst films were deposited onto a Pt RDE that had been pretreated to render any current due to Pt oxide formation negligible (see subheading 7 of the Experimental Section). For each electrolyte examined, the RDE was operated until a steady-state current value was attained at various ω. In cases where the [$\mathrm{B_i}$] was less than 100 mM, the observed currents were subject to mass transport limitations, as evidenced by the dependence of i on ω. In these instances, Koutecký−Levich (K−L) plots of i^{-1} as a function of $\omega^{-1/2}$ were constructed (Figure S5) to extract the activation-controlled current values by linear extrapolation to the limit of infinitely high rotation rates ($\omega^{-1/2} \rightarrow 0$).[57,58] In all cases, Ohmic potential losses amounted to less than 1 mV, and therefore, they were neglected. Figure 3 shows the logarithm of the activation−controlled current density plotted as a function of log$[B_i]$. For $[B_i] \geq 40$ mM, the slope of the plot establishes an inverse first order dependence of current density on B_i activity. In electrolytes of very low buffer strength ($[B_i] < 40$ mM), film activity deviates from this reaction order, and an ostensibly zeroth order regime is observed.

3. Determination of Reaction Order in H^+ Activity. Given the explicit reaction order in B_i, any measurements of reaction rate dependence on pH will inevitably alter the activity of boric acid, borate anion, or both. To evaluate the reaction order in H^+ activity, anodized films were deposited onto a Pt RDE, and steady-state data were collected as a function of pH. Initially, a galvanostatic titration at 10 μA cm^{-2} in an electrolyte with a constant $[B_i]_{total}$ = 100 mM was undertaken in the presence of 2 M KNO_3. The titration was commenced at pH 8.5, and the potential required to sustain constant current density was measured as the pH of the solution was raised incrementally. At low current density, no local pH gradients arise, even when the pH is adjusted outside of the ideal B_i buffering regime. Additionally, Ohmic potential losses were less than 0.5 mV, and they can be neglected. The plot of potential as a function of pH (Figure 4) shows two limiting slopes of −64 mV/pH unit and −96 mV/pH unit for pH ranges 8.5−9.8 and 10−12, respectively. The bifurcation observed at pH 10 indicates that either (1) there is a change in mechanism (such as a change in Tafel slope) at pH 10 or (2) there exists an inverse first order dependence of reaction rate on only borate anion (B_i^-), and not on boric acid, $B(OH)_3$, such that as the pH is increased from 8.5−10, the corresponding exponential increase in the concentration of B_i^- serves to skew the true dependence on H^+ activity. In this case, the intrinsic proton order is observed for pH > 10 where $[B_i^-]$ reaches saturation.

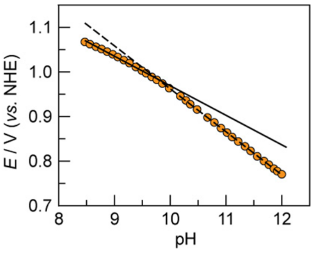

Figure 4. pH dependence of steady-state electrode potential at constant current density (j_{anodic} = 10 μA cm^{-2}) for an anodized 1.0 mC cm^{-2} catalyst film on FTO operated in 0.1 M B_i 2 M KNO_3 electrolyte. Slopes equal −64 (—) and −96 (---) mV/pH unit.

A separate experiment was conducted to distinguish between scenarios 1 and 2. Films were deposited onto a Pt RDE, and Tafel data were collected using B_i solutions at pH 8.5, 9.2, 10.2, 11.2, and 12.0 (Figure 5a). In each electrolyte, the total buffer concentration $[B_i]$ was varied such that the concentration of borate anion $[B_i^-]$ was maintained at 100 mM; 0.9 M KNO_3 was added to each solution to preserve a constant ionic strength of 1 M. Where necessary, the activation-controlled current densities were obtained from K−L analysis. There is no mechanistic change over the pH range explored; all Tafel slopes lie between 28 and 32 mV/decade. This suggests that scenario 2 is at the root of the change observed for pH > 10. Interpolation of each Tafel plot at 2.5, 0.25, and 0.025 mA cm^{-2} yields the potential dependence on pH (Figure 5b). The single observed slope $(\partial E/\partial \mathrm{pH})_j$ = −90 mV/pH over the pH range 8.5−12.0 is a convolution of the pH dependence of the current density $(\partial \log j/\partial \mathrm{pH})_E$ and the potential dependence of the current density $(\partial E/\partial \log j)_{\mathrm{pH}}$. That is[59]

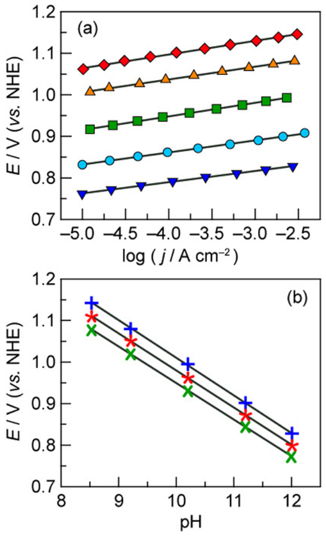

Figure 5. (a) Tafel plots, $E = (E_{appl} - iR)$, for anodized NiB_i catalyst films deposited on a Pt rotating disk electrode by passing 1.0 mC cm^{-2}, and operated in 0.60 M B_i pH 8.5 (red ◆), 0.20 M B_i pH 9.2 (orange ▲), 0.11 M B_i pH 10.2 (green ■), 0.10 M B_i pH 11.2 (light blue ●), and 0.10 M B_i pH 12.0 (dark blue ▼). Each electrolyte contained an additional 0.9 M KNO_3 as supporting electrolyte to maintain an ionic strength of about 1 M. Koutecký−Levich plots were constructed to extract activation-controlled current densities where necessary. (b) Interpolation of Tafel plots at 2.5 mA cm^{-2} (blue +), 0.25 mA cm^{-2} (red ∗), and 0.025 mA cm^{-2} (green ×). Slopes are −90, −89, and −88 mV/pH unit, respectively.

$$\left(\frac{\partial E}{\partial \mathrm{pH}}\right)_j = -\left(\frac{\partial \log j}{\partial \mathrm{pH}}\right)_E \left(\frac{\partial E}{\partial \log j}\right)_{\mathrm{pH}} \tag{3}$$

Substituting $(\partial E/\partial \mathrm{pH})_j$ = −90 mV/pH (from Figure 5b) and $(\partial E/\partial \log j)_{\mathrm{pH}}$ = 30 mV/decade (the Tafel slope) into eq 3 gives $(\partial \log j/\partial \mathrm{pH})_E$ = +3. The reaction order in H^+ activity $(\partial \log j/\partial \log a_{H+})_E$ may thus be determined as

$$\left(\frac{\partial \log j}{\partial \log a_{H^+}}\right)_E = -\left(\frac{\partial \log j}{\partial \mathrm{pH}}\right)_E \tag{4}$$

which yields a reaction order in proton activity a_H^+ of −3. We therefore deduce that the reaction rate is zeroth order in boric acid activity, inverse first order in borate anion activity for $[B_i^-]$ in excess of 20 mM, and inverse third order in proton activity between pH 8.5 and pH 12.

A galvanostatic titration in 100 mM B_i from pH 11 to 13 was used to investigate a change in the pH dependence under alkaline conditions, which might be expected to arise when the pH is elevated beyond the pK_a of an active site species. As shown in Figure 6, a plateau in the plot of η versus pH is observed at pH ~ 12.2. However, since Tafel data acquired in 0.1 and 1.0 M KOH (Figure 6 inset and Figure S8) continue to exhibit slopes close to 29 mV/decade, the mechanistic change that results in this plateau in the η versus pH plot does not arise from changes in Tafel slope. Instead, this behavior must arise exclusively from changes in the H^+ reaction order.

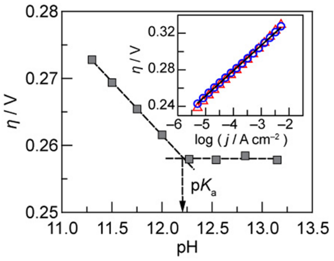

Figure 6. Plot of the pH dependence of steady-state electrode overpotential (gray ■), at constant current density (j_{anodic} = 10 > μA cm^{-2}) for an anodized 1.0 mC cm^{-2} catalyst film deposited onto FTO and operated in 0.1 M B_i 2 M KNO_3 electrolyte. The change in slope at pH 12.2 is consistent with the elevation of the bulk pH above the pK_a of an active site moiety. The inset shows Tafel plots, $\eta = (E - iR - E°)$, for anodized catalyst films deposited onto a Pt RDE by passage of 1.0 mC cm^{-2} and operated at 2000 rpm in 0.1 M KOH 1.9 M KNO_3 pH 12.9 (blue ○) and 1.0 M KOH 1.0 M KNO_3 pH 13.8 (red △) electrolyte. Tafel slopes are 28 and 30 mV/decade, respectively.

According to Figure 6, for pH > 12.2 there is no dependence of the current density on pH at constant overpotential. This parameter, $(\partial \log j/\partial \text{pH})_\eta$, is related to the pH dependence of the current density at constant potential, $(\partial \log j/\partial \text{pH})_E$, through the transfer coefficient, α ($\alpha = 2.3RT/bF$, where b is the Tafel slope):[59]

$$\left(\frac{\partial \log j}{\partial \text{pH}}\right)_E = \left(\frac{\partial \log j}{\partial \text{pH}}\right)_\eta + \alpha \tag{5}$$

Both Tafel slopes are close to 29 mV/decade, and therefore, $\alpha = 2.3RT/0.029F = 2$. Substituting $(\partial \log j/\partial \text{pH})_\eta = 0$ and $\alpha = 2$ into eq 5, we find $(\partial \log j/\partial \text{pH})_E = 2$. According to eq 4, this results in a reaction order in H^+ activity of −2. Therefore, the reaction order in H^+ activity transitions from a value of −3 over the range pH 8.5 to 12 (Figure 5a,b) to −2 at pH ≥ 12.2 (Figure 6). These results indicate that one of the three kinetically relevant protic centers of NiB_i active sites possesses a pK_a of 12.2. In strongly alkaline electrolytes, this species is deprotonated in the resting state of the catalyst and ceases to contribute to the electrochemical rate law.

4. Tafel Data in B_i-Free Electrolyte. To explore OER kinetics in the absence of a weak base, steady state polarization data were collected in 1 M $NaClO_4$ pH 8.5 solution. Films were deposited onto a Pt RDE by passage of 1.0 mC cm^{-2} and anodized in B_i buffered solutions. Tafel data were obtained in $NaClO_4$ electrolyte by extrapolation of K–L plots at each potential considered (Figure S6) in order to eliminate mass transport limitations through the bulk electrolyte. Over the course of the experiment, small aliquots (1–5 μL) of 1 M NaOH were added periodically to preserve the bulk pH at 8.50(1). Tafel data are the average of three runs. The resulting Tafel plot displays a greatly elevated slope compared to Tafel data acquired in B_i electrolyte, pH 8.5 (Figure 7). The kinetic profile of catalyst films in B_i buffered media following operation in B_i-free electrolyte was comparable to the activity of a freshly prepared film (Figure S7), indicating that the Tafel behavior obtained in the absence of B_i cannot be attributed to the corrosion of catalyst films in buffer−free electrolyte.

■ DISCUSSION

1. Steady-State Tafel Data. Tafel behavior describing the effect of potential, E, or overpotential, η, on steady-state current

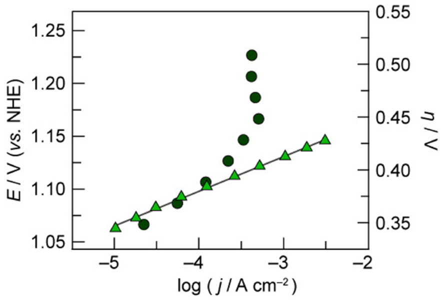

Figure 7. Tafel plots, $E = (E_{\text{appl}} - iR)$, $\eta = (E - E°)$, for anodized catalyst films deposited onto a Pt RDE by passage of 1.0 mC cm^{-2} and operated in 1 M $NaClO_4$ pH 8.5 electrolyte (●). Koutecký–Levich analysis of steady state current densities at various rotation rates was used to eliminate mass transport limitations through solution. The data shown is the average of three consecutive runs. A Tafel plot of an identical catalyst film in 0.6 M KB_i 0.9 M KNO_3 pH 8.5 (0.1 M B_i^-, total ionic strength = 1 M) electrolyte (green ▲), displaying a 32 mV/decade Tafel slope (—), is shown for comparison.

density, along with experimentally determined reaction orders, forms the basis of the mechanistic analysis of oxygen evolution by NiB_i catalyst films. Steady-state current densities are proportional to the activation-controlled velocity of the OER if the reaction is not subject to mass-transport limitations. This requirement is true of the electrokinetic studies described herein, since in well-buffered electrolytes Tafel data collected using an RDE is identical irrespective of rotation rate or whether stirring was the sole means of mass transport with the electrode stationary (Figure S1), resulting in Tafel slopes, b (where $b = \partial E \partial \log j)_{\text{pH}}$, of 28 mV/decade in each case. In cases where mass transport limitations were encountered (poorly buffered media, or electrolytes completely lacking a weak base electrolyte), Koutecký–Levich analysis was employed to extract activation-controlled current densities. Furthermore, the Tafel plots are the same for sequential runs and independent of the direction of potential change during data acquisition (Figure S2), verifying that catalyst films are not altered appreciably over the course of experiments. Precise control of catalyst film thickness was accomplished by managing the total charge passed during deposition. Although the resultant film thicknesses ranged from 1 to 5 nm (equivalent to 3–15 monolayers of catalyst), Tafel plots collected for each film gave similar slopes, close to 30 mV/decade (Figure 1). Since activated transport through the film can impose additional potential barriers to electronic/ionic conductivity,[60−62] consistent slopes over a range of film thicknesses (particularly at almost monolayer coverage) demonstrate the absence of non-Ohmic potential losses between the potential applied at the electrode and that experienced by active sites. In our initial report,[25] we explored considerably thicker films (>1 μm thick), and higher Tafel slopes were observed. However, the data reported here is for ultrathin (1–5 nm) films. Thus, these results are consistent with sluggish charge or mass transport through the mesoporous films leading to an inflation of the Tafel slope at high catalyst loadings. For anodized catalyst films, Tafel plots (Figure 1) yield 30 mV/decade slopes that are consistent with a mechanism involving a chemical turnover-limiting step (TLS) that follows a two-electron pre-equilibrium. The reciprocal of the Tafel slope in dimensionless form is known as the transfer coefficient, $\alpha = 2.3RT/bF = 2$ for $b = 29.5$ mV/decade at 25 °C.[59] Although the Tafel slopes are independent of film thickness, the apparent exchange current densities and hence the overall activity of films does increase with loading. This would be expected to occur, as anodes with thicker catalyst layers should possess more active sites per unit geometric area in these porous films. Lower-limit TOFs of 0.9 mol O_2 (mol Ni)$^{-1}$ s^{-1} are observed at η = 400 V in pH 9.2 electrolyte and 1.7 mol O_2 (mol Ni)$^{-1}$ s^{-1} at η = 325 mV in 1 M KOH. Lower-limit TOF for these catalysts may be calculated at any η by recognizing that the TOF decreases by an order of magnitude per 30 mV increment. Thus, these catalyst films rival the most active OER anodes reported to date.[40]

2. OER of Nonanodized NiB$_i$. Monitoring the decay in open circuit potential after interrupting an applied potential bias offers a complementary means of determining the Tafel slope of an electrokinetic reaction.[43,54,55] This method is the most appropriate means of extracting electrokinetic information on the OER at the less catalytically active nonanodized films, since polarization of the electrode for an extended period of time leads to anodization.[26] The higher activity of anodized films is immediately evident in the very rapid decay at early times due to more efficient O_2 evolution as compared to the less catalytically active nonanodized films (Figure 2). Indeed, since the Tafel slope for anodized films is found to be 33 mV/decade (in agreement with Figure 1), the corresponding OCP-decay transient indicates that the surface concentration of catalytic intermediates in anodized NiB$_i$ decreases by over 3 orders of magnitude in the first 100 ms after the potential is removed. In contrast, the Tafel slope of nonanodized films is considerably higher, approaching 100 mV/decade. Tafel slopes of 120 (±20) mV/decade are expected for mechanisms involving a turnover-limiting electron transfer (ET) from the resting state:[45,59]

$$\mathrm{A} \xrightarrow{\mathrm{TLS}} \mathrm{B} + \mathrm{e}^- \tag{6}$$

The turnover velocity for such a reaction will be given by

$$v = k_{\mathrm{ET}}\theta_{\mathrm{A}} \tag{7}$$

where k_{ET} is the rate constant for the turnover limiting electron transfer, and θ_{A} is the surface coverage of the resting state species, A:[63]

$$\frac{\Gamma_{\mathrm{A}}}{\Gamma_{\mathrm{max}}} \tag{8}$$

Γ_{A} is the surface concentration of active sites that exist in state A (expressed in mol/cm^2), and Γ_{max} is the total surface concentration of active sites. It is important to note that Γ_{max} need not equal the surface concentration of solvent-exposed metal centers, or even the concentration of electroactive Ni centers, since the number of active sites may actually represent a very small proportion of these centers. Under Langmuir conditions, since A is the resting state, θ_{A} may be assumed to be a constant equal to 1.[63] The rate constant k_{ET} is given by

$$k_{\mathrm{ET}} = k^0_{\mathrm{ET}} \exp\left(\frac{\beta\eta F}{RT}\right) \tag{9}$$

The parameter k^0_{ET} is the ET rate constant at $\eta = 0$, and β is the symmetry factor for the microscopic (irreversible) ET step, which determines the amount of the total driving force due to η (i.e., $\Delta G = -\eta F$), that causes a decrease in the activation energy barrier (i.e., $\Delta(\Delta G^{\ddagger}) = -\beta\eta F$).[53] Thus, the electrochemical rate law for a reaction that proceeds by eq 6 will be

$$j = 4Fk^0_{\mathrm{ET}} \exp\left(\frac{\beta\eta F}{RT}\right) \tag{10}$$

This will lead to a Tafel slope ($\partial\eta/\partial\log j$) of 2.3 × $RT/\beta F$. β is usually close to 0.5 (±0.1),[53] resulting in a Tafel slope of around 120 mV/decade at 298 K. Importantly, in this case, the symmetry factor, β, and the transfer coefficient for the overall OER, α, are numerically identical, since the kinetics of the overall multielectron reaction are governed entirely by the microscopic rate-limiting ET step.[53] In cases where one or more electron transfers exist in equilibrium, β and α are distinct.

It is unclear whether the suppression of the Tafel slope of nonanodized films from 120 mV/decade to 100 mV/decade arises due to the existence of a marginally altered β-value of 0.6, or is a result of the unavoidable partial anodization of the film during deposition.[26] However, the existence of a turnover-limiting electron transfer in nonanodized films is reasonable. The resting state nickel valency in nonanodized films is predominantly +3, and the local coordination environment of Ni centers in such films would be expected to exhibit a Jahn–Teller (J–T) distortion that is expected for low-spin d^7 ions.[26] Thus, the first oxidation process during turnover may be expected to be kinetically sluggish, as it would incur a large reorganizational energy penalty associated with a low-spin $d^7 \rightarrow d^6$ transformation. We conclude therefore that a higher reorganizational energy associated with Ni^{3+} oxidation may contribute to a slower electron transfer and thus to very low catalytic activity of nonanodized NiB$_i$ films.

3. OER of Anodized NiB$_i$. XAS shows that anodization of NiB$_i$ films leads to a gradual phase change (involving changes in both local structure and resting state nickel valency) that eliminates the J–T distortion present in nonanodized films.[26] In the absence of structural distortion in local geometry, the oxidation of Ni centers in anodized films should be more facile. Indeed, the 30 mV/decade Tafel slope obtained by steady-state Tafel plots (Figure 1) and open-circuit decay transients (Figure 2) indicates that the turnover-limiting step is chemical in nature and does not involve ET.

Before evaluating the dependence of activity on pH and therefore the existence of proton-transfer (PT) equilibria prior to the TLS, it was necessary to establish the dependence of reaction rate on buffer strength, since any [B$_i$] dependence would have to be accommodated during pH changes. The resulting inverse first order dependence of current density on [B$_i$] over almost 1.5 decades (Figure 3) is consistent with the reversible dissociation of a B$_i$ species from an active site over this range in buffer strength. Boric acid and borate species are known to adsorb to oxide surfaces in aqueous media by coordination to the metal centers.[64−67] The −1.0 reaction order in borate (Figure 3) establishes that the ligation of the buffer species is governed by the Langmuir isotherm with a high surface coverage of the adsorbate.[63] Accordingly, the B$_i$-free active sites necessarily exist in minor equilibrium with a B$_i$-bound resting state. We note that our data cannot distinguish adsorption of polyborate species[68−70] as opposed to $B(OH)_4^-$. Decreasing the concentration of B$_i$ in the electrolyte gives rise to an increase in activation-controlled current density until a point where there appears to be no dependence of reaction velocity on B$_i$ (<40 mM B$_i$).

While demonstrating an association between buffering species and active sites, B$_i$ dependence studies alone could not distinguish which B$_i$ species (boric acid, borate anion (B$_i^-$), or both) must dissociate from active sites during turnover for oxygen to be evolved. The pH dependence of the steady-state electrode potential at a constant high ionic strength changes from about −60 mV/pH over the B_i buffering range to about −90 mV/pH at B_i^- saturation (Figure 4). In contrast, Tafel data collected between pH 8.5 and pH 12 at a constant concentration of borate anion exhibit Tafel slopes of approximately 30 mV/decade (Figure 5a). The pH dependence of the steady-state electrode potential was determined to be about −90 mV/pH by interpolating the Tafel plots at constant current density (Figure 5b). These results identify that the observed desorption step involves the liberation of one borate anion into bulk electrolyte per active site, and confirms a three-proton equilibrium prior to the TLS. Were both species to be liberated from active sites, the activity of boric acid *and* borate in solution should appreciably modulate OER kinetics on NiB_i films, and an experiment in which the total B_i (boric acid + borate) concentration is held constant as the pH is varied (Figure 4) should yield a single slope and the genuine reaction order in H^+ activity. However, if the desorption equilibrium applies to only one species of the conjugate pair, the pH dependence of reaction rate will inevitably be convoluted with the reaction order in that species unless the total B_i concentration is adjusted to maintain a constant activity in the coordinated species alone (Figure 5a,b), or the pH regime is such that B_i speciation does not change appreciably with pH (pH > 10 in Figure 4).

Electrokinetic data should be acquired in an excess of supporting electrolyte. If not, the potential dependence of anion migration and the effects on local pH and specific adsorption of borate will skew Tafel data and lead to slopes that are dependent on B_i concentration, and apparent fractional reaction orders (Figure S3). These effects are eliminated by maintaining a constant, high ionic strength ($I \geq 1$ M) using an inert supporting electrolyte such as KNO_3, which when present at an appreciable concentration serves to reduce the transference number of borate anion (the fraction of the total ionic current that is carried by borate anions) (Figure S4).

Taken together, the results of Figures 1−5 reveal the electrochemical rate law for oxygen evolution in moderate to high borate ion concentrations (20−300 mM) at anodized NiB_i films to be

$$j = k_0(a_{B_i^-})^{-1}(a_{H^+})^{-3}\exp\left(\frac{2EF}{RT}\right) \tag{11}$$

where k_0 is proportional to the exchange current density and independent of potential. This rate expression contains the inverse first order dependence on borate activity as shown in Figure 3, the inverse third order dependence on proton activity (Figures 4 and 5), as well as the factor of 2 (transfer coefficient) in the exponential term in the applied potential, E. At constant borate activity and pH and $T = 25$ °C, the partial derivative of E with respect to log j ($\partial E/\partial \log j$) yields a Tafel slope of 30 mV/decade, consistent with Figures 1 and 5a.

The experimental rate law in eq 11 is consistent with the mechanistic sequence

$$A \rightleftharpoons B + B_i^- + 2e^- + 3H^+ \qquad K_1 \tag{12}$$

$$B \rightarrow C \qquad k_2 \tag{13}$$

which involves reversible borate dissociation from the resting state, and a two-electron, three-proton equilibrium followed by a chemical TLS. K_1 is the equilibrium constant at $E = 0$, and k_2 is the rate constant for the chemical TLS. Equation 12 may indeed proceed in a number of discrete steps; however, these would all exist as quasiequilibria, and such a sequence is kinetically indistinguishable from a single step. In addition, there may be any number of distinct chemical equilibrium steps prior to the TLS, but these cannot be resolved kinetically.

According to eq 13, the steady-state velocity of oxygen evolution can be expressed as[53]

$$v = k_2\theta_B \tag{14}$$

θ_B represents the partial surface coverage of intermediate B. θ_B can be defined in terms of the surface coverage of the resting state A (θ_A) as follows[53]

$$\theta_B = K_1\theta_A(a_{B_i^-})^{-1}(a_{H^+})^{-3}\exp\left(\frac{2EF}{RT}\right) \tag{15}$$

which involves the application of the Nernst equation to eq 12. Substituting for θ_B in eq 14 gives

$$v = k_2K_1\theta_A(a_{B_i^-})^{-1}(a_{H^+})^{-3}\exp\left(\frac{2EF}{RT}\right) \tag{16}$$

If Langmuir conditions are assumed, the surface coverage of the resting state is high, and θ_A would not be expected to change appreciably over the potential range, and may be considered a potential-independent constant equal to 1.[63] In this case, eq 16 approximates the experimental rate law (eq 11) with

$$k_0 = 4Fk_2K_1\theta_A \tag{17}$$

In situ XAS studies of anodized NiB_i films[26] show that there is no systematic shift in the nickel K-edge position with E_{appl} over the potential range used for Tafel data acquisition. This result is consistent with the assumption that the speciation of the resting state, A, is invariant over the potential range explored and therefore permits θ_A to be taken as a constant (eq 17 above). XANES[26,71] spectra and coulometric[26] studies also established that the average oxidation state of Ni in anodized catalyst films was +3.6 to +3.8, thereby indicating a substantial amount of formal Ni^{IV} valency in the catalyst resting state.[26] In fact, there appears to be even more formal +4 valency in NiB_i compared to Co−OEC.[22,23] Computational studies of Ni^{IV}-containing extended solid nickelates have demonstrated significant covalency in Ni−O bonding, and extensive delocalization of hole-density onto oxygen centers upon oxidation of the parent Ni^{III} compounds.[72−74] In addition, EPR studies of a tetracobalt cubane model compound possessing one formally Co^{IV} center as a molecular model of our cobalt-based catalyst revealed a radical distributed almost equally over all Co and O ions, effectively leading to a formal oxidation number of $[Co_4^{+3.125}O_4]$.[75] Thus, it is reasonable to expect that this Ni^{IV} valency in the catalyst resting state is distributed extensively over multiple Ni and O centers in the nickel−oxido clusters that form the ordered domains.

Figure 5 is effectively a Pourbaix diagram of the catalyst active sites, indicating that one of the protic species possesses a pK_a of about 12.2. At the pH regimes considered in this study, a $Ni^{III/IV}$—OH_2 resting state is unlikely, given the Pourbaix diagram for nickel.[76] In addition, the point of zero charge (pH_z) for nickel oxides, which defines the average of the pK_a values of surface-bound water (M−OH_2) and surface-bound hydroxyl (M−OH) groups,[77] has been found to be about 8 and 9.75 for $Ni(OH)_2$ and NiO, respectively.[78−80] Thus, we can anticipate the pK_a of a $Ni^{III/IV}$−OH_2 intermediate would be less than 8.

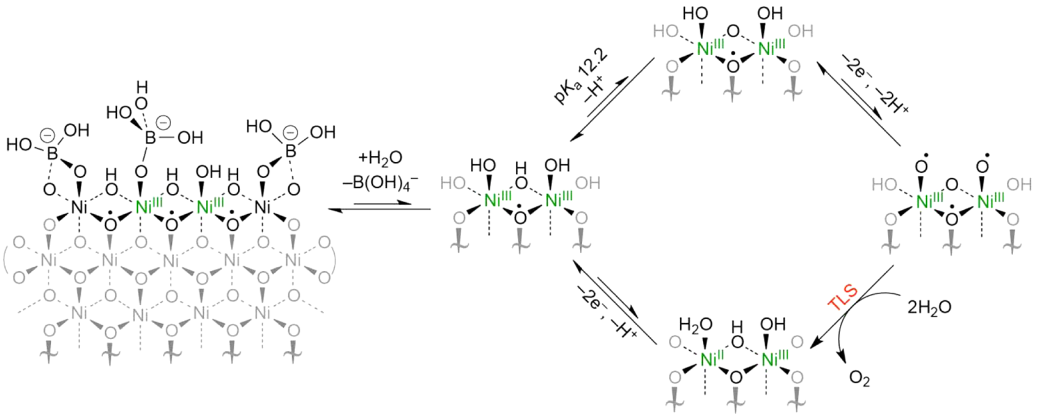

Figure 8. Proposed pathway for O_2 evolution by NiB_i in B_i ($[B(OH)_4^-] > 20$ mM) electrolyte, pH 8.5−14. The reversible dissociation of borate anion and an overall two-electron, three-proton equilibrium followed by a rate limiting chemical step is consistent with the experimental electrochemical rate law. A μ-OH site possessing a pK_a of 12.2 is fully deprotonated in the resting state under highly alkaline conditions. Oxidation state assignments are approximate; oxidizing equivalents are likely extracted from orbitals with predominantly O 2p character, particularly for the pre-TLS intermediate.

The moiety possessing a pK_a of 12.2 can therefore be more reasonably rationalized as a terminal or bridging Ni−OH. Under highly alkaline conditions (specifically pH > 12.2), this species is deprotonated in the resting state resulting in an overall two-electron, two-proton PCET transformation prior to a chemical turnover-limiting step. This gives rise to a 30 mV/decade Tafel slope and −60 mV/pH unit shift of E (Figures 6 and 7). Previous EPR studies[75] have pointed to the importance of proton loss in PCET steps for generating localized reactive intermediates. In the Co−OECs and Ni−OECs, the ensuing change in ligand field strength upon deprotonation could localize the unpaired spin density on specific centers leading to their subsequent reactivity toward O−O bond formation. This concept is validated by computational studies of cobalt oxido clusters as Co−OEC models.[81] Hence, while the resting state valency would be delocalized over the entire cluster, the catalytic intermediates are likely to possess spin density that is more localized due to proton loss.

A mechanistic scheme for oxygen evolution in B_i-buffered electrolyte that is consistent with the interfacial properties of the oxidic surface as well as the electrokinetic data presented herein is shown in Figure 8. For convenience, eq 12 has been described as a sequence of several steps in equilibrium. We assign the two-electron minor equilibrium step to the double oxidation of a dinickel active site, which proceeds with the overall deprotonation of a bridging and two terminal hydroxyl groups. These PCET processes are proposed to lead to a highly oxidized intermediate that may be tentatively described as $[Ni_2^{IV/V}]$ or $[Ni_2^{+4.6}]$. Since this intermediate exists in minor equilibrium at a very low surface coverage, its formal potential must lie well above the potential supplied at the electrode. Nevertheless, this formal $[Ni_2^{IV/V}]$ designation is likely not an accurate description of the true electronic structure of the intermediate; we expect that the electron-transfer pre-equilibria arise from orbitals with predominant O 2p contributions, resulting in oxyl radical character. The loss of three protons must contribute significantly to the accessibility of such highly oxidized intermediates by virtue of the PCET redox-potential leveling effect.[82−84] One hydroxyl group was found to possess a pK_a of 12.2, and hence its corresponding deprotonation step must occur prior to the remaining two-electron, two-proton PCET transformations. Since the turnover-limiting step is chemical in nature and unlikely to involve proton transfer to the electrolyte, we find it reasonable to propose that this step involves O−O bond formation and/or Ni−O bond scission. Computational studies on our Co-based system suggests that direct coupling of two terminal $Co^{IV}(O)$ groups to form an O−O bond is thermodynamically favorable and proceeds with a low kinetic barrier,[81] signifying that it may in fact be the breaking of the metal−oxygen bond that is the turnover-limiting step in these late transition metal oxide catalysts. Spectroscopic studies as well as extensive synthetic and computational modeling will be employed to shed light on the electronic structure of catalytic intermediates and the details of the turnover-limiting process. Further electrochemical studies, particularly on molecular models, are also needed to shed light on the details of the coupled multiproton, multielectron sequences.

4. OER in B_i-Free Electrolyte. Certainly, one important role of B_i is to preserve the local and bulk pH during O_2 evolution. However, the inverse first order dependence of reaction velocity on borate anion activity in eq 15 implicates a deleterious role of borate on OER kinetics. Despite this ostensibly "inhibitory" effect, the crucial importance of borate to the kinetics of water oxidation on NiB_i films is evident in Tafel plots acquired in B_i-free electrolyte (Figure 7). In the absence of B_i, very high Tafel slopes are observed and high current densities cannot be achieved. Since Koutecký−Levich analysis was used to eliminate effects associated with solution mass transport (Figure S6), and the bulk pH was preserved by constant addition of aqueous NaOH, the elevated Tafel slope in B_i-free electrolyte cannot be attributed to pH gradients at the film−solution interface. In addition, following operation in B_i-free electrolyte, films display no loss in activity in B_i-electrolyte (Figure S7), excluding the possibility of catalyst corrosion over the period of polarization in B_i-free electrolyte. The observed Tafel behavior may result from the transition to a turnover-limiting chemical step from the resting state; the absence of any preceding electrochemical steps results in a potential-independent kinetic profile, and therefore an extremely high ("infinite") Tafel slope. We observed a similar result for phosphate-free electrolytes of Co-based catalyst films.[24] These preliminary electrokinetic data suggest that proton transfer processes may become turnover-limiting in the absence of a

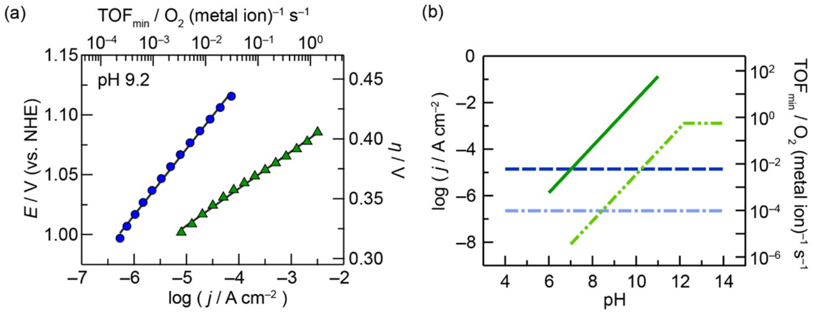

Figure 9. Comparison of ultrathin CoB_i and NiB_i OEC films with identical catalyst loadings of 6 nmol metal ions/cm^2. (a) Tafel plots of CoB_i (blue ●) and NiB_i (green ▲) in 0.5 M KB_i 1.75 M KNO_3 pH 9.2 electrolyte. Tafel slopes equal 55 and 31 mV/decade, respectively. (b) Schematic of the pH dependence of the current density and lower-limit turnover frequency of CoB_i at a constant overpotential of 400 mV (dark blue ---) and 300 mV (light blue —·—) compared to that of NiB_i at 400 mV (dark green —) and 300 mV (light green —··—) overpotential. Curves were calculated using the appropriate experimentally determined electrochemical rate laws. Ni-based films display a much higher *apparent* specific activity (since the true number of active sites cannot be known) than Co-based films above pH 8. However, due to their disparate electrochemical rate laws, a crossover is expected to occur around neutral pH, at which point Co-based films would yield higher activity anodes. The precise pH at which crossover occurs depends on the overpotential applied due to the different Tafel slopes.

good proton acceptor, at low hydroxide ion concentrations. Additional studies are ongoing to shed more light on the details of OER under such conditions, but these results underscore the critical importance of borate to facilitating proton transfers, thereby expediting the PCET sequences necessary for rapid O_2 evolution.

5. Differences in Mechanism and Activity of Co−OECs and Ni−OECs. Differences in activity between oxido Co−OECs and Ni−OECs are governed to a large extent by the characteristics of the PCET pre-equilibrium. A two-electron oxidation is required before the chemical turnover-limiting step in anodized NiB_i OEC films (30 mV/decade Tafel slope), whereas turnover at Co−OEC films involves a one-electron pre-equilibrium (60 mV/decade Tafel slope). We propose that this difference arises because O−O bond formation in both systems proceeds by radical coupling of two active site oxygen centers.[81] In Co−OEC, this oxygen-centered unpaired spin density arises upon generation of somewhat localized, low-spin formally d^5 Co^{4+} centers.[22,75,81]

Realization of a similar electronic structure would require more substantial oxidation for a nickel catalyst than for a cobalt-based system. As such, it would be expected to lead to a lower exchange current density, but also a lower Tafel slope, provided the ET steps remain kinetically facile. This is indeed what is observed when one compares Co−OEC with NiB_i at comparable catalyst loadings at pH 9.2 (Figure 9a). Additionally, the more extensive oxidation would also demand greater accompanying H^+ loss, leading to disparate pH dependences. Because of the differences in pH dependence for the two catalysts, NiB_i increasingly outperforms Co−OEC as the pH is elevated (Figure 9b). However, at neutral pH and slightly acidic conditions, Co−OEC surpasses NiB_i in activity. The majority of studies on the OER have been conducted in highly alkaline media,[85−87] and these have led to useful trends in correlating specific thermodynamic parameters (such as M−O bond strengths, enthalpies of formation of the metal(III) hydroxide compound, and adsorption enthalpies of proposed intermediates) with catalytic activity, resulting in the general consensus that, for first row transition metal oxides, OER activity increases in the order $MnO_x < FeO_x < CoO_x < NiO_x$.[45,62,88−90] However, as evident from Figure 9b, activity trends in concentrated base may not hold in intermediate pH electrolytes because of disparate PCET pre-equilibria involved in the mechanism of the OER at different catalysts.

■ CONCLUSION

Electrodeposited ultrathin anodized NiB_i catalyst films exhibit a Tafel slope of 30 mV/decade in well-buffered electrolytes between pH 8.5 and 14. Electrokinetic studies demonstrate that oxygen evolution in B_i-buffered electrolyte entails the reversible dissociation of borate anion from the resting state and a two-electron, three-proton equilibrium followed by a chemical turnover-limiting step. Under highly alkaline conditions, a change in reaction order in proton activity is observed that is attributed to the full deprotonation of a protic center with a pK_a of 12.2. On the basis of previous in situ XAS, a mixed valence $Ni^{III/IV}$ resting state is invoked, although radical character on oxygen ions in this resting state as well as the subsequent catalytic intermediate states is anticipated. These studies highlight the contradicting roles of borate as both an inhibiting adsorbate and a proton acceptor for PCET at intermediate pH. The much lower catalytic activity of nonanodized films may appear to arise, in part, from a large reorganizational energy arising from a Jahn−Teller distorted Ni^{III} resting state found in nonanodized films, thus resulting in a rate-limiting electron transfer. The low Tafel slope of anodized NiB_i films makes this catalyst ideal for integration with buried-junction semiconductors.

■ ASSOCIATED CONTENT

Ⓢ Supporting Information

Additional Tafel plots and representative K−L plots. This material is available free of charge via the Internet at http://pubs.acs.org.

■ AUTHOR INFORMATION

Corresponding Author

nocera@fas.harvard.edu

Notes

The authors declare no competing financial interest.

■ ACKNOWLEDGMENTS

D.K.B. gratefully acknowledges the MIT Energy Initiative for a predoctoral fellowship. Y.S. gratefully acknowledges the National Science Foundation for a predoctoral fellowship. This research was supported jointly by the DOE Solar Photochemistry and Catalysis programs, U.S. DOE Grant DE-FG02-13ER16377.

REFERENCES

(1) Cook, T. R.; Dogutan, D. K.; Reece, S. Y.; Surendranath, Y.; Teets, T. S.; Nocera, D. G. *Chem. Rev.* **2010**, *110*, 6474−6502.
(2) Nocera, D. G. *Inorg. Chem.* **2009**, *48*, 10001−10017.
(3) Barber, J. *Chem. Soc. Rev.* **2009**, *38*, 185.
(4) Lewis, N. S.; Nocera, D. G. *Proc. Natl. Acad. Sci. U.S.A.* **2006**, *103*, 15729−15735.
(5) Alstrum-Acevedo, J. H.; Brennaman, K. L.; Meyer, T. J. *Inorg. Chem.* **2005**, *44*, 6802−6827.
(6) Eisenberg, R.; Gray, H. B. *Inorg. Chem.* **2008**, *47*, 1697−1699.
(7) Betley, T. A.; Wu, Q.; Van Voorhis, T.; Nocera, D. G. *Inorg. Chem.* **2008**, *47*, 1849−1861.
(8) Surendranath, Y.; Nocera, D. G. *Prog. Inorg. Chem.* **2011**, *57*, 505−560.
(9) Nocera, D. G. *Acc. Chem. Res.* **2012**, *45*, 767−776.
(10) Walter, M. G.; Warren, E. L.; McKone, J. R.; Boettcher, S. W.; Mi, Q.; Santori, E. A.; Lewis, N. S. *Chem. Rev.* **2010**, *110*, 6446−6473.
(11) Khaselev, O.; Turner, J. A. *Science* **1998**, *280*, 425−427.
(12) Rocheleau, R. E.; Miller, E. L.; Misra, A. *Energy Fuel* **1998**, *12*, 3−10.
(13) Pijpers, J. J. H.; Winkler, M. T.; Surendranath, Y.; Buonassisi, T.; Nocera, D. G. *Proc. Natl. Acad. Sci. U.S.A.* **2011**, *108*, 10056−10061.
(14) Hanna, M. C.; Nozik, A. J. *J. Appl. Phys.* **2006**, *100*, 074510/1−8.
(15) Reece, S. Y.; Hamel, J. A.; Sung, K.; Jarvi, T. D.; Esswein, A. J.; Pijpers, J. J. H.; Nocera, D. G. *Science* **2011**, *334*, 645−648.
(16) Cox, C. R.; Winkler, M. T.; Pijpers, J. J. H.; Buonassisi, T.; Nocera, D. G. *Energy Environ. Sci.* **2013**, *6*, 532−538.
(17) Surendranath, Y.; Bediako, D. K.; Nocera, D. G. *Proc. Natl. Acad. Sci. U.S.A.* **2012**, *109*, 15617−15621.
(18) Surendranath, Y.; Lutterman, D. A.; Liu, Y.; Nocera, D. G. *J. Am. Chem. Soc.* **2012**, *134*, 6326−6336.
(19) Kanan, M. W.; Nocera, D. G. *Science* **2008**, *321*, 1072−1075.
(20) Surendranath, Y.; Dincă, M.; Nocera, D. G. *J. Am. Chem. Soc.* **2009**, *131*, 2615−2620.
(21) Lutterman, D. A.; Surendranath, Y.; Nocera, D. G. *J. Am. Chem. Soc.* **2009**, *131*, 3838−3839.
(22) McAlpin, J. G.; Surendranath, Y.; Dincă, M.; Stich, T. A.; Stoian, S. A.; Casey, W. H.; Nocera, D. G.; Britt, R. D. *J. Am. Chem. Soc.* **2010**, *132*, 6882−6883.
(23) Kanan, M. W.; Yano, J.; Surendranath, Y.; Dincă, M.; Yachandra, V. K.; Nocera, D. G. *J. Am. Chem. Soc.* **2010**, *132*, 13692−13701.
(24) Surendranath, Y.; Kanan, M. W.; Nocera, D. G. *J. Am. Chem. Soc.* **2010**, *132*, 16501−16509.
(25) Dincă, M.; Surendranath, Y.; Nocera, D. G. *Proc. Natl. Acad. Sci. U.S.A.* **2010**, *107*, 10337−10341.
(26) Bediako, D. K.; Lassalle, B.; Surendranath, Y.; Yano, J.; Yachandra, V. K.; Nocera, D. G. *J. Am. Chem. Soc.* **2012**, *134*, 6801−6809.
(27) Steinmiller, E. M. P.; Choi, K.-S. *Proc. Natl. Acad. Sci. U.S.A.* **2009**, *106*, 20633−20636.
(28) Young, E. R.; Costi, R.; Paydavosi, S.; Nocera, D. G.; Bulović, V. *Energy Environ. Sci.* **2011**, *4*, 2058−2061.
(29) Zhong, D. K.; Gamelin, D. R. *J. Am. Chem. Soc.* **2010**, *132*, 4202−4207.
(30) Zhong, D. K.; Cornuz, M.; Sivula, K.; Grätzel, M.; Gamelin, D. R. *Energy Environ. Sci.* **2011**, *4*, 1757−1764.
(31) McDonald, K. J.; Choi, K.-S. *Chem. Mater.* **2011**, *23*, 1686−1693.
(32) Seabold, J. A.; Choi, K.-S. *Chem. Mater.* **2011**, *23*, 1105−1112.
(33) Pilli, S. K.; Furtak, T. E.; Brown, L. D.; Deutsch, T. G.; Turner, J. A.; Herring, A. M. *Energy Environ. Sci.* **2011**, *4*, 5028−5034.
(34) Zhong, D. K.; Choi, S.; Gamelin, D. R. *J. Am. Chem. Soc.* **2011**, *133*, 18370−18377.
(35) Jeon, T. H.; Choi, W.; Park, H. *Phys. Chem. Chem. Phys.* **2011**, *13*, 21392−21401.
(36) Wang, D.; Li, R.; Zhu, J.; Shi, J.; Han, J.; Zong, X.; Li, C. *J. Phys. Chem. C* **2012**, *116*, 5082−5089.
(37) Pilli, S. K.; Deutsch, T. G.; Furtak, T. E.; Turner, J. A.; Brown, L. D.; Herring, A. M. *Phys. Chem. Chem. Phys.* **2012**, *14*, 7032−7039.
(38) Higashi, M.; Domen, K.; Abe, R. *J. Am. Chem. Soc.* **2012**, *134*, 6968−6971.
(39) Bledowski, M.; Wang, L.; Ramakrishnan, A.; Bétard, A.; Khavryuchenko, O. V.; Beranek, R. *ChemPhysChem* **2012**, *13*, 3018−3024.
(40) Trotochaud, L.; Ranney, J. K.; Williams, K. N.; Boettcher, S. W. *J. Am. Chem. Soc.* **2012**, *134*, 17253−17261.
(41) Lee, S. W.; Carlton, C.; Risch, M.; Surendranath, Y.; Chen, S.; Furutsuki, S.; Yamada, A.; Nocera, D. G.; Shao-Horn, Y. *J. Am. Chem. Soc.* **2012**, *134*, 16959−16962.
(42) Gras, J. M.; Pernot, M. In *Proceedings of the Symposium on Electrode Materials and Processes for Energy Conversion and Storage*; McIntyre, J. D. E., Srinivasan, S., Will, F. G., Eds.; The Electrochemical Society: Pennington, NJ, 1977; Vol. *77-6*, pp 425−440.
(43) Conway, B. E.; Bourgault, P. L. *Can. J. Chem.* **1959**, *37*, 292−307.
(44) Lu, P. W.; Srinivasan, S. *J. Electrochem. Soc.* **1978**, *125*, 1416−1422.
(45) Bockris, J. O'M.; Otagawa, T. *J. Phys. Chem.* **1983**, *87*, 2960−2971.
(46) Conway, B. E.; Liu, T. *J. Chem. Soc., Faraday Trans. 1* **1987**, *83*, 1063−1079.
(47) Ferreira, A. C.; Gonzalez, E. R.; Ticianelli, E. A.; Avaca, L. A.; Matvienko, B. *J. Appl. Electrochem.* **1988**, *18*, 894−898.
(48) Raj, I. A.; Trivdei, D. C.; Venkatesan, V. K. *Bull. Electrochem.* **1988**, *4*, 55−59.
(49) Lyons, M. E. G.; Brandon, M. P. *Int. J. Electrochem. Sci.* **2008**, *3*, 1386−1424.
(50) Conway, B. E.; Liu, T. C. *Mater. Chem. Phys.* **1989**, *22*, 163−182.
(51) Nickell, R. A.; Zhu, W. H.; Payne, R. U.; Cahela, D. R.; Tatarchuk, B. J. *J. Power Sources* **2006**, *161*, 1217−1224.
(52) Parsons, R. In *Advances in Electrochemistry and Engineering*; Delahay, P., Tobias, C. W., Eds.; Interscience: New York, 1961; Vol. *1*, pp 29−64.
(53) Gileadi, E. *Electrode Kinetics for Chemists, Chemical Engineers, and Materials Scientists*; Wiley-VCH: New York, 1993; Chapters 13−14.
(54) Corrigan, D. A. *J. Electrochem. Soc.* **1987**, *134*, 377−384.
(55) Gileadi, E. *Electrode Kinetics for Chemists, Chemical Engineers, and Materials Scientists*; Wiley-VCH: New York, 1993; Chapter 24.
(56) Gileadi, E. *Electrode Kinetics for Chemists, Chemical Engineers, and Materials Scientists*; Wiley-VCH: New York, 1993; Chapter 23.
(57) Gileadi, E. *Electrode Kinetics for Chemists, Chemical Engineers, and Materials Scientists*; Wiley-VCH: New York, 1993; Chapter 10.
(58) Bard, A. J.; Faulkner, L. R. *Electrochemical Methods: Fundamentals and Applications*, 2nd ed.; John Wiley and Sons: New York, 2001; pp 340−344.
(59) Gileadi, E. *Electrode Kinetics for Chemists, Chemical Engineers, and Materials Scientists*; Wiley-VCH: New York, 1993; Chapter 14.
(60) MacDonald, J. J.; Conway, B. E. *Proc. R. Soc. London* **1962**, *269*, 419−440.
(61) Damjanovic, A.; Jovanovic, B. *J. Electrochem. Soc.* **1976**, *123*, 374−381.
(62) Lyons, M. E. G.; Brandon, M. P. *Int. J. Electrochem. Sci.* **2008**, *3*, 1425−1462.
(63) Gileadi, E. *Electrode Kinetics for Chemists, Chemical Engineers, and Materials Scientists*; Wiley-VCH: New York, 1993; Chapters 17 and 19.
(64) Goldberg, S.; Criscenti, L. J.; Turner, D. J.; Davis, J. A.; Cantrell, K. J. *Vadose Zone J.* **2007**, *6*, 407−435.
(65) Peak, D.; Luther, G. W.; Sparks, D. L. *Geochem. Cosmochim. Acta* **2003**, *67*, 2551−2560.

(66) Scharifker, B. R.; Habib, M. A.; Carbajal, J. L.; Bockris, J. O'M. *Surf. Sci.* **1986**, *173*, 97−105.
(67) El-Shafei, A. A.; Aramata, A. *J. Solid State Electrochem.* **2007**, *11*, 430−433.
(68) Cotton, F. A.; Wilkinson, G.; Murillo, C.; Bochmann, M. *Advanced Inorganic Chemistry*, 6th ed.; Wiley: New York, 1999; pp 171−173.
(69) Farmer, J. B. In *Advances in Inorganic Chemistry and Radiochemistry*; Emeléus, H. J., Sharpe, A. G., Eds.; Academic Press: New York, 1982; Vol. 25, pp 187−237.
(70) Salentine, C. G. *Inorg. Chem.* **1983**, *22*, 3920−3924.
(71) Risch, M.; Klingan, K.; Heidkamp, J.; Ehrenberg, D.; Chernev, P.; Zaharieva, I.; Dau, H. *Chem. Commun.* **2011**, *47*, 11912−11914.
(72) Choisnet, J.; Evarestov, R. A.; Tupitsyn, I. I.; Veryazov, V. A. *J. Phys. Chem. Solids* **1996**, *57*, 1839−1850.
(73) Koyama, Y.; Kim, Y.-S.; Tanaka, I.; Adachi, H. *Jpn. J. Appl. Phys.* **1999**, *38*, 2024−2027.
(74) Koyama, Y.; Yabuuchi, N.; Tanaka, I.; Adachi, H.; Ohzuku, T. *J. Electrochem. Soc.* **2004**, *151*, A1545−A1551.
(75) McAlpin, J. G.; Stich, T. A.; Ohlin, C. A.; Surendranath, Y.; Nocera, D. G.; Casey, W. H.; Britt, R. D. *J. Am. Chem. Soc.* **2011**, *133*, 15444−15452.
(76) Beverskog, B.; Puigdomenech, I. *Corros. Sci.* **1997**, *39*, 969−980.
(77) Daghetti, A.; Lodi, G.; Trasatti, S. *Mater. Chem. Phys.* **1983**, *8*, 1−90.
(78) Trasatti, S. In *Electrochemistry of Novel Materials*; Lipkowski, J., Ross, P. N., Eds.; VCH: New York, 1994; Chapter 5.
(79) Tewari, P. H.; Campbell, A. B. *J. Colloid Interface Sci.* **1976**, *55*, 531−539.
(80) Faria, L. A.; Prestat, M.; Koenig, J.-F.; Chartier, P.; Trasatti, S. *Electrochim. Acta* **1998**, *44*, 1481−1489.
(81) Wang, L.−P.; Van Voorhis, T. *J. Phys. Chem. Lett.* **2011**, *2*, 2200−2204.
(82) Huynh, M. H. V.; Meyer, T. J. *Chem. Rev.* **2007**, *107*, 5004−5064.
(83) Constentin, C. *Chem. Rev.* **2008**, *108*, 2145−2179.
(84) Reece, S. Y.; Nocera, D. G. *Annu. Rev. Biochem.* **2009**, *78*, 673−699.
(85) Tarasevich, M. R.; Efremov, B. N. In *Electrodes of Conductive Metal Oxides, Part A*; Trasatti, S., Ed.; Elsevier: Amsterdam, 1980; Chapter 5.
(86) Trasatti, S. In *Electrochemistry of Novel Materials*; Lipkowski, J., Ross, P. N., Eds.; VCH: New York, 1994; Chapter 5.
(87) Kinoshita, K. *Electrochemical Oxygen Technology*; Wiley-Interscience: New York, 1992; Chapter 2.
(88) Man, I. C.; Su, H.-Y.; Calle-Vallego, F.; Hansen, H. A.; Martínez, J. I.; Inoglu, N. G.; Kitchin, J.; Jaramillo, T. F.; Nørskov, J. K.; Rossmeisl, J. *ChemCatChem* **2011**, *3*, 1159−1165.
(89) Suntivich, J.; May, K. J.; Gasteiger, H. A.; Goodenough, J. B.; Shao-Horn, Y. *Science* **2011**, *334*, 1383−1385.
(90) Subbaraman, R.; Tripkovic, D.; Chang, K.-C.; Strmcnik, D.; Paulikas, A. P.; Hirunsit, P.; Chan, M.; Greenley, J.; Stamenkovic, V.; Markovic, N. M. *Nat. Mater.* **2012**, *11*, 550−557.

JACS JOURNAL OF THE AMERICAN CHEMICAL SOCIETY

Article

pubs.acs.org/JACS

Nature of Activated Manganese Oxide for Oxygen Evolution

Michael Huynh,[†] Chenyang Shi,[‡] Simon J. L. Billinge,[‡,§] and Daniel G. Nocera*,[†]

[†]Department of Chemistry and Chemical Biology, Harvard University, Cambridge, Massachusetts 02138, United States

[‡]Department of Applied Physics and Applied Mathematics, Columbia University, New York, New York 10027, United States

[§]Condensed Matter Physics and Materials Science Department, Brookhaven National Laboratory, Upton, New York 11973, United States

Supporting Information

ABSTRACT: Electrodeposited manganese oxide films (MnOx) are promising stable oxygen evolution catalysts. They are able to catalyze the oxygen evolution reaction in acidic solutions but with only modest activity when prepared by constant anodic potential deposition. We now show that the performance of these catalysts is improved when they are "activated" by potential cycling protocols, as measured by Tafel analysis (where lower slope is better): upon activation the Tafel slope decreases from ∼120 to ∼70 mV/decade in neutral conditions and from ∼650 to ∼90 mV/decade in acidic solutions. Electrochemical, spectroscopic, and structural methods were employed to study the activation process and support a mechanism where the original birnessite-like MnOx (δ-MnO_2) undergoes a phase change, induced by comproportionation with cathodically generated $Mn(OH)_2$, to a hausmannite-like intermediate (α-Mn_3O_4). Subsequent anodic conditioning from voltage cycling or water oxidation produces a disordered birnessite-like phase, which is highly active for oxygen evolution. At pH 2.5, the current density of activated MnOx (at an overpotential of 600 mV) is 2 orders of magnitude higher than that of the original MnOx and begins to approach that of Ru and Ir oxides in acid.

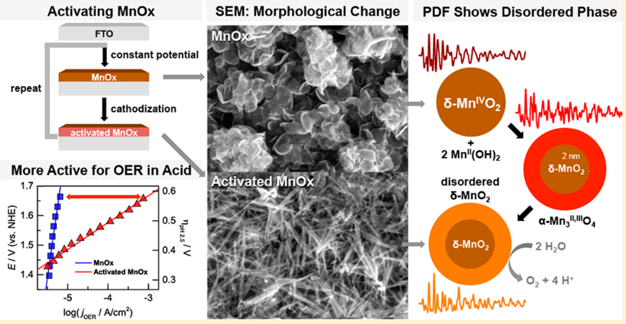

■ INTRODUCTION

A logical and sustainable response to the drastic growth in global energy needs is the use of solar energy for the production of inexpensive, scalable, sustainable, and carbon-neutral fuels.[1−6] Central to this process is the photoelectrochemical (PEC) driven splitting of water to oxygen and hydrogen.[5−10] We have championed buried junction devices for PEC water splitting where catalysts are interfaced to semiconductors such as silicon via conducting interfaces;[11−13] these constructs capture many of the basic functional elements of photosynthesis.[14,15] An advantage of the buried junction is that the light absorber and catalyst may be independently optimized.[16,17] This approach is generally being adopted by others[18,19] with the emphasis that the construction of a system requires both the photoelectrode and the catalysts to be active and stable under a given electrolyte environment.[13,20−22] In particular, the development of the photoanode is difficult because popular photovoltaic materials (such as silicon) are more stable in acidic pH,[22−25] while active and abundant oxygen evolution catalysts (OECs), such as oxidic cobalt and nickel films, operate best in neutral to alkaline conditions and quickly corrode at lower pH regimes.[26−32] We have addressed this challenge by developing an acid stable OEC based on an electrodeposited manganese oxide (MnOx).[33,34] By exploiting the intrinsic strength of the manganese−oxygen bond as well as the self-healing nature of MnOx, oxygen evolution in highly acidic electrolytes was demonstrated without degradation of the catalyst.[34] However, the low activity of MnOx in acid precluded its practical applicability as an earth-abundant alternative to Ru and Ir oxides, the only known active and acid stable OECs.[35−42]

Thus, we turned our attention to increasing the oxygen evolution reaction (OER) activity of MnOx. Recent literature suggests that the method of deposition can affect catalytic activity as manganese oxides have been studied extensively in neutral to alkaline conditions[43−56] and, to a lesser extent, acidic solutions,[34,54−59] yet their reported performances vary. Dau et al.[47] and Jaramillo et al.[49] reported that deposition via cyclic voltammetry (CV) results in more active manganese oxide films (in neutral and alkaline electrolyte) than those prepared at constant potential. They proposed that CV deposition introduces more Mn^{3+} valency in the oxide that promotes turnover. This perspective is shared by Dismukes et al. where they evaluated a variety of chemically prepared manganese oxide polymorphs and discovered that oxides containing more Mn^{3+} and Mn^{2+} exhibited the highest OER activities.[48]

Motivated by these results, we suspected the ability to access different compositions and polymorphs by electrochemical means (e.g., a Pourbaix diagram of Mn[25]) could explain the

Received: June 30, 2015
Published: November 2, 2015

DOI: 10.1021/jacs.5b06382
J. Am. Chem. Soc. 2015, 137, 14887−14904

increased activity of samples deposited by voltage cycling. We now elucidate the conditions necessary for activating MnOx and correlate functional changes with structural transformations. The activation process begins with a phase change driven by the comproportionation of the original birnessite-like (δ-MnO_2) film with cathodically generated $Mn(OH)_2$ to produce a hausmannite-like (α-Mn_3O_4) intermediate. Subsequent anodic conditioning during voltage cycling or oxygen evolution produces activated MnOx, which exhibits low Tafel slopes for OER of ~70 mV/decade in neutral pH (originally ~120 mV/decade) and ~90 mV/decade under acidic conditions (originally ~650 mV/decade). X-ray pair distribution function (PDF) analysis of these activated MnOx films reveals that the anodic conditioning results in a transformation of hausmannite back to birnessite but as a disordered phase, which is the active OER catalyst. In phosphate (P_i) buffer at pH 2.5, the activated MnOx exhibits current densities (1 mA/cm^2) that are 2 orders of magnitude greater than the original film when operated at an overpotential of 600 mV. These results represent a path toward replacing precious Ru and Ir oxides for oxygen evolution in acidic environments with oxide-based catalysts comprising noncritical materials.

■ EXPERIMENTAL SECTION

General Electrochemical Details. All electrochemical experiments (unless otherwise specified) employed a CH Instruments 760D potentiostat in a three-electrode configuration with a porous glass frit separating the working and auxiliary compartments of the glass H-cell. Glassware was cleaned by soaking in aqua regia and rinsing with type I reagent water (EMD Millipore, 18 MΩ cm resistivity). Fluorine-doped, tin oxide-coated glass (FTO) with 7 Ω per square surface resistivity (TEC-7, precut 1 cm × 2.5 cm slides from Hartford Glass) was used as the working electrode. FTO slides were sonicated in acetone and rinsed with type I water before use. A 1 cm^2 geometric electrode area was created by masking the FTO with Scotch tape. An Ag/AgCl reference electrode (BASi, filled with saturated KCl) and a Pt mesh (99.9%, Alfa Aesar) auxiliary electrode completed the setup. All experiments were conducted at ambient temperature (~23 °C) and employed automatic *iR* compensation where the electrode and solution resistance was determined by applying a small potential step at the open circuit potential. Potentials were converted to the NHE scale by the following relation, $E_{NHE} = E_{Ag/AgCl} + 0.197$ V, and overpotentials (η) for the oxygen evolution reaction from water were calculated by $\eta = E_{NHE} - (1.23 \text{ V} - 0.059 \text{ V} \times \text{pH})$.

Methods for Film Electrodeposition. MnOx catalyst films were prepared with varying electrodeposition protocols in solutions containing 0.5 mM Mn^{2+} (prepared from $MnCl_2 \cdot 4H_2O$, 99.995% trace metal basis, Strem) and 0.9 M KNO_3 (99.0−100.5%, Macron), unless otherwise specified. All films were then briefly immersed in type I water to remove any trace Mn^{2+}, and any subsequent electrochemical characterization was performed immediately to prevent films from drying. All deposition protocols were adjusted to obtain similar mass loadings of the catalyst films by using a QCM.

The first method for MnOx deposition was at constant potential, where 1.1 V (vs NHE unless otherwise specified) was applied to the electrode for 600 s. MnOx was also deposited at constant potential in the presence of buffer using procedures described previously:[33] 0.54 V potential at the electrode immersed in 0.5 mM Mn^{2+}, 50 mM methylphosphonate (MeP_i), and 0.9 M KNO_3 at pH 8.0. The second deposition method was by CV: the electrode was cycled 25 times between a potential from 1.7 to −0.8 V at a scan rate of 100 mV/s. A sample was also prepared via CV deposition without the presence of KNO_3 supporting electrolyte. The third approach for preparing MnOx films was by multipotential (MP) steps, where the electrode was initially held at 1.1 V for 3 s, followed by −0.4 V for 2 s, and this was repeated 50 times. The potential and duration of each pulse were varied to determine the optimal conditions for catalyst formation. Multipotential deposition was also performed in MeP_i buffer as a control. The fourth technique for MnOx deposition is called cathodization, where a pre-existing MnOx film deposited at constant anodic potential (described earlier) is subjected to a potential of −0.4 V for 2000 s. Finally, the fifth method for producing MnOx is by purely cathodic deposition, where the electrode was poised at −0.4 V for 2000 s. A variation in cathodic deposition employed a short anodic pulse of 1.0 V for 30 s following the end of the cathodic pulse.

Tafel Data Collection. The OER activity of MnOx films was evaluated by collecting steady-state current density (j) as a function of applied potential (E) during oxygen evolution in Mn^{2+}-free solutions of 0.10 M P_i buffer in acidic (pH 2.5) and neutral (pH 7.0) conditions. All solutions also contained 1.5−1.9 M KNO_3 supporting electrolyte (an innocent ion at high anodic potentials required to drive OER) to reach a total ionic strength (μ) of 2.0 M. During data collection, solutions were stirred at ~600 rpm with a Teflon stir bar (sufficient to remove mass transport limitations as shown previously[34]), and a series of discrete monotonically decreasing potentials were applied to the electrode for 30 s each to allow the current to reach a steady-state value. The highest potential (first point in the series) was held for 200 s to further minimize any pseudocapacitance. All potentials were automatically *iR* compensated for solution and FTO resistance (~17 Ω). Catalyst films were thin (<50 nm), and any resistivity through the film was negligible and not included in *iR* corrections: electrochemical impedance spectroscopy measurements (vide infra) estimate ~0.4 Ω. The current−potential data were plotted in the form of log j versus E (or η) to construct Tafel plots, which were reproducible with independently prepared MnOx samples. Control studies with bare FTO demonstrate that FTO is poor at oxygen evolution and serves as a good substrate because it exhibits high Tafel slopes and current densities for OER of at least an order of magnitude lower than that of MnOx catalyst films.

Faradaic Efficiency of Oxygen Evolution. To determine the percentage of charge passed that contributes to oxygen evolution on MnOx films, a fluorescence-based O_2 sensor (FOXY OR125-GT/AF-MG, Ocean Optics) was used to measure oxygen concentration during sustained electrolysis by chronoamperometry. A custom-built, gastight electrochemical H-cell was fit with the O_2 sensor (in a 14/20 port) in the working compartment, and the MnOx catalyst (1 cm^2 film deposited on FTO) and Ag/AgCl reference electrode were connected with glass-sealed electrical leads. The auxiliary compartment contained a Pt mesh electrode. Prior to all measurements, the cell was purged for 1 h with high-purity Ar gas, and a two-point calibration curve (air, 20.9% O_2 and Ar, 0% O_2) was constructed. Activated MnOx catalyst films prepared by multipotential deposition (described earlier) were operated at 0.1 mA/cm^2 in 0.10 M P_i with 1.75 M KNO_3 electrolyte solution at pH 2.5 and 7.0. The excitation and emission phase shifts of the O_2 sensor dye were recorded at 2 s intervals and converted to an excited state lifetime (τ). These lifetimes were used to calculate the partial pressure of oxygen (p_{O2}) using a modified Stern−Volmer relation:[60]

$$\tau_0/\tau = 1 + K \times p_{O_2} \tag{1}$$

where K is the Stern−Volmer coefficient, determined by calibration, and τ_0 is the lifetime for 0% O_2. No correction of the partial pressures by Henry's law was required because the amount of dissolved O_2 was small as compared to the amount of O_2 in the headspace. These pressures were converted to moles of O_2 by using the ideal gas law and headspace volume of the cell. Finally, the amount of detected O_2 was compared to the theoretical yield of O_2, calculated by dividing the charge passed by 4F.

Electrochemical Impedance Spectroscopy (EIS). Impedance measurements were conducted on a Gamry Interface 1000 potentiostat for 1 cm^2 FTO as a blank substrate as well as with constant potential deposited MnOx and activated MnOx in 0.10 M P_i buffer, 1.73 M KNO_3 at pH 2.5. Films were evaluated in the region of OER catalysis at 1.65 V with an initial conditioning for 60 s followed by the addition of 5 mV (rms) AC signals from 100 kHz to 0.1 Hz. No *iR* compensation was applied during these measurements. Collected data were analyzed by Gamry Echem Analyst (version 6.30) software to obtain Bode and Nyquist plots and to perform Kramers−Kronig analysis for data quality. Fits were calculated on the basis of a Randles equivalent circuit model employing constant phase and Warburg elements.

Inductively Coupled Plasma Mass Spectrometry (ICP-MS). Trace elemental analysis was performed with a quadrupole ICP-MS (Thermo Electron, X-Series ICP-MS with CCT). Because MnOx is resistant to passive dissolution in acid, as-deposited films were digested by voltage cycling (between 1.3 and −0.4 V) in 12 mL of 2% v/v nitric acid (TraceSELECT, Fluka). Manganese and iron calibration standards were prepared from corresponding ICP standard solutions (TraceCERT, Fluka), which enabled the construction of a calibration curve to convert the detected counts for ^{55}Mn and ^{57}Fe to concentrations (in ppm).

Stability during Oxygen Evolution. The ability of activated MnOx to sustain stable activity for oxygen evolution was assessed by chronoamperometry. Activated MnOx films prepared by multipotential deposition (described earlier) were operated at 0.1 mA/cm^2 in 100 mM P$_i$ buffer at pH 2.5 and 7.0 with 1.73 M KNO$_3$ supporting electrolyte and also 0.5 M H$_2$SO$_4$ at pH 0.3. Constant potential deposited MnOx, blank FTO, and electrodeposited IrOx (following literature procedures[61]) were also evaluated for comparison. A pre-electrolysis time of 200 s was applied to minimize any pseudocapacitance, and solutions were stirred at ∼600 rpm throughout the experiment. The potential was recorded over 8 h of continuous catalysis, and stability was evaluated by tracking the change in potential over time. The presence of peroxides in the final solution was tested immediately after the end of catalysis using Quantofix Peroxide 25 test strips (lower limit of detection of <0.5 ppm). In addition, chronoamperometry at higher current densities of 1 mA/cm^2 (geometric area) at pH 2.5 was conducted for activated and constant potential MnOx catalysts electrodeposited on a carbon cloth substrate (AvCarb 1071 HCB), which has ∼13 times the surface area of FTO as estimated by electrochemical surface area measurements (following literature procedures[41]).

Tracking Electrode Mass with a Quartz Crystal Microbalance (QCM). The change in mass on the electrode was recorded in situ using an electrochemical QCM (Gamry eQCM 10M). A 10 MHz platinum-coated quartz crystal (International Crystal Manufacturing Co, Inc.), connected to both the QCM resonator and the potentiostat, served as the working electrode, which was placed at the bottom of a static PTFE cell with a Ag/AgCl reference and Pt wire auxiliary electrode. Prior to all experiments, the resonator was locked to the resonant frequency of the crystal and permitted to stabilize for 15 min. The series and parallel resonant frequencies were sampled every second during the experiments and responded similarly (i.e., $\Delta f_s = \Delta f_p$). The change in resonant frequency (Δf) over time was correlated to a change in mass (Δm) on the electrode using the Saurbrey equation:[62]

$$\Delta f = -\frac{2f_0^2}{A\sqrt{\rho_q \mu_q}}\Delta m \qquad (2)$$

where f_0 is the resonant frequency of the crystal, A is the piezoelectrically active crystal area, ρ_0 is the density of quartz, and μ_0 is the shear modulus for the AT-cut quartz. None of the mass changes observed corresponded to a change of greater than 2% of f_0, which validated the use of the Saurbrey equation for analysis. After each experiment, any deposited MnOx film was removed from the Pt-coated quartz crystal by cycling the electrode between 1.7 and −0.1 V in 0.5 M H$_2$SO$_4$ (99.99% trace metals basis, Aldrich). Control experiments with only the Pt substrate in Mn^{2+}-free solution were performed for comparison.

Electron Microscopy. Morphological changes in MnOx films as a result of deposition protocol were observed by field emission scanning electron microscopy (SEM, Zeiss Supra 55VP). Samples were prepared with high catalyst loadings (32 mC/cm^2 for constant potential MnOx and 2000 cycles for multipotential deposited MnOx) on FTO. The FESEM was operated at a beam voltage of 15.0 kV, working distance of ∼8.5 mm, a 30 μm aperture, and an InLens detector.

The crystallinity of MnOx before and after activation was probed by high-resolution transmission electron microscopy (TEM) on a JEOL JEM-2100 equipped with a Gatan CCD. Samples were electrodeposited on a 400-mesh pure carbon film supported on an Au TEM grid (Electron Microscopy Sciences). The grid was partially immersed in the deposition solution and directly employed as the working electrode. Constant potential MnOx was prepared with a short 5 s pulse, and multipotential deposited MnOx utilized five complete cycles. Samples were immersed in type I water to remove any residual electrolyte, dried, and then imaged at a beam accelerating voltage of 200 keV using a 250 μm condenser aperture. Images were processed with Gatan DigitalMicrograph software. For constant potential deposited MnOx, crystal planes were identified by computing the FFT of the lattice fringes, masking to each maximum Fourier component, and taking the inverse FFT to isolate an interplanar spacing that was directly measured.

X-ray Photoelectron Spectroscopy (XPS). The oxidation state of manganese in MnOx samples was examined by XPS using a Thermo Scientific K-Alpha XPS system. MnOx catalyst films were electrodeposited on FTO as described above, and a series of high-purity manganese oxide control compounds were purchased to serve as calibration and comparison markers: Mn^{II}O (99.99% manganosite, Sigma-Aldrich), α-Mn$^{II,III}{}_3$O$_4$ (97% hausmannite, Sigma-Aldrich), α-Mn$^{III}{}_2$O$_3$ (99.99% bixbyite, Sigma-Aldrich), and β-Mn^{IV}O$_2$ (99.995% pyrolusite, Strem). The phases of these control compounds were verified with powder X-ray diffraction. All samples were illuminated with a 400 μm spot size, monochromated Al Kα X-ray source (1486.6 eV energy and 0.85 eV line width).[63] Surface charging was compensated by a low-energy (0−14 eV) electron flood gun. The system was precalibrated with Au, Ag, and Cu standards built into the sample stage using an automated routine. The MnO sample was sputtered with Ar ions in advance to remove surface oxidation from air.[49] Powders of the control compounds were mounted by drop casting on high-purity Cu foil (99.9%, Strem) or by attaching to double-sided Cu tape. Survey spectra were collected from 0 to 1350 eV with a step size of 1.0 eV, dwell time of 10 ms, average of 5 scans, and a pass energy of 200 eV. High-resolution spectra used an energy step of 0.1 eV, dwell time of 40 ms, average of at least 75 scans, and a pass energy of 40 eV. High-resolution scans were obtained for the Mn 2p, Mn 3s, Mn 3p, C 1s, and Cu 2p (for samples on Cu substrate) regions. Control and MnOx samples were calibrated to the Cu 2p$_{3/2}$ (932.6 eV)[64] and C 1s (284.8 eV)[65] peaks, respectively.

Thin-Film and Powder X-ray Diffraction (XRD). The composition and phase of MnOx thin-film and powder samples were interrogated by XRD. Electrodeposited MnOx films on FTO were prepared as described earlier. Thin-film diffraction patterns were obtained using a Bruker D8 Discover diffractometer configured with a Cu Kα X-ray source (λ = 1.5405 Å, generated at 40 kV and 40 mA) through a 1 mm antiscattering slit, Göbel mirror, and LynxEye detector with an 8 mm steckblende slit. Knife-edge attachments were used to remove low-angle scattering. The MnOx films on FTO were placed on a PMMA specimen holder, rotated at 3°/min, and scanned in Bragg−Brentano mode from 2θ = 10° to 70° in 0.02° increments with a 0.5 s/pt scan rate.

Powder MnOx samples were prepared by the same electrodeposition protocols as described earlier but on multiple 20 × 8 cm FTO plates. The thin films were briefly immersed in type I water to remove any residual solution, dried, and then carefully stripped from the FTO. Catalyst films were ground into a fine powder using a mortar and pestle. This process was repeated until sufficient material was obtained for XRD. The powders were loaded in a small cavity in a Si zero-diffraction plate (MTI Corporation) and inserted into a Bruker D2 Phaser powder diffractometer equipped with a Cu Kα X-ray source (generated at 20 kV and 20 mA; passed through a 1 mm slit) and LynxEye detector. A knife-edge attachment was used to reduce scattered signal, and the stage was rotated by 3°/min. Samples were examined in Bragg−Brentano mode from 2θ = 10° to 75° in 0.02° increments with a 0.5 s/pt scan rate.

DOI: 10.1021/jacs.5b06382
J. Am. Chem. Soc. 2015, 137, 14887−14904

Diffraction data were analyzed by search-match in Bruker's EVA 3.0 software using the JCPDS-ICDD PDF-2 (Release 2012) database. The data were also compared to patterns collected from control manganese oxide samples (same compounds used for XPS with the addition of δ-$Mn^{+3.7}O_2$, birnessite, synthesized by previously described procedures[66]), loaded in the Si zero-diffraction plate with the same XRD experimental parameters as for the MnOx powders.

Atomic Pair Distribution Function (PDF) Analysis. Synchrotron X-ray total scattering experiments were conducted at beamline X17A in the National Synchrotron Light Source (NSLS) at Brookhaven National Laboratory. MnOx powder samples and control manganese oxides (same as those for XRD) were packed into 0.0360 in. i.d. × 0.0400 in. o.d. Kapton capillary tubes (Cole Parmer) and measured at 100 K using a flowing nitrogen cryocooler. The rapid acquisition pair distribution function (RaPDF) technique[67] was used with an X-ray energy of 67.42 keV ($\lambda = 0.1839$ Å). A large area 2-D PerkinElmer detector (2084 × 2084 pixels and 200 × 200 μm pixel size) was mounted orthogonal to the beam path. The raw 2D data were azimuthally integrated and converted to 1-D intensity versus 2θ using FIT2D.[68] PDFgetX3[69] was used to correct and normalize the diffraction data before applying the Fourier transform to obtain the PDF, $G(r)$, according to

$$G(r) = \frac{2}{\pi}\int_{Q_{\min}}^{Q_{\max}} Q[S(Q) - 1] \sin Qr \, dQ \tag{3}$$

where Q is the magnitude of the momentum transfer on scattering and $S(Q)$ is the properly corrected and normalized powder diffraction intensity measured from $Q_{\min}$ to $Q_{\max}$.[70] $G(r)$ is a measure of the probability of finding a pair of atoms separated by a distance of r. Lanthanum hexaboride (LaB_6) or nickel was measured as the standard material to calibrate the sample-to-detector distance and to determine the values of Q_{damp} and Q_{broad} parameters, which are used during modeling to account for the instrument resolution effects on the PDF.[71,72] The sample-to-detector distances for constant potential deposited/cathodized samples and for multipotential deposited sample are 204.264 and 204.577 mm, respectively. The refined values were $Q_{damp} = 0.0387$ Å^{-1} and $Q_{broad} = 0.0184$ Å^{-1} for constant potential deposited and cathodized samples, while $Q_{damp} = 0.0409$ Å^{-1} and $Q_{broad} = 0.0207$ Å^{-1} for multipotential deposited sample. They are slightly different because the data were collected on different occasions and the setup was calibrated separately each time. These values were then used as fixed values in subsequent model fits to the PDF data.

PDF modeling was performed with the PDFgui[72] and SrFit[73] programs. Trial PDF fits used birnessite (δ-MnO_2), pyrolusite (β-MnO_2), akhtenkite (ε-MnO_2), hausmannite (α-Mn_3O_4), bixbyite (α-Mn_2O_3), manganosite (MnO), rancieite ($(Ca,Mn^{2+})Mn_4^{4+}O_9{\cdot}3H_2O$), and Mn_5O_8 structures. Final fits of the MnOx samples employed structures of birnessite and hausmannite. The birnessite model has the space group $C2/m$ (No. 12), where Mn, O_{OL}, K_{IL}, and O_{IL} atoms are positioned at (0, 0, 0), (x, 0, z), (x, 0, z), and (x, 0, z), respectively, where OL and IL stand for octahedral layer and interlayer, respectively. Water and potassium ion intercalants were introduced between the MnO_6 layers, as reported by Zhu et al.[74] The hausmannite model has the space group $I4_1/amd$ (origin choice 1), with Mn1, Mn2, and O atoms at (0, 0, 0), (1/2, 1/4, 1/8), and (0, y, z), respectively. The nanocrystalline nature of MnOx was modeled as the bulk PDF attenuated by a spherical characteristic function,[75−77] which allows us to estimate the crystallite size or the range of structural coherence in the samples.

RESULTS

The oxygen evolution activity of manganese oxide thin films (MnOx) changes as a function of electrodeposition protocol. As has been reported, MnOx films produced by cyclic voltammetry in Mn^{2+} aqueous solutions exhibit higher OER activities as compared to films deposited at constant anodic potential.[47] MnOx deposited on the first CV sweep becomes "activated" toward OER on the second cycle (Figure 1). Motivated by this observation, we prepared MnOx films by different electrodeposition protocols and set out to correlate the nature of this activation process with the electrochemistry and structure of the MnOx system.

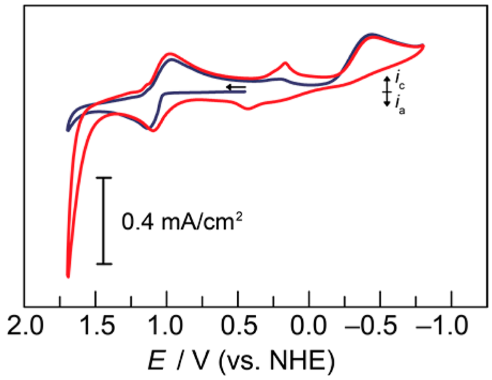

Figure 1. Cyclic voltammogram of a 1 cm² FTO electrode in 0.5 mM Mn^{2+} and 0.9 M KNO_3 solution at 100 mV/s scan rate showing the first (blue) and second (red) cycles.

Electrochemical Deposition and Tafel Analysis. *Constant Potential Deposition.* MnOx is typically deposited at constant anodic potential in an aqueous solution containing a Mn^{2+} salt. Following previously described procedures,[33] FTO-coated glass slides were polarized at a constant potential of 0.54 V (vs NHE unless otherwise stated) in quiescent solutions of Mn^{2+} buffered by MeP_i at pH 8. The resulting brown films were placed in Mn^{2+}-free P_i buffer solutions where the films' OER activity was defined by Tafel analysis. Because there are no methods to accurately normalize current densities to the number of true active sites in the films, Tafel slopes were used as the primary activity descriptor (where lower slope is better) because it is invariant to the number of active sites (vide infra). These MnOx films, deposited at constant potential, exhibit ~120 mV/decade Tafel slope at pH 7.0 (Figure 2) and ~650 mV/decade slope at pH 2.5 (Figure 3).[34] MnOx films deposited at constant potential in the absence of a buffer (in just aqueous solutions of Mn^{2+}) yield slightly less active films with Tafel slopes of ~221 mV/decade (Figure 2). Overall, these films display only modest OER activities and are

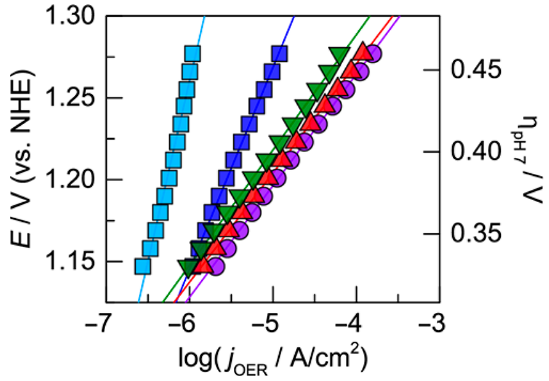

Figure 2. Tafel plots of oxygen evolution in 0.10 M P_i and 1.73 M KNO_3 at pH 7.0 on MnOx films deposited by different deposition protocols: constant potential without buffer (221 mV/decade Tafel slope; light blue ■), constant potential in MeP_i buffer at pH 8 (123 mV/decade; blue ■), CV (68 mV/decade; purple ●), multipotential pulses (67 mV/decade; red ▲), and cathodization (70 mV/decade; green ▼).

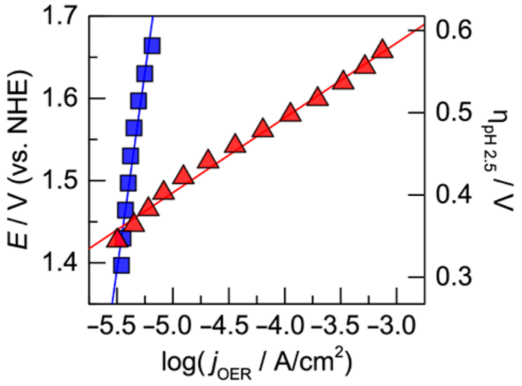

Figure 3. Tafel plots of oxygen evolution in 0.10 M P_i and 1.90 M KNO_3 at pH 2.5 on constant potential deposited MnOx (~650 mV/decade Tafel slope; blue ■) and activated MnOx (91 mV/decade; red ▲).

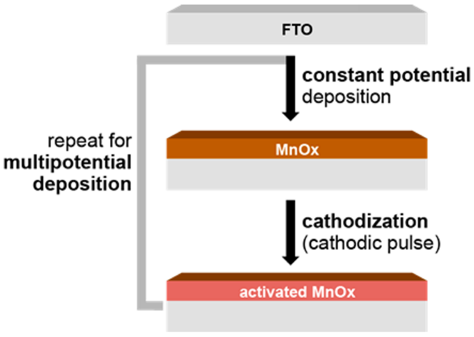

Figure 4. Electrochemical protocols for depositing MnOx on an FTO electrode. Unactivated (as-deposited) MnOx (brown) is produced by constant anodic potential deposition. Cathodizing this film by applying a negative potential results in activated MnOx (red). Activation can also occur by CV cycling (not shown) and multipotential deposition (which repeats the anodic−cathodic pulse sequence).

considered "unactivated". For clarity in the subsequent discussion, MnOx deposited at constant anodic potential will be denoted "as-deposited".

Cyclic Voltammetry Deposition. MnOx catalyst films can also be deposited by prolonged cyclic voltammetry (CV). Following previously reported procedures,[47] FTO electrodes were CV cycled in solutions of just aqueous Mn^{2+} (Figure S1a). Films obtained by this method exhibited Tafel slopes of ~74 mV/decade for OER in P_i buffer at pH 7 (Figure S1b). However, CV deposition was difficult to analyze by electrochemical methods because of high solution resistances (~4 kΩ/cm), which led to broad and shifted CV peaks. Adding KNO_3 supporting electrolyte resulted in sharper CV features (Figure 1) while still retaining the ability to deposit active films that exhibit Tafel slopes of 68 mV/decade for OER at neutral pH (Figure 2). CV-deposited films have lower Tafel slopes than that of as-deposited MnOx films and are considered "activated" for oxygen evolution. In this study, a Tafel slope of approximately 70 mV/decade serves as the benchmark for categorizing catalyst films as "activated".

Multipotential Deposition. CV deposition can be deconstructed into a primary anodic event at 1.1 V, where MnOx deposition occurs, followed by a series of reductions at ca. 1.0, 0.1, and −0.6 V (Figure 1). To study these redox processes more directly and rigorously, instead of sweeping the potential through these peaks, the potential was held constant at 1.1 V for a short period of time before briefly switching to a lower value, targeting the cathodic peaks near 0.1 and −0.6 V. For clarity, we call this method multipotential deposition. Alternating between anodic and cathodic potentials (see schematic in Figure 4) in a solution of Mn^{2+} and KNO_3 supporting electrolyte resulted in a brown film that grew thicker over cycles. Films produced using a 0.2 V cathodic pulse exhibited a Tafel slope of 92 mV/decade for OER in P_i buffer at pH 7.0. However, a lower slope was observed when a −0.4 V cathodic pulse was employed instead (Figure S2), and the best performing multipotential deposited films were deposited by stepping the electrode between 1.1 V for 3 s and −0.4 V for 2 s. These films displayed a Tafel slope of ~67 mV/decade at neutral pH (Figure 2) and ~91 mV/decade at pH 2.5 (Figure 3), establishing that multipotential deposition produces activated MnOx films.

Cathodization. A further simplification can be applied to multipotential deposition by reducing the procedure to a single cycle: an initial anodic deposition event followed by a final cathodic pulse without any further repetition (see schematic in Figure 4). We call this process "cathodization" in analogy to the more commonly known term "anodization", where an anodic pulse is applied to an existing film (as demonstrated in NiB_i catalyst films[31]). To cathodize MnOx, thin films (3 mC/cm^2 catalyst loading) were first deposited at 1.1 V in a Mn^{2+} solution with KNO_3 supporting electrolyte and then (in the same solution) poised at −0.4 V for 2000 s. These cathodized films were transferred to Mn^{2+}-free P_i buffer and subsequently evaluated by Tafel analysis for OER activity (Figure 2), demonstrating Tafel slopes of ~70 mV/decade at neutral pH, similar to those of CV and multipotential deposited films. Thus, cathodization in unbuffered Mn^{2+} solutions yields activated MnOx films.

In contrast, when cathodization is performed in Mn^{2+}-free solution or in buffered solutions containing Mn^{2+}, no activation was observed. As-deposited MnOx films were subjected to a cathodic potential of −0.4 V in Mn^{2+}-free solutions containing just KNO_3 supporting electrolyte, Mn^{2+} solutions buffered with P_i at pH 7.0, or Mn^{2+} solutions buffered with MeP_i at pH 8.0. In all cases, steep Tafel slopes of ~200−300 mV/decade were observed for OER at pH 7.0 (Figure 5). These high slopes indicate a regression in OER performance relative to the as-deposited MnOx (with a Tafel slope of ~123 mV/decade). These results show that the cathodization procedure activates MnOx only when performed in Mn^{2+} solutions that are unbuffered.

Cathodic Deposition. To check if the initial as-deposited MnOx was necessary for activation, deposition of MnOx films was attempted using only cathodic potentials. FTO electrodes were poised at −0.4 V (the same potential used for cathodization) in a deposition solution containing Mn^{2+} and KNO_3 supporting electrolyte. The FTO remained clear with faint darkening around the edges, which suggested that only a trace amount of catalyst formed. The electrode was evaluated for oxygen evolution in P_i buffer at pH 7, but the resulting Tafel plot (Figure 6) with a slope of ~221 mV/decade demonstrated poor OER performance relative to activated MnOx. When a short anodic pulse was applied to the FTO electrode immediately after cathodic deposition, a thin brown film instantly appeared. The Tafel slope of this film for OER in P_i buffer at neutral pH was ~126 mV/decade, an improvement over purely cathodic deposition but similar to the slope of as-

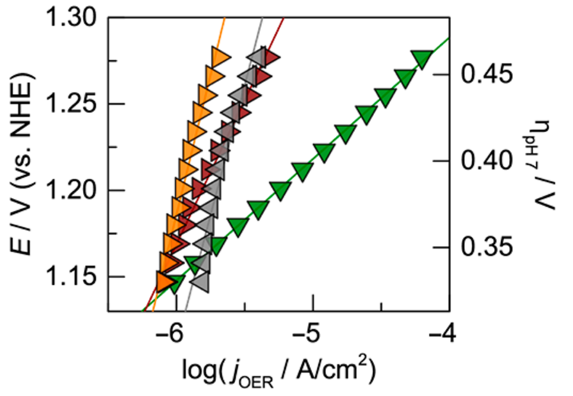

Figure 5. Tafel plots of oxygen evolution in 0.10 M P_i and 1.73 M KNO_3 at pH 7.0 on MnOx films produced by cathodization of MnOx in Mn^{2+}-less solution (300 mV/decade Tafel slope; gray left-facing ▲), 0.5 mM Mn^{2+} with 100 mM P_i buffer at pH 7.0 (181 mV/decade; brown right-facing ▲), and 0.5 mM Mn^{2+} with 100 mM MeP_i buffer at pH 8.0 (323 mV/decade; orange right-facing ▲). Activated MnOx by cathodization in 0.5 mM Mn^{2+} and 0.9 M KNO_3 solution (70 mV/decade; green ▼) is provided for comparison.

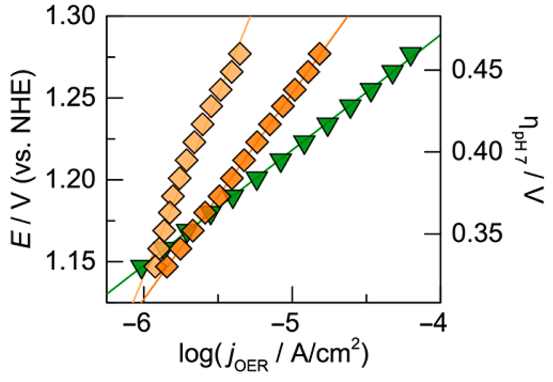

Figure 6. Tafel plots of oxygen evolution in 0.10 M P_i and 1.73 M KNO_3 at pH 7.0 on MnOx films produced by cathodic deposition (221 mV/decade Tafel slope; light orange ◆) and cathodic deposition followed by short anodic pulse (126 mV/decade; dark orange ◆). Activated MnOx by cathodization (70 mV/decade; green ▼) is provided for comparison.

deposited MnOx (∼123 mV/decade). However, the Tafel slopes of both cathodically deposited MnOx films were higher than that of activated MnOx (∼70 mV/decade), and thus cathodic deposition does not seem to produce activated MnOx films.

Faradaic Efficiency and Stability. Evolved oxygen from the catalyst films was measured by a fluorescence O_2 sensor in a gastight cell and compared to the amount of charge delivered to the films. The Faradaic efficiency for oxygen evolution was near unity for activated MnOx films operating in neutral and acidic solutions of P_i buffer (Figure S3). In addition, the stability of activated MnOx was evaluated by chronoamperometry at 0.1 mA/cm^2 over ∼8 h of sustained oxygen evolution. In P_i buffer at pH 7.0 and 2.5 and in sulfuric acid at pH 0.3, the films remained both chemically (i.e., no degradation of the film) and electrochemically stable (i.e., no significant change in potential) in both neutral and acidic pH solutions throughout the entirety of the stability test (Figure S4). No peroxides were detected in the final solutions, and Tafel plots of activated MnOx taken before and after the stability tests showed no change in slope (Figure S5). Overpotentials of ∼470 and ∼540 mV were required to maintain 0.1 mA/cm^2 in neutral and acidic (both pH 2.5 and 0.3) solutions, respectively. Consequently, to demonstrate higher current densities without increasing applied potential, as-deposited and activated MnOx were electrodeposited on a carbon cloth substrate and operated at 1 mA/cm^2 (geometric area) in pH 2.5 solution (Figure S4d). The measured electrochemical surface area of the carbon cloth is approximately 14 times greater than the FTO substrates (Figure S6), and this is reflected by the ca. 10-fold increase in current density of activated MnOx (from 0.1 to 1 mA/cm^2) at a similar overpotential.

Film Resistivity and Purity. To test if the lower Tafel slope of activated MnOx is the result of decreased electrical resistance of the film when compared to as-deposited MnOx, both systems and a blank FTO electrode were subjected to electrochemical impedance spectroscopy (EIS) during OER at 1.65 V in pH 2.5 solution. For EIS measurements, different electrochemical processes can be deconvoluted and isolated at certain frequencies, enabling separation of film properties from catalysis.[78] The resulting Bode and Nyquist plots (Figure S7) were fit to a modified Randles circuit (Figure S7g), which includes: resistive elements for uncompensated (R_u, comprising solution and film resistance) and Faradaic resistance (R_f, incorporating polarization and charge transfer resistance); and constant phase elements for solution and film capacitance, $Y(\alpha)$ where α is close to 1, as well as for diffusion limitations using a Warburg element (W_d). Kramers−Kronig analysis indicates high data quality, and calculated Bode and Nyquist fits were consistent with experimental data, suggesting that this basic Randles circuit was sufficient for describing the electrochemical system, that more complex equivalent circuits were unnecessary. The parameters from the fits (Table S1) show that the uncompensated resistance from FTO and solution resistance totaled ∼16.5 Ω and that the presence of either as-deposited or activated MnOx only adds ∼0.4 Ω of resistance. While the Faradaic resistance decreases from ∼18 kΩ to 27 Ω, it should be noted that this value primarily reflects OER kinetics and not film resistance: lower R_f values are inversely proportional to higher current densities in Tafel plots.[79] The large decrease in R_f between as-deposited and activated MnOx is consistent with Tafel plots (Figure 3), demonstrating a similar order of magnitude increase in current density. Thus, film resistivity for these thin films plays a negligible role when evaluating their Tafel slopes.

The presence of any trace Fe (in ppm-level concentrations in even high-purity reagents) is not responsible for the activation of MnOx films. As-deposited MnOx is not very active for OER, and when these films were anodized in pH 2.5 and 7.0 solutions at high anodic potentials for ∼8 h (Figure S4), no increase in OER activity was observed. Similarly, when these films were cathodized in Mn^{2+}-free solutions at neutral pH, subsequent Tafel plots showed that their OER activity diminishes relative to the original films (Figure 5); cathodization in acidic Mn^{2+}-free electrolyte results in slow film dissolution instead of activation. These results are consistent with the negligible amount of Fe in as-deposited MnOx (<10 ppb, corresponding to <0.6% of Mn concentration) as analyzed by inductively coupled plasma mass spectrometry. This is below the ∼5% and ∼8% Fe threshold where an increase in alkaline OER activity is observed for Ni and Co films, respectively.[80−82] Thus, activation and operation of MnOx films in acidic and neutral pH is not influenced by any trace Fe impurities.

Mass Change for Electrodeposition Protocols. An electrochemical quartz crystal microbalance (QCM) was employed to study the change in mass on a Pt-sputtered quartz electrode for different deposition protocols. For CV (Figures 7 and S8) and multipotential methods (Figure S9) in Mn^{2+} solutions with KNO_3 supporting electrolyte, the electrode mass increased with cycling. Potentials above ~0.9 V facilitated anodic deposition of MnOx. In contrast, a mass decrease was observed on the cathodic sweeps of CVs and on the cathodic pulses of multipotential deposition. However, this rate of decrease drops to zero at more cathodic potentials (below ~0.4 V in Figure 7). Because the total mass loss was always less than the amount of mass deposited, there was net deposition of MnOx over many cycles. For example, three CV cycles resulted in an increase of 1 μg on the electrode. In contrast, CVs taken in a Mn^{2+}-free solution exhibited only 10 ng of mass change, which was attributed to the reversible formation of Pt oxide on the electrode surface (Figure S10). Furthermore, CV deposition in Mn^{2+} solutions buffered with MeP_i at pH 8.0 was unsuccessful with completely reversible mass change and no net mass increase (Figure S11).

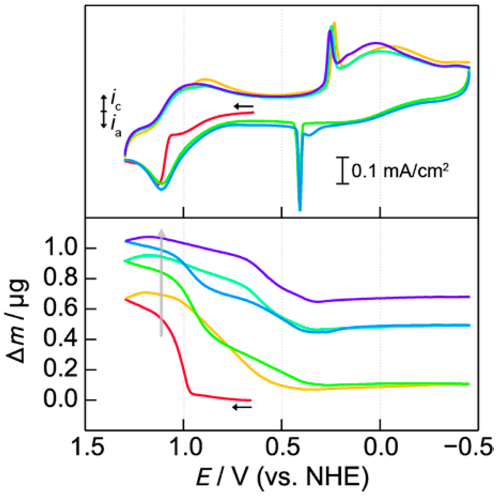

Figure 7. Cyclic voltammogram (top) and corresponding change in mass as measured by a quartz crystal microbalance (bottom) on a Pt-sputtered quartz electrode in 0.5 mM Mn^{2+} and 0.9 M KNO_3 solution at 50 mV/s scan rate. The scans progress from red to purple lines, and gray arrow indicates increase in mass over time. The current−time view of the same process is shown in Figure S6.

For the cathodization process, a thin as-deposited MnOx film on the QCM electrode was poised at −0.4 V in the same solution of Mn^{2+} with KNO_3 supporting electrolyte (Figure 8). As suggested by QCM results from CV and multipotential deposition, there was no mass loss on the electrode at these cathodic potentials. Instead, there was a slight mass increase during cathodization. For comparison, when cathodization was performed in Mn^{2+}-free solutions with KNO_3, no change in mass was observed. Finally, cathodization in Mn^{2+} solutions that are buffered with MeP_i at pH 8.0 led to complete desorption of the predeposited MnOx film.

For cathodic deposition, a blank QCM electrode was held at a constant cathodic potential in a solution of Mn^{2+} and KNO_3 supporting electrolyte. There was a faint linear increase in electrode mass of 0.2 μg over 1800 s. However, upon removal of potential, the electrode mass sharply decreased for an overall net zero change in mass (Figure S12a). As described earlier, application of a short anodic pulse immediately following cathodic deposition results in a rapid change in FTO electrode color from clear to brown. The same procedure, applied here with a 30 s anodic pulse on the QCM electrode, led to immediate darkening of the electrode accompanied by a sharp rise in mass, signifying film deposition (Figure S12b). The magnitude of this mass increase of ~0.7 μg over 30 s is approximately 7× greater than the mass increase of ~0.1 μg for 30 s of constant anodic potential deposition of MnOx.

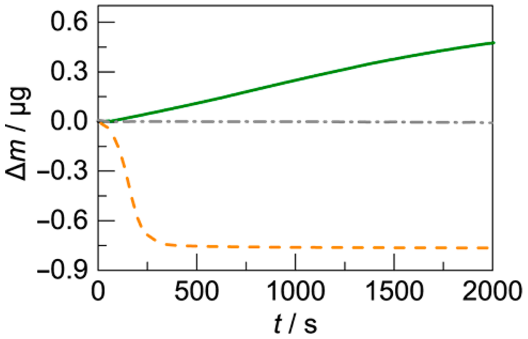

Figure 8. Change in mass as measured by a quartz crystal microbalance on a constant potential deposited MnOx film (of 3 mC/cm^2 loading, ~0.7 μg) cathodized in 0.5 mM Mn^{2+} and 0.9 M KNO_3 solution (green −), Mn^{2+}-free solution of 0.9 M KNO_3 (gray − · −), and 0.5 mM Mn^{2+} and 50 mM MeP_i at pH 8 (orange − − −).

Structural Studies. *SEM and TEM.* MnOx films prepared via different deposition routes have distinct morphologies. By SEM, as-deposited MnOx has pedal-like or plate-like features, while activated MnOx resembles needles or nanorods (Figure 9). TEM images show differences in crystallinity between as-deposited and activated MnOx films (Figure 10). While both samples are nanocrystalline, as-deposited MnOx exhibits coherent crystalline domains of ~8−10 nm, while activated MnOx is considerably disordered: the domain size decreases to ~2−4 nm, and edges of the catalyst become amorphous.

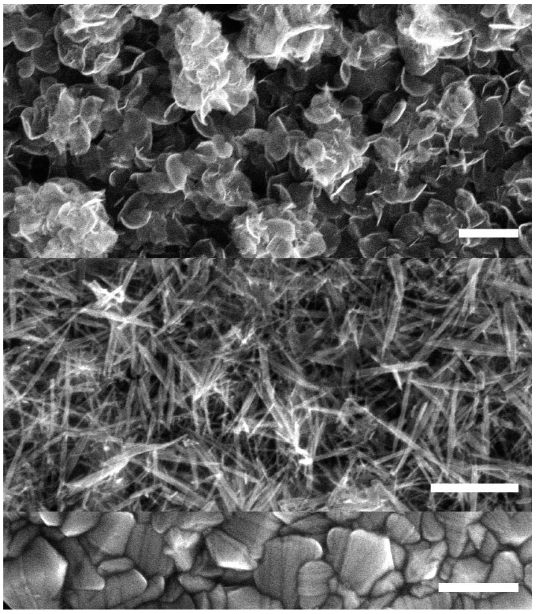

Figure 9. FESEM images of MnOx deposited at constant potential in MeP_i (top) and activated MnOx (middle). Both samples were electrodeposited on FTO substrate (bottom). Scale bars are 400 nm.

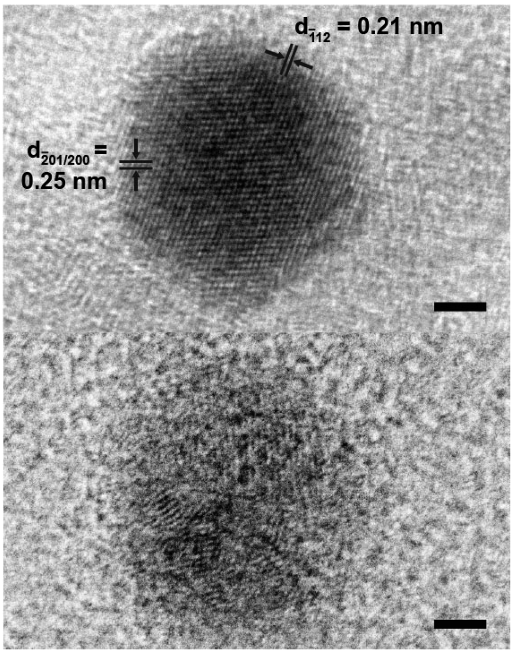

Figure 10. HRTEM images of isolated nanosized domains from MnOx deposited at constant potential (top) and from activated MnOx (bottom). All samples were electrodeposited on carbon film (visible as amorphous background). Scale bar is 2 nm. Interplanar spacing for constant potential MnOx was measured from the FFT and indexed according to birnessite.

X-ray Photoelectron Spectroscopy. XPS was employed for observing changes in the average manganese oxidation state of MnOx samples by monitoring the binding energy shift, satellite peak splitting, and exchange peak splitting for the Mn 2p, 3s, and 3p peaks. These parameters for a series of control manganese oxides ($Mn^{IV}O_2$, $Mn^{III}{}_2O_3$, $Mn^{II,III}{}_3O_4$, and $Mn^{II}O$) are well-documented as diagnostics of the Mn oxidation state,[49,83−92,107] and literature XPS data for manganese oxides have been included in subsequent analysis for comparison.

MnOx samples were prepared with the different electrodeposition protocols on FTO, and manganese oxide control samples were mounted on Cu tape. Survey spectra of all compounds indicated no presence of impurities. High-resolution scans were recorded for the Mn 2p, 3s, and 3p regions (Figure 11 and Figure S13). A reliable diagnostic for Mn oxidation state is the degree of Mn 3s peak splitting that is caused primarily by the exchange interaction between the 3s and 3d electrons.[85,89,93] When applied to control and MnOx samples (Figure 11a and b), as-deposited MnOx is MnO_2-like, which was expected from our previous mechanistic study.[33] However, cathodized MnOx is Mn_2O_3 or Mn_3O_4-like, where the larger Mn 3s peak splitting suggests that there is significant Mn^{3+} in the bulk cathodized film.

For multipotential deposited MnOx, the Mn 3s peak splitting is between that of as-deposited and cathodized MnOx (Figure 11a and b), which indicates that the average Mn oxidation state has increased slightly and is between +3 and +4. This "mixed" $Mn^{3+/4+}$ oxide retains its formal oxidation state even after operation at high anodic potentials for oxygen evolution, which demonstrates that this new phase is stable and does not simply convert slowly back to the as-deposited MnO_2-like film. Similarly, cathodized MnOx films after OER exhibit an oxidation state similar to that of multipotential deposited MnOx films, demonstrating that both methods of activation access the same mixed $Mn^{3+/4+}$ state during oxygen evolution.

Other diagnostics include the Mn $2p_{1/2}$ and 3p binding energies. The $2p_{1/2}$ peak arises from spin−orbit coupling of the 2p electrons, which splits the 2p orbitals into $2p_{1/2}$ and $2p_{3/2}$ energy levels.[85,88,94] Both $2p_{1/2}$ and 3p binding energies increase with higher Mn oxidation state, as observed in control manganese oxide compounds (Figure 11c−f). However, the

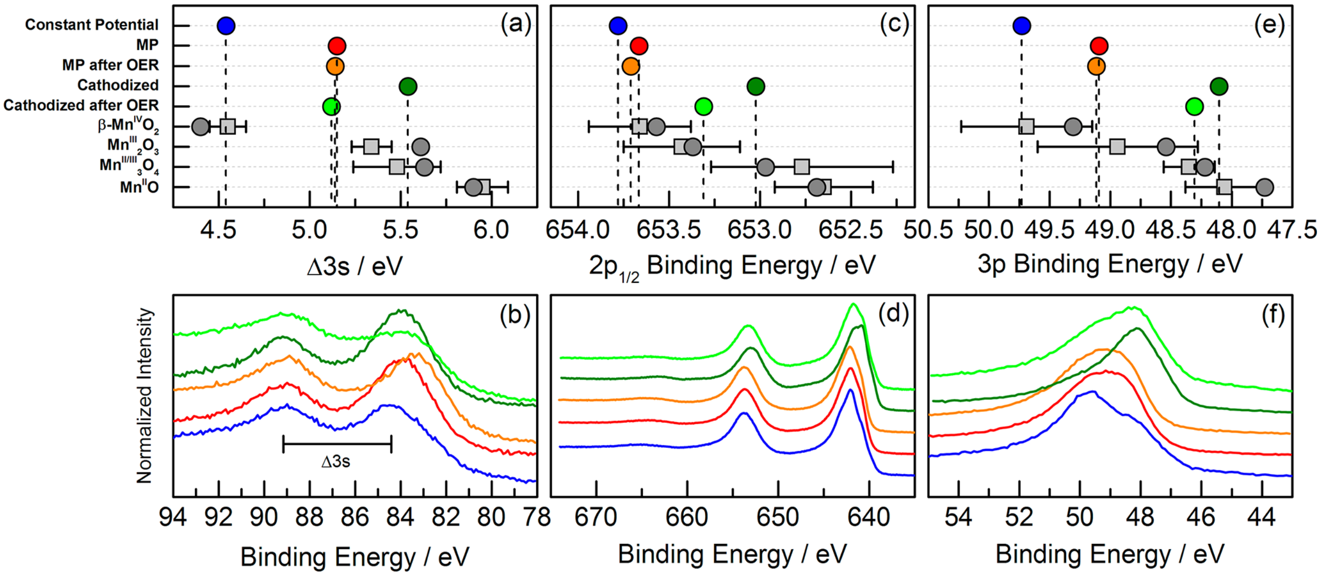

Figure 11. XPS diagnostics for assessing average Mn oxidation state in MnOx films: (a,b) Mn 3s peak splitting width (Δ3s); (c,d) Mn $2p_{1/2}$ binding energy; (e,f) Mn 3p binding energy. High-resolution spectra are shown in the bottom row for MnOx prepared by constant potential (blue ●, −), multipotential (red ●, −), multipotential followed by OER (orange ●, −), cathodization (dark green ●, −), and cathodization followed by OER (light green ●, −). The top row provides a simplified view of the diagnostic parameters extracted from the spectra with comparison to manganese oxide control compounds (gray, darker ● is from this Article; lighter ■ and black bars is compiled from the literature). High-resolution XPS spectra for control compounds are shown in Figure S13.

accuracy of absolute binding energies is affected by surface charging and depends on spectrometer calibration. As a consequence, literature compiled values for the control compounds exhibit wide standard deviations. To increase the accuracy of measured binding energies, the XPS spectrometer was calibrated to Au, Ag, and Cu standards before experiments, and binding energies were corrected via the Cu $2p_{3/2}$ peak for samples on Cu tape or via the C 1s peak for electrodeposited MnOx samples on FTO. Generally, results from binding energy analysis correlate with those from the Mn 3s exchange energy diagnostic: as-deposited MnOx is MnO_2-like, cathodized MnOx contains significant Mn^{3+}, and multipotential deposited as well as cathodized MnOx films after water oxidation have an average oxidation state between +3 and +4. We note that multipotential deposited MnOx retained the same oxidation state before and after OER.

Powder X-ray Diffraction (XRD). Composition and phase identification by XRD were initially applied to thin films of MnOx electrodeposited by different protocols on FTO. In the conventional Bragg−Brentano configuration, however, the observed diffraction patterns were all matched to the underlying FTO substrate (Figure S14). The as-deposited MnOx thin film produced a weak and broad peak at ca. 2θ = 12°, but there were no additional non-FTO features to facilitate a structural search.

To eliminate the intense FTO diffraction peaks, MnOx catalyst films were examined as powders: electrodeposited variants of MnOx films were mechanically separated from the FTO and ground into fine particles. XRD was performed on these samples (Figure 12) as well as a series of manganese oxide control compounds for comparative purposes (Figure S15). All control compounds displayed well-defined diffraction patterns that were phase matched to JCPDS-ICDD entries.

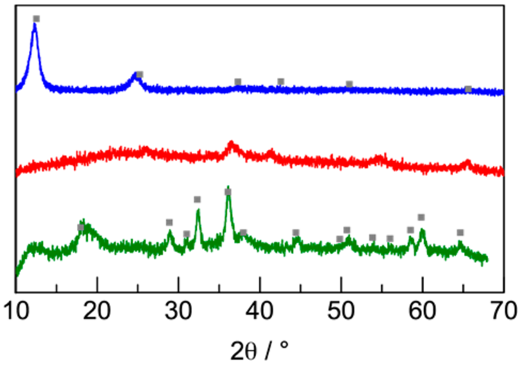

Figure 12. Powder X-ray diffraction patterns of MnOx prepared by constant potential (top blue), cathodization (bottom green), and multipotential (middle red) deposition. Constant potential MnOx (blue) matches birnessite (gray ■, JCPDS no. 01-087-1497), while cathodized samples (green) match hausmannite (gray ■, JCPDS no. 24-0734). Multipotential MnOx (red) was highly disordered, and the phase was undetermined by XRD.

For MnOx samples, as-deposited MnOx exhibited strong diffraction peaks at ca. 2θ = 12° and 25° that were characteristic of birnessite (δ-MnO_2). The diffraction pattern for cathodized MnOx matched hausmannite (α-Mn_3O_4) with three prominent characteristic peaks at ca. 2θ = 29°, 32°, and 37°. In contrast, multipotential deposited MnOx samples exhibited very faint and broad peaks that appeared atop an intense background. The poor crystallinity of multipotential deposited MnOx was insufficient for reliable phase matching using an in-house X-ray source and conventional XRD.

X-ray Pair Distribution Function (PDF). To obtain structural information on low crystallinity MnOx films (in particular, multipotential deposited MnOx), total X-ray scattering (both Bragg and diffuse) from sample powders over a wide range of momentum transfer (Q) was collected using a synchrotron X-ray source. Data were collected to short d-spacings of a few tenths of an angstrom and then Fourier transformed to obtain the probability density of atomic pairs as a function of atomic distance (i.e., the pair distribution function).[70,95,96] Structural analysis was performed by developing a model of the catalyst and then optimizing the model's computed PDF to fit the experimental PDF.[70,95,96]

The domain size or crystallinity of MnOx catalysts was estimated by examining the decay of the PDF plots for control manganese oxides (Figures S16) and MnOx samples prepared by different electrodeposition protocols (Figure 13). The PDF peaks for the control compounds extend beyond the plot cutoff of 40 Å, indicating that the control samples are highly crystalline as anticipated from their sharp XRD patterns (Figure S15). In contrast, the PDF peaks in electrodeposited MnOx samples disappear at lower r values, indicating a smaller structural coherence. Spherical PDF models of multipotential deposited and cathodized MnOx suggest a domain size of ∼30−50 Å for these samples, which is consistent with estimations by TEM.

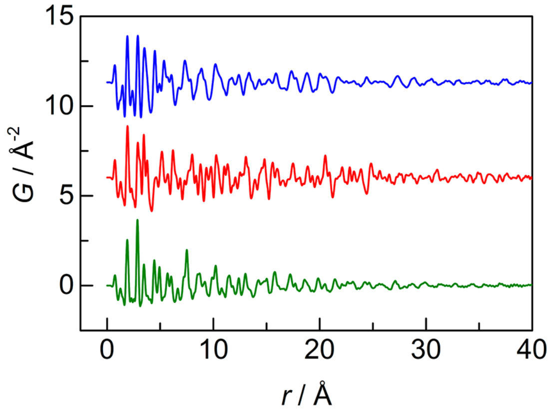

Figure 13. Atomic pair distribution functions (PDFs) of MnOx prepared by different deposition protocols: constant potential (top blue), multipotential (middle red), and cathodization (bottom green). PDFs are truncated at 40 Å. PDFs for manganese oxide control samples are in Figure S16.

The similarity of MnOx samples to control compounds was surveyed by calculating the Pearson's product−moment correlation coefficient R over discrete ranges of atomic distances (Table S2). This parameter indicates the similarity between two PDF data sets and is calculated by

$$R = \frac{1}{n-1}\sum_{i=1}^{n}\left(\frac{X_i - \overline{X}}{\sigma_x}\right)\left(\frac{Y_i - \overline{Y}}{\sigma_y}\right) \tag{4}$$

where $\overline{X}$, σ_x and $\overline{Y}$, σ_y are the mean value and standard deviation for the first and second data sets, respectively.[97,98] The Pearson's coefficient has the value between −1 and 1 where the two bounds indicate complete anticorrelation and correlation, respectively. Consistent with XRD results, as-deposited MnOx exhibits strong similarity to birnessite (R =

0.81−0.92), while cathodized MnOx is best correlated to hausmannite (R = ∼0.80). However, cathodized MnOx is also moderately similar to birnessite (R = 0.60−0.76) and suggests the presence of a mixed phase of hausmannite and birnessite, which was undetected by XRD. Multipotential deposited MnOx largely resembles birnessite, although the correlation diminishes in the intermediate range.

The composition and phases suggested by Pearson's coefficient analysis were employed in structural modeling of the PDF data. Initially, the birnessite structure was adopted for as-deposited and multipotential deposited MnOx, and the hausmannite structure for cathodized MnOx. The PDF fits (Figure 14 with fit results summarized in Table S3) were performed in an r range up to 40 Å that covers local to intermediate structure, and the nanoparticulate nature of the samples was accounted for by a spherical envelope function.

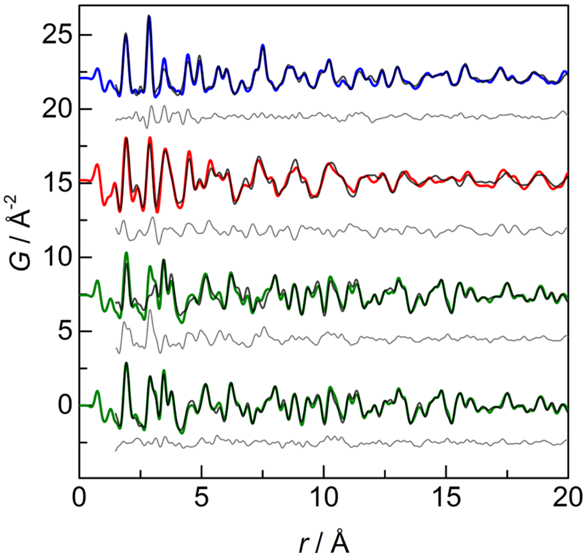

Figure 14. Calculated PDF model fits (black) overlaid on experimental PDF traces of MnOx catalysts prepared by different deposition methods: constant potential (blue), multipotential (red), and cathodization (green). The cathodized sample was fit in two ways: hausmannite structure alone (top green) and a two-phase birnessite and hausmannite fit (bottom green). The difference curves (gray) between the calculated and experimental PDFs are offset below each sample.

For as-deposited MnOx, the best fit was achieved with the birnessite model, whereas the PDF of cathodized MnOx required a two-phase fit of both birnessite and hausmannite (Figure 14). The initial guess for cathodized MnOx consisted of a single hausmannite phase where features in the r range above 10 Å were well-matched according to the difference curve between the experimental and calculated PDF. However, there remained a significant unfit signal in the low r range below 10 Å. According to the Pearson coefficients for cathodized MnOx, the experimental PDF in this short r range had a secondary correlation to birnessite, and thus a two-phase fit was introduced using both hausmannite and birnessite structures. The thermal factors, atomic positions, and occupancies were inherited from previous fits, and only scale factors, lattice parameters, and diameters (i.e., particle sizes) for both phases were tuned. The two-phase model improved the PDF fit for cathodized MnOx and successfully captured previously unfit structural features in the low r range. Structural coherence for the birnessite component exists at short r range, while the hausmannite component is correlated over longer intermediate r range. The mole fraction of birnessite refined from the fit is ∼68%, indicating that the majority of the sample is actually birnessite.

Trial fits of the multipotential deposited MnOx sample were performed against birnessite (δ-MnO_2), pyrolusite (β-MnO_2), akhtenkite (ε-MnO_2), hausmannite (α-Mn_3O_4), bixbyite (α-Mn_2O_3), manganosite (MnO), rancieite ($(Ca,Mn^{2+})Mn_4^{4+}O_9\cdot 3H_2O$), and Mn_5O_8 structures. The birnessite model had the best goodness-of-fit factor with low residuals in the short r range but displayed deviations between the experimental and calculated PDF in the intermediate r range (Figure 14). To account for the unfit signal at higher r, a two-phase fit was introduced with birnessite as the first component and the following candidates as the second phase: bixbyite (α-Mn_2O_3), hausmannite (α-Mn_3O_4), akhtenkite (ε-MnO_2), rancieite ($(Ca,Mn^{2+})Mn_4^{4+}O_9\cdot 3H_2O$), and Mn_5O_8. Both least-squares and differential evolution algorithms were employed to optimize the two-phase fits. However, no improvement to the fit was obtained as compared to a single-phase birnessite model. In addition, changing the shape function of the model from a spherical to a cylindrical envelope results in only a ∼1% improvement to the fit. The poor fit at high r range is not due to the model lacking inclusion of additional phases or an incorrect shape function but likely an inherent structural phenomenon of multipotential deposited MnOx.

■ DISCUSSION

The acid stability of electrodeposited manganese oxide (denoted MnOx) prepared at constant potential is derived from the interplay of deposition[33] and oxygen evolution[34] mechanisms. However, as-deposited MnOx catalysts, although stable in acid, exhibit only modest OER activity at neutral pH (∼120 mV/decade Tafel slope) and low activity (∼650 mV/decade) in acidic conditions.[34] Methods to increase catalyst activity include surface modification (e.g., binding polyallylamines to surface Mn sites[99]) or mixing other metals in the films (e.g., Mn/Fe,[100] Mn/Co,[101] Mn/Co/Fe,[102,103] Mn/Fe/Cr,[100,104] La/Mn,[105,106] La/Sr/Mn,[105,106] etc.). We show here that MnOx activity may be increased by an electrochemically induced phase change. By varying the voltage during electrodeposition, it is possible to access thermodynamically stable manganese oxide phases, as suggested by the Pourbaix diagram of manganese,[25] or trap the film in kinetically stable oxide phases. Polymorphs of chemically prepared manganese oxides containing lower valent Mn ions (such as Mn^{3+} and Mn^{2+}) exhibit greater OER activity than that of MnO_2 oxides,[48] which is the phase produced by constant anodic potential electrodeposition.[34,47,49,107] Similarly, manganese oxide films deposited by cyclic voltammetry[47,49] are more active for OER than those deposited at constant potential. X-ray absorption studies (XANES and EXAFS) on these CV deposited films demonstrate an average Mn oxidation state of +3.6 to +3.8, respectively, instead of the expected +4.0 of $Mn^{IV}O_2$ (i.e., pyrolusite).[47,49] In addition, powder X-ray diffraction on CV deposited film indicates the presence of α-Mn_2O_3.[49] These observations suggest that CV deposition may be a method for accessing different phases of manganese oxides. With this backdrop in mind, we explored other techniques for creating active electrodeposited manganese oxides and simplified the processes down to the essential steps required for activation.

Spectroscopic and structural analysis then guided our mechanistic proposal for the activation process.

Electrochemical Activation of MnOx. Tafel slopes for the OER differentiate between "non-activated" and "activated" MnOx films. Tafel slopes, as opposed to current densities, offer a more reliable method to compare catalyst films prepared by different electrodeposition protocols because it is difficult to correctly normalize current by the number of active sites in the electrodeposited material.[108] For example, the rate and amount of catalyst deposited vary between methods of preparation. Unlike in constant potential electrodeposition where the charge passed could be directly correlated with catalyst loading, these deposition protocols alternate between anodic and cathodic currents, and thus the total charge passed is in constant flux. By using a QCM, the deposition protocols were adjusted such that catalyst films had similar mass loadings. However, even then, the number of active sites in films of the same mass may differ because of changes in film structure or exposed surface area. Obtaining accurate surface area measurements of thin films is challenging, but the more fundamental issue is that the number of true active sites in a catalyst may be a fraction of its accessible surface area. For example, there are different catalyst regions: planes, edges, grain boundaries, and amorphous domains. Each region may have different manganese oxidation states and oxidic environments with one region containing the dominant "active sites", and it is still an open problem in the field to accurately quantify the number of active sites in catalyst films.

For a Tafel plot, increasing the number of active sites will raise the exchange current density (i.e., the *y*-intercept), which leads to shifting of the plot to higher activities. However, the Tafel slope will still remain the same, because it is only affected by the kinetics of the reaction (assuming that the data were collected in conditions of kinetic control), which involves the type of active site and not its quantity.[78] Thus, instead of emphasizing absolute activity in terms of current density normalized by mass or surface area, we compare the performance of MnOx catalysts by their Tafel slopes for OER, which does not depend on the quantity of active sites in the films.

The representative cases for describing "non-activated" and "activated" MnOx films are constant potential (denoted "as-deposited") and CV deposition, respectively. As-deposited MnOx establishes the baseline case that we sought to improve upon; these films are deposited in MeP$_i$ buffer at pH 8.0 and exhibit a ∼123 mV/decade slope at neutral pH (Figure 2).[34] They can also be formed in the absence of a buffer, but the resulting films are even less active with higher Tafel slopes. In contrast, CV deposited films are more active for the OER with Tafel slopes of ∼68 mV/decade at pH 7.0 (Figure 2 and consistent with values reported in literature).[47,49] For similar mass loading and geometric area, at an overpotential of 450 mV, CV deposited MnOx displays 10 and 100 times greater current density than MnOx deposited at constant potential from MeP$_i$ and without buffer, respectively. Thus, CV deposited films represent the benchmark for "activated" MnOx and serve as a reference point for comparison to other electrodeposition methods.

CV deposition was simplified by removing slow potential sweeping and by focusing instead on short anodic and cathodic pulses at fixed potentials. In the multipotential method, MnOx is deposited by alternating between two potentials continuously (see schematic in Figure 4) and results in an active MnOx film with a Tafel slope of ∼67 mV/decade at neutral pH (Figure 2). More fundamentally, a MnOx film can be deposited at an anodic potential and then subjected to a cathodic pulse. This procedure is called cathodization and also produces activated MnOx films with low Tafel slopes of ∼70 mV/decade (Figure 2). These results demonstrate that we can take a pre-existing MnOx film (deposited at constant potential) that has modest activity, apply a simple cathodic procedure (e.g., cathodization), and significantly increase the OER activity of the catalyst.

By simplifying CV deposition to cathodization, we observe that the use of a cathodic pulse is crucial for producing activated MnOx films. Cathodic deposition is prevalent for some materials including Mn,[109−112] Co,[113−117] and Ni[118−121] oxide films and even metal organic frameworks[122] deposited at negative potentials. In these cases, supporting electrolyte (such as NO_3^-) is reduced at the electrode surface leading to the generation of hydroxide species.[123] Hydroxide anions react with metal cations to precipitate an oxidic film. However, in practice, MnOx does not deposit well at cathodic potentials: the FTO electrode remained transparent when held at negative potentials. QCM studies demonstrate that there is a slight increase in electrode mass during deposition but that this species is poorly adhesive and desorbs back into solution when the electrode is at open circuit (Figure S12a). Tafel plots of these films (before complete mass loss) exhibit poor slopes (∼221 mV/decade, Figure 6) that resemble unactivated MnOx deposited at constant anodic potential from nonbuffering electrolyte. The lack of significant film formation and the decrease in electrode mass upon removal of applied potential are attributed to poorly adhesive $Mn(OH)_2$ species, generated by the reaction of Mn^{2+} with OH^- produced near the electrode.[25] To stabilize the film, a short anodic pulse was introduced immediately after cathodic deposition to convert the film into a more adhesive manganese oxide. This additional step tested if anodic conditioning of cathodically deposited MnOx resulted in active films and is conceptually similar to multipotential deposition where cathodic pulses are followed by anodic pulses in a repeating cycle. Indeed, as observed by QCM, application of a short 30 s anodic pulse to the cathodically deposited film resulted in a sharp mass increase (Figure S12b), and the resulting brown film was resistant to rinsing. However, the Tafel slope of these films was ∼126 mV/decade (Figure 6), which is similar to inactive as-deposited MnOx. Therefore, cathodic deposition is not responsible for activation of MnOx films.

Alternatively, we find that a cathodic pulse applied to as-deposited MnOx causes an irreversible phase change. Precedent for this process comes from the Pourbaix diagram[25] of manganese and also in the supercapacitor literature: MnO_2 supercapacitors normally exhibit reversible conversion between MnO_2 and MnOOH during charging and discharging, but if the potential range of cycling is extended cathodically, there is an irreversible compositional change from MnO_2 to a Mn_2O_3, which destroys the capacitor.[124,125] Our studies also point to a cathodically induced phase change but triggered by a chemical reaction between manganese in solution and on the electrode. Evidence for this process comes from the observation that inactive films (∼300 mV/decade, Figure 5) are obtained when as-deposited MnOx films are cathodized in a solution containing just KNO_3 supporting electrolyte. Thus, activation of as-deposited MnOx film does not occur in Mn^{2+}-free solution, suggesting that the presence of Mn^{2+} during the cathodic pulse is a crucial ingredient. Given that activation requires both Mn^{2+} in solution and a pre-existing MnOx film on the electrode, our results are in line with the well-known comproportionation reaction between Mn^{4+} and Mn^{2+} to yield Mn^{3+}:[54,126−128]

$$\delta\text{-}Mn^{IV}O_2 + 2Mn^{II}(OH)_2 \rightarrow \alpha\text{-}Mn_3{}^{II,III}O_4 + 2H_2O \quad (5)$$

The presence of δ-MnO_2 (birnessite) as the reactant and α-Mn_3O_4 (hausmannite) as the product is supported by structural studies (vide infra). Birnessite is a layered structure consisting of edge-sharing MnO_6 octahedra with water and K^+ ions intercalated between the layers (Figure 15). The hausmannite structure is of spinel type that contains corner-sharing MnO_4 tetrahedrons and edge-sharing MnO_6 octahedra where Mn^{2+} and Mn^{3+} ions reside in the former and the latter, respectively (Figure 15). The contention that hausmannite is a more active phase of manganese oxide for OER is consistent with previous proposals that hausmannite and bixbyite (both containing significant fraction of Mn^{3+}) are the most active polymorphs of manganese oxides.[48] Indeed, we find that our activated MnOx films contain greater Mn^{3+} valency than that of as-deposited MnOx films (Figure 11). For our case, hausmannite is the predominant material as neither XRD nor PDF could determine the presence of α-Mn_2O_3 (bixbyite) in cathodized films (vide infra).

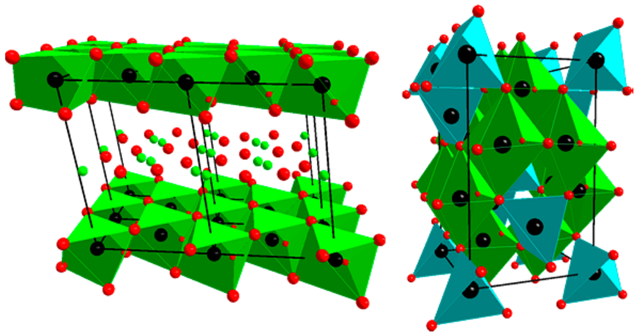

Figure 15. Polyhedral structural models for birnessite (δ-MnO_2, left) and hausmannite (α-Mn_3O_4, right) where Mn, O, and K atoms are in black, red, and green, respectively. In hausmannite, green and blue regions represent the MnO_6 octahedron and MnO_4 tetrahedron, respectively.

The Mn^{4+}/Mn^{2+} comproportionation reaction is accelerated in the presence of base and is consistent with the local alkaline pH gradient formed by the generation of OH^- during the reduction of nitrate. Indeed, when the mass of the electrode is monitored during the cathodization activation process, the mass increases during the cathodic pulse, signifying the deposition of additional material (Figure 8). In contrast, when cathodization of a pre-existing MnOx film is performed in Mn^{2+}-free solution, no mass change is observed, and the resulting film is not active (Figure 8). In addition, suppression of OH^- generation in well-buffered Mn^{2+} solutions such as MeP_i at pH 8 causes complete film loss (Figure 8) as the MnOx film in the absence of base can be fully reduced to soluble Mn^{2+}. As expected, films cathodized in MeP_i buffer display no increase in OER activity, as demonstrated by its high Tafel slopes for OER (~323 mV/decade, Figure 5). Although Wiechen et al. observe a dependence of the cation type in birnessite on OER activity,[129] the identity of the supporting electrolyte cation during deposition does not seem to affect activation in this study because CV deposition in Mn^{2+} solution without any supporting electrolyte still results in active films (Figure S1) as long as OH^- is generated (i.e., in this case, through hydrogen evolution). These control experiments establish that a crucial step in activation is a phase change triggered by the comproportionation of a pre-existing constant anodic potential deposited MnOx film with cathodically generated solution-phase $Mn(OH)_2$.

Nature of Activated MnOx. The phase change of MnOx during activation is qualitatively suggested by SEM, where MnOx films prepared via different deposition routes had different morphologies (Figure 9): as-deposited MnOx features plates or pedals, while activated MnOx resembles needles or nanorods. Similar morphologies have been observed for different manganese oxide compositions and polymorphs.[52,130−133] XPS was used to monitor the change in average Mn oxidation state in the films as a function of deposition method. Because XPS is a surface-confined technique, it is well suited for studying thin films. Using the Mn 3s peak splitting distance as the primary diagnostic for comparing electrodeposited films to control compounds, results from XPS were consistent with a birnessite-like phase for as-deposited MnOx and a hausmannite-like phase for cathodized MnOx (Figure 11), which support the comproportionation mechanism shown in eq 5. Notwithstanding, the limitations of using XPS for manganese oxide films have been emphasized;[49,107] the diagnostics for Mn_2O_3 and Mn_3O_4 are too similar to resolve with XPS. In addition, although it is possible to extract information about the chemical environment by XPS and thus further probe the phase of the film, in practice, the limitations of in-house X-ray sources lead to broad peaks; obtaining structural information required extensive peak fitting, which is complex for the Mn $2p_{3/2}$ peak.[92,88]

Direct structural information was obtained from X-ray diffraction. Diffraction off of MnOx thin films revealed only substrate peaks, suggesting that the catalyst films were poorly crystalline. Indeed, TEM images show domain sizes of ~8−10 nm for as-deposited MnOx and ~2−4 nm for activated MnOx (Figure 10). This nanocrystalline nature of MnOx significantly broadens any diffraction peak,[134] and given the low intensity of these peaks, the diffraction patterns were buried in the FTO substrate background (Figure S14). Weak signal intensity was exacerbated by the use of conventional Bragg−Brentano XRD, which is not well suited for thin-films because the micrometer penetration depth of X-rays in this configuration largely samples the underlying substrate and not the thin film. Moreover, thin films comprise a small amount of catalyst material over a wide area, which further reduces signal intensity. Grazing incidence XRD (recently employed for our CoP_i films on FTO[135]) and in-plane XRD can overcome these challenges;[136] however, for the studies reported herein, we found that the most direct solution was to separate catalyst films from the FTO and prepare the material as a powder for study with conventional Bragg−Brentano diffraction. XRD patterns of these catalyst powders obtained from as-deposited and cathodized MnOx match birnessite and hausmannite, respectively (Figure 12). These results further support MnOx activation by the comproportionation chemistry of eq 5.

Whereas the hausmannite phase is produced upon activation of MnOx films by eq 5, it is not preserved during OER. XPS spectra comparing the Mn 3s peak splitting in cathodized MnOx before and after OER demonstrate that the average oxidation state of Mn in these films increases with application of the higher anodic potentials required for oxygen evolution (Figure 11). The final state of cathodized films after OER is similar to that of multipotential deposited films. This result suggests that these films have converged to a similar active phase. Indeed, multipotential deposited MnOx may be viewed as cathodized films that have been subjected to additional anodic pulses (see schematic in Figure 4). This explains why both cathodized and multipotential deposited MnOx have similar Tafel slopes for OER (Figure 2).

To delve more deeply into defining the structure−activity relationship of these films, we employed pair distribution function (PDF) analysis of X-ray diffraction data, which describes the probability density of finding an atomic pair separated by a given distance. We and others have found PDF to be a powerful technique for studying electrodeposited materials that are amorphous.[137,138] Whereas XRD only uses the Bragg diffraction signal, PDF records the total X-ray scattering (both Bragg and diffuse). The technique is superior for multipotential deposited MnOx, because the material exhibits poor Bragg diffraction but strong diffuse scattering (which manifests as a broad background signal) in XRD diffraction patterns. Thus, PDF can elucidate the structure of disordered materials in cases where XRD cannot. First, the PDFs of as-deposited and cathodized MnOx were compared to the structural models determined by XRD. As expected for as-deposited MnOx, the birnessite model provides a good fit to PDF data, capturing all of the main structural features of the sample as demonstrated by deconstructing its PDF into component atomic pairs (Figure 16). Similarly, the initial fit of cathodized MnOx to a hausmannite model reproduced the primary structural components in the PDF (Figure 17), particularly in the intermediate *r* range above ~10 Å. However, the single phase fit was insufficient for fully describing the local *r* range (below ~10 Å) and required adding a secondary phase of birnessite in the model (Figure 14). The final fit comprising birnessite in the short-range and hausmannite in the intermediate range suggests that the cathodization procedure only converts the outer layers of unactivated MnOx domains (which have the birnessite phase) to hausmannite. This is consistent with the proposed mechanism of eq 5 where activation of MnOx involves a phase conversion induced by the comproportionation of birnessite with $Mn(OH)_2$, generated in solution, to produce hausmannite. This reaction occurs at the catalyst−solution interface, which is self-limiting and prevents full transformation of the catalyst domains to hausmannite.

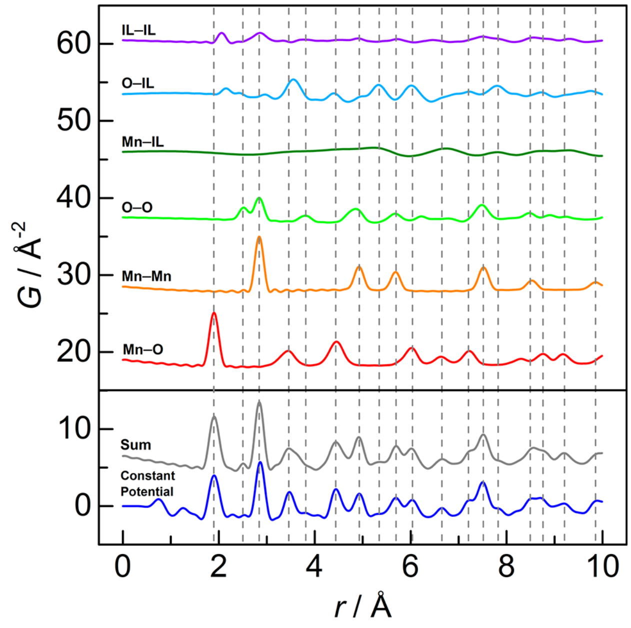

Figure 16. Decomposition of the PDF of the calculated birnessite fit (bottom gray) into contributions from primary atomic pairs where IL denotes interlayer species including K and O (from H_2O) atoms (see Figure 15a for 3D model). The intensity of the top four curves (IL−IL, O−IL, Mn−IL, and O−O) has been magnified 2× for clarity. The experimental PDF for constant potential deposited MnOx is provided for comparison (bottom blue).

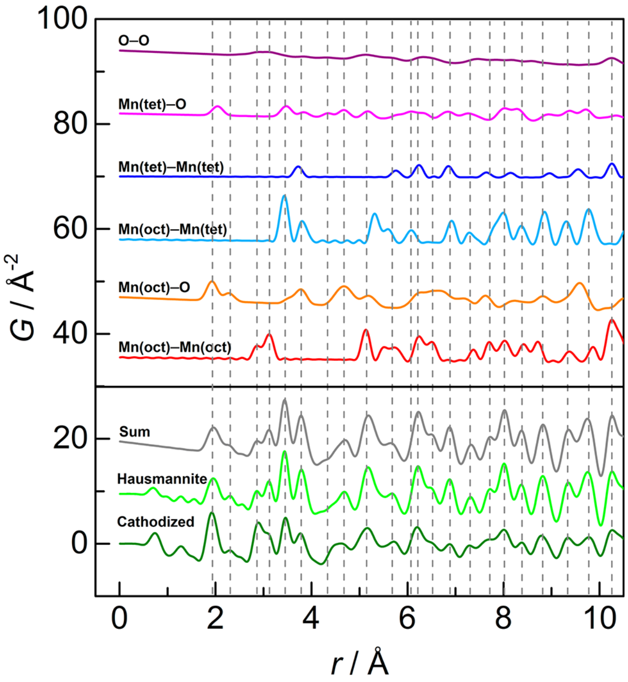

Figure 17. Decomposition of the PDF of the calculated hausmannite fit (bottom gray) into contributions from primary atomic pairs where Mn(oct) and Mn(tet) refer to a Mn atom in octahedral and tetrahedral geometry, respectively (see Figure 15b for 3D model). The experimental PDFs for α-Mn_3O_4 (hausmannite, bottom light green) and cathodized MnOx (bottom dark green) are provided for comparison.

Whereas XRD could not resolve the phase of multipotential deposited MnOx, PDF analysis revealed that the films are birnessite-like. A single phase structural model of birnessite produced low residuals in the PDF fit at low *r* range, although there were slight mismatches between the calculated and experimental PDFs at higher *r* values (Figure 14). Other single phase fits with pyrolusite (β-MnO_2), akhtenkite (ε-MnO_2), hausmannite (α-Mn_3O_4), bixbyite (α-Mn_2O_3), manganosite (MnO), rancieite ($(Ca,Mn^{2+})Mn_4^{4+}O_9\cdot 3H_2O$), and Mn_5O_8 structures resulted in poor goodness-of-fit factors. These candidate structures were selected from active manganese oxide phases for OER reported in recent literature.[48,49,54,139] For example, the Mn_5O_8 phase seemed promising because it is a metastable phase of manganese oxide that is active for OER[140] and exhibits structural similarities with birnessite since it is comprised of sheets of edge-sharing Mn^{4+} octahedra but with Mn^{2+} between the layers. Unfortunately, PDF does not support the fit of Mn_5O_8 to activated MnOx with predicted particle sizes that are too small and poor intermediate-range agreement to activated MnOx.

Introducing a two-phase model (by varying the second phase among a number of manganese oxide polymorphs including hausmannite and bixbyite) along with a more robust optimizer algorithm did not improve the fit residuals either. Typically, the possibility of a second phase manifests as extra unfit signal in the low *r* range (such as with cathodized MnOx), because this region describes the local coordination environments of Mn and O, which would significantly differ between phases. In contrast, deviations in the model fit in the high *r* region are often associated with an inaccurate shape function or with the incorrect assumption that the model is composed of repeating structural units. For all MnOx samples, a spherical shape function was employed to model the nanoparticulate nature of the catalyst domains, and changing the shape function to cylindrical resulted in only a negligible improvement to the fit.

Instead, the PDF of multipotential deposited MnOx was consistent with a single birnessite phase in "turbostratic disorder". This effect is commonly observed in layered materials,[140−143] such as in poorly crystalline manganese oxides including birnessite,[74,142−144] where each layer rotates or shifts relative to the adjacent one. This effect causes atomic pair distances between layers to vary, which results in the appearance of additional PDF peaks at higher *r* values. The increased disorder in multipotential deposited MnOx disrupts Bragg diffraction and explains why the XRD pattern of the sample lacks notable peaks. The $2\theta = \sim 12°$ peak of birnessite, which is very prominent in as-deposited MnOx (Figure 12), corresponds to a *d*-spacing of ~7 Å based on the Bragg equation. This value agrees with the *c*-lattice parameter of the birnessite structure (i.e., the interlayer spacing). The complete loss of this peak in the XRD pattern of multipotential deposited MnOx is due to turbostratic disorder that causes the layers in birnessite to be poorly stacked.

These structural studies support a model where activated MnOx is comprised of disordered birnessite, formed by a cycle of phase conversions from ordered birnessite to hausmannite and back to disordered birnessite (Figure 18). Nanosized domains of birnessite (formed at anodic potentials) are partially converted to hausmannite at the catalyst surface by comproportionation with $Mn(OH)_2$ in solution (generated at cathodic potentials). We propose that the hausmannite layer is then transformed to turbostratic-disordered birnessite when the catalyst domains are subjected to an anodic pulse from potential cycling deposition protocols or from oxygen evolution. This disordered birnessite phase is unique in that, unlike the original ordered birnessite phase, it is more active for OER in neutral and acidic solutions.

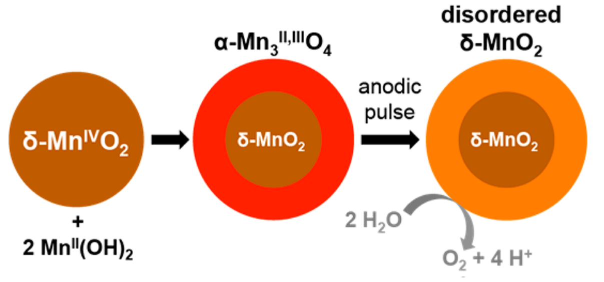

Figure 18. Schematic for the structure of nanosized MnOx domains during activation. First, birnessite (δ-MnO_2, from constant potential deposition) undergoes surface comproportionation with $Mn^{II}(OH)_2$, formed by cathodization. The resulting hausmannite (α-$Mn_3^{II,III}O_4$) then converts to disordered birnessite upon anodic conditioning (from either voltage cycling protocols or during oxygen evolution). This disordered birnessite layer is more active toward OER than the original birnessite phase.

Although redox-state cycling may improve transport properties in catalyst films,[144] the lower Tafel slopes of the disordered birnessite phase are consistent with more facile OER kinetics at active sites rather than better hole and proton transport between the electrode and active sites. Modeling transport throughout the bulk film as a series of self-exchange reactions between metal centers,[145] if the self-exchange process was turnover limiting during OER, then any film growth beyond a single monolayer should not result in additional activity. In contrast, the OER activity of MnOx increases with thicker films,[34] and no curvature of the Tafel plot to higher slopes (a possible indicator of transport limitations) is observed for activated MnOx. Similarly, the MnOx films prepared in this study were thin (estimated <50 nm by SEM), and so even assuming a worst-case resistivity for the films (e.g., 1 MΩ cm) results in through-film resistances (e.g., ~5 Ω) less than solution resistance (i.e., ~17 Ω). Tafel plots were recorded at low current densities (<1 mA/cm^2) to minimize the effect of any uncompensated resistance, which was negligible given the linearity of all Tafel plots; otherwise, significant curvature would be observed. Indeed, electrochemical impedance spectroscopy measurements comparing a blank FTO substrate to MnOx films electrodeposited on FTO estimate a negligible ~0.4 Ω of resistance through both as-deposited and activated MnOx. These control experiments further support that the lower Tafel slopes of activated MnOx are the result of improved OER kinetics.

The introduction of disordered birnessite explains why crystalline birnessite formed from chemical synthesis and annealing appears less active than birnessite prepared without annealing[43,48,54] or electrodeposited from CV cycling.[47,107] In addition, our results suggest that when lower valent manganese oxides (such as hausmannite or bixbyite) undergo OER, the samples begins to become amorphous and change into disordered birnessite, which is the actual species performing OER. Similar amorphization of crystalline MnO particles to an OER active birnessite-like phase by using a Ce^{IV} oxidant has been reported by Driess et al.[146,147] In general, many crystalline materials become disordered under anodic conditioning, with recent examples including $LiCoPO_4$,[148] Ba/Sr/Co/Fe perovskites,[149] and Co/Mn double layered hydroxides.[101]

An additional aspect of disordered birnessite is that the average Mn oxidation state is slightly lower than that of the original birnessite phase. XPS suggests that disordered birnessite contains a mixture of Mn^{4+} and Mn^{3+} valency in activated MnOx (Figure 11). X-ray absorption spectroscopy and other XPS studies on similar CV deposited manganese oxide films estimate an average oxidation state of +3.6−3.8, which is consistent with the presence of Mn^{3+}.[47,49,107] These Mn^{3+} sites are likely introduced when hausmannite is imperfectly converted to disordered birnessite. The large structural change when transforming from a spinel to a layered material is kinetically sluggish and may result in imperfections that trap Mn^{3+} species,[150] which logically comprise the resting state of highly active sites for oxygen evolution. The high spin electron configuration of Mn^{3+} is ideal for promoting fast self-exchange and labile Mn−O bonds.[34] Weakening of the metal−oxo bond can enhance OER kinetics yet retain structural stability because these Mn^{3+} sites are embedded in a robust oxidic Mn^{4+} matrix.

Performance of Activated MnOx in Acid. Activated MnOx has a Tafel slope of ~91 mV/decade in P_i buffer at pH 2.5 (Figure 3) and represents a significant improvement over as-deposited MnOx, which exhibits a Tafel slope of ~650 mV/decade in the same conditions. At an overpotential of ~600 mV, activated MnOx is 2 orders of magnitude more active for OER than as-deposited MnOx, and this gap will further increase as the films are operated at higher overpotential. In addition, activated MnOx is stable in acid where films sustaining oxygen evolution in P_i at pH 2.5 and sulfuric acid at pH 0.3 maintained low overpotentials (η = ~540 mV at 0.1 mA/cm^2) over 8 h of operation (Figure S4). For comparison, at pH 2.5, unactivated MnOx and FTO require overpotentials of ~990 and ~1250 mV, respectively. In addition, activated MnOx requires only 237 mV higher potential than IrOx (at similar mass loading) to operate at 0.1 mA/cm^2 in pH 2.5 (Figure S4). These results demonstrate that activated MnOx can achieve high OER activities while retaining the acid stability of as-deposited films.

However, an inherent limitation of manganese oxide films is the phase change from MnO_2 to MnO_4^- (permanganate) that occurs at high anodic potentials and leads to dissolution of the catalyst. The potential−pH dependence of this phase conversion is governed by the Pourbaix diagram of manganese oxide.[25] In practice, there is an additional overpotential for this process due to the kinetic barrier for the $3e^-/4H^+$ MnO_2/MnO_4^- transformation. The transition between OER on MnOx and permanganate formation manifests as a distinct mechanistic change in the Tafel slope. For example, at pH 2.5, the Tafel slope decreases from ~650 mV/decade (for as-deposited MnOx) to ~130 mV/decade above 1.67 V (Figure S17). Thus, all Tafel plots and stability tests in this Article were recorded at potentials with no permanganate formation. Consequently, to achieve higher current densities while maintaining long-term stability, the operating potential should be restricted while catalyst loading and electrode surface area are optimized. As a proof of concept demonstration, activated MnOx was electrodeposited on a carbon cloth substrate (with ~14 times the electrochemical surface area of FTO) to achieve stable 1 mA/cm^2 operation while remaining below potentials that form permanganate (Figure S4d). Use of highly porous electrodes with a 10−100-fold increase in surface area over planar FTO may enable activated MnOx to operate at 1−10 mA/cm^2 while retaining stability in acid, which is a target for practical applications.

CONCLUSION

The oxygen evolution activity of electrodeposited MnOx films can be increased by changing the deposition protocol from a constant anodic potential to a voltage cycling routine (alternating between positive and negative potentials). Activated MnOx has a considerably lower Tafel slope at pH 7.0 (~70 mV/decade vs ~120 mV/decade of as-deposited MnOx) and pH 2.5 (~90 mV/decade vs ~650 mV/decade of as-deposited MnOx). These lower Tafel slopes result in at least an order of magnitude increase in current density over unactivated MnOx at higher OER overpotentials, particularly in acidic solutions. The nature of the activated MnOx, as defined by the results combined from electrochemical, spectroscopic, and structural techniques, supports a comproportionation-driven phase change of the original birnessite-like phase to an intermediate hausmannite-like phase during cathodic pulse sequences before transforming into a disordered birnessite phase during oxygen evolution. These results explain why different manganese oxide systems in the literature have disparate OER activity profiles, because the preparation method of the films likely introduces different oxide compositions, polymorphs, and degrees of crystallinity that affect their performance. These factors influence the catalyst's mesoscale structure, which significantly impacts their reactivity, and should be considered when designing future systems for catalysis. The performance of activated MnOx provides an inroad to developing alternatives for the best acidic OER catalysts, Ru and Ir oxides, with the benefit that MnOx avoids the use of critical elements for OER.

ASSOCIATED CONTENT

Ⓢ Supporting Information

The Supporting Information is available free of charge on the ACS Publications website at DOI: 10.1021/jacs.5b06382.

> Figure S1, CV and Tafel plot (OER) of MnOx deposited by CV without buffer; Figure S2, Tafel plots (OER) of MP deposited MnOx, varying cathodic *E*; Figure S3, Faradaic efficiency of OER on activated MnOx by O_2 sensor; Figure S4, OER stability of activated MnOx at pH 7.0, 2.5, and 0.3; Figure S5, Tafel plots of OER on activated MnOx before and after stability test; Figure S6, electrochemical surface area measurements of FTO and C cloth; Figure S7, electrochemical impedance spectroscopy of MnOx films; Figure S8, CV−QCM *i*−*t* plot of MnOx deposition in Mn^{2+} solution with KNO_3; Figure S9, QCM plot of multipotential deposition of activated MnOx; Figure S10, CV−QCM plot in Mn^{2+}-free KNO_3 solution; Figure S11, CV−QCM plot in Mn^{2+} buffered by MeP_i at pH 8.0; Figure S12, QCM plot of cathodic deposition at −0.4 V and with anodic pulse; Figure S13, high-resolution XPS of manganese oxide control compounds; Figure S14, PXRD patterns of MnOx thin films; Figure S15, PXRD patterns of manganese oxide control compounds; Figure S16, PDF of manganese oxide control compounds; Figure S17, Tafel plot of as-deposited MnOx showing MnO_4^- region at high *E*; Table S1, fitting parameters for electrochemical impedance spectroscopy; Table S2, Pearson's coefficients of PDF pairs between MnOx and control samples; and Table S3, summary of PDF fitting results for MnOx samples and control samples (PDF)

AUTHOR INFORMATION

Corresponding Author

*dnocera@fas.harvard.edu

Notes

The authors declare no competing financial interest.

ACKNOWLEDGMENTS

We thank Shao-Liang Zheng and Miller Li for assistance in powder X-ray diffraction, Thomas J. Kempa for help with TEM imaging, and D. Kwabena Bediako, Andrew M. Ullman, and Chong Liu for helpful discussions. This material is based upon work supported by the U.S. Department of Energy Office of Science, Office of Basic Energy Sciences under Award number DE-SC0009565 (D.G.N.). SEM, TEM, and XPS were performed at Harvard University's Center for Nanoscale

Systems (CNS), a member of the National Nanotechnology Infrastructure Network (NNIN), which is supported by the National Science Foundation under ECS-0335765. X-ray PDF studies were supported by the Columbia University Energy Frontier Research Center funded by the U.S. Department of Energy, Basic Energy Sciences, under Grant no. DE-SC0001085 (S.J.L.B.) and the U.S. Department of Energy Office of Science, Office of Basic Energy Sciences Energy Frontier Research Center, Center for Next Generation of Materials by Design, Award number DE-AC36-086028308 (D.G.N.). NSLS is supported by the U.S. Department of Energy, Basic Energy Sciences (DOE-BES) under grant DE-AC02-98CH10886.

■ REFERENCES

(1) Hoffert, M. I.; Caldeira, K.; Jain, A. K.; Haites, E. F.; Harvey, L. D. D.; Potter, S. D.; Schlesinger, M. E.; Schneider, S. H.; Watts, R. G.; Wigley, T. M. L.; Wuebbles, D. J. *Nature* **1998**, *395*, 881−884.

(2) Nocera, D. G. *Energy Environ. Sci.* **2010**, *3*, 993−995.

(3) Abbott, D. *Proc. IEEE* **2010**, *98*, 42−66.

(4) Chu, S.; Majumdar, A. *Nature* **2012**, *488*, 294−303.

(5) Lewis, N. S.; Nocera, D. G. *Proc. Natl. Acad. Sci. U. S. A.* **2006**, *103*, 15729−15735.

(6) Cook, T. R.; Dogutan, D. K.; Reece, S. Y.; Surendranath, Y.; Teets, T. S.; Nocera, D. G. *Chem. Rev.* **2010**, *110*, 6474−6502.

(7) Bard, A. J.; Fox, M. A. *Acc. Chem. Res.* **1995**, *28*, 141−145.

(8) Liu, F.; Concepcion, J. J.; Jurss, J. W.; Cardolaccia, T.; Templeton, J. L.; Meyer, T. J. *Inorg. Chem.* **2008**, *47*, 1727−1752.

(9) Nocera, D. G. *Inorg. Chem.* **2009**, *48*, 10001−10017.

(10) Barber, J. *Chem. Soc. Rev.* **2009**, *38*, 185−196.

(11) Pijpers, J. J. H.; Winkler, M. T.; Surendranath, Y.; Buonassisi, T.; Nocera, D. G. *Proc. Natl. Acad. Sci. U. S. A.* **2011**, *108*, 10056−10061.

(12) Young, E. R.; Costi, R.; Nocera, D. G.; Bulović, V. *Energy Environ. Sci.* **2011**, *4*, 2058−2061.

(13) Cox, C. R.; Winkler, M. T.; Pijpers, J. J. H.; Buonassisi, T.; Nocera, D. G. *Energy Environ. Sci.* **2013**, *6*, 532−538.

(14) Reece, S. Y.; Hamel, J. A.; Sung, K.; Jarvi, T. D.; Esswein, A. J.; Pijpers, J. J. H.; Nocera, D. G. *Science* **2011**, *334*, 645−648.

(15) Nocera, D. G. *Acc. Chem. Res.* **2012**, *45*, 767−776.

(16) Winkler, M. T.; Cox, C. R.; Nocera, D. G.; Buonassisi, T. *Proc. Natl. Acad. Sci. U. S. A.* **2013**, *110*, E1076−E1082.

(17) Cox, C. R.; Lee, J. Z.; Nocera, D. G.; Buonassisi, T. *Proc. Natl. Acad. Sci. U. S. A.* **2014**, *111*, 14057−14061.

(18) Cristino, V.; Berardi, S.; Caramori, S.; Argazzi, R.; Carli, S.; Meda, L.; Tacca, A.; Bignozzi, C. A. *Phys. Chem. Chem. Phys.* **2013**, *15*, 13083−13092.

(19) Hu, S.; Shaner, M. R.; Beardslee, J. A.; Lichterman, M.; Brunschwig, B. S.; Lewis, N. S. *Science* **2014**, *344*, 1005−1009.

(20) Chen, Y. W.; Prange, P. D.; Dühnen, S.; Park, Y.; Gunji, M.; Chidsey, C. E. D.; McIntyre, P. C. *Nat. Mater.* **2011**, *10*, 539−544.

(21) Surendranath, Y.; Bediako, D. K.; Nocera, D. G. *Proc. Natl. Acad. Sci. U. S. A.* **2012**, *109*, 15617−15621.

(22) Sun, K.; Saadi, F. H.; Lichterman, M. F.; Hale, W. G.; Wang, H. P.; Zhou, X. H.; Plymale, N. T.; Omelchenko, S. T.; He, J. H.; Papadantonakis, K. M.; Brunschwig, B. S.; Lewis, N. S. *Proc. Natl. Acad. Sci. U. S. A.* **2015**, *112*, 3612−3617.

(23) Gerischer, H. In *Solar Energy Conversion: Solid-State Physics Aspects*; Seraphin, B. O., Ed.; Topics in Applied Physics; Springer: Berlin, Heidelberg, 1979; Vol. *31*, pp 115−172.

(24) Costi, R.; Young, E. R.; Bulović, V.; Nocera, D. G. *ACS Appl. Mater. Interfaces* **2013**, *5*, 2364−2367.

(25) Pourbaix, M. *Atlas of Electrochemical Equilibria in Aqueous Solutions*, 2nd ed.; National Association of Corrosion Engineers: New York, NY, 1974.

(26) Lutterman, D. A.; Surendranath, Y.; Nocera, D. G. *J. Am. Chem. Soc.* **2009**, *131*, 3838−3839.

(27) Gerken, J. B.; McAlpin, J. G.; Chen, J. Y. C.; Rigsby, M. L.; Casey, W. H.; Britt, R. D.; Stahl, S. S. *J. Am. Chem. Soc.* **2011**, *133*, 14431−14442.

(28) Esswein, A. J.; Surendranath, Y.; Reece, S. Y.; Nocera, D. G. *Energy Environ. Sci.* **2011**, *4*, 499.

(29) Surendranath, Y.; Lutterman, D. A.; Liu, Y.; Nocera, D. G. *J. Am. Chem. Soc.* **2012**, *134*, 6326−6336.

(30) Dincă, M.; Surendranath, Y.; Nocera, D. G. *Proc. Natl. Acad. Sci. U. S. A.* **2010**, *107*, 10337−10341.

(31) Bediako, D. K.; Surendranath, Y.; Nocera, D. G. *J. Am. Chem. Soc.* **2013**, *135*, 3662−3674.

(32) Jin, H.; Wang, J.; Su, D.; Wei, Z.; Pang, Z.; Wang, Y. *J. Am. Chem. Soc.* **2015**, *137*, 2688−2694.

(33) Huynh, M.; Bediako, D. K.; Liu, Y.; Nocera, D. G. *J. Phys. Chem. C* **2014**, *118*, 17142−17152.

(34) Huynh, M.; Bediako, D. K.; Nocera, D. G. *J. Am. Chem. Soc.* **2014**, *136*, 6002−6010.

(35) Yeo, R. S.; Orehotsky, J.; Visscher, W.; Srinivasan, S. *J. Electrochem. Soc.* **1981**, *128*, 1900−1904.

(36) Tseung, A. C. C.; Yeh, S.; Liu, X.; Kelsall, G. H.; Dykstra, P. *Novel Acid-Resistant Oxygen Evolution Electrodes*; EUR/European Commission; Commission of the European Communities: Luxembourg, 1991.

(37) Pauporté, T.; Andolfatto, F.; Durand, R. *Electrochim. Acta* **1999**, *45*, 431−439.

(38) Yagi, M.; Tomita, E.; Kuwabara, T. *J. Electroanal. Chem.* **2005**, *579*, 83−88.

(39) Reier, T.; Oezaslan, M.; Strasser, P. *ACS Catal.* **2012**, *2*, 1765−1772.

(40) Lee, Y.; Suntivich, J.; May, K. J.; Perry, E. E.; Shao-Horn, Y. *J. Phys. Chem. Lett.* **2012**, *3*, 399−404.

(41) McCrory, C. C. L.; Jung, S.; Peters, J. C.; Jaramillo, T. F. *J. Am. Chem. Soc.* **2013**, *135*, 16977−16987.

(42) Carmo, M.; Fritz, D. L.; Mergel, J.; Stolten, D. *Int. J. Hydrogen Energy* **2013**, *38*, 4901−4934.

(43) Iyer, A.; Del-Pilar, J.; King'ondu, C. K.; Kissel, E.; Garces, H. F.; Huang, H.; El-Sawy, A. M.; Dutta, P. K.; Suib, S. L. *J. Phys. Chem. C* **2012**, *116*, 6474−6483.

(44) Trotochaud, L.; Ranney, J. K.; Williams, K. N.; Boettcher, S. W. *J. Am. Chem. Soc.* **2012**, *134*, 17253−17261.

(45) Mette, K.; Bergmann, A.; Tessonnier, J.-P.; Hävecker, M.; Yao, L.; Ressler, T.; Schlögl, R.; Strasser, P.; Behrens, M. *ChemCatChem* **2012**, *4*, 851−862.

(46) Ramírez, A.; Bogdanoff, P.; Friedrich, D.; Fiechter, S. *Nano Energy* **2012**, *1*, 282−289.

(47) Zaharieva, I.; Chernev, P.; Risch, M.; Klingan, K.; Kohlhoff, M.; Fischer, A.; Dau, H. *Energy Environ. Sci.* **2012**, *5*, 7081−7089.

(48) Robinson, D. M.; Go, Y. B.; Mui, M.; Gardner, G.; Zhang, Z.; Mastrogiovanni, D.; Garfunkel, E.; Li, J.; Greenblatt, M.; Dismukes, G. C. *J. Am. Chem. Soc.* **2013**, *135*, 3494−3501.

(49) Gorlin, Y.; Lassalle-Kaiser, B.; Benck, J. D.; Gul, S.; Webb, S. M.; Yachandra, V. K.; Yano, J.; Jaramillo, T. F. *J. Am. Chem. Soc.* **2013**, *135*, 8525−8534.

(50) Fekete, M.; Hocking, R. K.; Chang, S. L. Y.; Italiano, C.; Patti, A. F.; Arena, F.; Spiccia, L. *Energy Environ. Sci.* **2013**, *6*, 2222−2232.

(51) Smith, R. D. L.; Prévot, M. S.; Fagan, R. D.; Zhang, Z.; Sedach, P. A.; Siu, M. K. J.; Trudel, S.; Berlinguette, C. P. *Science* **2013**, *340*, 60−63.

(52) Zhou, F.; Izgorodin, A.; Hocking, R. K.; Armel, V.; Spiccia, L.; Macfarlane, D. R. *ChemSusChem* **2013**, *6*, 643−651.

(53) Jin, K.; Park, J.; Lee, J.; Yang, K. D.; Pradhan, G. K.; Sim, U.; Jeong, D.; Jang, H. L.; Park, S.; Kim, D.; Sung, N.-E.; Kim, S. H.; Han, S.; Nam, K. T. *J. Am. Chem. Soc.* **2014**, *136*, 2−10.

(54) Pokhrel, R.; Goetz, M. K.; Shaner, S. E.; Wu, X.; Stahl, S. S. *J. Am. Chem. Soc.* **2015**, *137*, 8384−8387.

(55) Meng, Y.; Song, W.; Huang, H.; Ren, Z.; Chen, S.; Suib, S. L. *J. Am. Chem. Soc.* **2014**, *136*, 11452−11464.

(56) Takashima, T.; Hashimoto, K.; Nakamura, R. *J. Am. Chem. Soc.* **2012**, *134*, 1519−1527.

DOI: 10.1021/jacs.5b06382
J. Am. Chem. Soc. 2015, 137, 14887−14904

(57) Morita, M.; Iwakura, C.; Tamura, H. *Electrochim. Acta* **1979**, *24*, 357−362.

(58) Najafpour, M. M.; Leonard, K. C.; Fan, F.-R. F.; Tabrizi, M. A.; Bard, A. J.; King'ondu, C. K.; Suib, S. L.; Haghighi, B.; Allakhverdiev, S. I. *Dalt. Trans.* **2013**, *42*, 5085−5091.

(59) Bloor, L. G.; Molina, P. I.; Symes, M. D.; Cronin, L. *J. Am. Chem. Soc.* **2014**, *136*, 3304−3311.

(60) Krihak, M.; Murtagh, M. T.; Shahriari, M. R. *Proc. SPIE* **1996**, *2836*, 105−115.

(61) Petit, M. A.; Plichon, V. *J. Electroanal. Chem.* **1998**, *444*, 247−252.

(62) Hepel, M. In *Interfacial Electrochemistry: Theory: Experiment, and Applications*; Wieckowski, A., Ed.; Marcel Dekker, Inc.: New York, 1999; pp 599−630.

(63) Watts, J. F.; Wolstenholme, J. *An Introduction to Surface Analysis by XPS and AES*; John Wiley & Sons, Ltd: Chichester, UK, 2003.

(64) Anthony, M. T.; Seah, M. P. *Surf. Interface Anal.* **1984**, *6*, 95−106.

(65) Barr, T. L.; Seal, S. *J. Vac. Sci. Technol., A* **1995**, *13*, 1239−1246.

(66) Ching, S.; Landrigan, J. A.; Jorgensen, M. L. *Chem. Mater.* **1995**, 7.

(67) Chupas, P. J.; Qiu, X.; Hanson, J. C.; Lee, P. L.; Grey, C. P.; Billinge, S. J. L. *J. Appl. Crystallogr.* **2003**, *36*, 1342−1347.

(68) Hammersley, A. P.; Svenson, S. O.; Hanfland, M.; Hauserman, D. *High Pressure Res.* **1996**, *14*, 235−248.

(69) Juhás, P.; Davis, T.; Farrow, C. L.; Billinge, S. J. L. *J. Appl. Crystallogr.* **2013**, *46*, 560−566.

(70) Egami, T.; Billinge, S. J. L. *Underneath the Bragg Peaks: Structural Analysis of Complex Materials*; Elsevier: Amsterdam, 2012; Vol. *16*.

(71) Proffen, T.; Billinge, S. J. L. *J. Appl. Crystallogr.* **1999**, *32*, 572−575.

(72) Farrow, C. L.; Juhás, P.; Liu, J. W.; Bryndin, D.; Božin, E. S.; Bloch, J.; Proffen, T.; Billinge, S. J. L. *J. Phys.: Condens. Matter* **2007**, *19*, 335219−335226.

(73) Farrow, C. L.; Juhas, P.; Billinge, S. J. L. *SrFit*, 2010; http://www.diffpy.org/diffpy.srfit/ (accessed August 1, 2014).

(74) Zhu, M.; Farrow, C. L.; Post, J. E.; Livi, K. J. T.; Billinge, S. J. L.; Ginder-Vogel, M.; Sparks, D. L. *Geochim. Cosmochim. Acta* **2012**, *81*, 39−55.

(75) Farrow, C. L.; Billinge, S. J. L. *Acta Crystallogr., Sect. A: Found. Crystallogr.* **2009**, *65*, 232−239.

(76) Shi, C.; Redmond, E. L.; Mazaheripour, A.; Juhas, P.; Fuller, T. F.; Billinge, S. J. L. *J. Phys. Chem. C* **2013**, *117*, 7226−7230.

(77) Masadeh, A.; Božin, E.; Farrow, C.; Paglia, G.; Juhas, P.; Billinge, S.; Karkamkar, A.; Kanatzidis, M. *Phys. Rev. B: Condens. Matter Mater. Phys.* **2007**, *76*, 115413−115424.

(78) Gileadi, E. *Physical Electrochemistry: Fundamentals, Techniques and Applications*, 1st ed.; Wiley-VCH: Weinheim, 2011.

(79) Lyons, M. E. G.; Brandon, M. P. *Int. J. Electrochem. Sci.* **2008**, *3*, 1386−1424.

(80) Trotochaud, L.; Young, S. L.; Ranney, J. K.; Boettcher, S. W. *J. Am. Chem. Soc.* **2014**, *136*, 6744−6753.

(81) Bediako, D. K.; Li, N.; Kempa, T. J.; Nocera, D. G. *J. Am. Chem. Soc.* **2015**, submitted for publication.

(82) Burke, M. S.; Kast, M. G.; Trotochaud, L.; Smith, A. M.; Boettcher, S. W. *J. Am. Chem. Soc.* **2015**, *137*, 3638−3648.

(83) Carver, J. C.; Schweitzer, G. K.; Carlson, T. A. *J. Chem. Phys.* **1972**, *57*, 973.

(84) Oku, M.; Hirokawa, K.; Ikeda, S. *J. Electron Spectrosc. Relat. Phenom.* **1975**, *7*, 465−473.

(85) Rao, C. N. R.; Sarma, D. D.; Vasudevan, S.; Hegde, M. S. *Proc. R. Soc. London, Ser. A* **1979**, *367*, 239−252.

(86) Foord, J. S.; Jackman, R. B.; Allen, G. C. *Philos. Mag. A* **1984**, *49*, 657−663.

(87) Di Castro, V.; Polzonetti, G. *J. Electron Spectrosc. Relat. Phenom.* **1989**, *48*, 117−123.

(88) Nesbitt, H.; Banerjee, D. *Am. Mineral.* **1998**, *83*, 305−315.

(89) Nelson, A. J.; Reynolds, J. G.; Roos, J. W. *J. Vac. Sci. Technol., A* **2000**, *18*, 1072−1076.

(90) Chigane, M.; Ishikawa, M. *J. Electrochem. Soc.* **2000**, *147*, 2246−2251.

(91) Cerrato, J. M.; Hochella, M. F.; Knocke, W. R.; Dietrich, A. M.; Cromer, T. F. *Environ. Sci. Technol.* **2010**, *44*, 5881−5886.

(92) Biesinger, M. C.; Payne, B. P.; Grosvenor, A. P.; Lau, L. W. M.; Gerson, A. R.; Smart, R. S. C. *Appl. Surf. Sci.* **2011**, *257*, 2717−2730.

(93) Galakhov, V.; Demeter, M.; Bartkowski, S.; Neumann, M.; Ovechkina, N.; Kurmaev, E.; Lobachevskaya, N.; Mukovskii, Y.; Mitchell, J.; Ederer, D. *Phys. Rev. B: Condens. Matter Mater. Phys.* **2002**, *65*, 113102.

(94) Gupta, R.; Sen, S. *Phys. Rev. B* **1975**, *12*, 15−19.

(95) Proffen, T.; Billinge, S. J. L.; Egami, T.; Louca, D. *Z. Kristallogr. - Cryst. Mater.* **2003**, *218*, 132−143.

(96) Billinge, S. J. L.; Kanatzidis, M. G. *Chem. Commun.* **2004**, 749−760.

(97) Myers, J. L.; Well, A.; Lorch, R. F. *Research Design and Statistical Analysis*, 3rd ed.; Routledge: New York, 2010.

(98) Dykhne, T.; Taylor, R.; Florence, A.; Billinge, S. J. L. *Pharm. Res.* **2011**, *28*, 1041−1048.

(99) Takashima, T.; Hashimoto, K.; Nakamura, R. *J. Am. Chem. Soc.* **2012**, *134*, 18153−18156.

(100) Singh, R.; Singh, J.; Nguyencong, H.; Chartier, P. *Int. J. Hydrogen Energy* **2006**, *31*, 1372−1378.

(101) Song, F.; Hu, X. *J. Am. Chem. Soc.* **2014**, *136*, 16481−16484.

(102) Godinho, M. I.; Catarino, M. A.; da Silva Pereira, M. I.; Mendonça, M. H.; Costa, F. M. *Electrochim. Acta* **2002**, *47*, 4307−4314.

(103) Gerken, J. B.; Chen, J. Y. C.; Massé, R. C.; Powell, A. B.; Stahl, S. S. *Angew. Chem., Int. Ed.* **2012**, *51*, 6676−6680.

(104) Kumar, M.; Awasthi, R.; Sinha, A. S. K.; Singh, R. N. *Int. J. Hydrogen Energy* **2011**, *36*, 8831−8838.

(105) Bockris, J. O.; Otagawa, T. *J. Phys. Chem.* **1983**, *87*, 2960−2971.

(106) Suntivich, J.; May, K. J.; Gasteiger, H. A.; Goodenough, J. B.; Shao-Horn, Y. *Science* **2011**, *334*, 1383−1385.

(107) Gorlin, Y.; Jaramillo, T. F. *J. Electrochem. Soc.* **2012**, *159*, H782−H786.

(108) Trasatti, S.; Petrii, O. A. *J. Electroanal. Chem.* **1992**, *327*, 353−376.

(109) Nagarajan, N.; Humadi, H.; Zhitomirsky, I. *Electrochim. Acta* **2006**, *51*, 3039−3045.

(110) Zhitomirsky, I.; Cheong, M.; Wei, J. *JOM* **2007**, *59*, 66−69.

(111) Nayak, P. K.; Munichandraiah, N. *Electrochem. Solid-State Lett.* **2009**, *12*, A115−A119.

(112) Nayak, P. K.; Devaraj, S.; Munichandraiah, N. *Electrochem. Solid-State Lett.* **2010**, *13*, F29−F32.

(113) Salyer, D.; Sweet, T. R. *Anal. Chem.* **1958**, *30*, 1632−1635.

(114) Benson, P.; Briggs, G. W. D.; Wynne-Jones, W. F. K. *Electrochim. Acta* **1964**, *9*, 275−280.

(115) Cui, C. Q.; Jiang, S. P.; Tseung, A. C. C. *J. Electrochem. Soc.* **1990**, *137*, 3418−3423.

(116) Dinamani, M.; Kamath, P. V. *J. Appl. Electrochem.* **2000**, *30*, 1157−1161.

(117) Nguyen, Q.; Wang, L.; Lu, G. M. *Int. J. Nanotechnol.* **2007**, *4*, 588−596.

(118) Amadelli, R.; Ferro, S.; Barison, S.; Kötz, R.; Schnyder, B.; Velichenko, A. B. *Electrocatalysis* **2013**, *4*, 329−337.

(119) Sonavane, A. C.; Inamdar, A. I.; Shinde, P. S.; Deshmukh, H. P.; Patil, R. S.; Patil, P. S. *J. Alloys Compd.* **2010**, *489*, 667−673.

(120) El-Sherik, A. M.; Erb, U. *J. Mater. Sci.* **1995**, *30*, 5743−5749.

(121) Carpenter, M. K.; Conell, R. S.; Corrigan, D. A. *Sol. Energy Mater.* **1987**, *16*, 333−346.

(122) Li, M.; Dincă, M. *J. Am. Chem. Soc.* **2011**, *133*, 12926−12929.

(123) Duca, M.; Koper, M. T. M. *Energy Environ. Sci.* **2012**, *5*, 9726−9742.

(124) Athouël, L.; Moser, F.; Dugas, R.; Crosnier, O.; Bélanger, D.; Brousse, T. *J. Phys. Chem. C* **2008**, *112*, 7270−7277.

(125) Sopčić, S.; Peter, R.; Petravić, M.; Mandić, Z. *J. Power Sources* **2013**, *240*, 252−257.
(126) Davies, G. *Coord. Chem. Rev.* **1969**, *4*, 199−224.
(127) Hem, J. D. *Chem. Geol.* **1978**, *21*, 199−218.
(128) Lume-Pereira, C.; Baral, S.; Henglein, A.; Janata, E. *J. Phys. Chem.* **1985**, *89*, 5772−5778.
(129) Wiechen, M.; Zaharieva, I.; Dau, H.; Kurz, P. *Chem. Sci.* **2012**, *3*, 2330−2339.
(130) Subramanian, V.; Zhu, H.; Vajtai, R.; Ajayan, P. M.; Wei, B. *J. Phys. Chem. B* **2005**, *109*, 20207−20214.
(131) Wei, W.; Cui, X.; Chen, W.; Ivey, D. G. *Chem. Soc. Rev.* **2011**, *40*, 1697−1721.
(132) Zhou, F.; Izgorodin, A.; Hocking, R. K.; Spiccia, L.; MacFarlane, D. R. *Adv. Energy Mater.* **2012**, *2*, 1013−1021.
(133) Chen, W.; Rakhi, R. B.; Wang, Q.; Hedhili, M. N.; Alshareef, H. N. *Adv. Funct. Mater.* **2014**, *24*, 3130−3143.
(134) Klug, H. P.; Alexander, L. E. *X-ray Diffraction Procedures for Polycrystalline and Amorphous Materials*, 2nd ed.; Wiley: New York, 1974.
(135) Liu, Y.; Nocera, D. G. *J. Phys. Chem. C* **2014**, *118*, 17060−17066.
(136) Birkholz, M. *Thin Film Analysis by X-Ray Scattering*; Wiley-VCH Verlag GmbH: Weinheim, 2005.
(137) Du, P.; Kokhan, O.; Chapman, K. W.; Chupas, P. J.; Tiede, D. M. *J. Am. Chem. Soc.* **2012**, *134*, 11096−11099.
(138) Farrow, C. L.; Bediako, D. K.; Surendranath, Y.; Nocera, D. G.; Billinge, S. J. L. *J. Am. Chem. Soc.* **2013**, *135*, 6403−6406.
(139) Jeong, D.; Jin, K.; Jerng, S. E.; Seo, H.; Kim, D.; Nahm, S. H.; Kim, S. H.; Nam, K. T. *ACS Catal.* **2015**, *5*, 4624−4628.
(140) Petkov, V.; Trikalitis, P. N.; Bozin, E. S.; Billinge, S. J. L.; Vogt, T.; Kanatzidis, M. G. *J. Am. Chem. Soc.* **2002**, *124*, 10157−10162.
(141) Drits, V. A.; Lanson, B.; Gaillot, A.-C. *Am. Mineral.* **2007**, *92*, 771−788.
(142) Holland, K. L.; Walker, J. R. *Clays Clay Miner.* **1996**, *44*, 744−748.
(143) Manceau, A.; Marcus, M. A.; Grangeon, S.; Lanson, M.; Lanson, B.; Gaillot, A.-C.; Skanthakumar, S.; Soderholm, L. *J. Appl. Crystallogr.* **2013**, *46*, 193−209.
(144) Wang, H.; Lee, H.-W.; Deng, Y.; Lu, Z.; Hsu, P.-C.; Liu, Y.; Lin, D.; Cui, Y. *Nat. Commun.* **2015**, *6*, 7261.
(145) Bediako, D. K.; Costentin, C.; Jones, E. C.; Nocera, D. G.; Savéant, J. *J. Am. Chem. Soc.* **2013**, *135*, 10492−10502.
(146) Indra, A.; Menezes, P. W.; Zaharieva, I.; Baktash, E.; Pfrommer, J.; Schwarze, M.; Dau, H.; Driess, M. *Angew. Chem., Int. Ed.* **2013**, *52*, 13206−13210.
(147) Indra, A.; Menezes, P. W.; Ranjbar Sahraie, N.; Bergmann, A.; Das, C.; Tallarida, M.; Schmeißer, D.; Strasser, P.; Driess, M. *J. Am. Chem. Soc.* **2014**, *136*, 1.
(148) Lee, S. W.; Carlton, C.; Risch, M.; Surendranath, Y.; Chen, S.; Furutsuki, S.; Yamada, A.; Nocera, D. G.; Shao−Horn, Y. *J. Am. Chem. Soc.* **2012**, *134*, 16959−16962.
(149) May, K. J.; Carlton, C. E.; Stoerzinger, K. A.; Risch, M.; Suntivich, J.; Lee, Y.; Grimaud, A.; Shao-Horn, Y. *J. Phys. Chem. Lett.* **2012**, *3*, 3264−3270.
(150) Li, Y.; Bareñoa, J.; Bettgea, M.; Abrahama, D. P. *J. Electrochem. Soc.* **2015**, *162*, A155−A161.

J|A|C|S
JOURNAL OF THE AMERICAN CHEMICAL SOCIETY

Communication

pubs.acs.org/JACS

Oxygen Reduction Catalysis at a Dicobalt Center: The Relationship of Faradaic Efficiency to Overpotential

Guillaume Passard, Andrew M. Ullman, Casey N. Brodsky, and Daniel G. Nocera*

Department of Chemistry and Chemical Biology, Harvard University, 12 Oxford Street, Cambridge, Massachusetts 02138, United States

Ⓢ *Supporting Information*

ABSTRACT: The selective four electron, four proton, electrochemical reduction of O_2 to H_2O in the presence of a strong acid (TFA) is catalyzed at a dicobalt center. The faradaic efficiency of the oxygen reduction reaction (ORR) is furnished from a systematic electrochemical study by using rotating ring disk electrode (RRDE) methods over a wide potential range. We derive a thermodynamic cycle that gives access to the standard potential of O_2 reduction to H_2O in organic solvents, taking into account the presence of an exogenous proton donor. The difference in ORR selectivity for H_2O vs H_2O_2 depends on the thermodynamic standard potential as dictated by the pK_a of the proton donor. The model is general and rationalizes the faradaic efficiencies reported for many ORR catalytic systems.

Renewable energy resources have the potential to impact climate change by mitigating carbon emissions attendant to a fossil based fuel infrastructure.[1,2] Solar energy may be stored in the form of chemical bonds and subsequently recovered on demand in the form of electricity by using fuel cells.[3,4] The cathodic $4e^-$, $4H^+$ oxygen reduction reaction (ORR) of hydrogen-based fuel cells is kinetically challenging, and overall energy conversion efficiencies depend on the selective production of H_2O. Platinum can meet the demanding criteria of efficient ORR,[3,5] but the metal is critical, spurring efforts to develop catalysts based on earth abundant transition metals such as cobalt[6−10] and iron.[11−18] ORR in such systems is often performed in nonaqueous solution using a strong acid (e.g., trifluoroacetic acid (TFA), protonated *N*,*N*-dimethylformamide (DMF-H^+), or perchloric acid) as the proton donor.[14,15,19,20] In assessing activity, we and others often employ the faradaic efficiency for H_2O production as a performance benchmark.[14,19,20] However, faradaic efficiency is difficult to interpret in the absence of a thermodynamic potential that correctly accounts for the activity of the proton in nonaqueous solution.

Dicobalt complexes in acetonitrile (MeCN) and in the presence of O_2 and strong acid demonstrate excellent faradaic efficiencies for H_2O production.[21] We have prepared the pair of dicobalt complexes shown in Scheme 1 wherein a diamond $Co(III)_2(OH)_2$ core is stabilized by the six coordinate ligand, dipyridylethane naphthyridine (DPEN). The complex is similar to the first row metal complexes of DPEN (and its fluorinated analogue, DPFN) prepared by Tilley and co-workers[22−24] excepting the anionic bridging ligand. This dicobalt motif is useful because it is soluble in water and nonaqueous solutions and affords access to a wide range of overpotentials and faradaic efficiencies for ORR. We now develop a general framework to shed light on (a) how solvent and acid strength affect the overpotential of ORR catalysis and (b) the correlation between ORR overpotential and faradaic efficiency.

Scheme 1. Dicobalt Complexes Composed of a $Co(III)_2(OH)_2$ Diamond Core Stabilized by a DPEN Ligand with Anionic Acetamidate (1) and Acetate (2) Bridging Ligands

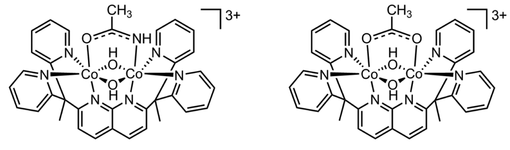

$[Co_2(OH)_2DPEN(\mu\text{-}1,3\text{-}OC(NH)CH_3)]^{3+}$
1

$[Co_2(OH)_2DPEN(\mu\text{-}1,3\text{-}OAc)]^{3+}$
2

Complex **1** was prepared by the addition of the DPEN ligand to $Co(NO_3)_2$ in a 1:1 water/acetone mixture. Air oxidation to furnish the two Co(III) centers is slow; thus H_2O_2 was used to drive the oxidation. The bridging acetamidate ligand was furnished by heating MeCN solutions of the PF_6 salt of the dicobalt complex. Complex **2** was prepared in a similar fashion, except using a $Co(OAc)_2$ precursor salt to furnish the bridging acetate ligand. The compounds were characterized by NMR, mass spectrometry, and elemental analysis (see SI for details).

Figure 1 shows CVs of **1** and **2** in MeCN in the absence of O_2 (red trace). The reversible CV wave corresponds to the

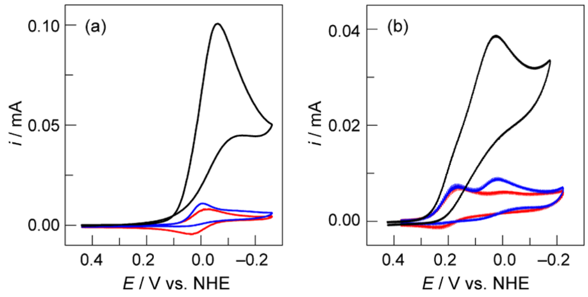

Figure 1. Cyclic voltammetry of (a) **1** and (b) **2** in MeCN (0.1 M *n*-Bu_4NPF_6) under Ar (red) and O_2 (blue), and in the presence of 50 mM AcOH (black); $\nu = 0.1\ V\ s^{-1}$.

Received: December 8, 2015
Published: February 13, 2016

DOI: 10.1021/jacs.5b12828
J. Am. Chem. Soc. 2016, 138, 2925−2928

Co_2(III,III)/Co_2(III,II) couple; redox processes of the DPEN ligand occur at a very negative potential (Figure S1). Consistent with the poorer electron-donating property of the acetate bridge, the Co_2(III,III)/Co_2(III,II) couple for **2** is shifted anodically by 250 mV as compared to that of **1**. The presence of O_2 (8.1 mM) causes a loss of reversibility for the Co_2(III,III)/Co_2(III,II) wave (blue trace, Figure 1) and concomitant slight increase in current. This loss of reversibility is a clear indication that O_2 binds to complexes **1** and **2** following the one-electron reduction of the dicobalt core. Whereas **1** exhibits a single reduction wave, **2** exhibits a small second wave that becomes more pronounced upon O_2 binding. In contrast to these small current−voltage perturbations of the complexes in the presence of O_2, addition of acetic acid (AcOH) to **1** and **2** in the presence of O_2 results in a single large reduction wave. Such a significant increase in current is consistent with a catalytic ORR process. The need for both AcOH and O_2 to engender the large current indicates that protons are necessary for catalytic ORR turnover. Moreover, the current increase exhibits a dependence on the amount of AcOH (Figure S2), which confirms the implication of protons in the mechanism of ORR. At the highest acid concentrations, the foot of the catalytic wave shifts toward less negative potentials, demonstrating that the kinetics of the catalytic reaction improve with increasing acid concentration. With [AcOH] concentration in excess of 50 mM (Figure S2), the current decreases due to deactivation of the catalyst via acidolysis.

The products of ORR are typically water and hydrogen peroxide with the latter being the undesirable product owing to its lower cell voltage. Consequently, the design of ORR catalysts typically emphasizes the selectivity of H_2O vs H_2O_2 production. The commonly used metric for this selectivity is faradaic efficiency as measured by RRDE, for which the theory is very well-defined.[25] The faradaic yield is often determined arbitrarily at the potential for which the disk current is highest, though it is more representative to take into account the average yield throughout the entire catalytic region. The faradaic efficiency for H_2O_2 production as a function of potential may be determined by using

$$\%H_2O_2(E) = \frac{2i_r(E)/N}{i_d(E) + i_r(E)/N} \qquad (1)$$

where $i_r(E)$ and $i_d(E)$ are the ring and the disk current, respectively, at potential E and N is the collection efficiency of the rotating ring disk electrode,[25] which was experimentally determined to be 0.26. The potential at the disk was scanned through the appropriate catalytic region while the potential at the ring was held at 1.17 V (all potentials are reported vs NHE) to ensure complete oxidization of H_2O_2. Figure 2a presents a representative experiment showing the ring and disk currents resulting from ORR of **1** in MeCN acidified with AcOH. Figure 2b shows the corresponding faradaic yield for H_2O_2 production across the potential range of ORR catalysis, obtained by application of eq 1 at different rotation rates. In applying eq 1, the average was taken over a potential range that gave a reliable measure of the current at the disk (i_d > 0.05 mA). Control experiments in the absence of catalyst show that there is no current on the ring regardless of the acid and its concentration within the limits of our potential window. Current from direct reduction of O_2 at the disk in the absence of catalyst occurs at more negative potentials ($E_{disk} < -0.3$ V vs NHE with strong acid to $E_{disk} < -0.64$ V vs NHE in the absence of acid). The faradaic efficiency should be the same at different rotation rates, unless hydrogen peroxide is an intermediate in the reaction leading to water. In this case, a decrease of the ring current would be observed with an increase in rotation rate. At a given potential, the ring and disk currents at various rotation rates show a small variance, however with no trend in rotation rate (Figure 2b). We attribute this variance (±10%) to arise in the collection efficiency. The average faradaic efficiency of H_2O production of 44% in Figure 2b was determined by taking 1 − [faradaic efficiency H_2O_2], which was determined as the average value across the entire trace for all rotation rates.

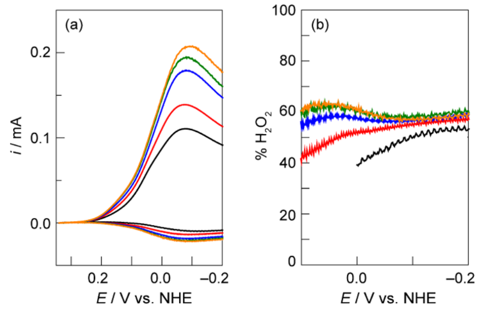

Figure 2. (a) Compound **1** (0.5 mM) in MeCN (0.1 M *n*-Bu_4PF_6) and AcOH (50 mM) under O_2 at different rotation rates: 100 (black), 250 (red), 500 (blue), 750 (green), and 1000 rpm (yellow). $\nu = 0.02$ V s^{-1}. Ring potential: 1.17 V. Disk current is positive, and ring current is negative. (b) Faradaic yield for H_2O_2 production obtained by application of eq 1 at different rotation rates.

This RRDE study of ORR by **1** was expanded to include proton donors of different strength in MeCN (Figures S5−S8) and DMF (Figures S9 and S10) at different acid concentrations. The pK_a of the acids used in these studies are given in Table 1 in DMF and MeCN.[26−29] For a given acid, the current increases and the foot of the wave shifts slightly to more positive potentials with acid concentration (e.g., Figure S2). These observations indicate that the effect of acid concentration is rooted in the kinetics of ORR. Most significantly, the H_2O yield in organic solvents increases with increasing acid strength. Figure 3a plots the average faradaic efficiency of H_2O for the different acids using eq 1. We note that the faradaic efficiency changed minimally with acid concentration (Table S1) over a range where acidolysis of the compound was minimal (≤50 mM acid concentration). As shown in Figure 3a, the faradaic efficiency varies substantially with pK_a (e.g., **1** with TFA in MeCN gives an average faradaic efficiency for H_2O production of 96% as compared to 33% for the more weakly acidic phenol).

Table 1. pK_a of Different Acids and Thermodynamic Standard Potential of O_2 Reduction to H_2O in MeCN and DMF

	MeCN		DMF	
acid, HA[a]	p$K_{a,HA}$	E^0/V vs NHE	p$K_{a,HA}$	E^0/V vs NHE
PhOH	27.2	0.430	18.8	−0.301
AcOH	22.3	0.720	13.3	0.020
ClAcOH	15.3	1.133	10.0	0.213
TFA	12.6	1.293	4.8	0.518

[a] Phenol (PhOH), acetic acid (AcOH), chloroacetic acid (ClAcOH), and trifluoroacetic acid (TFA).

The dependence of ORR faradaic yield on the different acids can be explained by considering the thermodynamic standard potential of the reduction of O_2 to H_2O as a function of acid pK_a (Table 1). We have developed a thermodynamic cycle akin to

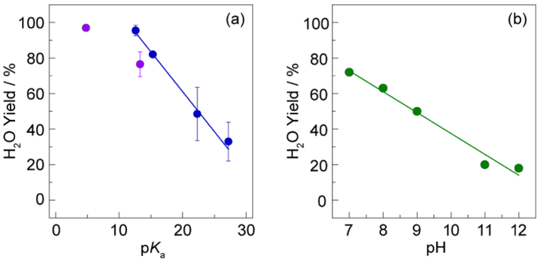

Figure 3. (a) Faradaic efficiency of **1** toward H_2O production as a function of acid pK_a of different acids listed in Table 1 in MeCN (blue) and DMF (green). (b) Faradaic efficiency of **1** toward H_2O production as a function of solution pH adjusted by aqueous phosphate buffer.

that developed by Costentin et al. for CO_2 reduction to CO (Scheme S1).[30] Using this cycle, the standard potential is given by

$$E^{0}_{O_2/2H_2O,HA,S} = E_{J,S} + E^{0}_{O_2/2H_2O,aq} - \frac{4\Delta G^{0}_{H^+,S\rightarrow aq} - 2\Delta G^{0}_{H_2O,S\rightarrow aq}}{2F} - \frac{RT\ln 10}{F} pK_{a\,HA,S} \quad (2)$$

where eq 2 accounts for the standard potential of ORR to furnish H_2O in solvent S and in the presence of HA ($E^{0}_{O_2/2H_2O,HA,S}$) from that in aqueous solution $E^{0}_{O_2/2H_2O,aq}$, corrected for the interliquid junction potential, $E_{J,S}$, between water and solvent S. The terms in eq 2 are defined within Scheme S1. Substituting the constants in eq 2 for MeCN and DMF, respectively, yields

$$E^{0}_{O_2/2H_2O,MeCN} = 2.038 - \frac{RT\ln 10}{F} pK_{a,HA,MeCN} \quad (3)$$

$$E^{0}_{O_2/2H_2O,DMF} = 0.799 - \frac{RT\ln 10}{F} pK_{a,HA,DMF} \quad (4)$$

We note that these equations contain no term for acid concentration, which is reflected in the lack of a noticeable concentration effect on selectivity (Table S1). For the case of water, the standard potential evolves with pH in a standard fashion:

$$\begin{aligned} E^{0'}_{O_2/2H_2O,aq} &= E^{0}_{O_2/2H_2O,aq} - \frac{RT\ln 10}{F}\mathrm{pH} \\ &= 1.23 - \frac{RT\ln 10}{F}\mathrm{pH} \end{aligned} \quad (5)$$

From eqs 3 and 4, we obtain the E^0 values presented in Table 1. These data reveal that the improved selectivity for H_2O production with increasing acid strength (Figure 3a) scales with the increasing standard potential of the ORR reaction for the different acids. Inasmuch as the applied potential to drive the ORR is defined by the reduction potential of the catalyst,

$$\Delta E_{ORR} = E^{0}_{O_2/2H_2O,HA,S} - E^{0}_{Co_2(III,III)/Co_2(II,III)} \quad (6)$$

the faradaic efficiency scales with ΔE_{ORR}, which is the effective overpotential. Thus, the ORR pathway leading to the O−O bond cleavage needed to produce H_2O becomes favored in the presence of strong acid where there is a high effective overpotential. Conversely, with weak acids, the effective overpotential for ORR to H_2O is small, and the pathway leading to H_2O production is disfavored relative to H_2O_2.

The same trend of improved H_2O selectivity with stronger acid is observed in DMF solution (Figure 3a, navy circles). Whereas the faradaic efficiency for H_2O production in DMF and MeCN are similar, ORR may be driven at much lower effective overpotential in DMF owing to the significantly reduced value of $E^{0}_{O_2/2H_2O,HA}$ (arising from a difference in $G^{0}_{H^+,S\rightarrow aq}$, Table S2). Indeed, Figure S3 shows the typical catalytic CVs of **1** in MeCN and DMF. A shift of 650 mV is observed at the foot of the catalytic wave caused by the difference of 779 mV between the two standard potentials (see Table 1). Nonetheless this gain in terms of thermodynamics is somewhat offset in terms of kinetics, as the catalytic current in DMF is significantly reduced as compared to MeCN.

Experiments performed on **1** in water at different pHs lead to results (Figure S11) that are similar to those observed for ORR in nonaqueous solutions. The apparent standard potential decreases with pH according to eq 5, and accordingly, ΔE_{ORR} decreases with increasing pH. Concomitant with this lowering in the effective overpotential, the faradaic efficiency for H_2O production decreases (Figure 3b).

Changing the bridging anion from the acetamidate in **1** to acetate in **2** yields similar RRDE results in MeCN (Figures S12 and S13) and water (Figure S14). The trend of the average faradaic efficiency with pK_a in MeCN (Figure S15) and pH in water (Figure S16) is similar to that observed for ORR catalyst **1**. A positive shift of the catalytic wave is observed for **2** resulting in a decrease in ΔE_{ORR} and an attendant decrease in the effective ORR overpotential (Figure S4). This gain in terms of thermodynamics is offset in terms of kinetics, as the current at the maximum of the catalytic wave is smaller in **2** than **1** (Figure S14a).

Our studies establish that an increase in the effective overpotential of ORR (i.e., increased ΔE_{ORR}) is accompanied by an increase in faradic efficiency. Our model is general, and it applies to previously published ORR catalysts. Figure 4 shows a plot of reported faradaic efficiencies versus effective overpotential for **1** and **2** together with selected ORR catalysts

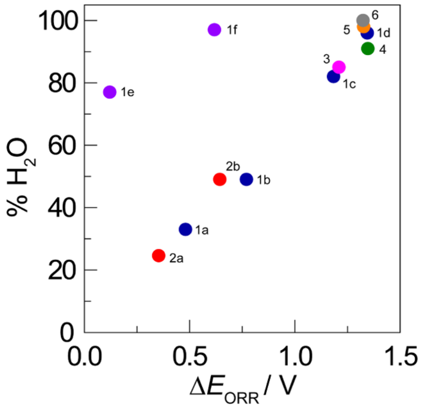

Figure 4. Faradaic efficiency for H_2O production vs ΔE_{ORR}($E^{0}_{O_2/2H_2O,HA,S}$ − $E^{0}_{catalyst}$) for: **1** in MeCN (blue) with (1a) PhOH, (1b) MeCN, (1c) ClAcOH, (1d) TFA; **1** in DMF with (purple) (1e) AcOH, (1f) TFA; **2** in MeCN (red) with (2a) PhOH, (2b) AcOH; (3) Fe tetraphenylporphyrin in DMF with $HClO_4$ (pink), ref 15; (4) Fe *meso*-tetra(2-carboxyphenyl)porphine in MeCN with $(HDMF)^+$ (yellow), ref 14; (5) Fe *meso*-tetra(4-carboxyphenyl)porphine in MeCN with $(HDMF)^+$ (green), ref 14; (6) $[Co^{III}_2(trpy)_2(\mu\text{-bpp})(\mu\text{-1,2-}O_2)]^{3+}$ (bpp = bis(pyridyl)-pyrazolate, trpy = terpyridine) in MeCN with TFA (gray), ref 21.

DOI: 10.1021/jacs.5b12828
J. Am. Chem. Soc. 2016, 138, 2925−2928

operating in organic solvents.[14,15,21] As conveyed by eq 6, the effective overpotential, ΔE_{ORR}, is obtained by subtracting the standard reduction potential of each catalyst from the standard potential of O_2 reduction in a given solvent as determined from eq 2. We note the value of $\Delta G^0_{H^+,S\rightarrow aq}$ used in eq 2 has recently been re-examined;[31] whereas the various values of $\Delta G^0_{H^+,S\rightarrow aq}$ (Table S3) alter the absolute value of ΔE_{ORR}, the trend in Figure 4 is maintained. We have confined our analysis to ORR catalysts operating in DMF and MeCN, as the thermodynamic parameters needed for other solvent systems are unknown or poorly defined; thus literature examples such as those in acetone[20] and benzonitrile[19] are not included in our analysis. Additionally, the standard potential for solid state catalysts is unknown; hence, Figure 4 does not include solid state catalyst in the comparison.

The result of Figure 4 is striking inasmuch as very different catalysts with respect to metal and ligand type are undistinguished with regard to ORR faradaic efficiency. High faradaic efficiencies are obtained only at high effective overpotentials. Per the model embodied by eq 2, most studies achieve these high overpotentials by employing strong acids in nonaqueous solutions. In this regard, compound **1** appears to exhibit better performance in DMF, but this is not a result of better intrinsic catalyst activity, but due to a lowering of the effective overpotential (eq 4 as compared to eq 3) as a result of greater activity of the proton in DMF (Table S3). It is interesting to note that the reported faradaic efficiencies for most catalysts to date are indifferent to the kinetics of the ORR reaction. For instance, in compounds **4** and **5**, a proton relay group is positioned toward and away from a Fe porphyrin ring, respectively. Whereas the kinetics of the ORR are affected by the involvement of the proton relay,[14] the faradaic efficiency for the two compounds is similar as consequence of similar effective overpotentials.

In summary, we have developed a model that shows that ORR selectivity of catalysts is largely dictated by the effective overpotential. Our model reveals that in most systems reported to date, high ORR selectivities for H_2O is a result of large effective overpotentials for the reaction, achieved by the use of strong acids. The challenge to developing better ORR catalysts will be to maintain high catalytic efficiencies under conditions where the overpotential for ORR is greatly reduced.

■ ASSOCIATED CONTENT

Ⓢ Supporting Information

The Supporting Information is available free of charge on the ACS Publications website at DOI: 10.1021/jacs.5b12828.

Full experimental details and additional electrochemical data (PDF)

■ AUTHOR INFORMATION

Corresponding Author

*dnocera@fas.harvard.edu

Notes

The authors declare no competing financial interest.

■ ACKNOWLEDGMENTS

This work was supported by the U.S. Department of Energy Office of Science under Award Number DE-SC0009758. We also thank the TomKat Charitable Trust for support of this work. C.N.B. acknowledges the NSF's Graduate Research Fellowship Program. We are grateful to Prof. Cyrille Costentin for helpful discussions.

■ REFERENCES

(1) Lewis, N. S.; Nocera, D. G. *Proc. Natl. Acad. Sci. U. S. A.* **2006**, *103*, 15729.

(2) Lewis, N. S.; Nocera, D. G. *Bridge* **2015**, *46*, 41.

(3) Borup, R.; Meyers, J.; Pivovar, B.; Kim, Y. S.; Mukundan, R.; Garland, N.; Myers, D.; Wilson, M.; Garzon, F.; Wood, D.; Zelenay, P.; More, K.; Stroh, K.; Zawodzinski, T.; Boncella, J.; McGrath, J. E.; Inaba, M.; Miyatake, K.; Hori, M.; Ota, K.; Ogumi, Z.; Miyata, S.; Nishikata, A.; Siroma, Z.; Uchimoto, Y.; Yasuda, K.; Kimijima, K.; Iwashita, N. *Chem. Rev.* **2007**, *107*, 3904.

(4) Cook, T. R.; Dogutan, D. K.; Reece, S. Y.; Surendranath, Y.; Teets, T. S.; Nocera, D. G. *Chem. Rev.* **2010**, *110*, 6474.

(5) Steele, B. C. H.; Heinzel, A. *Nature* **2001**, *414*, 345.

(6) Anson, F. C.; Shi, C.; Steiger, B. *Acc. Chem. Res.* **1997**, *30*, 437.

(7) Kadish, K. M.; Shen, J.; Frémond, L.; Chen, P.; Ojaimi, M. E.; Chkounda, M.; Gros, C. P.; Barbe, J.-M.; Ohkubo, K.; Fukuzumi, S.; Guilard, R. *Inorg. Chem.* **2008**, *47*, 6726.

(8) Dogutan, D. K.; Stoian, S. A.; McGuire, R.; Schwalbe, M.; Teets, T. S.; Nocera, D. G. *J. Am. Chem. Soc.* **2011**, *133*, 131.

(9) Geiger, T.; Anson, F. C. *J. Am. Chem. Soc.* **1981**, *103*, 7489.

(10) McGuire, R., Jr; Dogutan, D. K.; Teets, T. S.; Suntivich, J.; Shao-Horn, Y.; Nocera, D. G. *Chem. Sci.* **2010**, *1*, 411.

(11) Collman, J. P.; Devaraj, N. K.; Decréau, R. A.; Yang, Y.; Yan, Y.-L.; Ebina, W.; Eberspacher, T. A.; Chidsey, C. E. D. *Science* **2007**, *315*, 1565.

(12) Collman, J. P.; Decréau, R. A.; Lin, H.; Hosseini, A.; Yang, Y.; Dey, A.; Eberspacher, T. A. *Proc. Natl. Acad. Sci. U. S. A.* **2009**, *106*, 7320.

(13) Collman, J. P.; Ghosh, S.; Dey, A.; Decréau, R. A.; Yang, Y. *J. Am. Chem. Soc.* **2009**, *131*, 5034.

(14) Carver, C. T.; Matson, B. D.; Mayer, J. M. *J. Am. Chem. Soc.* **2012**, *134*, 5444.

(15) Wasylenko, D. J.; Rodríguez, C.; Pegis, M. L.; Mayer, J. M. *J. Am. Chem. Soc.* **2014**, *136*, 12544.

(16) Chatterjee, S.; Sengupta, K.; Samanta, S.; Das, P. K.; Dey, A. *Inorg. Chem.* **2015**, *54*, 2383.

(17) Samanta, S.; Mittra, K.; Sengupta, K.; Chatterjee, S.; Dey, A. *Inorg. Chem.* **2013**, *52*, 1443.

(18) Samanta, S.; Das, P. K.; Chatterjee, S.; Sengupta, K.; Mondal, B.; Dey, A. *Inorg. Chem.* **2013**, *52*, 12963.

(19) Rosenthal, J.; Nocera, D. G. *Acc. Chem. Res.* **2007**, *40*, 543.

(20) Kakuda, S.; Peterson, R. L.; Ohkubo, K.; Karlin, K. D.; Fukuzumi, S. *J. Am. Chem. Soc.* **2013**, *135*, 6513.

(21) Fukuzumi, S.; Mandal, S.; Mase, K.; Ohkubo, K.; Park, H.; Benet-Buchholz, J.; Nam, W.; Llobet, A. *J. Am. Chem. Soc.* **2012**, *134*, 9906.

(22) Davenport, T. C.; Tilley, T. D. *Angew. Chem., Int. Ed.* **2011**, *50*, 12205.

(23) Davenport, T. C.; Tilley, T. D. *Dalton Trans.* **2015**, *44*, 12244.

(24) Davenport, T. C.; Ahn, H. S.; Ziegler, M. S.; Tilley, T. D. *Chem. Commun.* **2014**, *50*, 6326.

(25) Allen, J. Bard, L. R. F. *Electrochemical Methods: Fundamentals and Applications*, 2nd ed.; Wiley: New York, 2001.

(26) Andrieux, C. P.; Gamby, J.; Hapiot, P.; Savéant, J.-M. *J. Am. Chem. Soc.* **2003**, *125*, 10119.

(27) Costentin, C.; Evans, D. H.; Robert, M.; Savéant, J.-M.; Singh, P. S. *J. Am. Chem. Soc.* **2005**, *127*, 12490.

(28) Kütt, A.; Rodima, T.; Saame, J.; Raamat, E.; Mäemets, V.; Kaljurand, I.; Koppel, I. A.; Garlyauskayte, R. Y.; Yagupolskii, Y. L.; Yagupolskii, L. M.; Bernhardt, E.; Willner, H.; Leito, I. *J. Org. Chem.* **2011**, *76*, 391.

(29) Izutsu, K. *Acid-Base Dissociation Constants in Dipolar Aprotic Solvents*; Blackwell: Boston, 1990.

(30) Costentin, C.; Drouet, S.; Robert, M.; Savéant, J.-M. *Science* **2012**, *338*, 90.

(31) Pegis, M. L.; Roberts, J. A. S.; Wasylenko, D. J.; Mader, E. A.; Appel, A. M.; Mayer, J. M. *Inorg. Chem.* **2015**, *54*, 11883.

JACS
JOURNAL OF THE AMERICAN CHEMICAL SOCIETY

Article

pubs.acs.org/JACS

Probing Edge Site Reactivity of Oxidic Cobalt Water Oxidation Catalysts

Andrew M. Ullman,[†] Casey N. Brodsky,[†] Nancy Li, Shao-Liang Zheng, and Daniel G. Nocera[*]

Department of Chemistry and Chemical Biology, Harvard University, 12 Oxford Street, Cambridge, Massachusetts 02138, United States

Supporting Information

ABSTRACT: Differential electrochemical mass spectrometry (DEMS) analysis of the oxygen isotopologues produced by ^{18}O-labeled Co-OEC in $H_2{}^{16}O$ reveals that water splitting catalysis proceeds by a mechanism that involves direct coupling between oxygens bound to dicobalt edge sites of Co-OEC. The edge site chemistry of Co-OEC has been probed by using a dinuclear cobalt complex. ^{17}O NMR spectroscopy shows that ligand exchange of OH/OH_2 at Co(III) edge sites is slow, which is also confirmed by DEMS experiments of Co-OEC. In borate (B_i) and phosphate (P_i) buffers, anions must be displaced to allow water to access the edge sites for an O−O bond coupling to occur. Anion exchange in P_i is slow, taking days to equilibrate at room temperature. Conversely, anion exchange in B_i is rapid (k_{assoc} = 13.1 ± 0.4 M^{-1} s^{-1} at 25 °C), enabled by facile changes in boron coordination. These results are consistent with the OER activity of Co-OEC in B_i and P_i. The P_i binding kinetics are too slow to establish a pre-equilibrium sufficiently fast to influence the oxygen evolution reaction (OER), consistent with the zero-order dependence of P_i on the OER current density; in contrast, B_i exchange is sufficiently facile such that B_i has an inhibitory effect on OER. These complementary studies on Co-OEC and the dicobalt edge site mimic allow for a direct connection, at a molecular level, to be made between the mechanisms of heterogeneous and homogeneous OER.

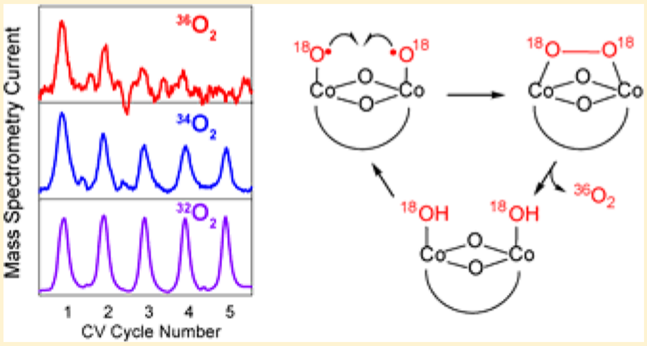

INTRODUCTION

The large scale implementation of renewable energy requires catalysts that can extract electrons and protons from water at low thermodynamic overpotentials.[1,2] The electron and proton reducing equivalents may be used directly as a fuel in the form of hydrogen or combined with CO_2 to furnish liquid fuels. Metal oxides have long been studied for this purpose, though most investigations have focused on the pH extremes, primarily precious metal oxide (e.g., RuO_2) catalysts in acidic solutions,[3,4] and first-row transition-metal oxide catalysts (e.g., cobalt oxides) in alkaline solutions.[5] Although there are advantages to reducing ohmic drops at extreme pH, large scale implementation of an energy conversion system using concentrated acid and base, especially in a distributed fashion, is impractical. Moreover, direct conversion of CO_2 and hydrogen to fuels is best accomplished at neutral pH, where pH gradients may be mitigated under flow conditions.[6] To this end, we have developed cobalt oxygen evolving catalysts (Co-OECs) that are active in neutral or near-neutral pH regimes.[7,8] In these systems, the active sites are cobaltate clusters,[9−12] which are likely to be the active sites in cobalt oxides operating in strong base as well. High-resolution transmission electron microscopy (HRTEM) has shown that crystalline cobalt oxides in neutral and alkaline solutions form amorphous overlayers comprising cobaltate aggregates,[13−16] which are the likely active sites for catalysis as opposed to the native oxide. This has led to the proposal that the catalysis of Co-OECs and cobalt oxides in neutral and concentrated base occurs at edge sites of the cobaltate clusters, with a dicobalt active site as the minimal structural unit that supports catalysis (Scheme 1).[17−19]

Scheme 1. Dicobalt Edge Site Is the Dimensionally Reduced Active Site of Co_3O_4 and Co-OEC

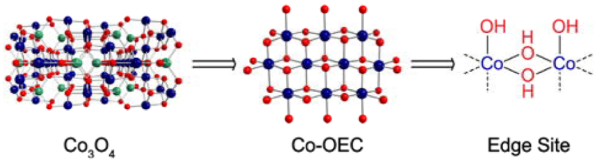

Nevertheless, little is known experimentally about the oxygen evolution reaction (OER) at edge sites of cobaltate clusters. Time-resolved infrared spectroscopy of Co_3O_4 nanoparticles in pH = 8 solution suggests the presence of superoxide/oxo intermediates formed at dicobalt edge sites during OER catalysis.[18] In a separate study, sensitive mass spectrometric measurements show the incorporation of a solvent $H_2{}^{18}O$ label

Received: January 21, 2016
Published: February 24, 2016

DOI: 10.1021/jacs.6b00762

into evolved dioxygen following water oxidation catalyzed by Co/methylenediphosphonate (Co/M2P) oxide nanoparticles.[20] Initial turnover analysis of the O_2 isotopologue ratio following the rapid (and simultaneous) injection of $H_2{}^{18}O$ and $Ru(bpy)_3{}^{3+}$ led to a proposed mechanism for water oxidation involving edge-site-mediated O−O bond formation via direct intramolecular coupling. Consistent with Scheme 1, the data from these experiments also suggested ∼2 cobalt atoms per catalytic site.

We report here mechanistic studies of Co-OECs and complementary investigations of molecular dicobalt analogs to shed light on the mechanism of OER at edge sites of cobaltic oxides. We have investigated the isotopologue distribution of labeled O_2 evolved from Co-OEC-mediated OER using differential electrochemical mass spectrometry (DEMS). This technique[21−23] identifies the distribution of ^{18}O in evolved dioxygen from an ^{18}O-labeled Co-OEC catalyst (in $H_2{}^{16}O$) under the exact electrochemically driven conditions of OER as a function of applied potential[24,25] and in doing so offers insights into the OER mechanism. To this end, the DEMS data support the notion that turnover is occurring at the edge sites of Co-OEC and that O−O bond formation occurs, at least in part, by intramolecular coupling between oxygen atoms ligated to cobalt at the edge sites. To further address the chemistry of edge sites, we prepared a dicobalt complex wherein a diamond $Co_2(OH)_4$ core (Scheme 2) is stabilized by the six coordinate ligand dipyridylethane naphthyridine (DPEN). The complex is akin to the first-row metal complexes of DPEN (and its fluorinated analog, DPFN) prepared by Tilley and coworkers.[26−28] We have identified edge site equilibrium reactions that deliver the open coordination sites needed for the intramolecular coupling reaction identified by the DEMS experiment. The kinetics of phosphate (P_i) and borate (B_i) binding to dicobalt centers differ by many orders of magnitude due to facile coordination chemistry between boric acid, $B(OH)_3$, and the edge of the cobalt dimer. Consistent with this observation, an inverse dependence of the activity of Co-OECs on [B_i] establishes the necessity of a *syn* configuration of the terminal hydroxo moieties of the diamond $Co_2(OH)_4$ core edge site. Together, the results of the authentic Co-OEC and dicobalt model compound demonstrate the important role of edge sites in controlling the OER activity of cobalt-oxide catalysts.

Scheme 2. Synthesis of Edge Site Mimic $[1(OH_2)_2]^{4+}$ Using the Ligand DPEN

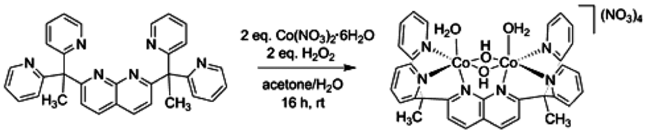

RESULTS

Differential Electrochemical Mass Spectrometry of Co-OEC. DEMS was used in conjunction with isotope labeling to probe the mechanism of O−O bond formation in Co-OEC thin-film catalysts. Catalyst films were deposited from solutions of 1 mM Co^{2+} in 100 mM KP_i at pH 7 in 97% $H_2{}^{18}O$ by performing a controlled potential electrolysis at 0.9 V vs Ag/AgCl (all potentials are referenced to Ag/AgCl unless noted otherwise) and passing a total charge of 10 mC. This labeled catalyst film was then inserted into the electrochemical flow cell of the DEMS instrument (instrument details provided in SI), while electrolyte (100 mM KP_i and 200 mM KNO_3 in $H_2{}^{16}O$ at pH 7) of natural isotopic abundance was flowed through the cell at a rate of 60 mL/h. An electrolyte flow for 30 min was maintained so that mass spectrometric (MS) O_2 baselines equilibrated to constant values. Because we anticipated fast exchange of surface OH/OH_2 species with bulk water at exposed Co(II) centers, the catalyst film was held at a constant potential of 0.9 V during this equilibration period to maintain an oxidation state of Co(III). Five consecutive cycles of cyclic voltammograms (CVs) were performed from 0.9 to 1.1 V at 10 mV/s and the three isotopologues $^{32}O_2$, $^{34}O_2$, and $^{36}O_2$ were detected by the online MS in real time (Figure 1). The CVs plateau at a maximum current of −0.5 mA due to sluggish ion conductance limited by the narrow capillaries of the flow cell, and each cycle plateaus to the same maximum current, indicating no loss of active catalyst during the experiment. All three isotopologues of O_2 were detected in the first four CV cycles; the $^{36}O_2$ signal is weak and by the fifth cycle the signal level could not be distinguished from the noise in the baseline.

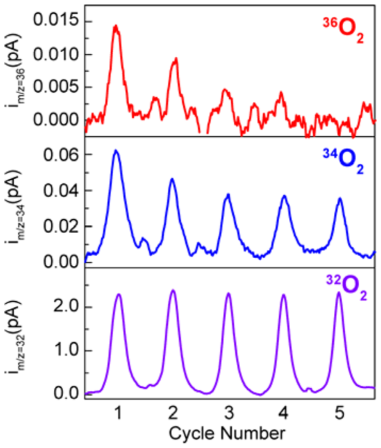

Figure 1. DEMS experimental data for ^{18}O-labeled Co-OEC operated in unlabeled P_i buffer of natural abundance at pH 7. Five consecutive CVs are scanned from 0.9 to 1.1 V vs Ag/AgCl at 10 mV/s, while MS ion current is detected for mass channels m/z = 32, 34, 36 (bottom to top).

Interpreting the data in Figure 1 requires knowledge of the exchange rate of OH/OH_2 bound to the Co(III) centers with bulk water on the time scale of the DEMS experiment. To examine the issue of exchange, the experiment in Figure 1 was repeated but using a longer equilibration time of 5 h, during which the catalyst was held at 0.9 V to maintain an oxidation state of Co(III). The result of this experiment at longer equilibration time (Figure S1) was the same as Figure 1 with a slight decrease in overall signal intensity. All three isotopologues were detected in non-negligible amounts in the first four cycles, while $^{36}O_2$ signal falls to the level of noise by the fifth cycle.

Whereas Co(III) is stable to OH/OH_2 exchange over hours of the DEMS experiment, Co(II) is not. The Co-OEC thin-film catalyst was equilibrated for a 30 min period with no applied potential bias. The films were then scanned from 0.6 to 1.1 V at a rate of 1 mV/s (Figure S2). Under these conditions, a significant population of Co(II) centers is generated in the film before the onset of OER catalysis. For this DEMS experiment, only $^{32}O_2$ is detected to any significant extent (Figure S2); $^{34}O_2$ was detected at low signal intensity only on the first two scans, and no $^{36}O_2$ was detected above the level of noise. These results informed us that a reliable DEMS experiment required that Co-OEC films be maintained in the Co(III) oxidation state (i.e., at 0.9 V applied potential), as performed for Figure 1.

Molecular Co_2(III,III) Edge Site Model. To acquire a more precise knowledge of OH/OH_2 exchange at Co(III) edge sites, a dicobalt edge-site model of Co-OEC, $[\mathbf{1}(OH_2)_2]^{4+}$, was employed. The complex (Scheme 2) features a dicobalt Co_2(III,III) $(OH)_2$ diamond core with *syn* geometry of terminal aquo/hydroxo ligands. This core is supported by a dipyridylethane naphthyridine (DPEN) ligand, which had previously been reported by Tilley et al. for stabilizing dinuclear copper complexes[28] and first-row metals (using the fluorinated analog, DPFN).[26,27] $[\mathbf{1}(OH_2)_2]^{4+}$ was assembled by oxidation of a mixture of 2:1 $Co(NO_3)_2$:DPEN with 2 equiv of aqueous peroxide (Scheme 2). Following precipitation with acetone, elementally pure compound was isolated as a pink solid. Single crystals of the complex were isolated from a pH = 5.5 aqueous solution in the presence of PF_6 anions. The solid-state structure of these crystals is shown in Figure 2 and showcases a dimer of dimers complex, $[\mathbf{1}(OH_2)_2|(HO)_2\mathbf{1}]^{6+}$, which is held together by the hydrogen bonds of an H_6O_4 dianion. The pK_as of the terminal aqua ligands in $[\mathbf{1}(OH_2)_2]^{4+}$ were measured by titration with NaOH and found to be pK_{a1} = 5.08 and pK_{a2} = 6.75 (Figure S3), supporting the notion that the monodeprotonated species, $[\mathbf{1}(OH)(OH_2)]^{3+}$, is stable in the pH regime in which the crystals were grown.

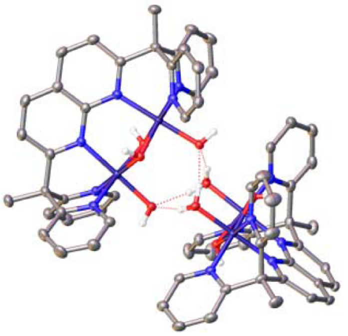

Figure 2. Solid-state structure of the hydrogen-bonded dimer $[\mathbf{1}(OH_2)_2|(HO)_2\mathbf{1}]^{6+}$ with PF_6 anions, solvent molecules, and DPEN hydrogen atoms removed for clarity. Atoms are color-coded: gray (C), blue (N), red (O), dark blue (Co), and white (H).

The cyclic voltammogram of $[\mathbf{1}(OH_2)_2]^{4+}$ in B_i buffer (pH = 9.2) shows no appreciable current signature beyond background at potentials <1.8 V vs NHE (Figure S4), indicating that oxidation of the complex to a Co(IV) species is not possible within the electrochemical window of this experiment. This electrochemical inertness to higher oxidation states contrasts that of Co-OEC, which exhibits access to Co(IV) at reasonably low potentials (~1.1 V vs NHE). Presumably, the polymetallic cobaltate cluster allows for redox leveling to attain the Co(IV) oxidation state, which is not accessible for the bimetallic core of $[\mathbf{1}(OH_2)_2]^{4+}$. Accordingly, $[\mathbf{1}(OH_2)_2]^{4+}$ does not support OER.

Water/Hydroxo Exchange at Co_2(III,III) Edge Site. The OH/OH_2 exchange was measured by ^{17}O NMR spectroscopy. The all-Co(III) complex $[\mathbf{1}(OH_2)_2]^{4+}$ was labeled with ^{17}O by heating in 40% $H_2{}^{17}O$ enriched water at pH 0 at 60 °C for 3 d, after which it was precipitated out of solution by acetone and collected as a solid. At this temperature and pH, both bridging and terminal OH/OH_2 moieties were able to incorporate the ^{17}O label. Labeled compound was freshly dissolved (100 mM) in an unlabeled buffer solution of 50 mM KP_i at pH = 7, and ^{17}O NMR spectra were collected every 20 min for 28 h at room temperature (Figure 3a). Three NMR peaks were observed. The peak at 420 ppm does not change during the 28 h, corresponding to bridging ^{17}OH. The peak at 0 ppm increases exponentially, corresponding to free $H_2{}^{17}O$ and the peak at −100 ppm decreases, corresponding to the terminal $^{17}OH/^{17}OH_2$ groups.[29] The broadness of this peak may be attributed to the mixture of terminal OH and OH_2 groups combined with fast proton exchange with solvent. The growth of the peak at 0 ppm for free $H_2{}^{17}O$ is due solely to exchange of the ^{17}O label from the terminal OH/OH_2 positions of the complex into bulk water; thus this sharp peak was integrated for quantitative analysis. The integration of the free $H_2{}^{17}O$ peak relative to the integration of bridging ^{17}OH was plotted against time (Figure 3b) and fit to a monoexponential curve, yielding a rate constant $k_{ex} = 4.9 \pm 0.1 \times 10^{-5}$ s^{-1}, with a lifetime of 5.7 ± 0.2 h. This result is consistent with the DEMS experiment; namely that exchange of terminal OH/OH_2 groups at Co(III) centers is slow, occurring on the order of hours.

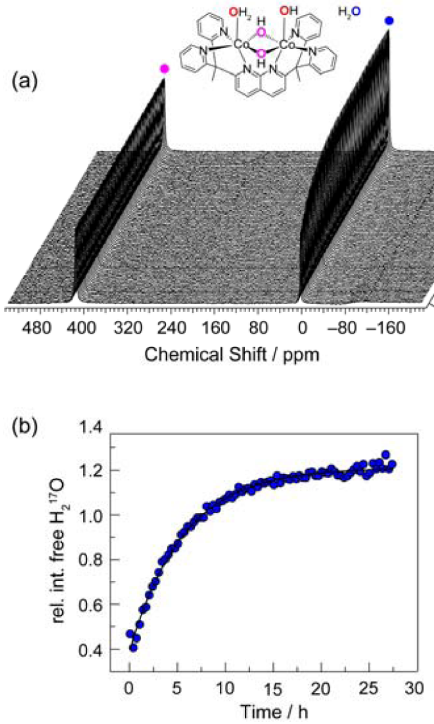

Figure 3. (a) ^{17}O NMR of ^{17}O-labeled $[\mathbf{1}(OH)\ (OH_2)]^{3+}$ in 50 mM natural abundance KP_i buffer at pH 7 over the span of 28 h at room temperature. (b) Relative integration of the free $H_2{}^{17}O$ peak (int. free $H_2{}^{17}O$/int. bound bridging ^{17}OH) versus time, fit to a monoexponential growth curve.

Anion Exchange at Co_2(III,III) Edge Site. In buffer solutions of borate (B_i) and phosphate (P_i), edge sites of Co-OEC are available for ligation. These anions must dissociate for OER to be performed. Complex **1** provides an ideal platform to examine the binding of B_i and P_i to a dicobalt edge site. The binding interaction with B_i was followed by using electronic absorption spectroscopy. The concentration of borate buffer B_i was adjusted by adding different volumes of a KB_i (1 M) stock solution to a $[\mathbf{1}(OH_2)_2][(NO_3)_4]$ = 250 μM solution; the samples were maintained at pH = 8.8, and ionic strength I = 1 M was maintained with addition of KNO_3. As shown in Figure 4, the titration of $[\mathbf{1}(OH)_2]^{2+}$ (pH = 8.8) with increasing concentrations of buffer, $[B_i]_T$, led to the growth of a shoulder at λ = 390 nm and an increase in intensity of the d–d transition at λ = 499 nm, with an isosbestic point at λ = 369 nm. Analysis of the Benesi–Hildebrand plot of this data (Figure 4a inset) furnishes a binding constant with respect to total borate buffer concentration, $[B_i]_T$, of K_{obs} = 28 M^{-1}. The total concentration of boron species $[B_i]_T$ in the buffer is the sum of the concentrations of boric acid, $[B(OH)_3]$, and borate anion, $[B(OH)_4^-]$. When $[B_i]_T$ was held constant at 250 mM, and the pH was increased gradually from 8.8 to 10.5 (Figure 4b), the spectrum reverts to that of the unbound $[\mathbf{1}(OH)_2]^{2+}$. As increasing the pH effectively increases the $B(OH)_4^-$ concentration and reduces the concentration of $B(OH)_3$ in solution, the result of Figure 4b indicates that $B(OH)_4^-$ does not bind to $[\mathbf{1}(OH)_2]^{2+}$, and it is the $B(OH)_3$ component of the buffer that binds to the dicobalt center of $[\mathbf{1}(OH)_2]^{2+}$ (Figure 4c). The association constant for boric acid is given by

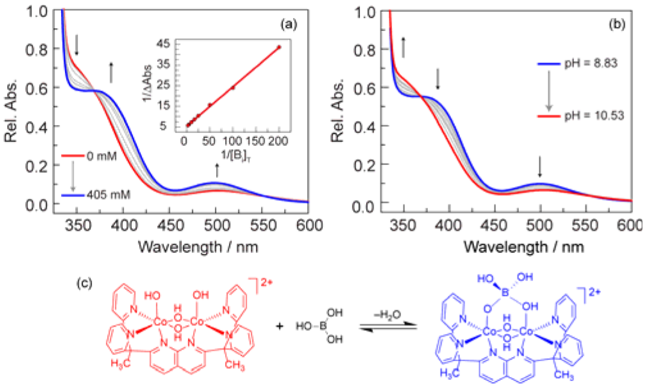

Figure 4. (a) UV–vis absorption changes during titration of 250 μM $[\mathbf{1}(OH)_2]^{2+}$ with borate buffer at pH = 8.8 and I = 1 M. (Inset) Benesi–Hildebrand plot with respect to total borate concentration, $[B_i]_T$. (b) UV–vis absorption changes during a pH titration of a solution of 250 μM $[\mathbf{1}(OH)_2]^{2+}$ and 225 mM $[B_i]_T$. (c) Color-coded schematic of the binding event between the $[\mathbf{1}(OH)_2]^{2+}$ and $B(OH)_3$.

$$K_{B(OH)_3} = K_{obs}\left(1 + \frac{K_a}{[H^+]}\right) \qquad (1)$$

where $K_a = 10^{-8.6}$ M is the acid dissociation constant of boric acid at I = 1 M,[30] and at pH = 8.8, $[H^+] = 10^{-8.8}$ M. Substituting the K_{obs} of 28 M^{-1} that was extracted from the Bensei–Hildebrand analysis furnishes $K_{B(OH)_3}$ = 73 M^{-1} for the equilibrium binding of $B(OH)_3$ to $[\mathbf{1}(OH)_2]^{2+}$. A Job plot constructed from the titration of $[\mathbf{1}(OH)_2]^{2+}$ with B_i (Figure S5) maximizes at a molar fraction of $B(OH)_3$ = ~0.5, consistent with a 1:1 association complex depicted in Figure 4c.

The association of $B(OH)_3$ to $[\mathbf{1}(OH)_2]^{2+}$ occurs rapidly upon mixing, and hence stopped flow measurements were required to measure the kinetics of association (k_{assoc}(B(OH)$_3$)) at room temperature. The extent of the reaction was monitored by following the growth (seen in Figure 4a) of the absorption at λ = 390 nm. Under pseudo-first-order conditions, the data were modeled well with a monoexponential fit, (Figure 5a, all fits, not shown, possess R^2 values exceeding 99.9%). The observed rate constant varied linearly with $[B(OH)_3]$ (Figure 5b), implying a first-order dependence; this result was consistent with that from the Job plot. The pseudo-first-order rate as a function of $[B(OH)_3]$ yielded a second-order rate constant of $k_{assoc}(B(OH)_3)$ = 13.1 ± 0.4 M^{-1} s^{-1} at 25 °C. Variable-temperature experiments were also conducted (Figure S6), and an Eyring analysis of the second-order rate constant revealed an activation enthalpy of $\Delta H^\ddagger$ = 34.5 ± 0.7 kJ mol^{-1} and activation entropy of $\Delta S^\ddagger$ = −107 ± 3 J mol^{-1} K^{-1}.

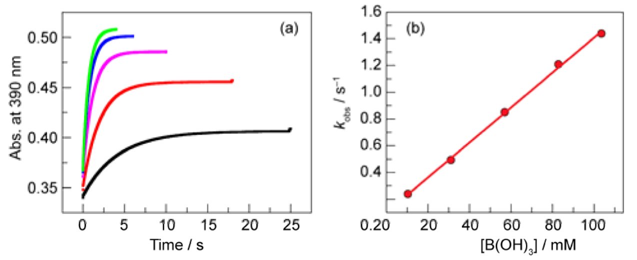

Figure 5. (a) Stopped-flow kinetic plots of the reaction at pH = 8.8 between 500 μM $\mathbf{1}(OH)_2^{2+}$ and $[B_i]_T$ at 250 mM (green), 200 mM (blue), 137.5 mM (magenta), 75 mM (red), and 25 mM (black). (b) Linear relationship between $[B(OH)_3]$ and observed rate constant from which the second-order rate constant is determined.

The UV–vis absorbance spectral changes resulting from anion association to the dicobalt center of $[\mathbf{1}(OH)_2]^{2+}$ in P_i buffer are qualitatively similar to that observed for B_i buffer but evolve over a much longer time scale. As shown in Figure 6, a shoulder near 400 nm appears with an attendant increase in intensity at λ = 507 nm in the absence of isosbestic points. At an elevated temperature of 70 °C, these absorption features require ~10 h to attain equilibrium (Figure 6a inset); as a comparison, the color changes associated with $B(OH)_3$ binding appear instantaneous to the eye at room temperature. At pH = 8.5, the speciation of P_i buffer is largely HPO_4^{2-}. The spectral changes for the association of HPO_4^{2-} to $[\mathbf{1}(OH)_2]^{2+}$ were monitored under pseudo-first-order conditions. A plot of the observed rate constant as a function of $[P_i]$ from 46 to 167 mM exhibits poor linearity (Figure S7), indicating more complicated kinetics for HPO_4^{2-} association. This contention is also supported by ^{1}H NMR experiments. Upon mixing 5 mM $[\mathbf{1}(OH)_2]^{2+}$ with 333 mM KP_i (I = 1 M) at pH = 8.6, the intensity of the resonances associated with $[\mathbf{1}(OH)_2]^{2+}$ decreases, while peaks (many of which were overlapping) associated with two new species appear (Figure S8).

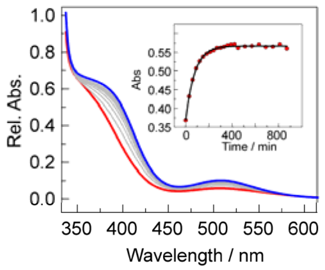

Figure 6. UV–vis absorption changes of a mixture of 250 μM $[\mathbf{1}(OH)_2]^{2+}$ and 167 mM KP_i at pH = 8.5 and 70 °C. (Inset) Monoexponential fit to the change in absorbance at 390 nm versus time.

Monitoring the integrated intensity with time reveals biexponential kinetics for the decrease in $[\mathbf{1}(OH)_2]^{2+}$ (Figure S9). The faster component has a lifetime of 4.9 ± 0.8 h, while the slower component exhibits a lifetime of 160 ± 30 h. The structural chemistry of phosphate with compound **1** is consistent with these observations. Both 1:1 and 2:1 phosphate:dicobalt complexes are known. A 2:1 dimer structure $[\mathbf{1}(O_2PO_2)\mathbf{1}]^{5+}$ is known to be a stable species for the similar metal−ligand DPFN architecture.[28] We report here the 1:1 complex shown in Figure 7. The crystal structure of $[\mathbf{1}(O_2PO(OH))]^{2+}$ was obtained from a mixture of $[\mathbf{1}(OH_2)_2]^{4+}$ and 10 equiv of P_i that was heated at 90 °C for 3 d at pH = 3. Thus, at pH = 3, the 1:1 complex forms from complexation by $H_2PO_4^-$ to the aquo species $[\mathbf{1}(OH_2)_2]^{4+}$. However, at I = 1 M and pH = 8.6 used in the kinetics measurements, $[\mathbf{1}(OH)_2]^{2+}$ is the stable species, and 99% of the phosphate buffer is the monoacidic form, HPO_4^{2-}. Therefore, we attribute the short lifetime component of Figure S9 to the facile formation of the 1:1 complex, $[\mathbf{1}(O_2PO(OH))]^{2+}$, which we expect to be deprotonated at pH = 8.6:

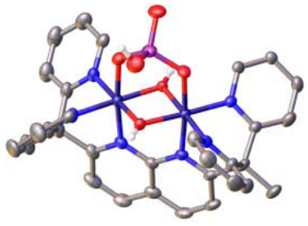

Figure 7. Solid-state crystal structure of phosphate bound complex $[\mathbf{1}(O_2PO(OH))]^{2+}$ with ClO_4^- anions, solvent molecules, and DPEN hydrogen atoms removed for clarity. Atoms are color-coded: gray (C), blue (N), red (O), dark blue (Co), white (H), and purple (P).

$$[\mathbf{1}(OH)_2]^{2+} + 2HPO_4^{2-} \overset{K_1}{\rightleftharpoons} [\mathbf{1}(O_2PO(O^-))]^{+} + 2H_2O + PO_4^{3-} \tag{2}$$

In the subsequent slower reaction (i.e., the longer lifetime component in Figure S9), deprotonated $[\mathbf{1}(O_2PO(OH))]^{2+}$ reacts with another $[\mathbf{1}(OH)_2]^{2+}$ to give the dimer structure, $[\mathbf{1}(O_2PO_2)\mathbf{1}]^{5+}$:

$$[\mathbf{1}(O_2PO(O^-)]^{+} + [\mathbf{1}(OH)_2]^{2+} + 2HPO_4^{2-} \overset{K_2}{\rightleftharpoons} [\mathbf{1}(O_2PO_2)\mathbf{1}]^{5+} + 2H_2O + 2PO_4^{3-} \tag{3}$$

Using this model for P_i binding, a lower limit for the association constants could be estimated from the relative distributions of the bound and unbound complexes after 25 d. The two relevant association constants were estimated to be K_1 = 0.08 M^{-1} for formation of 1:1 complex and K_2 = 0.5 M^{-1} for the dimer structure (see SI for details).

OER Activity of Co-OEC in B_i. To correlate the insights afforded from these molecular model studies with the interaction of anions at edge sites within Co-OEC films, we examined the dependence of OER activity of Co-OEC with anions. Whereas the activity of Co-OEC has been shown to exhibit a zero-order dependence on $[P_i]$,[12] the dependence of OER activity of CoP_i and CoB_i films in B_i has heretofore not been defined. Co-OEC films were deposited from Co^{2+} solutions containing either B_i buffer (Figure 8a) (CoB_i films) or P_i buffer (Figure 8b) (CoP_i films) onto glassy carbon rotating disk electrodes. The current density ($\log(j)$) associated with OER was monitored as a function of $[B_i]$, applied potential, and rotation rate. For both films, there exist two regions of interest. In the region of low $[B_i]$ (i.e., left of the dashed lines in Figure 8), the current density increases with increasing $[B_i]$. At a given $[B_i]$, the current density depends on the rotation rate (i.e., spread in current density at a given $[B_i]$ for a given potential); with increasing $[B_i]$ the spread in current density at a given $[B_i]$ converges with rotation rate. As we have shown, both the dependence on rotation rate (at a given $[B_i]$) and the increase in $\log(j)$ with $[B_i]$ (at a given potential) are indicative of partial mass transport control of protons diffusing from the catalyst films, mediated by the diffusion of buffer from solution into the catalyst films.[31] As current density is increased, evolution of H^+ by the films is fast, and hence mass transport becomes more pronounced (hence greater spread in $\log(j)$ with rotation rate at higher applied voltage). At high enough $[B_i]$, $\log(j)$ is independent of rotation rate, owing to sufficient buffering capacity, and the overall behavior transitions from mass transport to activation controlled kinetics (indicated by dashed line). The transition occurs at higher $[B_i]$ with higher applied potential (and consequently higher $\log(j)$) because a greater buffering capacity is needed with increased production of H^+. In the region of activation controlled catalysis, the dependence of OER on B_i is furnished from the slope of the solid lines shown in Figure 8. An inverse dependence on $[B_i]$ is observed for CoP_i and CoB_i films. For the latter (Figure 8a), the slopes resides between −0.52 and −0.42, whereas for the CoP_i films (Figure 8b), the slopes are between −0.20 and −0.16. Experiments on CoB_i films were also conducted at pH = 9.2 (Figure S10), and the slopes in the activation controlled region were similar to those collected at pH = 8.6.

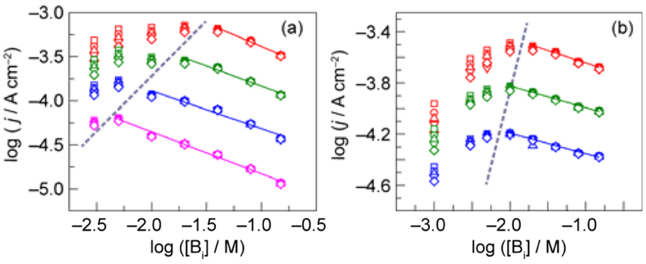

Figure 8. Dependence of the water oxidation current density on $[B_i]$ for 24 mC/cm^2 thick films of (a) CoB_i and (b) CoP_i at pH = 8.6 and I = 1 M using a rotating disk electrode at potentials vs Ag/AgCl of 0.95 V (red), 0.925 V (green), 0.90 V (blue), and 0.875 V (magenta). The shaped data points correspond to rotation rates in rpm of 2500 (square), 1600 (circle), 1225 (up triangle), 900 (down triangle), and 625 (diamond). Slopes of the linear fits (solid lines) are approximately (a) − 0.47 and (b) − 0.18.

■ DISCUSSION

The mechanism of Co-OEC catalyzed water oxidation involves a series of proton-coupled electron transfer (PCET) oxidations leading to an active catalyst. The pathway for OER by CoP_i is shown in Scheme 3.[32] The catalyst is deposited from solution in a Co(III) formal oxidation state (**D**, deposition state).[33] Cobalt K-edge X-ray absorption spectroscopy (XAS)[9] and EPR[34,35] confirm that the catalyst resides in a Co(IV) resting state (**R**). Localized at the edges of the Co-OEC clusters, these Co(IV) centers may be considered to have significant Co(III) oxyl radical character as a direct consequence of the electronic considerations embodied by the "Oxo Wall".[36] Such oxyl radical

Scheme 3. OER Pathway for Co-OEC As Determined from Electochemical Kinetics, EPR, and XAS Studies[a]

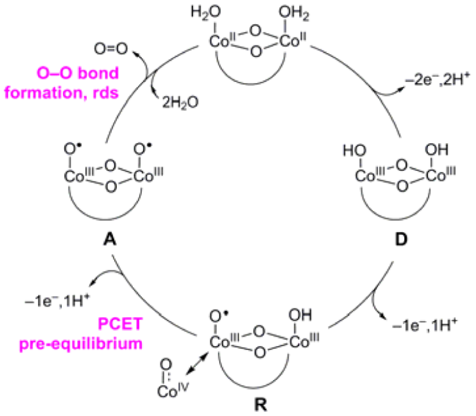

[a]Curved lines denote phosphate, or OH_x terminal or bridging ligands.

character is consistent with increasing evidence for the role of oxygen radicals in O−O bond formation by a PCET mechanism involving water.[18,37−39] A $1e^-/1H^+$ PCET minor equilibrium furnishes the active catalyst (**A**),[12] which drives O−O bond formation and the release of O_2 in a rate-limiting chemical step. The mechanism for O−O bond formation and O_2 generation remains undefined. Two prevailing mechanisms for O−O bond formation rely on the oxyl character of the high-valent metal-oxo: direct intramolecular oxygen coupling (IMOC) of two oxyl radicals leading to a bridging peroxo intermediate (eq 4):

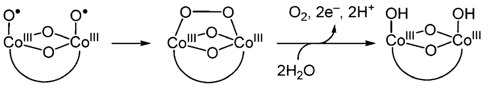

(4)

or water hydrogen atom abstraction (WHAA) of an associated water molecule by an oxyl radical, to generate a hydroperoxo intermediate (eq 5):

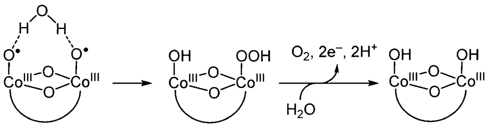

(5)

Experimental studies and computational analysis indicate that both mechanisms may be operative for cobalt oxo cubane catalysts. DFT analysis of a Co_4O_4 cubane has suggested that the IMOC mechanism of eq 4 is dominant,[37] and for computations where the WHAA mechanism of eq 5 prevails, it is only slightly favorable (∼5 kcal/mol) as compared to IMOC.[40] Isotopic labeling analysis of a chemically oxidized Co_4O_4 cubane at pH = 12 provides evidence for WHAA, but it is noted that IMOC is kinetically indistinguishable.[41] *In situ* FTIR analysis of crystalline Co_3O_4 nanoparticles (which are known to amorphize to cobaltate clusters at the edges)[13−16] in the presence of a $Ru(bpy)_3^{3+}$ photooxidant at pH = 8 provides evidence toward a WHAA mechanism, by observation of an IR stretching frequency consistent with a hydroperoxo intermediate as shown in eq 5.[18] Conversely, isotopic first turnover analysis of Co/M2P nanoparticles in conjunction with a $Ru(bpy)_3^{3+}$ photooxidant at pH = 7 supports IMOC.[20] The fast exchange that is noted in this work[20] is likely due to the relaxation of Co(III) to Co(II) upon OER,[42] since once the $Ru(bpy)_3^{3+}$ is depleted, a chemical potential does not exist to hold the majority of the cobalt atoms in the catalyst at the Co(III) oxidation state. In support of this contention, the DEMS data in Figure S2 show that oxidic Co(II) does exchange rapidly; indeed literature values for Co(II) ligand exchange are on the order of 10^6 s^{-1}.[43] This exchange, which complicates the interpretation of the isotope data obtained from a photochemical experiment, may be circumvented in electrochemically driven OER as the applied potential may be poised to maintain a Co(III) oxidation state. Indeed, Figure S1 shows that Co-OEC films composed of ^{18}O evolve significant $^{36}O_2$, even after the films have been equilibrated with natural abundance water for 5 h at room temperature, indicating exchange of terminal OH/OH_2 ligands to be slow. More quantitatively, ^{17}O NMR kinetic analysis of $[\mathbf{1}(OH)\ (OH_2)]^{3+}$ shows that terminal OH/OH_2 groups exchange slowly with k_{ex} = 4.9 × 10^{-5} s^{-1}. This result is in accordance with known exchange rates of terminal OH/OH_2 mononuclear Co(III) complexes (k_{ex} ∼ 10^{-3}–10^{-6} s^{-1}).[29,44] Additionally, the NMR experiment demonstrates that the bridging OH groups lack lability and do not exchange over the span of 28 h.

The detection of $^{36}O_2$ for electrochemically driven water oxidation by ^{18}O-labeled Co-OEC in $H_2{}^{16}O$ (Figure 1) provides direct evidence that OER proceeds, at least in part, by the IMOC mechanism (eq 4). We note that these isotopic DEMS experiments were only performed at pH = 7, and extrapolation of the results to other pH regimes may not be straightforward. With turnover, the ^{18}O label will be washed out by solvent exchange, accounting for the observation of $^{34}O_2$ and $^{32}O_2$. The appearance of a prompt $^{32}O_2$ signal is a result of partial exchange during equilibration. Based on the rate constant of k_{ex} = 4.9 × 10^{-5} s^{-1} measured from the ^{17}O NMR kinetic analysis, we expect 8% exchange during the 30 min equilibration time of the DEMS experiment. For the 5 h of equilibration experiment, we predict 59% exchange; indeed, we observe a 67% decrease in $^{36}O_2$ signal intensity during this longer equilibration period (Figure S1). A straightforward comparison of theoretical and experimental ratios of O_2 isotopologues is difficult to accurately quantitate because of (i) the low levels of turnover and exchange during the 30 min equilibration period and (ii) an unknown number of film active sites and therefore turnover frequency (TOF). With regard to the latter, in the absence of a measure of TOF, we cannot determine the rate of ^{16}O incorporation with turnover.

The DEMS results cannot distinguish between incorporation of O atoms into the evolved O_2 from either terminal or bridging positions. However, the recent isotopic cubane study by Tilley and co-workers suggests the bridging hydroxos may not be involved in catalysis.[41] The observation that bridging OH ligands are nonexchangeable in the ^{17}O NMR experiment of $[\mathbf{1}(OH)\ (OH_2)]^{3+}$ also indicates that bridging hydroxos are unreactive during OER. Moreover, we do not believe bridging hydroxos can assume terminal positions via structural rearrangement of the Co-OEC. If there was considerable structural rearrangement of the cobaltate cluster, sufficient ^{18}O label would be continually extruded from the cobaltate cluster interior to produce $^{36}O_2$ after many cycles. This is not the case in Figure 1; $^{36}O_2$ is depleted quickly upon cycling. We emphasize that the DEMS data in Figure 1 do not rule out WHAA as a contributing mechanism to OER. In this case, the $^{34}O_2$ isotopologue would be the primary oxygen product, with $^{32}O_2$ appearing as the label is washed out of the system. The key point with regard to the data in Figure 1 is that the $^{36}O_2$ is unique to the IMOC mechanism.

The DEMs results establish that O−O coupling occurs at the edges of the Co-OEC cobaltate cluster, and thus the OER activity should exhibit a dependence on the nature of the anion. Scheme 1 depicts the basic cobaltate structural unit of Co-OEC with interlayer buffer anions omitted; indeed the actual Co-OEC is capped by P_i or B_i anions that act in the roles of charge balance and proton management.[11,35] The manner in which anions associate and dissociate from the edge site determines whether OER exhibits a buffer dependence. Whereas OER activity of Co-OEC exhibits no dependence on P_i, Figure 8 establishes an inverse dependence on B_i. The more facile binding of B_i to the dicobalt edge site as opposed to P_i is illuminated by the association chemistry of these anions to $[\mathbf{1}(OH)_2]^{2+}$. Figure 4 establishes that $B(OH)_3$ is the binding agent in B_i buffer. $B(OH)_3$ can easily and rapidly accommodate coordination of a fourth OH^- to form $B(OH)_4^-$, so association of $B(OH)_3$ to a dicobalt edge site may proceed via nucleophilic attack of $B(OH)_3$ by a bound OH ligand of $[\mathbf{1}(OH)_2]^{2+}$. A condensation reaction may then take place between an intermediate borate complex and the adjacent η-OH ligand; a similar mechanism has been proposed for B_i association to FeOOH.[45] In support of this mechanism, we have found activation parameters ($\Delta H^‡ = 34.5 \pm 0.7$ kJ mol^{-1} and $\Delta S^‡ = -107 \pm 3$ J mol^{-1} K^{-1}) for this reaction that are consistent with a highly ordered transition state as opposed to breaking of an inert Co(III)−O bond, which would likely lead to a much higher activation enthalpy.[46] The microscopic reverse reaction will also facilitate $B(OH)_3$ dissociation from a dicobalt edge site (eq 6).

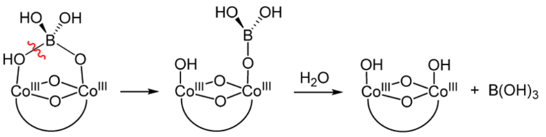

(6)

Conversely, direct attack of HPO_4^{2-} by a bound OH ligand of $[\mathbf{1}(OH)_2]^{2+}$ is unlikely as phosphate cannot accommodate the coordination of a fifth O atom. Generally, nucleophilic attack of phosphate occurs after Lewis acid activation by a transition-metal center.[47] Thus, the anation of the complex is expected to be very slow due to the rate-limiting dissociative cleavage of the inert Co(III)−O bond.[48] Phosphate dissociation from a dicobalt edge site may proceed by two pathways where HPO_4^{2-} is dissociative (eq 7, left) or is assisted by nucleophilic attack of an external hydroxide (eq 7, right).

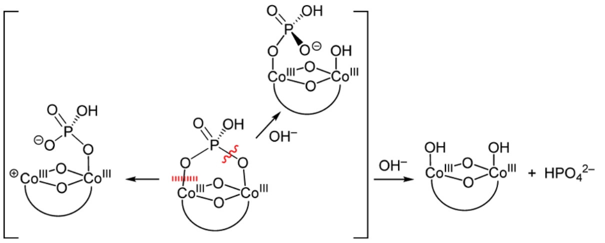

(7)

The importance of Co-OEC edge sites in promoting OER has been emphasized in computations.[49] The reactions in eqs 6 and 7 to furnish open coordination sites for O−O bond formation to occur at a dicobalt edge of Co-OEC are manifested in the observed OER activity of the catalysts in B_i and P_i. If anion association to an edge is competitively competent, then OER activity should be inhibited with increasing buffer concentration as fewer edge sites would be available to participate in the PCET activation cycle shown in Scheme 3. At modest to high buffer concentrations ($[P_i]$ = 40 mM to 1 M), there is no dependence of $[P_i]$ on water oxidation by Co-OEC.[12] Based on the binding studies of P_i to $[\mathbf{1}(OH)_2]^{2+}$, the P_i binding kinetics are likely too slow to establish a pre-equilibrium sufficiently fast to influence the electrochemically driven rate of catalysis, consistent with the zero-order dependence of P_i on the OER current density. Conversely, the B_i binding studies with $[\mathbf{1}(OH)_2]^{2+}$ establish that the binding to a dicobalt edge site is sufficiently fast that B_i will have an inhibitory effect on OER, as supported by the dependence of B_i in the activation controlled region of Figure 8. Accordingly, in B_i buffer, optimized OER requires a balance between the need for $B(OH)_4^-$ to accept the protons released from OER and the inhibitory effect of $B(OH)_3$. An additional role of the buffer is control of the morphology of the cobaltate structure.[10] PDF analysis of CoB_i vs CoP_i establishes that the former has a larger domain size of the cobaltate cluster than that in CoP_i. Finally, we propose that the larger domain sizes of CoB_i as compared to CoP_i may be rationalized by considering the disparate exchange kinetics of the capping buffer species on the edge of the growing films.[10] Irreversible binding of P_i to the edge sites may lead to the restriction of particle growth, whereas borate binding does not inhibit growth since borate may be rapidly displaced by incoming Co atoms.

■ CONCLUSION

The OER products of isotopically labeled Co-OEC water splitting catalyst, as determined by differential electrochemical mass spectrometry, indicate that the mechanism of O−O bond formation proceeds, at least in part, by an intramolecular coupling between oxygens atoms bound to the edge sites of the cobaltate catalyst. Binding studies of an edge site dicobalt molecular mimic show that buffer anions of B_i and P_i species mediate the OER activity. Facile changes in boron coordination and the ensuing interaction between B_i and terminal OH ligands explain the inhibitory effect that B_i has on water oxidation activity of Co-OEC, whereas exchange of P_i is too slow to influence the electrochemically driven rate of catalysis. More generally, the cobaltate clusters of Co-OEC lie at the border between extended solid heterogeneous catalysts and polynuclear homogeneous catalysts. We show here that the cobaltate clusters comprising a heterogeneous thin film are amenable to molecular level interrogation and thus exist at molecular/extended solid interface, a domain that has largely been neglected up until now. A dogma of heterogeneous systems is that "edges" matter in promoting catalytic transformations. We provide a rationale for such dogma by showing that OER in cobaltic oxides likely occurs at a dimensionally reduced dicobalt edge site. To this end, the studies reported here begin to unify heterogeneous and homogeneous catalysis at the molecular level.

■ ASSOCIATED CONTENT

Ⓢ Supporting Information

The Supporting Information is available free of charge on the ACS Publications website at DOI: 10.1021/jacs.6b00762.

Full experimental details, further DEMS data, crystallographic summary, pH titration data, ^{1}H NMR spectra, Job plot, and electrochemical data (PDF)

Crystallographic data (CIF)

Crystallographic data (CIF)

AUTHOR INFORMATION

Corresponding Author

*dnocera@fas.harvard.edu

Author Contributions

†These authors contributed equally.

Notes

The authors declare no competing financial interest.

ACKNOWLEDGMENTS

This material is based upon work supported by the U.S. Department of Energy Office of Science, Office of Basic Energy Sciences under award no. DE-SC0009565. C.N.B. acknowledges the NSF's Graduate Research Fellowship Program. We also thank the TomKat Foundation for support. We thank Prof. Joanne Stubbe for use of her stopped-flow spectrometer, Dr. Lisa Olshansky for assistance collecting the stopped-flow data, Dr. Kwabena Bediako for guidance collecting and analyzing the RDE data, Dr. Shaw Huang for assistance with ^{17}O NMR, and Michael Huynh and Dr. Chong Liu for assistance and helpful discussions regarding the DEMS experimental setup.

REFERENCES

(1) Lewis, N. S.; Nocera, D. G. *Proc. Natl. Acad. Sci. U. S. A.* **2006**, *103*, 15729.

(2) Lewis, N. S.; Nocera, D. G. *Bridge* **2015**, *46*, 41.

(3) *Electrodes of Conductive Metal Oxides*, Part A; Trasatti, S., Ed.; Elsevier: Amsterdam, 1980.

(4) Surendranath, Y.; Nocera, D. G. *Prog. Inorg. Chem.* **2011**, *57*, 505.

(5) Boggio, R.; Carugati, A.; Trasatti, S. *J. Appl. Electrochem.* **1987**, *17*, 828.

(6) Modestino, M. A.; Walczak, K. A.; Berger, A.; Evans, C. M.; Haussener, S.; Koval, C.; Newman, J. S.; Ager, J. W.; Segalman, R. A. *Energy Environ. Sci.* **2014**, *7*, 297.

(7) Kanan, M. W.; Nocera, D. G. *Science* **2008**, *321*, 1072.

(8) Surendranath, Y.; Dincă, M.; Nocera, D. G. *J. Am. Chem. Soc.* **2009**, *131*, 2615.

(9) Kanan, M. W.; Yano, J.; Surendranath, Y.; Dincă, M.; Yachandra, V. K.; Nocera, D. G. *J. Am. Chem. Soc.* **2010**, *132*, 13692.

(10) Farrow, C. L.; Bediako, D. K.; Surendranath, Y.; Nocera, D. G.; Billinge, S. J. L. *J. Am. Chem. Soc.* **2013**, *135*, 6403.

(11) Du, P.; Kokhan, O.; Chapman, K. W.; Chupas, P. J.; Tiede, D. M. *J. Am. Chem. Soc.* **2012**, *134*, 11096.

(12) Surendranath, Y.; Kanan, M. W.; Nocera, D. G. *J. Am. Chem. Soc.* **2010**, *132*, 16501.

(13) Lee, S. W.; Carlton, C.; Risch, M.; Surendranath, Y.; Chen, S.; Furutsuki, S.; Yamada, A.; Nocera, D. G.; Shao-Horn, Y. *J. Am. Chem. Soc.* **2012**, *134*, 16959.

(14) Friebel, D.; Bajdich, M.; Yeo, B. S.; Louie, M. W.; Miller, D. J.; Sanchez-Casalongue, H.; Mbuga, F.; Weng, T.-C.; Nordlund, D.; Sokaras, D.; Alonso-Mori, R.; Bell, A. T.; Nilsson, A. *Phys. Chem. Chem. Phys.* **2013**, *15*, 17460.

(15) Bergmann, A.; Martinez-Moreno, E.; Teschner, D.; Chernev, P.; Gliech, M.; Ferreira de Araujo, J.; Reier, T.; Dau, H.; Strasser, P. *Nat. Commun.* **2015**, *6*, 8625.

(16) Gonzalez-Flores, D.; Sanchez, I.; Zaharieva, I.; Klingan, K.; Heidkamp, J.; Chernev, P.; Menezes, P. W.; Driess, M.; Dau, H.; Montero, M. L. *Angew. Chem., Int. Ed.* **2015**, *54*, 2472.

(17) Zhang, M.; Frei, H. *Catal. Lett.* **2015**, *145*, 420.

(18) Zhang, M.; de Respinis, M.; Frei, H. *Nat. Chem.* **2014**, *6*, 362.

(19) Plaisance, C. P.; van Santen, R. A. *J. Am. Chem. Soc.* **2015**, *137*, 14660.

(20) Koroidov, S.; Anderlund, M. F.; Styring, S.; Thapper, A.; Messinger, J. *Energy Environ. Sci.* **2015**, *8*, 2492.

(21) Wang, H.; Rus, E.; Sakuraba, T.; Kikuchi, J.; Kiya, Y.; Abruna, H. D. *Anal. Chem.* **2014**, *86*, 6197.

(22) Peng, Z.; Freunberger, S. A.; Chen, Y.; Bruce, P. G. *Science* **2012**, *337*, 563.

(23) Jusys, Z.; Kaiser, J.; Behm, R. J. *Langmuir* **2003**, *19*, 6759.

(24) Baltruschat, H. *J. Am. Soc. Mass Spectrom.* **2004**, *15*, 1693.

(25) Wang, H.; Abruña, H. In *Electrocatalysis of Direct Alcohol Fuel Cells: Quantitative DEMS Studies Fuel Cells and Hydrogen Storage*; Bocarsly, A., Mingos, D. M. P., Eds.; Springer: Berlin, 2011; Vol. *141*, pp 33−83.

(26) Davenport, T. C.; Tilley, T. D. *Angew. Chem., Int. Ed.* **2011**, *50*, 12205.

(27) Davenport, T. C.; Tilley, T. D. *Dalton Trans.* **2015**, *44*, 12244.

(28) Davenport, T. C.; Ahn, H. S.; Ziegler, M. S.; Tilley, T. D. *Chem. Commun.* **2014**, *50*, 6326.

(29) Aygen, S.; Hanssum, H.; van Eldick, R. *Inorg. Chem.* **1985**, *24*, 2853.

(30) Müller, B. *ChemEQL*, ver. 3.1; Limnological Research Center EAWAG/ETH: Kastanienbaum, Switzerland, 2009.

(31) Bediako, D. K.; Costentin, C.; Jones, E. C.; Nocera, D. G.; Savéant, J.-M. *J. Am. Chem. Soc.* **2013**, *135*, 10492.

(32) Bediako, D. K.; Ullman, A. M.; Nocera, D. G. *Top. Curr. Chem.* **2015**, *371*, 173.

(33) Surendranath, Y.; Lutterman, D. A.; Liu, Y.; Nocera, D. G. *J. Am. Chem. Soc.* **2012**, *134*, 6326.

(34) McAlpin, J. G.; Surendranath, Y.; Dincaă, M.; Stich, T. A.; Stoian, S. A.; Casey, W. H.; Nocera, D. G.; Britt, R. D. *J. Am. Chem. Soc.* **2010**, *132*, 6882.

(35) Gerken, J. B.; McAlpin, J. G.; Chen, J. Y. C.; Rigsby, M. L.; Casey, W. H.; Britt, R. D.; Stahl, S. S. *J. Am. Chem. Soc.* **2011**, *133*, 14431.

(36) Winkler, J. R.; Gray, H. B. In *Structure and Bonding (Berlin)*; Mingos, D. M. P., Day, P., Dahl, J. P., Eds.; Springer: Berlin Heidelberg, 2012; Vol. *142*; p 17.

(37) Wang, L.-P.; Troy, V. V. *J. Phys. Chem. Lett.* **2011**, *2*, 2200.

(38) Jiang, Y.; Li, F.; Zhang, B.; Li, X.; Wang, X.; Huang, F.; Sun, L. *Angew. Chem., Int. Ed.* **2013**, *52*, 3398.

(39) Yang, X.-H.; Baik, M. *J. Am. Chem. Soc.* **2006**, *128*, 7476.

(40) Li, X.; Siegbahn, P. E M. *J. Am. Chem. Soc.* **2013**, *135*, 13804.

(41) Nguyen, A. I.; Ziegler, M. S.; Ona-Burgos, P.; Sturzbecher-Hoehne, M.; Kim, W.; Bellone, D. E.; Tilley, T. D. *J. Am. Chem. Soc.* **2015**, *137*, 12865.

(42) Lutterman, D. A.; Surendranath, Y.; Nocera, D. G. *J. Am. Chem. Soc.* **2009**, *131*, 3838.

(43) Ohlin, C. A.; Harley, s. J.; McAlpin, J. G.; Hocking, R. K.; Mercado, B. Q.; Johnson, R. L.; Villa, E. M.; Fidler, M. K.; Olmstead, M. M.; Spiccia, L.; Britt, R. D.; Casey, W. H. *Chem. - Eur. J.* **2011**, *17*, 4408.

(44) Bradley, S. M.; Doine, H.; Krouse, H. R.; Sisley, M. J.; Swaddle, T. W. *Aust. J. Chem.* **1988**, *41*, 1323.

(45) Peak, D.; Luther, G. W., III; Sparks, D. L. *Geochim. Cosmochim. Acta* **2003**, *67*, 2551.

(46) Swaddle, T. W. *Coord. Chem. Rev.* **1974**, *14*, 217.

(47) Williams, N. H.; Takasaki, B.; Wall, M.; Chin, J. *Acc. Chem. Res.* **1999**, *32*, 485.

(48) Chin, J.; Banaszczyk, M.; Jubian, V.; Zou, X. *J. Am. Chem. Soc.* **1989**, *111*, 186.

(49) Mattioli, G.; Giannozzi, P.; Bonapasta, A. A.; Guidoni, L. *J. Am. Chem. Soc.* **2013**, *135*, 15353.

JACS
JOURNAL OF THE AMERICAN CHEMICAL SOCIETY

Article

pubs.acs.org/JACS

X-ray Spectroscopic Characterization of Co(IV) and Metal–Metal Interactions in Co_4O_4: Electronic Structure Contributions to the Formation of High-Valent States Relevant to the Oxygen Evolution Reaction

Ryan G. Hadt,[†] Dugan Hayes,[†] Casey N. Brodsky,[∥] Andrew M. Ullman,[∥] Diego M. Casa,[‡]
Mary H. Upton,[‡] Daniel G. Nocera,[*,∥] and Lin X. Chen[*,†,§]

[†]Chemical Sciences and Engineering Division and [‡]Advanced Photon Source, Argonne National Laboratory, Lemont, Illinois 60439, United States

[§]Department of Chemistry, Northwestern University, Evanston, Illinois 60208, United States

[∥]Department of Chemistry and Chemical Biology, Harvard University, Cambridge, Massachusetts 02138, United States

S Supporting Information

ABSTRACT: The formation of high-valent states is a key factor in making highly active transition-metal-based catalysts of the oxygen evolution reaction (OER). These high oxidation states will be strongly influenced by the local geometric and electronic structures of the metal ion, which are difficult to study due to spectroscopically active and complex backgrounds, short lifetimes, and limited concentrations. Here, we use a wide range of complementary X-ray spectroscopies coupled to DFT calculations to study $Co(III)_4O_4$ cubanes and their first oxidized derivatives, which provide insight into the high-valent Co(IV) centers responsible for the activity of molecular and heterogeneous OER catalysts. The combination of X-ray absorption and 1s3p resonant inelastic X-ray scattering (K*β* RIXS) allows Co(IV) to be isolated and studied against a spectroscopically active Co(III) background. Co K- and L-edge X-ray absorption data allow for a detailed characterization of the 3d-manifold of effectively localized Co(IV) centers and provide a direct handle on the t_{2g}-based redox-active molecular orbital. K*β* RIXS is also shown to provide a powerful probe of Co(IV), and specific spectral features are sensitive to the degree of oxo-mediated metal–metal coupling across Co_4O_4. Guided by the data, calculations show that electron–hole delocalization can actually oppose Co(IV) formation. Computational extension of Co_4O_4 to CoM_3O_4 structures (M = redox-inactive metal) defines electronic structure contributions to Co(IV) formation. Redox activity is shown to be linearly related to covalency, and M(III) oxo inductive effects on Co(IV) oxo bonding can tune the covalency of high-valent sites over a large range and thereby tune E^0 over hundreds of millivolts. Additionally, redox-inactive metal substitution can also switch the ground state and modify metal–metal and antibonding interactions across the cluster.

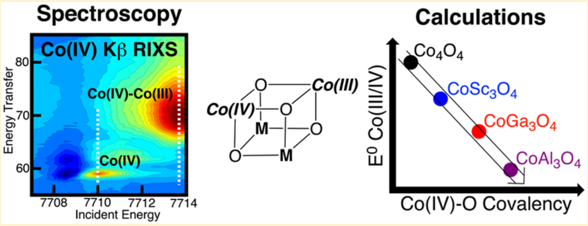

INTRODUCTION

The generation and storage of solar fuels is highly dependent on the efficiency of the oxygen evolution reaction (OER).[1−4] With the discovery of the proclivity of metalate oxidic clusters to promote OER,[5−8] research in the area has turned toward making better oxygen evolution catalysts (OECs) through geometric and electronic structural perturbations, which may involve metal substitution or alloying.[9−14] To understand the origin(s) of increased activity and to define structure/function relationships, the geometric and electronic structural perturbations of catalytic centers in their resting and active states need to be defined. Yet, reaction intermediates in OEC catalytic processes are often minority species in largely spectroscopically active backgrounds, thus severely limiting their detection and characterization. X-ray absorption spectroscopy (XAS) can be powerful in uncovering potential intermediates, as band edges can be sensitive to metal oxidation state. While metal K-edge XAS measurements in the hard X-ray regime can be insightful for both geometric and electronic structures, soft X-ray experiments provide access to metal L- and M-edges, which are subject to different selection rules and are more sensitive to electronic structure due to stronger interactions between 2p/3p and 3d electrons.[15] To this end, resonant inelastic X-ray scattering (RIXS) has become a powerful spectroscopic probe that provides "soft X-ray-like" data using hard X-rays,[16−18] opening the way for probing specific inner-shell processes with higher energy resolution and selectivity for various sample environments. In addition, as a two-photon process, RIXS provides rich and spectroscopically distinct information content relative to the single-photon X-ray absorption.[15−18]

Received: May 5, 2016
Published: August 12, 2016

ACS Publications

DOI: 10.1021/jacs.6b04663
J. Am. Chem. Soc. 2016, 138, 11017−11030

Properties intrinsic to heterogeneous catalysts such as geometric strain,[19−22] molecular engagement,[23−25] and redox-leveling[26] often allow for greater activity in the conversion of unreactive substrates. In defining the structure/function relationships that are at the root of this greater activity, comparisons drawn between molecular and heterogeneous analogs are beneficial.[27] Nonetheless, the design of homogeneous inorganic complexes as models of heterogeneous OEC catalysts is difficult to achieve, and few bona fide examples exist where both structure and activity are replicated. In recent years, inorganic molecular clusters have been developed as potential water oxidation catalysts, inspired by the Mn_4CaO_5 cluster of photosystem II (PSII) OEC.[28−30] An intensively studied heterogeneous/homogeneous pair with regard to OEC is the cobalt phosphate (CoP_i)/Co_4O_4 cubane pair, respectively, as CoP_i comprises Co_4O_4 cubanes as its basic structural element.[31,32] Co_4O_4 structures with different ligand sets (Figure 1 shows the $Co_4O_4(OAc)_4(py)_4$ primary ligation sphere) have been synthesized and characterized[33−40] and they have been intensively researched as molecular mimics of CoP_i.[41−53] The active sites of CoP_i are Co(IV) centers, and indeed, Co_4O_4 cubanes can house $S = {}^1/_2$ Co(IV) centers that exhibit electron paramagnetic resonance (EPR) signals comparable to those observed for Co(IV) in activated catalyst films.[51,52] The multifrequency EPR results (at <10 K) indicate that the Co(IV) spin density is symmetrically delocalized over the Co_4O_4 core,[52] and the X-ray crystal structure of the oxidized cubane has also been interpreted as fully delocalized.[53] These observations are related to the degree of electron−hole delocalization over the Co_4O_4 core, which can be described in terms of mixed-valency [i.e., effectively $Co(3.25)_4$ vs $Co(IV)Co(III)_3$]. In the Robin and Day classification, the effective oxidation states of the metals in a mixed-valent (MV) complex can be described as class I, II, or III.[54] The classification is dependent on the relative magnitudes of the vibronic trapping force vs the electronic coupling matrix element, H_{AB}. Class I complexes contain localized metal oxidation states at all temperatures, using all spectroscopic methodologies (i.e., strong vibronic trapping force, typically provided by asymmetric ligand fields, and small H_{AB}). At the other extreme, class III complexes give rise to spectral features reflecting average, effective oxidation states at all temperatures, using most spectroscopic methods (large H_{AB}, strong delocalization). In the latter case, it should be noted, even in the case of class III complexes, that core-hole spectroscopies can provide spectral features reflecting individual oxidation states.[55] The class II regime has a low-energy barrier for intramolecular ET (i.e., small vibronic trapping force, moderate H_{AB}, and delocalization) and typically exhibits either localized or delocalized characteristics, depending on spectroscopic time scale and/or temperature. Thus, the aforementioned results suggest significant class III mixed-valent (MV) character for oxidized Co_4O_4 on the EPR time scale ($\sim 10^{-9}$ s).[54]

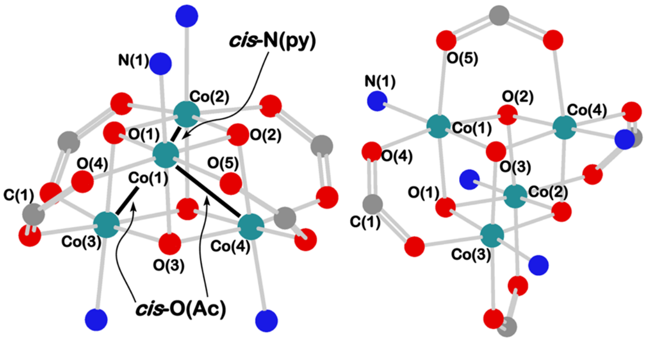

Figure 1. Different perspectives of the core structure of $Co_4O_4(OAc)_4(py)_4$ with (left) N(py) axial and (right) O(Ac) axial. Acetate and pyridine ligands have been truncated for clarity.

The ability to form high-valent Co(IV) within the Co_4O_4 topology has been attributed to efficient electron−hole delocalization,[41,47,56] which is also coupled to the formation of reactive species.[41,47,50] In CoP_i, the minimalist active core is composed of two adjacent formal Co(IV) centers, which promote the proton-coupled electron transfer (PCET) reactivity needed for water splitting.[31,57] Additionally, Co(IV) in CoP_i thin films likely facilitates PCET-driven conduction between active sites and the electrode via Co(III)/(IV) self-exchange or hopping,[31,50,58−60] which can be related directly to class II/III MV character.[54,61−65] Akin to the results for CoP_i, two electron−holes [formally 2Co(III)/2Co(IV)] have been proposed to be necessary for the observed OER activity of the $Co_4O_4(OAc)_4(py)_4$ cubane.[41,47] In light of the importance of Co(IV) in both CoP_i and cubane systems, direct spectroscopic detection and characterization of high-valent, partially or fully delocalized MV species is crucial to developing comparative structure activity relations between molecular and heterogeneous OEC catalysts.

Herein we utilize a combination of Co K- and L-edge X-ray absorption spectroscopies as well as 1s3p (Kβ) RIXS as sensitive probes of the geometric and electronic structures of Co_4O_4 cubanes. The combined XAS/RIXS measurements provide a powerful means of "mapping" Co(IV) contributions in these systems against a spectroscopically complex background. The XAS/RIXS methods effectively probe "localized" Co(IV) electronic structure, in part due to the intrinsically faster time scale of the inner-shell electronic transitions in X-ray spectroscopic measurements ($\sim 10^{-15}$ s) relative to EPR ($\sim 10^{-9}$ s). Both Co K-edge and L-edge XAS provide direct characterization of the low-spin 3d-manifold of Co(IV). Specific spectral features present in the Co K-edge and 1s3p RIXS have uncovered oxo-mediated metal−metal (M/M) interactions that are crucial to the basic electronic structure of the cubane core. The experimental data, combined with electronic structure calculations, indicate that the redox active molecular orbital (RAMO) of Co_4O_4 is relatively ionic, which can result from electron−hole delocalization and oppose Co(IV) formation. These observations have been extended to cubanes with substituted redox inactive metals (e.g., CoM_3O_4, M = Al, Ga, or Sc) to provide further insight into the interplay between electron−hole delocalization and the formation of high-valent species in a Co(IV) oxidic framework. These results together provide new insights into the redox transport and activity of molecular and heterogeneous OEC catalysts composed of cubane cores.

RESULTS

Co K-Edge XANES. The Co K-edge XANES spectra for the neutral $Co(III)_4$ (**1**) and oxidized $Co(IV)Co(III)_3$ (**2**) states of the $Co_4O_4(OAc)_4(py)_4$ cubane are given in Figure 2. The pre-edge region (labeled 1s → 3d in Figure 2) is given in the inset; pre-edge and edge energies of **1** are ∼7709.6 and 7722.1 eV, respectively. Upon one-electron oxidation, the edge energy of **2** shifts by ca. +0.4 eV to ∼7722.5 eV and the pre-edge shift is very slight (<0.2 eV). These XAS shifts upon oxidation are

DOI: 10.1021/jacs.6b04663
J. Am. Chem. Soc. 2016, 138, 11017−11030

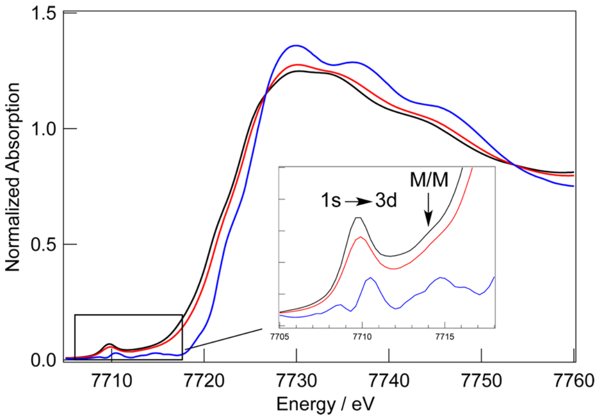

Figure 2. Co K-edge XAS: **1** (black line), **2** (red line), and Co(IV) (blue line). Co(IV) spectrum has been renormalized to the edge jump. Inset: expanded region of the pre-edge.

consistent with a partial increase in Z_{eff}. Another feature is observed at ~7714 eV (labeled M/M in Figure 2, vide infra) for both **1** and **2**, and its intensity does not appear to vary significantly with oxidation.

The rates of intramolecular self-exchange ET for delocalized class III complexes are on the order of ~10^{12} s^{-1}.[64,65] Given the ultrafast nature of the core-hole lifetimes (~1−4 fs), XAS provides an opportunity to spectroscopically resolve delocalized MV electronic structure. The formation of a core-hole potential in the final state will also result in partial or full localization.[55] Thus, the data are treated in terms of localized Co(IV) and Co(III) sites, and an approximate "Co(IV)" spectrum can be obtained by taking a scaled difference spectrum of **1** from **2** [i.e., **2** − ($^3/_4$)**1**]. It is noted that the subtraction method does not account for potential differences in Co(III)−ligand covalency and bond distances between **1** and **2**; however, for simplicity and the purposes of the work described herein, will use a metal oxidation state formalism and describe the oxidation as Co(IV) with the caveat that the oxidation may have some parentage involving oxygen. That said, the subtracted spectra exhibit strong similarities to iso-electronic, low-spin d^5 systems. The renormalized Co(IV) spectrum (Figure 2, blue spectrum) has an edge energy of ~7723.4 eV (~1.3 eV higher in energy relative to **1**), consistent with a complete Co oxidation state change from Co(III) to Co(IV).[7,66] The pre-edge region of Co(IV) exhibits a split structure, similar to isoelectronic, low-spin d^5 Fe(III) complexes[67] and Fe(III) in Fe(II)/Fe(III) mixed-valence complexes;[68] pre-edge peak maxima are at ~7708.6 and 7710.5 eV (Δ = 1.9 eV). For low-spin octahedral Fe(III) complexes, these peaks have been assigned as 1s → 3d transitions and correlate to the $(t_{2g})^6$ and $(t_{2g})^5(e_g)^1$ excited final states. Co(IV) also exhibits another broad feature centered at ~7714.5 eV, which is similar in energy to **1** but more pronounced. Similar features have been observed in α-Fe_2O_3[69] and $LiCoO_2$.[70,71]

Co K-edge EXAFS. The Co K-edge k^3-weighted EXAFS spectra and their Fourier transforms are given in Figure 3. The *R*-space data of **1** (black line, Figure 3A) shows intense features at *R* values of ~2.8 and 1.9 Å (at *R* ~ 2.35 and 1.4 Å, respectively, in Fourier transformed spectra without phase correction) associated with Co−Co and Co−O/N vectors, respectively. The spectrum of **2** shows a broadening and decreased amplitude of the Co−Co feature, consistent with multiple oxidation states arising from a mixture of Co(IV) and Co(III) in the oxidized Co_4O_4 cluster. The EXAFS data have been obtained from the weighted difference spectrum of Co(IV) from above [blue line in Figure 2, **2** − ($^3/_4$)**1**]. The Co−Co feature of Co(IV) is now similar in spectral width and intensity to that of Co(III) in **1**. The Co−Co and Co−O/N features of Co(IV) shift to slightly shorter *R*-values due to increased Z_{eff}.

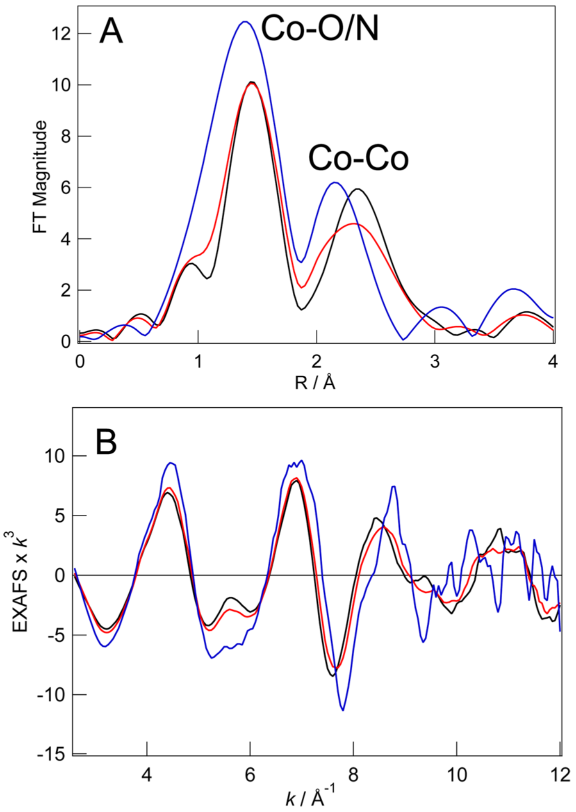

Figure 3. Co K-edge EXAFS data: (A) Fourier transforms and (B) k^3-weighted EXAFS oscillations of **1** (black line), **2** (red line), and Co(IV) (blue line).

Due to the presence of multiple different O/N and Co−Co distances, a full fit to the EXAFS data would be underdetermined. However, the experimental EXAFS data of **1** and Co(IV) can still be well-modeled using the neutral and Co(IV) DFT distorted geometries, respectively. These results are given in Table S1 and Figure S1 of the Supporting Information (SI). For more details, see the text below Table S1 (SI). The first-shell for **1** (Co−O/N in Figure 3) can be modeled with three shorter Co−O (~1.87 Å) and three longer Co−O/N bonds (~1.94 Å). The Co−Co peak can be modeled with two Co−Co single-scattering pathways of ~2.73 and 2.85 Å and one other single-scattering pathway [Co−C(1), 2.86 Å, *N* (degeneracy) = 2]. The longer Co−Co vector arises from the Co(1)−Co(2) interaction [*N* = 1; see Figure 1, *cis*-N(py)]. The other is the Co(1)−Co(3) and Co(1)−Co(4) interactions [*N* = 2, *cis*-O(Ac), Figure 1]. Analogous results were obtained for the Co(IV) data (blue line in Figure 2) and the Co(IV) localized DFT geometry (Table S1 and Figure S1, SI). Relative to **1**, most metal−ligand bond distances contract in Co(IV) (blue lines, Figure 3), reflecting increased Z_{eff}. The *cis*-N(py) Co−Co distance decreases slightly from 2.85 to 2.82 Å, while the 2-fold degenerate Co−Co [*cis*-O(Ac)] decreases from 2.73 to 2.68 Å. Additionally, the Co−O(oxo) bond distances

DOI: 10.1021/jacs.6b04663
J. Am. Chem. Soc. 2016, 138, 11017−11030

contract from 1.87 to 1.82 Å, and the Co−O(AcO) bond lengths decrease from 1.96 to 1.91 Å. The Co−N(py) distance increases from 1.93 to 2.00 Å. Thus, the EXAFS data of Co(IV) can be described and modeled using the Co(IV) distorted DFT geometry. Additionally, the relative intensity ratio of the first and second coordination shells in the *R*-space spectra of Co_4O_4 are more similar to ultrathin CoP_i[7] films than thicker CoP_i films and amorphous cobalt oxides,[72] reflecting the lower number of Co−Co vectors per Co ion in the surface CoP_i sites than in the bulk CoP_i.[7]

Co L-Edge XAS. The L-edge XAS data are given in Figure 4, normalized to unity at ~780 eV. Two intense features are observed at ~779 and 793 eV for **1**. The L-edge excites Co 2p core electrons to unoccupied 3d orbitals [e.g., $2p^63d^6 \rightarrow 2p^53d^7$ for Co(III)]. Two features, split by ~14 eV, are observed due to 2p core-hole spin−orbit coupling (SOC), resulting in a lower-energy L_3 ($J = {}^3/_2$) and higher-energy L_2 ($J = {}^1/_2$) edge. Upon oxidation, the L_3- and L_2-edges of **2** shift to higher energy (~0.5 and ~0.2 eV, respectively). Note that the energy positions are not necessarily reflective of energy differences between states without the 2p core-hole and are therefore also sensitive to the strong 2p/3d interactions. The L_3-edge of **2** broadens considerably, with growth of distinct shoulders on the lower and higher energy sides. The Co(IV) spectrum (Figure 4, blue line), obtained as for the Co K-edge, shows splitting on the L_3- and L_2-edges with peak maxima at ~777.4 and 779.5 eV ($\Delta \cong 2.1$ eV) and ~792.2 and 794 eV ($\Delta \cong 1.8$ eV), respectively. As in the K-edge XAS, the overall spectral shape of the L-edge is similar to isoelectronic, low-spin d^5 Fe(III).[73−75]

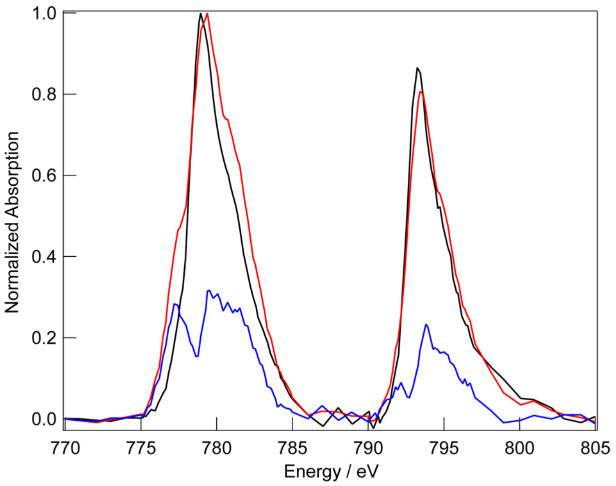

Figure 4. Co L-edge XAS: **1** (black line), **2** (red line), and Co(IV) (blue line).

Co 1s3p Resonant Inelastic X-ray Scattering. K*β* emission involves the decay of 3p electrons to a 1s core-hole formed from ionization or promotion to unoccupied bound states on the X-ray absorbing atom. The 3p/3d electron interactions are strong, thus making K*β* sensitive to the electronic structure of the metal, especially spin state.[76] The Co K*β* emission spectra obtained using 7730 eV excitation are given in Figure S2 (SI) and are consistent with an $S = 0$ to $S = {}^1/_2$ conversion.[76]

The Co 1s3p (K*β*) RIXS data were collected at Sector 27 at the Advanced Photon Source using the MERIX instrument.[77] RIXS planes for **1** and **2** are given in Figure 5. The data are normalized to the 1s → 3d pre-edge intensities (Figure 2).

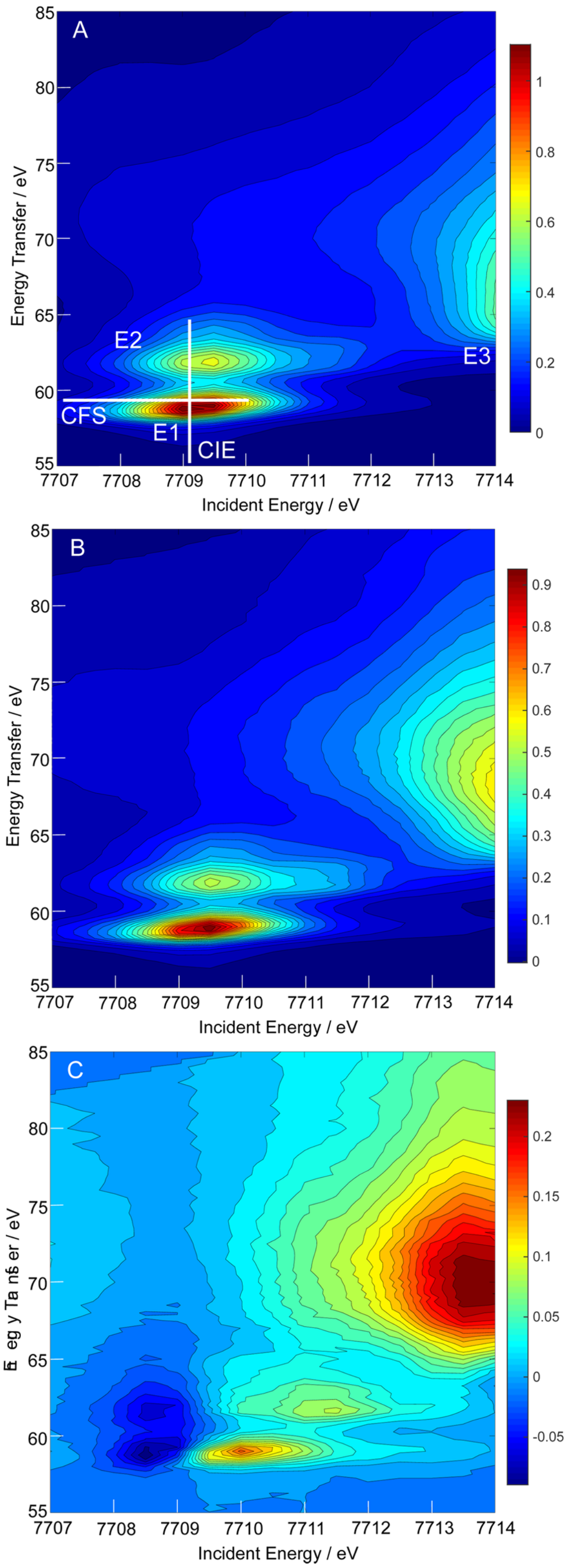

Figure 5. 1s3p RIXS planes for (A) **1**, (B) **2**, and (C) Co(IV) [e.g., **2** − (${}^3/_4$)**1**].

Figure S3 (SI) provides a schematic description of the overall RIXS process. Briefly, the two-dimensional plots have incident energy (Ω) and energy transfer (Ω − *ω*) axes. K*β* RIXS involves exciting at Co K-edge energies (e.g., 1s → 3d/4p

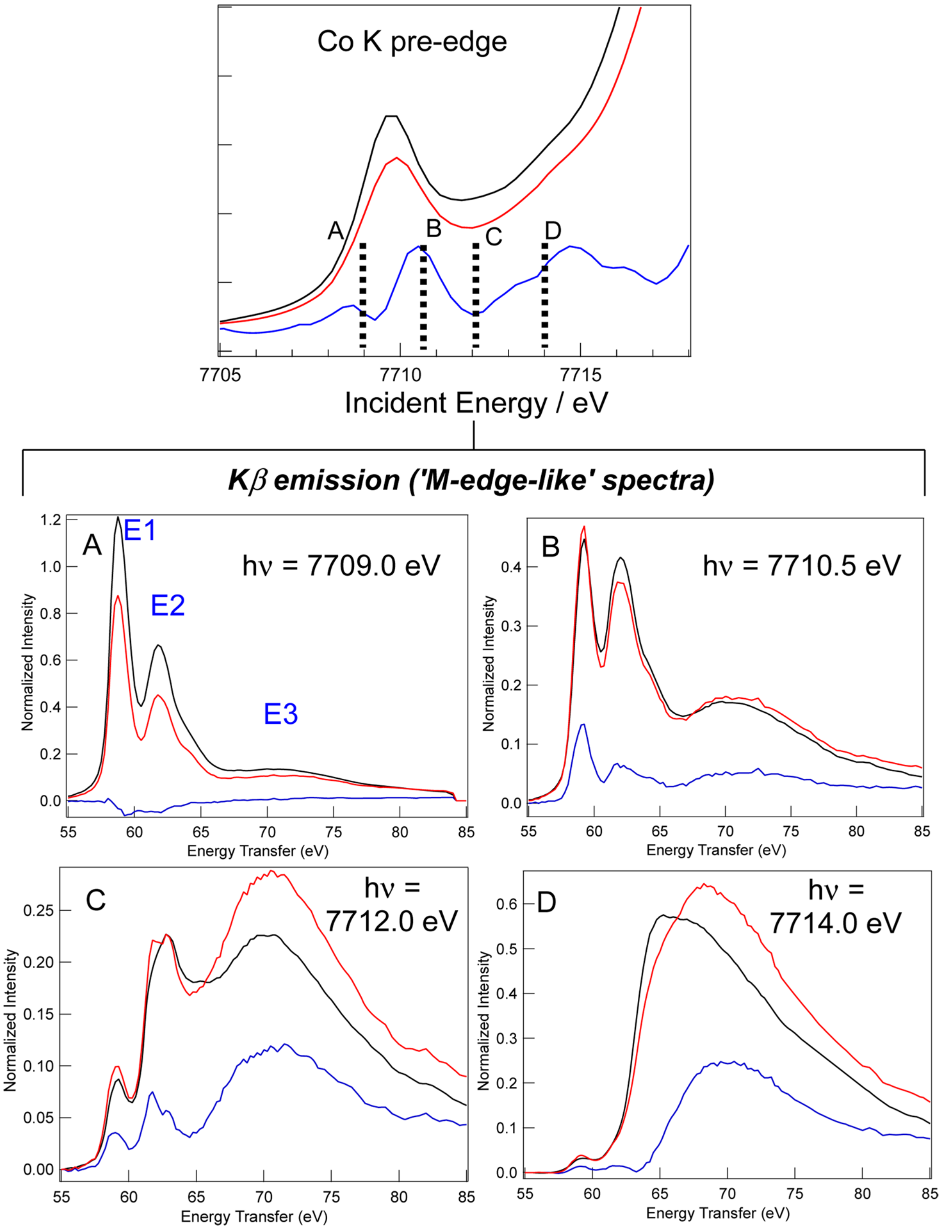

Figure 6. Constant incident energy cuts of the 1s3p RIXS planes: **1** (black line), **2** (red line), and Co(IV) (blue line).

transitions) and monitoring the resulting 3p → 1s K*β* emission. Taking a difference between the incident and fluorescence energies ($\Omega - \omega$) allows the data to be plotted with an energy transfer (ET) axis. The RIXS plane is constructed by measuring the K*β* emission as a function of incident energy. The two-photon process from initial to final state (gray dashed arrow in Figure S3, SI) corresponds roughly to a 3p → 3d absorption process (i.e., M-edge) located at ~60 eV for Co. However, the RIXS data can vary significantly from M/L-edge absorption due to different selection rules for the single-photon absorption (XAS) and two-photon RIXS process.[15,76]

The RIXS plane for **1** (Figure 5A) shows a strong feature centered at the 1s → 3d pre-edge energy (~7709.5 eV, Figure 2). The features in the RIXS plane are broadened in the incident energy axis from the 1s core-hole lifetime and along the ET axis from the 3p core-hole lifetime, resulting in anisotropy about the diagonal. Within the pre-edge region, **1** exhibits two sharper, strong ET features with energies of ~58.75 (E1) and 61.75 (E2) eV; a broader feature is observed at ~71 eV (E3), which increases in intensity as the incident energy increases, becoming dominant at incident energies greater than ~7712 eV.

The overall appearance of the RIXS plane of **2** appears similar to that of **1**, but several differences are observed. In the pre-edge, **2** also exhibits two sharp features with ET maxima at ~59.00 (E1) and 62.00 (E2) eV; the broader feature, E3, at ~71 eV is also present for **2** and increases in intensity with increasing incident energy. The relative intensity of E3 is greater for **2** than for **1**.

Similar to the difference spectra described above, a difference RIXS spectrum (Figure 5C) clearly displays the spectral contributions that derive from formation of Co(IV) in Co_4O_4. Spectral intensity is observed at incident energies >7709.5 eV, with larger differences observed from 7712 to 7714 eV (Figure 5C). These features appear in the energy regions labeled M/M in the Co(IV) K-edge XAS (Figure 2). A small amount of residual negative intensity is observed in the Co(IV) RIXS plane at energies less than 7709 eV, which is likely due to the very low signal intensity, large Co(III) background, and the approximate nature of the overall difference spectrum, as discussed above. Generally, the sharpness of the E1 and E2 features is consistent with localized, quadrupole excitations to 3d-based intermediate states. Interestingly, the resonantly excited E3 feature is very broad and provides strong evidence that it derives from delocalized intermediate state(s) that involve oxygen-mediated M/M bonding in Co_4O_4,[69] indicating that it is a direct probe of M/M interactions and oxidation state in clusters and anodes. In the following section, the RIXS data are further analyzed by taking slices or cuts along the *x*- and *y*-axes of Figure 5.

Constant Final State Cuts. Constant final state (CFS) cuts are slices in the RIXS plane through the ET axis (labeled CFS in Figure 5A). The CFS cuts provide a spectroscopic probe that fixes the final state [$\Omega - \omega$, 3p^{5}3d$^{7(6)}$ for Co(III) (Co(IV))] and scans the intermediate states (1s^{1}3d$^{7(6)}$) that decay to that particular final state, thus providing an effective probe of all 1s K-edge resonances that decay into a fixed final state.

A series of CFS cuts for **1** and **2** in the 7707−7714 eV region are shown in Figure S4 (SI). For these, CFS cuts are shown through E1 or E2 features, as labeled in Figure 5A. Representative CFS cuts for **1**, **2**, and Co(IV) at ET values of 59 (E1) and 63 (E2) eV are given in Figure S4, parts E and F (SI), respectively. The cuts through E1 result in sharp pre-edge-like features centered around 7709.5 eV. The Co(IV) spectrum (blue line, Figure S4E, SI) shows increased intensity at incident energies of ∼7710 eV, consistent with the sharp feature observed in the Co K-pre-edge (Figure 2). CFS cuts taken through E2 are given in Figure S4F (SI). Additional intensity is now observed at incident energies >7710 eV for both **1** and **2**. The Co(IV) spectrum taken through E2 now shows additional intensity across the 7710−7714 eV region. Thus, it appears that difference CFS cuts allow for Co(IV) contributions in the pre-edge region to be distinguished, and the intensity distribution is dependent on the specific final states that are selected (e.g., via slices in E1 vs E2). These cuts are also shifted toward higher incident energies than for Co(III) due to the higher Z_{eff} of Co(IV), similar to the Co(IV) K-pre-edge in Figure 2.

Constant Incident Energy Cuts. Constant incident energy cuts, labeled CIE in Figure 5A, are taken through the incident energy axis. These $K\beta$ emission spectra are representative of "M-edge like" spectra, with ETs around 60 eV for Co (dotted gray arrow in Figure S3, SI). The CIE cuts hold the 1s^{1}3d^{n+1} intermediate state (Ω) fixed while the final states ($\Omega - \omega$) are varied/scanned. This indicates what final states can be reached via a particular 1s resonance.

CIE cuts across the RIXS planes of **1** and **2** are given in Figure S5 (SI). Some representative CIE cuts are given in Figure 6, which also shows the CIE resonance profiling behavior. Respective excitation energies are indicated within the K-pre-edge, and E1, E2, and E3 are labeled in Figure 6A. The CIE cuts are strongly excitation energy dependent, with E1 and E2 being resonantly excited in the K-pre-edge features involving quadrupolar 1s → 3d excitation. E3 is resonantly excited at energies >7712 eV. Splitting/structure is evident for E2.

Co(IV) CIE cuts (Figure 6, blue line) grow in at excitation energies greater than ∼7709.5 eV and increase with increasing excitation energy, indicating resonant excitation. This interpretation is consistent with the above observations that Co(IV) contributes strongly at pre-edge energies higher than Co(III). However, the low-energy region of the pre-edge does not resolve specific emission spectral features associated with Co(IV).

Given the large differences observed in the ∼7712 eV pre-edge region in the Co K-edge and $K\beta$ RIXS, selective integrated spectra of Co(III)- and Co(IV)-based emission have been obtained by integrating the emission intensity through the 7112−7114 eV region (Figure 7). The data are highly sensitive to oxidation state. In particular, the lower-energy features (∼60−63 eV) show variations in intensity distribution, and the higher-energy region is strongly blue-shifted (∼3 eV) and shows differences in shape and structure. These data appear to represent a powerful probe of different oxidation states in high-valent, delocalized MV species.

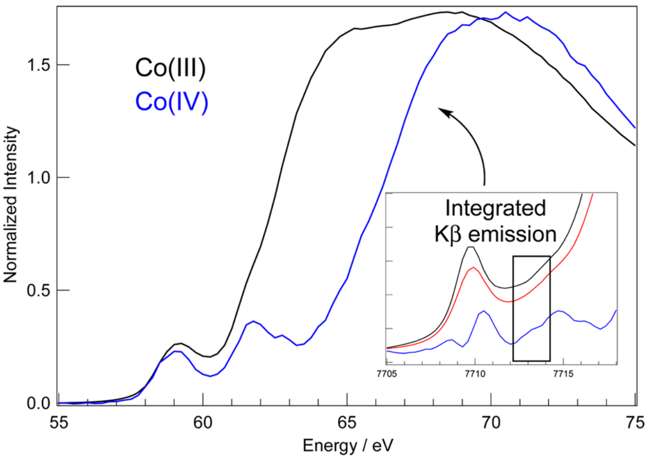

Figure 7. Integrated constant incident energy cuts of the 1s3p RIXS planes (sum of $K\beta$ emission in the 7112−7114 eV region is shown as an inset) of Co(III) in **1** (black) and Co(IV) in **2** (blue). Data are normalized for comparison.

In summary, the RIXS planes involve rich, oxidation state sensitive spectral features. E1, E2, and E3 are observed for **1**, **2**, and the difference spectrum obtained for Co(IV). While the absolute energies of E1 and E2 do not appear to be sensitive to oxidation state, intensity differences are observed in the Co(IV) spectra [Figures S5 (SI) and 6] with especially notable differences in splitting observed in the E2 energy region. E3 appears most sensitive to oxidation state. *Importantly, these spectroscopic data provide direct complementary probes of Co(IV) and M/M interactions (see below).*

Electronic Structure Calculations. Co_4O_4 Ground State. Several computational studies have explored mechanisms of water oxidation by Co_4O_4 cubanes with various ligand sets.[41,45,47,78,79] The majority employed the B3LYP functional [or a variation with 15% Hartree−Fock (HF) exchange] though one investigation used the PBE0 functional (25% HF exchange) to describe the spin delocalization over the cubane.[52] A computational goal was to evaluate the covalency of the ligand−metal bonds of the Co_4O_4 cubane and the oxidation potential as related to the experimental X-ray spectral data. Both of these experimental observables, covalency and oxidation potential, will be sensitive to the amount of HF exchange in the exchange−correlation functional. Several benchmarking calculations were therefore performed; full computational benchmarking results are given in the Supporting Information (see Tables S3−S5, SI). Briefly, the ground state of **2**, as determined by EPR measurements at 10

K, is mixed-valent and fully delocalized [i.e., 4Co(∼3.25)]. In this context, the localized electronic configuration [3Co(III)/Co(IV)] can be considered as an excited state. The energy separation between these states is sensitive to the amount of HF exchange.[80,81] Generally, delocalized MV ground states are favored using pure generalized gradient approximation (GGA) functionals (0% HF), which suffer from a self-interaction error;[81,82] increasing HF exchange will localize the ground state wave function. Accordingly, the localized wave function of Co_4O_4 becomes the ground state at values of HF exchange >15% (Table S3, SI). We find that values of 15% HF exchange or less are needed to reproduce the time-averaged delocalization as determined by EPR. The calculated oxidation potential [$E^0(1)$, obtained from the adiabatic ionization energies] of Co_4O_4 is also sensitive to HF exchange. The experimental oxidation potential $E^0(1)$ of Co_4O_4 is 0.94 V vs NHE in CH_3CN (Figure S7, SI), which involves one-electron oxidation of 4Co(III) to the delocalized Co(IV)-containing cluster. The calculated adiabatic ionization energy (IE) of Co_4O_4 is 5.41 eV, including CH_3CN solvation effects using the polarized continuum model (Table 2). $E^0(1)$ is calculated to be 0.97 V vs NHE in CH_3CN (Table 2: E^0 = IE − 4.44 eV) at 15% HF exchange. The calculated $E^0(1)$ is severely underestimated at values of HF <15% (Tables S4 and S5, SI); thus, 15% HF exchange was used for subsequent calculations.

Geometry-optimized bond distances of all models are given in Table S2 (SI). The neutral and localized structures can adequately reproduce the EXAFS data. The calculated Co(d) and oxo(p) characters for the t_{2g}- and e_g-based orbitals of the cubane are given in Tables 1 and S6 (SI) [Mulliken population analyses (MPAs)]. We focus on the singly unoccupied β molecular orbital (MO) [e.g., the β lowest-unoccupied MO (β-LUMO)], the t_{2g}-based RAMO of Co_4O_4. The contour of the β-LUMO for the delocalized wave function is shown in Figure 8A and is consistent with previous literature.[52] The Co(d) and oxo(p) characters for the delocalized t_{2g}-based ground state by MPA are 63.8 and 25.6, respectively (Table 1, sums of all four Co or oxo atoms). The Mulliken spin densities reflect the β-LUMO and are calculated to be 0.16 and 0.09 for individual Co and O(oxo) atoms. This is qualitatively similar to previous literature;[52] the values here are slightly more Co-based due to the use of 15% HF exchange vs the 25% as previously used (see Tables S4 and S5 of SI for HF dependence on covalency).

Table 1. Mulliken Population Analyses for the β-Based Unoccupied 3d MOs of Various Cubane Structures

	Co(d)	oxo(p)	OAc(p)	N(py)(p)
		Co_4O_4 (loc)[b]		
t_{2g} hole	61.8 (10.5)[a]	17.5	5.2	0.8
sum e_g	108.6 (12.7)[a]	53.8	14.2	6.2
		Co_4O_4 (deloc)[c,d]		
t_{2g} hole	63.8	25.6	4.6	1.1
sum e_g (/Co)	498.0 (124.5)	218.6 (48.3)	55.2 (13.8)	25.5 (6.4)
		$CoAl_3O_4$		
t_{2g} hole	46.1	47.5	2.2	0.4
sum e_g	117.5	53.2	21.0	0.4
		$CoGa_3O_4$		
t_{2g} hole	50.9	44.0	2.5	0.1
sum e_g	117.1	53.9	19.4	0.5
		$CoSc_3O_4$		
t_{2g} hole	57.6	33.8	4.6	0.0
sum e_g	113.0	48.0	18.5	0.2
	Co(d)	OH	H_2O	
		$Co(OH)_3(OH_2)_3$		
t_{2g} hole	63.5	35.0	0.4	
sum e_g	120.0	62.7	19.1	

[a]MPA characters of the other Co atoms for the localized wave function [formally Co(III)]. [b]Localized Co(IV). [c]Delocalized Co(IV). [d]Parenthetic values are total oxygen and nitrogen p-character.

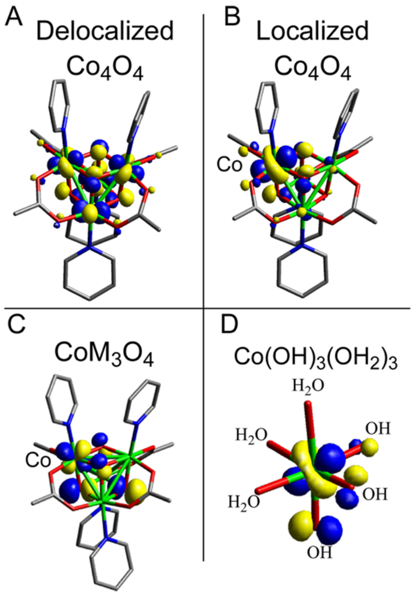

Figure 8. β-LUMOs for various versions and electronic structures of the cubane and a mononuclear model.

The calculated MPA value of 63.8 total Co(d) character for the t_{2g}-based electron−hole indicates that the wave function is mainly Co-centered, partially ionic, and consistent with the relatively intense t_{2g} feature in the L-edge results above. However, to directly compare to experiment, the covalency of the localized wave function must also be considered. As mentioned, the localized wave function is actually the ground state at >15% HF; therefore, the localized, distorted geometry is obtained using a BP(20HF)86 functional. Subsequent single-point calculations were performed using 15% HF exchange as applied to the delocalized wave function, allowing for a direct comparison. The β-LUMO of the localized wave function (Figure 8B) clearly shows that the electron−hole is primarily localized to a single Co center. The total Co(d) and oxo(p) characters are 61.8 and 17.5 (23.5), relative to 63.8 and 25.6 (31.3) for the delocalized state [parenthetic values in Table 1 are total oxygen and nitrogen p-character, thus accounting for small contributions from OAc and N(py) ligands]. Note that the value of 61.8 Co(d) is for the ionized Co atom only. A small amount of "spectator Co" character (10.5) is present in the t_{2g}-based hole for the localized state. Including this amount in the total Co(d) character gives 72.3. Thus, the total Co(d) character of the localized wave function is 61.8 or 72.3, depending on the spectator amount. Given the importance of this value, a few points are noted. With HF exchange <15%, the Co(d) character of all four Co atoms is similar for delocalized (deloc) and localized (loc) geometries (Table S5, SI; deloc/loc 70.8/70.0, 69.0/68.4, and 66.7/67.2 for 0, 5, 10% HF, respectively). At values of HF >15%, the Co(d) character of all four Co atoms is slightly larger for the localized wave function (deloc/loc 63.8/72.3, 60.4/77.7, and 55.8/80.7, for 15, 20, and 25% HF, respectively). This "spectator Co" character derives from partial electron−hole delocalization, even in the localized, distorted geometry. Thus, small amounts of electron−hole delocalization in distorted geometries of the Co_4O_4 cluster cannot be ruled out. Given that the L-edge measurement involves excitation of core electrons on Co, we tend to favor values closer to ~62% (i.e., no spectator Co). Future experiments, including perturbed Co_4O_4 structures, will help clarify this issue. Thus, delocalized and localized models appear to have similar amounts of Co d-character in their RAMOs (63.8 and 61.8, respectively), although, the localized state has less total ligand character than the delocalized state (23.5 and 31.3, respectively). This difference in ligand character occurs as localization decreases the effective number of oxo-ligands involved in bonding from four to three (see Figure 8, part A vs B), resulting in less oxo(p) character relative to delocalized Co(IV) (17.5 vs 25.6; a ratio of ~3/4). This decreased oxo character in the localized state is distributed over "spectator Co" due to a small degree of partial delocalization. Note, the β-LUMO of a mononuclear model of a corner site of Co_4O_4 [e.g., $Co(OH)_3(OH_2)_3$] gives calculated Co(d) and O(p) characters of 63.5 and 35.0, respectively, similar to the values of 63.8 and 31.3 of the delocalized wave function (Figure 8D). *Thus, electron delocalization does not appear to decrease the amount of Co d-character in the RAMO, but an intrinsic amount of Co(IV)-based d-character is delocalized, which can change the distribution of the ligand character.* This is important when considering how electron−hole delocalization contributes to the redox properties of Co_4O_4, as is discussed below.

In addition to the Co(d) character of the RAMO, it is important to consider the distribution of the t_{2g} hole over the t_{2g}-dπ orbitals. The t_{2g}-hole of delocalized Co_4O_4 has been described as d_{xy} with partial d_{xz}/d_{yz} mixing,[52] suggesting that the electron−hole undergoes partial localization in CoP_i. Indeed, the localized wave function calculated here takes on a different d-orbital mixing character (i.e., $d_{xz}/d_{yz}/d_{xy}$). As previously observed, the t_{2g}-hole of the delocalized state appears tilted or mixed $d_{xz}/d_{yz}/d_{xy}$ due to the canting of the Co(d)- and oxo(p)-orbitals to increase overlap (Figure 8A).[52] The degree of d-orbital mixing was not evaluated at that time, but it is calculated here to be ~45% d_{xz}/d_{yz} and ~55% d_{xy}. This mixing changes to ~56% $d_{xz/yz}$ and ~44% d_{xy} upon localization. *Thus, localization changes the nature of the d-orbital in the RAMO.* This is an important consequence for catalysis and redox properties, as different d-orbital characters allow for different orientations and metal−ligand bonding within the cubane core.

Oxidation Potential and Structural Perturbations of Co_4O_4: CoM_3O_4 (M = Al, Ga, and Sc). The RAMO of 2 is partially ionic, despite strong electron−hole delocalization over all Co and O(oxo) atoms. Given our experimental and computational considerations of localized vs delocalized wave functions, several structurally perturbed models of Co_4O_4 were targeted to gain insight into localized Co-based oxidation processes and to evaluate electron−hole delocalization contributions to redox chemistry. To do so, we evaluated the electronic structure of a single Co center within a CoM_3O_4 core, M = Al(III), Ga(III), or Sc(III), which were chosen because they are redox-inactive and conserve total charge on the cubane.

Table 2. Comparison between Experimental and Computational Oxidation Potentials

model	E^{0a}	$E^0(2)^a$	ΔE^b
Co_4O_4 (exp)	0.94	2.09	1.15
Co_4O_4 (calc)	0.97	2.15	1.18
$CoAl_3O_4{}^c$	0.64 (−0.33)	1.94 (−0.21)	1.30
$CoGa_3O_4{}^c$	0.72 (−0.25)	1.94 (−0.21)	1.22
$CoSc_3O_4{}^c$	0.86 (−0.11)	1.96 (−0.19)	1.10
$Co(OH)_3(OH_2)_3{}^c$	1.26 (0.29)		

[a] Ionization energies converted to V vs NHE (IE − 4.44 eV). [b] $E^0(2) - E^0(1)$. [c] Parenthetic values is the difference in calculated E^0 from that calculated for Co_4O_4.

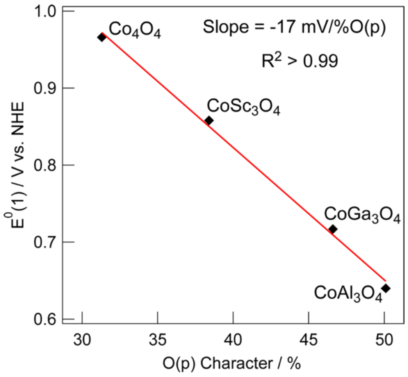

Figure 9. Linear dependence between oxidation potential and O(p) character.

The optimized bond distances are given in Table S6 (SI), and the calculated $E^0(1)$ values are given in Table 2. The $E^0(1)$ values for the substituted cubanes were all lower than for Co_4O_4 by 100−300 mV (Table 2). This indicates that it is easier to form localized Co(IV) centers in CoM_3O_4 than it is to form delocalized Co(IV) in Co_4O_4 and that electron delocalization is not necessary for Co(IV) formation as opposed to other electronic factors, most important of which appears to be Co−O covalency. The ground-state Co(d) characters of the β-LUMOs of $CoAl_3O_4$, $CoGa_3O_4$, and $CoSc_3O_4$ are 46.1, 50.9, and 57.6, respectively; the oxo(p) characters are 47.5 (50.1), 44.0 (46.6), and 33.8 (38.4), respectively. The Co(d)- and oxo(p)-characters of CoM_3O_4 are significantly more covalent than Co_4O_4 (63.8/25.6), and the covalency decreases across the series Al > Ga > Sc, which inversely parallels the oxidation potentials (e.g., Al < Ga < Sc). The correlation between $E^0(1)$ and covalency [total O(p) character from oxo and OAc ligands] is given in Figure 9 and exhibits an inverse linear relationship ($R^2 > 0.99$) with a slope of −17 mV/%O(p) character. The negative slope indicates that the oxidation potential lowers upon increasing covalency [e.g., ease of formation of Co(IV) is linearly related to covlency]. Correlations between covalency and oxidation potential have been observed in synthetic[83] and biological[84,85] FeS clusters and mononuclear, type I Cu proteins.[86] It is interesting to note that the slopes observed in those cases were ca. −8 mV/%S(p)[83,84] and −10 mV/%S(p),[86] on the order of what we observe in Figure 9. Thus, the different redox properties of Co_4O_4 and CoM_3O_4 are at least partially due to the difference in covalency of the RAMO. The origin of this difference is clear from the ground-state wave function [Figure 8C; this orbital is representative of all three M(III) substitutions]. Upon substituting 3Co(III) with redox-inactive metals, the ground-state wave function, and thus the RAMO, rotates from mainly d_{xy} to pure d_{xz}/d_{yz}. Interestingly, this change in d-orbital character is of the same type observed for electron–hole localization within Co_4O_4. This switch forms highly covalent Co–oxo bonds due to greater orbital overlap of the oxygen p-orbitals with the metal d_{xz}/d_{yz} orbitals, thus stabilizing the oxidized over the reduced state and decreasing $E^0(1)$.

Computation shows that substituting 3Co(III) of a Co_4O_4 cubane core by 3Al(III), 3Ga(III), or 3Sc(III) strongly influences the redox properties of the M_4O_4 topology. Co(IV) formation can become more favorable at localized, mononuclear sites rather than a delocalized Co_4O_4 cluster. For similar structures with the same ground state, $E^0(1)$, and thus formation of Co(IV), appears to be linearly related to the extent of metal–oxygen covalency. The inductive influence[87] of Al(III)/Ga(III)/Sc(III)–oxo bonding on Co(IV)–oxo bonding can tune covalency and hence $E^0(1)$ over hundreds of millivolts (Figure 9).

■ DISCUSSION

The formation of Co(IV) species is critical to the activity of cobalt-based homogeneous and heterogeneous OECs.[31,41,47] In comparing molecular Co_4O_4 cubanes to the catenated Co_4O_4 cubane structure of heterogeneous CoP_i, the hole equivalents in the form of Co(IV) are "stored" within the cubane core. The Co(IV) redox level is highly oxidizing and thus difficult to characterize. Whereas EPR measurements have shown the Co(IV) hole equivalents to be delocalized within the cubane cluster, X-ray spectroscopies have the potential to "look inside" this apparent delocalization owing to the many orders of magnitude faster detection of this method. Accordingly, X-ray spectroscopy can directly probe and define the precise nature of the formal Co(IV) oxidation state as well as its bonding with oxygen and with neighboring metals within the cubane core. Such analysis of the Co(IV) state is facilitated by its correspondence to isoelectronic systems that have benefited from rigorous spectroscopic characterization.

Co K- and L-Edge Spectral Features. Low-spin Co(III) (t_{2g}^6) and Co(IV) (t_{2g}^5) are isoelectronic to Fe(II) and Fe(III), respectively. The K-pre-edge and the L-edge provide a direct probe of the 3d manifold through 1s and 2p excitations to unoccupied 3d orbitals, respectively. These spectroscopic methods provide a high degree of complementarity, as they probe different final states ($1s^1 3d^{n+1}$ and $2p^5 3d^{n+1}$) and have different selection rules (quadrupole for 1s → 3d and dipole for 2p → 3d). The K-pre-edge features provide information on geometric and electronic structure through the energy splittings and intensity distributions. The former are reflective of the ligand field strength. In a centrosymmetric complex, pre-edge transitions exhibit quadrupole intensity; however, distortions eliminating inversion symmetry give rise to 4p mixing over the many-electron final states, which gives partial dipole character to the pre-edge, increasing intensity. The energy splittings and intensities can also be affected by covalency. Westre et al. have provided a rigorous interpretation of iron K-pre-edge data in terms of the excited state d^{n+1} electronic configurations.[67] While the d^{n+1} excited electronic configurations should be coupled to the 1s core-hole, it is symmetric (a_{1g}) and will not affect the overall symmetry of the final state. The presence of the core-hole does not change the relative energies of the final states but can reduce 10Dq by ~80% relative to the ground state by decreasing Z_{eff} on the metal.[67] Thus, parent d^{n+1} states are referred to, and the analysis provides a direct correlation to the strong-field many-electron excited states of the Tanabe–Sugano matrices.[88] The ground-state configuration of low-spin Co(III) is $(t_{2g})^6$; excitation of a 1s core electron results in a $(t_{2g})^6(e_g)^1$ excited configuration, which gives rise to a ^2E_g excited state and a single pre-edge feature, consistent with the K-pre-edge of **1** (Figure 2). Excitation of a 1s core electron in Co(IV) can result in either $(t_{2g})^6$ or $(t_{2g})^5(e_g)^1$ excited configurations. The $(t_{2g})^6$ excited configuration gives rise to the $^1A_{1g}$ final state, and coupling the electrons in $(t_{2g})^5(e_g)^1$ gives rise to $^1T_{1g}$, $^3T_{1g}$, $^1T_{2g}$, and $^3T_{2g}$ final states. The intensity ratio of the pre-edge features from excitations to the t_{2g}:e_g-based holes is 1:4 in the absence of spin–orbit coupling, electron–electron repulsion, and covalency. The K-pre-edge obtained here for Co(IV) exhibits two transitions split by ~1.9 eV with an ~1:4 intensity ratio. The relative energies of the many-electron excited states that contribute to the pre-edge can be estimated using the d^6 Tanabe–Sugano matrices. Using the covalency-scaled free ion B value of 1000 cm^{-1}, excited 10Dq = 21 500 cm^{-1}, and $C = 4B$, the energies of $^3T_{1g}$, $^3T_{2g}$, $^1T_{1g}$, and $^1T_{2g}$ final states are calculated to be 1.20, 2.15, 2.20, and 4.15 eV, respectively. These energy values, combined with an equal intensity weighting, reproduce the 1.9 eV energy splitting between the low- and high-energy Co(IV) pre-edge features (blue line in Figure 2). Only the $^3T_{1g}$, $^3T_{2g}$, and $^1T_{1g}$ states likely contribute to the intensity of the higher energy pre-edge feature, while the $^1T_{2g}$ state is ~4.2 eV higher in energy and likely contributes in the low-energy region of the broad ~7114 eV feature. We note the energy splitting of Co(IV) in Co_4O_4 is closer to $[Fe(prpep)_2](ClO_4)$ (~1.7 eV) and is significantly less than $K_3[Fe(CN)_6]$ (~3.2 eV). From the pre-edge splitting and intensity distribution, the ground state 10Dq of Co(IV) is estimated to be ~26 900 cm^{-1}. This agrees well with the value of ~27 000 cm^{-1}, determined from fits to magnetism and EPR data of $La_{1.5}Sr_{0.5}Li_{0.5}Co_{0.5}O_4$ (vide infra).[89]

As in the K-pre-edge, the Co(IV) L-edge spectrum in Figure 4 bears significant resemblance to low-spin Fe(III). Generally, 2p/3d interactions and the 2p spin–orbit spitting dominate the L-edge final states. Therefore, the overall spectral shape, energies, and intensities can be influenced by a number of interactions, including the amount of 3d character (i.e., charge transfer effects), crystal field splitting, and distortion from O_h. For low-spin d^5 systems, the L_3 feature exhibits splitting and multiplet structure, where the lower-energy component of the L_3-edge is largely associated with absorption to the t_{2g} hole [$^1A_{1g}$, $(t_{2g})^6$ final state].[75,90] Analogous to low-spin Fe(III), Co(IV) in Co_4O_4 exhibits this feature, which is energetically well-separated from the higher-energy packet; in some Fe(III) cases, this feature has been shown to be pure π in nature (i.e., only t_{2g} intensity). The higher-energy L_3 feature primarily arises from transitions to the e_g holes and has dominantly σ character with some π mixing, but exhibits strong multiplet character. Given the dipole-allowed nature of the L-edge, the total intensity is related to the amount of d-character or covalency. Detailed multiplet analyses, including wave function projection methods, can give a great deal of information content, including differential orbital covalencies, and are the subject of a future study on a series of perturbed cubanes and Co(IV) ground states. Thus, the L-edge data can provide a direct comparison to literature data where structures are also known and provide an important benchmark and reference for future studies involving

DOI: 10.1021/jacs.6b04663
J. Am. Chem. Soc. 2016, 138, 11017–11030

perturbed versions of Co_4O_4, Co clusters, and oxides containing Co(IV).

Comparing Molecular and Heterogeneous Systems. The valency of perovskites can be controlled via Sr substitution.[91] The Co(IV) L-edge spectrum of Co_4O_4 is compared to $La_{1.8}Sr_{0.2}Li_{0.5}Co_{0.5}O_4$[92] in Figure 10 (normalized to the e_g and t_{2g} features in parts A and B, respectively); differences in the intensity distribution patterns are observed in either case. Most striking is the relative intensities of the t_{2g} features, which are significantly less pronounced in $La_{1.8}Sr_{0.2}Li_{0.5}Co_{0.5}O_4$, and the increased intensity in the higher-energy region of the L_3 e_g feature for Co_4O_4. Additionally, the L_2 t_{2g} feature observed for Co_4O_4 is very weak or not present in $La_{1.8}Sr_{0.2}Li_{0.5}Co_{0.5}O_4$. This can reflect low overall t_{2g} intensity, even for the L_3-edge in $La_{1.8}Sr_{0.2}Li_{0.5}Co_{0.5}O_4$. However, the intensity of this feature is also related to symmetry-lowering distortions from O_h, such as structural or dynamic Jahn−Teller effects.[90,93,94] Additional insight can be gained from comparisons to other spectroscopic methods that do not involve core-hole formation.

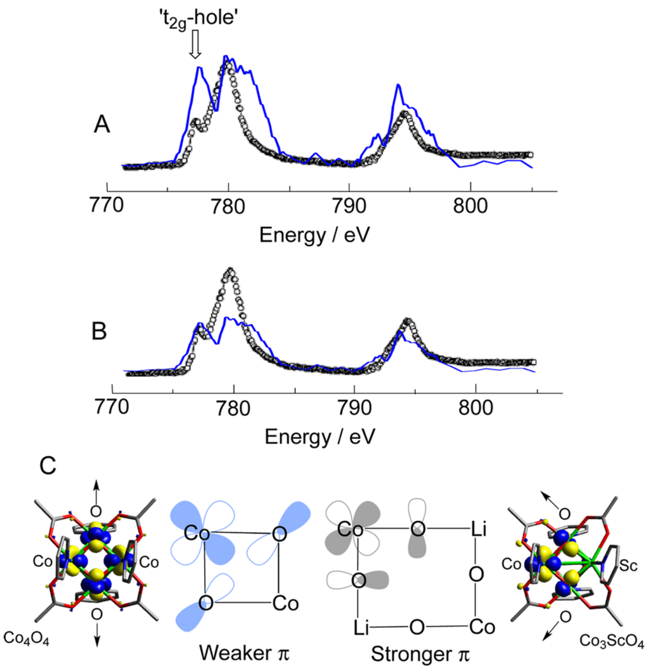

Figure 10. L-edge overlay between Co_4O_4 and $La_{1.8}Sr_{0.2}Li_{0.5}Co_{0.5}O_4$. Data are normalized to the e_g (A) and t_{2g} (B) features for comparison. The Co(IV) spectrum obtained here (blue line) is compared to the Co(IV) spectrum of $La_{1.8}Sr_{0.2}Li_{0.5}Co_{0.5}O_4$ obtained in ref 92. (C) Qualitative ground-state orbital overlaps for Co_4O_4 (blue, left center) and $La_{1.8}Sr_{0.2}Li_{0.5}Co_{0.5}O_4$ (gray, right center), as derived from EPR, are compared to DFT-derived β-LUMOs of Co_4O_4 (left) and Co_3ScO_4 (right).

Previous analyses of the $La_{2-x}Sr_xLi_{0.5}Co_{0.5}O_4$ magnetism and EPR data required significantly covalent Co−O bonding, as reflected by the low Stevens' orbital reduction factor (k)[95] of ∼0.65 (values <1 indicate covalent mixing).[89,96] It was also noted that Li−O bond linkages of neighboring octahedra (see Figure 10, bottom right) may provide an additional means of increasing the covalency of Co−O bonds.[89] The EPR g-values of $La_{1.5}Sr_{0.5}Li_{0.5}Co_{0.5}O_4$ are $2.32 \le g_\perp \le 2.55$, $g_\parallel \le 0.85$ (calcd $g_\perp = 2.32$, $g_\parallel = 0.80$)[89] and 2.442, 2.237, and 0.8 for $La_{1.8}Sr_{0.2}Li_{0.5}Co_{0.5}O_4$,[92] which are notably different than those of $[Co_4O_4(OAc)_2(py)_4]^+$ (2.3335, 2.3245, 2.0608).[53] These differences in g-values reflect different ground states, orbital orientations, and covalencies. The theory of Griffith[97] and Taylor[98] has been applied extensively to low-spin Fe(III) heme and nonheme centers to define the ground-state wave function, where $\sum g_i^2 = 16$ for a pure $d_{xy}{}^2 d_{xz/yz}{}^3$ ground state and $\sum g_i^2 = 12$ for a pure $d_{xy}{}^1 d_{xz/yz}{}^4$ ground state. Values of 15.1 and 11.6 are obtained for Co_4O_4 and $La_{1.8}Sr_{0.2}Li_{0.5}Co_{0.5}O_4$, respectively. The higher value for Co_4O_4 suggests a mixed $d_{xz/yz/xy}$ ground state, consistent with previous suggestions[52] and the DFT results obtained here. The low value for $La_{1.8}Sr_{0.2}Li_{0.5}Co_{0.5}O_4$ suggests a pure d_{xy} Co(IV) ground state.

Molecular orbital considerations gleaned from EPR and DFT calculations for Co_4O_4[52] and $La_{2-x}Sr_xLi_{0.5}Co_{0.5}O_4$[89] lead to the picture observed in Figure 10C (left and right center, respectively). The dπ orbital bisects the Co−O bonds in both structures; however, while the oxo-ligand p-orbitals are purely π-interacting with the metal 3d orbital in $La_{2-x}Sr_xLi_{0.5}Co_{0.5}O_4$ (Figure 10C, right center), they are misaligned and rotated off-axis in Co_4O_4 (Figure 10, left center). This misalignment derives from electron−hole delocalization in Co_4O_4, which directs the metal d-orbitals into the center of the diamond core to increase M/M coupling. Thus, the situation exists where maximizing delocalization misaligns the Co d- and oxo p-orbitals, decreasing the covalency of Co−O bonds. A recent study has found increased OER activity in structurally distorted $La_{1-x}Sr_xCo_3$ perovskites, rationalized by increased Co−O covalency and conductivity.[99] Our results here have showed that increased covalency decreases $E^0(1)$, driving Co(IV) formation, which will also enhance OER activity and conductivity. Future mechanistic studies will be necessary to better correlate and compare molecular and solid-state OER catalysis. Thus, knowledge of the 3d-orbital character is of limited importance if the resulting orientation with oxo p-orbitals is not known. The orientation clearly has a strong influence on the nature of the covalency and antibonding contributions to redox potentials. In testament, we can converge a wave function in a Co_3ScO_4 model that rotates the cubane oxo p-orbitals, resulting in orbital overlaps similar to those suggested for $La_{1.8}Sr_{0.2}Li_{0.5}Co_{0.5}O_4$. The β-LUMO is given in Figure 10C (far right) and can be directly compared to Co_4O_4 (far left). The arrows indicate the orientation of the oxo p-orbitals. In this model, Co(IV) formation takes place on a single Co center in Co_3ScO_4, with an $E^0(1)$ of 0.81 V vs NHE, 160 mV lower than that of Co_4O_4 (0.97 V).

Spectral Probes of Metal−Metal Interactions in Co_4O_4. Besides ligand−metal covalency, M/M interactions contribute strongly to the electronic structures and properties of MV species. Our combined K-edge and RIXS data provide a direct spectroscopic probe of both Co(IV) formation and M/M interactions in Co_4O_4. The Co K-edge exhibits a feature at ∼5 eV higher in energy than the pre-edge (labeled M/M in Figure 2), which is present for Co(III) in **1** and Co(IV) in **2**, appearing slightly more intense in the latter. Spectral features occur at this relative energy position for low-spin mononuclear compounds such as $K_3[Fe(III)(CN)_6]$[67,90] and $K_3[Co(III)(CN)_6]$.[100] Yet these spectral features have been assigned to transitions to low-lying π^* orbitals of CN^-, and they have been used as probes of backbonding. Interestingly, whereas this feature is not present in low-spin $Co(acac)_3$, it is observed in low-spin Co(III)-containing $LiCoO_2$, $AgCoO_2$, $EuCoO_3$, and $LaCoO_3$,[70] and it has been assigned to a dipolar transition to low-lying orbitals with significant M/M character [suggested to be a formally M($1s^13d^n$)M′($1s^23d^{n+1}$) XAS final state[69−71]]. This is based on several observations: (i) the intensity in the K-edge feature correlates with the Co−O−Co angle of edge-facing (for Li and Ag) and corner-facing (for Eu and La) octahedra, with the greatest intensity observed for structures with wider Co−O−Co angles (e.g., 152.9° for $EuCoO_3$ and 94.2° for $LiCoO_2$); (ii) the angular dependence of the K-edge intensity in a single crystal, and (iii) the dispersion (spectral broadness) of the resulting emission features obtained in RIXS measurements (i.e., emission features are broadened or elongated for dipolar and sharp for quadrupolar). The data presented here are specific to observation iii; for instance, resonant excitation into the ~7714 eV feature results in a dominant, broad feature, E3, which evolves and is enhanced in Figure 6, from part B to C to D. Additionally, E1 and E2 are sharp while E3 is broad, reflective of their quadrupole and dipole characters, respectively. E3 is also highly sensitive to oxidation state (Figures 6D and 7). This description of the quadrupolar and dipolar character observed in the XAS and RIXS data can also be described in terms of the amount of delocalization in the X-ray intermediate and final states. Specifically, excitation of the 1s/2p → 3d K-pre-edge (and L-edge absorption) results in data that reflect localized transitions on the Co(IV) and Co(III) X-ray absorbing/excited atom. However, the M/M feature can be assigned to a nonlocal 1s → 3d/4p transition that gains intensity through M(4p)−O(2p)−M′(3d) hybridization and can result in a formal electronic configuration of M($1s^13d^n$)/M′($1s^23d^{n+1}$), where contributions can now arise from neighboring Co 3d orbitals.[70,71] Thus, in comparing resonant excitation into the local and nonlocal 1s → 3d/4p regions, local excitation results in a RIXS final state that is M($1s^23p^53d^{n+1}$), which involves *intra*-atomic 3p/3d interactions. Conversely, nonlocal excitation can potentially result in RIXS final states with M($1s^23p^53d^n$)M′($1s^23p^63d^{n+1}$) character, which involves *inter*-atomic 3p/3d interactions.

It is interesting to note that, in $LiCoO_2$ (and other extended solids mentioned here), the local and nonlocal features are split by ~2−3 eV, which is significantly less than the splitting observed for Co_4O_4 (~5 eV). The energy splitting between these final states is thought to derive from differences in core-hole screening between the local and nonlocal excitations.[70,71,101] The 5 eV energy separation observed here implies a further perturbation of the relative energy of the nonlocal state relative to the local state, potentially through differences in relative core-hole screening in the molecular Co_4O_4 vs extended heterogeneous systems.

Thus, the combined XAS/RIXS data provide insight into the degree of M/M interactions and potentially electron−hole delocalization across Co_4O_4 through intensities and energy splittings. The XAS/RIXS data in the M/M region for Co_4O_4 will be further modeled in a future study using DFT and TDDFT calculations that will also evaluate the effect of the core-hole. These data can be directly compared to other clusters and cobalt oxide thin films, and the relative degrees of M/M interactions and charge delocalization should be able to be probed and quantified.

Electron−Hole Delocalization in Co_4O_4 and Comparisons to Heterometallic Cubane Clusters. It is important to consider that core-hole formation is considered to be instantaneous, with core-hole lifetimes varying from ~1−4 fs. This leads to a roughly 6 orders of magnitude decrease in the spectroscopic time-scale relative to EPR. Also, the core-hole potential can strongly influence the valence electrons of the X-ray absorbing *and* neighboring O and Co atoms, and the electron density will respond on the ultrafast time scale to screen the core-hole. These factors can contribute to a more localized Co(IV) description relative to longer time scale spectroscopies, such as EPR. Core-hole screening is especially important to consider in photoemission measurements where a true core-hole is created (as opposed to X-ray absorption to bound states where the excited electron can also partially screen the core-hole potential). Indeed, distinct features for localized oxidation states have been observed in photoemission studies of class III mixed-valence species, such as the Creutz−Taube ion,[55,102] which arise from final state effects. Electronic absorption spectroscopy provides an additional method with ultrafast time scales (~10^{-14} s) and can provide a direct correlation to the X-ray spectroscopic data. In this case, the core-hole is not present and therefore its effect on localization can be eliminated. In MV systems, the energy, intensity, and bandwidth of the intervalence charge transfer (IVCT) transition can be used to quantify electron−hole delocalization.[65] The room temperature electronic absorption spectra of **1** and **2** in the energy range of 400−3000 nm (25 000−3000 cm^{-1}) are given in Figure S8 (SI). Within this energy range, **1** exhibits weak features at ~600 nm (~16 670 cm^{-1}). Interestingly, **2** also exhibits absorption features at the same energy as **1**; however, an additional band, assignable to IVCT, grows in at ~4600 cm^{-1} upon oxidation to **2**. Bandwidth analysis indicates that **2** is a class II MV complex.

Electron−hole delocalization is thought to be a main factor for stabilizing Co(IV) in Co_4O_4. Certainly, a contribution from delocalization exists, as demonstrated by comparisons between the mononuclear corner site model and Co_4O_4. However, given that Co(IV) can be formed more easily at effectively mononuclear sites in perturbed cubane structures, other considerations such as covalency need to be considered. Electron delocalization may provide an electrostatic stabilization of the oxidized state over the reduced state, arising from distributing charge across multiple atoms of the cluster. This effect can be distinguished from the purely electronic effects of electron−hole delocalization, which we showed above can actually make it more difficult to form Co(IV). As an illustration, we calculated the relative energies of the reduced and oxidized states as a function of dielectric constant (Table S7, SI). In general, increasing the dielectric from 0 (gas phase) to ~36 (CH_3CN) significantly decreases the ionization energy for Co_4O_4 and CoM_3O_4 models (Table S7, SI) with the greatest stabilization observed for oxidized Co_4O_4 (Table S7, bolded, SI). This is due to delocalization of the charge over the cluster, which is considerably less for CoM_3O_4, as ionization is localized to mononuclear Co centers. While expected, this further illustrates that electron−hole delocalization does not necessarily intrinsically decrease $E^0(1)$ of Co_4O_4 but stabilizes the oxidized state over the reduced state by spreading charge across the cluster, and thus, additional effects are likely responsible for the stabilization of Co(IV) in Co_4O_4.

It is worth distinguishing time-averaged effective oxidation states (i.e., the result of fast hopping of electrons/holes between atoms, which may or may not be observed depending on the time scale of the measurement) from steady-state effective oxidation states due to orbital overlap and delocalization of states. These two pictures might correlate differently to catalysis. To a first approximation, the time-averaged, effective oxidation states are likely to be more ionic/less covalent, whereas the latter picture necessitates strongly covalent ligand−metal bonding interactions. Thus, on the basis of the results here, the time-averaged oxidation states may potentially be more oxidizing than the highly covalent counterparts, but they may then be less effective at PCET charge transport, which suggests an important interplay between covalency and mixed-valency on, specifically, OER by cobalt-based films.

Lastly, though the CoM_3O_4 complexes used here for insight into localized oxidation processes are likely very difficult synthetic targets, they have proved useful for better understanding the effects of redox-inactive metal substitution in redox tuning of heterometallic clusters. Two key observations can be made: (1) substitution can simply tune the potential via an inductive effect, which varies the covalency of the metal−oxo bonds, and perhaps more interestingly, (2) they can completely change the identity of the RAMO by rotating/switching the ground-state wave function and thus bonding with the ligands. This first factor is related to a growing body of literature on heterometallic oxido complexes.[103−106] Recent studies demonstrated a linear dependence between E^0 and the pK_a of the redox-inactive metal (~100 mV/pK_a).[103] The trend was linked to the Lewis acidity of the substituted metal, which (in the absence of PCET) is an indirect measure of the first factor and is related to the results shown in Figure 9. Here, we provide a direct correlation between the inductive effect of metal substitution, which gives rise to the linear relationship between E^0 and metal−oxo covalency. However, both covalency and the ground state can change for redox-inactive metal substitutions depending on how they are incorporated. Additionally, switching the ground state can result in variable degrees of metal−metal interactions across the cluster (i.e., mixed-valency) based on the nature of the molecular orbital. This large variation in electronic structure can be utilized in the rational design and improvement of water-oxidizing catalysts, both homogeneous and heterogeneous.

Higher Oxidation States of Co_4O_4. As a final consideration, Co(V) states have been proposed for promoting Co_4O_4 reactivity.[41,47] A second oxidation, $E^0(2)$, of Co_4O_4 occurs at 2.09 V vs NHE in CH_3CN (Figure S7, SI), giving a $\Delta E^0(2-1)$ splitting of 1.15 V. $E^0(2)$ of Co_4O_4 is calculated here to be 2.15 V vs NHE, giving a $\Delta E^0(2-1)$ splitting of 1.18 V; the absolute and relative calculated values are in excellent agreement with experiment. Note that the second oxidation of the Co_4O_4 is preliminarily modeled as a $Co(III)_2Co(IV)_2$ triplet ($S = 1$), not a Co(V) localized state. Future studies are necessary to define the electronic structure of this state. We do note, however, that the calculated $E^0(2)$ values of $CoAl_3O_4$, $CoGa_3O_4$, and $CoSc_3O_4$ clusters (also triplets) are 1.94, 1.94, and 1.96 V vs NHE, respectively (Table 2), all of which are again less than Co_4O_4, suggesting that a formally Co(V) could be formed in CoM_3O_4 clusters.

Examining the ground-state wave functions (Figure S9, SI), we find that CoM_3O_4 effectively houses one of two redox equivalents within the oxo-bonding framework [e.g., effective ionization of O(2p)-based electrons or extremely covalent Co−oxo bonding for one of the unoccupied 3d-orbitals]. This can be viewed as a form of "redox-potential leveling" or "ligand noninnocence", potentially analogous to Co(III)−corroles, where one of two electron−holes necessary for water oxidation is delocalized within the corrole π-electron system.[107] Indeed, oxidation of oxo(2p) electrons has been proposed for Co and Ni oxides as well as $Li_{1.2}[Ni_{0.13}{}^{2+}Co_{0.13}{}^{3+}Mn_{0.54}{}^{4+}]O_2$.[108−112] Interestingly, in the latter example, holes generated upon oxidation are proposed to be effectively localized on Mn(IV)−O and not Co(IV)− or Ni(IV)−O bonds.[112] This form of redox noninnocence may allow perturbed clusters with effectively "mononuclear" sites to reach high formal oxidation states in a fashion similar to metal oxides.

In terms of oxidic metal OER catalysts, the formation of highly covalent surface exposed active sites within a covalent, mixed-valent matrix will lower Co-OEC Co(III/IV) redox potentials and drive OER activity by increasing Co(IV) content and by facilitating the regeneration of active sites via self-exchange proton-coupled electron transport. Increased covalency can also thus lower the necessary operating overpotential of the catalyst.

■ CONCLUSIONS

The formation of Co(IV) species is critical to the activity of cobalt-based homogeneous and heterogeneous OECs.[31,41,47] In comparing molecular Co_4O_4 cubanes to the catenated Co_4O_4 cubane structure of heterogeneous CoP_i, the hole equivalents in the form of Co(IV) are "stored" within the cubane core. Whereas EPR measurements have shown that these hole equivalents are delocalized within the cubane cluster, the XAS studies reported here indicate that the hole equivalents are localized on the much shorter time scale of an XAS experiment, suggesting that delocalization is thus achieved by a very fast hopping rate. Complementary X-ray spectroscopies have provided a direct probe of the Co(IV) d-orbital manifold in a Co_4O_4 cubane and have allowed for a comparison to isoelectronic d^5 molecular and heterogeneous species. Future studies are aimed at extending to 1s2p RIXS, which provide these data using hard X-rays. The combined K-edge and 1s3p RIXS data allow for the experimental "mapping" of Co(IV) contributions to the K-edge and RIXS planes in the presence of a spectroscopically active MV background. This sensitivity lends promise for applications to in situ measurements of cobalt oxides. Additionally, application of the XAS/RIXS combination has allowed spectral features to be identified that provide a direct handle on both Co(IV) and oxygen-mediated M/M interactions.

DFT calculations guided by the experiment indicate that electron−hole delocalization is not necessary for Co(IV) formation in clusters, and other factors such as covalency, antibonding, and inductive effects may be more important. In particular, maximizing electron−hole delocalization can result in a partial decrease in the covalency and orbital overlap of ligand−metal bonds and oppose the formation of high-valent states. Additionally, substituting redox-inactive metals results in a rotation of the ground-state wave function and increased ligand−metal covalency. This strongly helps drive the formation of Co(IV). For similar structures with the same ground state, $E^0(1)$, and thus formation of Co(IV), is shown to be linearly related to covalency, and the inductive influence of Al(III)/Ga(III)/Sc(III)−oxo bonding on Co(IV)−oxo bonding can tune covalency over a large range and thus $E^0(1)$ over hundreds of millivolts. Covalency-driven formation of high-valent species increases the number of active sites and facilitates regeneration.

■ ASSOCIATED CONTENT

Ⓢ Supporting Information

The Supporting Information is available free of charge on the ACS Publications website at DOI: 10.1021/jacs.6b04663.

Full experimental details, supporting tables and figures, and Cartesian coordinates of DFT-optimized geometries (PDF)

■ AUTHOR INFORMATION

Corresponding Authors

*dnocera@fas.harvard.edu

*lchen@anl.gov; l-chen@northwestern.edu

Notes

The authors declare no competing financial interest.

■ ACKNOWLEDGMENTS

Work at ANL was supported by funding from the Division of Chemical Sciences, Biosciences, Office of Basic Energy Science (OBES), DOE through Grant DE-AC02-06CH11357. Synchrotron facilities were provided by the Advanced Photon Source (APS) and Advanced Light Source (ALS) operated by DOE BES. Work at Harvard was performed under a grant from the U.S. DOE Office of Science (DE-SC0009758). D.H. is supported by the Joseph J. Katz Postdoctoral Fellowship at Argonne National Laboratory (ANL). C.N.B. acknowledges the National Science Foundation's Graduate Research Fellowship. We acknowledge Sungsik Lee for assistance in making Co K-edge measurements and Robert Schoenlein and Amy Cordones-Hahn for assistance in making Co L-edge measurements. We acknowledge Edward Solomon, Michael Mara, Thomas Kroll, and Bryce Anderson for helpful discussions. We gratefully acknowledge the computing resources provided on Blues and Fusion, both high-performance computing clusters operated by the Laboratory Computing Resource Center at ANL.

■ REFERENCES

(1) Lewis, N. S.; Nocera, D. G. *Proc. Natl. Acad. Sci. U. S. A.* **2006**, *103*, 15729.

(2) Cook, T. R.; Dogutan, D. K.; Reece, S. Y.; Surendranath, Y.; Teets, T. S.; Nocera, D. G. *Chem. Rev.* **2010**, *110*, 6474.

(3) Nocera, D. G. *Acc. Chem. Res.* **2012**, *45*, 767.

(4) Lewis, N. S.; Nocera, D. G. *Bridge* **2015**, *46*, 41.

(5) Kanan, M. W.; Nocera, D. G. *Science* **2008**, *321* (5892), 1072.

(6) Lutterman, D. A.; Surendranath, Y.; Nocera, D. G. *J. Am. Chem. Soc.* **2009**, *131*, 3838.

(7) Kanan, M. W.; Yano, J.; Surendranath, Y.; Dincă, M.; Yachandra, V. K.; Nocera, D. G. *J. Am. Chem. Soc.* **2010**, *132*, 13692.

(8) Dincă, M.; Surendranath, Y.; Nocera, D. G. *Proc. Natl. Acad. Sci. U. S. A.* **2010**, *107*, 10337.

(9) Trotochaud, L.; Young, S. L.; Ranney, J. K.; Boettcher, S. W. *J. Am. Chem. Soc.* **2014**, *136*, 6744.

(10) Hunter, B. M.; Blakemore, J. D.; Deimund, M.; Gray, H. B.; Winkler, J. R.; Müller, A. M. *J. Am. Chem. Soc.* **2014**, *136*, 13118.

(11) Smith, R. D. L.; Prévot, M. S.; Fagan, R. D.; Trudel, S.; Berlinguette, C. P. *J. Am. Chem. Soc.* **2013**, *135*, 11580.

(12) Song, F.; Hu, X. *J. Am. Chem. Soc.* **2014**, *136*, 16481.

(13) Qiu, Y.; Xin, L.; Li, W. *Langmuir* **2014**, *30*, 7893.

(14) Friebel, D.; Louie, M. W.; Bajdich, M.; Sanwald, K. E.; Cai, Y.; Wise, A. M.; Cheng, M.-J.; Sokaras, D.; Weng, T.-C.; Alonso-Mori, R.; Davis, R. C.; Bargar, J. R.; Nørskov, J. K.; Nilsson, A.; Bell, A. T. *J. Am. Chem. Soc.* **2015**, *137*, 1305.

(15) Lundberg, M.; Kroll, T.; DeBeer, S.; Bergmann, U.; Wilson, S. A.; Glatzel, P.; Nordlund, D.; Hedman, B.; Hodgson, K. O.; Solomon, E. I. *J. Am. Chem. Soc.* **2013**, *135*, 17121.

(16) Kroll, T.; Hadt, R. G.; Wilson, S. A.; Lundberg, M.; Yan, J. J.; Weng, T.-C.; Sokaras, D.; Alonso-Mori, R.; Casa, D.; Upton, M. H.; Hedman, B.; Hodgson, K. O.; Solomon, E. I. *J. Am. Chem. Soc.* **2014**, *136*, 18087.

(17) Kotani, A.; Shin, S. *Rev. Mod. Phys.* **2001**, *73*, 203.

(18) Ament, L. J. P.; van Veenendaal, M.; Devereaux, T. P.; Hill, J. P.; van den Brink, J. *Rev. Mod. Phys.* **2011**, *83*, 705.

(19) Li, C. W.; Ciston, J.; Kanan, M. W. *Nature* **2014**, *508*, 504.

(20) Feng, X.; Jiang, K.; Fan, S.; Kanan, M. W. *J. Am. Chem. Soc.* **2015**, *137*, 4606.

(21) Verdaguer-Casadevall, A.; Li, C. W.; Johansson, T. P.; Scott, S. B.; McKeown, J. T.; Kumar, M.; Stephens, I. E. L.; Kanan, M. W.; Chorkendorff, I. *J. Am. Chem. Soc.* **2015**, *137*, 9808.

(22) Petrie, J. R.; Cooper, V. R.; Freeland, J. W.; Meyer, T. L.; Zhang, Z.; Lutterman, D. A.; Lee, H. N. *J. Am. Chem. Soc.* **2016**, *138*, 2488.

(23) Woertink, J. S.; Smeets, P. J.; Groothaert, M. H.; Vance, M. A.; Sels, B. F.; Schoonheydt, R. A.; Solomon, E. I. *Proc. Natl. Acad. Sci. U. S. A.* **2009**, *106*, 18908.

(24) Vanelderen, P.; Hadt, R. G.; Smeets, P. J.; Solomon, E. I.; Schoonheydt, R. A.; Sels, B. F. *J. Catal.* **2011**, *284*, 157.

(25) Vanelderen, P.; Snyder, B. E. R.; Tsai, M.-L.; Hadt, R. G.; Vancauwenbergh, J.; Coussens, O.; Schoonheydt, R. A.; Sels, B. F.; Solomon, E. I. *J. Am. Chem. Soc.* **2015**, *137*, 6383.

(26) Gagliardi, C. J.; Vannucci, A. K.; Concepcion, J. J.; Chen, Z.; Meyer, T. J. *Energy Environ. Sci.* **2012**, *5*, 7704.

(27) Ullman, A. M.; Brodsky, C. N.; Li, N.; Zheng, S.-L.; Nocera, D. G. *J. Am. Chem. Soc.* **2016**, *138*, 4229.

(28) Ferreira, K. N.; Iverson, T. M.; Maghlaoui, K.; Barber, J.; Iwata, S. *Science* **2004**, *303*, 1831.

(29) Umena, Y.; Kawakami, K.; Shen, J.-R.; Kamiya, N. *Nature* **2011**, *473*, 55.

(30) Zhang, C.; Chen, C.; Dong, H.; Shen, J.-R.; Dau, H.; Zhao, J. *Science* **2015**, *348*, 690.

(31) Bediako, D. K.; Ullman, A. M.; Nocera, D. G. *Top. Curr. Chem.* **2015**, *371*, 173.

(32) Kanan, M. W.; Surendranath, Y.; Nocera, D. G. *Chem. Soc. Rev.* **2009**, *38*, 109.

(33) Beattie, J. K.; Hambley, T. W.; Klepetko, J. A.; Masters, A. F.; Turner, P. *Polyhedron* **1998**, *17*, 1343.

(34) Dimitrou, K.; Folting, K.; Streib, W. E.; Christou, G. *J. Am. Chem. Soc.* **1993**, *115*, 6432.

(35) Dimitrou, K.; Sun, J.-S.; Folting, K.; Christou, G. *Inorg. Chem.* **1995**, *34*, 4160.

(36) Dimitrou, K.; Brown, A. D.; Christou, G.; Concolino, T. E.; Rheingold, A. L. *Chem. Commun.* **2001**, 1284.

(37) Chakrabarty, R.; Bora, S. J.; Das, B. K. *Inorg. Chem.* **2007**, *46*, 9450.

(38) Sarmah, P.; Chakrabarty, R.; Phukan, P.; Das, B. K. *J. Mol. Catal. A: Chem.* **2007**, *268*, 36.

(39) Chakrabarty, R.; Sarmah, P.; Saha, B.; Chakravorty, S.; Das, B. K. *Inorg. Chem.* **2009**, *48*, 6371.

(40) Das, B. K.; Chakrabarty, R. *J. Chem. Sci.* **2011**, *123*, 163.

(41) Smith, P. F.; Hunt, L.; Laursen, A. B.; Sagar, V.; Kaushik, S.; Calvinho, K. U. D.; Marotta, G.; Mosconi, E.; De Angelis, F.; Dismukes, G. C. *J. Am. Chem. Soc.* **2015**, *137*, 15460.

(42) McCool, N. S.; Robinson, D. M.; Sheats, J. E.; Dismukes, G. C. *J. Am. Chem. Soc.* **2011**, *133*, 11446.

(43) La Ganga, G.; Puntoriero, F.; Campagna, S.; Bazzan, I.; Berardi, S.; Bonchio, M.; Sartorel, A.; Natali, M.; Scandola, F. *Faraday Discuss.* **2012**, *155*, 177.

(44) Berardi, S.; La Ganga, G.; Natali, M.; Bazzan, I.; Puntoriero, F.; Sartorel, A.; Scandola, F.; Campagna, S.; Bonchio, M. *J. Am. Chem. Soc.* **2012**, *134*, 11104.

(45) Li, X.; Siegbahn, P. E. M. *J. Am. Chem. Soc.* **2013**, *135*, 13804.

(46) Mattioli, G.; Giannozzi, P.; Amore Bonapasta, A.; Guidoni, L. *J. Am. Chem. Soc.* **2013**, *135*, 15353.

(47) Nguyen, A. I.; Ziegler, M. S.; Oña-Burgos, P.; Sturzbecher-Hohne, M.; Kim, W.; Bellone, D. E.; Tilley, T. D. *J. Am. Chem. Soc.* **2015**, *137*, 12865.

(48) Ullman, A. M.; Liu, Y.; Huynh, M.; Bediako, D. K.; Wang, H.; Anderson, B. L.; Powers, D. C.; Breen, J. J.; Abruña, H. D.; Nocera, D. G. *J. Am. Chem. Soc.* **2014**, *136*, 17681.

(49) Symes, M. D.; Lutterman, D. A.; Teets, T. S.; Anderson, B. L.; Breen, J. J.; Nocera, D. G. *ChemSusChem* **2013**, *6*, 65.

(50) Symes, M. D.; Surendranath, Y.; Lutterman, D. A.; Nocera, D. G. *J. Am. Chem. Soc.* **2011**, *133*, 5174.

(51) McAlpin, J. G.; Surendranath, Y.; Dinca, M.; Stich, T. A.; Stoian, S. A.; Casey, W. H.; Nocera, D. G.; Britt, R. D. *J. Am. Chem. Soc.* **2010**, *132*, 6882.

(52) McAlpin, J. G.; Stich, T. A.; Ohlin, C. A.; Surendranath, Y.; Nocera, D. G.; Casey, W. H.; Britt, R. D. *J. Am. Chem. Soc.* **2011**, *133*, 15444.

(53) Stich, T. A.; Krzystek, J.; Mercado, B. Q.; McAlpin, J. G.; Ohlin, C. A.; Olmstead, M. M.; Casey, W. H.; David Britt, R. *Polyhedron* **2013**, *64*, 304.

(54) Robin, M. B.; Day, P. *Adv. Inorg. Chem. Radiochem.* **1968**, *10*, 247.

(55) Hush, N. S. *Chem. Phys.* **1975**, *10*, 361.

(56) Smith, P. F.; Kaplan, C.; Sheats, J. E.; Robinson, D. M.; McCool, N. S.; Mezle, N.; Dismukes, G. C. *Inorg. Chem.* **2014**, *53*, 2113.

(57) Surendranath, Y.; Kanan, M. W.; Nocera, D. G. *J. Am. Chem. Soc.* **2010**, *132*, 16501.

(58) Bediako, D. K.; Costentin, C.; Jones, E. C.; Nocera, D. G.; Savéant, J.-M. *J. Am. Chem. Soc.* **2013**, *135*, 10492.

(59) Ullman, A. M.; Nocera, D. G. *J. Am. Chem. Soc.* **2013**, *135*, 15053.

(60) Costentin, C.; Porter, T. R.; Savéant, J.-M. *J. Am. Chem. Soc.* **2016**, *138*, 5615.

(61) Day, P.; Hush, N. S.; Clark, R. J. H. *Philos. Trans. R. Soc., A* **2008**, *366*, 5.

(62) Glover, S. D.; Lear, B. J.; Salsman, J. C.; Londergan, C. H.; Kubiak, C. P. *Philos. Trans. R. Soc., A* **2008**, *366*, 177.

(63) Glover, S. D.; Goeltz, J. C.; Lear, B. J.; Kubiak, C. P. *Eur. J. Inorg. Chem.* **2009**, *2009*, 585.

(64) Glover, S. D.; Goeltz, J. C.; Lear, B. J.; Kubiak, C. P. *Coord. Chem. Rev.* **2010**, *254*, 331.

(65) Brunschwig, B. S.; Creutz, C.; Sutin, N. *Chem. Soc. Rev.* **2002**, *31*, 168.

(66) Poltavets, V. V.; Croft, M.; Greenblatt, M. *Phys. Rev. B: Condens. Matter Mater. Phys.* **2006**, *74*, 125103.

(67) Westre, T. E.; Kennepohl, P.; DeWitt, J. G.; Hedman, B.; Hodgson, K. O.; Solomon, E. I. *J. Am. Chem. Soc.* **1997**, *119*, 6297.

(68) Iwai, K.; Iwai, M.; Suto, K.; Nakashima, S.; Motoyama, I.; Sano, H.; Ikemoto, I.; Kosugi, N.; Kuroda, H. *Bull. Chem. Soc. Jpn.* **1986**, *59*, 2675.

(69) Glatzel, P.; Mirone, A.; Eeckhout, S. G.; Sikora, M.; Giuli, G. *Phys. Rev. B: Condens. Matter Mater. Phys.* **2008**, *77*, 115133.

(70) Vanko, G.; de Groot, F. M. F.; Huotari, S.; Cava, R. J.; Lorenz, T.; Reuther, M. *ArXiv.org e-Print Arch., Condens. Matter* **2008**, arXiv:082.2744v1 [cond-mat.str-el].

(71) de Groot, F. M. F.; Vankó, G.; Glatzel, P. *J. Phys.: Condens. Matter* **2009**, *21*, 104207.

(72) Risch, M.; Ringleb, F.; Kohlhoff, M.; Bogdanoff, P.; Chernev, P.; Zaharieva, I.; Dau, H. *Energy Environ. Sci.* **2015**, *8*, 661.

(73) Wasinger, E. C.; de Groot, F. M. F.; Hedman, B.; Hodgson, K. O.; Solomon, E. I. *J. Am. Chem. Soc.* **2003**, *125*, 12894.

(74) Hocking, R. K.; DeBeer George, S.; Raymond, K. N.; Hodgson, K. O.; Hedman, B.; Solomon, E. I. *J. Am. Chem. Soc.* **2010**, *132*, 4006.

(75) Cartier dit Moulin, C.; Rudolf, P.; Flank, A. M.; Chen, C. T. *J. Phys. Chem.* **1992**, *96*, 6196.

(76) Glatzel, P.; Bergmann, U. *Coord. Chem. Rev.* **2005**, *249*, 65.

(77) Shvyd'ko, Y. V.; Hill, J. P.; Burns, C. A.; Coburn, D. S.; Brajuskovic, B.; Casa, D.; Goetze, K.; Gog, T.; Khachatryan, R.; Kim, J. H.; Kodituwakku, C. N.; Ramanathan, M.; Roberts, T.; Said, A.; Sinn, H.; Shu, D.; Stoupin, S.; Upton, M.; Wieczorek, M.; Yavas, H. *J. Electron Spectrosc. Relat. Phenom.* **2013**, *188*, 140.

(78) Wang, L.-P.; Van Voorhis, T. *J. Phys. Chem. Lett.* **2011**, *2*, 2200.

(79) Mavros, M. G.; Tsuchimochi, T.; Kowalczyk, T.; McIsaac, A.; Wang, L.-P.; Voorhis, T. V. *Inorg. Chem.* **2014**, *53*, 6386.

(80) Hadt, R. G.; Nemykin, V. N. *Inorg. Chem.* **2009**, *48*, 3982.

(81) Lundberg, M.; Siegbahn, P. E. M. *J. Chem. Phys.* **2005**, *122*, 224103.

(82) Neese, F. *Coord. Chem. Rev.* **2009**, *253*, 526.

(83) Anxolabehere-Mallart, E.; Glaser, T.; Frank, P.; Aliverti, A.; Zanetti, G.; Hedman, B.; Hodgson, K. O.; Solomon, E. I. *J. Am. Chem. Soc.* **2001**, *123*, 5444.

(84) Glaser, T.; Bertini, I.; Moura, J. J. G.; Hedman, B.; Hodgson, K. O.; Solomon, E. I. *J. Am. Chem. Soc.* **2001**, *123*, 4859.

(85) Dey, A.; Jenney, F. E., Jr.; Adams, M. W. W.; Babini, E.; Takahashi, Y.; Fukuyama, K.; Hodgson, K. O.; Hedman, B.; Solomon, E. I. *Science* **2007**, *318*, 1464.

(86) Hadt, R. G.; Sun, N.; Marshall, N. M.; Hodgson, K. O.; Hedman, B.; Lu, Y.; Solomon, E. I. *J. Am. Chem. Soc.* **2012**, *134*, 16701.

(87) Etourneau, J.; Portier, J.; Ménil, F. *J. Alloys Compd.* **1992**, *188*, 1.

(88) Tanabe, Y.; Sugano, S. *J. Phys. Soc. Jpn.* **1954**, *9*, 753.

(89) Buffat, B.; Demazeau, G.; Pouchard, M.; Dance, J. M.; Hagenmuller, P. *J. Solid State Chem.* **1983**, *50*, 33.

(90) Hocking, R. K.; Wasinger, E. C.; de Groot, F. M. F.; Hodgson, K. O.; Hedman, B.; Solomon, E. I. *J. Am. Chem. Soc.* **2006**, *128*, 10442.

(91) Abbate, M.; de Groot, F. M. F.; Fuggle, J. C.; Fujimori, A.; Strebel, O.; Lopez, F.; Domke, M.; Kaindl, G.; Sawatzky, G. A.; Takano, M.; Takeda, Y.; Eisaki, H.; Uchida, S. *Phys. Rev. B: Condens. Matter Mater. Phys.* **1992**, *46*, 4511.

(92) Warda, S. A.; Massa, W.; Reinen, D.; Hu, Z.; Kaindl, G.; de Groot, F. M. F. *J. Solid State Chem.* **1999**, *146*, 79.

(93) de Groot, F. M. F. *Coord. Chem. Rev.* **2005**, *249*, 31.

(94) de Groot, F. M. F.; Hu, Z. W.; Lopez, M. F.; Kaindl, G.; Guillot, F.; Tronc, M. *J. Chem. Phys.* **1994**, *101*, 6570.

(95) Stevens, K. W. H. *Proc. R. Soc. London, Ser. A* **1953**, *219*, 542.

(96) Figgis, B. N. *Trans. Faraday Soc.* **1961**, *57*, 198.

(97) Griffith, J. S. *Proc. R. Soc. London, Ser. A* **1956**, *235*, 23.

(98) Taylor, C. P. S. *Biochim. Biophys. Acta, Protein Struct.* **1977**, *491*, 137.

(99) Cheng, X.; Fabbri, E.; Nachtegaal, M.; Castelli, I. E.; El Kazzi, M.; Haumont, R.; Marzari, N.; Schmidt, T. J. *Chem. Mater.* **2015**, *27*, 7662.

(100) Obashi, M. *Jpn. J. Appl. Phys.* **1977**, *16*, 167.

(101) Juhin, A.; de Groot, F.; Vankó, G.; Calandra, M.; Brouder, C. *Phys. Rev. B: Condens. Matter Mater. Phys.* **2010**, *81*, 115115.

(102) Creutz, C.; Taube, H. *J. Am. Chem. Soc.* **1969**, *91*, 3988.

(103) Tsui, E. Y.; Tran, R.; Yano, J.; Agapie, T. *Nat. Chem.* **2013**, *5*, 293.

(104) Lin, P.-H.; Takase, M. K.; Agapie, T. *Inorg. Chem.* **2015**, *54*, 59.

(105) Krewald, V.; Neese, F.; Pantazis, D. A. *Phys. Chem. Chem. Phys.* **2016**, *18*, 10739.

(106) Evangelisti, F.; Moré, R.; Hodel, F.; Luber, S.; Patzke, G. R. *J. Am. Chem. Soc.* **2015**, *137*, 11076.

(107) Dogutan, D. K.; McGuire, R.; Nocera, D. G. *J. Am. Chem. Soc.* **2011**, *133*, 9178.

(108) Rao, G. R. R.; Hegde, M. S.; Sarma, D. D.; Rao, C. N. R. *J. Phys.: Condens. Matter* **1989**, *1*, 2147.

(109) Uchimoto, Y.; Sawada, H.; Yao, T. *J. Power Sources* **2001**, *97–98*, 326.

(110) Kuiper, P.; Kruizinga, G.; Ghijsen, J.; Sawatzky, G. A.; Verweij, H. *Phys. Rev. Lett.* **1989**, *62*, 221.

(111) Mizokawa, T.; Wakisaka, Y.; Sudayama, T.; Iwai, C.; Miyoshi, K.; Takeuchi, J.; Wadati, H.; Hawthorn, D. G.; Regier, T. Z.; Sawatzky, G. A. *Phys. Rev. Lett.* **2013**, *111*, 056404.

(112) Luo, K.; Roberts, M. R.; Hao, R.; Guerrini, N.; Pickup, D. M.; Liu, Y.-S.; Edström, K.; Guo, J.; Chadwick, A. V.; Duda, L. C.; Bruce, P. G. *Nat. Chem.* **2016**, *8*, 684.

DOI: 10.1021/jacs.6b04663
J. Am. Chem. Soc. 2016, 138, 11017−11030

THE JOURNAL OF
PHYSICAL CHEMISTRY C

Article

pubs.acs.org/JPCC

Nucleation and Growth Mechanisms of an Electrodeposited Manganese Oxide Oxygen Evolution Catalyst

Michael Huynh,[†,‡] D. Kwabena Bediako,[†] Yi Liu,[†] and Daniel G. Nocera*[,†]

[†]Department of Chemistry and Chemical Biology, Harvard University, 12 Oxford Street, Cambridge, Massachusetts 02138, United States

[‡]Department of Chemistry, Massachusetts Institute of Technology, 77 Massachusetts Avenue, Cambridge, Massachusetts 02139, United States

Supporting Information

ABSTRACT: We investigate the mechanisms of nucleation and steady-state growth of a manganese oxide catalyst (MnOx) electrodeposited from Mn^{2+} solutions in a weakly basic electrolyte. Early catalyst growth was probed through chronoamperometry transients, which were fit to reveal a progressive nucleation mechanism for initial catalyst formation. Time-dependent atomic force microscopy snapshots of the electrode surface reveal a rapid increase in nucleus size together with a sluggish rise in coverage, which is also characteristic of progressive nucleation. Electrochemical kinetic studies of the catalyst growth yield a Tafel slope of approximately $2.3 \times RT/2F$ and a rate law consisting of a second-order and inverse fourth-order dependence on $[Mn^{2+}]$ and proton activity, respectively. These results are consistent with a deposition mechanism involving rate-limiting disproportionation of aqueous Mn^{3+}, resolving a longstanding ambiguity surrounding the deposition of manganese oxides under nonacidic conditions.

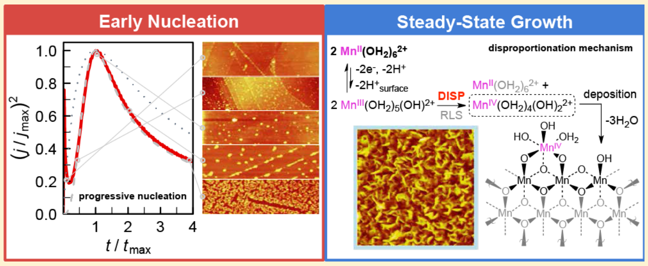

■ INTRODUCTION

First-row transition-metal oxides are materials of choice for energy storage and conversion applications.[1−6] Manganese oxides have found particular use as the functional materials of capacitors[7,8] and batteries[9−11] owing to the redox versatility of manganese ion (from Mn^{2+} to Mn^{7+}).[12,13] Inspired by nature's use of a Mn_4Ca-oxo cubane in Photosystem II, there has been a resurgence of interest in using manganese oxides as catalysts to drive solar-to-fuels conversions derived from the oxygen evolving reaction (OER). The activity of manganese oxides toward OER has been observed to depend on the method of preparation of the oxide, whether that be by electrodeposition,[14−18] thermal decomposition,[19−21] or chemical precipitation.[22,23] An emerging trend from these studies is that the presence of Mn^{3+} in the oxides confers higher catalytic activity.[14−23] However, a description of the manganese oxidation state is incomplete without consideration of the dynamical processes attendant to manganese oxides. These dynamical processes find their origins in the redox versatility of manganese ion. For instance, synthetic tetranuclear-manganese clusters liberate Mn^{2+} ions during operation, which are then reoxidized to furnish a $Mn^{3+/4+}$ oxide.[16] Similarly, manganese-oxo complexes embedded in a Nafion membrane transform into a birnessite-like manganese oxide upon application of anodic potentials.[23] Results such as these provide an imperative to understand the role of the manganese ion oxidation state during the formation of manganese oxide OER catalysts. However, little attention has been devoted to understanding the deposition of manganese oxides in the context of OER catalysis.

Previous deposition studies have largely been devoted to the production of electrolytic manganese dioxide (EMD) from highly acidic electrolytes (0.1 to 5.0 M H_2SO_4) owing to interest in this material as a battery electrode.[24−30] These conditions do not reflect those for OER, where catalyst films are deposited or evaluated at neutral to alkaline pHs.[14−23] Moreover, even for EMD formation, the deposition mechanism is unresolved. Cyclic voltammetry (CV) was unable to distinguish between deposition by an ECE (i.e., two one-electron transfer steps separated by a chemical step) and a disproportionation (DISP) process because ECE and DISP CV traces are almost identical and can only be distinguished by a subtle trace-crossing effect upon variation of scan rate.[31]

To discern the mechanism of manganese oxide deposition in neutral to alkaline electrolytes of relevance to OER, we now provide a detailed study of both nucleation and growth pathways of an electrodeposited manganese oxide (denoted MnOx) by using a combination of electrochemical methods. CV and coulometry, in conjunction with X-ray diffraction data, suggest the overall formation of an amorphous MnOx with an

Special Issue: Michael Grätzel Festschrift

Received: February 19, 2014
Revised: March 28, 2014
Published: March 31, 2014

dx.doi.org/10.1021/jp501768n | *J. Phys. Chem. C* 2014, 118, 17142−17152

average Mn oxidation state of +3.68. Application of chronoamperometry and atomic force microscopy (AFM) reveal the nature of catalyst nucleation in the stage of early film growth. Electrochemical kinetic experiments using Tafel and reaction-order plots establish the rate law for MnOx nucleation and growth and guided mechanistic proposals for steady-state catalyst deposition. Together, these studies are able to differentiate between the longstanding issue of ECE versus DISP as the mechanism for manganese oxide deposition by demonstrating the latter to be operative and initiated by a progressive nucleation process.

■ EXPERIMENTAL SECTION

A. Materials. $MnCl_2 \cdot 4H_2O$ (99.995% trace metals basis, Strem), phosphoric acid (85 wt % in H_2O, 99.99% trace metals basis, Aldrich), KOH (88%, Macron), and KNO_3 (99.0 to 100.5%, Macron) were used as received. Methylphosphonic acid (98%, Aldrich) was twice recrystallized from boiling acetonitrile (HPLC grade, Aldrich). Electrodes and glassware were rinsed with Type-I water (EMD Millipore, 18.2 MΩ-cm resistivity), which was also used to prepare solutions.

B. Solution Preparation. Stock solutions of 10 mM Mn^{2+} and 1.0 M methylphosphonate (MeP_i, pK_{a1} = 2.35, pK_{a2} = 7.1,[32] preadjusted to target pH with KOH) were diluted with type-I reagent-grade water to prepare electrolytes for deposition studies. The concentrated stock MeP_i stock solution was first diluted before adding Mn^{2+}, and the electrolyte was permitted to equilibrate for ca. 8 h prior to experiments. Additional KNO_3 was added to maintain ~2 M ionic strength (μ).

C. General Electrochemical Methods. A CH Instruments 760D bipotentiostat, a BASi Ag/AgCl reference electrode (filled with saturated KCl), and a Pt-mesh counter electrode were employed for all electrochemical experiments with ohmic potential loss correction (iR compensation). The electrochemical cell was a standard three-electrode configuration with a porous glass frit separating the working and auxiliary compartments. Glassware and cells were cleaned by soaking in aqua regia and rinsing with reagent-grade water. All measurements were performed at ambient temperature (23 ± 1 °C), and electrode potentials were converted to the normal hydrogen electrode (NHE) scale using E(NHE) = E(Ag/AgCl) + 0.197 V. Unless otherwise specified, all reported potentials are referenced to NHE.

D. Cyclic Voltammetry. Solutions of 0.5 mM Mn^{2+} with 50 mM of MeP_i at pH 3 and 8 were prepared. For each quiescent solution, cyclic voltammograms (CVs) were taken at 10 and 50 mV/s scan rates on an immersed 1 cm^2 fluorine-doped tin-oxide-coated glass (FTO, TEC-7 purchased from Hartford Glass). All FTO slides were sonicated in acetone and rinsed with reagent-grade water prior to use, and a 1 cm^2 electrode area was produced by using a 0.5 cm wide strip of Scotch tape as a mask. The potential range of the scans depended on the pH of the electrolyte (Figure 1), and CVs were permitted to cycle 100 times to visualize the progression of the peaks over time.

E. Coulometric Titration. Films of electrodeposited manganese oxide (MnOx) at loadings of 6, 32, 100, and 250 mC/cm^2 were prepared on 1 cm^2 FTO by controlled potential deposition at 0.577 V in quiescent solutions of 0.5 mM Mn^{2+} with 50 mM MeP_i buffer at pH 8.0. The films were dipped in reagent-grade water to remove any remaining solution, dried under ambient conditions, and the Scotch tape used to mask the FTO was carefully removed from the plates. Each plate was placed in a polypropylene test tube (Falcon) and sonicated in a small aliquot of 69.7% nitric acid (Fluka Analytical, Trace-Select) and left to dissolve overnight. The blank FTO plate was removed from the tube, and reagent-grade water was added to dilute the existing solution to 5% v/v nitric acid concentration. Samples were analyzed for manganese content by inductively coupled plasma atomic emission spectrometery (ICP-AES; HORIBA Jobin ACTIVA instrument) and quadrupole inductively coupled plasma mass spectrometry (ICP-MS; Elemental Analysis, Inc., Lexington, KY); see Table S1 in the Supporting Information. Manganese standards were prepared from solutions purchased from Fluka, designated suitable for ICP analysis.

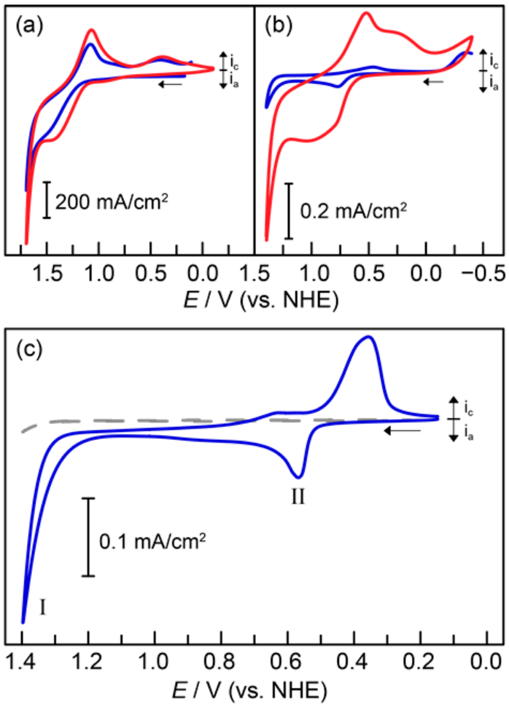

Figure 1. Cyclic voltammograms of a 1 cm^2 FTO electrode in 0.5 mM Mn^{2+} and 50 mM MeP_i solution at (a) pH 3.0 and (b) pH 8.0, 50 mV/s scan rate showing the 1st (blue line) and 200th (red line) cycles. (c) Representative CV at pH 8.0 at 10 mV/s (blue line). Region I is attributed to water oxidation while region II denotes MnOx deposition. For comparison, background CV of same electrolyte but without Mn^{2+} (gray dashed line).

F. Potential Step Chronoamperometry. Potential step chronoamperometry traces were recorded in 0.5 mM Mn^{2+}, 50 mM MeP_i, and 1.90 M KNO_3 solution with the following electrodes: 2 mm diameter platinum disk button electrode (CH Instruments), 3 mm diameter glassy carbon (GC) disk button electrode (CH Instruments), 1 cm^2 TEC-7 FTO on glass slide (Hartford Glass), and 0.15 mm^2 highly oriented pyrolytic graphite (HOPG, grade SPI-2, SPI Supplies). The Pt and GC button electrodes were polished to a mirror shine for 60 s with 0.05 μm alumina (CH Instruments) and sonicated for 60 s in reagent-grade water. Prior to each experiment, the Pt button electrodes were cycled ~50 times from −0.2 to 1.5 V in 0.5 M sulfuric acid (99.999% trace metals basis, Aldrich) and then rinsed with reagent-grade water. GC button electrodes were repolished with alumina before each experiment. Electrodes were initially polarized at 0.397 V for 5 s to charge only the double-layer and then stepped to a more anodic potential sufficient for catalyst nucleation for 60 s (Figure 2 and Figure

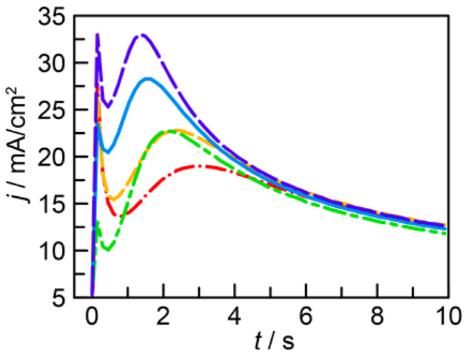

Figure 2. Potential step chronoamperograms of a platinum disk electrode in a solution of 0.5 mM Mn^{2+} and 50 mM MeP_i with 1.90 M KNO_3 electrolyte at pH 8. Step potentials of 0.517 (red dashed dotted line), 0.522 (yellow dashed line), 0.527 (green dashed line), 0.532 (blue line), and 0.537 V (purple dashed line) were applied. All experiments were preceded by an initial 5 s pulse at 0.397 V (not shown) to partially precharge the double layer.

S1 in the Supporting Information). In all cases, data points were sampled every 0.03 s, and *i*R compensation was applied. Multiple independent experiments on fresh electrodes using the same potential step parameters reproduced the values of peak current (j_{max}) and time of peak current (t_{max}) within 5%.

G. Atomic Force Microscopy of Nucleation. AFM employed HOPG electrodes (Grade SPI-2, SPI Supplies) prepared by cleaving a thin layer of HOPG from a bulk slab using double-sided Scotch tape and mounting onto a glass slide. The HOPG layer was contacted using a toothless alligator clip, and a 0.1 to 0.15 cm^2 area was immersed in solution. A series of partially nucleated catalyst islands on HOPG were prepared by potential step chronoamperometry with a step potential of 0.637 V and times of 0.2, 0.5, 1.0, 2.0, 4.0, and 8.0 × t_{max} (for $t_{max} \approx 13$ s under these conditions) in 0.5 mM Mn^{2+}, 50 mM MeP_i, and 1.90 M KNO_3 solution (Figure 3 and Figure S2 in the Supporting Information). For longer electrolysis times, the amperometric trace was monitored, and electrolysis was manually terminated at the appropriate time relative to the observed t_{max} in each run. This procedure served to limit errors due to slight variations (<2 s) in the absolute value of t_{max} between independent experiments. In all cases, after termination of electrolysis, the electrode was immediately removed from solution, rinsed in reagent-grade water, and dried in preparation for imaging by AFM. AFM images were collected using a Veeco Nanoscope Dimension 4100 (Veeco Instruments, Santa Barbara, CA) operating in tapping mode with a Veeco silicon nitride probe with a resonance frequency of ~200 kHz and average tip radius of 3 nm. All measurements were performed in air and at room temperature. Nucleus size, height, number, and percent coverage values were determined using Nanoscope V5.31 software (Figure 4).

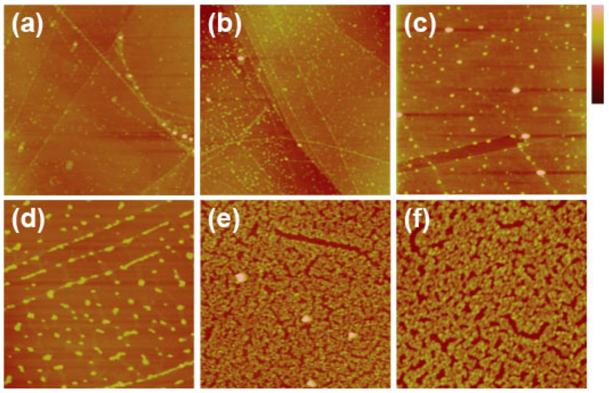

Figure 3. Representative 5 × 5 μm AFM images of a highly oriented pyrolytic graphite electrodes after being subjected to potential step polarization at 0.637 V in 0.5 mM Mn^{2+} and 50 mM MeP_i with 1.90 M KNO_3 electrolyte at pH 8 for ca. (a) 0.2, (b) 0.5, (c) 1, (d) 2, (e) 4, and (f) 8 × t_{max} (~13 s). Bar to the right of image indicates the depth with a full-scale value of (a) 25, (b) 25, (c) 25, (d) 50, (e) 75, and (f) 100 nm.

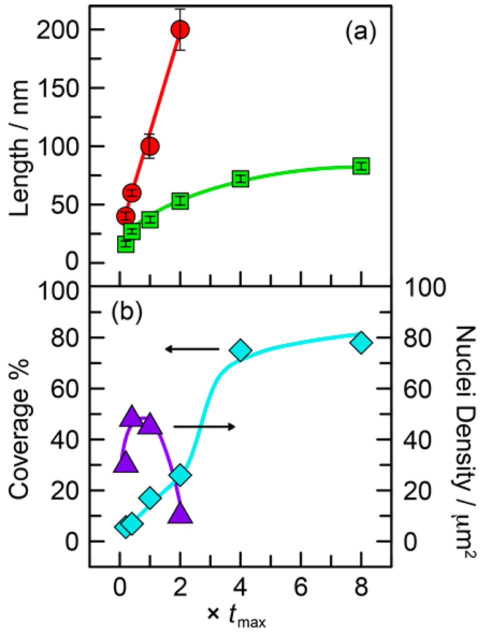

Figure 4. Nucleus size, density, and surface coverage percentages as a function of the time to achieve peak current (t_{max}) derived from analysis of MnOx AFMs in Figure 3. (a) Diameter (red ●) and height (green ■) of catalyst nuclei with error bars. (b) Percent of surface coverage (light blue ◆) and nucleus density (purple ▲) of the 5 × 5 μm HOPG surfaces. Diameters and nucleus densities could not be obtained for merged nuclei for $t \geq 4 \times t_{max}$. In both figures, lines are presented to guide the eye.

H. Tafel Data Collection. Current−potential data (or Tafel data) was obtained by controlled potential electrolysis of MnOx films in 0.5 mM Mn^{2+}, 50 mM MeP_i, and 1.90 M KNO_3 buffer solutions at pH 8. A 0.196 cm^2 Pt RDE in a Pine Instruments MSR rotator served as the working electrode and was polished to mirror shine with 0.05 μm alumina (CH Instruments) and cycled ~50 times at 300 mV/s from −0.2 to 1.5 V in 0.5 M H_2SO_4 (99.999% trace metals basis, Aldrich) before each experiment. To remove the influence of early nucleation processes, a thin 2.55 mC/cm^2 MnOx film was predeposited on the Pt RDE at 0.577 V and 2500 rpm. Next, Tafel data were collected by sweeping the electrode potential from high to low values, in 5 mV decrements, across the linear Tafel region. At each potential, the electrode was rotated at 2500, 1600, 1225, 900, and 625 rpm, and data were collected for 60−90 s at each rotation rate such that steady-state current density was reached. pH was continuously monitored during the experiment with a pH probe (VWR) positioned in the working compartment, and the pH was held within 0.05 units of the desired value with periodic addition of 1 to 2 μL of concentrated KOH.

Importantly, KOH was only added at the beginning of a new potential step rather than during the sweep of rotation rates to minimize the impact of transient current spikes resulting from base addition from affecting subsequent Koutecký–Levich (K–L) analysis. The solution in the working compartment was stirred gently during Tafel data collection to prevent the formation of large concentration gradients and allow efficient mixing of any added KOH. K–L analysis by plotting the inverse of steady-state current density (j^{-1}) against the inverse square root of the rotation rate ($\omega^{-1/2}$) yielded activation-controlled current density (j_{ac}) for each potential (Figure S3 in the Supporting Information). The potentials were then plotted against log j_{ac} to yield a Tafel plot for the deposition process (Figure 5). Running the same experiment in Mn^{2+}-free solution resulted in current densities two orders of magnitude lower than for solutions with Mn^{2+}, demonstrating negligible background contribution (Figure S4 in the Supporting Information).

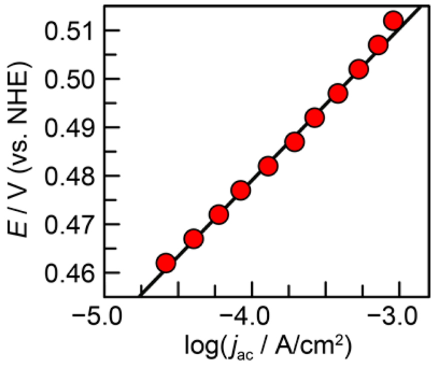

Figure 5. Tafel plot of MnOx deposition on a platinum rotating disk electrode (RDE, surface area = 0.196 cm^2) in solution of 0.5 mM Mn^{2+} with 50 mM MeP_i and 1.90 M KNO_3 electrolyte at pH 8. A 2.55 mC/cm^2 of catalyst film was predeposited on the RDE before Tafel data collection. The Tafel slope is 31.1 mV/decade. Normalized activation currents were obtained from Koutecký–Levich (K–L) analysis (Figure S3 in the Supporting Information).

I. Mn^{2+} Concentration Dependence. The dependence of MnOx catalyst formation rate on Mn^{2+} concentration was determined by constructing Tafel plots, using the procedure previously described, from 50 mM MeP_i, 1.90 M KNO_3 solutions at pH 8.0 containing 0.010, 0.018, 0.032, 0.056, and 0.100 Mn^{2+} (Figure S5 in the Supporting Information). The data were interpolated at potentials of 0.497, 0.502, 0.507, and 0.512 V by slicing horizontally across the linear Tafel plots to yield the dependence of j_{ac} on Mn^{2+} concentration (Figure 6).

J. Methylphosphonate Concentration Dependence. The dependence of MnOx catalyst formation rate on MeP_i concentration was determined by constructing Tafel plots, using the procedure previously described, from 0.5 mM Mn^{2+} solutions at pH 8.0 containing 3.2, 5.6, 10.0, 17.8, 31.6, and 56.2 mM MeP_i (Figure S6 in the Supporting Information). Additional KNO_3 was added to achieve a fixed μ = 2 M. The data were interpolated at potentials of 0.497, 0.502, 0.507, 0.512, 0.517, and 0.522 V, by slicing horizontally across the linear Tafel plots, to yield the dependence of j_{ac} on MeP_i concentration (Figure 7).

Because pK_a changes with μ, a fixed μ = 2 M was required to reliably prepare solutions of known MeP_i concentration. The adjusted pK_a for MeP_i was computed using specific ion interaction theory (SIT),[33] as implemented in the program *Ionic Strength Corrections using Specific Interaction Theory* (version 2.0).[34] Equilibrium constants were calculated for 50 mM MeP_i in solution under μ = 2 M with KNO_3 background electrolyte. The reported first and second pK_a values of methylphosphonic acid at μ = 0.1 M are 2.10 and 7.51, respectively.[35] These values were corrected using the cation SIT parameter for H^+ (0.07), the anion SIT parameters for $MePO_3H^-$ and $MePO_3^-$ (−0.14), and HPO_4^{2-} surrogates, $H_2PO_4^{2-}$ (−0.10). This yielded corrected values of pK_{a1} = 1.7 and pK_{a2} = 7.0. These pK_a values were used to calculate the speciation of MeP_i at various concentrations and determine the amount of KNO_3 required to achieve a target μ = 2 M.

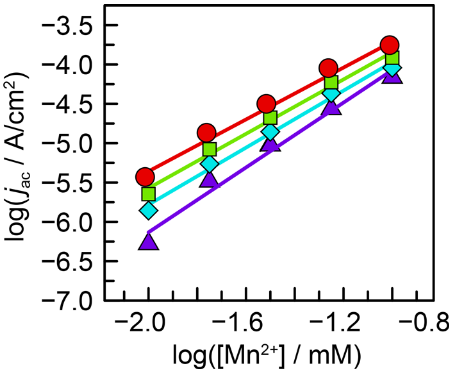

Figure 6. [Mn^{2+}] dependence of MnOx deposition in 50 mM MeP_I and 1.90 M KNO_3 electrolyte at pH 8. Data were interpolated at fixed potentials of 0.512 (red ●), 0.507 (green ■), 0.502 (blue ◆), and 0.497 V (purple ▲) from Tafel plots collected for Mn^{2+} concentrations from 0.010 to 0.100 mM (Figure S5 in the Supporting Information). Average slope is 1.8 ± 0.2.

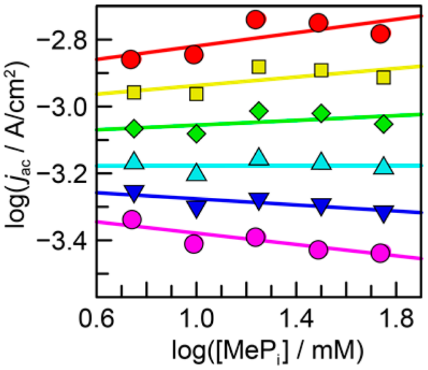

Figure 7. [MeP_i] dependence for MnOx catalyst film growth in 0.5 mM Mn^{2+} at pH 8.0 with KNO_3 adjusted to maintain an ionic strength of 2 M. Data were interpolated at fixed potentials of 0.522 (red ●), 0.517 (yellow ■), 0.512 (green ◆), 0.507 (blue ▲), 0.502 (purple ▼), and 0.497 V (magenta ●) from Tafel plots collected for MeP_i concentrations from 3.2 to 56.2 mM (Figure S6 in the Supporting Information). The average slope is 0.0 ± 0.1.

K. pH Dependence. The dependence of MnOx catalyst formation rate on pH was determined by constructing Tafel plots, using the procedure previously described, from 0.5 mM Mn^{2+}, 50 mM MeP_i, and 1.90 M KNO_3 solutions at pH 6.0, 6.2, 6.4, 6.6, 6.8, 7.0, 7.2, 7.4, 7.6, 7.8, 8.0, 8.2, 8.4, and 8.6 (Figure S7 in the Supporting Information). The data were interpolated at values of log(j_{ac}) = −5.0, −4.4, −3.7, and −3.0 by slicing vertically across the linear Tafel plots to yield the dependence of applied potential on pH (Figure 8). The slope of *E* versus pH plots was divided by the negative of the Tafel slope to extract the reaction order in pH.

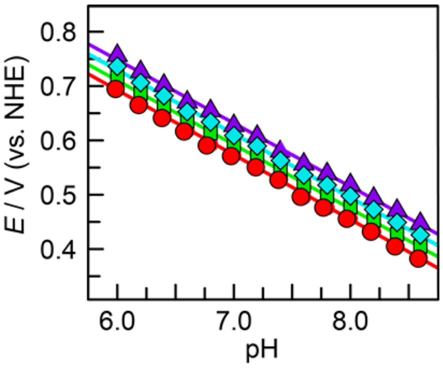

Figure 8. pH dependence for MnOx deposition in 0.5 mM Mn^{2+} with 50 mM MeP_i, and 1.90 M KNO_3 electrolyte. Data were interpolated at fixed current densities of log j = −5.0 (red ●), −4.4 (green ■), −3.7 (blue ◆), and −3.0 (purple ▲) from Tafel plots collected at pH values from 6.0 to 8.6, incrementing by 0.2 (Figure S7 in the Supporting Information). The average slope is −117.6 ± 1.1 mV/pH unit.

L. Powder X-ray Diffraction. Powder X-ray diffraction patterns (pXRD) of MnOx films (Figure S8 in the Supporting Information) were obtained with a PANAlytical X'Pert Pro MPD diffractometer with Motorized Open Eularian Cradle platform and X'Celerator Detector under Cu Kα radiation (λ = 1.5405 Å). The diffractometer contained a programmable divergence slit, exchangeable Soller slits, and exchangeable antiscatter slits. All measurements were taken under fixed slit mode using instrument parameters of 0.04 rad Soller slits, 1/8° antiscatter slit, and 1/16° divergence slit with a 10 mm beam mask. Crystalline peaks observed on the FTO substrate correspond to tin oxide (SnO_2, JCPDS file no. 01-075-9494, CSD#157449). The MnOx sample was prepared by constant potential deposition of 32 mC/cm^2 in MeP_i as described previously, lightly rinsed with reagent-grade water, and immediately anodized at 1.10 V in Mn^{2+}-free 1.0 M P_i buffer at pH 9.0 for 4 h. The film was then rinsed again, air-dried, and examined using pXRD from 2θ = 5 to 45°. Crystalline features corresponded to the FTO substrate. No peaks were observed for MnOx, which indicated that the electrodeposited films were amorphous.

■ RESULTS

MnOx catalyst films were prepared by controlled-potential electrolysis of solutions containing 0.5 mM Mn^{2+} and 50 mM methylphosphonate (MePi) at pH 8.0. These solutions remained clear over the course of all depositions, and the resulting MnOx films were examined using powder X-ray diffraction (pXRD) from 2θ = 5 to 45°. As shown in Figure S8 in the Supporting Information, the only peaks in the resulting diffraction pattern for MnOx deposited on fluorine-doped tin oxide (FTO) correspond to the underlying FTO substrate. The broad feature at low angles indicates the amorphous nature of electrodeposited MnOx.

Figure 1a,b shows the CVs recorded for an FTO electrode immersed in a solution of MeP_i at pH 3.0 and 8.0. Continued cycling of the electrode was accompanied by peak growth and formation of a light brown film on the FTO slide. Two distinct regions appear in the CV. The feature labeled I in Figure 1c is a sharp catalytic wave at high positive potentials assigned to water oxidation, where the current density increases exponentially with applied potential. The region labeled II at less positive potentials comprises two coupled peaks. The diffusive anodic peak (E_P = 0.57 V) is assigned to oxidation of solution Mn^{2+} to deposited Mn^{4+}, and the surface cathodic peak (E_P = 0.36 V) is assigned to the reduction of the Mn^{4+} film. These peaks are not electrochemically reversible because a complex multistep mechanism is responsible for both the oxidation and reduction processes. Accordingly, more detailed electrochemical experiments were required to elucidate the mechanism. However, because of the complexity of the peaks in the CVs, subsequent experiments focused only on illuminating the oxidative deposition process.

The CVs of Figure 1 indicate that MnOx films may be electrodeposited at low potentials distinctly separate from the onset of water oxidation. Consequently, the deposition current could be recorded without extraneous contributions from the OER, which enabled coulometric titration studies to determine accurately the number of electrons passed per deposited manganese center during catalyst growth. Films of various loadings were prepared by the passage of a fixed amount of charge on FTO by controlled potential deposition in MeP_i buffered solutions of Mn^{2+} at pH 8.0. The films were then dissolved in 5% nitric acid and analyzed for manganese content by inductively coupled plasma. The detected manganese loadings were compared with the charge passed during deposition (Table S1 in the Supporting Information) to reveal a calculated average number of electrons passed per deposited Mn center of 1.68 ± 0.06, which indicates an average Mn oxidation state of +3.68 for the electrodeposited MnOx films.

Nucleation and Early Growth of Film. The early stages of catalyst formation were probed, without interference from the OER, by collecting chronoamperograms on freshly polished platinum electrodes in Mn^{2+} solutions of MeP_i buffer and potassium nitrate (KNO_3) supporting electrolyte at pH 8 (Figure 2). A high ionic strength was maintained to avoid diffuse double-layer effects and to minimize interference from migration of charged reactants in solution.[31,36] Chronoamperograms were also collected on GC, HOPG, and FTO to verify that the same nucleation process occurs on different electrode surfaces (Figure S1 in the Supporting Information). The electrode was initially polarized at a potential lower than required for catalyst growth (e.g., 0.397 V on Pt, not shown in Figure 2) for 5 s to charge the double layer marginally, which minimizes double-layer charging currents. The potential was then stepped to sufficiently more anodic voltages for electrodeposition. Upon initiating this potential step, the chronoamperograms displayed the characteristics of: (i) an initial current spike followed by rapid decay; (ii) a rise and fall in current that culminates at a peak, j_{max}; and finally, (iii) a slow decrease in current that approaches a nonzero limiting value. The time at which j_{max} appeared, denoted t_{max}, is potential-dependent; we observed that as the step potential increases, t_{max} decreases.

Nucleated growth was confirmed by imaging the electrode surface with AFM. The requirements of an atomically smooth electrode surface necessitated the use of HOPG. Figure 3 shows a series of AFM images of HOPG electrodes with deposited MnOx that was prepared with varying polarization times. These images were algorithmically processed based on the difference in contrast between the bare HOPG and MnOx deposited surface to determine catalyst island diameter, height, density, and percent coverage as a function of t_{max}; these results are summarized in Figure 4. At 0.2 × t_{max}, the average island size was 40 nm with 6% coverage and increased to 100 nm and 17% coverage at 1 × t_{max}. At 4 × t_{max}, catalyst islands began to merge and surface coverage advanced to 75%, where it began to plateau. This rapid increase in nucleus size with sluggish rise in nucleus density and coverage is characteristic of progressive nucleation. A landscape AFM image of a HOPG electrode subjected to 64 mC/cm^2 MnOx loading is shown in Figure S2 in the Supporting Information and reveals a porous surface with disc-shaped features.

Electrokinetics. Tafel plots were employed to interrogate mechanistic information about the role of electron transfer with respect to the rate-limiting step (RLS) for electrodeposition. Steady-state current densities (j) for the electrodeposition process were measured at varying rotation rates (ω) and applied potentials (E) on a platinum rotating disk electrode (RDE) with a thin-layer of predeposited MnOx catalyst. The predeposited film prevented early nucleation and growth processes from influencing steady-state measurements.

For each potential in the Tafel analysis, a K–L plot of j^{-1} versus $\omega^{-1/2}$ was constructed and extrapolated to infinite rotation rate, where $\omega^{-1/2} = 0$, to determine the activation-controlled current density (j_{ac}), free from any mass-transport limitations (Figure S3 in the Supporting Information).[37] A Tafel plot of E versus log j_{ac} exhibited linearity over two decades of current densities and a slope of 31.1 mV/decade (Figure 5; Figure S4 in the Supporting Information includes background). The plot displays excellent run-to-run reproducibility, and the same slope was obtained regardless of initial film thickness or the direction (increasing or decreasing) of applied potentials.

Electrokinetics were also used to determine the reaction order (ρ) of reactants by obtaining the slope of log j versus log [c_i] plots at fixed potentials (where c_i denotes the concentration of a species). The reaction order is defined as the dependence of the logarithm of the reaction rate (v) on the logarithm of the species concentration when the concentration of all other species ($c_{k\neq i}$) are held constant

$$\rho = \left(\frac{\partial \log v}{\partial \log c_i}\right)_{c_{k\neq i}} = \left(\frac{\partial \log j}{\partial \log c_i}\right)_{c_{k\neq i}} \tag{1}$$

where the current density (j) driving that reaction replaces the rate of the reaction because these quantities are directly proportional.[37] Thus, the dependence of electrodeposition rate on Mn^{2+} concentration was probed by constructing log j_{ac} versus log [Mn^{2+}] plots at different fixed potentials for solutions of varying Mn^{2+} concentrations (Figure S5 in the Supporting Information). Higher Mn^{2+} concentrations could not be evaluated owing to solubility limitations of Mn^{2+} in the MeP_i electrolyte. The Tafel plots demonstrated linearity over two decades of current density, and an average Tafel slope of 30.6 ± 3.0 mV/decade was obtained. Interpolation of the plots, by taking horizontal slices of the data at fixed potentials, produced plots of steady-state activation controlled current densities as a function of Mn^{2+} concentration (Figure 6). The slope of this plot furnishes the reaction order, which was determined to be second-order in [Mn^{2+}].

The role of MeP_i buffer on MnOx electrodeposition was similarly evaluated by constructing Tafel plots in Mn^{2+} solutions with MeP_i concentrations varied from 3.2 to 56.2 mM (Figure S6 in the Supporting Information). The total ionic strength was maintained at 2.0 M with the addition of KNO_3 supporting electrolyte. The Tafel plots were linear over two decades of current density for an average Tafel slope close to 36.3 mV/decade. As shown in Figure S6 in the Supporting Information, changing [MeP_i] over a decade of concentrations did not significantly affect observed activity. Indeed, horizontal interpolation of the Tafel data at fixed potentials generated plots of log j_{ac} as a function of log [MeP_i], which possessed an average slope of 0.0 ± 0.1 (Figure 7). On the basis of these results, we conclude that electrodeposition of MnOx is zeroth-order in [MeP_i].

Finally, the pH dependence of catalyst formation rate was determined by collecting Tafel data in MeP_i-buffered Mn^{2+} solutions with KNO_3 at a range of pH from the near-neutral to weakly alkaline regimes (Figure S7 in the Supporting Information). The plots displayed linearity over one to two decades of current density with an average slope of 31.6 ± 2.1 mV/decade. The consistency of this slope over a wide pH range provided verification that the mechanism of deposition remained the same. However, the Tafel plots exhibited significant shift with pH. The consequence of this higher activity is that a single horizontal slice through all data, as employed for interpolating [Mn^{2+}] and [MeP_i] dependence data, cannot encompass all Tafel plots. However, a vertical slice (i.e., at constant current density) through all plots may be achieved. Vertical interpolation at fixed current densities yields the pH dependence of the steady-state potential at constant current density $(\partial E/\partial \mathrm{pH})_j$ (Figure 8). In this form, the reaction order in pH (ρ_{pH}) may be calculated from the following partial derivative[37]

$$\rho_{pH} = \left(\frac{\partial \log j}{\partial \mathrm{pH}}\right)_E = -\left(\frac{\partial E}{\partial \mathrm{pH}}\right)_j \Big/ \left(\frac{\partial E}{\partial \log j}\right)_{\mathrm{pH}} \tag{2}$$

where the reaction order in pH (ρ_{pH}) can be determined by dividing the negative of the slope of the potential versus pH plot by the Tafel slope. The average slope of these plots was −117.6 ± 1.1 mV/pH. Dividing this slope by the negative of the average Tafel slope then produced a reaction order in pH of 3.7 ± 0.2. Therefore, MnOx deposition is inverse fourth-order in H^+ activity.

DISCUSSION

Chronoamperometry was employed to probe details of catalyst growth at early and steady-state times of deposition. In solutions of Mn^{2+} buffered by MeP_i at pH 8, the chronoamperograms shown in Figure 2 at anodic MnOx deposition potentials (region II of Figure 1) show that the oxidation event is not a mere diffusion-controlled process characteristic of a simple outer-sphere oxidation of Mn^{2+} but is rather a quasi-3-D nucleation pathway, as demonstrated by the early peak in current density and its subsequent decay to a limiting diffusion-controlled current. The initial rise and peak in current represents the formation of small islands of catalyst nuclei.[38,39] As more nuclei appear, the effective surface area of the electrode increases, thus leading to a corresponding gain in the geometric current density. The fact that the current density quickly attains a maximum (denoted j_{max}) at time t_{max} is consistent with the local depletion of Mn^{2+} ions. As the depletion zones around the deposited nuclei expand and overlap, the decay of current as a function of $t^{-1/2}$ is characteristic of diffusion-controlled growth where Mn^{2+} ions move in a linear fashion perpendicular to the plane of the electrode surface. Because current density is exponentially proportional to potential, higher applied potentials (more anodic in this case) increase the rate of nucleus growth and consequently j_{max}. However, the rate of depletion zone formation also increases concurrently, which lead to earlier onset of t_{max}.

There are two limiting regimes for the competition between nucleation and growth: instantaneous nucleation where the nucleation rate constant is fast and dominates the growth rate constant versus progressive nucleation where nucleation is slower than growth.[38,39] Analytical models can be fit to experimental data to discern the type of nucleation behavior, but they require experimental specific variables such as diffusion coefficients, nucleus density, and nucleation rate constants. These parameters may be effectively deconvoluted from models by normalizing j and t to the peak current density and peak time, respectively. This normalization is convenient because it permits the comparison of chronoamperograms taken with different substrates, step potentials, and electrolytes. Figure 9 reformulates the j versus t plots of Figure 2 as normalized $(j/j_{max})^2$ versus t/t_{max} plots. Theoretical traces of instantaneous and zeroth-order progressive nucleation (i.e., the Scharifker–Hill (SH) model) have been overlaid for comparison. The fits to the experimental normalized current transients on platinum closely follow the progressive nucleation model. The slight deviations from the exact theoretical progressive nucleation curve are largely within experimental error and likely result from the models not accounting for concentration dependence on nucleation rate[40] and surface diffusion of adatoms.[41−45] Indeed, AFM snapshots of the electrode surface during the nucleation process (Figure 3) show that the nuclei density decreases after t_{max} (Figure 4b), which suggests that some nuclei are diffusing and coalescing. Similar analysis applied to GC, HOPG, and FTO chronoamperograms demonstrated the same progressive nucleation model for early catalyst growth (Figure S9 in the Supporting Information). Current transients for GC, HOPG, and FTO electrodes, in contrast with Pt, were slightly more complicated owing to a significant delay in the onset of nucleation (denoted t_0). This delay caused the normalized plots to have sharper peaks and precluded the comparison to theoretical curves.[46] A t_0 correction can be applied to the chronoamperograms to obtain correct normalization traces. For a progressive nucleation model, t_0 was estimated from the x axis intercept of a linear fit to the rising portion of $j^{2/3}$ versus t plots (Figure S10 in the Supporting Information), and all time points were subtracted by t_0 before normalization.

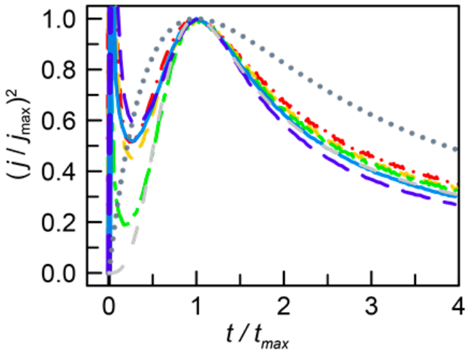

Figure 9. Normalized potential step chronoamperograms for platinum disk electrodes in 0.5 mM Mn^{2+} and 50 mM MeP_i with 1.90 M KNO_3 electrolyte at pH 8. Data from Figure 2 were normalized to t_{max} and j_{max} for step potentials of 0.517 (red dashed dotted line), 0.522 (yellow dashed line), 0.527 (green dashed line), 0.532 (blue line), and 0.537 V (purple dashed line). For comparison, theoretical normalized traces for instantaneous (dark gray dotted line) and zeroth-order progressive (light gray dashed line) nucleated growth are overlaid with experimental results.

An important consequence of the nucleation results is that nuclei size and surface coverage of catalyst can be precisely controlled by modulating the magnitude and duration of the applied potential, much like what the Penner group reported for size-selective electrodeposition of metal particles[47,48] and enabling the possibility for regulating bimetallic particle deposition.[49] The ability to manipulate catalyst coverage via progressive nucleation was confirmed through AFM imaging of a series of initial depositions at short times from $t = 0.2$ to $8 \times t_{max}$ (Figure 3). Tracking nucleus size, density, and surface coverage over time demonstrated the sluggish formation of new surface nucleus sites relative to the growth of existing nuclei (Figure 4), a characteristic expected of progressive nucleation.

Beyond early nucleation lies steady-state catalyst growth. The electrochemical rate law for catalyst growth may be discerned from Tafel analysis of the current density as a function of Mn^{2+}, MeP_i, and H^+ concentrations and under the conditions: (i) that current is analyzed beyond the stage of initial nucleation kinetics and (ii) that the activation-controlled current be absent of mass-transport limitations. The first condition was ensured by the predeposition of a thin MnOx film that fully covered the Pt electrode surface prior to Tafel analysis. This pretreatment eliminated any early nucleation kinetics from influencing the observed current density. The second condition was met by using a RDE to collect mass-transport limited current at various rotation velocities. A K–L plot of RDE data enabled the extrapolation of current to infinite rotation velocity to obtain activation-controlled current density (Figure S3 in the Supporting Information). A K–L analysis was performed for each point of the Tafel plots.

Tafel plots were linear over two decades of current densities and exhibited an average slope close to 31 mV/decade (Figure 5), which is close to $2.3 \times RT/2F$ (at 298 K) and is indicative of a deposition mechanism involving a two-electron pre-equilibrium, followed by a chemical RLS.[37] A comprehensive mechanistic picture further entails probing the dependence of deposition kinetics on other solution species including Mn^{2+}, MeP_i, and H^+. For Mn^{2+}, the average reaction order was ~1.8, which indicated that electrodeposition of MnOx is second-order in Mn^{2+} concentration (Figure 6). Therefore, assembly of MnOx catalyst clusters involves two Mn^{2+} ions prior to or during the RLS. A similar reaction order analysis was performed for MeP_i dependence. In these experiments, it was especially important to maintain a constant ionic strength of 2 M because the pK_a values of methylphosphonic acid vary with ionic strength. Phosphate pK_a values were corrected using SIT. (See the Experimental Section for details.) The Tafel plots of Figure 7 indicate no dependence on MeP_i concentration. Likewise, the reaction order analysis furnished from Figure 8 for the H^+ dependence of deposition yielded an inverse fourth-order dependence on H^+ activity.

Together, the forgoing Tafel results establish an electrochemical rate law for MnOx deposition as

$$j_{ac} = 2Fk_0[Mn^{2+}]^2[H^+]^{-4}\exp\left[\frac{2FE}{RT}\right] \quad (3)$$

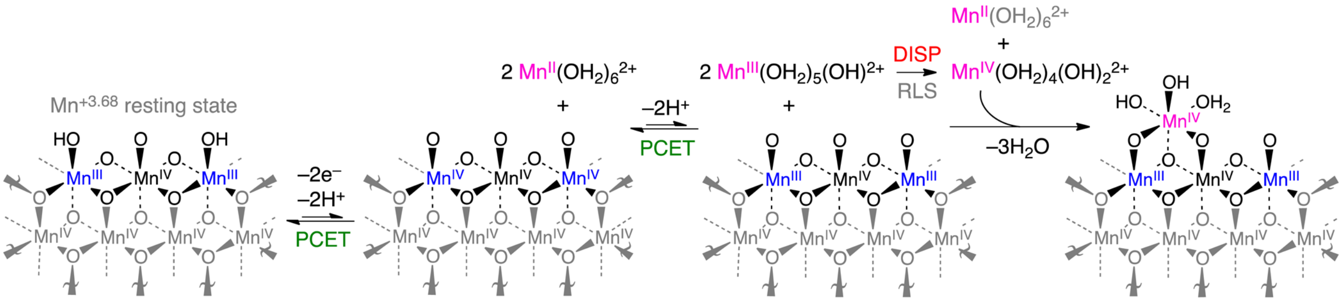

Figure 10. Proposed mechanism of MnOx catalyst film formation. The predeposited MnOx film (with an average Mn oxidation state of +3.68, determined by coulometry in Table S1 in the Supporting Information) first undergoes electrochemical oxidation in a two-electron, two-proton PCET minor equilibrium. The catalyst film then chemically oxidizes two Mn^{2+} hexaaquo complexes, each in a one-electron, one-proton PCET minor equilibrium to form two solution Mn^{3+} species that disproportionate, in the rate-limiting step, to Mn^{2+} and Mn^{4+}. Subsequent dehydration facilitates the deposition of a single Mn^{4+} site.

where k_0 is a potential-independent rate constant with units of $(\text{mol M}^2)/(\text{s cm}^2)$ that is proportional to the exchange current density. Tafel analysis for deposition of MnOx, albeit under acidic conditions,[24] also reports a 30 mV/decade Tafel slope and inverse fourth-order proton dependence but a first-order dependence on Mn^{2+}, which may be the result of an inability to distinguish between a first- and second-order dependence owing to the limited window of Mn^{2+} concentrations within which measurements were taken.

An overall stoichiometry of MnOx deposition from homogeneous solutions of Mn^{2+} that is consistent with the rate law established from electrokinetics is

$$2Mn^{2+} + 2H_2O \rightleftharpoons MnO_2 + 4H^+ + 2e^- + Mn^{2+} \quad (4)$$

The initial step entails the participation of two Mn^{2+} aqua complexes, each in a one-electron, one-proton proton-coupled electron transfer (PCET) minor equilibrium, to form two Mn^{3+} species in solution. The most likely PCET event involves the concomitant deprotonation of the manganous aqua complex upon oxidation

$$2Mn^{II}(H_2O)_6{}^{2+} \rightleftharpoons 2Mn^{III}(H_2O)_5(OH)^{2+} + 2H^+ + 2e^- \quad (5)$$

Indeed, the pK_a values for first-row transition-metal(III) ion hexaaqua complexes are typically <4, and hence a PCET oxidation is favored.[50] PCET facilitates the redox leveling of deposition potentials. That is, the thermodynamic potential associated with the Mn^{3+}/Mn^{2+} redox couple is 1.5 V,[51] yet deposition is observed at less anodic potentials (ca. 0.5 V at pH 8, see Figure 1). Subsequent rate-limiting disproportionation of the two Mn^{3+} complexes reforms the Mn^{2+} aquo and a Mn^{4+} species, which can then add to the MnOx surface via a standard dehydration reaction; deprotonation of two terminal hydroxyl groups completes the observed inverse fourth-order dependence on $[H^+]$. Overall, two Mn^{2+} solution ions are necessary for the formation of one Mn^{4+} surface site, which explains the second-order dependence on Mn^{2+}. This sequence repeats to facilitate steady-state growth, as schematically described in Figure 10. The mechanism is shown within the context of pyrolusite- (β-MnO_2) and birnessite- (δ-MnO_2) like structures because it has now been established with structural X-ray absorption and diffraction (XRD) studies[16−18,27,30] that electrodeposited MnOx films from acidic and neutral pH assume these structural polymorphs.

There is an additional caveat that arises from the reconciliation of the coulometric titration data with the proposed mechanism of Figure 10. Approximately 1.68 electrons are passed per Mn atom that is deposited for an average bulk Mn oxidation state of +3.68. This suggests that a minority fraction of Mn^{3+} oxide is present in the catalyst resting state; this fraction is depicted at edge sites in Figure 10. Because the thicknesses of these films are on the order of 10 nm (estimated for 6 mC/cm² catalyst loadings), direct oxidation of solution Mn^{2+} by the Pt electrode is improbable. Therefore, growth of MnOx must occur via charge transport by self-exchange through the predeposited catalyst.[52,53] Per our Tafel results, the catalyst film in its resting state participates in a $2e^-$−$2H^+$ minor equilibrium that then chemically oxidizes solution Mn^{2+} in subsequent PCET. The Mn^{4+} formed at newly deposited edge sites may subsequently react with solution Mn^{2+} to form Mn^{3+} (not shown in Figure 10). Given that manganese dioxides have been experimentally observed to have stoichiometric compositions of $MnO_{1.7-2.0}$,[54] our results are in agreement with the majority reaction comprising an overall two-electron oxidation to a Mn^{4+} oxide with a minority population of Mn^{3+} sites. Moreover, our results support the contention of Takashima et al., who have used electronic absorption spectroscopy to correlate enhanced OER of MnOx materials to conditions that stabilize Mn^{3+}.[19,20]

Tafel data also provides insight into the mechanism of progressive nucleation of MnOx on Pt from calculated nucleation rates as a function of applied potential. Under the SH model for progressive nucleation, the nucleation rate is proportional to $t_{max}{}^{-2}$ (derivation shown in the Supporting Information). Substituting this value into the Tafel equation results in a final expression where the Tafel slope can be determined by plotting potential versus log $t_{max}{}^{-2}$. This plot is shown in Figure 11 and exhibits a slope of 27.8 mV/decade. Although the slope was derived from nucleation measurements taken over a narrow potential range of only 20 mV, it agrees with Tafel measurements taken for steady-state deposition (Figure 5) and implies that a similar mechanism occurs for early catalyst growth. Such a low Tafel slope also explains the narrow range of potentials for observing nucleation current transients: small changes in potential result in a large increase in nucleation rate, which quickly obscures t_{max} in initial double-layer capacitive charging signal. Similarly, small decreases in potential rapidly extend and bury t_{max} into broad convectional features that appear at longer times.

The MnOx deposition mechanism contrasts that of Co−OEC under similar conditions. For Co−OEC deposition, a Tafel slope of 60 mV/decade and first-order dependence on

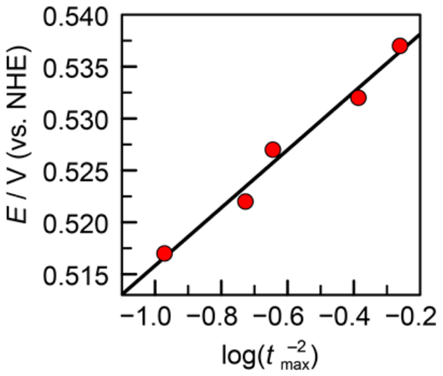

Figure 11. Tafel plot of early MnOx nucleation on a Pt disk electrode. Under the SH model for progressive nucleation, the nucleation rate is proportional to $t_{\max}^{-2}$ (derivation in the Supporting Information). Using $t_{\max}$ derived from Figure 2 yields a Tafel plot with slope of 27.8 mV/decade.

[Co^{2+}] corresponds to a net one-electron minor equilibrium resulting in the oxidation of aqueous Co^{2+} to surface-bound Co^{3+} that then associates to the surface in a RLS.[55] Conversely, a Tafel slope of 31 mV/decade for MnOx together with a second-order dependence on [Mn^{2+}] establishes the involvement of two Mn^{3+} species in a DISP reaction, which is the RLS for catalyst film growth. Moreover, Co−OEC displays an inverse first-order dependence on [MeP_i] and inverse third-order dependence on H^+ activity, whereas MnOx exhibits no dependence on [MeP_i] and is inverse fourth-order in H^+ activity. These details are only revealed by electrochemical kinetics analysis and are transparent in CV traces. Notwithstanding, the majority of literature on electrodeposition of oxidic manganese species is from CVs of Mn^{2+} in unbuffered acidic electrolytes (e.g., molar concentrations of H_2SO_4).[24−30] Proposed pathways for deposition involve either an ECE mechanism, where oxidation of Mn^{2+} to Mn^{3+} is followed by MnOOH formation and subsequent oxidation to MnO_2[25,28] or a DISP mechanism, similar to the finding here, in which two Mn^{3+} formed from oxidation combine to generate Mn^{2+} and MnO_2 species.[24,26,27] Studies seeking to unify these two mechanisms were unable to obtain kinetics information with sufficient fidelity from CV traces.[29−31] In the absence of such data, the mechanisms have been distinguished on the basis of chemical principles. Most notably, the ECE mechanism has been preferred over that of a DISP mechanism for MnO_2 deposition based on expected slower disproportionation kinetics at higher pH. However, the data presented here and particularly the second-order dependence of Mn^{2+} in the rate law strongly point to a DISP mechanism for deposition and growth of MnOx materials under near-neutral and weakly basic conditions. This different interpretation is based on the phase in which Mn^{3+} undergoes disproportionation: solution-based Mn^{3+} versus surface-bound Mn^{3+}. The equilibrium constant for disproportionation of surface MnOOH to Mn^{2+} and MnO_2 decreases by eight orders of magnitude from pH 3.0 to 7.0;[30] similarly, Mn^{3+} exhibits enhanced stability above pH 9 when associated with surfaces.[19] In contrast, solution-based Mn^{3+} complexes are more stable in concentrated acids and disproportionate readily upon decrease in acidity.[56−59] In accordance with the Pourbaix diagram for manganese,[60] disproportionation is averted under highly alkaline conditions because Mn ions are not stable in solution and precipitate as hydroxides and oxides.

■ CONCLUSIONS

The separation of the potentials between MnOx deposition onset and the OER allows for the two processes to be studied in isolation from each other. Fitting current chronoamperometric transients combined with AFM image analysis establish that early catalyst growth follows a progressive nucleation mechanism. Steady-state growth was interrogated through electrochemical kinetics and revealed a rate law that is consistent with a second-order dependence on [Mn^{2+}] and a two-electron, four-proton pre-equilibrium, followed by a rate-limiting chemical step. These results support a DISP mechanism of aqueous Mn^{3+} in near-neutral electrolyte, which addresses a longstanding issue of distinguishing between the ECE and DISP mechanisms for manganese oxide electrodeposition under nonacidic conditions. Overall, the results reported herein lay the foundations for controlling and fine-tuning catalyst nuclei size and coverage on a variety of substrates and defines the kinetics parameters that influence growth, which is important for the integration of oxidic manganese catalysts with photoelectrochemical cells in a buried junction architecture.

■ ASSOCIATED CONTENT

Ⓢ Supporting Information

Calculations, coulometry data, AFM images, chronoamperograms, K−L plots, Tafel plots, and XRD traces. This material is available free of charge via the Internet at http://pubs.acs.org.

■ AUTHOR INFORMATION

Corresponding Author

*E-mail: dnocera@fas.harvard.edu.

Notes

The authors declare no competing financial interest.

■ ACKNOWLEDGMENTS

We thank Minyuan Li for assistance with collecting XRD data. This research was supported by DOE DE-SC0009565. This work made use of the MRSEC Shared Experimental Facilities at MIT, supported by the National Science Foundation under award number DMR-08-19762.

■ REFERENCES

(1) Trasatti, S. Transition Metal Oxides: Versatile Materials for Electrocatalysis. In *The Electrochemistry of Novel Materials*; Lipkowski, J., Ross, P. N., Eds.; VCH: New York, 1994; pp 207−251.

(2) Lewis, N. S.; Nocera, D. G. Powering the Planet: Chemical Challenges in Solar Energy Utilization. *Proc. Natl. Acad. Sci. U.S.A.* **2006**, *103*, 15729−15735.

(3) Nocera, D. G. Chemistry of Personalized Solar Energy. *Inorg. Chem.* **2009**, *48*, 10001−10017.

(4) Cook, T. R.; Dogutan, D. K.; Reece, S. Y.; Surendranath, Y.; Teets, T. S.; Nocera, D. G. Solar Energy Supply and Storage for the Legacy and Nonlegacy Worlds. *Chem. Rev.* **2010**, *110*, 6474−6502.

(5) Pletcher, D.; Li, X. Prospects for Alkaline Zero Gap Water Electrolysers for Hydrogen Production. *Int. J. Hydrogen Energy* **2011**, *36*, 15089−15104.

(6) Desilvestro, J.; Haas, O. Metal Oxide Cathode Materials for Electrochemical Energy Storage: A Review. *J. Electrochem. Soc.* **1990**, *137*, 5C−22C.

(7) Belanger, D.; Brousse, T.; Long, J. W. Manganese Oxides: Battery Materials Make the Leap to Electrochemical Capacitors. *Electrochem. Soc. Interface* **2008**, *17*, 49−52.

(8) Wei, W.; Cui, X.; Chen, W.; Ivey, D. G. Manganese Oxide-Based Materials as Electrochemical Supercapacitor Electrodes. *Chem. Soc. Rev.* **2011**, *40*, 1697−721.

(9) Thackeray, M. M. Manganese Oxides for Lithium Batteries. *Prog. Solid State Chem.* **1997**, *25*, 1−71.

(10) Ji, L.; Lin, Z.; Alcoutlabi, M.; Zhang, X. Recent Developments in Nanostructured Anode Materials for Rechargeable Lithium-Ion Batteries. *Energy Environ. Sci.* **2011**, *4*, 2682−2699.

(11) Scarr, R. F.; Hunter, J. C.; Slezak, P. J. Alkaline-Manganese Dioxide Batteries. In *Handbook of Batteries*; Linden, D.,Reddy, T. B., Eds.; McGraw-Hill: New York, 2002; pp 10.1−10.32.

(12) Greenwood, N. N.; Earnshaw, A. Manganese, Technetium and Rhenium. In *Chemistry of the Elements*; Butterworth-Heinemann: Oxford, U.K., 2006; pp 1040−1069.

(13) Hunter, J. C.; Kozawa, A. Manganese, Technetium, and Rhenium. In *Standard Potentials in Aqueous Solution*; Bard, A. J.; Parsons, R.; Jordan, J., Eds.; CRC Press: New York, 1985; pp 429−452.

(14) Gorlin, Y.; Jaramillo, T. F. A Bifunctional Nonprecious Metal Catalyst for Oxygen Reduction and Water Oxidation. *J. Am. Chem. Soc.* **2010**, *132*, 13612−13614.

(15) Zhou, F.; Izgorodin, A.; Hocking, R. K.; Spiccia, L.; MacFarlane, D. R. Electrodeposited MnOx Films from Ionic Liquid for Electrocatalytic Water Oxidation. *Adv. Energy Mater.* **2012**, *2*, 1013−1021.

(16) Hocking, R. K.; Brimblecombe, R.; Chang, L.-Y.; Singh, A.; Cheah, M. H.; Glover, C.; Casey, W. H.; Spiccia, L. Water-Oxidation Catalysis by Manganese in a Geochemical-like Cycle. *Nat. Chem.* **2011**, *3*, 461−466.

(17) Zaharieva, I.; Chernev, P.; Risch, M.; Klingan, K.; Kohlhoff, M.; Fischer, A.; Dau, H. Electrosynthesis, Functional, and Structural Characterization of a Water-Oxidizing Manganese Oxide. *Energy Environ. Sci.* **2012**, *5*, 7081−7089.

(18) Gorlin, Y.; Lassalle-Kaiser, B.; Benck, J. D.; Gul, S.; Webb, S. M.; Yachandra, V. K.; Yano, J.; Jaramillo, T. F. In Situ X-Ray Absorption Spectroscopy Investigation of a Bifunctional Manganese Oxide Catalyst with High Activity for Electrochemical Water Oxidation and Oxygen Reduction. *J. Am. Chem. Soc.* **2013**, *135*, 8525−8534.

(19) Takashima, T.; Hashimoto, K.; Nakamura, R. Mechanisms of pH-Dependent Activity for Water Oxidation to Molecular Oxygen by MnO_2 Electrocatalysts. *J. Am. Chem. Soc.* **2012**, *134*, 1519−1527.

(20) Takashima, T.; Hashimoto, K.; Nakamura, R. Inhibition of Charge Disproportionation of MnO_2 Electrocatalysts for Efficient Water Oxidation under Neutral Conditions. *J. Am. Chem. Soc.* **2012**, *134*, 18153−18156.

(21) Trotochaud, L.; Ranney, J. K.; Williams, K. N.; Boettcher, S. W. Solution-Cast Metal Oxide Thin Film Electrocatalysts for Oxygen Evolution. *J. Am. Chem. Soc.* **2012**, *134*, 17253−17261.

(22) Robinson, D. M.; Go, Y. B.; Mui, M.; Gardner, G.; Zhang, Z.; Mastrogiovanni, D.; Garfunkel, E.; Li, J.; Greenblatt, M.; Dismukes, G. C. Photochemical Water Oxidation by Crystalline Polymorphs of Manganese Oxides: Structural Requirements for Catalysis. *J. Am. Chem. Soc.* **2013**, *135*, 3494−3501.

(23) Fekete, M.; Hocking, R. K.; Chang, S. L. Y.; Italiano, C.; Patti, A. F.; Arena, F.; Spiccia, L. Highly Active Screen-Printed Electrocatalysts for Water Oxidation Based on β-Manganese Oxide. *Energy Environ. Sci.* **2013**, *6*, 2222−2232.

(24) Fleischmann, M.; Thirsk, H. R.; Tordesillas, I. M. Kinetics of Electrodeposition of γ-Manganese Dioxide. *Trans. Faraday Soc.* **1962**, *58*, 1865−1877.

(25) Paul, R.; Cartwright, A. The Mechanism of the Deposition of Manganese Dioxide Part III. Rotating Ring-Disk Studies. *J. Electroanal. Chem.* **1986**, *201*, 123−131.

(26) Kao, W.-H.; Weibel, V. J. Electrochemical Oxidation of Manganese(II) at a Platinum Electrode. *J. Appl. Electrochem.* **1992**, *22*, 21−27.

(27) Rodrigues, S.; Munichandraiah, N.; Shukla, A. K. A Cyclic Voltammetric Study of the Kinetics and Mechanism of Electrodeposition of Manganese Dioxide. *J. Appl. Electrochem.* **1998**, *28*, 1235−1241.

(28) Nijjer, S.; Thonstad, J.; Haarberg, G. Oxidation of Manganese-(II) and Reduction of Manganese Dioxide in Sulphuric Acid. *Electrochim. Acta* **2000**, *46*, 395−399.

(29) Clarke, C.; Browning, G.; Donne, S. An RDE and RRDE Study Into the Electrodeposition of Manganese Dioxide. *Electrochim. Acta* **2006**, *51*, 5773−5784.

(30) Batchelor-McAuley, C.; Shao, L.; Wildgoose, G. G.; Green, M. L. H.; Compton, R. G. An Electrochemical Comparison of Manganese Dioxide Microparticles versus α and β Manganese Dioxide Nanorods: Mechanistic and Electrocatalytic Behaviour. *New J. Chem.* **2008**, *32*, 1195−1203.

(31) Saveant, J.-M. *Elements of Molecular and Biomolecular Electrochemistry: An Electrochemical Approach to Electron Transfer Chemistry*; John Wiley: Hoboken, NJ, 2006.

(32) Jencks, W. P.; Regenstein, J. Ionization Constants of Acids and Bases. In *Handbook of Biochemistry and Molecular Biology*; Lundblad, R. L., MacDonald, F. M., Eds.; CRC Press: New York, 2010; pp 595−635.

(33) Grenthe, I.; Plyasunov, A. On the Use of Semiempirical Electrolyte Theories for Modeling of Solution Chemical Data. *Pure Appl. Chem.* **1997**, *69*, 951−958.

(34) Pettit, L. D.; Puigdomenech, I.; Wanner, H.; Sukhno, I.; Buzko, V. *Ionic Strength Corrections Using Specific Interaction Theory*, 2008. http://old.iupac.org/projects/2006/2006-010-1-500.html (accessed Jan 12, 2013).

(35) Sigel, H.; Da Costa, C. P.; Song, B.; Carloni, P.; Gregáň, F. Stability and Structure of Metal Ion Complexes Formed in Solution with Acetyl Phosphate and Acetonylphosphonate: Quantification of Isomeric Equilibria. *J. Am. Chem. Soc.* **1999**, *121*, 6248−6257.

(36) Parsons, R. The Structure of the Electrical Double Layer and Its Influence on the Rates of Electrode Reactions. In *Advances in Electrochemistry and Electrochemical Engineering*; Delahay, P., Ed.; Interscience: New York, 1961; pp 1−64.

(37) Gileadi, E. *Physical Electrochemistry: Fundamentals, Techniques and Applications*, 1st ed.; Wiley-VCH: Weinheim, Germany, 2011.

(38) Gunawardena, G.; Hills, G.; Montenegro, I.; Scharifker, B. Electrochemical Nucleation Part I. General Considerations. *J. Electroanal. Chem. Interfacial Electrochem.* **1982**, *138*, 225−239.

(39) Scharifker, B.; Hills, G. Theoretical and Experimental Studies of Multiple Nucleation. *Electrochim. Acta* **1983**, *28*, 879−889.

(40) Zheng, M.; West, A. C. Simulation of the Influence of Reactant Depletion on Nucleation Rate in Electrodeposition. *J. Electrochem. Soc.* **2004**, *151*, C502−C507.

(41) Radisic, A.; Vereecken, P. M.; Hannon, J. B.; Searson, P. C.; Ross, F. Quantifying Electrochemical Nucleation and Growth of Nanoscale Clusters Using Real-Time Kinetic Data. M. *Nano Lett.* **2006**, *6*, 238−242.

(42) Guo, L.; Searson, P. C. Influence of Anion on the Kinetics of Copper Island Growth. *Nanoscale* **2010**, *2*, 2431−2435.

(43) Guo, L.; Oskam, G.; Radisic, A.; Hoffmann, P. M.; Searson, P. C. Island Growth in Electrodeposition. *J. Phys. D. Appl. Phys.* **2011**, *44*, 443001−443012.

(44) Ustarroz, J.; Ke, X.; Hubin, A.; Bals, S.; Terryn, H. New Insights Into the Early Stages of Nanoparticle Electrodeposition. *J. Phys. Chem. C* **2012**, *116*, 2322−2329.

(45) Ustarroz, J.; Hammons, J. A.; Altantzis, T.; Hubin, A.; Bals, S.; Terryn, H. A Generalized Electrochemical Aggregative Growth Mechanism. *J. Am. Chem. Soc.* **2013**, *135*, 11550−11561.

(46) Rigano, P. M.; Mayer, C.; Chierchie, T. Electrochemical Nucleation and Growth of Copper on Polycrystalline Palladium. *J. Electroanal. Chem. Interfacial Electrochem.* **1988**, *248*, 219−228.

(47) Liu, H.; Penner, R. M. Size-Selective Electrodeposition of Mesoscale Metal Particles in the Uncoupled Limit. *J. Phys. Chem. B* **2000**, *104*, 9131−9139.

(48) Liu, H.; Favier, F.; Ng, K.; Zach, M. P.; Penner, R. M. Size-Selective Electrodeposition of Meso-Scale Metal Particles: A General Method. *Electrochim. Acta* **2001**, *47*, 671−677.

(49) Ng, K. H.; Penner, R. M. Electrodeposition of Silver−Copper Bimetallic Particles Having Two Archetypes by Facilitated Nucleation. *J. Electroanal. Chem.* **2002**, *522*, 86.

(50) Sisley, M. J.; Jordan, R. B. First Hydrolysis Constants of Hexaaquacobalt(III) and -Manganese(III): Longstanding Issues Resolved. *Inorg. Chem.* **2006**, *45*, 10758−10763.

(51) Bard, A. J.; Faulkner, L. R. *Electrochemical Methods: Fundamentals and Applications*; Wiley: New York, 2001.

(52) Bediako, D. K.; Costentin, C.; Jones, E. C.; Nocera, D. G.; Savéant, J.-M. Proton-Electron Transport and Transfer in Electrocatalytic Films. Application to a Cobalt-Based O_2-Evolution Catalyst. *J. Am. Chem. Soc.* **2013**, *135*, 10492−10502.

(53) Ullman, A. M.; Nocera, D. G. Mechanism of Cobalt Self-Exchange Electron Transfer. *J. Am. Chem. Soc.* **2013**, *135*, 15053−15061.

(54) Pisarczyk, K. Manganese Compounds. In *Kirk-Othmer Encyclopedia of Chemical Technology*; John Wiley: Hoboken, NJ, 2000; pp 1−78.

(55) Surendranath, Y.; Lutterman, D. A.; Liu, Y.; Nocera, D. G. Nucleation, Growth, and Repair of a Cobalt-Based Oxygen Evolving Catalyst. *J. Am. Chem. Soc.* **2012**, *134*, 6326−6336.

(56) Waters, W. A. Mechanisms of Oxidation by Compounds of Chromium and Manganese. *Q. Rev. Chem. Soc.* **1958**, *12*, 277−300.

(57) Davies, G. Some Aspects of the Chemistry of Manganese(III) in Aqueous Solution. *Coord. Chem. Rev.* **1969**, *4*, 199−224.

(58) Lume-Pereira, C.; Baral, S.; Henglein, A.; Janata, E. Chemistry of Colloidal Manganese Dioxide. 1. Mechanism of Reduction by an Organic Radical (A Radiation Chemical Study). *J. Phys. Chem.* **1985**, *89*, 5772−5778.

(59) Armstrong, F. A. Why Did Nature Choose Manganese to Make Oxygen? *Philos. Trans. R. Soc., B* **2008**, *363*, 1263−1270.

(60) Pourbaix, M. *Atlas of Electrochemical Equilibria in Aqueous Solutions*, 2nd ed.; National Association of Corrosion Engineers: New York, 1974; p 644.

THE JOURNAL OF
PHYSICAL CHEMISTRY C

Spectroscopic Studies of Nanoparticulate Thin Films of a Cobalt-Based Oxygen Evolution Catalyst

Yi Liu and Daniel G. Nocera*

Department of Chemistry and Chemical Biology, Harvard University, 12 Oxford Street, Cambridge, Massachusetts 02138, United States

Supporting Information

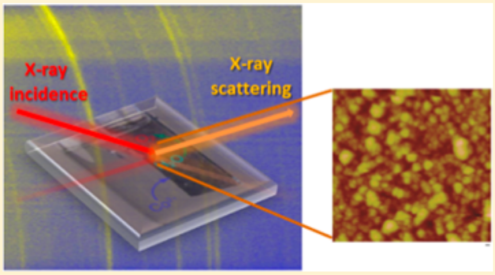

ABSTRACT: Nanoparticle (NP) cobalt−phosphate (Co-P_i) water oxidation catalysts are prepared as thin films by anodic electrodeposition from solutions of Co^{2+} dissolved in proton-accepting electrolytes. Compositional and structural insight into the nature of the catalyst film is provided from advanced spectroscopy. Infrared spectra demonstrate that counteranions incorporate into the Co-P_i thin films and that the phosphate ion, among various anion electrolytes, exhibits the highest binding affinity to the cobalt centers. Atomic force microscopy images show a highly porous morphology of the thin film that is composed of Co-P_i NPs. Whereas conventional X-ray powder diffraction technique shows catalyst films to be amorphous, synchrotron-based X-ray grazing incidence diffraction reveals well-defined diffraction patterns that are indicative of long-range ordering within the film. Azimuthal scans imply that as-prepared films possess a highly preferred orientation and texture on the electrode surface.

INTRODUCTION

Increasing demand for renewable and sustainable energy utilization[1,2] has motivated substantial efforts to develop novel materials for solar energy conversion and storage. Solar-to-fuels energy conversion is an especially attractive method of storage owing to the high energy density of chemical fuels.[3,4] The solar-driven splitting of water to H_2 and O_2 is an important reaction for this purpose because water provides a renewable and carbon-neutral source of hydrogen, which can effectively be harnessed to electricity by fuel cell devices[5,6] or converted to liquid fuels upon its combination with CO or CO_2.[7−11] Of the two half-reactions composing water splitting, the oxygen evolution reaction (OER) is particularly demanding because it is a coupled four-electron, four-proton process involving the formation of an oxygen−oxygen double bond.[12−17] Although water splitting can be achieved at very high efficiency at pH extremes, high costs are attendant to performing water splitting under harsh conditions.[18] To circumvent these limitations, catalysts with appreciable activities under benign conditions has benefits for the development of low-cost solar energy storage.[19,20] We have developed water oxidation catalysts that readily self-assemble upon anodic oxidation of Co^{2+} from phosphate (P_i) (pH 7) or borate (B_i) (pH 9.2)[21,22] and oxidation of Ni^{2+} from borate (B_i).[23−25] The catalysts may be coupled to the surfaces of semiconducting surfaces either via electrodeposition or photodeposition.[26−35] Buried junction devices based on interfacing the catalyst to silicon[36,37] have been realized to permit the creation of the artificial leaf,[38,39] which captures many of the basic functional elements of photosynthesis. The solar-to-fuels efficiency (SFE) of these devices depends critically on morphology of the catalyst film and semiconductor|catalyst interface.[40,41] Hence, insight into the structure of such catalyst films is an imperative for the continued development of higher SFE devices.

Extended X-ray absorption fine structure (EXAFS) models have established that the catalyst films comprise cobaltate clusters.[42] Atomic pair distribution function (PDF) analysis[43,44] of synchrotron data collected on active films of Co−phosphate (Co-P_i) and Co−borate (Co-B_i) reveals that the cobaltate clusters of the latter assemble into stacked superstructures whereas Co-P_i are isolated. The arrangement of the clusters into a network is manifest by overall catalytic activity owing to the dominating effects of proton and ion transport through the mesostructure of the catalyst films.[45] To this end, the role of the electrolyte in establishing the cobaltate clusters and their arrangement within the film is important to understanding overall catalytic activity. Accordingly, we now characterize films formed from different electrolytes with advanced electrochemical spectroscopic measurements. We show by Fourier transform infrared (FT-IR) spectroscopy that selected electrolytes are preferred structural elements of the catalyst film and a highly porous morphology formed from nanoparticles of the catalyst is in evidence from AFM images. Using synchrotron-based X-ray grazing incidence diffraction, we establish, for the first time, crystalline ordering within Co-P_i catalyst thin films and the arrangement of the cobaltate clusters into nanoparticles (NPs).

Special Issue: Michael Grätzel Festschrift

Received: January 23, 2014
Revised: March 17, 2014
Published: March 28, 2014

EXPERIMENTAL SECTION

Materials. $Co(NO_3)_2$ 99.999%, CH_3COONa, C_2H_5COONa, $CH_2(COONa)_2$, and $(CH_2COONa)_2$ (Aldrich) and KOH, H_3BO_3, and KH_2PO_4 (Mallinckrodt) were used as received. All electrolytic solutions were prepared with reagent grade deionized water (18 MΩ cm resistivity). Fluorine-doped tin oxide (FTO) electrodes, with 8−12 Ω/sq surface resistivity, were purchased from Aldrich. Au and Pt electrodes were purchased from Pine Instruments. Ag/AgCl (sat. KCl) reference electrodes were purchased from BASi.

Electrochemical Measurements. All electrochemical measurements were performed in a typical H-cell with Ag/AgCl as reference electrode, Pt wire as auxiliary electrode, and respective working electrode (FTO, Au, or Pt) at ambient temperature with CH Instruments 760C or 760D potentiostats. Unless specifically stated, all potentials were referred to the Ag/AgCl reference electrode. Cyclic voltammetric (CV) profiles were recorded with IR compensation at a scan rate of 100 mV s^{-1}.

Preparation of Cobalt-Based Thin-Film Electrocatalysts. Co−phosphate (Co-P_i) thin films were prepared via anodic electrodeposition. Electrochemically cleaned FTO electrode was immersed in freshly prepared 100 mM potassium phosphate (KP_i) buffer solution (pH 7) with 0.1 mM $Co(NO_3)_2$ as the cobalt source. Co-P_i thin films steadily grew on the electrode surface while holding potential constant at +0.90 V versus Ag/AgCl. This potential was 100 mV negative from the onset of the catalytic wave for OER, thus allowing films to be deposited without interference from OER. The typical thickness of the film was controlled by the total charge passed during electrodeposition. The electrodeposition process used for the preparation of Co-B_i thin films was analogous to that used for Co-P_i. A FTO electrode was immersed in freshly prepared 0.1 M potassium borate (KB_i) solution at pH 9.2 with 0.1 mM $Co(NO_3)_2$ as the cobalt source. A Co-B_i thin film steadily grew on the electrode surface while holding the potential constant at +0.77 V so as to avoid interference from OER. All other Co-X (X = acetate (Ac), propionate (Pr), malonate (Ma), or succinate (Su)) thin films were prepared by anodic electrodepostion from 0.1 M NaAc (pH 8), 0.1 M NaPr (pH 8), 0.1 M NaMa (pH 9), or 0.1 M NaSu (pH 8) electrolyte, respectively. Film formation was performed 100 mV removed from the onset of OER (E_{appl} = +0.84 V for Co-Ac, +0.84 V for Co-Pr, +0.77 V for Co-Ma, and +0.84 V for Co-Su).

FT-IR Characterization. FT-IR spectra were recorded at ambient temperature with a PerkinElmer Spectrum 400 FT-IR/FT-NIR spectrometer via reflection mode. Co-X films (80 mC cm^{-2}) were thoroughly rinsed with reagent grade water and completely air-dried before FTIR interrogation. For ion exchange experiments, FT-IR spectra were collected before and after Co-X thin films were immersed for 30 min in KP_i solutions of various concentrations.

AFM Morphology Investigation. AFM images were collected using a Veeco Nanoscope Dimension 4100 operating in tapping mode with a Veeco silicon nitride probe with a resonance frequency of ∼200 KHz and average tip radius of 3 nm. All measurements were performed in air and at room temperature. Nanoparticle diameters were determined using Nanoscope V5.31 software. AFM studies were conducted on an electrochemically cleaned FTO electrode. Co-X films were thoroughly rinsed with reagent grade water prior to measurement. The recording image scale was gradually decreased from a landscape 10 × 10 μm^2 field of view to a higher 250 × 250 nm^2 field of view.

Synchrotron-Based X-ray GID Characterization. X-ray grazing incidence diffraction (GID) experiments were performed at the G-line Station of the Cornell High Energy Synchrotron Source (CHESS). All diffraction experiments were carried out on a homemade six-circle K-diffractometer. The experimental X-ray incidence energy was 9.374 keV (1.323 Å). The beam size was 2 mm horizontal × 200 μm vertical. This asymmetric beam shape was deliberately chosen so as to optimize surface sensitivity. The typical photon flux intensity at the center of rotation (COR) of the diffractometer was ca. 10^{13} photons sec^{-1} mm^{-2}. A linear position sensitive 1-D detector (LPSD) was utilized for collecting the diffracted beam. The detector's angular resolution was ca. 0.18°. A horizontal in-plane X-ray scattering geometry was employed. In this geometry, the electrode surface normal is perpendicular to the laboratory frame, and the detector moves within a plane that is parallel to the electrode surface. More detailed information about the diffractometer and the experimental geometry can be found elsewhere.[46] Diffraction signals from Co-P_i films on different substrates (FTO, Au, and Pt), with thickness of ca. 150 nm (total deposition charge of 150 mC cm^{-2}) were collected over 2θ of 18−55°, which encompassed a range that included the characteristic major peaks from substrates and Co-P_i films. Two types of GID measurements were performed: (1) a survey scan to furnish characteristic diffraction peaks and (2) an azimuthal scan to offer information on the crystalline orientation and texture. For the azimuthal scan, LPSD was recorded at selected 2θ position and scattering signals as function of azimuthal rotating angle of the sample.

RESULTS AND DISCUSSION

Catalyst thin films were formed from oxidation of Co^{2+} (10 mM) ions in the presence of various electrolytes: X = acetate (Ac), propionate (Pr), malonate (Ma), succinate (Su), borate (B_i), and phosphate (P_i). All films were prepared from the same 0.1 mM $Co(NO_3)_2$ stock solution and from 0.1 M electrolyte solution. Accordingly, any differences in the catalyst film formation and morphology are a result of the effect of the supporting electrolyte. Figure 1 shows CV profiles of Co-X film formation on a FTO working electrode in different proton-accepting electrolyte solutions. A prewave at +0.92 V is due to the oxidation of Co^{2+} to Co^{3+}; the current response is characteristic of a nucleation and growth mechanism.[47] The large subsequent wave in the CV at potentials greater than 1.2 V is due to the OER reaction, which occurs with 100% Faradaic efficiency. The different films exhibit almost identical Co $2p_{3/2}$ XPS spectra (Figure S1 of Supporting Information), thus establishing that the formal oxidation state of the Co centers, as well as their local chemical environment in films prepared from different electrolytes, is similar.[42,43]

Figure 2 displays the FT-IR spectra of various films prepared from different proton-accepting electrolytes. The weak band appearing at ca. 740 cm^{-1} in all samples is due to Sn−O vibration of the FTO substrate. Bands at 604 and 637 cm^{-1} are characteristic of breathing vibrational modes of Co−O stretches within the Co−oxo core of the cobaltate cluster.[31] Consistent with XPS results, the similarity of these bands in this region for the different samples suggests cobaltate clusters of similar structure for Co-X thin films prepared from the different proton-accepting electrolytes. Characteristic bands within the

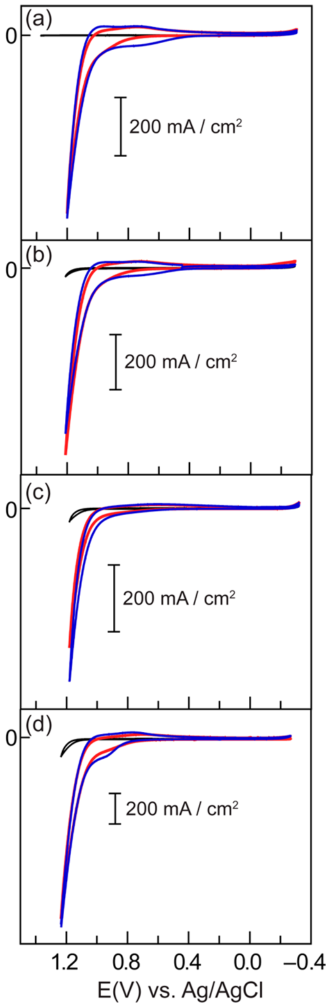

Figure 1. Cyclic voltammetric profiles of 0.5 mM $Co(NO_3)_2$ in the presence of electrolytes using FTO as a working electrode at a scan rate of 20 mV s^{-1} where the electrolyte is (a) 0.1 M NaAc pH 8, (b) 0.1 M NaPr pH 9, (c) 0.1 M NaMa pH 9, or (d) 0.1 M NaSu pH 8 (first scan, red; fifth scan, blue; background in the absence of a cobalt source, black).

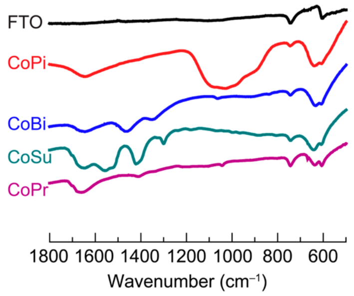

Figure 2. IR spectra of catalyst films (80 mC cm^{-2}) deposited from 0.1 M KPi pH 7 with 0.5 mM $Co(NO_3)_2$ (red), 0.1 M KB_i pH 9.2 with 0.5 mM $Co(NO_3)_2$ (blue), 0.1 M NaPr with 0.5 mM $Co(NO_3)_2$ (green), 0.1 M NaPr with 0.5 mM $Co(NO_3)_2$ (purple), and bare FTO electrode (black).

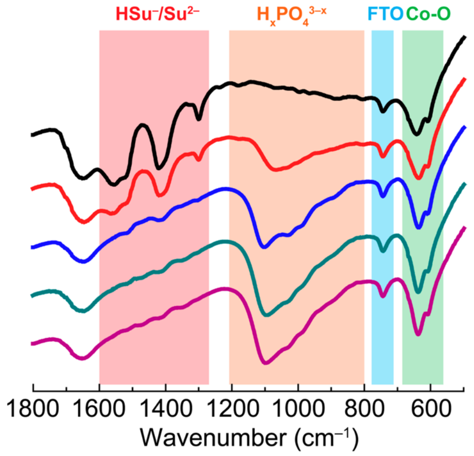

Figure 3. IR spectra of catalyst films (80 mC cm^{-2}) deposited from succinate (black) and the succinate film immersed in solutions containing phosphate at 0.1 M (red), 0.2 M (blue), 0.5 M (green), and 1.0 M (purple) .

range of 800−1800 cm^{-1} indicate the presence of the electrolyte anion as a structural element within the films. To investigate the affinity of different anions to cobaltate cluster centers, ion exchange experiments were performed while monitoring the IR spectra of films under exchange. Figure 3 displays the IR spectra of films prepared from P_i and Su. The Co-Su catalyst film exhibits convenient and characteristic IR bands for Su at 1300, 1420, and 1558 cm^{-1},[48] clearly establishing the presence of succinate in the film. We note that cobalt oxo cubane clusters,[49] which are structural analogs of Co-P_i,[50,51] and molecular cobaltate complexes[52] show an affinity for carboxylate and other anions as a terminal, capping ligand of cobalt. When the Co-Su films are immersed in KP_i solutions, the IR bands of succinate are depressed and a broad band appears at 1072 cm^{-1}, corresponding to the phosphate anion. Over time, the characteristic bands of succinate completely vanish and only the IR bands of the phosphate ion and the cobalt−oxo core (at 637 and 604 cm^{-1}) are observed. The IR spectrum of succinate is not recovered upon reimmersion of the catalyst films in succinate solution (Figure S2 of Supporting Information). Similar results were obtained for all other Co-X films, establishing that the phosphate anion is a preferred structural element of the catalyst films.

Figure 4 shows AFM images of a Co-Su catalyst film deposited onto a FTO working electrode from 0.5 mM $Co(NO_3)_2$ and 0.1 M NaSu while holding the potential constant at 0.84 V after 80 mC cm^{-2} of charge was passed. The film exhibits uniformly stacked nanoparticles (NPs) of the catalyst with a diameter of 200−250 nm. This stacking morphology results in a highly porous thin film, which is consistent with previous electrochemical results.[45,47] The particle size was dependent on the film thickness; particle sizes ranged from 50 to 450 nm for films prepared from passing current from 15 to 275 mC cm^{-2}, respectively. High-resolution AFM images in Figure 4e,f reveal that the NPs are not compact spheres but possess layered structures with high surface areas. Figure 5 displays the morphology change as a function of deposition time/total charge/film thickness for a set of Co-Pr thin films, with deposition total charge of 15, 45, and 80 mC cm^{-2}. For the thinnest films (15 mC cm^{-2}), the morphology of the catalytic film reflects characteristics of the FTO substrate; a thin layer of catalyst covers on the surface of FTO crystals. No well-defined NPs formed at this stage. With the continuous passing of charge and attendant growth of the film (80 mC cm^{-2}), well-defined NPs appear with a narrow size distribution: NPs 80 nm in diameter formed for 45 mC cm^{-2} of charge

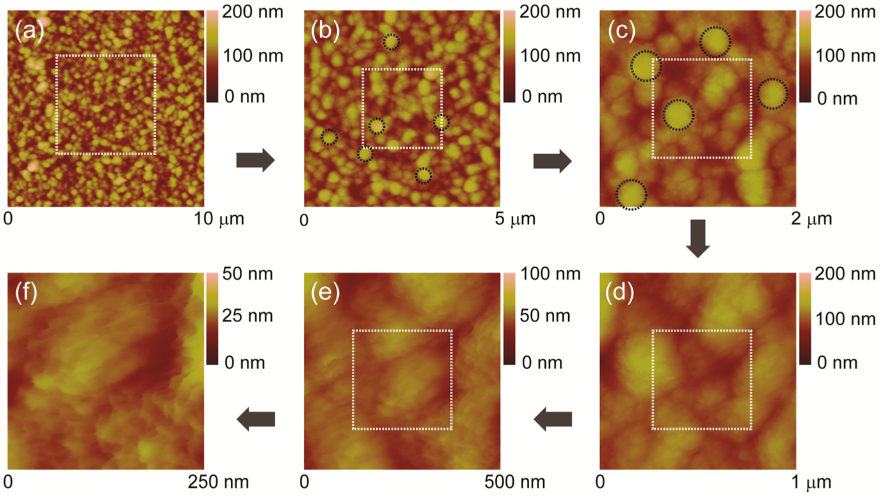

Figure 4. AFM images of a 80 mC cm^{-2} Co-Su thin film with different magnification scale: scanning range of 10 × 10 μm^2 (a), 5 × 5 μm^2 (b), 2 × 2 μm^2 (c), 1 × 1 μm^2 (d), 500 × 500 nm^2 (e), and 250 × 250 nm^2 (f). White dashed line squares indicate the scanning range of the next image, and black dashed line circles highlight well-defined nanoparticles in the film.

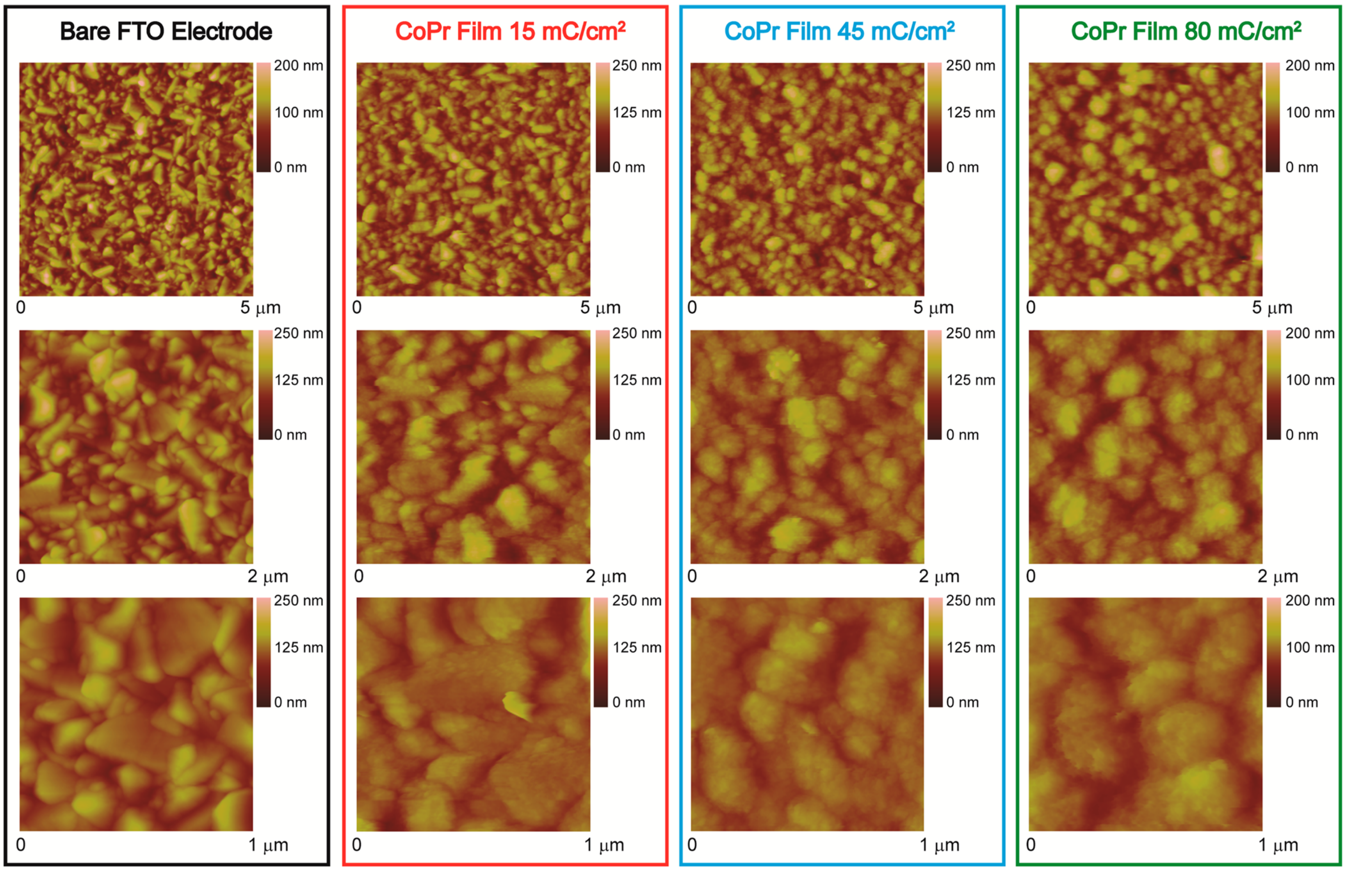

Figure 5. AFM images of Co-Pr thin films at different thickness: bare electrode (black), 15 mC cm^{-2} (red), 45 mC cm^{-2} (blue), and 80 mC cm^{-2} (green).

passed and NPs 200 nm in diameter formed for 80 mC cm^{-2} of charge passed.

The supposition of microcrystalline NP domains is supported by synchrotron-based X-ray grazing incidence diffraction (GID) of Co-X films. The GID technique is particularly well-suited to distinguish long-range structural ordering in thin films.[53] For the case of Co-P$_i$ GID studies, the thin film was electrodeposited onto freshly prepared and polished Au, Pt, and FTO electrodes. For all substrates, the film was electrodeposited upon passing 150 mC cm^{-2} overall charge through a 0.1 M KPi (pH 7) and 0.5 mM Co(NO$_3$)$_2$ solution at a constant current of 5 μA and constant potential of +0.80 V. These experimental conditions provided the smoothest films for GID experiments.

The three strong diffraction peaks in the GID diffraction pattern beyond 2θ of 30° in Figure 6a corresponds to the Au

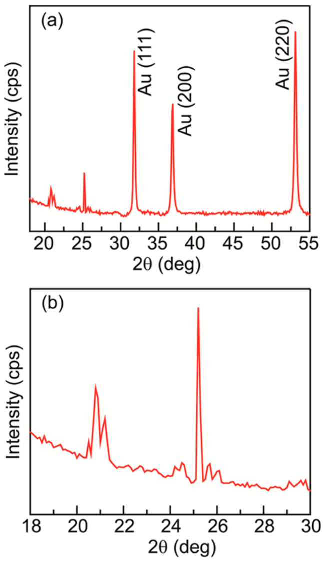

Figure 6. Partial survey GID scans at the incidence angle of 0.2° from Co-P$_i$ thin films (150 mC cm^{-2}) deposited on polycrystalline Au electrode without azimuthal rotation: (a) scan from 18 to 55° including characteristic peaks of Au; (b) scan from 18 to 30° focusing characteristic peaks of Co-P$_i$ film.

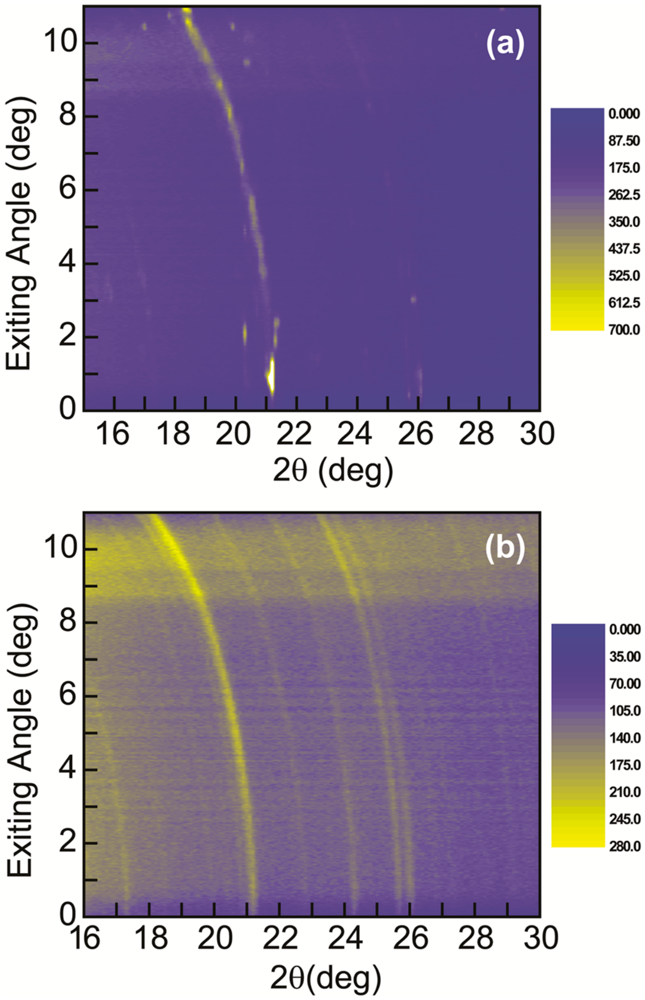

Figure 7. Peusdo-2D mapping images of partial survey GID scans at the incidence angle of 0.2° from Co-P$_i$ thin films (150 mC cm^{-2}) deposited on polycrystalline Pt electrode (a) without azimuthal rotation and (b) with azimuthal rotation of 180°.

substrate. Diffraction peaks below 2*θ* of 30° in Figure 6b arise from the Co-P$_i$ catalyst film because they possessed reproducibility and consistency among samples grown on different substrates, such as Au, Pt, and FTO electrodes. The relatively intense peak at 25.4° in Figure 6b appeared to have its origins arising from nonazimuthal rotation owing to its sharpness and intensity. We ascribe the peak to preferred orientation at this 2*θ* position within the thin-film sample. Nonazimuthal survey scan shown in Figure 6a confirmed nonuniformity and preferred orientation in crystalline structure. To account for the nanocrystalline domain size within Co-P$_i$ films, the unusual sharpness of peaks, such as 25.4° and 21°, are due to the nonuniformity of crystalline domains and preferred orientations. For this specific measuring position, the preferred facets correlated strongly with incident X-ray photons to give strong scattering signals. The nonconsistent sharpness of different Bragg peaks arises from the random crystalline facet distributions within the Co-P$_i$ thin-film catalyst. To investigate the possibility of reflections due to surface texture of the substrate, a partial survey GID scan of Co-P$_i$ films on Pt electrodes was recorded with and without azimuthal rotation; these results are shown in Figure 7. Azimuthal rotation averages out diffraction signals at particular 2*θ* values and consequently furnishes uniform powder-like diffraction rings. If the sample has no preferred orientations or texture, the survey scans for the two scanning methods (with and without azimuthal rotation) will be the same. Otherwise, differences in diffraction patterns confirm potential crystalline orientations within the film. A pseudo-2D mapping image was obtained by integrating signals from all channels of PSLD. Discontinuous rings decorated with spots of various intensities in Figure 7a suggest that uneven ordered structures, akin to single-crystalline domains, are arranged along specific directions and orientations within the film. These results are consistent with nanosize domains of Co-P$_i$ subunits that are confined to specific crystalline facets of the underlying support because of either intrinsic ordering upon deposition or preferred ordering induced by the underlying substrate.

The "powder-like" diffraction pattern shown in Figure 7b was obtained by averaging the intensity variations via azimuthal rotation of 180°. There were ca. 7 well-defined diffraction peaks in the range of 16 to 30°. These peaks were utilized for indexing and simulation to furnish crystal symmetry and unit cell information. The patterns of X-ray GID data were indexed by using either CrystalMaker or Hi-Index softwares. Two possible unit cells were obtained based on the indexing: either an orthorhombic cell with parameters of 10.34 Å (*a*), 10.34 Å (*b*), and 11.27 Å (*c*) or a monoclinic cell with parameters of 7.16 Å (*a*), 15.03 Å (*b*), and 4.32 Å (*c*), and *β* = 96.6°. These cell dimensions are inconsistent with crystalline cobalt oxides, such as Co_2O_3, CoO and Co(OH), but they account for the dimer unit cell of the cobaltate cluster core, as identified from EXAFS and PDF data.

AFM images and GID diffraction patterns of Co-P$_i$ NPs indicate that catalyst films grown on Au were similar to thin films grown on Pt and FTO electrodes, though the diffraction patterns from FTO were much less well-defined than those of the others. The less well-defined diffraction patterns observed from films deposited on FTO substrates refer to broader diffraction peaks, worse signal-to-noise levels, and more ill-defined peak shape. The quality of diffraction signals corresponded to electrode surface roughness. Crystal domains of 300−400 nm were observed on FTO, which displayed a surface roughness of ca. 200 nm (Figure S3 of Supporting Information). This surface roughness was much greater than that for freshly polished Au and Pt electrodes, which was on the order of ca. 40−50 nm (Figure S4 of Supporting Information). The Co-P_i film on the smoother surfaces of Au and Pt exhibited NP domain sizes of 40 and 15 nm, respectively (Figure S5 of Supporting Information). It is worth mentioning that the diffraction patterns were quite similar for the Co-P_i films grown on the smoother surfaces of Au and Pt, if not significantly better than rougher ones. We did not observe peak broadening, which indicated similar crystalline domain sizes. The particle sizes of 40 and 15 nm were observed from AFM experiment and defined as morphological particle size, as opposed to the crystalline domain size indicated from diffraction data.

The Co-Pi nucleation process occurs by a progressive mechanism followed by steady-state growth from islands of nucleation. The results described herein suggest that these early nucleation events find their origins in the small crystalline domains observed here, formed during the early stages of electrodeposition. We note that the dimensions of particles observed in AFM images are larger than the physical domain size of the NPs. As is often the case, morphological domain sizes are larger than crystalline domain sizes that are estimated from X-ray diffraction measurements.[53] Our results indicate that the NPs aggregate to form larger structures that lead to porosity within the film.

■ SUMMARY

The cobalt-based water oxidation catalyst that forms from the electrodeposition of cobalt ions from phosphate electrolyte does so as nanoparticles. The anion electrolyte is a critical compositional and structural element of Co-X films. Mechanistic studies have established that phosphate is particularly important to the OER reaction[54] and film nucleation, growth,[47] and repair.[55] The results reported here begin to unveil the basic structural element that establishes its criticality to film morphology. Synchrotron-based GID reveals that Co-P_i thin films exhibit crystalline NPs, which is most pronounced for thin films, at the earliest stages of catalyst nucleation and deposition. The basic unit cell of the crystalline form is either orthorhombic or monoclinic symmetry and is unique, exhibiting structural similarities to extended cobalt oxides. These results are consistent with EXAFS and PDF studies, which model the active site as a molecular cobaltate cluster. We now establish that these cobaltate clusters may arrange into NPs, which are nucleation sites for the catalyst film formation.

■ ASSOCIATED CONTENT

Ⓢ Supporting Information

Co $2p_{3/2}$ XPS spectra of different Co-X films, various Co-X thin-film formation conditions, FTIR spectra of recovery experiment, and SEM and AFM images of Co-P_i on Au and Pt electrodes. This material is available free of charge via the Internet at http://pubs.acs.org.

■ AUTHOR INFORMATION

Corresponding Author

*E-mail: dnocera@fas.harvard.edu. Tel: 1-617-495-8904.

Notes

The authors declare no competing financial interest.

■ ACKNOWLEDGMENTS

This work was supported by DOE DE-SC0009565 (D.G.N.). We thank Dr. Arthur Woll and Dr. Detlef Smilgies at CHESS for assistance and discussion of GID experiments. Beam time at CHESS G2 station is highly appreciated for NSF/NIH-funded facility (Grant DMR-0936384).

■ REFERENCES

(1) Lewis, N. S.; Nocera, D. G. Powering the Planet: Chemical Challenges in Solar Energy Utilization. *Proc. Natl. Acad. Sci. U.S.A.* **2006**, *103*, 15729−15735.

(2) Abbott, D. Keeping the Energy Debate Clean: How Do We Supply the World's Energy Needs. *Proc. IEEE* **2010**, *98*, 42−66.

(3) Nocera, D. G. Chemistry of Personalized Solar Energy. *Inorg. Chem.* **2009**, *48*, 10001−10017.

(4) Cook, T. R.; Dogutan, D. K.; Reece, S. Y.; Surendranath, Y.; Teets, T. S.; Nocera, D. G. Solar Energy Supply and Storage for the Legacy and Non-Legacy Worlds. *Chem. Rev. (Washington, DC, U.S.)* **2010**, *110*, 6474−6502.

(5) Crabtree, G. W.; Dresselhaus, M. S. The Hydrogen Fuel Alternative. *MRS Bull.* **2008**, *33*, 421−428.

(6) *Handbook of Fuel Cells: Fundamentals, Technology and Applications*; Vielstch, W., Lamm, A. Gasteiger, H. A., Eds.; John Wiley: Chichester, U.K., 2003.

(7) Chen, Y. H.; Li, C. W.; Kanan, M. W. Aqueous CO_2 Reduction at Very Low Overpotential on Oxide-Derived Au Nanoparticles. *J. Am. Chem. Soc.* **2012**, *134*, 19969−19972.

(8) Li, C. W.; Kanan, M. W. CO_2 Reduction at Low Overpotential on Cu Electrodes Resulting from the Reduction of Thick Cu_2O Films. *J. Am. Chem. Soc.* **2012**, *134*, 7231−7234.

(9) Chen, Y. H.; Kanan, M. W. Tin Oxide Dependence of the CO_2 Reduction Efficiency on Tin Electrodes and Enhanced Activity for Tin/Tin Oxide Thin-Film Catalysts. *J. Am. Chem. Soc.* **2012**, *134*, 1986−1989.

(10) DiMeglio, J. L.; Rosenthal, J. Selective Conversion of CO_2 to CO with High Efficiency Using an Inexpensive Bismuth-Based Electrocatalyst. *J. Am. Chem. Soc.* **2013**, *135*, 8798−8801.

(11) Kuhl, K. P.; Cave, E. R.; Abram, D. N.; Jaramillo, T. F. New Insights Into the Electrochemical Reduction of Carbon Dioxide on Metallic Copper Surfaces. *Energy Environ. Sci.* **2012**, *5*, 7050−7059.

(12) Cukier, R. I.; Nocera, D. G. Proton-Coupled Electron Transfer. *Annu. Rev. Phys. Chem.* **1998**, *49*, 337−369.

(13) Eisenberg, R.; Gray, H. B. Preface on Making Oxygen. *Inorg. Chem.* **2008**, *47*, 1697−1699.

(14) Betley, T. A.; Wu, Q.; Van Voorhis, T.; Nocera, D. G. Electronic Design Criteria for O−O Bond Formation via Metal-Oxo Complexes. *Inorg. Chem.* **2008**, *47*, 1849−1861.

(15) Betley, T. A.; Surendranath, Y.; Childress, M. V.; Alliger, G. E.; Fu, R.; Cummins, C. C.; Nocera, D. G. Ligand Field Chemistry of Oxygen Generation by the Oxygen Evolving Complex and Synthetic Active Sites. *Phil. Trans. Royal Soc., B* **2008**, *363*, 1293−1303.

(16) Hammes-Schiffer, S. Theory of Proton-Coupled Electron Transfer in Energy Conversion Processes. *Acc. Chem. Res.* **2009**, *42*, 1881−1889.

(17) Concepcion, J. J.; Jurss, J. W.; Brennaman, M. K.; Hoertz, P. G.; Patrocinio, A. O. T.; Murakami Iha, N. Y.; Templeton, J. L.; Meyer, T. J. Making Oxygen with Ruthenium Complexes. *Acc. Chem. Res.* **2009**, *42*, 1954−1965.

(18) Turner, J. A. A Realizable Renewable Energy Future. *Science* **1999**, *285*, 687−689.

(19) Nocera, D. G. "Fast Food" Energy. *Energy Environ. Sci.* **2010**, *3*, 993−995.

(20) Esswein, A. J.; Surendranath, Y.; Reece, S. R.; Nocera, D. G. Highly Active Cobalt Phosphate and Borate Based Oxygen Evolving

Catalysts Operating in Neutral and Natural Waters. *Energy Environ. Sci.* **2011**, *4*, 499−504.

(21) Kanan, M. W.; Nocera, D. G. In-situ Formation of an Oxygen-Evolving Catalyst in Neutral Water Containing Phosphate and Co^{2+}. *Science* **2008**, *321*, 1072−1075.

(22) Surendranath, Y.; Dincă, M.; Nocera, D. G. Electrolyte-Dependent Electrosynthesis and Activity of Cobalt Based Water Oxidation Catalysts. *J. Am. Chem. Soc.* **2009**, *131*, 2615−2620.

(23) Dincă, M.; Surendranath, Y.; Nocera, D. G. A Nickel-Based Water Oxidation Catalyst that Functions under Benign Conditions. *Proc. Natl. Acad. Sci. U.S.A.* **2010**, *107*, 10337−10341.

(24) Bediako, D. K.; Lassalle−Kaiser, B.; Surendranath, Y.; Yano, J.; Yachandra, V. K.; Nocera, D. G. Structure−Activity Correlations in a Nickel−Borate Oxygen Evolution Catalyst. *J. Am. Chem. Soc.* **2012**, *134*, 6801−6809.

(25) Bediako, D. K.; Surendranath, Y.; Nocera, D. G. Mechanistic Studies of the Oxygen Evolution Reaction Mediated by a Nickel−Borate Thin Film Electrocatalyst. *J. Am. Chem. Soc.* **2013**, *135*, 3662−3674.

(26) Zhong, D. K.; Sun, J.; Inumaru, H.; Gamelin, D. R. Solar Water Oxidation by Composite Catalyst/α-Fe_2O_3 Photoanodes. *J. Am. Chem. Soc.* **2009**, *131*, 6086−6087.

(27) Zhong, D. K.; Gamelin, D. R. Photoelectrochemical Water Oxidation by Cobalt Catalyst ("Co−Pi")/α-Fe_2O_3 Composite Photoanodes: Oxygen Evolution and Resolution of a Kinetic Bottleneck. *J. Am. Chem. Soc.* **2010**, *132*, 4202−4207.

(28) Steinmiller, E. M. P.; Choi, K. S. Photochemical Deposition of Cobalt-Based Oxygen Evolving Catalyst on a Semiconductor Photoanode for Solar Oxygen Production. *Proc. Natl. Acad. Sci. U.S.A.* **2009**, *106*, 20633−20636.

(29) Seabold, J. A.; Choi, K. S. Effect of a Cobalt-Based Oxygen Evolution Catalyst on the Stability and the Selectivity of Photo-Oxidation Reactions of a WO_3 Photoanode. *Chem. Mater.* **2011**, *23*, 1105−1112.

(30) Zhong, D. K.; Cornuz, M.; Sivula, K.; Grätzel, M.; Gamelin, D. R. Photo-Assisted Electrodeposition of Cobalt−Phosphate (Co−Pi) Catalyst on Hematite Photoanodes for Solar Water Oxidation. *Energy Environ. Sci.* **2011**, *4*, 1759−1764.

(31) Tang, C.-W.; Wang, C.-B.; Chien, S.-H. Characterization of Cobalt Oxides Studied by FT-IR, Raman, TPR and TG-MS. *Thermochim. Acta* **2008**, *473*, 68−73.

(32) Zhong, D. K.; Choi, S.; Gamelin, D. R. Near-Complete Suppression of Surface Recombination in Solar Photoelectrolysis by "Co-Pi" Catalyst-Modified W:$BiVO_4$. *J. Am. Chem. Soc.* **2011**, *133*, 18370−18377.

(33) Young, E. R.; Nocera, D. G.; Bulović, V. Direct Formation of a Water Oxidation Catalyst from Thin-Film Cobalt. *Energy Environ. Sci.* **2010**, *3*, 1726−1728.

(34) Costi, R.; Young, E. R.; Bulović, V.; Nocera, D. G. Stabilized CdSe-CoP_i Composite Photoanode for Light-Assisted Water Oxidation by Transformation of a CdSe/Cobalt Metal Thin Film. *ACS Appl. Mater. Inter.* **2013**, *5*, 2364−2367.

(35) Klahr, B.; Gimenez, S.; Fabregat-Santiago, F.; Bisquert, J.; Hamann, T. W. Photoelectrochemical and Impedance Spectroscopic Investigation of Water Oxidation with "Co−Pi"-Coated Hematite Electrodes. *J. Am. Chem. Soc.* **2013**, *134*, 16693−16700.

(36) Pijpers, J. J. H.; Winkler, M. T.; Surendranath, Y.; Buonassisi, T.; Nocera, D. G. Light-Induced Water Oxidation at Silicon Electrodes Functionalized with a Cobalt Oxygen-Evolving Catalyst. *Proc. Natl. Acad. Sci. U.S.A.* **2011**, *108*, 10056−10061.

(37) Young, E. R.; Costi, R.; Nocera, D. G.; Bulović, V. Photo-Assisted Water Oxidation with Cobalt-Based Catalyst Formed from Thin-Film Cobalt Metal on Silicon Photoanodes. *Energy Environ. Sci.* **2011**, *4*, 2058−2061.

(38) Reece, S. Y.; Hamel, J. A.; Sung, K.; Jarvi, T. D.; Esswein, A. J.; Pijpers, J. J. H.; Nocera, D. G. Wireless Solar Water Splitting Using Silicon-Based Semiconductors and Earth-Abundant Catalysts. *Science* **2011**, *334*, 645−648.

(39) Nocera, D. G. The Artificial Leaf. *Acc. Chem. Res.* **2012**, *45*, 767−776.

(40) Cox, C. R.; Winkler, M. T.; Pijpers, J. J. H.; Buonassisi, T.; Nocera, D. G. Interfaces Between Water Splitting Catalysts and Buried Silicon Junctions. *Energy Environ. Sci.* **2013**, *6*, 532−538.

(41) Winkler, M. T.; Cox, C. R.; Nocera, D. G.; Buonassisi, T. Modeling Integrated Photovoltaic−Electrochemical Devices Using Steady-State Equivalent Circuits. *Proc. Natl. Acad. Sci. U.S.A.* **2013**, *110*, E1076−E1082.

(42) Kanan, M. W.; Yano, J.; Surendranath, Y.; Dincă, M.; Yachandra, V. K.; Nocera, D. G. Structure and Valency of a Cobalt-Phosphate Water Oxidation Catalyst Determined by in Situ X-Ray Spectroscopy. *J. Am. Chem. Soc.* **2010**, *132*, 13692−13701.

(43) Farrow, C. L.; Bediako, D. K.; Surendranath, Y.; Nocera, D. G.; Billinge, S. J. L. Intermediate-Range Structure of Self-Assembled Cobalt-Based Oxygen-Evolving Catalyst. *J. Am. Chem. Soc.* **2013**, *135*, 6403−6406.

(44) Du, P. W.; Kokhan, O.; Chapman, K. W.; Chupas, P. J.; Tiede, D. M. Elucidating the Domain Structure of the Cobalt Oxide Water Splitting Catalyst by X-ray Pair Distribution Function Analysis. *J. Am. Chem. Soc.* **2012**, *134*, 11096−11099.

(45) Bediako, D. K.; Costentin, C.; Jones, E. C.; Nocera, D. G.; Savéant, J.−M. Proton−Electron Transport and Transfer in Electrocatalytic Films. Application to a Cobalt-Based O_2-Evolution Catalyst. *J. Am. Chem. Soc.* **2013**, *135*, 10492−10502.

(46) Nowak, D. E.; Blasini, D. R.; Vodnick, A. M.; Blank, B.; Tate, M. W.; Deyhim, A.; Smilgies, D. M.; Abruña, H.; Gruner, S. M.; Baker, S. P. Six-Circle Diffractometer with Atmosphere- and Temperature-Controlled Sample Stage and Area and Line Detectors for Use in the G2 Experimental Station at CHESS. *Rev. Sci. Instrum.* **2006**, *77*, 113301−113309.

(47) Surendranath, Y.; Lutterman, D. A.; Liu, Y.; Nocera, D. G. Nucleation, Growth, and Repair of a Cobalt-Based Oxygen Evolving Catalyst. *J. Am. Chem. Soc.* **2012**, *134*, 6326−6336.

(48) Hug, S. J.; Bahnemann, D. Infrared Spectra of Oxalate, Malonate and Succinate Adsorbed on the Aqueous Surface of Rutile, Anatase and Lepidocrocite Measured with In Situ ATR-FTIR. *J. Electron Spectrosc. Relat. Phenom.* **2006**, *150*, 208−219.

(49) Dimitrou, K.; Folting, K.; Streib, W. E.; Christou, G. "Dimerization" of the $[Co^{III}{}_2(OH)_2]$ Core to the First Example of a $[Co^{III}{}_4O_4]$ Cubane: Potential Insights into Photosynthetic Water Oxidation. *J. Am. Chem. Soc.* **1993**, *115*, 6432−6433.

(50) Kanan, M.; Surendranath, Y.; Nocera, D. G. Cobalt-Phosphate Oxygen-Evolving Compound. *Chem. Soc. Rev.* **2009**, *38*, 109−114.

(51) Symes, M. D.; Surendranath, Y.; Lutterman, D. A.; Nocera, D. G. Bidirectional and Unidirectional PCET in a Molecular Model of a Cobalt-Based Oxygen Evolving Catalyst. *J. Am. Chem. Soc.* **2011**, *133*, 5174−5177.

(52) Ullman, A. M.; Nocera, D. G. Mechanism of Cobalt Self-Exchange Electron Transfer. *J. Am. Chem. Soc.* **2013**, *135*, 15053−15061.

(53) Liu, Y.; Lowe, M. A.; DiSalvo, F. J.; Abruña, H. D. Kinetic Stabilization of Ordered Intermetallic Phases as Fuel Cell Anode Materials. *J. Phys. Chem. C* **2010**, *114*, 14929−14938.

(54) Surendranath, Y.; Kanan, M. W.; Nocera, D. G. Mechanistic Studies of the Oxygen Evolution Reaction by a Cobalt-Phosphate Catalyst at Neutral pH. *J. Am. Chem. Soc.* **2010**, *132*, 16501−16509.

(55) Lutterman, D. A.; Surendranath, Y.; Nocera, D. G. A Self-Healing Oxygen-Evolving Catalyst. *J. Am. Chem. Soc.* **2009**, *131*, 3838−3839.

Influence of iron doping on tetravalent nickel content in catalytic oxygen evolving films

Nancy Li[a,1], **D. Kwabena Bediako**[a,1], **Ryan G. Hadt**[b], **Dugan Hayes**[b], **Thomas J. Kempa**[a], **Felix von Cube**[c], **David C. Bell**[c], **Lin X. Chen**[b,d], **and Daniel G. Nocera**[a,2]

[a]Department of Chemistry and Chemical Biology, Harvard University, Cambridge, MA 02138; [b]Chemical Sciences and Engineering Division, Argonne National Laboratory, Lemont, IL 60439; [c]Center for Nanoscale Systems, Harvard University, Cambridge, MA 02138; and [d]Department of Chemistry, Northwestern University, Evanston, IL 60208

Contributed by Daniel G. Nocera, December 19, 2016 (sent for review July 12, 2016; reviewed by Curtis P. Berlinguette and Shannon W. Boettcher)

Iron doping of nickel oxide films results in enhanced activity for promoting the oxygen evolution reaction (OER). Whereas this enhanced activity has been ascribed to a unique iron site within the nickel oxide matrix, we show here that Fe doping influences the Ni valency. The percent of Fe^{3+} doping promotes the formation of formal Ni^{4+}, which in turn directly correlates with an enhanced activity of the catalyst in promoting OER. The role of Fe^{3+} is consistent with its behavior as a superior Lewis acid.

water splitting | renewable energy | electrocatalysis | oxygen evolution reaction | catalysis

Increasing the solar-to-fuels conversion efficiency of artificial photosynthetic systems relies on continued improvements in understanding the chemistry of catalytic water splitting, especially the oxygen evolution reaction (OER) (1–3). It is known since the studies of Corrigan in the 1980s that oxidic Ni thin films with trace Fe content exhibit exceptional OER activity (4–8). The behavior of Fe-doped Ni (Fe:Ni) oxide films under basic conditions (1 M KOH) has been revisited (9–19) and in this recent body of work, the role of Fe in these films has come under debate. X-ray absorption spectra of Fe:Ni oxide films supported by computational studies have led to the contention that Fe^{3+} species are the active sites for water oxidation (13). The conductivity of the metal (Ni and Co) oxido framework has been observed to increase with Fe content, with the oxide also potentially serving as a scaffold for Fe active sites (16, 17). Interestingly, unary Fe oxide films, however, are inferior OER catalysts. Whereas iron oxide displays modest intrinsic activity at high overpotentials ($\eta > 350$ mV) (17), at low overpotentials ($\eta < 300$ mV) the activity of the films is poor (17, 18, 20–22), even as ultrathin submonolayer films (22). Interestingly, the Tafel slope of Fe:Ni oxido films changes with increasing Fe content (7). Based on the reaction–diffusion behavior of multilayer oxygen evolving catalyst (OEC) films (23), Fe centers as isolated (i.e., noninteracting) sites embedded in a conductive matrix may be expected to alter the exchange current density with Fe content but not necessarily the Tafel slope. In contradistinction to an Fe active site model for Fe:Ni oxides, although Mössbauer studies of Fe:Ni layered double hydroxides provide direct evidence for the formation of Fe^{4+} in Fe:Ni oxide catalysts during OER, these Fe^{4+} sites do not account for the observed catalytic activity (24). Moreover, the formed "active oxygen" species have been found to be adsorbed on nickel sites in Fe:Ni films in borate buffer (25–27), suggesting Ni centers as active sites for OER. These results together suggest that the presence of Fe active sites may not be the primary reason for the enhanced activity of Fe:Ni catalysts films and point to another chemical role for Fe in oxidic Ni films.

Fe:Ni oxide films may be prepared by nitrate electroreduction, which creates a basic pH at the electrode resulting in rapid precipitation induced by local pH increases. Under these basic conditions, Fe oxide/hydroxide is prone to preferential deposition owing to differences in solubility product constants for $Ni(OH)_2$ versus $Fe(OH)_2$ ($K_{sp} = 5.5 \times 10^{-16}$ and 4.9×10^{-17}, respectively) (28). Segregation of Fe and Ni oxido subdomains would make it difficult to examine the role of Fe in films at a mechanistic level. In contrast, addition of Fe through incidental doping or the more gradual anodic deposition technique is a more controlled deposition method that prevents rapid Fe precipitation. We have developed methods that permit metal oxido films to be anodically electrodeposited in a controlled fashion under near-neutral pH conditions where Fe precipitation is not prevalent (29–34). Oxidic Ni-based films may be deposited at intermediate pH by using borate (B_i) electrolyte and high activity from these NiB_i films may be achieved by anodic conditioning (31–33). In conjunction with these studies, electrochemical redox titrimetry and in situ (32) and ex situ (35) X-ray absorption spectroscopy (XAS) at the nickel K edge has revealed a correlation of the catalytic activation with a rise beyond 3 in the formal valence of the Ni resting state. Indeed, immediately following deposition, nickel centers persist as Ni^{3+} in a low-activity β-NiOOH-like phase; anodization results in oxidation to a mixed-valence $Ni^{3.6+}$ γ-NiOOH-like phase, which serves as the resting state for the active catalyst (32). These studies support the notion that the active Ni phase in NiOOH-mediated OER is the Ni^{4+}-containing γ-NiOOH phase. Taking into account the spectroscopic data demonstrating the correlation between activity and Ni^{4+} content (32), we have now interrogated the influence of Fe content on Ni valence by electrochemical redox titration of ultrathin (<10 nm) catalyst films, with additional characterization using Ni K-edge XAS and O K-edge electron energy loss spectroscopy (EELS). We show that the resting state

Significance

Iron-doped nickel oxide films are the most active nonnoble metal oxygen evolution reaction (OER) catalysts in alkaline electrolyte. Since Corrigan's original discovery of enhanced activity with Fe doping in nickel oxides, the chemical basis for this synergy remains unclear. Recent studies suggest iron to assume a high valent oxidation state, thus promoting OER. We provide evidence for an alternative role of Fe^{3+} as a Lewis acid in the host nickel oxide. We observe that Fe^{3+} promotes the formation of Ni^{4+}, which leads to enhanced catalytic activity. This result is consistent with Fe^{3+} to be one of the strongest Lewis acidic metals by any measure of Lewis acidity, including hard–soft acid base theory, metal ion pK_as, and chemical inertness.

Author contributions: N.L., D.K.B., R.G.H., D.C.B., L.X.C., and D.G.N. designed research; N.L., D.K.B., R.G.H., D.H., T.J.K., and F.v.C. performed research; N.L., D.K.B., and R.G.H. contributed new reagents/analytic tools; N.L., D.K.B., R.G.H., D.H., and D.G.N. analyzed data; and N.L., D.K.B., R.G.H., and D.G.N. wrote the paper.

Reviewers: C.P.B., University of British Columbia; and S.W.B., University of Oregon.

The authors declare no conflict of interest.

[1]N.L. and D.K.B. contributed equally to this work.

[2]To whom correspondence should be addressed. Email: dnocera@fas.harvard.edu.

This article contains supporting information online at www.pnas.org/lookup/suppl/doi:10.1073/pnas.1620787114/-/DCSupplemental.

Table 1. Summary of film preparation, analysis, and Fe content

Entry	Film	Fe incorporation method	Film preparation*	Fe content, mol %†
			NiB$_i$ films	
1	NiB$_i$	None	As-deposited	1.04 ± 0.46
2	NiB$_i$	None	Anodized in Fe-free solution (1 M KOH)	1.60 ± 0.38
3	NiB$_i$	None	Anodized in Fe-free solution (1 M KB$_i$ pH 9.2)	0.58
			Fe:NiB$_i$ films from trace Fe incorporation	
4	Fe^{tr}:NiB$_i$	Incubate in reagent grade 1 M KB$_i$ pH 9.2	Anodized in Fe-free solution (1 M KOH)	2.91 ± 0.74–4.75 ± 1.87#
5	Fe^{tr}:NiB$_i$	Incubated in reagent grade 1 M KB$_i$ pH 9.2	Anodized in Fe-free solution (1 M KB$_i$ pH 9.2)	2.66–6.45#
6	Fe^{tr}:NiB$_i$	Anodized in reagent grade buffer	Anodized in reagent grade solution (1 M KOH)	11.43 ± 1.55
7	Fe^{tr}:NiB$_i$	Anodized in reagent grade buffer	Anodized in reagent grade solution (1 M KB$_i$ pH 9.2)	27.34 ± 3.51
			Fe:NiB$_i$ films from intentional Fe incorporation	
8	Fe^{cod}:NiB$_i$	None	As-deposited	4.47 ± 0.59
9	Fe^{cod}:NiB$_i$	Codeposition from Ni/Fe solution	Anodized in Fe-free solution (1 M KOH)	4.90 ± 0.64

*Electrodeposited films studied with no applied anodic preconditioning are designated as-deposited; electrodeposited films obtained from applying an anodic potential for 3 h either at 0.75 V vs. NHE in 1 M KOH or 1.15 V in 1 M KBi pH 9.2. are designated as anodized.

†Fe concentration determined from ICP-MS of dissolved films.

#Incubation times from 5 to 30 min.

of the Ni valence in these materials increases with Fe content to 10%, after which increased Fe content does not affect the Ni valency. Our results point to the role of Fe as a Lewis acid to increase the Ni valency, which in turn leads to the increase in OER activity of Fe-doped Ni oxido films.

Results and Discussion

Table 1 lists the three types of NiB$_i$ films examined in this study: pure NiB$_i$ films with no Fe, and NiB$_i$ films with Fe incorporation either from trace Fe (11, 14, 15) in reagent-grade KOH and B$_i$ electrolytes (i.e., Fe^{tr}:NiB$_i$) or from Fe codeposited (14) from a known solution concentration (i.e., Fe^{cod}:NiB$_i$). Electrolyte solutions for the preparation of authentic NiB$_i$ films must be either scrubbed of Fe in very basic pH conditions by subjecting the solutions to treatment with solid $Ni(OH)_2$ as previously described (11, 14) or cleaned by chelating resin complex in more neutral pH conditions as previously described (36) (see *SI Appendix* for details). Table 1 also lists different methods of film treatment. Films were studied either directly upon electrodeposition (designated as-deposited) or after holding the film at an anodic potential for 3 h either at 0.75 V in 1 M KOH or 1.15 V in 1 M KB$_i$ pH 9.2 (designated anodized). All potentials are in reference to the normal hydrogen electrode (NHE).

As-deposited and KOH-anodized NiB$_i$ films (entries 1 and 2 in Table 1, entries 1–1 and 1–2, respectively) exhibit Fe content and OER activity similar to previous reports (14, 31–33). Ni and Fe metal ion concentrations were determined by inductively coupled plasma-mass spectrometry (ICP-MS) on solutions of digested films (rinsed in type I water) in ultrapure (doubly distilled) 2% nitric acid. All glassware was thoroughly acid-washed before use. The detection of Fe in as-deposited NiB$_i$ films (Table 1, entry 1–1) at a level of 1.04 ± 0.46% and for films anodized in scrubbed electrolyte (Table 1, entry 1–2) at a level of 1.60 ± 0.38% is likely due to remnant trace Fe in glassware and the general experimental setup. As noted previously (14, 31–33), the OER activity of as-deposited NiB$_i$ films in Fe-scrubbed electrolyte (Table 1, entry 1–1) is low (red trace, *SI Appendix*, Fig. S1), consistent with the high Tafel slopes (90–100 mV/decade) characteristic of such films (14, 31–33). That the OER current density (j) does not vary over time suggests that an anodic potential alone does not modify NiB$_i$ films operating in Fe-free media. Also consistent with previous results (14, 31–33), the operation of these as-deposited NiB$_i$ films (Table 1, entry 1–1) in reagent-grade electrolyte (which contains adventitious amounts of Fe) shows a dramatic increase in activity (blue trace, *SI Appendix*, Fig. S1), attendant to a decreased Tafel slope of 30 mV/decade (33).

The valencies of Ni in these films (Table 1, entries 1–1 and 1–2) were electrochemically assessed by coulometric titration in Fe-free 1 M KOH. This measurement was also carried out on Fe^{tr}:NiB$_i$ films (Table 1, entries 1–4, 1–6, and 1–7). Films ≤7 nm (a few monolayers) thick are obtained by terminating deposition upon the passage of 1.0 mC/cm^2 (32, 33). The use of such ultrathin films ensures that charge transport is not a predominant factor in evaluating film redox properties. The total charge passed in the electroreduction of Ni centers in NiB$_i$ and Fe^{tr}:NiB$_i$ films (blue trace, Fig. 1*A*) was determined from the cyclic voltammogram (red trace, Fig. 1*A*), permitting the total number of electrons consumed upon reduction to Ni^{2+} to be quantified.

Fig. 1*A* shows exemplary data for the cyclic voltammogram and current integration (charge) curve for NiB$_i$ films anodized in Fe-free electrolyte (Table 1, entry 1–2). By determining the total Ni and Fe content in these films from ICP-MS analysis, the Ni valency may be calculated. For NiB$_i$ films (Table 1, entry 1–2), we observe that 1.2 ± 0.1 electrons are consumed per Ni center, revealing that a Ni valency of +3.2(1) is sustained upon anodization

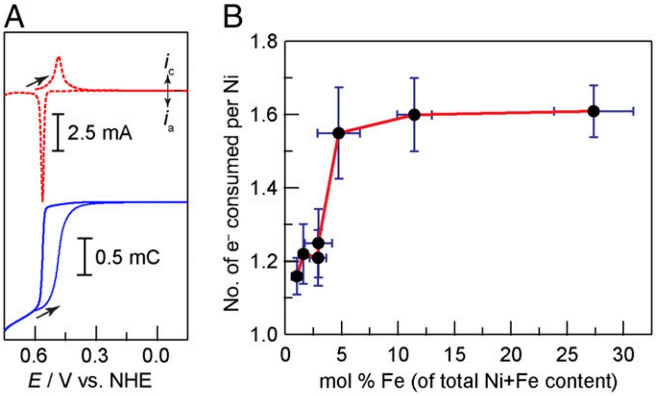

Fig. 1. (*A*) CV in Fe-free 1 M KOH of a NiB$_i$ film deposited onto a fluorine-doped tin oxide (FTO)-coated glass slide and anodized for 3 h in Fe-free 1.0 M KOH (Table 1, entry 1–2). Scan rate: 0.1 V/s. Current (top, dashed line) and total charge (bottom, solid line) data are offset for clarity. (*B*) Plot of coulometric titration data against the Fe content for NiB$_i$ and Fe^{tr}:NiB$_i$ films in the as-deposited (Table 1, entry 1–1) and reagent-grade anodized states (Table 1, entries 1–6 and 1–7), as well as upon anodization in Fe-free KOH following exposure to reagent-grade 1 M KB$_i$ electrolyte for 0, 5, 10, or 30 min (Table 1, entries 1–2 and 1–4). Error bars derived from three independent measurements.

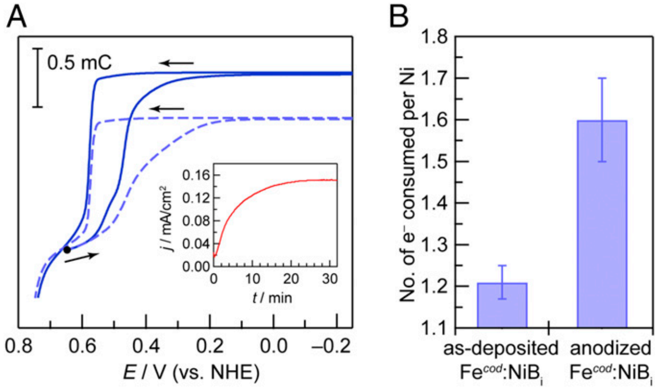

Fig. 2. Fe^{cod}:NiB$_i$ films deposited in the presence of Fe^{3+}. (*A*) Coulometric titration of as-deposited (Table 1, entry 1–8) (blue, dashed line) and anodized (Table 1, entry 1–9) (dark blue, solid line) films showing a significantly greater amount of charge passed following anodization. The dot marks the start of the scan and arrows show scan direction. (*Inset*) Chronoamperometric trace over the course of anodization at 0.75 V in Fe-free 1 M KOH showing activation. (*B*) Coulometric titration data for codeposited Fe:Ni oxide films (Table 1, entries 1–8 and 1–9).

in Fe-free solution. A similar result of 1.16 ± 0.05 e$^-$/Ni (Ni valency of +3.2) is also obtained for films in the as-deposited state (Table 1, entry 1–1), matching previous values for as-deposited NiB$_i$ films (32). Our analysis assumes that Fe^{4+} sites, if present (as has been reported for a 3:1 Ni:Fe layered double hydroxide, LDH) (24), do not consume electrons to produce Fe^{3+} sites. Indeed, at most, 1/5 of the Fe sites in these LDHs are Fe^{4+}; with this benchmark, even if all of the iron content in NiB$_i$ films were reduced to Fe^{3+}, this would account for negligible electron consumption given our low Fe content (under 5% for Fe incorporated through incubation, *vide infra*). We note that integration of the cathodic wave is more reliable than integrating the corresponding anodic wave of the Ni$^{3+/2+}$ redox feature (*SI Appendix*, Fig. S2). As shown by *SI Appendix*, Fig. S2*B*, the integrated charge curve for cyclic voltammogram (CV) scans recorded toward reductive potentials is defined clearly by an extended plateau where the film has been completely reduced to Ni^{2+}. This is not the case for integration of the anodic feature, which merges into the OER wave. This likely explains the observation of Corrigan and Bendert (8) and Merrill et al. (37) that NiB$_i$ in the absence of significant Fe incorporation exhibits a redox level of 1.6 e$^-$/Ni above Ni^{2+}. In these measurements, the Ni valency was determined from the anodic wave of the Ni$^{3+/2+}$ redox feature where contributions of OER to the measured current would lead to inflated values in the Ni redox level. Furthermore, we note that the films used by Corrigan were much thicker than reported here (∼470 nm versus ∼7 nm based on average Ni loading comparison). In thick films, a CV sweep conducted for coulometric analysis may not capture all Ni center reductions because of poor electron transfer as the film is made increasingly insulating by Ni^{2+} centers during the reduction. We avoid this issue by using ultrathin films to ensure that the entirety of the film is subject to interrogation by redox titrimetry. We also note that different materials and conditions lead to different values of Ni valency. Smith and Berlinguette have observed 4 e$^-$/Ni transferred for photochemically prepared α-NiO$_x$ films upon integration of the first anodic peak (38), although with repeated cycling of the film, the e$^-$/Ni calculated with subsequent cycling converges to ∼1.2 e$^-$ per Ni, as we observe here. Studies of other NiFe-based LDHs show a trend in decreased Ni valency with increasing Fe (39) which may be explained by a different resting state species such as a NiFe hydroperoxide (40). Also of note, at high iron concentrations, phase-segregated Fe hydroxide phases may be prevalent and thus could complicate accurate measurements of Ni valency.

NiB$_i$ films were doped with increasing quantities of Fe by incubating the as-deposited films in reagent-grade 1 M KB$_i$ pH 9.2 electrolyte (that had not been subject to the Fe scrubbing procedure) at open circuit for varying times (5, 10, 30 min) and subsequently anodized in Fe-free KOH (Table 1, entry 1–4). The amount of iron incorporated into these films increases steadily with incubation time (*SI Appendix*, Fig. S3) as the onset potential to OER decreases (*SI Appendix*, Fig. S2*A*). Incorporation of Fe via this incubation method is advantageous because it allows us to resolve the behavior of uniform films with low Fe content (<5 mol %). Fig. 1*B* plots the coulometric titration data versus the percentage of Fe doping for films prepared by this incubation process (Table 1, entry 1–4) along with that obtained from films prepared by the aforementioned methods (Table 1, entries 1–1, 1–2, 1–6, and 1–7). The maximal mixed-valence resting state of Ni$^{3.6+}$ is achieved at Fe doping levels of 4%, and beyond a doping level of 10% Fe, there is no further increase in average Ni valence. Interestingly, the plateau at ≥10% Fe content observed here matches previous reports of maximal film activity at ∼10% Fe doping (10, 13, 15, 18). Moreover, the Ni$^{3.6+}$ value matches that previously measured for NiB$_i$ films anodized in reagent-grade 1 M KB$_i$ buffer (33), which likely contains Fe as a contaminant on par with the highest Fe content in Fe^{tr}:NiB$_i$ (Table 1, entry 1–7) measured here (*SI Appendix*, Fig. S3). This plateau in Ni valence with Fe content again emphasizes that electrons consumed during coulometric titrations are going toward reduction of higher valence nickel centers to Ni^{2+} as opposed to the reduction of Fe^{4+} to Fe^{3+}.

To distinguish the role of increasing Fe content during an applied anodic potential, coulometric titration/ICP-MS analysis was conducted on films prepared by codeposition of Ni and Fe (Fe^{cod}:NiB$_i$) in the as-deposited and anodized state (Table 1, entries 1–8 and 1–9, respectively). Here, we followed previously published (14) procedures to anodically electrodeposit ultrathin films (deposition charge of 1.0 mC/cm^2) from a pH 9.2 KB$_i$ electrolyte containing a 9:1 molar ratio of Ni^{2+} and Fe^{2+}. Table 1, film entry 1–8 shows a steady increase in activity with a plateau after 1 h (Fig. 2*A*, *Inset*), similar to that observed upon anodization of NiB$_i$ films in reagent-grade electrolyte (*SI Appendix*, Fig. S1, blue trace) (33, 34). Redox titrimetry followed by elemental analysis of digested films reveals that the average Ni valence in these Fe^{cod}:NiB$_i$ films increases over the course of the electrochemical activation from +3.21(4) (as-deposited, Table 1, entry 1–8) to +3.6(1) (anodized, Table 1, entry 1–9) as shown in

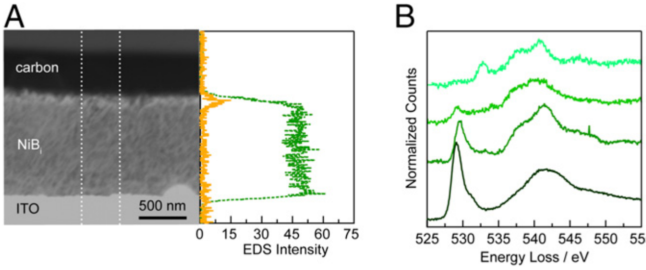

Fig. 3. (*A*, *Left*) Dark-field STEM image of a typical cross-sectioned catalyst film sample showing: a portion of the indium tin oxide (ITO) substrate, the Fe^{tr}:NiB$_i$ (Table 1, entry 1–7) catalyst layer (anodized in reagent-grade KB$_i$ electrolyte), and protective carbon overcoats applied before focused ion beam milling. (*Right*) Energy-dispersive X-ray spectroscopy (EDS) elemental profile (Ni: green; Fe: orange) with EDS counts summed across the region between the dotted lines. (*B*) Oxygen K-edge EELS of nickel oxide model compounds. From top to bottom: Ni^{II}O, Ni^{II}(OH)$_2$, LiNi^{III}O$_2$, and γ-Ni$^{III/IV}$OOH. Spectra were normalized to the edge jump and offset for clarity.

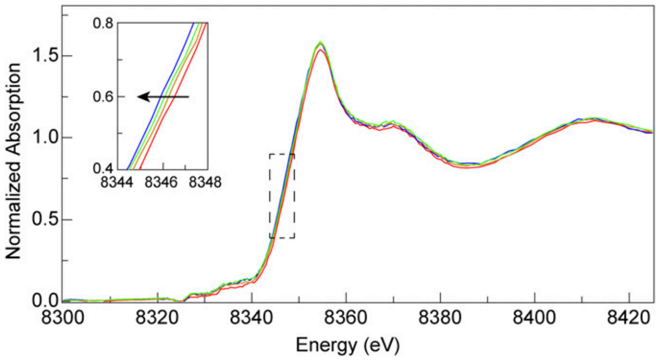

Fig. 4. Ni K-edge XANES spectra of reagent-grade 1 M KB_i pH 9.2 anodized Fe^{tr}:NiB_i film (12.30 mol % Fe) (Table 1, entry 1–7) (blue), as well as Fe^{tr}:NiB_i films anodized in Fe-free 1 M KB_i pH 9.2 following exposure to reagent-grade 1 M KB_i electrolyte for 0 (red), 15 (orange), or 25 (green) min to obtain Fe content of 0.58, 2.66, and 6.45 mol % Fe, respectively (Table 1, entries 1–3 and 1–5). (*Inset*) Zoomed-in K-edge shift of spectra as indicated by dotted box in *A*. All films were poised at 1.3 V during anodization and XAS scans.

Fig. 2*B*. This result agrees with previous work that shows anodization results in significant increase in turnover frequency even for codeposited Fe^{cod}:NiB_i films (14).

The results of Figs. 1 and 2 show that the presence of Fe alone does not promote the formation of higher valent Ni species. Instead, the combination of Fe and electrochemical polarization at moderately high potentials (anodization) is necessary for activation. Previous XAS studies show that anodization drives a phase change from β-NiOOH (valency 3.2) to γ-NiOOH (valency 3.6) (32). Fe dopants make this phase transition more accessible but Fe incorporation alone cannot achieve this transformation. That the presence of Fe facilitates the formation of Ni^{4+} to yield an overall average $Ni^{3.6+}$ formal oxidation of the resting state suggests that Fe dopants make this phase transition more accessible. It remains undefined if Fe increases Ni valency to drive the structural change or vice versa.

To study the difference between anodized Fe:NiB_i films formed from codeposition (Fe^{cod}:NiB_i, Table 1, entry 1–9) versus incidental doping (Fe^{tr}:NiB_i, Table 1, entry 1–7), we conducted cross-sectional elemental analysis of a thick NiB_i catalyst film (~1 μm) that was anodized in reagent-grade KB_i pH 9.2 electrolyte (Table 1, entry 1–7). The results reveal an anisotropic distribution of Fe in the film with the predominant localization of Fe in the outermost ~100 nm of the catalyst film (Fig. 3*A*). Similarly, thick as-deposited films that were not subjected to anodization (Table 1, entry 1–1) do not display significant Fe counts across the film (*SI Appendix*, Fig. S4). This result again emphasizes the need to make measurements of Ni valency on thin films, as performed in our studies here. Importantly, this result also offers insight into the possible origin of the apparently higher activity observed upon codeposition of Fe^{cod}:NiB_i in thicker films (14). Codeposition gives rise to a more homogeneous distribution of Fe throughout a thick film. Consequently, a greater proportion of the Ni centers throughout a thick film would attain a Ni^{4+} valency upon anodization, resulting in higher activity.

To investigate why greater Ni^{4+} valence is beneficial to greater catalytic OER activity, we probed the influence of formal Ni valence on the electronic structure of oxygen ions in Ni oxide models (Fig. 3*B*). Oxygen K-edge spectroscopy largely probes transitions between O 1*s* and unoccupied metal orbitals (i.e., 3*d*, and 4*s*/4*p*). Such spectra typically feature a preedge feature centered at ~530 eV and a broader set of overlapping bands spanning the 535–550-eV range. The preedge results from transitions to unoccupied metal 3*d* orbitals that are hybridized with O 2*p* character (formally a 1*s* → 3*d* transition that gains dipole allowed intensity via O 2*p* mixing).

Spectral intensity above the preedge is associated with states that have O 2*p* character hybridized with unoccupied metal 4*s* and 4*p* orbitals (41–43). The intensity of the preedge has been shown to be a powerful measure of the covalency of metal–oxygen bonds (41). As shown in Fig. 3*B*, EELS (see *SI Appendix* for details) of a series of model Ni oxide compounds reveals a pronounced increase in the intensity of the preedge feature as the formal oxidation state of Ni increases from NiO to γ-NiOOH. These data indicate increased covalency in Ni–O bonding as the formal Ni oxidation state is increased. As a direct consequence of the electronic considerations embodied by the "Oxo Wall" (44), the formal oxidation state of Ni(IV)–oxo (Ni(IV) $\stackrel{...}{=}$ O) will possess significant Ni(III)–$O^\bullet$ resonance character with increased covalency. Such oxyl radical character is consistent with increasing evidence for the role of oxygen radicals in O–O bond formation by a proton-coupled electron transfer (PCET) mechanism involving water (45–47), most likely to generate a hydroperoxide intermediate from which oxygen is generated (48). To this end, increased Ni^{4+} generation by Fe incorporation will lead to greater Ni–O covalency, and thus greater oxyl character, which can manifest in increased OER activity.

XAS of Ni centers in NiB_i during OER also show increased Ni–O covalency as Fe loading is increased. The in situ X-ray absorption near-edge spectra data are given in Fig. 4 for anodized NiB_i (Table 1, entry 1–3) and Fe^{tr}:NiB_i films (Table 1, entry 1–5 and entry 1–7). A systematic red-shift of the Ni K edge is observed upon increased Fe incorporation from 0.58 mol % to 12.30 mol % Fe. The magnitude of this edge shift (−0.8 eV) is less than that associated with reducing $Ni^{3+/4+}$ in the anodized

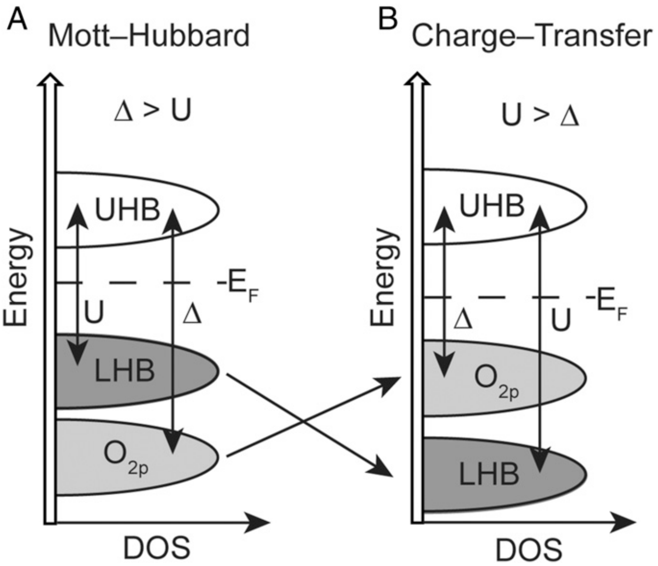

Fig. 5. Schematic energy-band vs. density of states (DOS) diagrams of (*A*) a Mott–Hubbard insulator and (*B*) a charge-transfer insulator. The occupied O 2*p* bands are shaded in light gray whereas the metal *d* bands are shaded in dark gray for occupied bands and unshaded for unoccupied bands. The unoccupied and occupied *d* bands are represented by the UHB and LHB, respectively. The *d*-*d* coulomb and exchange energy transfer (U) between UHB and LHB of the metal *d* bands and the *p*-to-*d* charge-transfer energy (Δ) terms are also indicated. The Fermi energy (E_F) level is indicated by the dotted dashed line. Mott–Hubbard insulators and charge-transfer insulators are differentiated by their relative values of U versus Δ to result in the highest occupied band being either metal or ligand character, which in turn results in either metal oxidation (Mott–Hubbard insulator) or ligand oxygen oxidation (charge-transfer insulator), respectively.

film to Ni^{2+} (*SI Appendix*, Fig. S5). Additionally, the edge shift upon Fe incorporation is less than that previously observed (40, 49) with the caveats that the results of Fig. 4 have been obtained under OER conditions with less Fe incorporation. If X-ray–induced photoreduction were to give rise to this <1-eV change in edge energy (50, 51), we would expect a systematic, instantaneous photoreduction across the different films. However, spectral changes do not change over multiple scans, suggesting that photoreduction of the film is not occurring upon continuous X-ray exposure. On the other hand, it is well established that the Ni K edge is sensitive to changes in oxidation and spin state as well as ligand–metal covalency. Increased Ni–O covalency results in a decreased effective nuclear charge, Z_{eff}, of the metal, which in turn results in a red-shift of the edge transition(s) (i.e., $1s \rightarrow 4p$). Additionally, increased metal–ligand covalency can result in a broadening and increased intensity of the edge transitions due to delocalization of the metal $4p$ orbitals (52). Our observations are also in line with comparative Ni K-edge X-ray absorption near edge structure (XANES) spectra of Ni/Mn molecular complexes with hard O, N-donor and soft Cl, S-donor ligands, which show that the edge energy shifts to lower energy with increased Ni–ligand covalency (52–54). Thus, the Ni K-edge data corroborate the O K-edge data of Fig. 3*B*—an increase in Fe loading results in an increase in Ni–O covalency.

The contributions of Ni(IV) $\stackrel{\cdot\cdot}{=}$ O versus Ni(III)–O$^{\bullet}$ resonances with covalency can be understood within the context of a Zaanen–Sawatzky–Allen scheme. In this treatment, transition-metal compounds may be classified as either Mott–Hubbard or charge-transfer insulators (55, 56). The electronic structure for these two regimes is determined by the relative values of U and Δ (57), where U is related to the *d-d* Coulomb and exchange interactions resulting from d_i^n, $d_j^n \leftrightarrow d_i^{n-1}$, d_j^{n+1} (i and j are electrons on neighboring metals) charge fluctuations, and Δ is related to the ionization energy of the ligand and electron affinity of the metal, and is therefore related to the ligand-to-metal charge-transfer (LMCT) energy ($d_i^n \rightarrow d_i^{n+1}\mathrm{L}$, where the electron-hole is located on the ligand) (56). The relative values of U and Δ tune the metal–ligand character of the highest occupied band, which results in metal versus oxide oxidation (Fig. 5). For large Δ ($\Delta > \mathrm{U}$), the oxygen valence band lies below the occupied *d*-orbital band [i.e., lower Hubbard band (LHB)], giving rise to a Mott–Hubbard-type insulator, as depicted in Fig. 5. Conversely, for small Δ ($\mathrm{U} > \Delta$), the oxygen valence band lies above the occupied d-orbital band, giving rise to a charge-transfer-type insulator. The relative values of U and Δ are determinants of the Ni(IV) $\stackrel{\cdot\cdot}{=}$ O $\leftrightarrow$ Ni(III)–O$^{\bullet}$ resonance structures. Decreasing Δ (more covalent interaction due to greater ligand–metal orbital mixing) and increasing U will favor covalency and hence a greater Ni(III)–O$^{\bullet}$ resonance contribution (owing to the ordering of the O_{2p} band above LHB). This model is consistent with our results of a greater Ni–O covalency arising from a higher effective formal oxidation state of Ni with Fe doping. The result is also consistent with the observation of increased conductivity of the Ni oxide lattice with Fe doping (11) inasmuch as a decrease in Δ and increase in U induces more charge-transfer character within the lattice.

Conclusions

The ability to access the Ni^{4+} in the resting state of Ni oxido OECs at modest overpotentials ($\eta \sim 350$–250 mV) is directly correlated to the presence of Fe in NiB_i films. Coulometric titration results reveal that the resting state valency of Ni increases by 0.5 for Fe loadings of 5–10%. Attendant to this increase in Ni valency, O and Ni K-edge spectra reveal a greater Ni–O covalency. On the basis of the studies reported herein, the role of Fe in promoting the OER at nickel oxide catalysts appears in large part to be a Lewis acid effect. By any measure, Fe^{3+} is strong Lewis acid. The chemical hardness scale of Parr et al. places Fe^{3+} as one of the "hardest" ions in the periodic table (58, 59), which is also supported by the less quantitative predictions of hard–soft acid–base theory (60). Within the context of the study herein, a very relevant measure of the Lewis acidity is offered by the pK_a of the hexaqua metal complex. Computation and experiment show Fe^{3+} to be the most acidic transition metal ion with a $pK_a = 2.2$ for the deprotonation of coordinated water (61). Accordingly, the incorporation of the Lewis acid Fe^{3+} into Ni oxido catalyst clusters would serve to increase the acidity of OH_x (aqua/hydroxo) moieties that are coordinated to nickel, thereby lowering the reduction potential for the $Ni^{4+/3+}$ couple and thus engendering a greater population of Ni^{4+} in the Fe-doped catalysts. This in turn leads to greater oxyl character arising from the Ni(IV) $\stackrel{\cdot\cdot}{=}$ O $\leftrightarrow$ Ni(III)–O$^{\bullet}$ resonance contribution. In light of the recognized role of the oxyl radical in promoting O–O bond formation via PCET (62–69), the role of Fe^{3+} in NiB_i to promote increased oxyl character is of beneficial consequence to increasing OER activity in metal oxidic catalyst films.

ACKNOWLEDGMENTS. We are grateful to Adam Graham for assistance with scanning transmission electron microscopy (STEM), Zhongxing Chen for assistance with ICP, and Michael Huynh for helpful discussions. We also acknowledge Tianpin Wu, Lu Ma, and George Sterbinsky for assistance with XAS measurements. This material is based upon work supported under the Solar Photochemistry Program of the Chemical Sciences, Geosciences, and Biosciences Division, Office of Basic Energy Sciences of the US Department of Energy. R.G.H. is an Enrico Fermi Fellow at Argonne National Laboratory (ANL). D.H. is supported by the Joseph J. Katz Postdoctoral Fellowship at ANL. Work by D.C.B. and F.v.C. was supported by the Science and Technology Center for Integrated Quantum Materials, National Science Foundation (NSF) Grant DMR-1231319. Use of beamline 9BM-B at the Advanced Photon Source at ANL was supported by the US Department of Energy, Office of Science, Office of Basic Energy Sciences, under Contract DE-AC02-06CH11357. The Center for Nanoscale Systems at Harvard University is a member of the National Nanotechnology Infrastructure Network, which is supported by the National Science Foundation under ECS-0335765.

1. Lewis NS, Nocera DG (2006) Powering the planet: chemical challenges in solar energy utilization. *Proc Natl Acad Sci USA* 103(43):15729–15735.
2. Lewis NS, Nocera DG (2015) The solar opportunity. *The Bridge* 46:41–47.
3. Cook TR, et al. (2010) Solar energy supply and storage for the legacy and nonlegacy worlds. *Chem Rev* 110(11):6474–6502.
4. Conway BE, Bourgault PL (1959) The electrochemical behavior of the nickel–nickel oxide electrode: Part I. Kinetics of self-discharge. *Can J Chem* 37:292–307.
5. Lu PW, Srinivasan S (1978) Electrochemical-ellipsometric studies of oxide film formed on nickel during oxygen evolution. *J Electrochem Soc* 125:1416–1422.
6. Bockris JO'M, Otagawa T (1983) Mechanism of oxygen evolution on perovskites. *J Phys Chem* 87:2960–2971.
7. Corrigan DA (1987) The catalysis of the oxygen evolution reaction by iron impurities in thin film nickel oxide electrodes. *J Electrochem Soc* 134:377–384.
8. Corrigan DA, Bendert RM (1989) Effect of coprecipitated metal ions on the electrochemistry of nickel hydroxide thin films: Cyclic voltammetry in 1M KOH. *J Electrochem Soc* 136:723–728.
9. Trotochaud L, Ranney JK, Williams KN, Boettcher SW (2012) Solution-cast metal oxide thin film electrocatalysts for oxygen evolution. *J Am Chem Soc* 134(41):17253–17261.
10. Louie MW, Bell AT (2013) An investigation of thin-film Ni-Fe oxide catalysts for the electrochemical evolution of oxygen. *J Am Chem Soc* 135(33):12329–12337.
11. Trotochaud L, Young SL, Ranney JK, Boettcher SW (2014) Nickel-iron oxyhydroxide oxygen-evolution electrocatalysts: The role of intentional and incidental iron incorporation. *J Am Chem Soc* 136(18):6744–6753.
12. Hunter BM, et al. (2014) Highly active mixed-metal nanosheet water oxidation catalysts made by pulsed-laser ablation in liquids. *J Am Chem Soc* 136(38):13118–13121.
13. Friebel D, et al. (2015) Identification of highly active Fe sites in (Ni,Fe)OOH for electrocatalytic water splitting. *J Am Chem Soc* 137(3):1305–1313.
14. Smith AM, Trotochaud L, Burke MS, Boettcher SW (2015) Contributions to activity enhancement via Fe incorporation in Ni-(oxy)hydroxide/borate catalysts for near-neutral pH oxygen evolution. *Chem Commun (Camb)* 51(25):5261–5263.
15. Klaus S, Cai Y, Louie MW, Trotochaud L, Bell AT (2015) Effects of Fe electrolyte impurities on $Ni(OH)_2$/NiOOH structure and oxygen evolution activity. *J Phys Chem C* 119:7243–7254.
16. Burke MS, Kast MG, Trotochaud L, Smith AM, Boettcher SW (2015) Cobalt-iron (oxy)hydroxide oxygen evolution electrocatalysts: The role of structure and composition on activity, stability, and mechanism. *J Am Chem Soc* 137(10):3638–3648.

17. Burke MS, et al. (2015) Revised oxygen evolution reaction activity trends for first-row transition-metal (oxy)hydroxides in alkaline media. *J Phys Chem Lett* 6(18): 3737–3742.
18. Swierk JR, Klaus S, Trotochaud L, Bell AT, Tilley TD (2015) Electrochemical study of the energetics of the oxygen evolution reaction at nickel iron (oxy)hydroxide catalysts. *J Phys Chem C* 119:19022–19029.
19. Ahn HS, Bard AJ (2016) Surface interrogation scanning electrochemical microscopy of $Ni_{1-x}Fe_xOOH$ ($0 < x < 0.27$) oxygen evolving catalyst: Kinetics of the "fast" iron sites. *J Am Chem Soc* 138(1):313–318.
20. Lyons MEG, Brandon MP (2008) The oxygen evolution reaction on passive oxide covered transition metal electrodes in alkaline solution. Part III – Iron. *Int J Electrochem Sci* 3:1463–1503.
21. Man IC, et al. (2011) Universality in oxygen evolution electrocatalysis on oxide surfaces. *ChemCatChem* 3:1159–1165.
22. Subbaraman R, et al. (2012) Trends in activity for the water electrolyser reactions on 3d M(Ni,Co,Fe,Mn) hydr(oxy)oxide catalysts. *Nat Mater* 11(6):550–557.
23. Bediako DK, Costentin C, Jones EC, Nocera DG, Savéant J-M (2013) Proton-electron transport and transfer in electrocatalytic films. Application to a cobalt-based O_2-evolution catalyst. *J Am Chem Soc* 135(28):10492–10502.
24. Chen JYC, et al. (2015) Operando analysis of NiFe and Fe oxyhydroxide electrocatalysts for water oxidation: Detection of Fe^{4+} by Mössbauer spectroscopy. *J Am Chem Soc* 137(48):15090–15093.
25. Trześniewski BJ, et al. (2015) In situ observation of active oxygen species in Fe-containing Ni-based oxygen evolution catalysts: The effect of pH on electrochemical activity. *J Am Chem Soc* 137(48):15112–15121.
26. Morales OD, Ferrus-Suspedra D, Koper MTM (2016) The importance of nickel oxyhydroxide deprotonation on its activity towards electrochemical water oxidation. *Chem Sci* 7:2639–2645.
27. Yoshida M, et al. (2015) Direct observation of active nickel oxide cluster in nickel–borate electrocatalyst for water oxidation by in situ O K–edge X–ray absorption spectroscopy. *J Phys Chem C* 119:19279–19286.
28. Lide, DR, ed (2003) CRC Handbook of Chemistry and Physics, ed Lide, DR (CRC Press, Boca Raton, FL), 84th Ed, Sect 8, No. 120–121.
29. Kanan MW, Nocera DG (2008) In situ formation of an oxygen-evolving catalyst in neutral water containing phosphate and Co^{2+}. *Science* 321(5892):1072–1075.
30. Surendranath Y, Dincă M, Nocera DG (2009) Electrolyte-dependent electrosynthesis and activity of cobalt-based water oxidation catalysts. *J Am Chem Soc* 131(7):2615–2620.
31. Dincă M, Surendranath Y, Nocera DG (2010) Nickel-borate oxygen-evolving catalyst that functions under benign conditions. *Proc Natl Acad Sci USA* 107(23):10337–10341.
32. Bediako DK, et al. (2012) Structure-activity correlations in a nickel-borate oxygen evolution catalyst. *J Am Chem Soc* 134(15):6801–6809.
33. Bediako DK, Surendranath Y, Nocera DG (2013) Mechanistic studies of the oxygen evolution reaction mediated by a nickel-borate thin film electrocatalyst. *J Am Chem Soc* 135(9):3662–3674.
34. Huynh M, Bediako DK, Nocera DG (2014) A functionally stable manganese oxide oxygen evolution catalyst in acid. *J Am Chem Soc* 136(16):6002–6010.
35. Risch M, et al. (2011) Nickel-oxido structure of a water-oxidizing catalyst film. *Chem Commun (Camb)* 47(43):11912–11914.
36. Wuttig A, Surendranath Y (2015) Impurity ion complexation enhances carbon dioxide reduction catalysis. *ACS Catal* 5:4479–4484.
37. Merrill M, Worsley M, Wittstock A, Biener J, Stadermann M (2014) Determination of the "NiOOH" charge and discharge mechanisms at ideal activity. *J Electroanal Chem* 717:177–188.
38. Smith RDL, Berlinguette CP (2016) Accounting for the dynamic oxidative behavior of nickel anodes. *J Am Chem Soc* 138(5):1561–1567.
39. Görlin M, et al. (2016) Oxygen evolution reaction dynamics, faradaic charge efficiency, and the active metal redox states of Ni-Fe oxide water splitting electrocatalysts. *J Am Chem Soc* 138(17):5603–5614.
40. Black JF (1978) Metal-catalyzed autoxidation. The unrecognized consequences of metal-hydroperoxide complex formation. *J Am Chem Soc* 100:527–535.
41. Grioni M, Fuggle JC, Ghijsen J, Sawatzky GA, Petersen H, de Groot FM (1989) Oxygen 1s x-ray-absorption edges of transition-metal oxides. *Phys Rev B Condens Matter* 40(8):5715–5723.
42. Kuiper P, Kruizinga G, Ghijsen J, Sawatzky GA, Verweij H (1989) Character of holes in $Li_xNi_{1-x}O$ and their magnetic behavior. *Phys Rev Lett* 62(2):221–224.
43. Yoon W-S, Chung KY, McBreen J, Fischer DA, Yang X-Q (2006) Changes in electronic structure of the electrochemically Li-ion deintercalated $LiNiO_2$ system investigated by soft X-ray absorption spectroscopy. *J Power Sources* 163:234–237.
44. Winkler J, Gray H (2012) Electronic structures of oxo-metal ions. *Molecular Electronic Structures of Transition Metal Complexes I, Structure and Bonding*, eds Mingos DMP, Day P, Dahl JP (Springer, Berlin), Vol 142, pp 17–28.
45. Wang L-P, Troy VV (2011) Direct-coupling O_2 bond forming a pathway in cobalt oxide water oxidation catalysts. *J Phys Chem Lett* 2:2200–2204.
46. Yang X, Baik MH (2006) *cis,cis*-$[(bpy)_2Ru^VO]_2O^{4+}$ catalyzes water oxidation formally via in situ generation of radicaloid Ru^{IV}–O*. *J Am Chem Soc* 128(23):7476–7485.
47. Jiang Y, et al. (2013) Promoting the activity of catalysts for the oxidation of water with bridged dinuclear ruthenium complexes. *Angew Chem Int Ed Engl* 52(12): 3398–3401.
48. Zhang M, de Respinis M, Frei H (2014) Time-resolved observations of water oxidation intermediates on a cobalt oxide nanoparticle catalyst. *Nat Chem* 6(4):362–367.
49. Bates MK, Jia Q, Doan H, Liang W, Mukerjee S (2016) Charge-transfer effects in Ni–Fe and Ni–Fe–Co mixed-metal oxides for the alkaline oxygen evolution reaction. *ACS Catal* 6:155–161.
50. Dubois L, Jacquamet L, Pécaut J, Latour J-M (2006) X-ray photoreduction of a di(μ-oxo)$Mn^{III}Mn^{IV}$ complex occurs at temperatures as low as 20 K. *Chem Commun (Camb)* 43(43):4521–4523.
51. Yi J, Orville AM, Skinner JM, Skinner MJ, Richter-Addo GB (2010) Synchrotron X-ray-induced photoreduction of ferric myoglobin nitrite crystals gives the ferrous derivative with retention of the O-bonded nitrite ligand. *Biochemistry* 49(29):5969–5971.
52. Sarangi R (2013) X-ray absorption near-edge spectroscopy in bioinorganic chemistry: Application to M-O_2 systems. *Coord Chem Rev* 257(2):459–472.
53. Penner-Hahn JE, et al. (1990) Structural characterization of the manganese sites in the photosynthetic oxygen-evolving complex using x-ray absorption spectroscopy. *J Am Chem Soc* 112:2549–2557.
54. Colpas GJ, et al. (1991) X-ray spectroscopic studies of nickel complexes, with application to the structure of nickel sites in hydrogenases. *Inorg Chem* 30:920–928.
55. Zaanen J, Sawatzky GA, Allen JW (1985) Band gaps and electronic structure of transition-metal compounds. *Phys Rev Lett* 55(4):418–421.
56. Imada M, Fujimori A, Tokura Y (1998) Metal-insulator transitions. *Rev Mod Phys* 70(4): 1039–1263.
57. Greiner MT, Lu Z-H (2013) Thin-film metal oxides in organic semiconductor devices: Their electronic structures, work functions and interfaces. *NPG Asia Mater* 5:e55.
58. Parr RG, Pearson RG (1983) Absolute hardness: Companion parameter to absolute electronegativity. *J Am Chem Soc* 105:7512–7516.
59. Yang W, Parr RG (1985) Hardness, softness, and the Fukui function in the electronic theory of metals and catalysis. *Proc Natl Acad Sci USA* 82(20):6723–6726.
60. Pearson RG (1968) Hard and soft acids and bases, HSAB, part 1: Fundamental principles. *J Chem Educ* 45:581–587.
61. Jerome SV, Hughes TF, Friesner RA (2014) Accurate pKa prediction in first-row hexaaqua transition metal complexes using the B3LYP-DBLOC method. *J Phys Chem B* 118(28): 8008–8016.
62. Siegbahn PEM, Blomberg MRA (2010) Quantum chemical studies of proton-coupled electron transfer in metalloenzymes. *Chem Rev* 110(12):7040–7061.
63. Lundberg M, Siegbahn PEM (2004) Theoretical investigations of structure and mechanism of the oxygen-evolving complex in PSII. *Phys Chem Chem Phys* 6:4772–4780.
64. Siegbahn PEM (2013) Water oxidation mechanism in photosystem II, including oxidations, proton release pathways, O-O bond formation and O_2 release. *Biochim Biophys Acta* 1827(8-9):1003–1019.
65. Meyer TJ, Huynh MH, Thorp HH (2007) The possible role of proton-coupled electron transfer (PCET) in water oxidation by photosystem II. *Angew Chem Int Ed Engl* 46(28): 5284–5304.
66. Sproviero EM, Gascón JA, McEvoy JP, Brudvig GW, Batista VS (2008) A model of the oxygen-evolving center of photosystem II predicted by structural refinement based on EXAFS simulations. *J Am Chem Soc* 130(21):6728–6730.
67. Hull JF, et al. (2009) Highly active and robust Cp* iridium complexes for catalytic water oxidation. *J Am Chem Soc* 131(25):8730–8731.
68. Weinberg DR, et al. (2012) Proton-coupled electron transfer. *Chem Rev* 112(7): 4016–4093.
69. Lundberg M, Blomberg MRA, Siegbahn PEM (2004) Oxyl radical required for o-o bond formation in synthetic Mn-catalyst. *Inorg Chem* 43(1):264–274.

ENERGY RESOURCES

10.1126/sciadv.1501425

Room temperature stable CO_x-free H_2 production from methanol with magnesium oxide nanophotocatalysts

Zhengqing Liu,[1]* Zongyou Yin,[2,3]*† Casandra Cox,[3] Michel Bosman,[4] Xiaofeng Qian,[2] Na Li,[1] Hongyang Zhao,[1] Yaping Du,[1]† Ju Li,[1,2]† Daniel G. Nocera[3]†

Methanol, which contains 12.6 weight percent hydrogen, is a good hydrogen storage medium because it is a liquid at room temperature. However, by releasing the hydrogen, undesirable CO and/or CO_2 byproducts are formed during catalytic fuel reforming. We show that alkaline earth metal oxides, in our case MgO nanocrystals, exhibit stable photocatalytic activity for CO/CO_2-free H_2 production from liquid methanol at room temperature. The performance of MgO nanocrystals toward methanol dehydrogenation increases with time and approaches ~320 μmol g^{-1} $hour^{-1}$ after a 2-day photocatalytic reaction. The CO_x-free H_2 production is attributed to methanol photodecomposition to formaldehyde, photocatalyzed by surface electronic states of unique monodispersed, porous MgO nanocrystals, which were synthesized with a novel facile colloidal chemical strategy. An oxygen plasma treatment allows for the removal of organic surfactants, producing MgO nanocrystals that are well dispersible in methanol.

INTRODUCTION

Because of the high mobility of protons, hydrogen can be efficiently converted into electricity by using low-temperature proton exchange membrane fuel cells. However, it is not easy to store and transport pure hydrogen. A liquid methanol–formaldehyde cycle could be useful for storing hydrogen (*1*)

$$CH_3OH \rightleftharpoons H_2(g) + CH_2O \qquad (1)$$

Methanol (CH_3OH) has a boiling point of 64.7°C and is a liquid under ambient conditions. Formaldehyde (CH_2O) has a boiling point of −19.3°C, so only moderate pressure (~5 atm) is needed to liquefy it; furthermore, it exhibits 37 weight percent solubility in liquid water. Reaction (1) in a closed loop releases no carbon into the atmosphere (*2*, *3*). The difficulty in reaction (1) lies in efficient methanol dehydrogenation to produce H_2 at the site of end use (as opposed to hydrogenation, which can be accomplished centrally), and so far, this has been far from economical. The reported dehydrogenation catalysts to producing hydrogen from methanol mainly include aqueous methanol reforming and pure methanol decomposition. Aqueous methanol reforming, with H_2O added for the water-gas (CO) shift reaction, normally requires high temperatures (≥200°C) and pressures (≥25 bar) (*4*, *5*), or mild temperatures (<100°C) but the use of ruthenium complexes (*6*) or lower-stability metal-organic complexes (*7*). For pure methanol decomposition, thermal decomposition is achieved at high temperatures (≥160°C) with noble metals (Pt and Pd) (*8*–*12*), although photodecomposition has been reported at room temperature with Ti-β and noble metals (Pt, Rh, Ir, Pd, and Au) deposited on TiO_2 as photocatalysts. However, the photocatalytic reactions require methanol vapor, and a Pt-TiO_2 catalyst is plagued by low H_2 yields (<7 μmol H_2 g^{-1} $hour^{-1}$) and low stability (*13*–*15*).

Here, we show that magnesium oxide (MgO), a stable and cheap alkaline earth metal oxide that has been used as a photocatalyst for CO_2 reduction and organic contaminant degradation, an additive in refractory materials, and an adsorbent for air purification, toxic waste remediation, and biomedicine (*16*–*25*), is also an ultrastable photocatalyst for hydrogen production from methanol. We can mass produce monodispersed, porous MgO nanoparticles (NPs) with diameters ranging from 40 to 170 nm that demonstrate stable CO_x-free H_2 production from liquid methanol near room temperature.

Various wet chemical synthesis strategies have been developed to obtain MgO nanocrystals. Examples include sol-gel processes, hydrothermal/solvothermal methods, polyol-mediated thermolysis reactions, and microwave-assisted synthesis (*26*–*29*). However, most of the current routes initially yield hydroxide precursors, such as $Mg(OH)_2$ and $Mg_2(OH)_2CO_3$, which must be calcinated at high temperatures to produce crystalline MgO. These high-temperature processes are costly and usually result in fusion of NPs into aggregates (*30*–*33*). To date, only one study focused on the preparation and properties of nearly monodispersed MgO nanocrystals using an organometallic decomposition method (*34*). However, the raw materials used in this approach are toxic and expensive. To the best of our knowledge, until now, a facile, environmentally friendly, and inexpensive synthetic route to mass produce well-defined, porous MgO nanocrystals still remains a challenge, and a systematic study on the synthesis and properties of monodispersed, porous MgO nanocrystals has yet to be performed.

Here, we demonstrate an inexpensive and green approach to synthesizing monodispersed, porous monocrystalline MgO NPs (Scheme 1) using magnesium acetylacetonate dihydrate [$Mg(acac)_2 \cdot 2H_2O$]. The size of the porous MgO nanocrystals can be tuned from ~40 to 170 nm, all showing ultraviolet (UV) to blue emissions under UV light excitation

---

[1] Frontier Institute of Science and Technology jointly with College of Science, State Key Laboratory for Mechanical Behavior of Materials, Xi'an Jiaotong University, Xi'an 710049, China. [2] Department of Nuclear Science and Engineering, and Materials Science and Engineering, Massachusetts Institute of Technology, Cambridge, MA 02139, USA. [3] Department of Chemistry and Chemical Biology, Harvard University, 12 Oxford Street, Cambridge, MA 02138, USA. [4] Institute of Materials Research and Engineering, A*STAR (Agency for Science, Technology and Research), 2 Fusionopolis Way, Singapore 138634, Singapore.
*These authors contributed equally to this work.
†Corresponding author. Email: ypdu2013@mail.xjtu.edu.cn (Y.D.); zyyin@mit.edu (Z.Y.); liju@mit.edu (J.L.); dnocera@fas.harvard.edu (D.G.N.)

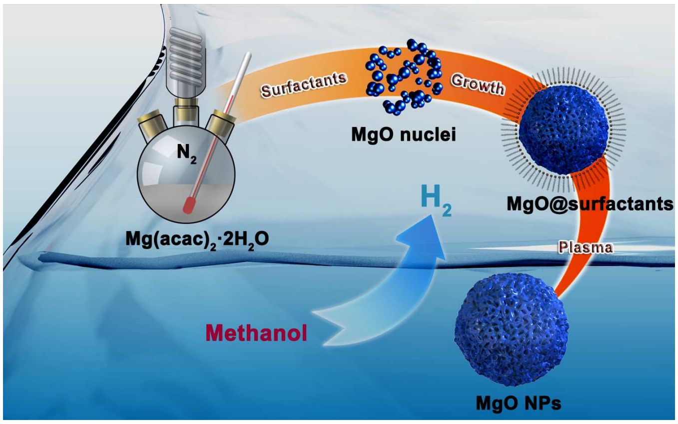

Sheme 1. Process of synthesis of MgO NPs and activity in H_2 production from methanol photodecomposition.

that indicates high density of mid-gap surface electronic states. After oxygen plasma treatment, we modified the surfaces of as-obtained MgO NPs, improving their surface purity and hydrophilicity. The superior activity in CO_x-free H_2 production from MgO NPs was associated with the local photoexcitation and charge separation among MgO defect energy levels, where excited holes oxidize methanol to generate protons that subsequently get reduced by hot electrons to produce H_2.

RESULTS

Synthesis and characterization of monodispersed porous MgO nanocrystals

The synthesized MgO NPs have an exclusively face-centered cubic phase [periclase type, space group: *Fm*3*m*, JCPDS (Joint Committee on Powder Diffraction Standards): 45-0946], as confirmed by powder x-ray diffraction (XRD) analysis (Fig. 1A) for various-sized MgO NPs, with the calculated crystal parameters $a = b = c = 4.211$ Å. No diffraction peaks from other chemical species, such as $Mg(OH)_2$ or $MgCO_3$, are detectable in all the samples. The average particle sizes of MgO NPs determined by XRD using the Debye-Scherrer equation to the (200) reflection were around 40, 85, 115, and 170 nm, respectively. Sharpening of the diffraction peaks indicates the increased crystallinity of MgO NPs with increasing size.

Figure 1B shows a transmission electron microscopy (TEM) image of as-synthesized MgO nanocrystals; the MgO NPs are relatively monodispersed with an average size of ~85 nm (inset for a histogram of particle diameters). This suggests retention of capping ligands on the nanocrystal surfaces, as validated by Fourier transform infrared (FTIR) spectroscopy (fig. S1). The scanning electron microscopy (SEM; fig. S2A) image shows that the MgO NPs are spherically shaped. Energy-dispersive x-ray (EDX) spectroscopy (fig. S2B) confirms that stoichiometric MgO is formed with an atomic ratio of Mg/O = 1:1.

The size of the MgO NPs was readily controlled by varying the reaction temperature and time. For instance, with 2 mmol of $Mg(acac)_2·2H_2O$ as the precursor in oleylamine/oleic acid/1-octadecene (OM/OA/ODE) = 4:1:5 (molar ratio), a reaction time of 30 min at 265°, 280°, 300°, or 320°C produced MgO NPs with an average diameter of ~40 nm (Fig. 1C), ~85 nm (Fig. 1D), ~115 nm (Fig. 1E), or ~170 nm (Fig. 1F), respectively, which is well consistent with the XRD analysis (Fig. 1A). Moreover, as indicated by the TEM images in Fig. 1, the as-obtained MgO NPs gradually became smooth as the reaction temperature was elevated. Under a fixed reaction temperature of 265°C, the thermolysis of 2 mmol of $Mg(acac)_2·2H_2O$ in OM/OA/ODE = 4:1:5 (molar ratio) for 60 min produces MgO NPs with a size of ~60 nm (fig. S3A). When the reaction temperature was raised to 280°C with all other conditions unchanged, the size of MgO NPs increased to ~100 nm (fig. S3B). Our results show that the size of the as-obtained MgO NPs did not significantly change with the reaction time (30 to 60 min) and when the temperature was kept constant at 300° or 320°C (Fig. 1E versus fig. S3C and Fig. 1F versus fig. S3D). This suggests a temperature-driven "size-focusing" process with increasing reaction temperature (*35*).

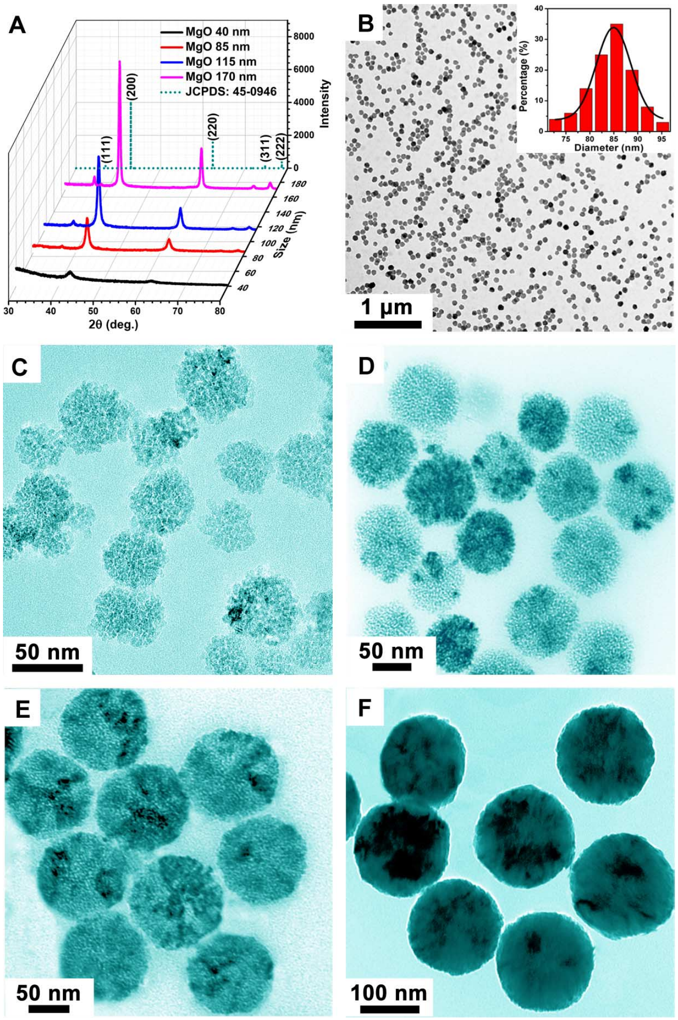

Fig. 1. Composition and morphology characterization of MgO NPs. (**A**) XRD pattern of various-sized MgO NPs. (**B**) TEM image of 85-nm-sized porous MgO NPs, with a plane size distribution analysis (inset). (**C** to **F**) Temperature effect on NP size. TEM images of MgO NPs with different sizes obtained from the thermolysis of 2 mmol of $Mg(acac)_2·2H_2O$ in OM/OA/ODE = 4:1:5 (molar ratio) at different temperatures for the same reaction time of 30 min: 265°C (C), 280°C (D), 300°C (E), and 320°C (F). From the TEM images, the average sizes of MgO NPs can be estimated to be ~40 nm (C), ~85 nm (D), ~115 nm (E), and ~170 nm (F), respectively.

The crystal structure of the individual MgO NPs was determined with high-resolution TEM (HRTEM) imaging and selected-area electron diffraction (SAED), as shown in Fig. 2. Figure 2A represents a typical TEM image for a single MgO NP; an amorphous surface layer can be clearly observed at the edge of the MgO NPs (inset of Fig. 2A). This amorphous surface layer may result from the applied capping ligands (OM and OA), which is consistent with the FTIR spectroscopy (fig. S1). The enlarged TEM image in the inset of Fig. 2A and the high-angle annular dark-field scanning TEM (HAADF-STEM) image in Fig. 2B demonstrate the local variation in density due to the porous nature of the MgO NPs. As seen in Fig. 2C, the HRTEM images taken from Fig. 2A show clear rock salt crystal lattice along the [100]. The observed interplanar distances between the lattice fringes are 0.21 and 0.15 nm, corresponding to the (200) and (220) planes of MgO, respectively. The SAED pattern acquired on a single MgO NP displays a single set of clear diffraction spots (Fig. 2D), confirming the monocrystalline nature of the porous MgO NPs (*36*).

In the present synthesis, the combination of different capping ligands was found to play a key role in obtaining monodispersed porous MgO nanocrystals. For example, aggregated MgO NPs (fig. S4A) were produced when 2 mmol of $Mg(acac)_2{\cdot}2H_2O$ was used as a precursor for a reaction at 280°C for 30 min, with the sole use of OM as the capping ligand and ODE as the solvent. In pure OA and ODE, almost no solid matter appeared after the precipitation treatment. In addition, we found that different ratios of solvents had great influence on the dispersibility of the porous MgO nanocrystals (fig. S4, B to D). High yields of monodispersed porous MgO nanocrystals were only obtained at an optimized OM/OA/ODE ratio of 4:1:5 (Fig. 1B) because of a well-maintained balance between nucleation and growth during synthesis.

Through manipulation of capping ligands, solvents, and their relative ratios, we have successfully synthesized size-controlled monodispersed porous MgO NPs. One unique characteristic of MgO is its chemical stability, which is essential for long-term performance under strong illumination. To remove surface capping ligands, we used an oxygen plasma treatment on dried MgO powders. As an example, fig. S1 shows a comparison between the FTIR spectrum of the 85-nm MgO NPs before (black) and after (red) treatment. The oxygen plasma treatment thus efficiently modifies the nanomaterial surface by removing the organic capping ligands.

Figure 3 shows the room temperature UV-vis (visible) absorption and photoluminescence (PL) spectra for MgO NPs. Figure 3A shows the UV-vis absorption spectra for MgO NPs of different sizes. All of the colloidal MgO NPs exhibited continuous absorption across the UV wavelength range, with two broad absorption peaks centered around 220 nm (5.6 eV) and 270 nm (4.6 eV). These peaks arise from the excitation of O^{2-} surface anions on the edge (fourfold coordinated) and on the corner (threefold coordinated) of the nanocrystal (*37*, *38*), respectively. Although MgO is a wide–band gap insulator (E_g = 7.8 eV) (*39*, *40*), optical transitions in the visible range were observed for our porous MgO NPs. Figure 3B shows PL spectra of MgO NPs at an excitation wavelength of 270 nm. The broad spectra covering from 300 to 450 nm indicate the presence of structural defects, such as oxygen vacancies (*41*–*43*), in the insulating MgO. All of the various sizes of the MgO NPs exhibited a strong visible blue emission if under 365-nm UV irradiation (fig. S5).

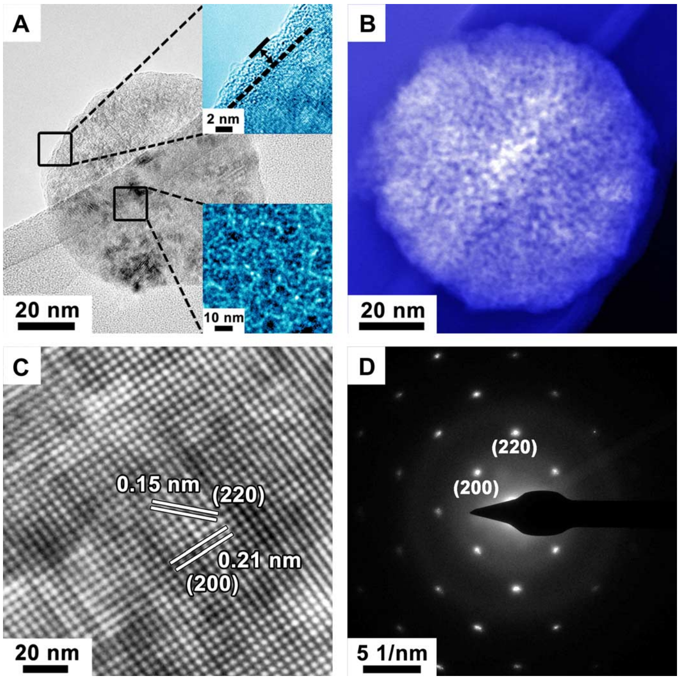

Fig. 2. Crystal structure analysis of MgO NP. (**A** and **B**) TEM (A) and HAADF-STEM (B) image of a single porous MgO NP with a diameter of ~85 nm. Inset of (A): Enlarged TEM images for the edge and center of the MgO NPs. (**C** and **D**) HRTEM image (C) and the corresponding SAED pattern (D) recorded from (A).

Stable H_2 production from liquid-methanol photodecomposition near room temperature

The photocatalytic activity for hydrogen production from high-purity liquid methanol at room temperature was examined for the MgO NPs (see Materials and Methods for details). The excitation wavelength dependence was studied by using various long-pass filters. As shown in Fig. 4A, there is no H_2 production when 530- or 380-nm long-pass filters are used. However, full-wavelength illumination (200 to 2500 nm) resulted in the production of H_2. This result is consistent with photoactivity arising from 220- and 270-nm excitation of the MgO nanocrystals (Fig. 3A). Hydrogen production was sensitive to MgO concentration in methanol. Figure 4B shows that suspensions of

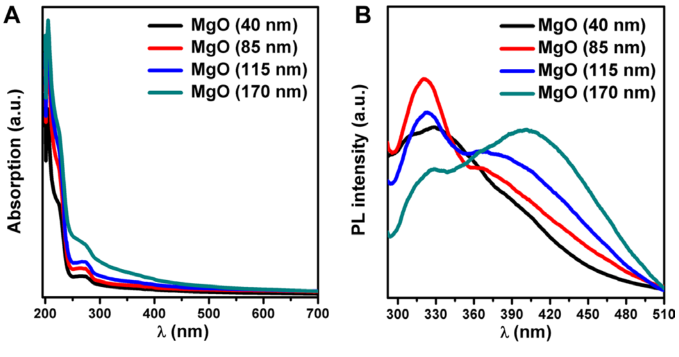

Fig. 3. Optical properties of MgO nanocrystals. (**A** and **B**) Room temperature UV-vis absorption (A) and PL (λ_{ex} = 270 nm) spectra (B) of differently sized porous MgO NPs. a.u., arbitrary units.

~0.38 mg ml^{-1} exhibit the best performance. Lower concentrations likely dilute the concentration of intermediate products, radicals, and/or protons because of the lower availability of surface active sites or photoexcited charges from MgO, resulting in a lower performance. On the other hand, high concentrations can cause light blocking/screening between the adjoining MgO nanocrystals, thus lowering light-harvesting efficiency. This is further supported by the fact that MgO's absorbance of light rises much slower compared with its concentration increase (fig. S6A).

The H_2 production yields for various sizes of MgO nanocrystals are presented in fig. S6. Among the different sizes, the highest H_2 production rates (~55 μmol g^{-1} $hour^{-1}$) occur from 85-nm MgO NPs. The higher surface area of the smaller-sized MgO nanocrystals (85 nm), as compared to the larger-sized MgO nanocrystals (115 and 170 nm), leads to an enhanced photocatalytic reaction with methanol. The surface area was verified using the Brunauer-Emmett-Teller (BET) method: the 40-, 85-, 115-, and 170-nm-sized MgO NPs have surface areas of 28.5, 19.7, 17.4, and 13.9 m^2 g^{-1}, respectively (fig. S7).

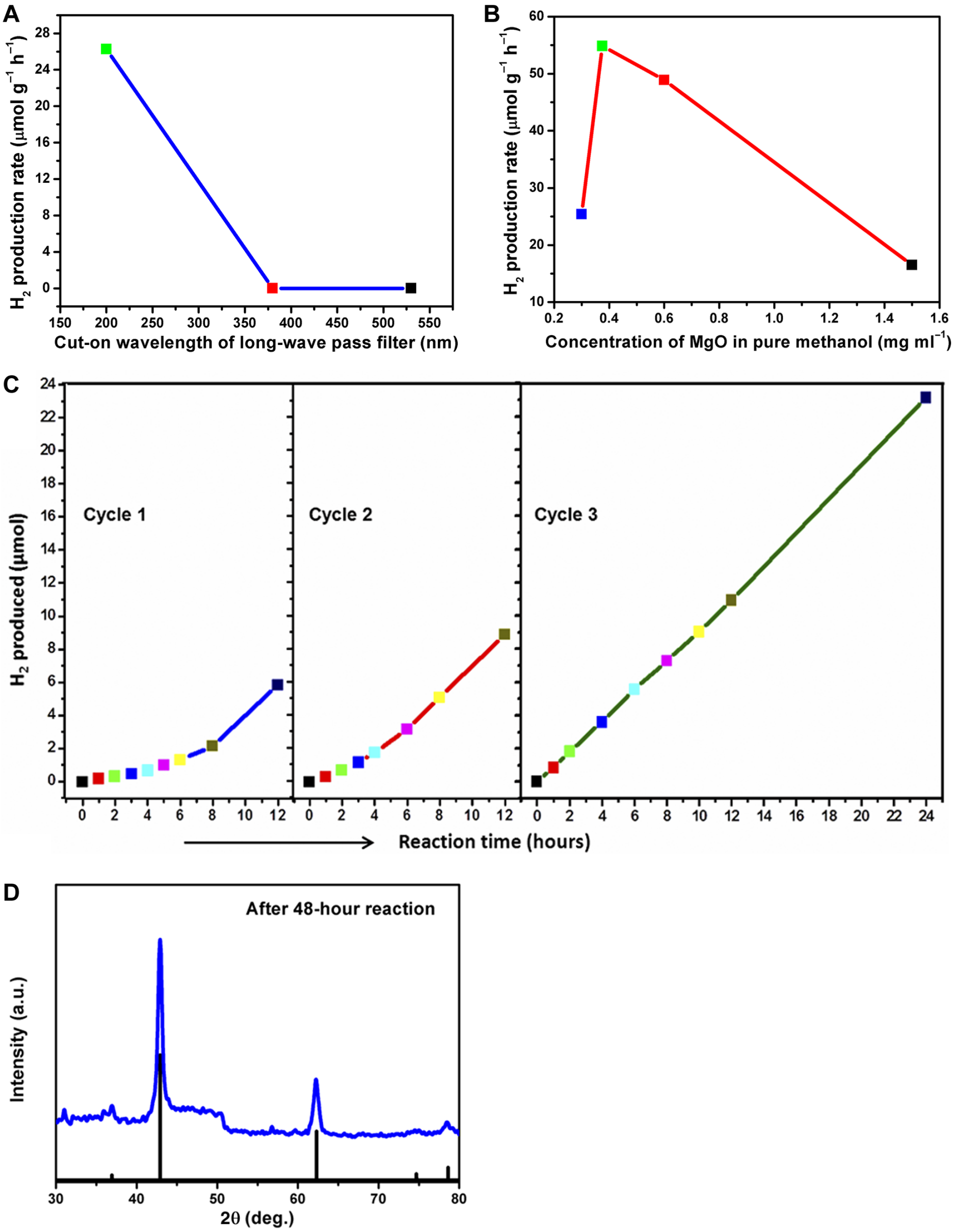

Fig. 4. H_2 production from methanol photodecomposition based on ~85-nm MgO nanocrystals. (**A**) Illumination wavelength effect using the long-wave pass filters with different cut-on wavelengths. (**B**) MgO concentration effect with constant 3 mg of MgO powder dispersed in different volumes of methanol. (**C**) Performance endurance of H_2 production by continuing to use the same MgO (3 mg)/methanol (8 ml) reaction materials for the whole three-cycle testing. (**D**) XRD pattern for MgO after a total 48-hour photocatalytic reaction.

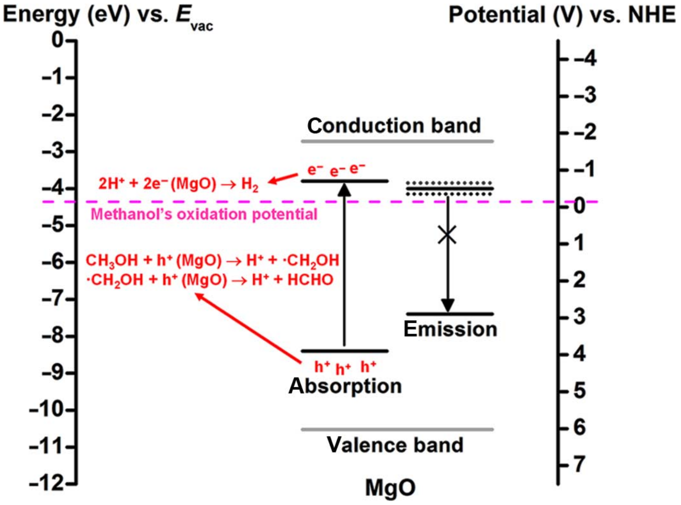

Fig. 5. Schematic diagram of proposed hydrogen production mechanism for MgO nanocrystals. On the basis of the UPS results (fig. S11), the valence band maximum for MgO, that is, E_v, is ~−10.5 eV relative to vacuum. Combined with the 7.8-eV band gap of MgO, we infer a conduction band minimum, E_c, of −2.7 with respect to the vacuum energy level ($E_{vac} = 0$). The energy levels of the absorption at 4.6 eV arise from surface excitons, as described in the main text. The energy levels of the emission in MgO are derived from the PL spectrum of 85-nm-sized MgO in Fig. 3B, that is, an emission peak at 330 nm with a broad shoulder at around 400 nm. NHE, normal hydrogen electrode.

The smallest-sized MgO nanocrystals (40 nm), with the largest BET surface area, did not yield the highest H_2 production rate per weight. This is most likely the result of the lower crystal quality of 40-nm-sized MgO nanocrystals (fig. S8) as compared to the 85-nm-sized MgO nanocrystals (Fig. 2D). The production of H_2 from pure MgO nanocrystals indicates that photoexcited electrons and holes in the surface defect energy levels of MgO can be harvested to oxidize methanol and reduce the generated protons (H^+) for H_2 production. At the same time, this result demonstrates that an oxygen plasma treatment is an effective method to remove the organic surfactants from nanomaterials synthesized via this oil phase strategy. After oxygen plasma treatment, MgO crystals have hydrophilic surfaces and become dispersible in polar liquids, such as methanol and water. This method enhances the direct contact between the MgO nanocrystal surface and methanol, enabling a more efficient photoreaction.

The H_2 production from MgO NPs is stable, and the rate actually improves with time (Fig. 4C and fig. S9). This is in contrast to many H_2 production systems, which often deteriorate in performance over time (*5*, *7*, *15*, *44*, *45*). To test MgO's performance stability, we monitored product analysis of the same MgO/methanol system under photocatalytic reaction over the course of 2 days. To avoid undesirable gas leakage from the capped septum of a reactor during periodic syringe removal of products from the cell, the reaction system was interrupted and then vented in fume hood between testing cycles. During the first cycle, the produced H_2 rises steadily, increasing with time. After the interruption following cycle 1, the production of H_2 continues and its rate increases with time in cycle 2. Hydrogen production continues in cycle 3, although to a lesser extent in rate increase. Notably, the rate reaches ~320 μmol g^{-1} $hour^{-1}$ at the end of a 2-day photocatalytic reaction. The local temperature induced by the lamp illumination around the photoreactor was observed to vary from 25° to 37°C over the 2-day reaction period. Note here that the temperature does not rise with illumination time strictly linearly: the temperature is relatively high, ~37°C, around noon and does not surpass 33°C during other times. The temperature therefore did not affect the performance, and the rising performance during the first 24-hour reaction (Fig. 4C and fig. S9) occurred as the surface sites on MgO NPs were gradually activated while the reaction was ongoing. On the basis of our experimental results, MgO nanocrystals are extremely stable under operating conditions for H_2 production near room temperature. This is attributed not only to the large band gap and high chemical stability of MgO (the heat of formation is 601.24 kJ mol^{-1} of oxygen, in contrast to 469.36 kJ mol^{-1} of oxygen for TiO_2) but also to photocatalytic surface states. To our knowledge, this work is the first to demonstrate catalytic methanol photodecomposition using the surface states of a dielectric oxide nanomaterial synthesized with a low-cost, high-throughput, green process.

Insight into H_2 production from MgO/methanol

Figure 5 proposes a mechanism for the H_2 production of MgO in methanol (*46*, *47*). In this figure, the black dotted lines close to the central solid line represent the broad emission feature of MgO. For comparison, the energy scale versus E_{vac} is scaled to the redox potential versus the normal hydrogen electrode (*46*, *47*). The oxidation potential for methanol, ~−4.3 eV versus E_{vac} at pH 7, is indicated by the dashed pink line. Absolute energy levels for emission and absorption are set on the basis of the fact that MgO NPs have photocatalytic activity in H_2 production. This requires that the oxidation potential of methanol lies between the energy levels of excitonic electrons and holes in the absorption region of MgO. Surface-bound electron-hole pairs from threefold/low-coordinate surface sites of MgO NPs are ionized after absorption of UV light mainly at 220 nm (5.6 eV) and 270 nm (4.6 eV) (see Fig. 3A) (*37*, *38*, *43*). For simplicity, only the energy levels in the absorption region relating to the 270-nm peak are illustrated in Fig. 5. The energy level of the photogenerated holes of MgO is over −8 eV, negative to the oxidation potential of methanol at ~−4.3 eV versus the vacuum energy level E_{vac} at pH 7 (*48*). This enables photogenerated holes to oxidize CH_3OH and generate intermediate hydroxyalkyl radical, $\cdot CH_2OH$. These dynamically unstable radicals are easily oxidized to formaldehyde (CH_2O) (*3*, *49*). During the two-step oxidation, two protons are generated and reduced to H_2 from the electrons residing in surface states of MgO. This H_2 production behavior is closely correlated with the unique structure of our synthesized MgO nanocrystals. As shown in fig. S10, we compared time-dependent H_2 production between MgO in this work, commercial MgO, commercial SiO_2, and commercial TiO_2 (P25) NPs. The sizes of commercial MgO, SiO_2, and TiO_2 are about 80 to 100 nm, 30 to 60 nm, and 20 to 40 nm, respectively. Before H_2 production, all samples are treated with the same O_2 plasma. With the continuous light illumination time for 24 hours, H_2 produced from commercial SiO_2 is only 0.4 μmol, and that from commercial MgO reaches 1.1 μmol. However, MgO in this work can reach 2.4 μmol, which is 2.2 and 6.0 times of that from commercial MgO and SiO_2, respectively. Compared with SiO_2 and MgO, commercial TiO_2 (P25) produced H_2 more efficiently at first but slowed down after 12-hour reaction and was surpassed by MgO in this work after 16 hours. This indicates an unendurable performance from commercial TiO_2 (P25). The low performance of commercial SiO_2 implies that O_2 plasma treatment itself does not make a notable contribution to H_2 production in this work; O_2 plasma treatment is mainly used to make MgO nanocrystals hydrophilic. The obviously more H_2 produced from the MgO in this work, as compared with commercial MgO, demonstrates that the unique structure with low-coordinate surface sites of our MgO directly contributes to efficient H_2 production from methanol under photocatalytic reaction.

Aqueous methanol reforming, one of the methanol dehydrogenation reactions, produces carbon dioxide (CO_2) via the water-gas shift reaction. Conversely, complete decomposition of methanol generates carbon monoxide (CO) and H_2 (*5*). In our MgO/methanol reaction system, neither CO_2 (fig. S11, A and C) nor CO (fig. S12, A and B) was observed in the products. On the basis of this observation, the two main products from MgO/methanol after photodecomposition are H_2, as observed from the chromatogram of fig. S11A, and CH_2O. This indicates that methanol, catalyzed by MgO, is not completely photodecomposed. Although this partial decomposition of methanol is not ideal in terms of H_2 production capacity, the CH_2O product is a convenient liquid in a closed loop (under ~5-atm pressure), as opposed to CO_2 or CO gases. Note here that there is a trace of unknown gaseous component (fig. S11A), which is attributed to the impurities in methanol because this component is also produced after illumination of pure methanol (fig. S11B). Additionally, negligible amounts of oxygen are also present because of the manual injection of gas into the gas chromatograph. Furthermore, to check whether methanol itself produces H_2 under UV light illumination (*50*), H_2 production was monitored from 8 ml of methanol in the absence of the MgO photocatalyst. As shown in fig. S5B, the amount of H_2 produced is only ~0.1 μmol after 10-hour reaction, which is only 2.5% of that (~4 μmol) produced from the MgO/methanol (3 mg of MgO dispersed in 8 ml of methanol). The negligible H_2 produced from pure methanol starts to saturate after a 9-hour reaction (fig. S6B), which implies that the hydrogen is probably produced from the impurities in methanol that eventually decomposed to the inactive species. This saturation in H_2 production is in contrast to the increasing H_2 production for MgO/methanol (Fig. 4C and fig. S9). MgO not only exhibited stable performance; its crystal structure was well maintained after the 48-hour photocatalytic reaction. This is confirmed by the XRD taken after 48 hours of operation, which is still well matched to the standard pattern of JCPDS: 45-0946, as shown in Fig. 4D.

DISCUSSION

Here, we demonstrate to have successfully synthesized porous, monocrystalline MgO NPs via a green and cheap thermolysis process with high yields. The diameter of the MgO nanocrystals can be well controlled from 40 to 170 nm, and these nanocrystals exhibit intense defect-induced blue luminescence under UV excitation. To widen the application of MgO synthesized via an oil phase solution process, we successfully used an oxygen plasma treatment to remove the capping ligands and increase hydrophilicity and dispersion in polar liquids, such as methanol and water. The resulting MgO NPs are photocatalysts for liquid-methanol photodecomposition, resulting in fast CO_x-free H_2 production. The ultrastable catalytic activity for CO_x-free H_2 production demonstrated herein points to new paths to develop environmentally friendly and scalable photocatalysts.

MATERIALS AND METHODS

Chemicals

Magnesium 2,4-pentanedionate hydrate [$Mg(acac)_2{\cdot}2H_2O$, >98%, Alfa Aesar], OM (70%, Sigma-Aldrich), OA (90%, Sigma-Aldrich), ODE (>90%, Sigma-Aldrich), ethanol [analytical reagent (AR)], acetone (AR), glycerin (AR), and cyclohexane (AR) were used as received without further purification.

Synthesis of porous MgO NPs

The synthesis of the 85-nm-sized porous MgO NPs was used as an example. A slurry containing 2 mmol (0.445 g) of $Mg(acac)_2{\cdot}2H_2O$, 16 mmol (4.288 g) of OM, 4 mmol (1.128 g) of OA, and 20 mmol (5.05 g) of ODE in a three-necked flask (100 ml) was heated to 140°C to remove water and oxygen, thus forming a homogeneous light yellow solution. The resulting mixture was heated to 280°C under N_2 and kept at that temperature for 30 min. Upon cooling to room temperature, the nanocrystals were precipitated by adding an excess of ethanol and glycerin (volume ratio of 4:1) and separated from the solution by centrifugation (10,000 rpm, 10 min), followed by drying in an oven at 60°C. The glycerin was used to remove impurities, such as NaCl. The as-prepared dried nanocrystals could be dispersed in various nonpolar organic solvents, such as cyclohexane and toluene. The average yield of nanocrystals was around 55%.

Characterization

TEM images were acquired with a Hitachi HT7700 transmission electron microscope operated at 100 kV. HRTEM micrographs and STEM images were obtained with a Philips Tecnai F20 FEG (field emission gun)–TEM operated at 200 kV. SEM images were characterized through a Quanta F250. Samples for TEM analysis were prepared by drying a drop of cyclohexane solution containing the nanocrystals on the surface of a carbon-coated copper grid. The XRD patterns were obtained using Rigaku D/MAX-RB with monochromatized Cu Kα radiation (λ = 1.5418 Å) and 2θ ranging from 20° to 80°C. Infrared spectra were recorded on a Nicolet 6700 FT-IR spectrometer. UV-vis absorption spectra were measured on a PerkinElmer Lambda 35 UV-vis spectrophotometer. PL spectra were recorded on a Hitachi F-4600 spectrofluorophotometer at room temperature. Nitrogen adsorption-desorption isotherms were measured on a Micromeritics TriStar 3000 porosimeter (mesoporous characterization) and Micromeritics ASAP 2020 (microporous characterization) at 77 K. All MgO NPs samples were outgassed at 160°C for 6 hours under vacuum before measurements. The specific surface areas were calculated on the basis of the BET method. Ultraviolet photoelectron spectroscopy (UPS) measurements were carried out with a Shimadzu/Kratos AXIS Ultra DLD spectrometer, using the HeI radiation (21.21 eV) from a He discharge lamp. Peaks were recorded with a constant energy of 5 eV and a step size of 0.05 eV. The pressure in the analysis chamber was maintained at 4.3×10^{-9} torr.

Measurement of H_2 production

Here, four kinds of materials/powders were tested for the photocatalytic hydrogen production, including MgO nanocrystals with sizes of 40, 85, 115, and 170 nm. Note here that, before the photocatalytic experiments, all the MgO powders were treated with the same oxygen plasma for 1 hour to generate hydrophilic surfaces by removing the hydrophobic organic ligands. The photocatalytic hydrogen production experiments were performed in a ~16-ml quartz flask under atmospheric pressure at room temperature. For hydrogen production testing, 3 mg of MgO powder was dispersed in pure methanol (anhydrous, 99.8% from Sigma-Aldrich) with its volume varied from 2 to 10 ml, followed by sonication for ~45 min. Then, the quartz flask was sealed with silicone rubber septum, and then the reaction suspension in the flask was degassed with pure nitrogen gas for ~30 min to remove the air inside, keeping the reaction suspension in an inert environment. After degassing, the quartz flask with reaction suspension was transferred and placed before the light source. A 1000-W mercury lamp (MAX-1000, Newport Corporation) was used as a broadband light source covering the wavelength band between 200 and 2500 nm, to trigger the photocatalytic reaction. The light illumination intensity on the flask was ca. 388 mW cm^{-2}. The hydrogen was analyzed by gas chromatography (Agilent 7890A) with the installed gas valve system. During multiple-cycle performance endurance testing, the reaction material MgO/methanol in the reactor was sonicated for ~30 min, and then the whole reaction system was sealed for the subsequent ~30-min degassing to drive away air before the H_2 production testing.

SUPPLEMENTARY MATERIALS

Supplementary material for this article is available at http://advances.sciencemag.org/cgi/content/full/2/9/e1501425/DC1

fig. S1. FTIR analysis of synthesized and oxygen plasma–treated MgO NPs.
fig. S2. SEM image and EDX analysis of synthesized MgO NPs.
fig. S3. Temperature-dependent experiments of synthesized MgO NPs.
fig. S4. Solvent composition–dependent experiments of synthesized MgO NPs.
fig. S5. Digital photographs of different-sized MgO colloidal solution.
fig. S6. Optical properties for ~85-nm MgO nanocrystals and H_2 production from methanol photodecomposition.
fig. S7. Specific surface area of four different-sized MgO NPs.
fig. S8. TEM and SAED images of an MgO NP with a size of 40 nm.
fig. S9. The rate pattern of H_2 production for ~85-nm MgO nanocrystals.
fig. S10. SEM analysis and H_2 production of commercial MgO, SiO_2, and TiO_2 (P25).
fig. S11. Chromatogram analysis of a mixture of gases.
fig. S12. Chromatogram analysis of a mixture of gases.
fig. S13. UPS spectrum for ~85-nm-sized MgO NPs.

REFERENCES AND NOTES

1. G. A. Olah, A. Goeppert, G. K. Surya Prakash, *Beyond Oil and Gas: The Methanol Economy* (Wiley-VCH, Weinheim, ed. 2, 2009).
2. K.-i. Aika, H. Sekiya, A. Ozaki, Selectivities of group VIII metals for the hydrogenation of formaldehyde and the effect of support and promoter. *Chem. Lett.* **12**, 301–304 (1983).
3. R. Hirschl, A. Eichler, J. Hafner, Hydrogenation of ethylene and formaldehyde on Pt (111) and $Pt_{80}Fe_{20}$ (111): A density-functional study. *J. Catal.* **226**, 273–282 (2004).
4. J. W. Shabaker, R. R. Davda, G. W. Huber, R. D. Cortright, J. A. Dumesic, Aqueous phase reforming of methanol and ethylene glycol over alumina-supported platinum catalysts. *J. Catal.* **215**, 344–352 (2003).
5. D. R. Palo, R. A. Dagle, J. D. Holladay, Methanol steam reforming for hydrogen production. *Chem. Rev.* **107**, 3992–4021 (2007).
6. M. Nielsen, E. Alberico, W. Baumann, H.-J. Drexler, H. Junge, S. Gladiali, M. Beller, Low-temperature aqueous-phase methanol dehydrogenation to hydrogen and carbon dioxide. *Nature* **495**, 85–89 (2013).
7. E. Alberico, P. Sponholz, C. Cordes, M. Nielsen, H.-J. Drexler, W. Baumann, H. Junge, M. Beller, Selective hydrogen production from methanol with a defined iron pincer catalyst under mild conditions. *Angew. Chem. Int. Ed.* **52**, 14162–14166 (2013).
8. Y. Matsumura, M. Okumura, Y. Usami, K. Kagawa, H. Yamashita, M. Anpo, M. Haruta, Low-temperature decomposition of methanol to carbon monoxide and hydrogen with low activation energy over Pd/ZrO_2 catalyst. *Catal. Lett.* **44**, 189–191 (1997).
9. Y. Matsumura, K. Tanaka, N. Tode, T. Yazawa, M. Haruta, Catalytic methanol decomposition to carbon monoxide and hydrogen over nickel supported on silica. *J. Mol. Catal. A Chem.* **152**, 157–165 (2000).
10. W. J. Shen, Y. Matsumura, Low-temperature methanol decomposition to carbon monoxide and hydrogen catalysed over cationic palladium species in Pd/CeO_2. *Phys. Chem. Chem. Phys.* **2**, 1519–1522 (2000).
11. J. C. Brown, E. Gulari, Hydrogen production from methanol decomposition over Pt/Al_2O_3 and ceria promoted Pt/Al_2O_3 catalysts. *Catal. Commun.* **5**, 431–436 (2004).
12. W. Cui, L. Feng, C. Xu, S. Lü, F. Qiu, Hydrogen production by photocatalytic decomposition of methanol gas on Pt/TiO_2 nano-film. *Catal. Commun.* **5**, 533–536 (2004).
13. W. Cui, C. Xu, S. Zhang, L. Feng, S. Lü, F. Qiu, Hydrogen evolution by photocatalysis of methanol vapor over Ti-beta. *J. Photochem. Photobiol. A* **175**, 89–93 (2005).
14. G. Halasi, G. Schubert, F. Solymosi, Comparative study on the photocatalytic decomposition of methanol on TiO_2 modified by N and promoted by metals. *J. Catal.* **294**, 199–206 (2012).
15. A. Gazsi, G. Schubert, T. Bánsági, F. Solymosi, Photocatalytic decomposition of methanol and ethanol on Au supported by pure or N-doped TiO_2. *J. Photochem. Photobiol. A* **271**, 45–55 (2013).
16. C.-J. Jia, Y. Liu, H. Bongard, F. Schüth, Very low temperature CO oxidation over colloidally deposited gold nanoparticles on $Mg(OH)_2$ and MgO. *J. Am. Chem. Soc.* **132**, 1520–1522 (2010).
17. K. Teramura, T. Tanaka, H. Ishikawa, Y. Kohno, T. Funabiki, Photocatalytic reduction of CO_2 to CO in the presence of H_2 or CH_4 as a reductant over MgO. *J. Phys. Chem. B* **108**, 346–354 (2004).
18. S. Demirci, B. Öztürk, S. Yildirim, F. Bakal, M. Erol, O. Sancakoğlu, R. Yigit, E. Celik, T. Batar, Synthesis and comparison of the photocatalytic activities of flame spray pyrolysis and sol–gel derived magnesium oxide nano-scale particles. *Mater. Sci. Semicond. Process.* **34**, 154–161 (2015).
19. K. Mageshwari, S. S. Mali, R. Sathyamoorthy, P. S. Patil, Template-free synthesis of MgO nanoparticles for effective photocatalytic applications. *Powder Technol.* **249**, 456–462 (2013).
20. J. I. Di Cosimo, V. K. Díez, C. Ferretti, C. R. Apesteguía, Basic catalysis on MgO: Generation, characterization and catalytic properties of active sites. *Catalysis* **26**, 1–28 (2014).
21. H. Niu, Q. Yang, K. Tang, Y. Xie, Large-scale synthesis of single-crystalline MgO with bone-like nanostructures. *J. Nanopart. Res.* **8**, 881–888 (2006).
22. A. Khaleel, P. N. Kapoor, K. J. Klabunde, Nanocrystalline metal oxides as new adsorbents for air purification. *Nanostruct. Mater.* **11**, 459–468 (1999).
23. R. Richards, W. Li, S. Decker, C. Davidson, O. Koper, V. Zaikovski, A. Volodin, T. Rieker, K. J. Klabunde, Consolidation of metal oxide nanocrystals. Reactive pellets with controllable pore structure that represent a new family of porous, inorganic materials. *J. Am. Chem. Soc.* **122**, 4921–4925 (2000).
24. C. Feldmann, S. Matschulo, S. Ahlert, Polyol-mediated synthesis of nanoscale $Mg(OH)_2$ and MgO. *J. Mater. Sci.* **42**, 7076–7080 (2007).
25. L. Huang, D.-Q. Li, Y.-J. Lin, M. Wei, D. G. Evans, X. Duan, Controllable preparation of Nano-MgO and investigation of its bactericidal properties. *J. Inorg. Biochem.* **99**, 986–993 (2005).
26. S. Utamapanya, K. J. Klabunde, J. R. Schlup, Nanoscale metal oxide particles/clusters as chemical reagents. Synthesis and properties of ultrahigh surface area magnesium hydroxide and magnesium oxide. *Chem. Mater.* **3**, 175–181 (1991).
27. Y. Ding, G. Zhang, H. Wu, B. Hai, L. Wang, Y. Qian, Nanoscale magnesium hydroxide and magnesium oxide powders: Control over size, shape, and structure via hydrothermal synthesis. *Chem. Mater.* **13**, 435–440 (2001).
28. A. Subramania, G. V. Kumar, A. R. Sathiya Priya, T. Vasudevan, Polyol-mediated thermolysis process for the synthesis of MgO nanoparticles and nanowires. *Nanotechnology* **18**, 225601 (2007).
29. S. Makhluf, R. Dror, Y. Nitzan, Y. Abramovich, R. Jelinek, A. Gedanken, Microwave-assisted synthesis of nanocrystalline MgO and its use as a bacteriocide. *Adv. Funct. Mater.* **15**, 1708–1715 (2005).
30. K. Zhu, J. Hu, C. Kübel, R. Richards, Efficient preparation and catalytic activity of MgO (111) nanosheets. *Angew. Chem. Int. Ed.* **118**, 7435–7439 (2006).
31. O. B. Koper, I. Lagadic, A. Volodin, K. J. Klabunde, Alkaline-earth oxide nanoparticles obtained by aerogel methods. Characterization and rational for unexpectedly high surface chemical reactivities. *Chem. Mater.* **9**, 2468–2480 (1997).
32. P. P. Fedorov, E. A. Tkachenko, S. V. Kuznetsov, V. V. Voronov, S. V. Lavrishchev, Preparation of MgO nanoparticles. *Inorg. Mater.* **43**, 502–504 (2007).
33. C. Yan, D. Xue, Novel self-assembled MgO nanosheet and its precursors. *J. Phys. Chem. B* **109**, 12358–12361 (2005).
34. H. R. Moon, J. J. Urban, D. J. Milliron, Size-controlled synthesis and optical properties of monodisperse colloidal magnesium oxide nanocrystals. *Angew. Chem. Int. Ed.* **48**, 6278–6281 (2009).
35. X. Peng, J. Wickham, A. P. Alivisatos, Kinetics of II-VI and III-V colloidal semiconductor nanocrystal growth: "Focusing" of size distributions. *J. Am. Chem. Soc.* **120**, 5343–5344 (1998).
36. F. Wang, C. Li, L.-D. Sun, C.-H. Xu, J. Wang, J. C. Yu, C.-H. Yan, Porous single-crystalline palladium nanoparticles with high catalytic activities. *Angew. Chem. Int. Ed.* **51**, 4872–4876 (2012).

37. S. Stankic, M. Sterrer, P. Hofmann, J. Bernardi, O. Diwald, E. Knözinger, Novel optical surface properties of Ca^{2+}-doped MgO nanocrystals. *Nano Lett.* **5**, 1889–1893 (2005).
38. M. Sterrer, T. Berger, O. Diwald, E. Knözinger, Energy transfer on the MgO surface, monitored by UV-induced H_2 chemisorption. *J. Am. Chem. Soc.* **125**, 195–199 (2003).
39. R. C. Whited, W. C. Walker, Exciton spectra of CaO and MgO. *Phys. Rev. Lett.* **22**, 1428–1430 (1969).
40. M. Klaua, D. Ullmann, J. Barthel, W. Wulfhekel, J. Kirschner, R. Urban, T. L. Monchesky, A. Enders, J. F. Cochran, B. Heinrich, Growth, structure, electronic, and magnetic properties of MgO/Fe (001) bilayers and Fe/MgO/Fe (001) trilayers. *Phys. Rev. B* **64**, 134411 (2001).
41. G. H. Rosenblatt, M. W. Rowe, G. P. Williams Jr., R. T. Williams, Y. Chen, Luminescence of F and F^+ centers in magnesium oxide. *Phys. Rev. B* **39**, 10309–10318 (1989).
42. E. Feldbach, R. Jaaniso, M. Kodu, V. P. Denks, A. Kasikov, P. Liblik, A. Maaroos, H. Mändar, M. Kirm, Luminescence characterization of ultrathin MgO films of high crystallinity prepared by pulsed laser deposition. *J. Mater. Sci. Mater. Electron.* **20** (Suppl. 1), 321–325 (2009).
43. P. Rinke, A. Schleife, E. Kioupakis, A. Janotti, C. Rödl, F. Bechstedt, M. Scheffler, C. G. Van de Walle, First-principles optical spectra for *F* centers in MgO. *Phys. Rev. Lett.* **108**, 126404 (2012).
44. C. G. Silva, R. Juárez, T. Marino, R. Molinari, H. García, Influence of excitation wavelength (UV or Visible light) on the photocatalytic activity of titania containing gold nanoparticles for the generation of hydrogen or oxygen form water. *J. Am. Chem. Soc.* **133**, 595–602 (2011).
45. Y. Hou, A. B. Laursen, J. Zhang, G. Zhang, Y. Zhu, X. Wang, S. Dahl, I. Chorkendorff, Layered nanojunctions for hydrogen-evolution catalysis, *Angew. Chem. Int. Ed.* **52**, 3621–3625 (2013).
46. C. G. Zoski, *Handbook of Electrochemistry* (Elsevier, Amsterdam, 2007).
47. S. Linic, P. Christopher, D. B. Ingram, Plasmonic-metal nanostructures for efficient conversion of solar to chemical energy. *Nat. Mater.* **10**, 911–921 (2011).
48. M. J. Berr, P. Wagner, S. Fischbach, A. Vaneski, J. Schneider, A. S. Susha, A. L. Rogach, F. Jäckel, J. Feldmann, Hole scavenger redox potentials determine quantum efficiency and stability of Pt-decorated CdS nanorods for photocatalytic hydrogen generation. *Appl. Phys. Lett.* **100**, 223903 (2012).
49. A. A. Ismail, L. Robben, D. W. Bahnemann, Study of the efficiency of UV and visible-light photocatalytic oxidation of methanol on mesoporous RuO_2–TiO_2 nanocomposites. *Chemphyschem* **12**, 982–991 (2011).
50. K. I. Öberg, R. T. Garrod, E. F. van Dishoeck, H. Linnartz, Formation rates of complex organics in UV irradiated CH_3OH-rich ices. *Astron. Astrophys.* **504**, 891–913 (2009).

Acknowledgments

Funding: We gratefully acknowledge financial support from NSF DMR-1120901 (Massachusetts Institute of Technology), the start-up funding from Xi'an Jiaotong University, 973 Program of China (2012CB619402), the National Natural Science Foundation of China (grant no. 21371140), and China National Funds for Excellent Young Scientists (grant no. 21522106). D.G.N. acknowledges support from the U.S. Department of Energy, Office of Basic Energy Sciences (DE-SC0009565). **Author contributions:** Y.D., Z.Y., D.G.N., and J.L. proposed the whole research direction and guided the project. Y.D. and Z.L. designed and performed the series of synthesis and characterization experiments. Z.Y. and C.C. preformed the H_2 production test. All authors analyzed the experimental results and drafted the manuscript. **Competing interests:** The authors declare that they have no competing interests. **Data and materials availability:** All data needed to evaluate the conclusions in the paper are present in the paper and/or the Supplementary Materials. Additional data related to this paper may be requested from the authors.

Submitted 11 October 2015
Accepted 2 August 2016
Published 2 September 2016
10.1126/sciadv.1501425

Citation: Z. Liu, Z. Yin, C. Cox, M. Bosman, X. Qian, N. Li, H. Zhao, Y. Du, J. Li, D. G. Nocera, Room temperature stable CO_x-free H_2 production from methanol with magnesium oxide nanophotocatalysts. *Sci. Adv.* **2**, e1501425 (2016).

Top Curr Chem (2015)
DOI: 10.1007/128_2015_649

Catalytic Oxygen Evolution by Cobalt Oxido Thin Films

D. Kwabena Bediako, Andrew M. Ullman, and Daniel G. Nocera

Abstract The contemporary demand to generate fuels from solar energy has stimulated intense effort to develop water splitting catalysts that can be coupled to light-absorbing materials. Cobalt oxido catalyst (Co-OECs) films deposited from buffered Co^{II} solutions have emerged as arguably the most studied class of heterogeneous oxygen evolution catalysts. The interest in these materials stems from their formation by self-assembly, their self-healing properties, and their promising catalytic activity under a variety of conditions. The structure and function of these catalysts are reviewed here together with studies of molecular Co-O cluster compounds, which have proven invaluable in elucidating the chemistry of the Co-OECs.

Keywords Artificial leaf · Cluster compounds · Cobalt oxide · Electrocatalysis · Oxygen evolution reaction · Proton-coupled electron transfer · Self-assembly · Self-healing · Solar fuels · Water splitting

Contents

D.K. Bediako, A.M. Ullman, and D.G. Nocera (✉)
Department of Chemistry and Chemical Biology, Harvard University, 12 Oxford Street, Cambridge, MA, USA
e-mail: dnocera@fas.harvard.edu

1 Introduction

The way we power the planet is changing. Distributed energy generation and storage is now within scientific and technological reach and accordingly has the promise of supplanting traditional energy infrastructure. Centralized power plants are giving way to utility-scale wind and solar farms, and, in combination with smaller scale commercial and residential forms of renewable generation, a new energy ecosystem is evolving before our eyes. In Germany, the country's largest energy supplier, E.ON, announced in late 2014 that it plans to spin off the portion of the company centered around conventional fossil fuels to focus on the increasingly important renewable energy sector (http://www.eon.com/en/media/news/press-releases/2014/11/30/new-corporate-strategy-eon-to-focus-on-renewables-distribution-networks-and-customer-solutions-and-to-spin-off-the-majority-of-a-new-publicly-listed-company-specializing-in-power-generation-global-energy-trading-and-exploration-and-production.html). The impetus for this historic restructuring originates with the rise of marketable renewable technology innovations and the increased demand for individualized consumer products. There is an increasing desire for individuals to control their energy, and hence this has turned them to the Sun as their direct energy supply.

Standing at the crossroads of these drivers of change is energy storage. The intermittency of renewable energy (solar and wind) sources necessitates suitable storage. Flow and solid-state battery technologies maintain a dominant position in the energy storage marketplace [1]. However, marketable improvements in these technologies are sporadic, sprouting mainly from cost-saving measures in engineering and manufacturing. Moreover, truly outstanding improvements in these technologies are limited by the finite energy density of materials used at the battery anode and cathode [2].

Fuels possess the energy density needed for large scale global energy storage [2]. Of the various solar fuel cycles, water splitting is perhaps the most attractive chemical reaction for storing intermittent renewable energy because the source of fuel, water, is ubiquitous, and significant energy density may be achieved in the O–O and H–H bonds of oxygen and hydrogen, which greatly increases the maximum energy density [3]. The thermodynamic potential for this reaction is given in (3), and formal potentials for the constituent half-reactions are given in (1) and (2).

$$2H_2O \rightarrow O_2 + 4H^+ + 4e^-;\ E^o_{OER} = 1.23V - 0.059\ V \times pH, \tag{1}$$

$$4H^+ + 4e^- \rightarrow 2H_2;\ E^o_{HER} = 0V - 0.059\ V \times pH, \tag{2}$$

$$2H_2O \rightarrow O_2 + 2H_2;\ E^o = E^o_{HER} - E^o_{OER} = -1.23\ V. \tag{3}$$

This E° voltage defines the minimum amount of energy required to carry out the reaction, and the maximum amount of energy that can be stored and later recovered from the bonds of H_2 and O_2. Driving this reaction inevitably requires an additional voltage in excess of E°, which is termed the overpotential. Minimizing this overpotential is a critical parameter in maximizing the efficiency of a solar fuels device. Of the two half reactions (1) and (2), the four electron, four proton oxidation of water to dioxygen (i.e., the oxygen evolution reaction, OER) is the more kinetically challenging reaction, and therefore executing this reaction at any given rate typically demands a more substantial input of overpotential than the hydrogen evolution reaction, HER (2).

Existing methods used to split water commercially (mainly for the production of high purity H_2) involve the use of proton-exchange membrane (PEM) electrolyzers that operate in acidic electrolytes, alkaline electrolyzers that operate in strongly basic solution, and solid-oxide electrolyzers that operate at high temperatures of ~1,000°C [4]. In all cases, water splitting is performed under very harsh conditions, and as a result the overall balance of system cost is too high to allow these technologies to be economically viable renewable solar fuel generators [5, 6]. PEM electrolyzers incur additional costs associated with the precious metals that are required as electrodes. Moreover, extremely harsh conditions are invariably at odds with: materials stability if the catalyst is to be interfaced directly to light harvesting systems [7, 8], other processes such as CO_2 reduction (which is best performed at pH 7), the construction of inorganic/biological hybrid systems [9], and the use of distributed energy storage schemes where water is at a premium by allowing the use of "dirty" water [10, 11]. To this end, there are advantages in performing water splitting under more benign conditions, such as at intermediate (close to neutral) pH.

The focus of this review is the oxidic thin film catalysts of cobalt that we have found to be active OER catalysts at neutral and near-neutral pHs. This Co-based catalyst has been a springboard for the development of other oxidic catalysts based on Mn [12, 13] and Ni [14–16], as well as mixed-metal oxidic catalysts [17–34]. We discuss the preparation of Co-OEC and its structural interrogation using X-ray absorption spectroscopy and X-ray total scattering methods together with pair distribution function analysis. The kinetics of catalytic turnover and film growth, which form the basis for the inherent self-repair property of these catalysts, are also reviewed. We also discuss the advances in our understanding of this catalyst that have arisen from the investigation of molecular complexes.

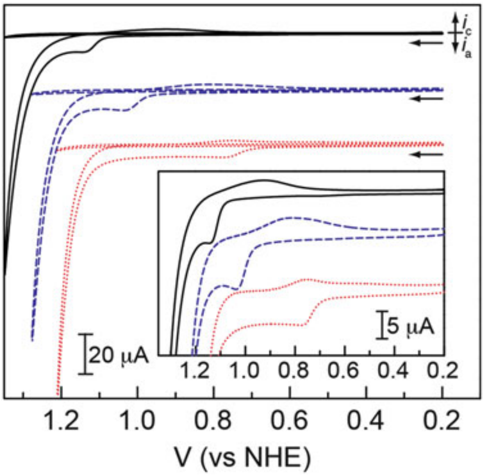

Fig. 1 Cyclic voltammograms using a glassy carbon working electrode, 50 mV/s scan rate, of aqueous 0.5 mM Co^{2+} in 0.1 M Pi electrolyte, pH 7.0 (*solid line*, *black*), 0.1 M MeP_i electrolyte, pH 8.0 (*dashed line*, *blue*), and 0.1 M Bi electrolyte, pH 9.2 (*dotted line*, *red*). Background traces in each electrolyte medium in the absence of Co^{2+} are overlaid. *Inset* shows CVs in the presence of Co^{2+} on an expanded current scale. Figure adapted from [37]

2 Self-Assembly of Co-OEC Thin-Films

A film that is catalytically active for water oxidation is formed on the surface of inert conducting electrodes upon anodic polarization at >1.0 V (vs NHE) in pH 7 phosphate (P_i)-buffered solutions containing sub-millimolar concentrations of simple Co^{2+} salts [35, 36]. Cyclic voltammograms (CVs) in buffered Co^{2+}-containing electrolytes at pH 7, 8 and 9.2 (Fig. 1) display sharp anodic waves that are well separated from a subsequent catalytic wave [35, 37], which is a result of oxygen evolution. A Faradaic efficiency of 100% indicates that OER occurs in the absence of side reactions. The initial anodic pre-feature (Fig. 1) reflects the primary process for catalyst formation; after catalyst deposition, subsequent CVs in Co-containing or Co-free electrolytes display broader waves that are representative of the redox changes within the electrodeposited film [35].

Film formation and O_2 evolution catalysis occur over a wide range of electrolyte types and pH conditions (Fig. 1). The presence of the electrolyte was observed to be crucial to film formation at low potentials as well as its long-term stability (Fig. 2). These materials stand in contrast to cobalt-based films that are formed in non-buffering electrolytes such as sulfate or nitrate, which require high metal salt concentrations and large voltages to drive deposition of films that are ultimately unstable in neutral pH electrolytes [38, 39]. Although we collectively term these oxygen-evolving catalyst films Co-OEC, they may be further distinguished as CoP_i, CoB_i, and $CoMeP_i$ depending on the electrolyte used during electrodeposition and catalysis.

Co-OEC films were shown to be permeable and conductive, because O_2 evolution activity scales with film thickness (Fig. 3) [40]. This result indicated early on that active sites are present and accessible throughout the entire thickness of the film, and not just at the outermost layer of the material. This property was exploited to prepare highly active anodes that achieved geometric current densities of 100 mA/cm^2 at an overpotential of 363 mV in pH 9.2 B_i electrolyte by extending all three dimensions of the catalyst film. Unlike commercial electrolyzer systems

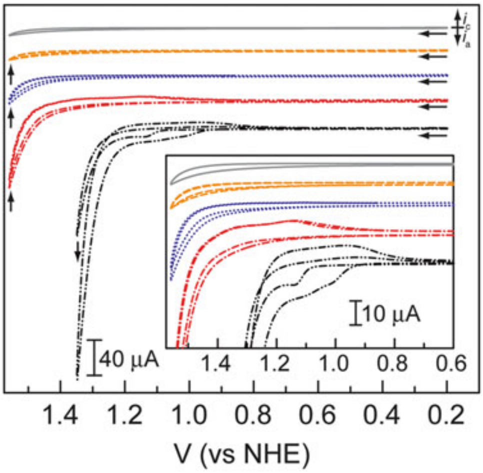

Fig. 2 Cyclic voltammogram using a glassy carbon working electrode, 50 mV/s scan rate, of 0.1 M K_2SO_4 electrolyte, pH 7.0, containing from top to bottom 0 (*solid line*), 0.5 (*dashed line*), 5 (*dotted line*), and 50 (*dot-dashed line*) mM Co^{2+}. CV traces of glassy carbon working electrode, 50 mV/s scan rate, of 0.5 mM Co^{2+} in P_i electrolyte, pH 7.0 (*dash-dotted line*) are shown for comparison. *Vertical arrows* indicate progression between the first and fifth scans taken without pause. *Inset* shows all CVs on an expanded current and potential scale. Figure adapted from [37]

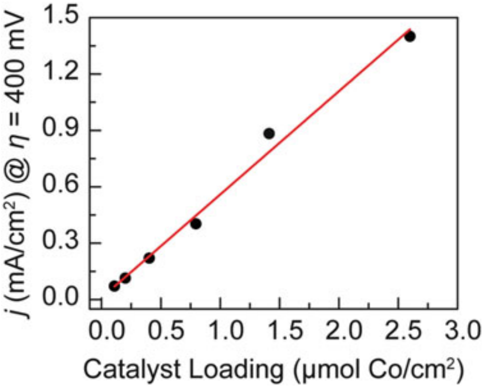

Fig. 3 CoB_i film activity (current density at 400 mV overpotential) vs catalyst loading for films deposited at 0.72 V vs Ag/AgCl in 0.1 M KB_i solution (pH 9.2). Figure adapted from [40]

that require water of high purity for sustained optimal operation, Co-OEC activities were found to be resistant to degradation in impure waters [40], making them potential targets for future cheap, distributed energy storage systems in impoverished regions. This resistance to degradation, along with the ease of preparation and good activity characteristics, prompted us to investigate the structural and mechanistic basis for Co-OEC formation and catalysis.

3 Co-OEC Structure and Valency

Insights into catalyst structure and valency are critical parameters for uncovering the mechanistic basis for catalyst activity. In particular, the construction of structure–activity relationships is a vital part of all catalyst development (homogeneous and heterogeneous), potentially revealing key insights that lead to the design of catalysts with enhanced activity. However, obtaining structural information on Co-OEC films has been impeded by their ostensibly amorphous nature within the resolution of conventional crystallographic methods [35] signifying minimal long-range structural order [41]. In this regard, they stand in contrast to the crystalline brucite, spinel, and perovskite Co compounds which have been the subject of the vast majority of heterogeneous OER mechanistic studies [42]. Although presenting challenges to structural characterization, the absence of long-range structural coherence in these films also means that they offer a unique platform for the study of water oxidation at hitherto underexplored structurally disordered heterogeneous OECs. In this section, we discuss X-ray absorption spectroscopy (XAS) and X-ray pair distribution function (PDF) studies that have shed light on complementary aspects of the local coordination environment in these catalyst systems. Together with X-ray absorption near edge structure (XANES) studies, electron paramagnetic resonance (EPR) spectroscopy methods have also been particularly useful for developing a clear picture of the valency of these catalyst films, and particularly of the resting state, which is the predominant form of the catalyst during turnover.

3.1 *Structural Studies*

Cobalt *K*-edge extended X-ray absorption fine structure (EXAFS) studies have been performed on CoP_i films to elucidate the structural connectivity of the catalyst [43, 44]. Figure 4 compares the Fourier transform (FT) of EXAFS spectra of two CoP_i samples collected in situ at room temperature during catalysis with that of a crystalline CoO(OH) model compound [44]. The abscissa is the apparent distance, which is shorter than the actual distance, between a given absorber–backscatterer pair of atoms produced by a phase shift. Peaks I and II at actual distances of about 1.9 and 2.8 Å reflect Co–O and Co–Co vectors, respectively. Notably, the relative intensity of the Co–Co vector is considerably greater in CoO(OH) than in either CoP_i sample, indicating a larger average number of Co–Co vectors per Co ion in CoO(OH) than in CoP_i. In addition, the EXAFS FT for CoO(OH) displays prominent peaks at distances greater than 3 Å (peaks III and IV), consistent with contributions from scattering interactions in outer shells, as expected for a crystalline compound. However, the analogous features are considerably weaker in CoP_i films, indicating a much smaller coherent domain size.

The EXAFS data shown in Fig. 4 also suggest that the deposition conditions and/or film thickness can impact the domain size (or distribution of domain sizes) in

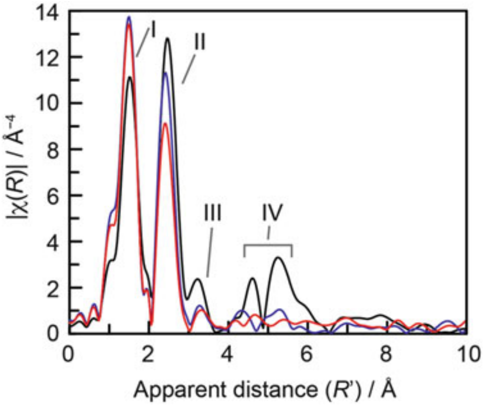

Fig. 4 Fourier transforms of EXAFS spectra for CoP$_i$ and CoO(OH). Fourier transforms of *k*-space oscillations for "thick" CoP$_i$ film deposited at 1.25 V (*blue*), "thin" CoP$_i$ deposited at 1.1 V (*red*), and crystalline CoO(OH) (*black*). Figure adapted from [44]

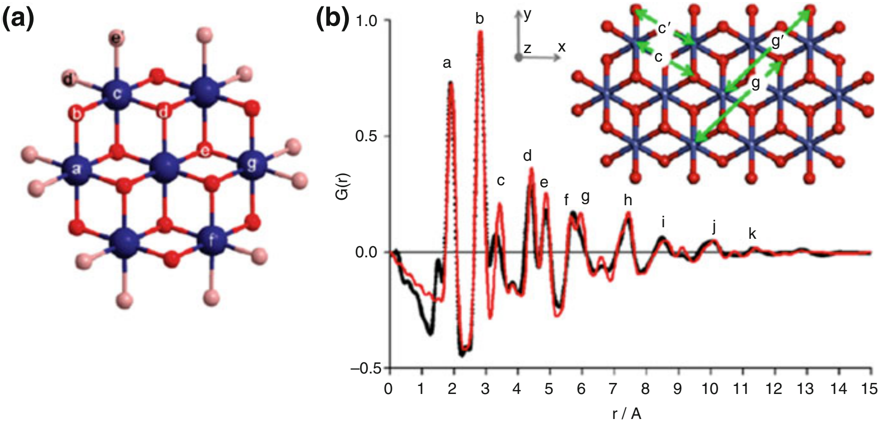

Fig. 5 (**a**) Edge-sharing molecular cobaltate cluster (MCC) obtained for "thin" CoP$_i$ films deposited at 1.1 V, as determined from EXAFS measurements. Bridging oxo/hydroxo ligands are shown in *red*, and nonbridging oxygen ligands (including water, hydroxide, and phosphate, *light red*) complete the octahedral coordination geometry of each peripheral Co ion (*blue*). Figure adapted from [44]. (**b**) Comparison between the experimental electron pair distribution function, $G(r)$ measured for CoP$_i$ (*black trace*) and the $G(r)$ calculated from the structural model (*inset*). Figure adapted from [48]

catalyst films. Fitting to the EXAFS spectra establishes that ordered domains in CoP$_i$ consist of edge-sharing molecular cobaltate clusters (MCCs) with the minimal structural unit shown in Fig. 5a [44]. Differences in cluster sizes (or distributions of sizes) between the two CoP$_i$ materials may arise as a consequence of the difference in the amount of material deposited. The absence of detectable crystallites in diffraction experiments indicated that these molecular clusters are not infinitely stacked in ordered arrays, but are to a large extent disordered relative to one another.

Attempts to incorporate cobalt–potassium vectors into the fits for this in situ cobalt *K*-edge EXAFS data were unsuccessful [44], leading to substantially increased error values or negligible effects on the fitting quality. A CoP_i catalyst was prepared with sodium phosphate used in place of potassium phosphate as the electrolyte during electrodeposition. The replacement of K^+ with Na^+ slightly increases the intensity of peaks in the FT EXAFS at apparent distances >3 Å, which is the opposite trend from what would be expected if one of these peaks had a Co–K component, because potassium is a stronger scatterer than sodium; any peaks that result from a Co–K vector in the FT of the CoP_i EXAFS data would certainly be reduced upon substitution with sodium. On the basis of these results we concluded that alkali cations are most likely coordinated to the peripheral ligands of the MCC or to interstitial lattice water molecules. Risch et al. [45] subsequently reported ex situ XAS data on frozen Co-OEC samples deposited in KP_i and $CaCl_2$ at the respective potassium and calcium *K*-edges to interrogate specifically any structural role of redox-inert cations in these catalyst films. They found that potassium binding appears largely nonspecific and disordered, in agreement with our previous in situ report. However, on the basis of Ca *K*-edge EXAFS data of films deposited in Ca^{2+}-containing electrolytes, they proposed the formation of $CaCo_3O_4$ cubanes, which are analogous to the $CaMn_3O_4$ cubane moiety found in the oxygen-evolving center of photosystem II. Nevertheless, they found that substitution of these redox-inert cations did not lead to any major differences in catalytic activity, suggesting that these ions are not directly involved in the catalytic mechanism in Co-OEC.

High energy X-ray total scattering and pair distribution function (PDF) analysis is a powerful tool for structural studies of disordered and nanocrystalline systems, because it permits consideration of a wider range of atom–atom distances that are not accessible by EXAFS [46, 47]. Tiede and co-workers employed PDF analysis to shed more light on the coherent domain size and structure of CoP_i [48]. Their results indicate that atom pair correlations persist out to about 13 Å, and PDF patterns were fit to a model consisting of a 13–14 Co ion lattice domain consisting of edge-sharing CoO_6 octahedra (Fig. 5b), in good correspondence with the in situ EXAFS results discussed above. Phosphate was found as a disordered component in the films, and minority "defect" sites consisting of complete Co_4O_4 cubanes were also proposed. In addition, the PDF data suggested that the clusters might possess distorted coordination geometries at their periphery, such as alterations in the terminal O ion positions. It was proposed that these terminal Co–O distortions could play a key role in O_2 evolution catalysis at CoP_i by facilitating the formation of terminal peroxo intermediates.

We employed an X-ray PDF analysis set to explore the influence of deposition conditions on the structure of Co-OEC films. These studies established that the nature of the buffering electrolyte (P_i and B_i) affects the intermediate structure of the catalyst [49]. The refined PDF fits and models for CoB_i and CoP_i catalysts are shown in Fig. 6a, b. Films of the CoB_i comprise three layers on average of the

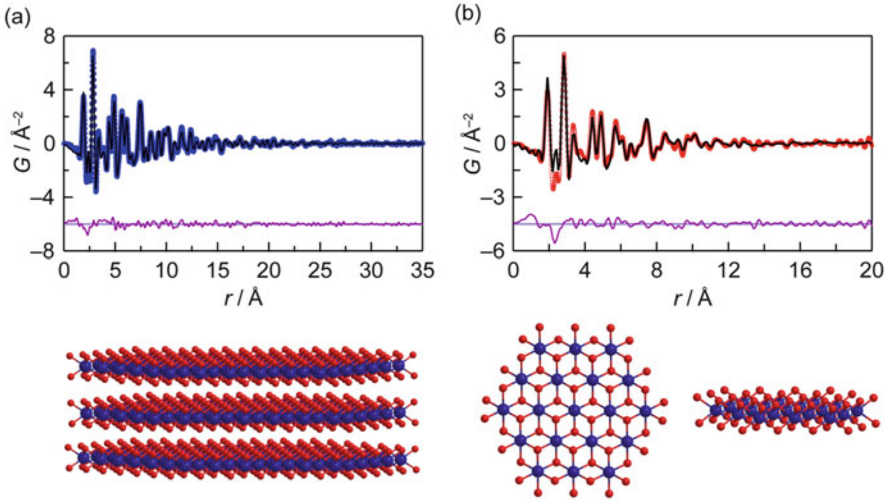

Fig. 6 *Top*: Cylindrical atomistic model fit (*black lines*) to the (**a**) CoB_i catalyst PDF data (*blue circles*) and (**b**) CoP_i catalyst PDF data (*red circles*). The difference curves are shown in *purple*, and are offset for clarity. *Bottom*: (**a**) View of the refined model for the average coherent domain in CoB_i films, and (**b**) two views of the refined model for the average coherent domain in CoP_i films. Figure adapted from [49]

MCC, and the diameter of each MCC layer is approximately 35 Å. Constraining the model to a single layer results in a poorer fit, suggesting that the coherent domains of CoB_i do indeed consist of multiple layers of MCCs with weak but significant interlayer correlations. The PDF data also reveal significant interlayer expansion relative to crystalline CoOOH, possibly to accommodate something larger than protons in the interlayer region such as weakly scattering or disordered electrolyte ions, though B_i was not identified explicitly. The refined CoP_i model and fit (Fig. 6b) indicates that the diameter of the clusters is approximately 14 Å, considerably smaller than those of CoB_i and on a par with the EXAFS data as well as the PDF studies of Tiede et al. Unlike CoB_i, modeling PDF data could not accommodate significant interlayer correlations in CoP_i, suggesting that the coherent domains of the catalyst consist of single layer MCCs whose arrangements are significantly disordered in the film.

3.2 Catalyst Resting State Valency

Electrocatalytic intermediates are typically formed in minor equilibrium. Though crucial for catalysis, such intermediates tend to contribute negligibly to spectroscopic data of the catalyst under steady state conditions. Insight into such intermediates is provided from the catalyst resting state, because it sheds light on the character of the catalyst prior to subsequent redox transformations. Cobalt *K*-edge XAS was used to probe the resting state oxidation state of Co in catalyst films by

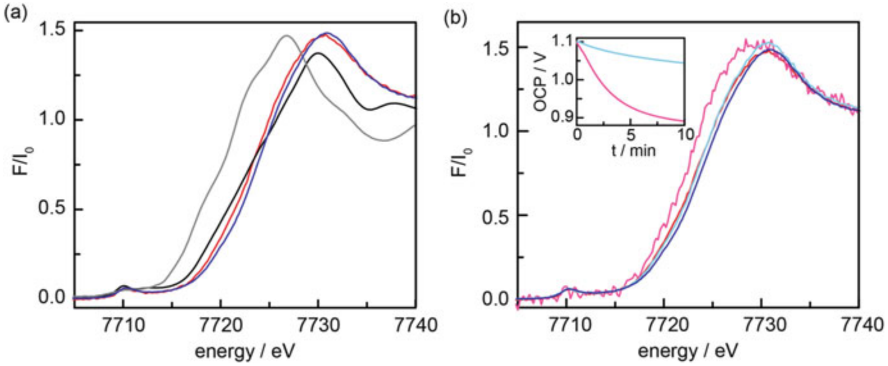

Fig. 7 XANES spectra for CoP$_i$ samples and model compounds. (**a**) Thin 1.1 V deposited-CoP$_i$ during operation at 1.25 V (*red*), thick 1.25 V deposited-CoP$_i$ during operation at 1.25 V (*blue*), CoOOH (*black*), and CoO (*gray*). (**b**) Thin 1.1 V deposited-CoP$_i$ at OCP (*magenta*) and 1.25 V (*red*), thick 1.25 V deposited-CoP$_i$ at OCP (*cyan*) and 1.25 V (*blue*). *Inset*: open circuit potential vs time traces. Figure adapted from [44]

comparison of the XANES spectra to those of model compounds [44]. XANES spectra of CoP$_i$ samples collected in situ during catalysis at 1.25 V are shown in Fig. 7a along with the spectra of solid samples of CoO and CoOOH. The observed edge positions are consistent with an average Co valency ≥ 3 for the CoP$_i$ samples at 1.25 V, indicative of some formal Co^{IV} valency in the resting state. However, it is not straightforward to determine precise metal valency based on XANES spectra alone because of their sensitivity to geometry and the specific ligand environment [50]. However, this qualitative assignment is supported by several pieces of independent data, including CV data and the observed bond lengths in the cobalt-oxido clusters compared to bond lengths in crystalline cobaltate compounds.

As described in Sect. 2, CVs of CoP$_i$ exhibit an anodic wave as a pre-feature to a catalytic wave. The half-wave potential of the pre-feature is observed at ~+0.95 V. The $Co(H_2O)_6{}^{3+/2+}$ couple is about 1.9 V [51] and the pK_a values of $Co(H_2O)_6{}^{3+}$ and $Co(H_2O)_6{}^{2+}$ are 2.9 [52] and 9.2 [53], respectively. Therefore, it is reasonable to consider that at pH 7 the proton-coupled oxidation of $Co^{2+}{}_{(aq)}$ could lead to a Co^{3+} film if more than one proton is transferred in the process (see Sect. 5) [53]. In addition, the $Co(OH)_2{}^{+/0}$ couple is estimated to be +1.1 V and the Pourbaix diagram of cobalt indicates that the thermodynamic potential for the conversion of Co_3O_4 to CoOOH occurs at ~0.75 V at pH 7 [54]. The $Co^{3+/2+}$ couple for CoP$_i$ at 0.95 V occurs ~0.14 V negative of the catalytic wave for water oxidation, consistent with a formal oxidation state of Co^{3+}, prior to any catalytic behavior. The catalytic wave is therefore obtained only upon further oxidation of the Co^{3+} film.

The first shell Co–O distances and the nearest neighbor Co–Co distances deduced from EXAFS data [44] support the assignment of a Co valency greater than 3 by comparison to corresponding distances in alkali cobaltates of various valencies [55]. In the stoichiometric Co^{3+} oxides, CoOOH and $LiCoO_2$, the Co–Co distances are 2.85 and 2.81 Å, and the Co–O distances are 1.90 and 1.92 Å, respectively. For the series Na_xCoO_2, the corresponding distances range from 2.89 and 1.94 Å for $x = 1$ (all Co^{3+}), to 2.81 and 1.81 Å for $x = 0.3$ (i.e., formally 70% Co^{IV}). The Co–Co distance (2.82 Å) observed for the CoP_i samples under an applied potential is at the short end of the range of distances observed in cobaltates with valencies greater than 3 and the Co–O distance (1.89 Å) is in the middle of the corresponding range, suggesting a significant presence of Co^{IV} during turnover.

XANES results (Fig. 7a) indicate that there is a greater average Co valency in the CoP_i film that was deposited at 1.25 V (a potential at which water oxidation is coincident with catalyst deposition) compared to that prepared at 1.1 V (where water oxidation is negligible) [44]. Furthermore, in situ XANES spectra acquired for CoP_i films at open circuit (OC) conditions together with OC decay transients (Fig. 7b) indicate that film deposition at high potentials permits the trapping of some of the Co^{IV} centers within the film, thereby delaying their eventual discharge (reduction upon the OER) when the cell is held at OC. This trapping effect was exploited to confirm more precisely the existence of Co^{IV} centers in the resting state of CoP_i films during turnover using EPR spectroscopy.

McAlpin et al. [56] and Gerken et al. [57] conducted EPR studies of CoP_i samples freeze-quenched after deposition at a variety of potentials. Continuous wave (CW) X-band EPR spectra of frozen catalyst samples display a broad resonance at $g_{\mathrm{eff}} \approx 5$ along with a broad derivative lineshape at $g_{\mathrm{eff}} = 2.27$ (Fig. 8a). The $g_{\mathrm{eff}} \approx 5$ feature was assigned to an $S = 3/2$ Co^{II} species based on EPR spectra of model Co^{II} compounds. The progressive rise of the $g_{\mathrm{eff}} = 2.27$ feature as the deposition potential is increased along with its similarity to the g value of the signal observed in a tetracobalt cubane model compound ($[Co_4O_4(C_5H_5N)_4(CH_3CO_2)_4]$ (ClO_4)) possessing Co centers with formal cobalt oxidation states of III, III, III, IV (Fig. 8b), provides strong evidence for the assignment of the $g_{\mathrm{eff}} = 2.27$ signal to low-spin Co^{IV}-containing species in the catalyst film. Moreover, the potential dependence of this signal suggests that it arises predominantly from species generated during electrocatalytic water oxidation, corroborating the finding of the in situ XANES study.

As observed in the XAS studies above (Fig. 7b), removal of the applied potential causes the open circuit potential to decay, implying a change in the average valency of the film. In correspondence with the XAS and electrochemical results, EPR spectra of films prepared identically, but with variable delay times between catalyst isolation from the film and freezing at 77 K, revealed that the Co^{IV} signal decays over the course of minutes at room temperature even in a dry, isolated film (Fig. 8c) [56].

These EPR studies permitted an estimation of the population of Co^{IV} spins in the catalyst films. By comparison to an $S = ½$ spin standard, Cu(EDTA)(SO_4), it was estimated that Co^{IV} centers represented 3% and 7% of the total cobalt centers in trapped films grown at 1.14 and 1.34 V, respectively [56]. It was also shown that the Co^{IV} valency was not merely trapped in films deposited at elevated potentials, but was important to the electronic structure of the resting state of CoP_i during turnover. By preparing two catalyst films in an identical manner at 1.04 V, below the onset of

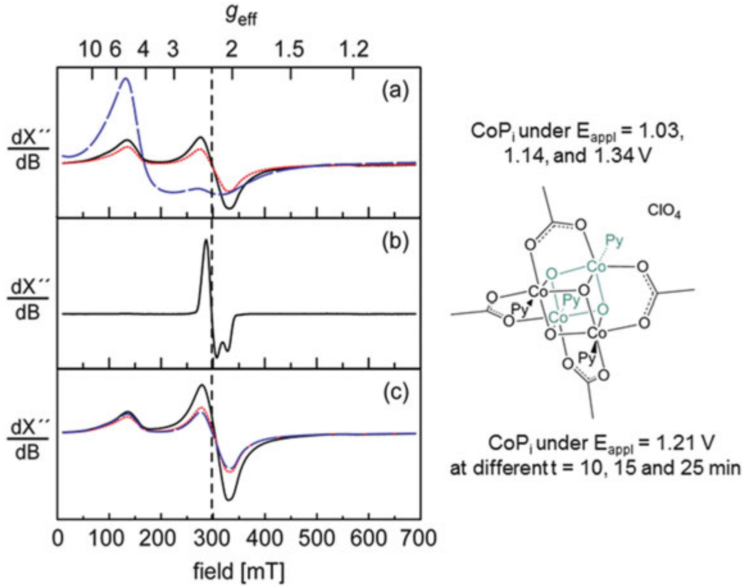

Fig. 8 CW X-band EPR spectra at $T = 5.7$ K and microwave power $= 1.02$ mW. (**a**) CoP$_i$ catalyst films deposited from aqueous 0.5 mM $Co(NO_3)_2$ solutions in 0.1 M P$_i$ electrolyte (pH 7.0) at 1.03 V (*blue dashed curve*), 1.14 V (*red dotted curve*), and 1.34 V (*black solid curve*). Spectra were scaled by the amount of cobalt in each sample, as measured by atomic absorption spectroscopy. (**b**) The $Co^{III}{}_3Co^{IV}$ cluster $[Co_4O_4(C_5H_5N)_4(CH_3CO_2)_4]$-$(ClO_4)$. The *vertical dotted line* indicates $g = 2.27$. (**c**) CoP$_i$ catalyst films electrodeposited at 1.21 V with 10 (*solid line*), 15 (*red-dotted line*) and 25 (*blue-dashed line*) min of delay between the termination of electrolysis and freezing of the sample at 77 K. Spectra were scaled relative to the mass of CoP$_i$ in each sample, as measured by atomic absorption spectroscopy. Figures adapted from [56]

water oxidation catalysis, it was ensured that the as-deposited film exists almost completely in its Co^{III} form (Sect. 5). Catalyst material was isolated from the one electrode immediately following deposition, whereas the other electrode was transferred to Co-free P$_i$ electrolyte solution and electrolyzed at a potential sufficient for water oxidation catalysis (>1.2 V). The catalyst film subjected to water oxidation in the absence of additional film formation in this fashion exhibited a decrease in the Co^{II} signal concomitant with an increase in the Co^{IV} signal, just as observed in Fig. 8a.

Additional multifrequency EPR studies and electronic structure calculations were performed on the Co^{IV}-containing cubane compound to investigate further the electronic and geometric structure relationships of MCCs such as those found in CoP$_i$ [58]. The magnetic parameters determined by electron nuclear double resonance (ENDOR) and spectroscopic results from electron spin echo envelope modulation (ESEEM) combined with density functional theory (DFT) calculations revealed that the unpaired spin of the cubane is highly delocalized. Each octahedrally coordinated cobalt ion was found to possess a low-spin electron configuration resulting from the anionic oxo and carboxylato ligands, and a fractional electron

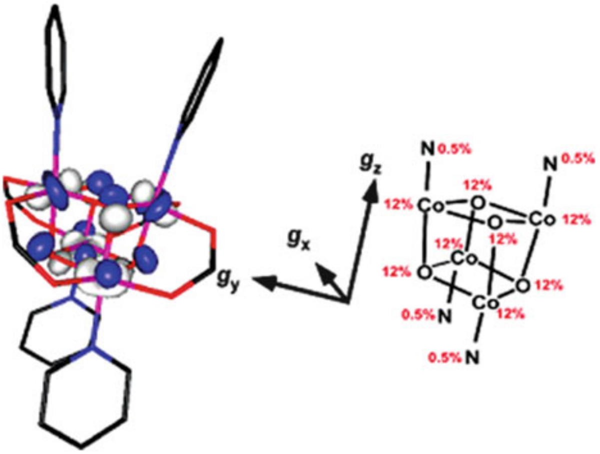

Fig. 9 Singly occupied molecular orbitals of $[Co_4O_4(C_5H_5N)_4(CH_3CO_2)_4](ClO_4)$ from DFT calculations. Calculations show the unpaired electron spin density spread almost equally over the eight core atoms of the cubane based on their Löwdin spin populations. Reproduced from [58]

hole resides on each metal center in a Co $3d_{xz,yz}$-based molecular orbital, essentially giving a $[Co^{+3.125}{}_4O_4]$ cluster (Fig. 9). However, closer inspection of the EPR spectra of the molecular model and those of CoP_i revealed features consistent with less delocalization of the unpaired electron spin in the case of CoP_i compared to the model. It was proposed that because the $Co^{III/IV}$ redox transformations in the film (Sect. 2) and at active sites during turnover (Sect. 4) are coupled to proton loss from bound OH_x ligands, the increase in ligand-field strength accompanying this proton loss could result in substantial localization of unpaired spin density [58]. This localization of the oxidized equivalent is consistent with subsequent reactivity of the Co^{IV} moieties in CoP_i compared to the molecular model. These findings implicate the importance of PCET, not only for redox/potential leveling but also for hole/radical localization, leading to efficient oxygen evolution in Co-OEC films.

The aforementioned EXAFS and X-ray PDF studies combined with the geometric structure of Co-OEC films support a structural model wherein Co-OEC is composed of cobaltate clusters of molecular dimensions. In addition, XANES and EPR studies are consistent with a proportion of Co centers achieving a formal oxidation state of +4 at potentials sufficient for water oxidation catalysis, indicating a $Co^{III/IV}$ mixed valence resting state during oxygen evolution. Together with the mechanistic studies discussed in the following section, a cohesive picture of water oxidation by Co-OEC films is unveiled.

4 Mechanistic Insights into O_2 Evolution Catalysis at Co-OEC Thin Films

The preceding sections address the electrosynthesis of Co-OECs and the structural and electronic characterization of its resting state. Against this backdrop, we discuss electrokinetic studies that provide insight into the mechanism of oxygen evolution mediated by this thin-film catalyst over a wide pH range. Because of the extreme kinetic demands of the OER, the efficiency and conditions required for this reaction are key determinants of the overall viability of energy storage via water splitting. Therefore, the continued development of effective OER catalysts and elucidation of their mechanisms stand as central scientific and technological challenges in energy conversion. For porous catalyst films of this type, the relationship between film thickness (catalyst loading) and film activity is of central importance to the search for solar water splitting at high efficiency. This is because the overpotential is an extrinsic parameter that depends on the current density desired. Hence, in addition to making more active catalyst materials, low overpotentials may be realized by preparing thicker films where a higher active site density (per projected geometric area) may be accessed. This allows faster rates to be achieved with thicker films (Fig. 3), but demands that charge hopping between active sites is well matched to catalytic rates. Thus the mechanisms of catalytic turnover and charge hopping are equally important design elements. These topics are addressed in the following sections.

4.1 Active Site Electrokinetics

Steady-state electrokinetic data were acquired over a range of electrolyte conditions between pH 4 and 12 in order to uncover the electrochemical rate law for O_2 evolution [59]. Tafel plots, which describe the variation of the steady state current density with the potential or overpotential supplied at the electrode [60], provide key mechanistic insights for electrochemical reactions that are not mass-transport limited. Under these conditions, the current density measured at steady state is directly proportional to the rate of the underlying reaction [60]. It was shown that this condition applies to the electrokinetic studies of CoP_i; Tafel plots collected at 1,000 and 2,000 rpm of CoP_i films on a Pt rotating disk electrode exhibited similar slopes (61 mV/decade) to those collected on a stationary FTO electrode (62 mV/decade) in a stirred solution, indicating that the observed currents are not limited by mass transport to the catalyst films over the sampled current/potential range. In addition, the Tafel data were shown to be reproducible between sequential potential sweeps and insensitive to the direction of potential sweep, indicating that the film is not appreciably altered over the course of Tafel data collection. Furthermore, measurable steady-state current is observed upon application of an overpotential of >0.2 V to CoP_i films. At these overpotentials, any current arising from the

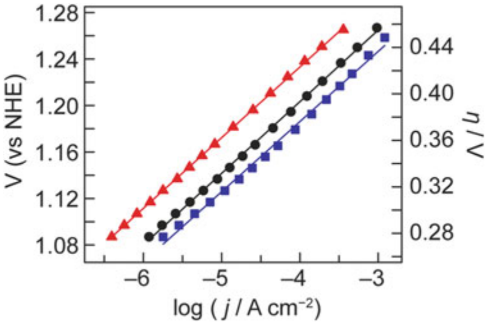

Fig. 10 Tafel plots, $V = (V_{\text{appl}} - iR)$, $\eta = (V - E°)$, for CoP$_i$ catalyst films grown with passage of 6 (*red-filled triangle*), 24 (*filled circle*), and 60 (*blue-filled square*) mC/cm^2. Adapted from [59]

oxygen reduction back reaction can be safely ignored and, thus, kinetic information about the OER can be deduced directly from the steady state current density measurements.

Tafel slopes were found to be similar over the same range of current densities for CoP$_i$ films of varying thickness (Fig. 10), and the activity of the film increases markedly as the film thickness is increased from 10 to 90 nm [59]. All three film thicknesses exhibited similar lower limit turnover frequencies (TOF) of ~2×10^{-3} s^{-1} per Co at an overpotential of 410 mV. This TOF estimate assumed that every Co center in the film is catalytically active. Because the vast majority of the cobalt centers in the film are expected to play a purely structural role, this is likely a gross underestimate of the real TOF of active sites. However, in the absence of a direct measure of the electrocatalytically active surface area or the active site density, this value is offered purely for the purposes of comparing different film thicknesses. The similarity in TOF amongst the films of varying thickness highlights the porous and conductive nature of the catalyst films, because the active sites are accessible throughout the film and not merely at the film/solution interface. Moreover, the independence of Tafel slope with film thickness indicated that the reaction kinetics are not influenced by barriers to electron transport or mass transport within the film – factors that can severely skew the activation-controlled electrokinetic data. These barriers can be particularly problematic for oxide films formed by the anodization of a metal substrate, where a compact barrier oxide layer between the buried metal and the catalytic hydrous oxide can pose significant challenges for charge transport [61–63].

The Tafel slope of nearly 59 mV/decade observed for the thin CoP$_i$ films indicated that a single mechanism is dominant over the potential range investigated [60]. The observed Tafel slope defines a transfer coefficient (usually denoted α) of 1, consistent with a one-electron pre-equilibrium from the resting state followed by a turnover-limiting chemical step. It is important to note here that α (which is a purely experimental parameter equal to the reciprocal Tafel slope in dimensionless form) is distinct from the fundamental symmetry factor (usually denoted β) characterizing the position of the activated complex along the reaction coordinate in a microscopic one-electron transfer reaction. In multielectron catalysis, the transfer coefficient can take any value between 0 and the total number of electrons

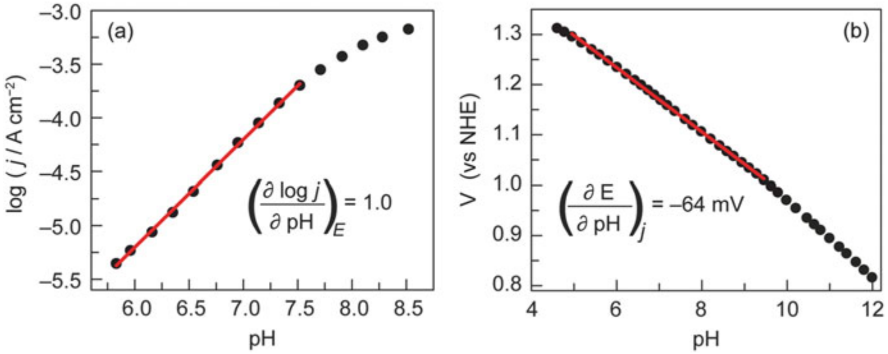

Fig. 11 (**a**) pH dependence of steady-state catalytic current density at constant potential ($E = 1.18$ V) for a catalyst film functioning in 0.1 M P_i electrolyte. Attenuated current densities are observed for pH > 8, because under these conditions P_i (p$K_a = 7.2$) cannot maintain a constant local pH. (**b**) pH dependence of steady-state electrode potential at constant current density ($j_{\text{anodic}} = 30\ \mu\text{A/cm}^2$) for a catalyst film operated in 0.1 M P_i electrolyte. Maintaining a low current density ensures that the buffering capacity of P_i is not overwhelmed even when the bulk pH is adjusted outside of the ideal P_i buffering range. Adapted from [59]

transferred per turnover, n (for the OER $n = 4$ and therefore $0 \leq \alpha \leq 4$). Therefore, for any multielectron reaction, the lowest Tafel slope attainable is $2.3 \times RT/nF$ [60]. On the other hand, β by definition must lie between 0 and 1, because it represents the ratio between the changes in the electrochemical free energy of activation and the electrochemical free energy of the reaction. For an irreversible one-electron reaction, α (which is always the parameter that can be measured directly) is taken as numerically equal to β [60].

Examination of the pH dependence of the reaction rate by both potentiostatic (Fig. 11a) and galvanostatic (Fig. 11b) techniques is consistent with an inverse first-order dependence on proton activity, indicative of the loss of a single proton in an equilibrium step prior to the turnover-limiting process [59]. Although phosphate is neither reactant nor product in the overall water oxidation reaction, it can serve as a proton acceptor in reactions involving PCET transformations. Notwithstanding, a zeroth-order dependence of phosphate was observed over a >1.5 decade range of phosphate concentration, indicating that proton transfer to phosphate is not involved in the turnover-limiting step and therefore proton transfer to bulk solution is also not turnover-limiting because phosphate is the most likely proton acceptor in P_i electrolyte. Moreover, turnover-limiting proton transfer to surface-bound phosphate is unlikely provided that phosphate has not saturated the catalyst film over the potential range studied. It was, however, noted that turnover-limiting internal proton transfers, as might be required for oxo-hydroxo exchange between catalyst active sites, could not be ruled out.

To a first approximation, these electrokinetic studies define an electrochemical rate law described by the following expression [59]:

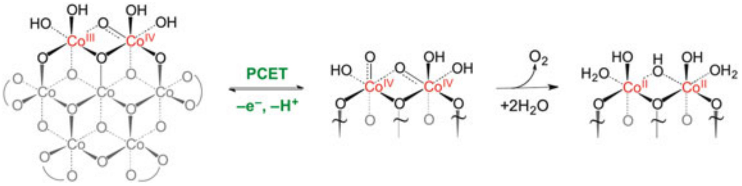

Fig. 12 Proposed pathway for OER by CoP_i. A PCET minor equilibrium proceeded by a turnover-limiting O–O bond forming step is consistent with current dependencies on proton and electron equivalencies. *Curved lines* denote phosphate, or OH_x terminal or bridging ligands. Reproduced from [59]

$$j = k_0^{\mathrm{OER}} (a_{\mathrm{H}^+})^{-1} \exp\left[\frac{FE}{RT}\right], \tag{4}$$

where k_0^{OER} is a potential-independent constant. This constant is proportional to the exchange current density and increases with catalyst loading as observed in Fig. 12. The exact mechanistic basis for the proportionality between this constant and film thickness is addressed in Sect. 4.2. Rearrangement of the logarithmic form of (4) yields a Tafel slope, $b = \partial \mathrm{E}/\partial \log(j)$, of 59 mV/decade that is also consistent with the experimental data shown in Fig. 11 and is equivalent to a transfer coefficient of $\alpha = RT/bF = 1$. Equation (4) is consistent with a mechanistic sequence involving a reversible one-electron, one-proton minor equilibrium step followed by a turnover-limiting chemical step [59]:

$$\mathrm{A} \rightleftharpoons \mathrm{B} + e^- + \mathrm{H}^+, \tag{5}$$

$$\mathrm{B} \rightarrow \mathrm{C}. \tag{6}$$

The assignment of chemical species to A, B, and C in (5) and (6) was aided by knowledge of the oxidation state changes in the film as a function of the applied potential. As described in Sect. 3, CV features of CoP_i are consistent with a predominant Co oxidation state of >+3 during catalysis. Accordingly, the pre-equilibrium step ($\mathrm{A} \rightleftharpoons \mathrm{B}$) was assigned to a formal $\mathrm{Co^{III}} \rightleftharpoons \mathrm{Co^{IV}}$ redox transition that is coupled to a proton transfer. It was suggested that the electrokinetic behavior described by (4) was in accord with $\mathrm{Co^{IV}}$ (i.e., B) as the minor component of this pre-equilibrium. Because the surface coverage of B, denoted θ_B, must be less than 10% for the pre-equilibrium to exhibit the observed Nernstian dependence on potential at the highest potential (1.27 V) that Tafel data were collected, the maximum fractional surface coverage of $\mathrm{Co^{IV}}$ ($\theta_{\mathrm{B,max}}$) must be 10%, and θ_B is expected to diminish by an order of magnitude per ~60 mV decrease in potential [60].

As discussed in Sect. 3, EPR spectra of CoP_i films subjected to prolonged electrolysis at 1.14 V, a value sufficient for water oxidation, exhibit a $\mathrm{Co^{IV}}$ signal estimated to arise from 3% of the cobalt centers in the film [56]. Noting the sizeable dead time (~25 min) between termination of electrolysis and freezing of the EPR sample, it is to be expected that the population of Co^{IV} in the film during electrolysis at 1.14 V would be significantly in excess of the residual 3% observed by EPR. Correspondingly, the in situ XANES data [44] discussed in Sect. 3 are consistent with an appreciable population of Co^{IV} when the films are held at potentials sufficient for water oxidation catalysis. The large population of Co^{IV} observed by EPR and in situ XANES studies, therefore, indicated that the catalyst resting state, A, is comprised of $Co^{III/IV}$ mixed valence clusters. The pre-equilibrium redox process ($A \rightleftharpoons B$) was therefore assigned to further oxidation of the $Co^{III/IV}$ mixed valence clusters preceding a turnover-limiting chemical process [59].

Based on the pH titration data shown in Fig. 11b, it was inferred that the reactant in the equilibrium step defined in (5) possessed a pK_a greater than 12 [59]. Indeed, additional studies under more alkaline conditions undertaken by Gerken et al. [57] extend the pK_a of this species beyond 14. By comparison to the pK_as of known Co aqua species [52] and to potentiometric titrations of crystalline cobalt oxide compounds [64, 65], we deduced that the reactant in (5) was most likely a [Co^{III}–OH] moiety present in a $Co^{III/IV}$ mixed valence cluster (species A), which is oxidized in a PCET equilibrium to a [Co^{IV}–O] center (species B).

Films prepared in isotopically labeled $^{18}OH_2$-enriched electrolyte and operated in non-isotopically labeled water were shown to extrude $^{32}O_2$ and $^{34}O_2$ and, to a lesser extent, $^{36}O_2$ [59]. The observation of $^{34}O_2$ and $^{36}O_2$ was ascribed to the participation of μ-oxo/μ-hydroxide moieties in oxygen production given that (1) the terminal Co–$^{18}OH_x$ moieties of the films used in the ^{18}O experiments are subject to exchange with bulk solvent over the time required to purge the gas-tight electrochemical cell used in these measurements and (2) the μ-oxo/μ-hydroxide moieties in the catalyst clusters exchange at a much slower rate. Importantly, although these results are consistent with the participation of μ-oxo/μ-hydroxo sites in O–O bond formation as a plausible mechanistic pathway in the OER, it does not necessarily imply that this pathway is the *predominant* route for O_2 formation; the slow extrusion of ^{18}O could simply reflect a minor pathway for O_2 evolution that contributes minimally to the observed electrokinetics. Because of the ambiguities associated with interpreting these ^{18}O-labeling results, it was noted that studies identifying the rate and nature of oxo-exchange in these films are needed before specific conclusions can be drawn. Once these exchange rates are identified, experiments that permit more rapid switching between isotopically enriched and non-isotopically enriched electrolytes (along with in-line analysis of products) could be leveraged to shed more light on the mechanism of O−O bond formation.

The proposed reaction pathway for the overall transformation is shown in Fig. 12 using the MCC model derived from EXAFS [44] and X-ray PDF analysis [48] (Sect. 3.1). Given the pre-equilibrium in (5) and the observed 60 mV/decade Tafel slope, the [Co^{IV}−O] product must participate in a turnover-limiting chemical step. The electrochemical rate law is consistent with a chemical step that does not involve proton transfer to bulk electrolyte, and as such, it was concluded that the O–O bond is formed in this irreversible chemical process.

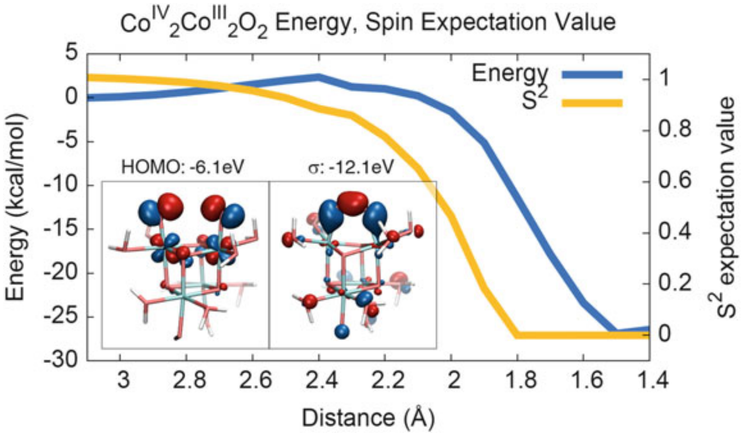

Fig. 13 DFT energies (*left Y*-axis, in *blue*) and $\langle S^2 \rangle$ (*right Y*-axis, in *orange*) as a function of O–O distance for a tetracobalt cubane model catalyst in the [Co$^{III}{}_2$Co$^{IV}{}_2$] state. *Left inset*: highest occupied molecular orbital (HOMO) at $r_{O\text{–}O} = 3.0$ Å. *Right inset*: σ bonding orbital at $r_{O\text{–}O} = 1.4$ Å. Reprinted from [66]. Copyright 2011 American Chemical Society

Wang and Van Voorhis [66] explored the catalytic mechanism of O_2 evolution at a cobalt cubane model compound using DFT . They computed the energetics and barriers for the steps leading up to and including the O–O bond formation reaction using an explicit solvent model within a hybrid quantum mechanics/molecular mechanics (QM/MM) framework. Their studies on this model compound indicated that the formation of two cofacial terminal Co^{IV}–O generated a stable O–O bond with a low activation barrier (Fig. 13) and a low thermodynamic driving force. Based on the low barrier for O–O bond formation, it was proposed that the turnover-limiting step in CoP$_i$ could be the addition of a water molecule or an intramolecular proton transfer, both of which would be consistent with the electrokinetic data. However, the authors noted one important deficiency of this cubane model relative to CoP$_i$: the model lacks any μ$_2$-(hydr)oxo centers, which are present in the MCC structure (Figs. 5 and 6), and which are implicated in O–O bond formation by the ^{18}O-labeling studies described above. We note that alternative turnover-limiting steps could also be the scission of the Co–O bond following O–O bond formation or hydrogen atom abstraction from H_2O by a Co oxyl (Co^{III}–O$^{\bullet}$). This computational study revealed that the localization of the hole density was severely dependent on the precise OH center deprotonated in the proton-coupled oxidation, providing further evidence for the role of PCET in hole/radical localization, which was suggested by the EPR studies [58] discussed in Sect. 3.2.

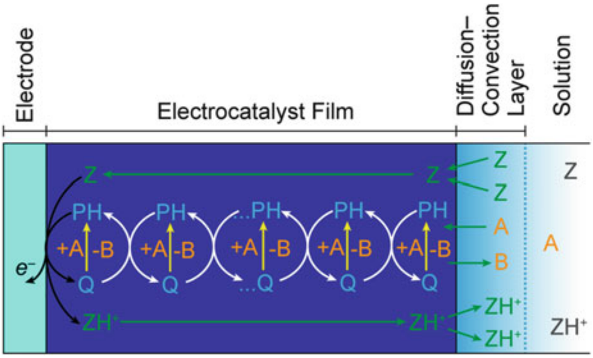

Fig. 14 Electrocatalytic oxidation of the substrate A into the products B in the presence of an acid-base pair ZH^+/Z by means of an immobilized $PH/Q + e^-$ catalyst couple. Adapted from [67]

4.2 Proton-Electron Transport-Catalysis Mechanism

In addition to the catalytic reaction, a major controlling factor in overall observed activity is electron transport through the film to the electrode to regenerate the catalyst [67]. Because protons are generated during the catalytic reaction, proton transfer – and therefore proton-coupled electron transfer [68–76] – reactions play a key role in both catalysis and transport. Using the active site turnover mechanism discussed in Sect. 4.1 [59], we set out to provide a more complete electrochemical rate law than the simplified version in (4).

The general scheme for the analysis is displayed in Fig. 14. Here "PH" represents the resting $Co^{III}(OH)/Co^{IV}(O)$ state (Fig. 12, left) and "Q" represents the preturnover-limiting $[Co^{IV}(O)]_2$ state, colloquially referred to as the "active form" of the catalyst (Fig. 12, middle). The substrate (A) and product (B) are H_2O and O_2, respectively. The acid-base pair, ZH^+/Z, is $H_2PO_4^-/HPO_4^{2-}$, $B(OH)_3/B(OH)_4^-$, or H_3O^+/H_2O (under appropriate electrolyte conditions).

The permeation of electrolyte into the film and the fact that the hopping involves no net charge transport (e^- plus H^+) ensures that transport is not driven by a gradient in the electric field across the film; instead proton coupled electron hopping proceeds down a gradient in electrochemical potential, akin to the description used for polymer electrode coatings – the so-called "redox conductors" [77–79]. In this model, proton coupled electron hopping through the film may be likened to a linear diffusion transport obeying Fick's law that is modified by a catalytic rate constant term, k_{cat}:

$$D_{H,e}\frac{d^2C_{\mathrm{PH}}}{dx^2} + k_{\mathrm{cat}}C_{\mathrm{Q}} = 0, \qquad (7)$$

$$D_{H,e}\frac{d^2C_{\mathrm{Q}}}{dx^2} - k_{\mathrm{cat}}C_{\mathrm{Q}} = 0. \qquad (8)$$

Here, x is the distance between any specified site in the film and the electrode substrate, and "C" represents the concentrations of the subscript species.

At the electrode, the following expression of the Nernst law is appropriate at the electrode surface ($x = 0$):

$$\frac{(C_{\mathrm{Q}})_{x=0} \times (C_{\mathrm{H^+}})_{x=0}}{(C_{\mathrm{PH}})_{x=0} \times C^0} = \exp\left[\frac{F}{RT}\left(E - E^o_{\mathrm{Q+H^+/PH}}\right)\right], \tag{9}$$

where C^0 is a normalizing concentration of 1 M.

A detailed analysis of the implications of these diffusion–reaction equations leads to an equation for the Tafel plot at high buffer concentration (where there is no pH gradient at the film–electrolyte interface):

$$\log j = \log j_0 + \frac{F}{RT\ln 10}\eta, \tag{10}$$

where j_0 is the nominal exchange current density (current density at overpotential, $\eta = 0$). Increasing film thickness increases j_0 in accordance with the following relation:

$$\log j_0 = \log\left[F\frac{C^0}{C^0_{\mathrm{H^+}}} C_{\mathrm{cat}} k_{\mathrm{cat}} d_f^{\mathrm{opt}} \tanh\left(\frac{d_f}{d_f^{\mathrm{opt}}}\right)\right] + \frac{F\left(E_A^{\mathrm{eq}} - E^0_{\mathrm{Q+H^+/PH}}\right)}{RT\ln 10}, \tag{11}$$

with an optimal film thickness defined as

$$d_f^{\mathrm{opt}} = \sqrt{\frac{D_{H,e}}{k_{\mathrm{cat}}}}. \tag{12}$$

C_{cat} represents the total concentration of catalyst active sites and E_A^{eq} is the thermodynamic potential for the reaction catalyzed (OER).

Equations (10)–(12) describe Tafel plots that possess a slope of 59 mV and whose exchange current densities change progressively with film thickness as shown in Fig. 15a. Below an “optimal” film thickness value, d_f^{opt}, the current density response increases in proportion to film thickness, but beyond d_f^{opt} the response displays a plateau. The variation of the exchange current density with the film thickness is shown in Fig. 15b where the maximal value reached by j_0, denoted j_0^{max}, may be expressed by

$$j_0^{\mathrm{max}} = F\frac{C^0}{C^0_{\mathrm{H^+}}} C_{\mathrm{cat}} \sqrt{k_{\mathrm{cat}} D_{H,e}} \exp\left[\frac{F\left(E_A^{\mathrm{eq}} - E^0_{\mathrm{Q+H^+/PH}}\right)}{RT}\right]. \tag{13}$$

This reveals that a high film activity can be achieved by improving the intrinsic activity of the catalyst (increasing k_{cat}) and/or by increasing the film thickness (d_f),

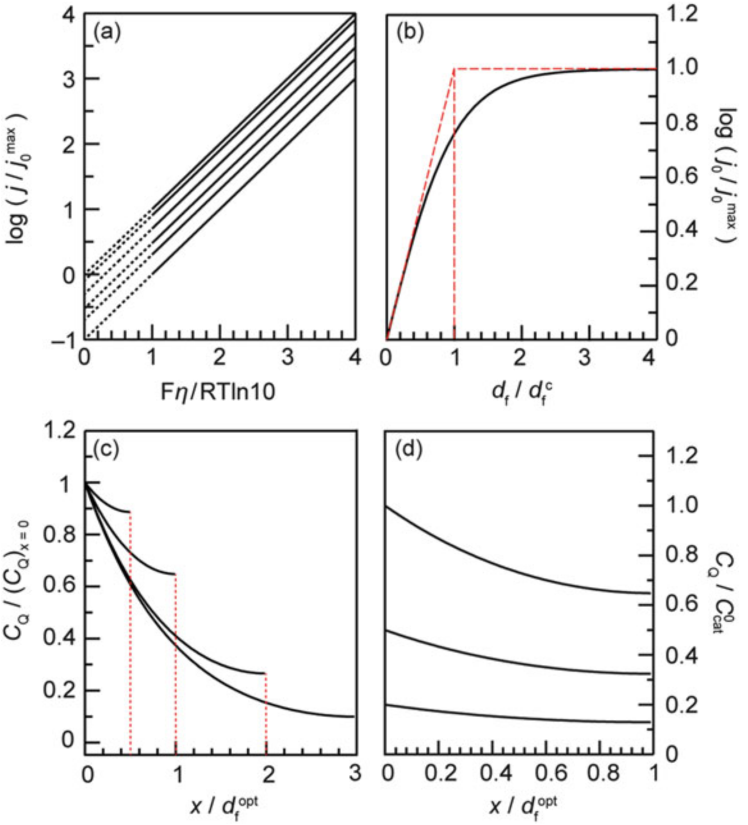

Fig. 15 Electrokinetic profile at large buffer concentrations. (**a**) Tafel plot trends predicted for a series of increasing thicknesses, from *bottom* to *top*. (**b**) Variation of the current density with the film thickness (relative to the optimal film thickness ($d_\mathrm{f}^\mathrm{opt}$), at $\eta = 0$. j_0 and j_0^max are defined in (11)–(13). For $d_\mathrm{f}^\mathrm{opt}$ see (12). (**c**) Concentration profile of oxidized catalyst form, Q (relative to the concentration of Q at the electrode–film interface), in the case of mixed control by the turnover-limiting reaction and the diffusion-like proton–electron hopping under pure kinetic conditions for a series of films with thicknesses equal to 0.5 d_f^opt, d_f^opt, 2 d_f^opt, and 3 d_f^opt. (**d**) Concentration profile of Q (relative to total catalyst concentration in the film) as a function of increasing electrode potential (from *bottom* to *top*) for a film of thickness equal to d_f^opt. Figures adapted from [67]

but only up to a point. Once $d_f \times \sqrt{k_\mathrm{cat}} > \sqrt{D_{H,e}}$, the film activity no longer improves with thickness. A crucial implication is, to the extent that catalyst film development focuses on improving intrinsic activity, one must also address the issue of proton-coupled electron transport (represented by the effective diffusion coefficient, $D_{H,e}$), in order to extract maximal benefit from a more active catalyst.

The underlying reason for the plateau in activity is described by Fig. 15c where the concentration of the oxidized form of the catalyst (Q) is plotted as a function of the distance from the electrode substrate (for films of different thicknesses). Beyond

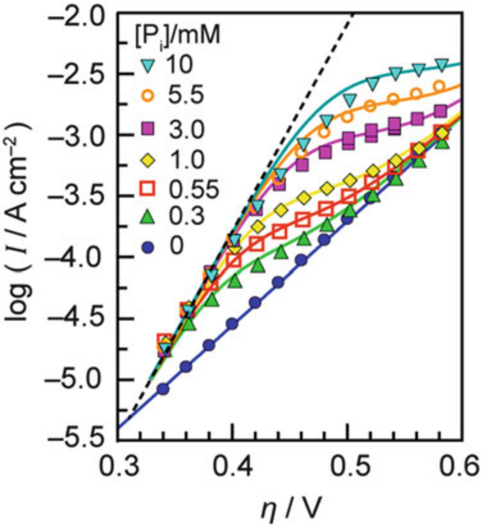

Fig. 16 Tafel plots of a CoP_i film (ca. 200 nm thick) deposited onto a platinum rotating disk electrode and operated at 2,500 rpm in varying concentrations of NaP_i pH 6 with 1 M $NaClO_4$ as supporting electrolyte. The slopes of the straight lines are F/RT ln 10 (*dashed black*) and $F/2RT$ ln 10 (*solid blue*). Adapted from [67]

d_f^{opt} the total integrated concentration of Q over the electrode surface ceases to increase appreciably with film thickness, leading to no net gain in film activity. The role of the actual electrode potential is then only to define the concentration of oxidized catalyst at the immediate film–electrode interface. Increasing the electrode potential shifts the position of the PH/(Q+H^+) equilibrium at the interface. This consequently leads to greater values of C_Q throughout the film (Fig. 15d) and therefore a greater current density (Fig. 15a).

This mechanistic framework was tested against the electrokinetic data acquired over a wide range of buffering conditions (including non-buffered electrolytes) (Fig. 16). We found that the model was fully consistent with proton-coupled electron transport turnover in Co-OEC films. More broadly, these concepts are readily applicable to systems comprising molecular catalysts that are coated onto electrode surfaces [80, 81] or to the increasing number of crystalline oxides that become amorphous and electrochemically porous during turnover [82, 83].

Having discussed the structural and mechanistic basis for the catalytic behavior of these materials, we turn our attention to the fundamental underpinnings of the self-healing behavior of these systems.

5 Catalyst Life Cycle: Growth and Repair

All catalytic systems to our knowledge require the catalyst to be repaired. In deactivation, the catalyst is transformed to an inactive species, which then must be regenerated, usually by a chemical process that lies outside the catalytic cycle.

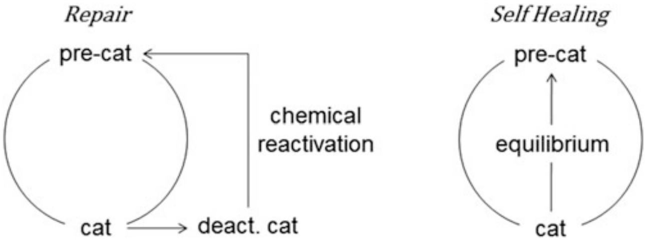

Fig. 17 The difference between a catalyst that is repaired vs self-healing. The CoP_i catalyst is unique among all catalysts in that it is self-healing

The CoP_i catalyst is self-healing, i.e., the catalyst may be regenerated by an equilibrium within the catalytic cycle. These two processes are compared in Fig. 17.

Self-healing in CoP_i is established from the interplay of the potential at which OER occurs vs the potential at which the catalyst nucleates and grows. Accordingly, the kinetics of the oxidative self-assembly process are critical to developing a coherent picture of the full life cycle of the catalyst from nucleation to dissolution and, ultimately, self-repair. Mechanistic insights into catalyst formation are now discussed.

The separation in potentials between water oxidation and catalyst formation [35, 37] (Sect. 2) were exploited to isolate the kinetics for the latter [53]. Chronoamperograms (Fig. 18) with step potentials spanning the initial rising portion of the anodic pre-feature wave discussed in Sect. 2 revealed that the deposition process is not merely a diffusion-controlled oxidation of Co^{2+} ions. The initial decay in current immediately after the potential step is followed by a rise in current produced by the formation of catalyst nuclei on the surface [84] which, in effect, increases the surface area of the electrode. Quasi three-dimensional growth of these catalyst particles gives rise to a rapid increase in current until the reactant-depleted diffusion zones surrounding each growing catalyst particle begin to overlap, causing the onset of semi-infinite linear diffusion and an associated $t^{-1/2}$ decay of the current [85]. Importantly, the step potential has a marked impact on the time, $t_{\max}$, and current density, $j_{\max}$, at which the chronoamperogram exhibits its characteristic peak. These characteristic features established that Co-OEC formation occurs via nucleation, followed by diffusion-limited growth [53].

Examination of the chronoamperometric transients indicated that the nucleated growth process was characterized by progressive nucleation, as opposed to instantaneous nucleation. In the instantaneous case, all potential nucleation sites, N_0, on the surface are assumed to give rise to nuclei at time zero following the potential step. In contrast, for progressive nucleation the number of occupied nucleation sites, N, increases with time, leading to a nucleation rate defined by [86]

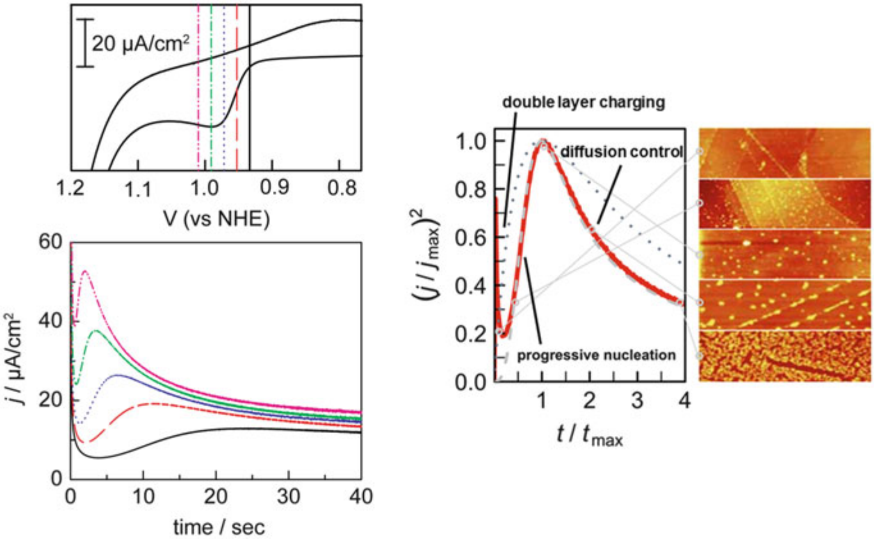

Fig. 18 *Top left*: Cyclic voltammogram (scan rate = 5 mV/s) and (*bottom left*) potential step chronoamperograms of a freshly polished glassy carbon disk electrode in 0.4 mM Co^{2+}, and 0.02 M MeP_i, 1.97 M KNO_3 electrolyte at pH 7.5. Chronoamperometry data recorded with a step voltage of 1.01 (*magenta*, *dot-dashed line*), 0.99 (*green*, *dot-dashed line*), 0.97 (*blue*, *dotted line*), 0.95 (*red*, *dashed line*), and 0.93 V (*black*, *solid line*) following a 100-s pulse at 0.75 V (not shown). Step voltages used to collect chronoamperograms are indicted with vertical lines overlaid on the CV trace. *Right*: Comparison of simulated nucleation transients (*gray dashed line*) with the experimental data (*red line*) modeled by (14) for a progressive growth mechanism with $n = 4$. The *dotted line* is the predicted growth curve for an instantaneous nucleation growth mechanism. Atomic force microscopy (AFM) images of Co-OEC on the electrode surface are shown for various points along the experimental curve. Adapted from [53]

$$\frac{\partial N}{\partial t} = k_N \left(\frac{c}{c_0}\right)^n (N_0 - N), \tag{14}$$

where k_N is the nucleation rate constant, and the term $N_0 - N$ represents the number of unoccupied nucleation sites on the electrode surface. In (14), c and c_0 represent the local and bulk concentrations of all solution species upon which the nucleation rate depends, with the exponent, n, characterizing the overall reaction order. Comparison of simulated nucleation transients with the experimental data indicated that Co-OEC nucleation was best modeled by an $n = 4$ curve (Fig. 18), highlighting the complexity of the initial catalyst formation process relative to simple metal deposition/plating.

Atomic force microscopy (AFM) imaging of Co-OEC early on during deposition on highly-ordered pyrolytic graphite (HOPG) was also explored to study catalyst formation (Figs. 18 and 19) [53]. The number of nuclei was observed to increase dramatically at times between 0.2 and $1 \times t_{\max}$, after which relatively few new nuclei are formed. Instead, the already formed nuclei grow and coalesce to coat a

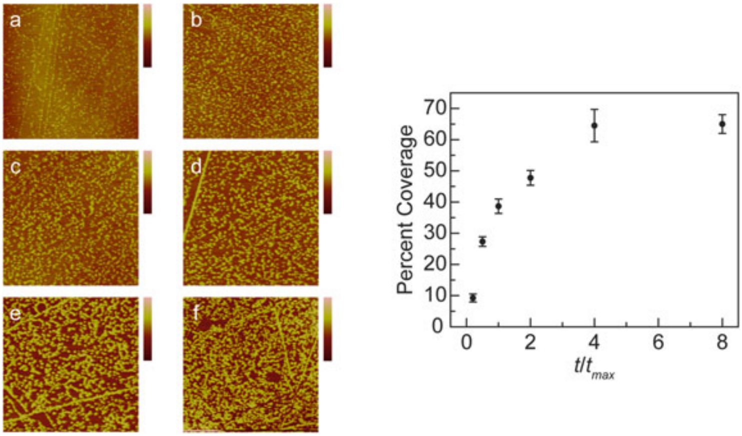

Fig. 19 *Left*: Representative 5 × 5 μm^2 AFM images of a highly oriented pyrolytic graphite electrode after being subjected to potential step polarization from 0.75 to 0.97 V for (**a**) 0.2, (**b**) 0.5, (**c**) 1, (**d**) 2, (**e**) 4, and (**f**) 8 × $t_{\max}$ (~10 s). *Bars* to the right of each image indicate the depth with full scale values of (**a**) 20, (**b**) 30, (**c**) 50, (**d**) 75, (**e**) 75, and (**f**) 50 nm. Electrolyte conditions: 0.4 mM Co^{2+} and 0.02 M MeP_i, 1.97 M KNO_3 electrolyte at pH 7.5 (2 M ionic strength). *Right*: Plot displays coverage percentage of catalyst vs the normalized duration of potential step polarization, $t/t_{\max}$. Reproduced from [53]

greater proportion of the surface between 1 and 4 × $t_{\max}$. Besides confirming the progressive nature of catalyst nucleation, these AFM studies highlight a convenient method for patterning semiconductor surfaces with catalyst islands. The appropriate choice of (photo)potential would enable modulation of the $t_{\max}$ parameter for any desired surface, and controlling the deposition time relative to this $t_{\max}$ would permit control over the coverage of the catalyst islands on the conducting or semiconducting surface. More recently, a high throughput, scalable, and low cost method for patterning periodic sub-micron structures of CoP_i over large areas of silicon has been developed, called reactive interface patterning promoted by lithographic electrochemistry (RIPPLE) [87]. Through an interplay of electrochemical and hydrodynamic effects, the RIPPLE method allows for catalyst to be deposited with tunable and high spatial resolution using cyclic voltammetry; the number of patterns scales with N–1 CV scans. In addition to planar substrates, three-dimensional surfaces and their vertical sidewalls may be patterned. Patterns of sufficient fidelity are realized that optical light control may also be achieved [88].

Activation-controlled current densities for steady state catalyst growth were determined as a function of the applied potential by extrapolating current densities measured at variable rotation rates on a rotating disk electrode (RDE) to infinite rotation speed (Fig. 20a). Tafel plots of steady state catalyst deposition displayed a Tafel slope of 60 mV/decade (Fig. 20b) [53]. The observed 60 mV/decade slope implies a catalyst assembly mechanism involving a one-electron reversible equilibrium preceding a chemical rate-limiting step for catalyst formation [60].

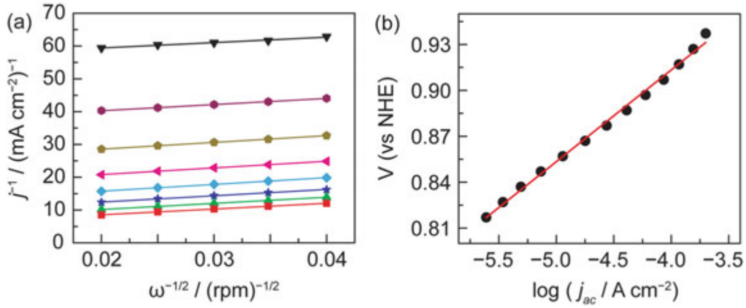

Fig. 20 (**a**) Koutecký–Levich plots Co-OEC catalyst film formation from 0.4 mM Co^{2+}, 0.02 M MeP_i, 1.97 M KNO_3 electrolyte, pH 7.5 at applied potentials of (from *top* to *bottom*) 0.87, 0.88, 0.89, 0.90, 0.91, 0.92, 0.93, and 0.94 V. (**b**) Tafel plot of Co-OEC catalyst film formation from 0.4 mM Co^{2+}, 0.02 M MeP_i, 1.97 M KNO_3 electrolyte, pH 7.5 onto a Pt rotating disk electrode. Activation controlled current density values (j_{ac}) were derived from Koutecký–Levich analysis of plots in (**a**). The Tafel slope is 60 mV/decade. Reproduced from [53]

Additional electrokinetic data was acquired as a function of Co^{2+} concentration, pH, and buffer (methyl phosphonate, MeP_i) concentration. In each case, Tafel plots relating potential to the activation-controlled current density were obtained over the range of electrolyte conditions. Interpolation of these plots permitted determination of the respective reaction orders in Co^{2+} concentration, proton activity, and buffer concentration [53]. These studies uncovered a first-order dependence on Co^{2+} concentration, indicating the reversible one-electron equilibrium defined by the 60 mV/decade Tafel slope involves one Co^{2+} ion, thereby excluding the possibility of multi-nuclear solution species participating in the one-electron equilibrium in question. It was also observed that the rate of deposition possesses an inverse third-order dependence on proton activity. This result suggested that the coupling of three proton transfers to the single cobalt one-electron transfer is what permits access to Co^{3+} at these low potentials. The high degree of proton coupling in the oxidation of the Co^{2+} precursor implicates a critical role for the MeP_i buffering species. Notwithstanding its role as a PCET proton acceptor, MeP_i may coordinate to Co centers in a conflicting inhibitory role. Interestingly, an inverse second-order dependence in MeP_i is observed for buffer concentrations in excess of ~30 mM. At intermediate buffer strengths, an inverse first-order dependence in MeP_i is found, and below 2 mM MeP_i, a plateau is observed implying that, at these concentrations, MeP_i is no longer explicitly represented in the rate law for electrodeposition. On the basis of Co^{2+}/MeP_i binding calculations, one half of the second-order behavior was explained as caused by coordination of the buffer to dissolved Co^{2+}, whereas the underlying first-order behavior, was attributed to buffering species that were bound to clusters of the growing catalyst film. Thus, it was proposed that equilibrium dissociation of buffering species from the surface was a critical prerequisite for incorporation of newly oxidized Co centers. These findings are summarized in the electrochemical rate law for catalyst formation [53]:

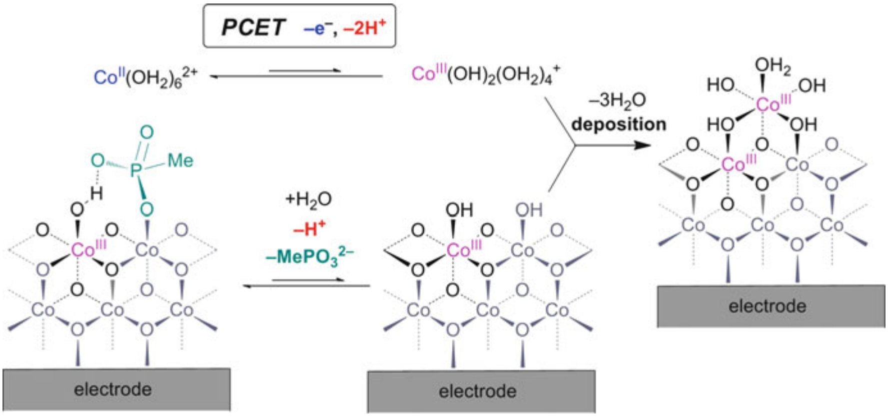

Fig. 21 Proposed mechanism of Co-OEC catalyst film formation. Adapted from [53]

$$v = k_0^{\mathrm{de\,p}}\left[\mathrm{Co}^{2+}\right](a_{\mathrm{H}^+})^{-3}[\mathrm{MeP_i}]^{-1}\exp\left[\frac{FE}{RT}\right], \tag{15}$$

where k_0^{dep} is a potential-independent constant which is proportional to the exchange current density for the electrodeposition process.

Within the framework of the Co-OEC structural model discussed in Sect. 3, it was proposed that growth of the MCCs, and thus of the catalyst film itself, proceeds via attachment of new Co fragments to the exposed edges of these clusters. The proposed mechanistic model for Co-OEC film growth is shown in Fig. 21 [53]. A portion of the expanding cobaltate cluster is shown to present the surface active sites from which growth is proposed to occur. In this mechanistic model, surface and solution phase reactions exist in equilibrium prior to the rate-limiting phase transfer of Co to the growing catalyst surface. The exposed edge sites were proposed to be directly coordinated to MeP_i buffering species in the resting state. Further studies on model complexes (Sect. 6) suggest that the mode of inhibition by MeP_i may more likely involve H-bonding to the surface of the clusters. Thus, the $\mathrm{Co(OH_2)_6}^{2+}$ solution precursor is proposed to undergo a one electron-proton minor equilibrium PCET reaction to form a $\mathrm{Co(OH)_2(OH_2)_4}^+$ intermediate. Simultaneously, a surface equilibrium involving $\mathrm{MePO_3}^{2-}$ dissociation and deprotonation of a surface aquo species takes place. This heterogeneous equilibrium forms a surface intermediate poised for rate-limiting binding of the solution-based Co $\mathrm{(OH)_2(OH_2)_4}^+$ intermediate to effect catalyst growth by one Co center [53].

The above mechanistic insights into catalyst formation are critical for explaining the self-repair process of Co-OEC films. We had shown previously through ^{57}Co radiolabeling of CoP_i films that, when held at open circuit, cobalt slowly leached out of films into bulk solution. Yet upon application of a potential bias sufficient to trigger O_2 evolution, Co was taken up from solution and redeposited on the catalyst

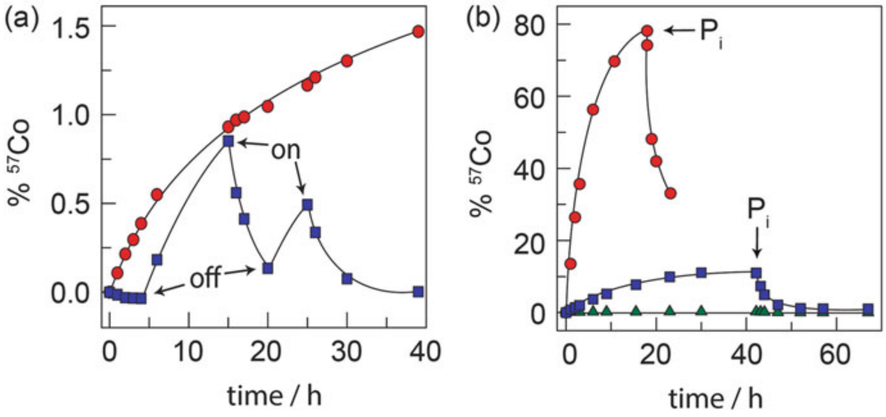

Fig. 22 (**a**) Percentage of ^{57}Co leached from a CoP_i catalyst film on an electrode: with a potential bias of 1.3 V (NHE) (*blue squares*) turned on and off at the times designated and held at open circuit potential (*red circles*). (**b**) Percentage of ^{57}Co leached from Co-X (where X is a non-buffering electrolyte such as SO_4^{2-} or NO_3^{-}) films on an electrode under a potential bias of 1.3 V (*red circles*) and 1.5 V (*blue squares*) (NHE) and held at open circuit potential (*green triangles*). Phosphate was added at the time points indicated by the *arrows*. Adapted from [89]

film (Fig. 22a) [89]. Moreover, it was shown that phosphate was a critical ingredient to enabling this self-healing capacity (Fig. 22b) [89].

The mechanistic basis for Co-OEC self-healing is shown in Fig. 23a. The electrodeposition process displays an inverse third-order dependence on proton activity (see (5)) [53] compared to the inverse first-order dependence on proton activity found for the OER mediated by Co-OEC [59] (see (4) and (11)). Thus, as the pH is lowered, the potential necessary for catalyst formation increases much faster than the corresponding rise in potential required for water oxidation catalysis as shown in Fig. 23a. Extrapolation of the kinetic profile for catalyst assembly reveals a crossover point at ca. pH 5.2. This self-healing behavior arises because, at pH > 5.2, the potentials necessary to sustain catalyst film formation and growth are well below the potentials required for water oxidation catalysis. Thus, upon application of a potential sufficient to generate O_2, ample driving force exists to redeposit any Co^{2+} in solution that may have leached from the film in between catalyst operation cycles. This repair process is only possible in the presence of a good proton acceptor such as P_i, B_i, or MeP_i because these buffers not only maintain a stable local pH at the electrode in order to prevent local acidification that can trigger film dissolution, but they are also crucial for permitting the high degree of proton coupling inherent in the oxidative deposition process itself (see (15)) [53].

Direct measurement of catalyst corrosion agrees with the results of Fig. 23a. Whereas no dissolution is observed in pH > 6 P_i electrolyte under an applied bias, catalyst corrosion is observed at pH 5 and below, even in the presence of P_i and under anodic polarization [53]. This predicted dependence of the pH regime of catalyst stability on Co^{2+} concentration (Fig. 23b) is in line with the observation in the literature that adding 1 mM Co^{2+} to the electrolyte solution during catalyst

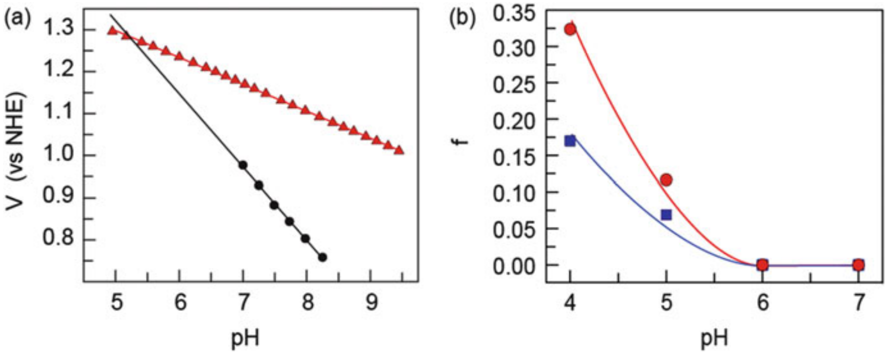

Fig. 23 (**a**) pH dependence of the potential for catalyst film formation (*black filled circle*) and oxygen evolution (*red-filled square*) at $j_{ac} = 30\ \mu A/cm^2$. (**b**)Fraction (f) of catalyst film dissolved after 1 h vs pH for electrodes poised at 1 (*blue-filled square*) and 0 (*red-filled square*) mA/cm^2 in 0.04 M Britton−Robinson buffer. *Lines* are presented to guide the eye. Adapted from [53]

operation for oxygen evolution was critical to maintain functional stability at pH 3.7 [57, 90]. The much lower potentials required for Co-OEC deposition in buffered electrolytes at intermediate pH, relative to those required for O_2 evolution also provide an explanation for the observation that some molecular compounds that are designed to be water oxidation catalysts form oxidic films upon decomposition of the precursor compound [91–94]. This issue is discussed in further detail in the next section. As we discuss below, it is critical that ligand scaffolds targeted for homogeneous water oxidation catalysts both preclude the dissociation of free Co ions into solution and maintain their integrity under the highly oxidizing conditions during the OER.

6 Molecular Cobalt Complexes as Models for Co-OEC

Unlike the amorphous solids of Co-OECs, where structure at the most precise atomistic level is undetermined, inorganic molecular complexes may be structurally characterized precisely using X-ray diffraction. Accordingly, we turned our attention to the use of multinuclear cobalt molecules, especially those with oxidic ligands (O^{2-}, OH^{-}, and OH_2), as models for the Co-OEC. We sought to use spectroscopic handles of multinuclear molecular cobalt complexes to provide direct comparisons to Co-OEC. For example, in Sect. 3.2 it was shown how EPR studies on the molecular cobalt cubane $Co_4O_4(OAc)_4(py)_4^+$ provided evidence that the EPR signal that arises from Co-OEC at anodic potentials is produced by a delocalized Co^{IV} valency.

Following in this theme, this section is organized to provide an overview of our research efforts in this area of cobalt model complexes. The aim is not to provide a review of the molecular water oxidation catalysts, cobalt-containing or otherwise, but to highlight the results obtained from studying molecules that have refined our thinking with regard to the mechanisms germane to the activity of Co-OEC.

6.1 Co_4O_4 Cubanes Model Complexes: Co(III)/Co(IV) Self-Exchange and Film Conductivity

The Co_4O_4 cubanes have proven to be very useful models of the Co-OEC. A number of molecules in this class have been reported, and they are distinguished by the ligands, such as pyridines, bipyridines, acetates, or benzoates, which stabilize the metal-oxo core [95–100]. The $Co_4O_4(OAc)_4(py)_4$ cubane, **1**, and the derivatives thereof, first synthesized by Das and coworkers [95], were not only shown to be useful for EPR studies, but have also been explored as discrete water oxidation catalysts [101–103]. Though some evidence of electrochemical water oxidation was presented in these studies, the primary mode of characterization of the water oxidation activity was through the use of a photochemical assay, utilizing $Ru(bpy)_3^{2+}$/persulfate as the photosensitizer/sacrificial oxidant. Because two oxidizing species (i.e., $Ru(bpy)_3^{3+}$ and $SO_4^{-\bullet}$) are created following the absorption of a photon, it is difficult to draw mechanistic conclusions from this photochemical assay as the driving force is not well defined. Therefore, we decided to explore the mechanism by electrochemical methods, which permit precise control over the electrode potential, and thus the driving force of the reaction.

It was discovered during these studies that the reported oxygen evolution activity could not be reproduced. Further investigation revealed that the earlier reports had used samples of **1** that had not been purified by silica gel chromatography, which was found to be essential for removing Co^{II} impurities from the as-synthesized material [104]. The Co^{II} impurity was found to be a precursor to the formation of the active catalyst, Co-OEC. Figure 24 shows a comparison of the electrochemical and photochemical responses of purified and crude samples of **1**. In both experiments, the oxygen evolution activity decreases significantly once the impurity is removed.

The lack of significant water oxidation activity for **1** suggests the need for a solvent accessible coordination site on the periphery of the metal cluster. For the Co-OECs, the edge sites of the cobaltate clusters provide these points of access and are the likely active sites for catalysis. However, because the metal ligand bonds in the oxidized cubane $\mathbf{1}^+$ are inert because of the low-spin electronic structure of the Co^{III} and Co^{IV} atoms, the complex is resistant to protonolysis and hydrolysis. This leads to a stable molecule, but the peripherally coordinated ligands present a barrier to the formation of Co^{IV}–O intermediate, which is presumably a key catalytic intermediate. Further research is needed to develop novel ligand architectures that can stabilize a Co_4O_4 core and at the same time provide open coordination sites for water or hydroxide ligands capable of participating in redox-leveling PCET events.

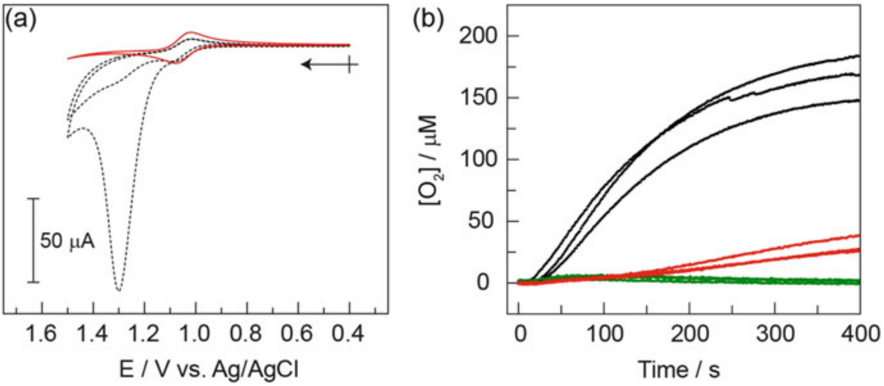

Fig. 24 (**a**) Background corrected CVs of crude (*black-dashed line*) and purified (*red-solid line*) samples of **1** (0.852 mg/mL) in 0.2 M KP_i buffer, pH 7. (**b**) Solution [O_2] measurements during illumination of (*black-solid line*) crude and (*red-solid line*) purified samples of **1** (0.33 mM), and (*green-solid line*) without added **1**. Photochemical reactions were performed in the presence of 0.5 mM $Ru(bpy)_3^{2+}$, 35 mM $Na_2S_2O_8$, and 100 mM KP_i pH 7 buffer. Adapted from [104]

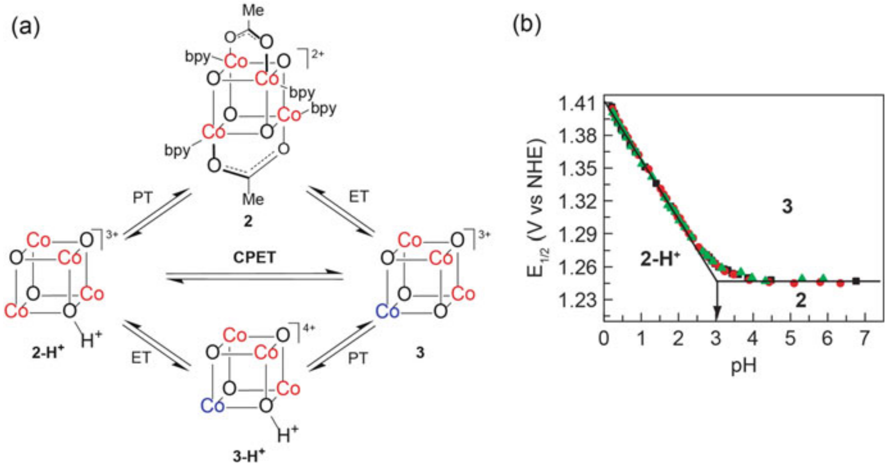

Fig. 25 (**a**) PCET square scheme for the oxidation of the molecular model cubane, **2**-**H**$^+$. Though the hole in the oxidized cubane is delocalized, we depict the Co^{IV} centers (*blue*) and Co^{III} centers (*red*) solely for illustrative purposes. For clarity, the ligands are not depicted for **2**-**H**$^+$, **3**, and **3**-**H**$^+$. (**b**) Pourbaix diagram of cubane **2** constructed from CV scans at 0.1 V s^{-1}. The *green*, *red*, and *black dots* correspond to three separate sets of data. Labels depicted the zones of thermodynamic stability for **2**, **2**-**H**$^+$, and **3**. Adapted from [105]

The Co_4O_4 core has provided a platform for the study of the PCET properties associated with charge transfer through the films. The molecule $Co_4O_4(OAc)_2(bpy)_4^{2+}$, **2**, first synthesized by Christou and coworkers [97], also contains a Co_4O_4 core, but differs in overall charge from the cubane of Das, **1**, because of the replacement of two acetate ligands by neutral bipyridines (Fig. 25a).

Cubane **2** exhibits a reversible $Co^{IV}Co^{III}_3/Co^{III}_4$ couple with an $E_{1/2} = 1.25$ V vs NHE at pH > 4. Below pH 4, the $E_{1/2}$ value becomes progressively more positive, exhibiting a slope of –55 mV/pH unit at pH < 2 (Fig. 25b). The electrochemical response in the low pH region of the Pourbaix diagram is indicative of a one-electron, one-proton transfer of a protonated species, **2-H**$^+$, with a p$K_a = 3.1$, to a deprotonated, oxidized cubane, **3**. Because a second plateau region was not observed at high potentials, the pK_a of the protonated form of **3** must be pH < 0.

As charge transport through Co-OEC films is thought to proceed via electron and proton hopping between Co^{III}–OH to Co^{IV}–O species (Sect. 4.2), we sought to isolate the kinetics of this PCET event by interrogating the mechanism by which **2-H**$^+$ is converted to **3** [105]. We were interested in comparing the bidirectional reaction, in which the electron and proton are transferred to separate chemical species, to the unidirectional reaction, in which they are transferred to the same species. By varying the scan rate in cyclic voltammogram experiments, the heterogeneous ET rate constant was extracted by comparing the simulated CV overlaid with the experimental data. Using this method, it was found that the rate constant for the PCET reaction at pH 1 was $k_{\mathrm{PCET}} = 0.17$ cm s^{-1}, an order of magnitude smaller than the simple ET rate constant measured at pH 4, $k_{\mathrm{ET}} = 2$ cm s^{-1}. The lack of an observable kinetic isotope effect (KIE) at pD = 1 indicated that the PCET reaction at the electrode surface is stepwise, proceeding by an equilibrium proton transfer followed by a rate-limiting electron transfer (PTET). This stepwise pathway was also found to be manifested in the bidirectional PCET reaction between $[Ru(bpy)_3]^{2+}$ and **3** at pH or pD = 1. In this homogeneous reaction, **3** was reduced to **2-H**$^+$ by $[Ru(bpy)_3]^{2+}$ with a driving force of ~100 mV. Stopped-flow kinetic measurements resulted in near identical second-order rate constants (~1×10^6 M^{-1} s^{-1}) in H_2O and D_2O. As in the heterogeneous reaction, the lack of an observable KIE indicated a stepwise PTET mechanism.

The unidirectional PCET self-exchange reaction between **3** and **2-H**$^+$ was interrogated further using NMR line broadening analysis. The rate constant for this reaction at pH 1, $k_{\mathrm{SE1}} = 5.6 \times 10^4$ M^{-1} s^{-1}, was found to be only a factor of ~5 slower than the simple self-exchange ET reaction at pH 4, $k_{\mathrm{SE4}} = 3.0 \times 10^5$ M^{-1} s^{-1}. As a comparison, the expected rate constant at pH 1 for the stepwise self-exchange PTET reaction constant can be calculated using k_{SE4} and the acid dissociation constant of **2-H**$^+$ according to

$$k_{\mathrm{SE1}} = k_{\mathrm{SE4}} \frac{K_a}{[\mathrm{H}^+]} = 3.0 \times 10^5\ \mathrm{M}^{-1}\ \mathrm{s}^{-1} \frac{10^{-3.1}\mathrm{M}}{10^{-1}\mathrm{M}} = 2400\ \mathrm{M}^{-1}\ \mathrm{s}^{-1}. \qquad (16)$$

Because the calculated rate constant is less than one twentieth of the experimentally determined value, a concerted proton-electron transfer, CPET, mechanism is implicated for this unidirectional PCET event. This supposition was confirmed by the measurement of a significant KIE = 4.3 for the self-exchange reaction at pH 1, which suggests that proton tunneling is involved in the rate-limiting step. Taken together, these results indicate that the unidirectional pathway provides an activation barrier significantly lower in energy than the intermediates of the stepwise reactions.

The $Co^{III/IV}$ self-exchange reaction is directly relevant to Co-OEC catalysis. During OER, the catalyst is poised at a potential to maintain the Co^{IV} oxidation state. Hole propagation through the film may occur by self-exchange with Co^{III}. In this way the oxidizing hole equivalents may move from the electrode surface through the film. The fairly high self-exchange $Co^{III/IV}$ rate constant measured for the cubane indicates that the Co-OEC film may be sufficiently conductive by a hole hopping mechanism.

6.2 Co_7 Clusters: Co^{II}-Co^{III} Self-Exchange and Co-OEC Deposition

Co-OEC deposition and growth is driven by the oxidation of aqueous Co^{2+} to Co^{3+}. When considering the mechanism of how this oxidation is coupled to deposition, we were confronted by the unresolved issue regarding the anomalously high observed self-exchange rate constant for the $Co(OH_2)_6^{3+/2+}$ couple [106, 107]. Because of the low-spin to high-spin transformation that takes place when $Co(OH_2)_6^{3+}$ is reduced to $Co(OH_2)_6^{2+}$, a large (~0.2 Å) change in inner-sphere bond lengths is observed. Consequently, Marcus theory predicts a very slow self-exchange rate constant for this reaction. However, experiment does not bear this out, as a k_{SE} of 5 M^{-1} s^{-1} has been measured [108], which is six orders of magnitude higher than predicted by theory [109].

We sought to address this issue by interrogating this redox couple in the context of a relevant molecular framework [110]. Such a framework is afforded by a heptanuclear cluster, **4**, shown in Fig. 26. The heptanuclear core of this molecule closely resembles the minimal cobaltate cluster unit of the Co-OEC, as determined from EXAFS studies on thin films (Fig. 5a).

Complex **4** has, as have a number of heptanuclear cobalt clusters, previously been synthesized as a potential single-molecular magnet, [111, 112]. Cluster **4** is distinguished from other known clusters by the μ_3-OH bridging units surrounding the central cobalt atom. This oxidic ligand environment is precisely that of Co-OEC and additionally provides a similar ligand field stabilization for the central cobalt atom as is found for cobalt hexaaqua complexes. Chemical oxidation of **4** with 1 equiv. of Ag^+ leads to an oxidized complex, **5**, which was structurally characterized using X-ray diffraction. Bond distance analysis in conjunction with magnetic measurements confirmed that the central cobalt's oxidation state was Co^{III} with a low-spin electronic configuration. The crystal structure also revealed hydrogen bond interactions between the triflate anions and the protons of the μ_3-OH ligands (Fig. 26), and NMR measurements established that this interaction was strong enough with **5**, but not **4**, to be maintained in solution.

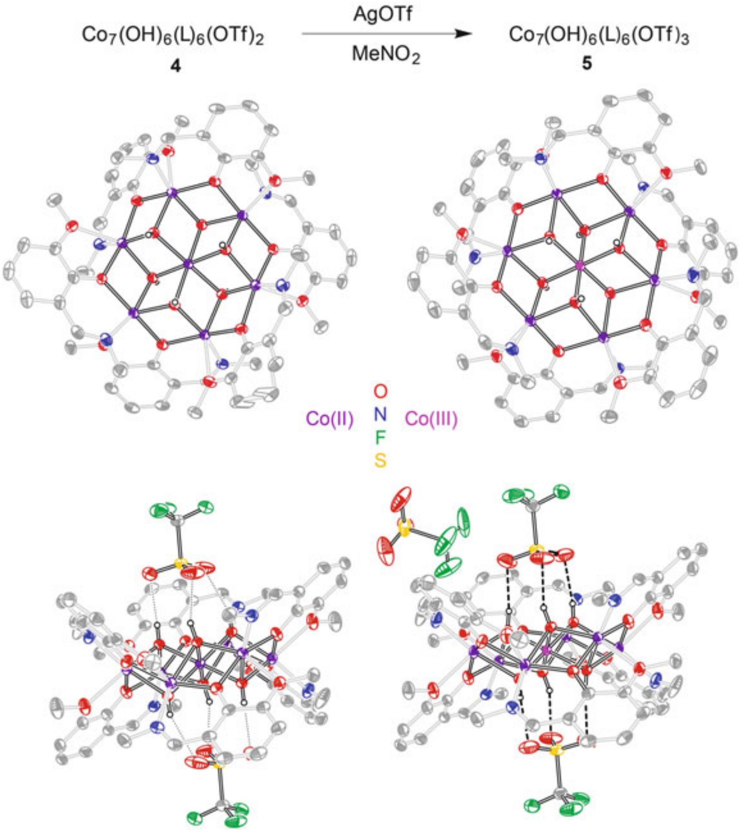

Fig. 26 *Top*: Synthetic scheme for the oxidation of **4** to **5**. *Middle*: Top down view of co-crystallized (*left*) **4** and (*right*) **5** with anions removed for clarity. *Bottom*: Side-on view of co-crystallized (*left*) **4** and (*right*) **5** with triflate anions shown. Adapted from [110]

The kinetics of the self-exchange electron transfer (ET) between **4** and **5** were measured using an isotope scrambling experiment. The second-order rate constant was found to be 1.53×10^{-3} M^{-1} s^{-1} at 40°C and to depend inversely on triflate concentration. This observation defined a mechanism for the self-exchange which involved an equilibrium dissociation of a hydrogen-bonded anion from **5** prior to rate-determining electron transfer (Fig. 27).

The slow observed rate constant is important in the context of the anomalous self-exchange rate constant for $Co(OH_2)_6^{3+/2+}$ electron transfer. For the $Co(OH_2)_6^{3+/2+}$ self-exchange reaction, an inner-sphere ET mechanism involving a water bridge was hypothesized to account for the fast rate of electron exchange. Because the two exchanging cobalt atoms, at the center of the clusters in **4** and **5**, are shielded from each other by the surrounding cobalt atoms and ligands, an inner sphere ET between these centers is precluded. Because a slow self-exchange ET rate constant was measured in this model study – consistent with the large bond

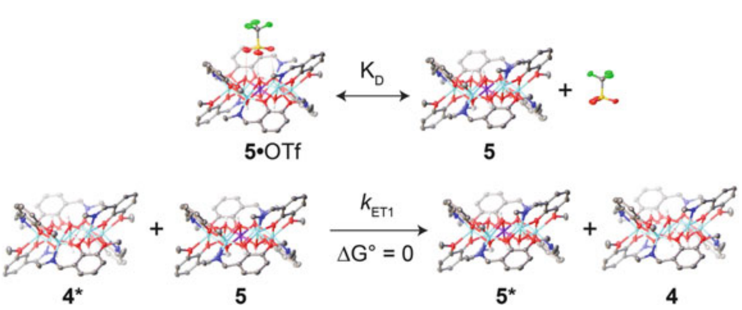

Fig. 27 Electron transfer scheme for the self-exchange reaction between model clusters **4** and **5**. K_D is the dissociation constant of the hydrogen bonded triflate anion from the oxidized cluster, **5**. The *asterisks* signify the isotopic label used to monitor the exchange reaction. Adapted from [110]

distance changes associated with a low-spin Co^{III} to high-spin Co^{II} transformation – it was concluded that an inner-sphere water bridge mechanism can account for the anomalous k_{SE} for the $Co(OH_2)_6^{3+/2+}$ exchange reaction.

Taken together, these results, in combination with others discussed above, have led to a new proposed mechanism of Co-OEC deposition. The original proposed mechanism, shown in Fig. 21, is consistent with the experimental rate law (15), which is distinguished by an inverse dependence on the $MePO_3^{2-}$ anion and a potential-dependent equilibrium ET. However, in an initial analysis, it was proposed that the $MePO_3^{2-}$ anion was bound as an inner-sphere ligand to a surface exposed Co^{III}. It is known that ligand substitution at Co^{III} atoms is usually slow because of the inert nature of d^6, low spin complexes, and therefore it is unlikely that this type of bond cleavage could exist in a fast equilibrium step. A more plausible explanation for the equilibrium dissociation of the buffer anion, which is consistent with the model studies above, involves a hydrogen-bonded $MePO_3^{2-}$ species, which rapidly associates and dissociates with surface edge site of the Co-OEC. Once the anion dissociates, a site is opened for solution-based Co^{2+} to bind before subsequent oxidation to Co^{III}.

The precise mechanism by which Co^{II} is oxidized to Co^{III} during steady state film growth can now also be re-evaluated. Based on the studies described in Sect. 4.2, it is now known that ET occurs by hole hopping through the film. This is in contrast to the initial proposal, which involved an ET from Co^{II} in solution directly to the underlying electrode. Moreover, a film-mediated ET mechanism is implicated because film growth proceeds efficiently even when the thickness of the film exceeds length scales that could allow electrons to tunnel from the solution directly to the electrode (i.e., 5–10 nm). The issue then becomes what is the nature of the ET process that supports catalyst deposition.

The EPR studies on the Co-OEC films demonstrated that at 1.03 V (vs NHE) a signal for Co^{IV} can be observed (Fig. 8a). This potential is only 100–200 mV more positive than the potential region investigated by Tafel analysis for the deposition mechanism (Fig. 20b). Therefore, these data suggest that the minor equilibrium ET leads to the oxidation of the Co^{III} film to a minor Co^{IV} species – the same species as

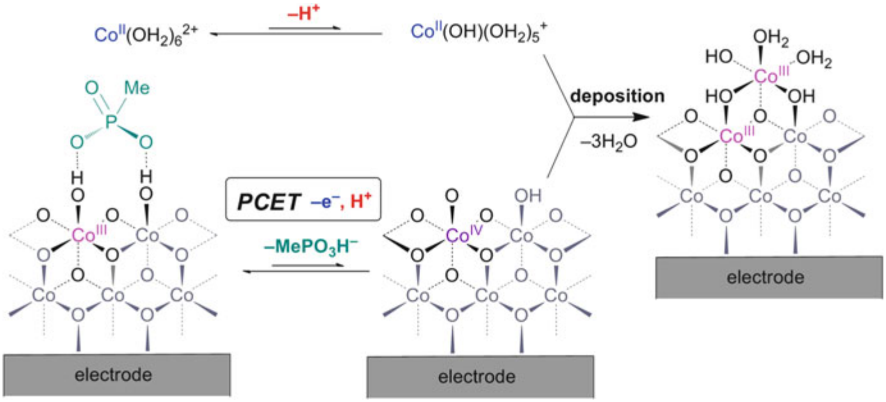

Fig. 28 New proposed mechanism of Co-OEC film formation

the resting state of the Co-OEC catalyst during catalytic turnover – which then "diffuses" to the surface of film in a series of self-exchange ET events. The diffusion process is analogous to the one described in Sect. 4.2 for the catalytic intermediate Co_2^{IV} form of the catalyst (Fig. 14), but instead involves a lower oxidation state of the film. Because the hopping mechanism can be thought of as a PCET self-exchange reaction between small domains in the Co-OEC films, $Co^{III/IV}$ self-exchange studies with molecular model complexes, such as the cubanes, **2-H**$^+$ and **3**, offer helpful insights. Studies of these Co_4 cubanes showed that the $Co^{III/IV}$ CPET self-exchange reaction is indeed rapid (possessing a rate constant on the order of 10^5 M^{-1} s^{-1}) and revealed that intrafilm $Co^{III/IV}$ hole hopping can indeed sustain the facile film growth. As a point of comparison, an exchange reaction between Co^{II} and Co^{III} in an oxidic ligand field (as in the case of the Co_7 compounds **4** and **5**) is eight orders of magnitude slower (~10^{-3} M^{-1} s^{-1}).

A revised model for the mechanism of Co-OEC growth is presented in Fig. 28. The dissociation of a hydrogen-bonded $MePO_3^{2-}$ is coupled to proton loss from the film. This increases the electron-donating ability of the inner-sphere hydroxide ligands, which in turn makes the surface-exposed Co^{III} species more susceptible to oxidation. The oxidation of the exposed Co^{III} to Co^{IV} is coupled to a deprotonation in a PCET event, and, in solution, a $Co(OH_2)_6^{2+}$ species is in minor equilibrium with its deprotonated form, $Co(OH)(OH_2)_5^+$. Following the interaction of the solution species with the surface of the film, likely through an inner-sphere bridging species, a comproportionation of the Co^{IV} and Co^{II} species into two Co^{III} species leads to the growth of the film by one cobalt atom. The rate-determining chemical step is likely the inner-sphere ET comproportionation. This is predicted to be a slow event because a Co^{II} species is being oxidized to Co^{III}, leading to large changes in bond lengths. Importantly, because this ET does not involve the electrode directly, its influence on the Tafel slope is indistinguishable from a "chemical" step, which is usually considered to involve the formation or cleavage of chemical bonds.

7 Outlook

The electrodeposition and OER catalysis of molecular cobaltate clusters may be established by self-assembly from solution. They are comprised of disordered Co–O clusters with sizes within the molecular to nanoscale range. The Co-OECs are the first self-healing catalysts of any type and they function at neutral pH. Catalysis occurs at active sites throughout the porous films and as a result proton-electron transport is a crucial determinant of the overall activity of these materials. A mixed valence $Co^{III/IV}$ resting state is revealed from spectroscopic studies and Co^{IV} intermediates are implicated in the catalytic cycle. Molecular model compounds have shed light on the kinetics of proton-coupled self-exchange reactions within the film as well as the buffer-binding process at electrolyte-exposed sites. The interaction of buffer oxoanions with the edges of the clusters during growth appears to be the basis for the electrolyte-dependent domain sizes observed in these materials. As such, these systems may be ideal for the exploration of redox leveling in electrocatalysis. Yet this requires the elucidation of precisely how deposition conditions direct catalyst structure. The exact details of the rate-limiting step (possibly O–O bond formation) are yet to be revealed, and additional isotopic labeling studies are required (in concert with a determination of aquo and hydroxo exchange rates in these materials) in order to understand this step more definitively. Analogous catalyst films based on Ni [14–16] and Mn [12, 13] have also been developed. These systems are also highly promising OECs under slightly alkaline (Ni) and acidic (Mn) conditions. The lessons learned from the CoP_i system offers encouragement that new reaction pathways and redox tuning may be realized by the self-assembly of mixed-metal films with a rationally controlled mesostructure.

References

1. Yang Z, Zhang J, Kintner-Meyer MCW et al (2011) Chem Rev 111:3577–3613
2. Cook TR, Dogutan DK, Reece SY, Surendranath Y, Teets TS, Nocera DG (2010) Chem Rev 110:6474
3. Lewis NS, Nocera DG (2006) PNAS 103:15729
4. Grimes CA, Varghese OK, Ranjan S (2008) Light, water, hydrogen: the solar generation of hydrogen by water photoelectrolysis. Springer, New York
5. Lewis NS (2007) Science 315:798
6. Turner JA (1999) Science 285:687
7. Pijpers JJH, Winkler MT, Surendranath Y, Buonassisi T, Nocera DG (2011) Proc Natl Acad Sci USA 108:10056
8. Reece SY, Hamel JA, Sung K, Jarvi TD, Esswein AJ, Pijpers JJH, Nocera DG (2011) Science 334:645
9. Torella JP, Gagliardi CJ, Chen JS, Bediako DK, Colón B, Way JC, Silver PA, Nocera DG (2015) Proc Natl Acad Sci USA 112:2337
10. Nocera DG (2009) Inorg Chem 48:10001
11. Nocera DG (2009) ChemSusChem 2:387
12. Huynh M, Bediako DK, Nocera DG (2014) J Am Chem Soc 136:6002

13. Huynh M, Bediako DK, Liu Y, Nocera DG (2014) J Phys Chem C 118:17142
14. Dincă M, Surendranath Y, Nocera DG (2010) Proc Natl Acad Sci USA 107:10337
15. Bediako DK, Lassalle-Kaiser B, Surendranath Y, Yano J, Yachandra VK, Nocera DG (2012) J Am Chem Soc 134:6801
16. Bediako DK, Surendranath Y, Nocera DG (2013) J Am Chem Soc 135:3662
17. Gerken JB, Chen JYC, Massé RC, Powell AB, Stahl SS (2012) Angew Chem Int Ed 51:6676
18. Gerken JB, Shaner SE, Massé RC, Porubsky NJ, Stahl SS (2014) Energy Environ Sci 7:2376
19. Suntivich J, Gasteiger HA, Yabuuchi N, Nakanishi H, Goodenough HB, Shao-Horn Y (2011) Nat Chem 3:546
20. Li X, Walsh FC, Pletcher D (2011) Phys Chem Chem Phys 13:1162
21. Suntivich J, Gasteiger HA, Yabuuchi N, Nakanishi H, Goodenough HB, Shao-Horn Y (2011) Science 334:1383
22. Trotochaud L, Ranney JK, Williams KN, Boettcher SW (2012) J Am Chem Soc 134:17253
23. Subbaraman R, Tripkovic D, Chang K-C, Strmcnik D, Paulikas AP, Hirunsit P, Chan M, Greeley J, Stamenkovic V, Markovic NM (2012) Nature Mat 11:550
24. Smith RDL, Prévot MS, Fagan RD, Zhang Z, Sedach PA, Siu MKJ, Trudel S, Berlinguette CP (2013) Science 340:60
25. Louie MW, Bell AT (2013) J Am Chem Soc 135:12329
26. McCrory CCL, Jung S, Peters JC, Jaramillo TF (2013) J Am Chem Soc 135:16977
27. Lu Z, Wang H, Kong D, Yan K, Hsu P-C, Zheng G, Yao H, Liang Z, Sun X, Cui Y (2014) Nature Commun 5:4345
28. Trotochaud L, Young SL, Ranney JK, Boettcher SW (2014) J Am Chem Soc 136:6744
29. Hunter BM, Blakemore JD, Deimund M, Gray HB, Winkler JR, Müller AM (2014) J Am Chem Soc 136:13118
30. Li C, Han X, Cheng F, Hu Y, Chen C, Chen J (2015) Nature Commun 6:7365
31. Friebel D, Louie MW, Bajdich M, Sanwald KE, Cai Y, Wise AM, Cheng M-J, Sokaras D, Weng T-C, Alonso-Mori R, Davis RC, Barger JR, Nørskov JK, Nilsson A, Bell AT (2015) J Am Chem Soc 137:1305
32. Zakaria MB, Hu M, Pramanik M, Li C, Tang J, Aldalbani A, Alshehri SM, Malgras V, Yamauchi Y (2015) Chem Asian J. doi:10.1002/asia.201500245
33. Du J, Chen C, Cheng F, Chen J (2015) Inorg Chem 54:5467
34. Gong M, Dai H (2014) Nano Res 8:239
35. Kanan MW, Nocera DG (2008) Science 321:1072
36. Kanan MW, Surendranath Y, Nocera DG (2009) Chem Soc Rev 38:109
37. Surendranath Y, Dinca M, Nocera DG (2009) J Am Chem Soc 131:2615
38. Suzuki O, Takahashi M, Fukunaga T, Kuboyama J (1968) US Pat 3 399 966
39. Shafirovich VY, Strelets VV (1978) Nouv J Chim 2:199
40. Esswein AJ, Surendranath Y, Reece SY, Nocera DG (2011) Energy Environ Sci 4:499
41. Liu Y, Nocera DG (2014) J Phys Chem C 118:17060
42. Surendranath Y, Nocera DG (2011) Prog Inorg Chem 57:505
43. Risch M, Khare V, Zaharieva I, Gerencser L, Chernev P, Dau H (2009) J Am Chem Soc 131:6936
44. Kanan MW, Yano J, Surendranath Y, Dincă M, Yachandra VK, Nocera DG (2010) J Am Chem Soc 132:13692
45. Risch M, Klingan K, Ringleb F, Chernev P, Zaharieva I, Fischer A, Dau H (2012) ChemSusChem 5:542
46. Egami T, Billinge SJL (2003) Underneath the Bragg-peaks: structural analysis of complex materials. Plenum, Oxford
47. Billinge SJL, Kanatzidis MG (2004) Chem Commun 2004:749
48. Du P, Kokhan O, Chapman KW, Chupas PJ, Tiede DM (2012) J Am Chem Soc 134:11096
49. Farrow CL, Bediako DK, Surendranath Y, Nocera DG, Billinge SJL (2013) J Am Chem Soc 135:6403

50. Bianconi A (1988) In: Koningsberger DC, Prins R (eds) X-Ray absorption: principles, applications, techniques of EXAFS, SEXAFS and XANES. Wiley, New York, pp 573–662
51. Brunschwig BS, Chou MH, Creutz C, Ghosh P, Sutin N (1983) J Am Chem Soc 105:4832
52. Sisley MJ, Jordan RB (2006) Inorg Chem 45:10758
53. Surendranath Y, Lutterman DA, Liu Y, Nocera DG (2012) J Am Chem Soc 134:6326
54. Chivot J, Mendoza L, Mansour C, Pauporte T, Cassir M (2008) Corrosion Sci 50:62
55. Strobel P, Muguerra H, Hebert S, Pachoud E, Colin C, Julien M (2009) J Sol State Chem 182:1872
56. McAlpin JG, Surendranath Y, Dincă M, Stich TA, Stoian SA, Casey WH, Nocera DG, Britt RD (2010) J Am Chem Soc 132:6882
57. Gerken JB, McAlpin JG, Chen JYC, Rigsby ML, Casey WH, Britt RD, Stahl SS (2011) J Am Chem Soc 133:14431
58. McAlpin JG, Stich TA, Ohlin CA, Surendranath Y, Nocera DG, Casey WH, Britt RD (2011) J Am Chem Soc 133:15444
59. Surendranath Y, Kanan MW, Nocera DG (2010) J Am Chem Soc 132:16501
60. Gileadi E (1993) Electrode kinetics for chemists, chemical engineers, and materials scientists. Wiley-VCH, New York, pp 127–184
61. Lyons MEG, Brandon MP (2008) Int J Electrochem Sci 3:1425
62. MacDonald JJ, Conway BE (1962) Proc R Soc Lond 269:419
63. Damjanovic A, Jovanovic B (1976) J Electrochem Soc 123:374
64. Trasatti S (1994) In: Ross PN, Lipkowski J (eds) Electrochemistry of novel materials. VCH, New York, Chap 5
65. Daghetti A, Lodi G, Trasatti S (1983) Mater Chem Phys 8:1
66. Wang L-P, Van Voorhis T (2011) J Phys Chem Lett 2:2200
67. Bediako DK, Costentin C, Jones EC, Nocera DG, Savéant J-M (2013) J Am Chem Soc 135:10492
68. Cukier RI, Nocera DG (1998) Annu Rev Phys Chem 49:337
69. Hammes-Schiffer S (2010) Chem Rev 110:6937
70. Savéant J-M (2012) Energy Environ Sci 5:7718
71. Mayer JM (2004) Annu Rev Phys Chem 55:363
72. Huynh MHV, Meyer TJ (2007) Chem Rev 107:5004
73. Costentin C (2008) Chem Rev 108:2145
74. Hammarström L, Styring S (2008) Phil Trans R Soc B 363:1283
75. Reece SY, Nocera DG (2009) Annu Rev Biochem 78:763
76. Hammes-Schiffer S (2009) Acc Chem Res 42:1881
77. Savéant J-M (1991) J Electroanal Chem 302:91
78. Chidsey CED, Feldman BJ, Lundgren C, Murray RW (1986) Anal Chem 58:601
79. Ofer D, Crooks RM, Wrighton MS (1990) J Am Chem Soc 112:7869
80. Jurss JW, Concepcion JC, Norris MR, Templeton JL, Meyer TJ (2010) Inorg Chem 49:3980
81. Chen Z, Concepcion JJ, Hull JF, Hoertz PG, Meyer TJ (2010) Dalton Trans 39:6950
82. May KJ, Carlton CE, Stoerzinger KA, Risch M, Suntivich J, Lee Y-L, Grimaud A, Shao-Horn Y (2012) J Phys Chem Lett 49:3980
83. González-Flores D, Sánchez I, Zaharieva I, Klingan K, Heidkamp J, Chernev P, Menezes PW, Driess M, Dau H, Montero ML (2015) Angew Chem Int Ed 54:2472
84. Scharifker B, Hills G (1983) Electrochim Acta 28:879
85. Bard AJ, Faulkner LR (2001) Electrochemical methods: fundamentals and applications. Wiley, New York, Chap 5
86. Zheng M, West AC (2004) J Electrochem Soc 151:C502
87. Kempa TJ, Bediako DK, Jones EC, Lieber CM, Nocera DG (2015) J Am Chem Soc 137:3739
88. Kempa TJ, Bediako DK, Kim SK, Park HG, Nocera DG (2015) Proc Natl Acad Sci USA 112:5309
89. Lutterman DA, Surendranath Y, Nocera DG (2009) J Am Chem Soc 131:3838
90. Gerken JB, Landis EC, Hamers RJ, Stahl SS (2010) ChemSusChem 3:1176

91. Stracke JJ, Finke RG (2011) J Am Chem Soc 133:14872
92. Limburg B, Bouwman E, Bonnet S (2012) Coord Chem Rev 256:1451
93. Hong D, Jung J, Park J, Yamada Y, Suenobu T, Lee Y-M, Nam W, Fukuzumi S (2012) Energy Environ Sci 5:7606
94. Crabtree RH (2012) Chem Rev 112:1536
95. Chakrabarty R, Bora SJ, Das BK (2007) Inorg Chem 46:9450
96. Chakrabarty R, Sarmah P, Saha B et al (2009) Inorg Chem 48:6371
97. Dimitrou K, Folting K, Streib WE, Christou G (1993) J Am Chem Soc 115:6432
98. Dimitrou K, Brown AD, Folting K, Christou G (1999) Inorg Chem 38:1834
99. Dimitrou K, Brown AD, Christou G et al (2001) Chem Comm 2001:1284
100. Ama T, Okamoto K, Yonemura T et al (1997) Chem Lett 26:1189
101. McCool NS, Robinson DM, Sheats JE, Dismukes GC (2011) J Am Chem Soc 133:11446
102. Berardi S, La Ganga G, Natali M et al (2012) J Am Chem Soc 134:11104
103. Zhang B, Li F, Yu F, Wang X, Zhou X, Li H, Jiang Y, Sun L (2014) ACS Catal 4:804
104. Ullman AM, Liu Y, Huynh M, Bediako DK, Wang H, Anderson BL, Powers DC, Breen JJ, Abruña HD, Nocera DG (2014) J Am Chem Soc 136:17681
105. Symes MD, Surendranath Y, Lutterman DA, Nocera DG (2011) J Am Chem Soc 133:5174
106. Macartney DH, Sutin N (1985) Inorg Chem 24:3403
107. Endicott JF, Durham B, Kumar K (1982) Inorg Chem 21:2437
108. Habib HS, Hunt JP (1966) J Am Chem Soc 88:1668
109. Marcus RA, Sutin N (1985) Biochim Biophys Acta 811:265
110. Ullman AM, Nocera DG (2013) J Am Chem Soc 135:15053
111. Zhou Y-L, Zeng M-H, Wei L-Q et al (2010) Chem Mater 22:4295
112. Murrie M (2010) Chem Soc Rev 39:1986

Hydrogen Bonding **Hot Paper**

International Edition: DOI: 10.1002/anie.201508060
German Edition: DOI: 10.1002/ange.201508060

Activation of Electron-Deficient Quinones through Hydrogen-Bond-Donor-Coupled Electron Transfer

Amanda K. Turek, David J. Hardee, Andrew M. Ullman, Daniel G. Nocera, and Eric N. Jacobsen**

Abstract: *Quinones are important organic oxidants in a variety of synthetic and biological contexts, and they are susceptible to activation towards electron transfer through hydrogen bonding. Whereas this effect of hydrogen bond donors (HBDs) has been observed for Lewis basic, weakly oxidizing quinones, comparable activation is not readily achieved when more reactive and synthetically useful electron-deficient quinones are used. We have successfully employed HBD-coupled electron transfer as a strategy to activate electron-deficient quinones. A systematic investigation of HBDs has led to the discovery that certain dicationic HBDs have an exceptionally large effect on the rate and thermodynamics of electron transfer. We further demonstrate that these HBDs can be used as catalysts in a quinone-mediated model synthetic transformation.*

Hydrogen bonding influences the rates and product distributions of many organic reactions of interest through direct stabilization of transition structures and reactive intermediates.[1,2] In a largely different context, H-bonding is also known to have a significant effect on the thermodynamics and kinetics of electron transfer,[3–13] especially in biological systems. Quinones are especially important cofactors that play critical roles in electron transfer (ET) pathways, including those of photosystem II.[14,15] In this system, a quinone serves as the terminal electron acceptor in a chain of ET events. Hydrogen bonds formed within the quinone binding site play a critical role in stabilizing the semiquinone radical anion after ET,[16] governing a conformational shift[17] that is proposed to constitute the rate-determining step for the first ET to the quinone.[18]

With the knowledge that the behavior of quinones is strongly influenced by H-bonding interactions, we became interested in employing small-molecule hydrogen-bond donors (HBDs) to activate quinone oxidants in a synthetically interesting context. The effect of H-bonding on the redox chemistry of quinones has been investigated in synthetic model systems using a variety of HBDs, including simple alcohols,[3,4] ammonium salts,[5] amino acids,[6] amides,[7,8] and neutral dual HBDs such as ureas[9,10] and thioureas.[11] Whereas these important studies revealed that HBDs can indeed couple with ET to enhance the reactivity of quinone oxidants, this effect was only observed with weakly oxidizing quinones that are good Lewis bases. In contrast, the HBDs used in these studies had little discernible effect on the ET to quinones bearing electron-withdrawing substituents (Figure 1), which increase their oxidizing ability but diminish their Lewis basicity and binding ability.

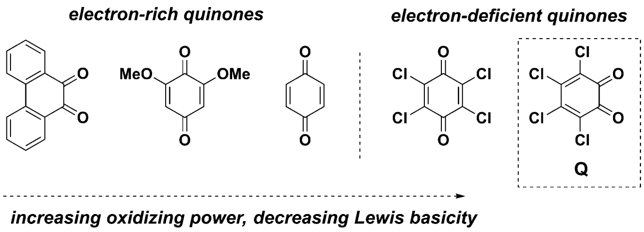

Figure 1. Effect of quinone structure on oxidizing ability and Lewis basicity.

From a thermodynamic standpoint, HBD-coupled ET using quinone oxidants [Eq. (1)] can be parsed into two elementary steps: ET between the quinone (**Q**) and an electron donor [**D**, Eq. (2)], and binding of the reduced quinone to an HBD [Eq. (3)]. Althoughthe actual transformation does not necessarily proceed by this mechanism (e.g., binding of the HBD to **Q** may precede ET), dissection of the overall process in this manner is instructive in defining the challenge that is presented to achieving favorable ET reactions ($\Delta G_{\text{net}} < 0$) using HBDs.

$$\text{HBD} + \mathbf{Q} + \mathbf{D} \rightleftharpoons \text{HBD} \cdot \mathbf{Q}^{\bullet -} + \mathbf{D}^{\bullet +}\ (\Delta G_{\text{net}}) \tag{1}$$

$$\mathbf{Q} + \mathbf{D} \rightleftharpoons \mathbf{Q}^{\bullet -} + \mathbf{D}^{\bullet +}\ (\Delta G_{\text{ET}}) \tag{2}$$

$$\text{HBD} + \mathbf{Q}^{\bullet -} \rightleftharpoons \text{HBD} \cdot \mathbf{Q}^{\bullet -}\ (\Delta G_{\text{assoc}}) \tag{3}$$

$$\Delta G_{\text{net}} = \Delta G_{\text{ET}} + \Delta G_{\text{assoc}}$$

The activating effect of an HBD on the overall reaction can be understood in terms of Eq. (3), which describes the binding of the HBD to the reduced quinone ($\mathbf{Q}^{\bullet -}$). That interaction must offset the thermodynamic penalty of the ET (given a $\Delta G_{\text{ET}} > 0$), which depends on the substrate **D** and the intrinsic oxidizing ability of the quinone. The oxidation of organic functional groups of interest (e.g., alkenes, aromatic rings) by electron-rich quinones is so unfavorable that an unattainably high binding energy (ΔG_{assoc}) would be necessary to enable the overall reaction with HBDs. ET in

---

[*] A. K. Turek, Dr. D. J. Hardee, A. M. Ullman, Prof. D. G. Nocera, Prof. E. N. Jacobsen
Department of Chemistry and Chemical Biology, Harvard University
Cambridge, MA 02138 (USA)
E-mail: dnocera@fas.harvard.edu
jacobsen@chemistry.harvard.edu

Supporting information for this article is available on the WWW under http://dx.doi.org/10.1002/anie.201508060.

synthetically interesting contexts with electron-deficient quinones is less unfavorable.[19] However, as noted above, these quinones and their reduced counterparts are inherently weak H-bond acceptors. As such, the success of the proposed HBD-coupled ET strategy relies on finding the appropriate balance between HBD strength and quinone reactivity.

Herein, we report a systematic evaluation of several small-molecule hydrogen-bond donors, with the goal of activating electron-deficient quinones (Figure 2). *ortho*-Chloranil (**Q**) was selected as the oxidant as it is an electron-deficient quinone that nonetheless lacks the intrinsic reactivity necessary to oxidize many organic substrates of synthetic interest. Our examination of the influence of H-bonding on the single-electron transfer chemistry of *ortho*-chloranil has led to the discovery that dicationic bis(amidinium) salts can exert a remarkable influence on the thermodynamics and kinetics of ET. By taking advantage of this effect, we demonstrate that these HBDs can also catalyze a model oxidative transformation that is mediated by *ortho*-chloranil.

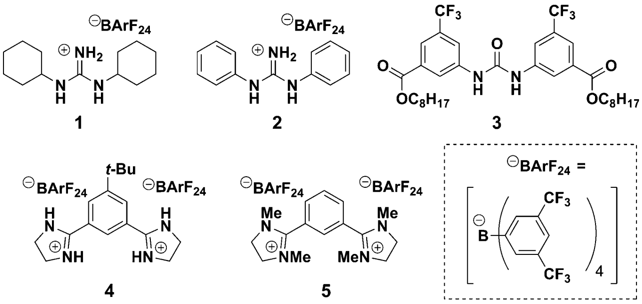

Figure 2. HBDs and additives examined in this study.

In aprotic media, quinones undergo two sequential single-electron transfers, proceeding via the semiquinone radical anion $\mathbf{Q}^{\bullet-}$.[20] Protic and H-bonding molecules influence the mechanism by which ET proceeds. This study is concerned primarily with the effect of HBDs on the first ET step. To quantify the ability of an HBD to modulate the thermodynamics of ET, the association of the HBD with $\mathbf{Q}^{\bullet-}$ must be quantified; in other terms, we need to determine how strongly the HBD favors the reduced state over the oxidized, neutral state.

The mechanistic methods used to quantify HBD-coupled ET are borrowed from the study of proton-coupled ET.[21] Eq. (4), which is related to the Nernst equation, describes HBD-coupled ET (Scheme 1 a). The apparent potential of a quinone involved in HBD-coupled ET will undergo a shift ($\Delta E_{1/2}$) that is dependent on the HBD concentration and the association constants for the binding of the quinone and semiquinone (K_Q and $K_{Q^{\bullet-}}$, respectively) to the HBD.

$$\Delta E_{1/2} = 0.059 V \log \frac{1 + K_{Q^{\bullet-}}[\mathrm{HBD}]}{1 + K_Q[\mathrm{HBD}]} \tag{4}$$

This relationship between $\Delta E_{1/2}$ and the association constants shows that as long as $K'_{Q^{\bullet-}} > K'_Q$, increasing the concentration of the HBD results in a more positive $\Delta E_{1/2}$, effectively creating a more potent oxidant by favoring the reduced state through binding. As illustrated by the square scheme in Scheme 1 a, $K'_{Q^{\bullet-}}$ specifically describes this stabilizing interaction. The equilibrium constants that govern this shift in the potential can be elucidated electrochemically through cyclic voltammetry and provide a quantitative measure of the stabilization provided by the HBD to $\mathbf{Q}^{\bullet-}$.

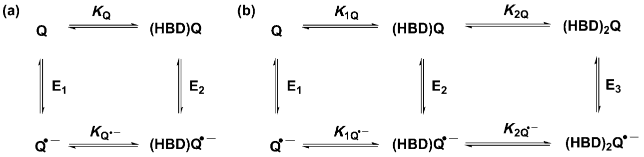

Scheme 1. a) Square scheme describing pathways for HBD-coupled ET to quinones and their associated equilibrium constants. b) Extended square scheme accounting for two binding events.

Our investigations were carried out with a range of HBDs, including the representative dual HBDs **1**–**3**, with the aim of understanding how H-bonding interactions affect $\Delta G_{\mathrm{assoc}}$ [Eq. (3)] when electron-deficient quinones are used. Electrochemical titrations of **Q** were performed with each HBD, using cyclic voltammetry to record the $\Delta E_{1/2}$ value as a function of HBD concentration (Figure 3 a–c). Each of the HBDs studied has a significant, measurable effect on the apparent potential that corresponds to the first ET.[22] Furthermore, the reversibility of the CVs recorded in all titration experiments indicate that the effect on $E_{1/2}$ is the result of H-bonding to $\mathbf{Q}^{\bullet-}$ and not protonation, which would manifest as irreversibility in the CV traces.

To elucidate the equilibrium constants that describe the binding of $\mathbf{Q}^{\bullet-}$ to **1**–**3**, the full set of electrochemical data for these titrations was subjected to simulations.[23] This analysis revealed that the experimental data are best described by a mechanism in which two HBD molecules are involved in the stabilization of $\mathbf{Q}^{\bullet-}$. This mechanistic interpretation provides a good fit to the experimental data with respect to the overall $\Delta E_{1/2}$ values, and also reproduces the distinct features of the cyclic voltammogram at low HBD concentrations (e.g., Figure 3 a, scan (——) and corresponding simulation (-----)).[24]

An HBD-coupled ET to **Q** that involves two binding events requires the use of an expanded square scheme to outline all mechanistic possibilities (Scheme 1 b), wherein $K_{1Q^{\bullet-}} K_{2Q^{\bullet-}}$ provides a quantitative description of the stabilization provided to $\mathbf{Q}^{\bullet-}$ through binding, and a measure of the oxidizing strength of **Q** in the presence of a given HBD.

The electrochemical simulations allow us to distinguish between the pathways for HBD-coupled ET outlined in Figure 1 d and to determine the binding constants associated with each individual step. The simulations for **1**–**3** reveal that these HBDs all promote a mechanism in which binding of the neutral quinone (K_{1Q}) precedes ET (E_2), and a second binding event follows ($K_{2Q^{\bullet-}}$).[25] A simulation of this mechanism explicitly determines values for these equilibrium constants, from which $K_{1Q^{\bullet-}}$ can be calculated. Independent determination of K_{1Q} using spectroscopic methods resulted in values that were consistent with those obtained from the simulations (Supporting Information, Figures S1–S4).

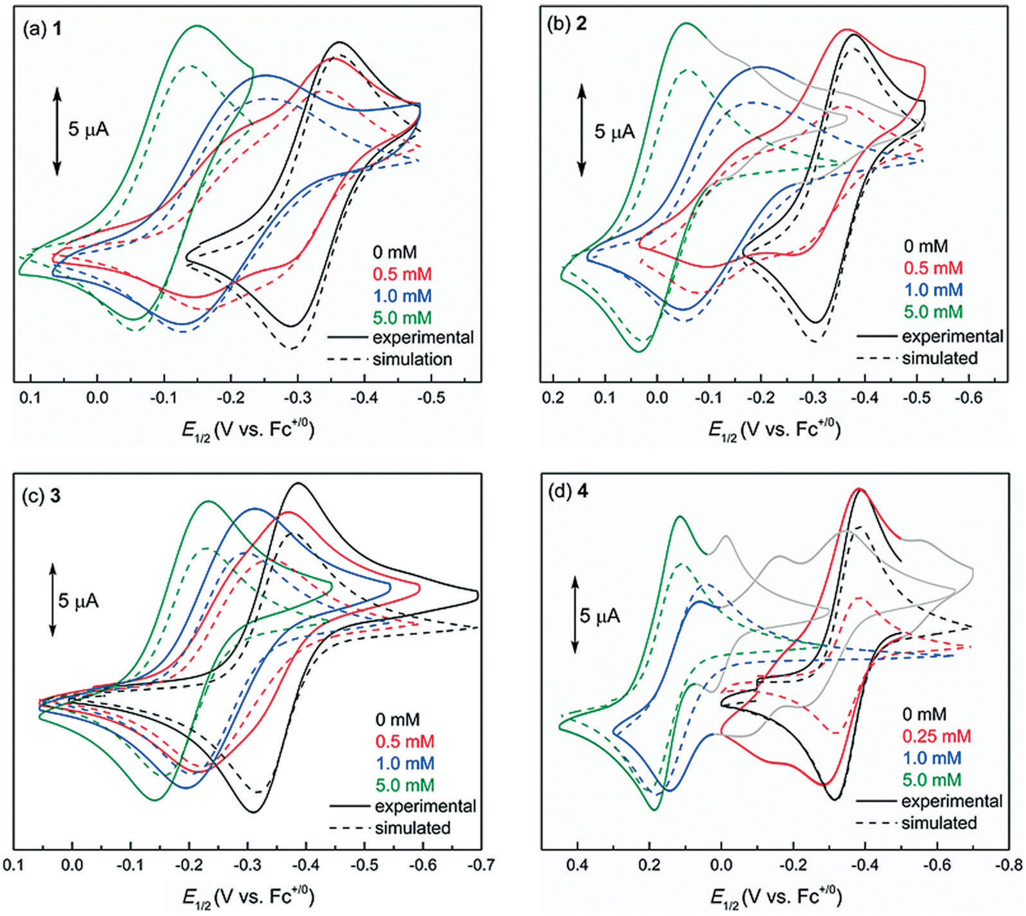

Figure 3. Experimental CV data and comparison with simulation. CVs ($0.1\ \mathrm{V\,s^{-1}}$) recorded for 0.5 mM **Q** in 0.1 M $n\mathrm{Bu_4NBArF_{24}/CH_2Cl_2}$ (glovebox) in the presence of increasing concentrations of a) **1**, b) **2**, c) **3**, and d) **4**.

The values for $K_{1\mathrm{Q}^{\bullet-}}K_{2\mathrm{Q}^{\bullet-}}$ were thus determined for the HBDs **1**–**3** (Table 1). All three HBDs afforded similar results with respect to mechanism and stoichiometry (Figure 3 b,c). Diphenylguanidinium **2** offers the greatest degree of stabilization to $\mathbf{Q}^{\bullet-}$, and urea **3** offers the weakest, with a difference of three orders of magnitude between them. A comparison of these values provides insight into the ways in which the nature of the HBD can influence its interaction with $\mathbf{Q}^{\bullet-}$. The enhanced binding of **2** relative to **1** can be ascribed to a difference in acidity.[26] Such an effect implicates hydrogen-bonding interactions in the modulation of $\Delta G_{\mathrm{assoc}}$ and increased favorability of ET to **2**. On the other hand, neutral **3** and cationic **1** have similar $\mathrm{p}K_{\mathrm{a}}$ values,[27] yet $K_{1\mathrm{Q}^{\bullet-}}K_{2\mathrm{Q}^{\bullet-}}$ for **3** is smaller by one order of magnitude, demonstrating the importance of electrostatic effects in HBD-coupled ET. Combined with the required 2:1 stoichiometry between the HBD and $\mathbf{Q}^{\bullet-}$, this result has important implications for the HBD-coupled ET strategy, as the data from the titration with **2** clearly indicate that the most substantial stabilization of $\mathbf{Q}^{\bullet-}$ is achieved in a complex that involves two cationic HBDs. We conclude that both H-bonding and electrostatic effects play a crucial role in HBD-coupled ET.

Table 1: Equilibrium constants for HBD-coupled ET determined by CV.[a]

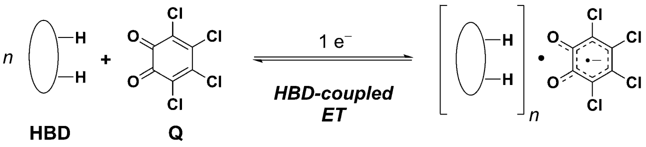

HBD[a]	$K_{1\mathrm{Q}^{\bullet-}}$ [$\mathrm{M^{-1}}$][b]	$K_{1\mathrm{Q}^{\bullet-}}K_{2\mathrm{Q}^{\bullet-}}$ [$\mathrm{M^{-2}}$]
1	(3.4×10^{4})	6.1×10^{8}
2	(3.5×10^{5})	1.8×10^{10}
3	(5.6×10^{4})	1.0×10^{7}
4	9.2×10^{10}	–
5	5.7×10^{5}	–

[a] Parameters were determined by titrating 0.5 mM **Q** in 0.1 M $n\mathrm{Bu_4NBArF_{24}/CH_2Cl_2}$ (glovebox) with [HBD] and simulating the experimental CVs obtained. [b] Values for $K_{1\mathrm{Q}^{\bullet-}}$ in parentheses are thermodynamically redundant and were calculated from E_1, E_2, and $K_{1\mathrm{Q}}$.

The observation that the HBDs **1**–**3** all bind $\mathbf{Q}^{\bullet-}$ in 2:1 complexes, with the charge of the HBD playing a critical role, prompted us to examine bis(amidinium) salt **4**,[28] which features a covalent linkage between two cationic subunits (Figure 3 d). Reversible waves are obtained for the cyclovoltammetry of **Q** in the presence of **4**, indicating that the $\mathbf{4}\cdot\mathbf{Q}^{\bullet-}$ complex is stable under the experimental conditions and does not experience full proton transfer. Simulations reproduce the overall $\Delta E_{1/2}$ value and the observed reversibility over the course of the titration. A mechanism involving a single binding step ($K_{1\mathrm{Q}}$) with subsequent ET (E_2) was found to best describe the experimental data.[29]

As noted above, these simulations revealed that bis(amidinium) salt **4** binds $\mathbf{Q}^{\bullet-}$ as a 1:1 complex, in contrast with HBDs **1**–**3**, which form 2:1 complexes with $\mathbf{Q}^{\bullet-}$. Because of this change in stoichiometry, the efficacy of the different HBDs in promoting ET to **Q** was gauged by comparing the value of $K_{\mathrm{Q}^{\bullet-}}$ for **4** to that of $K_{1\mathrm{Q}^{\bullet-}}K_{2\mathrm{Q}^{\bullet-}}$ for **1**–**3**. This analysis reveals that **4** is exceptionally effective at promoting ET and six orders of magnitude more potent than **2** at binding $\mathbf{Q}^{\bullet-}$.

Tetramethylated bis(amidinium) salt **5**, which bears the same net charge as **4** but lacks the ability to form H-bonds, has a substantially smaller $K_{1\mathrm{Q}^{\bullet-}}$ value than **4**. The large difference in the potencies of **4** and **5** shows that the pronounced effect of **4** in promoting HBD-coupled ET is not purely electrostatic in nature. Instead, both the dual charge and the H-bonding capability underlie the ability of **4** to modulate the thermodynamics of ET to **Q**. Furthermore, the CVs recorded with **5** are best simulated by a pathway in which ET (E_1) precedes association ($K_{1Q^{\bullet -}}$; Figure S5). This change in mechanism establishes that H-bonding is necessary for pre-association between **Q** and the HBD, and thereby dictates the pathway by which HBD-coupled ET occurs.

Having established that dicationic HBDs can exert a strong influence on the thermodynamics of ET to an electron-deficient quinone through tight binding of $\mathbf{Q}^{\bullet -}$, we investigated whether HBDs can similarly affect the kinetics of ET. This was addressed by measuring the rate of ET between **Q** and ferrocene (Fc) derivatives in the presence of HBDs to generate HBD·$\mathbf{Q}^{\bullet -}$ Fc^+ salts stoichiometrically (Table 2). The reactions were monitored by UV/Vis spectrophotometry under homogeneous conditions. The rate constants were obtained under pseudo-first-order conditions, varying the concentration of excess HBD. As the HBDs were found to span a broad range of reactivity, multiple reductants with a range of reduction potentials were required for this study. Two reductants were studied with each HBD, and the relative rates were scaled according to the intrinsic reactivity differences of those reductants.

Bis(amidinium) salt **4** is found to provide remarkable acceleration of the rate of ET, with a relative rate constant that is twelve orders of magnitude larger than that for urea **3** (Table 2). A comparison of the relative rate constants with the corresponding equilibrium constants revealed a good correlation between the thermodynamics and kinetics of ET, demonstrating the ability of these HBDs to thoroughly influence the energetics of ET.

Table 2: Relative rate constants for HBD-coupled ET.[a]

HBD	K_{rel} [s^{-1}] Fc	k_{rel} [s^{-1}] BrFc	k_{rel} [s^{-1}] $\mathrm{Br_2Fc}$	k_{rel} [s^{-1}]	$K_{1Q^{\bullet -}}$ [M^{-1}]	$K_{1Q^{\bullet -}}\,K_{2Q^{\bullet -}}$ [M^{2}]
3	1	–	–	1	5.6×10^{4}	1.0×10^{7}
1	486	1	–	4.9×10^{2}	3.4×10^{4}	6.1×10^{8}
2	–	124	1	2.3×10^{7}	3.5×10^{5}	1.8×10^{10}
4	–	–	104	9.0×10^{11}	9.2×10^{10}	–

[a] Pseudo-first-order rate constants were determined at 25 °C by monitoring the reaction between **Q** (2.5 mM) and the indicated ferrocene (0.5 mM) in $\mathrm{CH_2Cl_2}$ in the presence of the indicated HBD (5.0 mM).

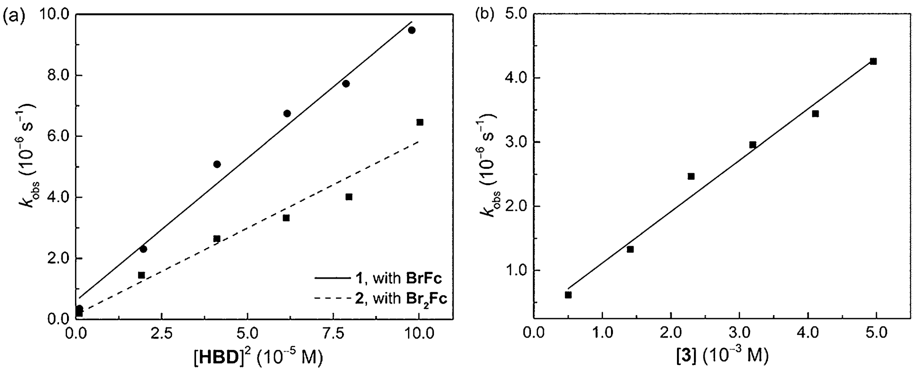

Figure 4. Initial rate constants (k_{obs}) vs. $[\mathrm{HBD}]^2$ or [HBD] for ET from ferrocene derivatives to **Q** in $\mathrm{CH_2Cl_2}$ at 25 °C under $\mathrm{N_2}$ atmosphere. a) Second-order plots for **1** (10–1.0 mM), **Q** (1.0 mM), and bromoferrocene (BrFc; 1.0 mM); and **2** (10–1.0 mM), **Q** (1.0 mM), and 1,1′-dibromoferrocene ($\mathrm{Br_2Fc}$; 1.0 mM). b) First-order plot for **3** (5.0–0.5 mM), **Q** (0.5 mM), and 1,1′-dimethylferrocene ($\mathrm{Me_2Fc}$; 0.5 mM).

To further probe the mechanism of HBD-coupled ET and provide independent verification for the stoichiometries ascertained electrochemically, the reaction order with respect to each HBD was determined. The ET reaction obeys a second-order kinetic dependence on both guanidinium salts **1** and **2** (Figure 4a), which is consistent with the contention that two cationic HBDs act cooperatively to stabilize $\mathbf{Q}^{\bullet -}$. ET promoted by urea **3**, in contrast, was found to follow a first-order dependence on HBD (Figure 4b). This result may still be consistent with the formation of a 2:1 complex between **3** and $\mathbf{Q}^{\bullet -}$, as a rate-determining ET step may precede complexation by the second urea molecule. The kinetic order in **4** was not accurately quantified owing to the extremely high reactivity observed with this HBD. However, a Job plot obtained with excess reductant clearly shows that the reaction stoichiometry between **4** and **Q** is 1:1 (Figure S6), thereby corroborating the electrochemical thermodynamic studies.

Examining the free energy differences associated with these homogenous ETs offers a different perspective on the effectiveness of **4** as a promoter of HBD-coupled ET. ET between 1,1′-dibromoferrocene and **Q** is highly unfavorable in the absence of an HBD ($\Delta G_{\mathrm{ET}} = +15.3\ \mathrm{kcal\,mol^{-1}}$).[30] Yet **4** modulates the kinetics and thermodynamics of this inherently disfavored process such that it proceeds rapidly. In comparison, DDQ, a more powerful oxidant than **Q** that finds widespread use in organic synthesis, lacks the intrinsic reactivity to perform this ET reaction independently ($\Delta G_{\mathrm{ET}} = +4.4$ kcal $\mathrm{mol^{-1}}$).[31] The ability of **4** to participate in HBD-coupled ET was examined further with additional electron donors, and it was found to facilitate oxidation of perylene in a yet more unfavorable process ($\Delta G_{ET} = +19.8$ kcal mol^{-1};[32] Figure S7).

Having identified HBDs capable of promoting ET to electron-deficient quinones, we sought to probe their possible utility as catalysts for synthetic reactions involving ET. An oxidative lactonization was selected as a model transformation that would illustrate the catalytic use of HBDs to promote quinone-mediated ET (Scheme 2a). The HBDs **1–4** were evaluated, and the conversions observed after a reaction time of 24 hours are found to correlate well with both the thermodynamic and kinetic trends discussed previously. Bis(amidinium) salt **4** is the most effective catalyst, affording the product in 70% yield, whereas urea **3** provides no acceleration over background. The bis(amidinium) salt **6**, which lacks the *tert*-butyl substituent of **4**, is even more reactive, affording the lactonization product in nearly quantitative yield. This difference in reactivity may be ascribed to an inductive deactivating effect of the *tert*-butyl substituent of **4**.[33]

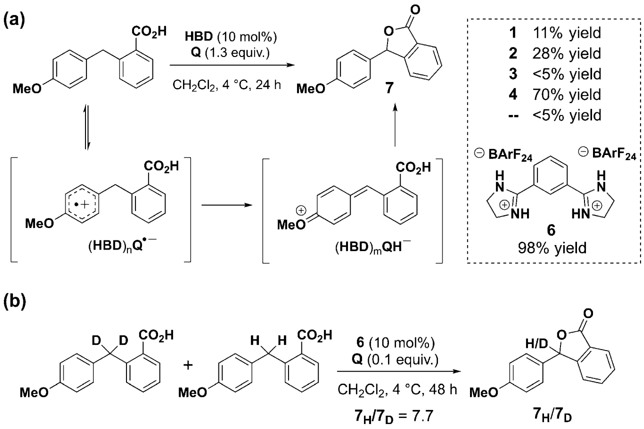

Scheme 2. a) Proposed oxidative lactonization mechanism and yields obtained at 24 hours. b) Kinetic isotope effect experiment.

A large KIE was measured for the lactonization ($k_H/k_D = 7.7$ with **6**), and points to rate-limiting cleavage of the benzylic C−H bond. This finding can be reconciled with rapid and reversible single-electron transfer preceding a subsequent, rate-limiting H-atom abstraction (Scheme 2b), although a direct hydride abstraction mechanism cannot be ruled out unambiguously.[34] Nonetheless, the strong correlation between the effect of different HBDs on the thermodynamics and kinetics of ET to **Q** and on the reaction rate of the lactonization is consistent with a mechanism in which the HBD affects a pre-equilibrium ET by binding **Q** and remains associated with $\mathbf{Q}^{\bullet-}$ throughout the H-atom transfer.

As demonstrated in the electrochemical and kinetic studies described above, HBD-coupled ET can be applied as an effective strategy to activate electron-deficient quinones. The application of **4** and **6** as catalysts in a model organic transformation further shows that this strategy has potential in synthetically useful contexts. The results obtained from this mechanistic study with simple dual hydrogen-bond donors highlight the promise of dicationic scaffolds as catalysts for promoting ET. The evidence that association of the HBD occurs prior to ET demonstrates the potential of this strategy for application in enantioselective processes, wherein binding to the chiral catalyst prior to generation of reactive intermediates would be expected to be crucial. We anticipate that the findings outlined here will help guide the discovery of new catalysts that are capable of promoting highly efficient and selective ET reactions mediated by quinone oxidants.

Acknowledgements

This work was supported by the NIH (GM043214 to E.N.J.) and the DOE (DE-SC0009565 to D.G.N.), by an NSF predoctoral fellowship to A.K.T., and by an NIH post-doctoral fellowship to D.J.H. We thank Robert Knowles for many helpful discussions.

Keywords: catalysis · electron transfer · hydrogen bonding · oxidation · quinones

How to cite: *Angew. Chem. Int. Ed.* **2016**, *55*, 539–544
Angew. Chem. **2016**, *128*, 549–554

---

[1] M. S. Taylor, E. N. Jacobsen, *Angew. Chem. Int. Ed.* **2006**, *45*, 1520–1543; *Angew. Chem.* **2006**, *118*, 1550–1573.
[2] R. R. Knowles, E. N. Jacobsen, *Proc. Natl. Acad. Sci. USA* **2010**, *107*, 20678–20685.
[3] N. Gupta, H. Linschitz, *J. Am. Chem. Soc.* **1997**, *119*, 6384–6391.
[4] N. A. Macías-Ruvalcaba, I. González, M. Aguilar-Martínez, *J. Electrochem. Soc.* **2004**, *151*, E110–E118.
[5] K. Okamoto, K. Ohkubo, K. M. Kadish, S. Fukuzumi, *J. Phys. Chem. A* **2004**, *108*, 10405–10413.
[6] J. Yuasa, S. Yamada, S. Fukuzumi, *J. Am. Chem. Soc.* **2008**, *130*, 5808–5820.
[7] S. Fukuzumi, H. Kitaguchi, T. Suenobu, S. Ogo, *Chem. Commun.* **2002**, 1984–1985.
[8] M. Gómez, C. Z. Gómez-Castro, I. I. Padilla-Martínez, F. J. Martínez-Martínez, F. J. González, *J. Electroanal. Chem.* **2004**, *567*, 269–276.
[9] Y. Ge, R. R. Lilienthal, D. K. Smith, *J. Am. Chem. Soc.* **1996**, *118*, 3976–3977.
[10] Y. Ge, L. Miller, T. Ouimet, D. K. Smith, *J. Org. Chem.* **2000**, *65*, 8831–8838.
[11] M. D. Greaves, A. Niemz, V. M. Rotello, *J. Am. Chem. Soc.* **1999**, *121*, 266–267.
[12] L. A. Clare, A. T. Pham, F. Magdaleno, J. Acosta, J. E. Woods, A. L. Cooksy, D. K. Smith, *J. Am. Chem. Soc.* **2013**, *135*, 18930–18941.
[13] E. A. Mader, J. M. Mayer, *Inorg. Chem.* **2010**, *49*, 3685–3687.
[14] K. N. Ferreira, T. M. Iverson, K. Maghlaoui, J. Barber, S. Iwata, *Science* **2004**, *303*, 1831–1838.
[15] M. S. Graige, M. L. Paddock, J. M. Bruce, G. Feher, M. Y. Okamura, *J. Am. Chem. Soc.* **1996**, *118*, 9005–9016.
[16] A. T. Taguchi, P. J. O'Malley, C. A. Wraight, S. A. Dikanov, *J. Phys. Chem. B* **2015**, *119*, 5805–5814.
[17] M. H. B. Stowell, T. M. McPhilliips, D. C. Rees, S. M. Soltis, E. Abresch, G. Feher, *Science* **1997**, *276*, 812–816.
[18] M. S. Graige, G. Feher, M. Y. Okamura, *Proc. Natl. Acad. Sci. USA* **1998**, *95*, 11679–11684.
[19] H.-D. Becker, A. B. Turner in *The Chemistry of the Quinonoid Compounds, Vol. II* (Eds.: S. Patai, Z. Rappoport), Wiley, New York, **1988**, pp. 1352–1384.

[20] J. Q. Chambers in *The Chemistry of the Quinonoid Compounds, Vol. II* (Eds.: S. Patai, Z. Rappoport), Wiley, New York, **1988**, pp. 719–757.

[21] C. Costentin, *Chem. Rev.* **2008**, *108*, 2145–2179.

[22] A large effect on the second ET was also observed with **2** and **4** (see the Supporting Information for a discussion).

[23] M. Rudolph, *J. Electroanal. Chem.* **2003**, *543*, 23–39; DigiElch from Elchsoft under http://www.elchsoft.com.

[24] Discrepancies in the current magnitude may be attributed to variations in the diffusion coefficients across the range of species involved in the simulation, which have no bearing on $\Delta E_{1/2}$ (see the Supporting Information for a discussion).

[25] Efforts to simulate alternative mechanisms are described in the Supporting Information.

[26] The pK_a values in DMSO for *N,N'*-dialkylguanidinium ions and **2** are 14.1 and 10.1, respectively; see: C. H. Uyeda, *Catalysis of the Claisen Rearrangement by Hydrogen Bond Donors*, Ph.D. Thesis, Harvard University, Cambridge, MA **2010**.

[27] The pK_a value of **3** is 13.8 in DMSO; see: F. Jakab, C. Tancon, Z. Zhang, K. M. Lippert, P. R. Schreiner, *Org. Lett.* **2012**, *14*, 1724–1727.

[28] V. R. Annamalai, E. C. Linton, M. C. Kozlowski, *Org. Lett.* **2009**, *11*, 621–624.

[29] The current that appears at 0.1 V in scan (c) is not reproduced by this mechanism. This extra current has been observed in cyclic voltammograms of quinones, and has been attributed to the formation of oxides on the glassy carbon electrode surface; see: a) P. A. Staley, C. M. Newell, D. P. Pullman, D. K. Smith, *Anal. Chem.* **2014**, *86*, 10917–10924; mechanisms that involve the formation of quinone dimers, which have been observed with some *ortho*-quinones containing electron-withdrawing groups, may also play a role in the appearance of this extra current; see: b) N. A. Macías-Ruvalcaba, D. H. Evans, *J. Phys. Chem. C* **2010**, *114*, 1285–1292.

[30] T. Daeneke, A. J. Mozer, Y. Uemura, S. Makuta, M. Fekete, Y. Tachibana, N. Koumura, U. Bach, L. Spiccia, *J. Am. Chem. Soc.* **2012**, *134*, 16925–16928.

[31] N. G. Connelly, W. E. Geiger, *Chem. Rev.* **1996**, *96*, 877–910.

[32] X. Cui, A. Charaf-Eddin, J. Wang, B. Le Guennic, J. Zhao, D. Jacquemin, *J. Org. Chem.* **2014**, *79*, 2038–2048.

[33] A rigorous comparison of the abilities of **4** and **6** to promote ET was not possible because of the very low solubility of **6** in dichloromethane.

[34] X. Guo, H. Zipse, H. Mayr, *J. Am. Chem. Soc.* **2014**, *136*, 13863–13873.

Received: August 27, 2015
Revised: October 23, 2015